Introduction Dredging Engineering

OE4607

Miedema, Sape

Publication date
2015

Document Version
Final published version

Citation (APA)
Miedema, S. (2015). *Introduction Dredging Engineering: OE4607*. (1 ed.) SA Miedema / Delft University of Technology.

OE4607 Introduction Dredging Engineering.
MSc Offshore & Dredging Engineering
Delft University of Technology

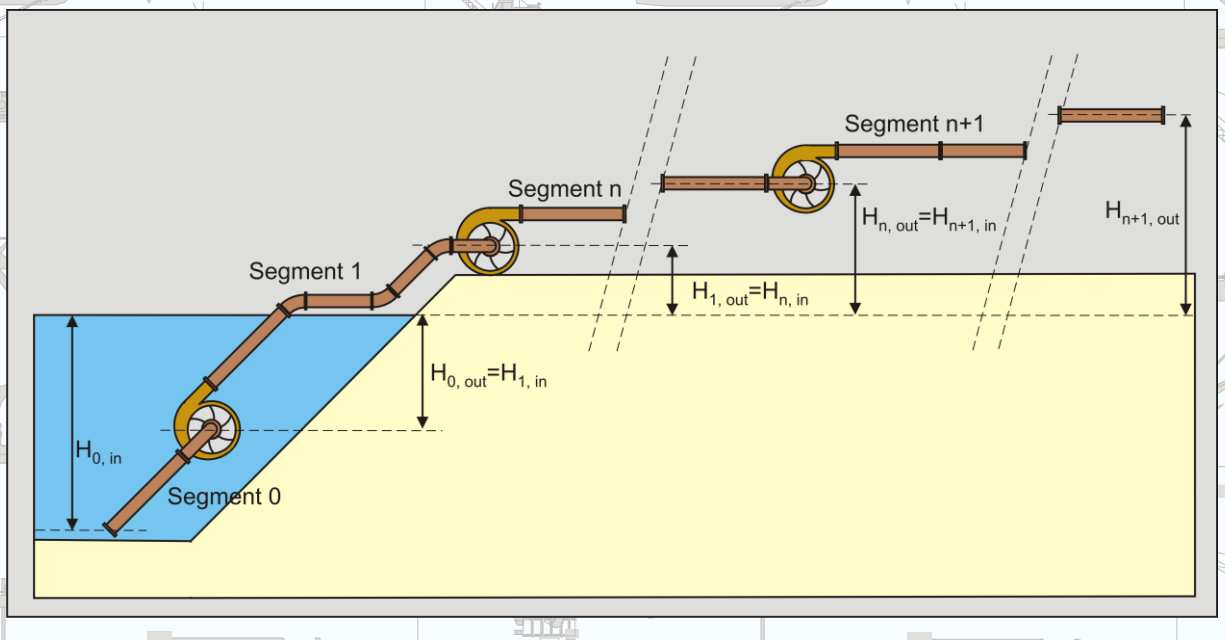

by
Dr.ir. Sape A. Miedema

Preface

In dredging, trenching, (deep sea) mining, drilling, tunnel boring and many other applications, sand, clay or rock has to be excavated. The productions (and thus the dimensions) of the excavating equipment range from mm^3/sec - cm^3/sec to m^3/sec. In oil drilling layers with a thickness of a magnitude of 0.2 mm are cut, while in dredging this can be of a magnitude of 0.1 m with cutter suction dredges and meters for clamshells and backhoe's. Some equipment is designed for dry soil, while others operate under water saturated conditions. Installed cutting powers may range up to 10 MW. For both the design, the operation and production estimation of the excavating equipment it is important to be able to predict the cutting forces and powers. After the soil has been excavated it is usually transported hydraulically as a slurry over a short (TSHD's) or a long distance (CSD's) or mechanically. Estimating the pressure losses and determining whether or not a bed will occur in the pipeline is of great importance. Fundamental processes of sedimentation, initiation of motion and erosion of the soil particles determine the transport process and the flow regimes. In TSHD's the soil has to settle during the loading process, where also sedimentation and erosion will be in equilibrium. In all cases we have to deal with soil and high density soil water mixtures and its fundamental behavior.

The lecture notes are complemented with the book The Delft Sand, Clay & Rock Cutting Model, by Dr.ir. Sape A. Miedema and available at www.iospress.nl.

Additional information can be found on www.delftdredging.com, www.dredgingengineering.com, www.dhlldv.com and www.dscrcm.com.

Targets/Goals of OE4607.

1. What is dredging (projects and equipment)?
2. What are the important dredging processes?
3. The working methods of a CSD and a TSHD.
4. Which dredging processes can be identified related to a CSD and TSHD?
    a. CSD.
    b. TSHD.
5. Basic Soil Mechanics (OE4624-15 for advanced theory).
    a. Which soil mechanical properties are involved?
    b. Failure criteria.
    c. Soil mechanical tests.
    d. Mohr circles, active and passive soil failure.
6. Basic saturated sand cutting theory (OE4626 for advanced theory and OE4627 for jetting).
    a. The forces involved.
    b. The generic force and moment equilibrium equations.
    c. Dilatation in saturated sand.
    d. Simplified cutting equations.
    e. Simplified specific energy equations.
    f. The terminal settling velocity (including hindered settling).
7. The terminal setting velocity.
    a. The force equilibrium and theoretical equation.
    b. The drag coefficient.
    c. Practical equations.
8. Volume, volume flow, concentration and density relations.
9. Basic pumps and slurry transport (OE4625 for advanced theory).
    a. Flow (Q)-Head (H) curves.
    b. Darcy Weisbach and ELM for pure liquid.
    c. The Dacry Weisbach friction factor.
    d. The DHLLDV Framework, Jufin Lopatin and Wilson for mixture.
    e. The Limit Deposit Velocity.
10. Basic hopper sedimentation and overflow losses (OE4627 for advanced theory).
    a. The TSHD loading cycle.
    b. The optimum loading time.
    c. The Camp theory.
    d. The settling efficiency.
    e. Overflow losses.
11. Case study CSD, showing the relation between the different processes.
12. Case study TSHD, showing the relation between the different processes.

Book ISBN: 978-94-6186-536-6
EBook ISBN: 978-94-61864-57-4
DOI: 10.13140/RG.2.1.2643.2488

Version: Tuesday, October 13, 2015

About the Author.

Dr.ir. Sape A. Miedema (November 8th 1955) obtained his M.Sc. degree in Mechanical Engineering with honours at the Delft University of Technology (DUT) in 1983. He obtained his Ph.D. degree on research into the basics of soil cutting in relation with ship motions, in 1987. From 1987 to 1992 he was Assistant Professor at the chair of Dredging Technology. In 1992 and 1993 he was a member of the management board of Mechanical Engineering & Marine Technology of the DUT. In 1992 he became Associate Professor at the DUT with the chair of Dredging Technology. From 1996 to 2001 he was appointed Head of Studies of Mechanical Engineering and Marine Technology at the DUT, but still remaining Associate Professor of Dredging Engineering. In 2005 he was appointed Head of Studies of the MSc program of Offshore & Dredging Engineering and he is also still Associate Professor of Dredging Engineering. In 2013 he was also appointed as Head of Studies of the MSc program Marine Technology of the DUT.

Dr.ir. S.A. Miedema teaches (or has taught) courses on soil mechanics and soil cutting, pumps and slurry transport, hopper sedimentation and erosion, mechatronics, applied thermodynamics related to energy, drive system design principles, mooring systems, hydromechanics and mathematics. He is (or has been) also teaching at Hohai University, Changzhou, China, at Cantho University, Cantho Vietnam, at Petrovietnam University, Baria, Vietnam and different dredging companies in the Netherlands and the USA.
His research focuses on the mathematical modeling of dredging systems like, cutter suction dredges, hopper dredges, clamshell dredges, backhoe dredges and trenchers. The fundamental part of the research focuses on the cutting processes of sand, clay and rock, sedimentation processes in Trailing Suction Hopper Dredges and the associated erosion processes. Lately the research focuses on hyperbaric rock cutting in relation with deep sea mining and on hydraulic transport of solids/liquid settling slurries.

Table of Contents

Chapter 1: Basic Soil Mechanics.

1.1. Introduction.

Cutting processes of soil distinguish from the classical soil mechanics in civil engineering in the fact that:

Classical soil mechanics assume:
1. Small to very small strain rates.
2. Small to very small strains.
3. A very long time span, years to hundreds of years.
4. Structures are designed to last forever.

Cutting processes assume:
1. High to very high strain rates.
2. High to very high strains and deformations in general.
3. A very short time span, following from very high cutting velocities.
4. The soil is supposed to be excavated, the coherence has to be broken.

For the determination of cutting forces, power and specific energy the criterion for failure has to be known. In this book the failure criterion of Mohr-Coulomb will be applied in the mathematical models for the cutting of sand, clay and rock. The Mohr–Coulomb theory is named in honor of Charles-Augustin de Coulomb and Christian Otto Mohr. Coulomb's contribution was a 1773 essay entitled "*Essai sur une application des règles des maximis et minimis à quelques problèmes de statique relatifs à l'architecture*". Mohr developed a generalized form of the theory around the end of the 19th century. To understand and work with the Mohr-Coulomb failure criterion it is also necessary to understand the so called Mohr circle. The Mohr circle is a two dimensional graphical representation of the state of stress at a point. The abscissa, $\boldsymbol{\sigma}$, and ordinate, $\boldsymbol{\tau}$, of each point on the circle are the normal stress and shear stress components, respectively, acting on a particular cut plane under an angle $\boldsymbol{\alpha}$ with the horizontal. In other words, the circumference of the circle is the locus of points that represent the state of stress on individual planes at all their orientations. In this book a plane strain situation is considered, meaning a two-dimensional cutting process. The width of the blades considered $\mathbf{w}$ is always much bigger than the layer thickness $\mathbf{h_i}$ considered. In geomechanics (soil mechanics and rock mechanics) compressive stresses are considered positive and tensile stresses are considered to be negative, while in other engineering mechanics the tensile stresses are considered to be positive and the compressive stresses are considered to be negative. Here the geomechanics approach will be applied. There are two special stresses to be mentioned, the so called principal stresses. Principal stresses occur at the planes where the shear stress is zero. In the plane strain situation there are two principal stresses, which are always under an angle of 90° with each other.

In order to understand the cutting processes in sand, clay and rock, it is required to have knowledge of basic soil and rock mechanics. The next chapters 1.2-1.7 cover this knowledge and have been composed almost entirely from information from the public domain, especially internet. Most information comes from Wikipedia and Answers.com.

1.2. Soil Mechanics.

1.2.1. Definition.

McGraw-Hill Science & Technology Encyclopedia gives the following description of Soil Mechanics:
The study of the response of masses composed of soil, water, and air to imposed loads. Because both water and air are able to move through the soil pores, the discipline also involves the prediction of these transport processes. Soil mechanics provides the analytical tools required for foundation engineering, retaining wall design, highway and railway sub base design, tunneling, earth dam design, mine excavation design, and so on. Because the discipline relates to rock as well as soils, it is also known as geotechnical engineering. Soil consists of a multiphase aggregation of solid particles, water, and air.

This fundamental composition gives rise to unique engineering properties, and the description of the mechanical behavior of soils requires some of the most sophisticated principles of engineering mechanics. The terms multiphase and aggregation both imply unique properties. As a multiphase material, soil exhibits mechanical properties that show the combined attributes of solids, liquids, and gases. Individual soil particles behave as solids, and show relatively little deformation when subjected to either normal or shearing stresses. Water behaves as a liquid, exhibiting little deformation under normal stresses, but deforming greatly when subjected to shear. Being

a viscous liquid, however, water exhibits a shear strain rate that is proportional to the shearing stress. Air in the soil behaves as a gas, showing appreciable deformation under both normal and shear stresses. When the three phases are combined to form a soil mass, characteristics that are an outgrowth of the interaction of the phases are manifest. Moreover, the particulate nature of the solid particles contributes other unique attributes.

Figure 1-1: Earthwork in Germany (source Wikimedia).

When dry soil is subjected to a compressive normal stress, the volume decreases nonlinearly; that is, the more the soil is compressed, the less compressible the mass becomes. Thus, the more tightly packed the particulate mass becomes, the more it resists compression. The process, however, is only partially reversible, and when the compressive stress is removed the soil does not expand back to its initial state.

When this dry particulate mass is subjected to shear stress, an especially interesting behavior owing to the particulate nature of the soil solids results. If the soil is initially dense (tightly packed), the mass will expand because the particles must roll up and over each other in order for shear deformation to occur. Conversely, if the mass is initially loose, it will compress when subjected to a shear stress. Clearly, there must also exist a specific initial density (the critical density) at which the material will display zero volume change when subjected to shear stress. The term dilatancy has been applied to the relationship between shear stress and volume change in particulate materials. Soil is capable of resisting shear stress up to a certain maximum value. Beyond this value, however, the material undergoes large, uncontrolled shear deformation.

The other limiting case is saturated soil, that is, a soil whose voids are entirely filled with water. When such a mass is initially loose and is subjected to compressive normal stress, it tends to decrease in volume; however, in order for this volume decrease to occur, water must be squeezed from the soil pores. Because water exhibits a viscous resistance to flow in the microscopic pores of fine-grained soils, this process can require considerable time, during which the pore water is under increased pressure. This excess pore pressure is at a minimum near the drainage face of the soil mass and at a maximum near the center of the soil sample. It is this gradient (or change in pore water pressure with change in position within the soil mass) that causes the outflow of water and the corresponding decrease in volume of the soil mass. Conversely, if an initially dense soil mass is subjected to shear stress, it tends to expand. The expansion, however, may be time-dependent because of the viscous resistance to water being drawn into the soil pores. During this time the pore water will be under decreased pressure. Thus, in saturated soil masses, changes in pore water pressure and time-dependent volume change can be induced by either changes in normal stress or by changes in shear stress.

1.2.2. Soil Creation.

The primary mechanism of soil creation is the weathering of rock. All rock types (igneous rock, metamorphic rock and sedimentary rock) may be broken down into small particles to create soil. Weathering mechanisms are physical weathering, chemical weathering, and biological weathering. Human activities such as excavation, blasting, and waste disposal, may also create soil. Over geologic time, deeply buried soils may be altered by pressure and temperature to become metamorphic or sedimentary rock, and if melted and solidified again, they would complete the geologic cycle by becoming igneous rock.
Physical weathering includes temperature effects, freeze and thaw of water in cracks, rain, wind, impact and other mechanisms. Chemical weathering includes dissolution of matter composing a rock and composition of soils. Physical weathering includes temperature effects, freeze and thaw of water in cracks, rain, wind, impact and other mechanisms. Chemical weathering includes dissolution of matter composing a rock and precipitation in the form of another mineral. Clay minerals, for example can be formed by weathering of feldspar, which is the most common mineral present in igneous rock. The most common mineral constituent of silt and sand is quartz, also called silica, which has the chemical name silicon dioxide. The reason that feldspar is most common in rocks but silicon is more prevalent in soils is that feldspar is much more soluble than silica. Silt, Sand, and Gravel are basically little pieces of broken rocks. According to the Unified Soil Classification System, silt particle sizes are in the range of 0.002 mm to 0.075 mm and sand particles have sizes in the range of 0.075 mm to 4.75 mm. Gravel particles are broken pieces of rock in the size range 4.75 mm to 100 mm. Particles larger than gravel are called cobbles and boulders.

Figure 1-2: Fox glacier, New Zealand (source Wikimedia).

Soil deposits are affected by the mechanism of transport and deposition to their location. Soils that are not transported are called residual soils -- they exist at the same location as the rock from which they were generated. Decomposed granite is a common example of a residual soil. The common mechanisms of transport are the actions of gravity, ice, water, and wind. Wind-blown soils include dune sands and loess. Water carries particles of different size depending on the speed of the water, thus soils transported by water are graded according to their size. Silt and clay may settle out in a lake, and gravel and sand collect at the bottom of a river bed. Wind-blown soil deposits (aeolian soils) also tend to be sorted according to their grain size. Erosion at the base of glaciers is powerful enough

to pick up large rocks and boulders as well as soil; soils dropped by melting ice can be a well graded mixture of widely varying particle sizes. Gravity on its own may also carry particles down from the top of a mountain to make a pile of soil and boulders at the base; soil deposits transported by gravity are called colluvium.
The mechanism of transport also has a major effect on the particle shape. For example, low velocity grinding in a river bed will produce rounded particles. Freshly fractured colluvium particles often have a very angular shape.

1.2.3. Soil Classification.

Soil classification deals with the systematic categorization of soils based on distinguishing characteristics as well as criteria that dictate choices in use.

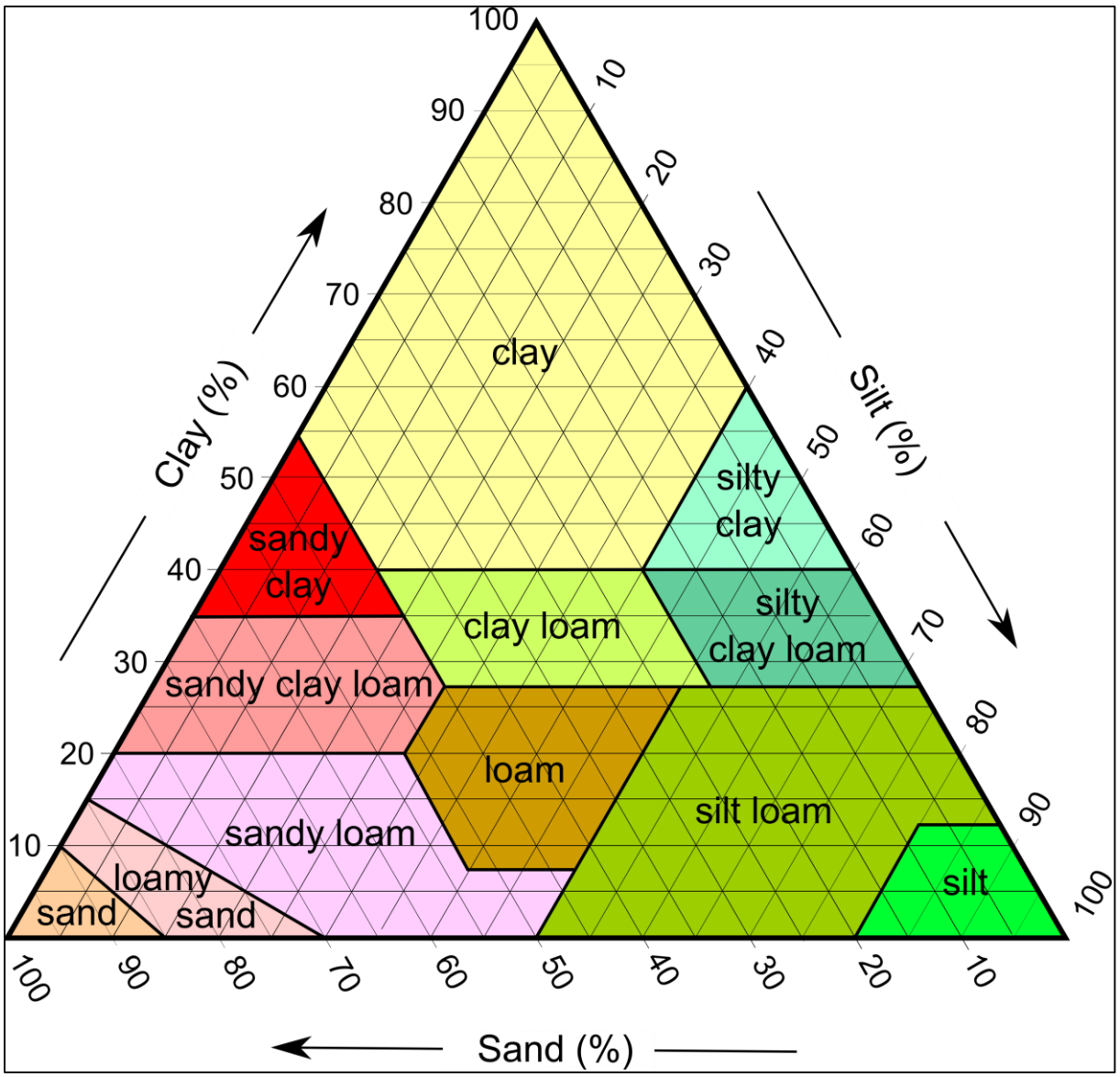

Figure 1-3: Soil naming according to USDA.

Soil texture is a qualitative classification tool used in both the field and laboratory to determine classes for agricultural soils based on their physical texture. The classes are distinguished in the field by the 'textural feel' which can be further clarified by separating the relative proportions of sand, silt and clay using grading sieves: The Particle Size Distribution (PSD). The class is then used to determine crop suitability and to approximate the soils responses to environmental and management conditions such as drought or calcium (lime) requirements. A qualitative rather than a quantitative tool it is a fast, simple and effective means to assess the soils physical characteristics. Although the U.S.D.A. system uses 12 classes whilst the U.K.-ADAS uses just 11 the systems are mutually compatible as shown in the combined soil textural triangle below.

Hand analysis, whilst an arbitrary technique, is an extremely simple and effective means to rapidly assess and classify a soils physical condition. Correctly executed the procedure allows for rapid and frequent assessment of soil characteristics with little or no equipment. It is thus an extremely useful tool for identifying spatial variation both within and between plots (fields) as well as identifying progressive changes and boundaries between soil classes and orders. The method involves taking a small sample of soil, sufficient to roll into a ball of approximately 2.5 cm diameter, from just below the surface. Using a small drop of water or 'spit' the sample is then moisten to the sticky point (the point at which it begins to adhere to the finger). The ball is then molded to determine its workability and its class according to the steps in the chart opposite.
Soil separates are specific ranges of particle sizes. In the United States, the smallest particles are clay particles and are classified by the USDA as having diameters of less than 0.002 mm. The next smallest particles are silt particles and have diameters between 0.002 mm and 0.05 mm. The largest particles are sand particles and are larger than 0.05 mm in diameter. Furthermore, large sand particles can be described as coarse, intermediate as medium, and the smaller as fine. Other countries have their own particle size classifications.

Table 1-1: Soil Classification.

Name of Soil	Diameter Limits (mm)
Clay	<0.002
Fine silt	0.002–0.006
Medium silt	0.006-0.020
Coarse silt	0.020-0.060
Very fine sand	0.060–0.100
Fine sand	0.100–0.200
Medium sand	0.200–0.600
Coarse sand	0.600–1.000
Very coarse sand	1.000–2.000
Fine gravel	2-6
Medium gravel	6-20
Coarse gravel	20-60
Cobbles	60-200
Boulders	>200

Figure 1-4: Soil failure (www.4isfge.org).

Figure 1-5: The Wenjiagou landslide (blogs.agu.org).

Figure 1-6: Karl von Terzaghi, one of the founders of modern soil mechanics.

1.3. Soils.

1.3.1. Sand.

Sand is any material composed of loose, stony grains between 1/16 mm and 2 mm in diameter. Larger particles are categorized as gravel; smaller particles are categorized as silt or clay. Sands are usually created by the breakdown of rocks, and are transported by wind and water, before depositing to form soils, beaches, dunes, and underwater fans or deltas. Deposits of sand are often cemented together over time to form sandstones.
The most common sand-forming process is weathering, especially of granite. Granite consists of distinct crystals of quartz, feldspar, and other minerals. When exposed to water, some of these minerals (e.g., feldspar) decay chemically faster than others (especially quartz), allowing the granite to crumble into fragments. Sand formed by weathering is termed epiclastic.

Figure 1-7: Sand from the Gobi desert, Mongolia (source Wikimedia).

Where fragmentation is rapid, granite crumbles before its feldspar has fully decayed and the resulting sand contains more feldspar. If fragmentation is slow, the resulting sand contains less feldspar. Fragmentation of rock is enhanced by exposure to fast-running water, so steep mountains are often source areas for feldspar-rich sands and gentler terrains are often source areas for feldspar-poor sands. Epiclastic sands and the sandstones formed from them thus record information about the environments that produce them. A sedimentologist can deduce the existence of whole mountain ranges long ago eroded, and of mountain-building episodes that occurred millions of years ago from sandstones rich in relatively unstable minerals like feldspar.
The behavior of sand carried by flowing water can inscribe even more detailed information about the environment in sand deposits. When water is flowing rapidly over a horizontal surface, any sudden vertical drop in that surface splits the current into two layers, (1) an upper layer that continues to flow downstream and (2) a slower backflow that curls under in the lee of the drop-off. Suspended sand tends to settle out in the backflow zone, building a slope called a "slip face" that tilts downhill from the drop-off. The backflow zone adds continually to the slip face, growing it downstream, and as the slip face grows downstream its top edge continues to create a backflow zone. The result is the deposition of a lengthening bed of sand. Typically, periodic avalanches of large grains down the slip face (or other processes) coat it with thin layers of distinctive material. These closely-spaced laminations are called "cross bedding" because they angle across the main bed. Cross-bedding in sandstone records the direction of the current that deposited the bed, enabling geologists to map currents that flowed millions of years ago (paleocurrents).
Evidence of grain size, bed thickness, and cross-bedding angle, allows geologists to determine how deep and fast a paleocurrent was, and thus how steep the land was over which it flowed.

Figure 1-8: Sand in the Sahara desert (source Luca Galuzzi – www.galuzzi.it)

Ripples and dunes—probably the most familiar forms created by wind- or waterborne sand—involve similar processes. However, ripples and dunes are more typical of flow systems to which little or no sand is being added. The downstream slip faces of ripples and dunes are built from grains plucked from their upstream sides, so these structures can migrate without growing. When water or wind entering the system (e.g., water descending rapidly from a mountainous region) imports large quantities of sand, the result is net deposition rather than the mere migration of sand forms.

Grain shape, too, records history. All epiclastic grains of sand start out angular and become more rounded as they are polished by abrasion during transport by wind or water. Quartz grains, however, resist wear. One trip down a river is not enough to thoroughly round an angular grain of quartz; even a long sojourn on a beach, where grains are repeatedly tumbled by waves, does not suffice. The well-rounded state of many quartz sands can be accounted for only by crustal recycling. Quartz grains can survive many cycles of erosion, burial and cementation into sandstone, uplift, and re-erosion. Recycling time is on the order of 200 million years, so a quartz grain first weathered from granite 2.4 billion years ago may have gone through 10 or 12 cycles of burial and re-erosion to reach its present day state. An individual quartz grain's degree of roundness is thus an index of its antiquity. Feldspar grains can also survive recycling, but not as well, so sand that has been recycled a few times consists mostly of quartz.

Sand can be formed not only by weathering but by explosive volcanism, the breaking up of shells by waves, the cementing into pellets of finer-grained materials (pelletization), and the precipitation of dissolved chemicals (e.g., calcium carbonate) from solution.

Pure quartz sands are mined to make glass and the extremely pure silicon employed in microchips and other electronic components.

1.3.2. Clay.

Clay is a fine-grained (small particle size) sedimentary rock. Clay is so fine-grained it is rarely possible to see the individual mineral particles with the naked eye. The definition of clays describes rocks with particle sizes of less than 4 μm in diameter. Most sedimentary rocks are described using both mineral content and particle size. While this is also true for clays, the particle size description is most reliable and most often used.

Figure 1-9: Quaternary clay in Estonia (source Wikimedia)

The majority of common types of minerals found in clays are kaolinite (a soapy-feeling and lightweight mineral), talc, pyrophyllite, all types of micas, minerals from the chlorite group, feldspars, and a lesser amount of tectosilicates (including quartz).
The mineral content of clays is less variable than other types of sedimentary rock. This is a direct result of the way clays are formed. Water carries the bulk of sediments to their resting place where they are cemented together. The transport of sediments is directly related to the force or velocity of water carrying them. The stronger the velocity of water, the larger and heavier the particle it can move. Conversely, the weaker the flow, the smaller the particle that is carried by the water. As a result, water acts as a winnowing filter for certain types of minerals. The heavier minerals are not carried as far by water currents as are the lighter ones. When water finally comes to rest, it deposits its load of minerals. The last to be released are the lighter and smaller particles, the clay minerals.
Where rivers meet oceans, the clay minerals are so light they are usually carried far out to sea where they fall gently to the bottom forming a fine-grained sediment. These deposits cover organic materials and trap them at the edges of deltas and continental slopes. Over millions of years, the organic materials convert to petroleum and remain trapped by the clays. This relationship makes the study of clays extremely important for petroleum geologists. In addition to this important economic consideration, clays provide important economic resources for a wide variety of other industries.

Depending on the academic source, there are three or four main groups of clays: kaolinite, montmorillonite, smectite, illite, and chlorite. Chlorites are not always considered a clay, sometimes being classified as a separate group within the phyllosilicates. There are approximately 30 different types of "pure" clays in these categories, but most "natural" clays are mixtures of these different types, along with other weathered minerals.

Varve (or varved clay) is clay with visible annual layers, formed by seasonal differences in erosion and organic content. This type of deposit is common in former glacial lakes. When glacial lakes are formed there is very little movement of the water that makes the lake, and these eroded soils settle on the lake bed. This allows such an even distribution on the different layers of clay.

Figure 1-10: Varved clay, Little River State Park, Waterbury, Vermont (source www.anr.state.vt.us).

Quick clay is a unique type of marine clay indigenous to the glaciated terrains of Norway, Canada, Northern Ireland, and Sweden. It is highly sensitive clay, prone to liquefaction, which has been involved in several deadly landslides.

Clays exhibit plasticity when mixed with water in certain proportions. When dry, clay becomes firm and when fired in a kiln, permanent physical and chemical changes occur. These reactions, among other changes, cause the clay to be converted into a ceramic material. Because of these properties, clay is used for making pottery items, both utilitarian and decorative. Different types of clay, when used with different minerals and firing conditions, are used to produce earthenware, stoneware, and porcelain. Prehistoric humans discovered the useful properties of clay, and one of the earliest artifacts ever uncovered is a drinking vessel made of sun-dried clay. Depending on the content of the soil, clay can appear in various colors, from a dull gray to a deep orange-red.

Clay tablets were used as the first known writing medium, inscribed with cuneiform script through the use of a blunt reed called a stylus.

Clays sintered in fire were the first form of ceramic. Bricks, cooking pots, art objects, dishware, and even musical instruments such as the ocarina can all be shaped from clay before being fired. Clay is also used in many industrial processes, such as paper making, cement production, and chemical filtering. Clay is also often used in the manufacture of pipes for smoking tobacco. Until the late 20th century bentonite clay was widely used as a mold binder in the manufacture of sand castings.

Clay, being relatively impermeable to water, is also used where natural seals are needed, such as in the cores of dams, or as a barrier in landfills against toxic seepage (lining the landfill, preferably in combination with geotextiles).

Recent studies have investigated clay's absorption capacities in various applications, such as the removal of heavy metals from waste water and air purification.

1.3.3. Rock.

To the geologist, the term rock means a naturally occurring aggregate of minerals that may include some organic solids (e.g., fossils) and/or glass. Rocks are generally subdivided into three large classes: igneous, sedimentary, and metamorphic. These classes relate to common origin, or genesis. Igneous rocks form from cooling liquid rock or related volcanic eruptive processes. Sedimentary rocks form from compaction and cementation of sediments. Metamorphic rocks develop due to solid-state, chemical and physical changes in pre-existing rock because of elevated temperature, pressure, or chemically active fluids.
With igneous rocks, the aggregate of minerals comprising these rocks forms upon cooling and crystallization of liquid rock. As crystals form in the liquid rock, they become interconnected to one another like jigsaw puzzle pieces. After total crystallization of the liquid, a hard, dense igneous rock is the result. Also, some volcanic lavas, when extruded on the surface and cooled instantaneously, will form a natural glass.

Figure 1-11: Sample of igneous gabbro, Rock Creek Canyon, California (source Wikimedia).

Glass is a mass of disordered atoms, which are frozen in place due to sudden cooling, and is not a crystalline material like a mineral. Glass composes part of many extrusive igneous rocks (e.g., lava flows) and pyroclastic igneous rocks. Alternatively, some igneous rocks are formed from volcanic processes, such as violent volcanic eruption. Violent eruptions eject molten, partially molten, and non-molten igneous rock, which then falls in the vicinity of the eruption. The fallen material may solidify into a hard mass, called pyroclastic igneous rock. The texture of igneous rocks (defined as the size of crystals in the rock) is strongly related to cooling rate of the original liquid. Rapid cooling of liquid rock promotes formation of small crystals, usually too small to see with the unaided eye. Rocks with this cooling history are called fine-textured igneous rocks. Slow cooling (which usually occurs deep underground) promotes formation of large crystals. Rocks with this cooling history are referred to as coarse-textured igneous rocks.
The mineral composition of igneous rocks falls roughly into four groups: silicic, intermediate, mafic, and ultramafic. These groups are distinguished by the amount of silica (SiO_4), iron (Fe), and magnesium (Mg) in the constituent minerals. Mineral composition of liquid rock is related to place of origin within the body of the earth. Generally speaking, liquids from greater depths within the earth contain more Fe and Mg and less SiO_4 than those from shallow depths.
In sedimentary rocks, the type of sediment that is compacted and cemented together determines the rock's main characteristics. Sedimentary rocks composed of sediment that has been broken into pieces (i.e., clastic sediment),

such as gravel, sand, silt, and clay, are clastic sedimentary rocks (e.g., conglomerate, sandstone, siltstone, and shale, respectively). Sedimentary rocks composed of sediment that is chemically derived (i.e., chemical sediment), such as dissolved elements like calcium (Ca), sodium (Na), iron (Fe), and silicon (Si), are chemical sedimentary rocks. Examples of chemical sedimentary rocks are limestone (composed of calcium carbonate), rock salt (composed of sodium chloride), rock gypsum (composed of calcium sulfate), ironstones (composed of iron oxides), and chert (composed of hydrated silica). Biochemical sedimentary rocks are a special kind of chemical sedimentary rock wherein the constituent particles were formed by organisms (typically as organic hard parts, such as shells), which then became sedimentary particles. Examples of this special kind of sedimentary rock include chalk, fossiliferous limestone, and coquina. Sedimentary rocks are formed from sediment in two stages: compaction and cementation. Compaction occurs when sediments pile up to sufficient thickness that overlying mass squeezes out water and closes much open space. Cementation occurs when water flowing through the compacted sediment deposits mineral crystals upon particles thus binding them together. The main cement minerals are calcite ($CaCO_3$), hematite (Fe_2O_3), and quartz (SiO_2).
With metamorphic rocks, the nature of the pre-existing rock (protolith) determines in large part the characteristics of the ultimate metamorphic rock. Regardless of protolith, however, almost all metamorphic rocks are harder and more dense than their protoliths. A protolith with flat or elongate mineral crystals (e.g., micas or amphiboles) will yield a metamorphic rock with preferentially aligned minerals (due to directed pressure). Such metamorphic rocks are called foliated metamorphic rocks (e.g., slate and schist). Non-foliated metamorphic rocks (e.g., marble and quartzite) come from protoliths that have mainly equidimensional mineral crystals (e.g., calcite and quartz, respectively). For example, a protolith shale will yield a foliated metamorphic rock, and a protolith limestone will yield marble, a non-foliated metamorphic rock. Metamorphic rocks possess distinctive grades or levels of metamorphic change from minimal to a maximum near total melting. Low-grade metamorphic rocks generally have fine-textured crystals and low-temperature indicator minerals like the mica chlorite. High-grade metamorphic rocks generally have coarse-textured crystals and very distinctive foliation, plus high-temperature indicator minerals like the silicate mineral staurolite.
Rock is a brittle natural solid found mainly in the outer reaches of Earth's crust and upper mantle. Material that would be brittle rock at such shallow depths becomes to one degree or another rather plastic within the body of the earth. The term "rock" is not generally applied to such non-brittle internal Earth materials. Therefore, rock is a concept related to the outer shell of the earth. The term rock may also be properly applied to brittle natural solids found on the surfaces of other planets and satellites in our solar system. Meteorites are rock. Naturally occurring ice (e.g., brittle water ice in a glacier, H_2O) is also a rock, although we do not normally think of ice this way.
Rock has been an important natural resource for people from early in human evolution. Rocks' properties are the key to their specific usefulness, now as in the past. Hard, dense rocks that could be chipped into implements and weapons were among the first useful possessions of people. Fine-textured and glassy rocks were particularly handy for these applications. Later on, rock as building stone and pavement material became very important, and this continues today in our modern world. All of Earth's natural mineral wealth, fossil energy resources, and most groundwater are contained within rocks of the earth's crust.

Rock is a natural occurrence mass of cohesive organic or inorganic material, which forms a part earth crest of which most rocks are composed of one or more minerals. Rocks can be classified in different ways. The most used classification is based on their origin, in which the following classes can be distinguished.
Igneous rock; a rock that has solidified from molten rock material (magma), which was generated within the Earth. Well known are granite and basalt
Sedimentary rock; a rock formed by the consolidation of sediment settle out in water, ice of air and accumulated on the Earth’s surface, either on dry land or under water. Examples are sandstone, lime stone and clay stone
Metamorphic rock; any class of rocks that are the result of partial or complete recrystallization in the solid state of pre-existing rocks under conditions of temperature and pressure that are significantly different from those obtaining at the surface of the Earth.
When deterring the dredge-ability of rock, distinction has to be made between the properties of intact rock and that of a rock mass. Depending on the fracture density of the rock the cutter will cut intact rock or break out rock blocks.
In the first case the strength (tensile- and compressive strength), deformation properties (E-value) and the petrography (mineralogical proposition) of the intact rock determines the production completely. The second case the fracture frequency and the weathering of the rock is more important than the strength of the intact rock. It is known that the absence of water in rock is important for the rock strength. When saturated with water the rock strength can be 30 to 90 % of the strength of dry rock. Therefore rock samples have to be sealed immediately after drilling in such a way that evaporation of or intake of water is avoided. It has to be mentioned that this does not mean that cutting forces in saturated rock are always lower than in dry rock. The petrography is important for the weir of rock cutting tools.

Figure 1-12: Sandstone formations, Vermillion Cliffs, Arizona (source www.reddit.com).

Figure 1-13: Columns of Basalt of the Scottish Island of Staffa (National Geographic).

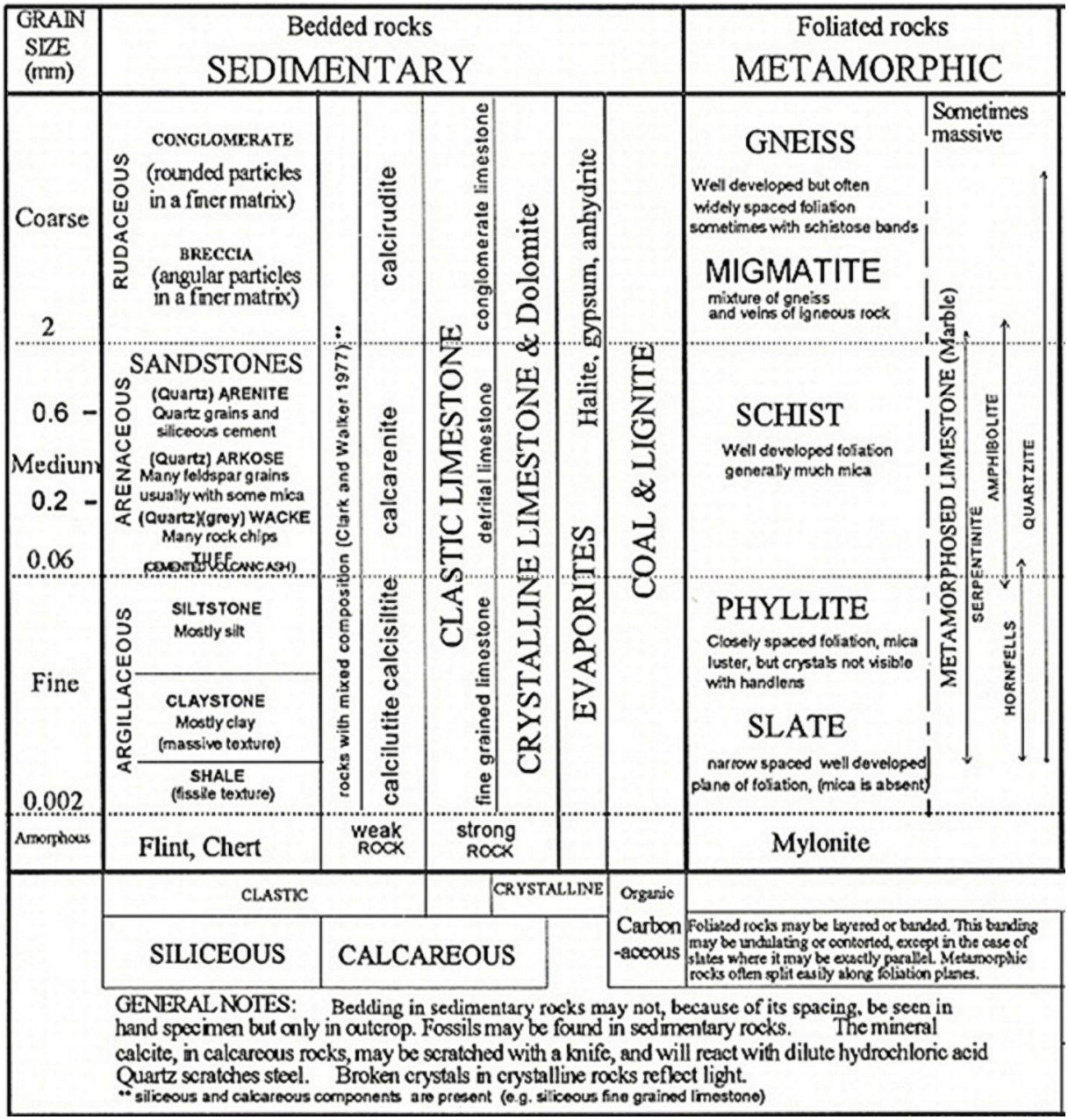

Figure 1-14 A: Aid to identification of rock for engineering purposes (After BS 5930:1981).

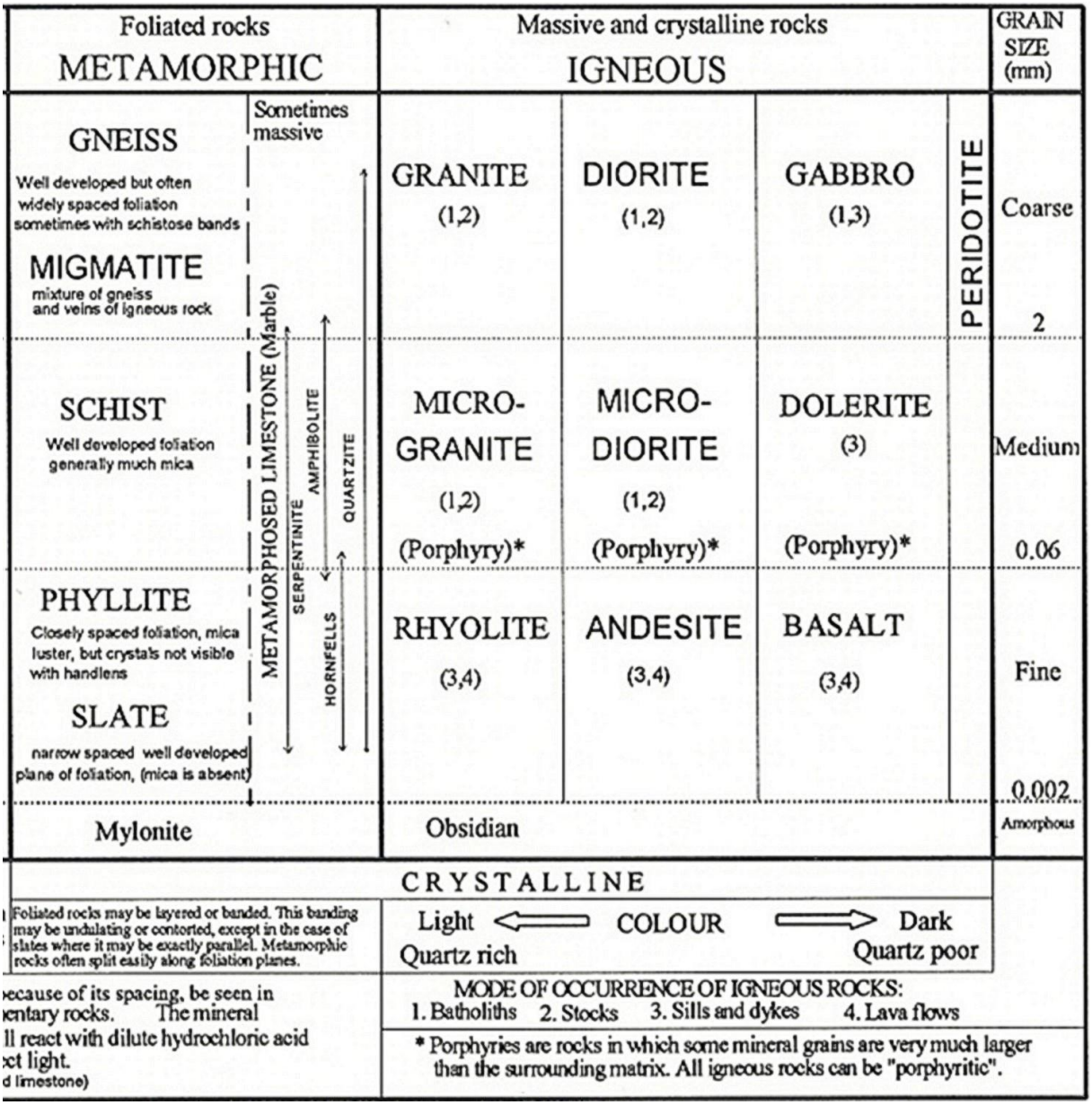

Figure 1-15 B: Aid to identification of rock for engineering purposes (After BS 5930:1981).

Figure 1-16: Utica Shale, Fort Plain, New York (Wikipedia).

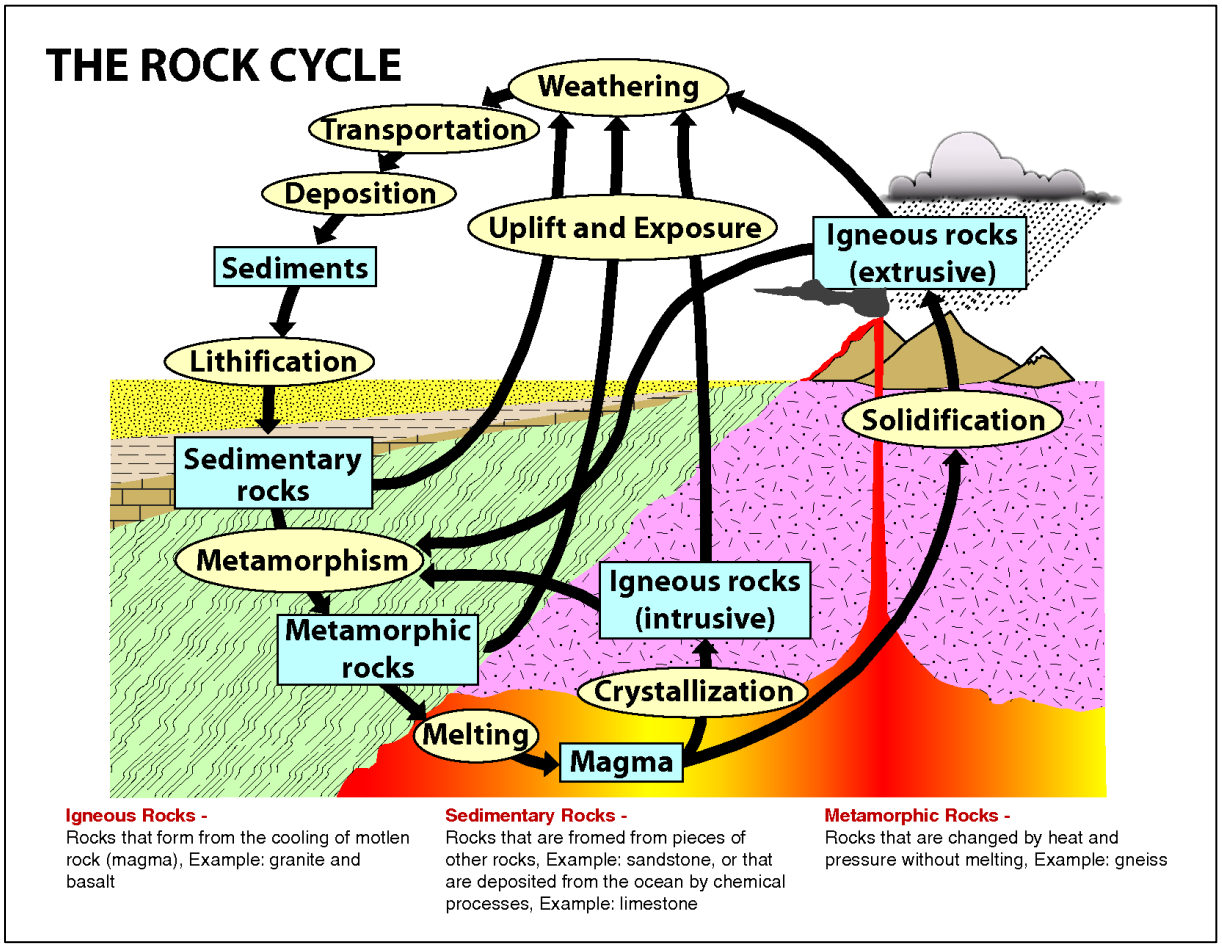

Figure 1-17: The rock formation cycle (galleryhip.com).

1.4. Soil Mechanical Parameters.

1.4.1. Grain Size Distribution/Particle Size Distribution.

Soils consist of a mixture of particles of different size, shape and mineralogy. Because the size of the particles obviously has a significant effect on the soil behavior, the grain size and grain size distribution are used to classify soils. The grain size distribution describes the relative proportions of particles of various sizes. The grain size is often visualized in a cumulative distribution graph which, for example, plots the percentage of particles finer than a given size as a function of size. The median grain size, d_{50}, is the size for which 50% of the particle mass consists of finer particles. Soil behavior, especially the hydraulic conductivity, tends to be dominated by the smaller particles; hence, the term "effective size", denoted by d_{10}, is defined as the size for which 10% of the particle mass consists of finer particles.
Sands and gravels that possess a wide range of particle sizes with a smooth distribution of particle sizes are called well graded soils. If the soil particles in a sample are predominantly in a relatively narrow range of sizes, the soil is called uniformly graded soils. If there are distinct gaps in the gradation curve, e.g., a mixture of gravel and fine sand, with no coarse sand, the soils may be called gap graded. Uniformly graded and gap graded soils are both considered to be poorly graded. There are many methods for measuring particle size distribution. The two traditional methods used in geotechnical engineering are sieve analysis and hydrometer analysis.

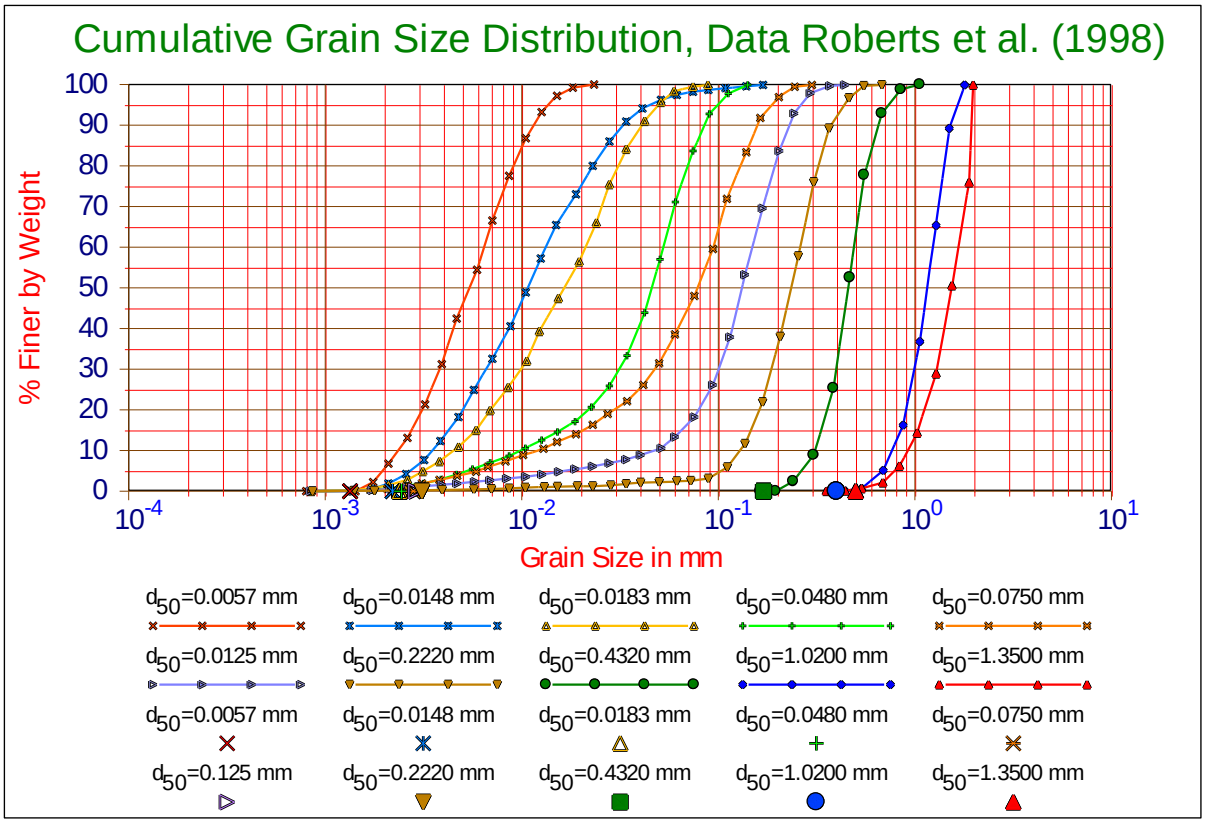

Figure 1-18: The particle size distributions of the sands used by Roberts et al. (1998).

1.4.2. Atterberg Limits.

The **Atterberg limits** are a basic measure of the nature of a fine-grained soil. Depending on the water content of the soil, it may appear in four states: solid, semi-solid, plastic and liquid. In each state the consistency and behavior of a soil is different and thus so are its engineering properties. Thus, the boundary between each state can be defined based on a change in the soil's behavior. The Atterberg limits can be used to distinguish between silt and clay, and it can distinguish between different types of silts and clays. These limits were created by Albert Atterberg, a Swedish chemist. They were later refined by Arthur Casagrande. These distinctions in soil are used in picking the soils to build structures on top of. These tests are mainly used on clayey or silty soils since these are the soils that expand and shrink due to moisture content. Clays and silts react with the water and thus change sizes and have varying shear strengths. Thus these tests are used widely in the preliminary stages of building any structure to

insure that the soil will have the correct amount of shear strength and not too much change in volume as it expands and shrinks with different moisture contents.

Figure 1-19: Liquid limit device.

Figure 1-20: Liquid limit device.

1.4.2.1. Shrinkage Limit.

The shrinkage limit (SL) is the water content where further loss of moisture will not result in any more volume reduction. The test to determine the shrinkage limit is ASTM International D4943. The shrinkage limit is much less commonly used than the liquid and plastic limits.

1.4.2.2. Plastic Limit.

The plastic limit (PL) is the water content where soil transitions between brittle and plastic behavior. A thread of soil is at its plastic limit when it begins to crumble when rolled to a diameter of 3 mm. To improve test result consistency, a 3 mm diameter rod is often used to gauge the thickness of the thread when conducting the test. The Plastic Limit test is defined by ASTM standard test method D 4318.

1.4.2.3. Liquid Limit.

The liquid limit (LL) is the water content at which a soil changes from plastic to liquid behavior. The original liquid limit test of Atterberg's involved mixing a pat of clay in a round-bottomed porcelain bowl of 10-12cm diameter. A groove was cut through the pat of clay with a spatula, and the bowl was then struck many times against the palm of one hand. Casagrande subsequently standardized the apparatus and the procedures to make the measurement more repeatable. Soil is placed into the metal cup portion of the device and a groove is made down its center with a standardized tool of 13.5 millimeters (0.53 in) width. The cup is repeatedly dropped 10mm onto a hard rubber base during which the groove closes up gradually as a result of the impact. The number of blows for the groove to close is recorded. The moisture content at which it takes 25 drops of the cup to cause the groove to close over a distance of 13.5 millimeters (0.53 in) is defined as the liquid limit. The test is normally run at several moisture contents, and the moisture content which requires 25 blows to close the groove is interpolated from the test results. The Liquid Limit test is defined by ASTM standard test method D 4318. The test method also allows running the test at one moisture content where 20 to 30 blows are required to close the groove; then a correction factor is applied to obtain the liquid limit from the moisture content.
The following is when you should record the N in number of blows needed to close this 1/2-inch gap:
The materials needed to do a Liquid limit test are as follows

- Casagrande cup (liquid limit device)
- Grooving tool
- Soil pat before test
- Soil pat after test

Another method for measuring the liquid limit is the fall cone test. It is based on the measurement of penetration into the soil of a standardized cone of specific mass. Despite the universal prevalence of the Casagrande method, the fall cone test is often considered to be a more consistent alternative because it minimizes the possibility of human variations when carrying out the test.

1.4.2.4. Importance of Liquid Limit Test.

The importance of the liquid limit test is to classify soils. Different soils have varying liquid limits. Also to find the plasticity index of a soil you need to know the liquid limit and the plastic limit.

1.4.2.5. Derived Limits.

The values of these limits are used in a number of ways. There is also a close relationship between the limits and properties of a soil such as compressibility, permeability, and strength. This is thought to be very useful because as limit determination is relatively simple, it is more difficult to determine these other properties. Thus the Atterberg limits are not only used to identify the soil's classification, but it allows for the use of empirical correlations for some other engineering properties.

1.4.2.6. Plasticity Index.

The plasticity index (PI) is a measure of the plasticity of a soil. The plasticity index is the size of the range of water contents where the soil exhibits plastic properties. The PI is the difference between the liquid limit and the plastic limit (PI = LL-PL). Soils with a high PI tend to be clay, those with a lower PI tend to be silt, and those with a PI of 0 (non-plastic) tend to have little or no silt or clay.
PI and their meanings

- 0 – Non-plastic
- (1-5)- Slightly Plastic
- (5-10) - Low plasticity
- (10-20)- Medium plasticity
- (20-40)- High plasticity
- >40 Very high plasticity

1.4.2.7. Liquidity Index.

The liquidity index (LI) is used for scaling the natural water content of a soil sample to the limits. It can be calculated as a ratio of difference between natural water content, plastic limit, and plasticity index:
LI=(W-PL)/(LL-PL) where W is the natural water content.

1.4.2.8. Activity.

The activity (A) of a soil is the PI divided by the percent of clay-sized particles (less than 2 μm) present. Different types of clays have different specific surface areas which controls how much wetting is required to move a soil from one phase to another such as across the liquid limit or the plastic limit. From the activity one can predict the dominant clay type present in a soil sample. High activity signifies large volume change when wetted and large shrinkage when dried. Soils with high activity are very reactive chemically. Normally the activity of clay is between 0.75 and 1.25, and in this range clay is called normal. It is assumed that the plasticity index is approximately equal to the clay fraction (A = 1). When A is less than 0.75, it is considered inactive. When it is greater than 1.25, it is considered active.

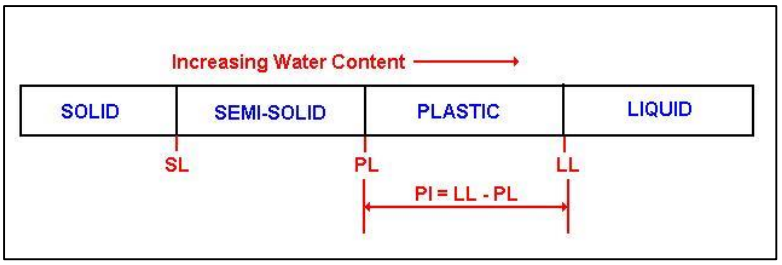

Figure 1-21: The relation between SL, PL, LL and PI.

1.4.3. Mass Volume Relations.

There are a variety of parameters used to describe the relative proportions of air (gas), water (liquid) and solids in a soil. This section defines these parameters and some of their interrelationships. The basic notation is as follows:
$\mathbf{V_g}$, $\mathbf{V_l}$, and $\mathbf{V_s}$ represent the volumes of gas, liquid and solids in a soil mixture;
$\mathbf{W_g}$, $\mathbf{W_l}$, and $\mathbf{W_s}$ represent the weights of gas, liquid and solids in a soil mixture;
$\mathbf{M_g}$, $\mathbf{M_l}$, and $\mathbf{M_s}$ represent the masses of gas, liquid and solids in a soil mixture;
$\boldsymbol{\rho_g}$, $\boldsymbol{\rho_l}$, and $\boldsymbol{\rho_s}$ represent the densities of the constituents (gas, liquid and solids) in a soil mixture;
Note that the weights, **W**, can be obtained by multiplying the mass, **M**, by the acceleration due to gravity, **g**; e.g., $\mathbf{W_s = M_s \cdot g}$

1.4.3.1. Specific Gravity.

Specific Gravity is the ratio of the density of one material compared to the density of pure water ($\boldsymbol{\rho_l}$ = 1000 kg/m^3).

$$G_s = \frac{\rho_s}{\rho_l} \tag{1-1}$$

1.4.3.2. Density.

The terms density and unit weight are used interchangeably in soil mechanics. Though not critical, it is important that we know it. Density, Bulk Density, or Wet Density, $\boldsymbol{\rho_t}$, are different names for the density of the mixture, i.e., the total mass of air, water, solids divided by the total volume of air, water and solids (the mass of air is assumed to be zero for practical purposes. To find the formula for density, divide the mass of the soil by the volume of the soil, the basic formula for density is:

$$\rho_t = \frac{M_t}{V_t} = \frac{M_s + M_l + M_g}{V_s + V_l + V_g} \tag{1-2}$$

Unit weight of a soil mass is the ratio of the total weight of soil to the total volume of soil. Unit Weight, $\boldsymbol{\gamma_t}$, is usually determined in the laboratory by measuring the weight and volume of a relatively undisturbed soil sample obtained from a brass ring. Measuring unit weight of soil in the field may consist of a sand cone test, rubber balloon or nuclear densitometer, the basic formula for unit weight is:

$$\gamma_t = \frac{M_t \cdot g}{V_t} \tag{1-3}$$

Dry Density, $\boldsymbol{\rho_d}$, is the mass of solids divided by the total volume of air, water and solids:

$$\rho_d = \frac{M_s}{V_t} = \frac{M_s}{V_s + V_l + V_g} \tag{1-4}$$

Submerged Density, $\boldsymbol{\rho_{st}}$, defined as the density of the mixture minus the density of water is useful if the soil is submerged under water:

$$\rho_{sd} = \rho_t - \rho_l \tag{1-5}$$

Table 1-2: Empirical values for ρ_t, of granular soils based on the standard penetration number, (from Bowels, *Foundation Analysis*).

SPT Penetration, N-Value (blows/ foot)	ρ_t (kg/m^3)
0 - 4	1120 - 1520
4 - 10	1520 - 1800
10 - 30	1800 - 2080
30 - 50	2080 - 2240
>50	2240 - 2400

Table 1-3: Empirical values for ρ_s, of cohesive soils based on the standard penetration number, (From Bowels, *Foundation Analysis*).

SPT Penetration, N-Value (blows/ foot)	$\rho_{s,\,sat}$ (kg/m^3)
0 - 4	1600 - 1840
4 - 8	1840 - 2000
8 - 32	2000 - 2240

Table 1-4: Typical Soil Characteristics (From Lindeburg, Civil Engineering Reference Manual for the PE Exam, 8th edition).

Soil Type	ρ_s (kg/m^3)	$\rho_{s,\,sat}$ (kg/m^3)
Sand, loose and uniform	1440	1888
Sand, dense and uniform	1744	2080
Sand, loose and well graded	1584	1984
Sand, dense and well graded	1856	2160
Glacial clay, soft	1216	1760
Glacial clay, stiff	1696	2000

Table 1-5: Typical Values of Soil Index Properties (From *NAVFAC 7.01*).

Soil Type	ρ_s (kg/m^3)
Sand; clean, uniform, fine or medium	1344 - 2176
Silt; uniform, inorganic	1296 - 2176
Silty Sand	1408 - 2272
Sand; Well-graded	1376 - 2368
Silty Sand and Gravel	1440 - 2480
Sandy or Silty Clay	1600 - 2352
Silty Clay with Gravel; uniform	1840 - 2416
Well-graded Gravel, Sand, Silt and Clay	2000 - 2496
Clay	1504 - 2128
Colloidal Clay	1136 - 2048
Organic Silt	1392 - 2096
Organic Clay	1296 - 2000

1.4.3.3. Relative Density.

Relative density is an index that quantifies the state of compactness between the loosest and densest possible state of coarse-grained soils. The relative density is written in the following formulas:

$$D_r = \frac{e_{max} - e}{e_{max} - e_{min}} = \frac{n_{max} - n}{n_{max} - n_{min}} \quad \textbf{(1-6)}$$

Table 1-6: Designation of Granular Soil Based on Relative Density.

D_r (%)	Description
0 - 20	Very loose
20 - 40	Loose
40 - 70	Medium dense
70 - 85	Dense
85 - 100	Very dense

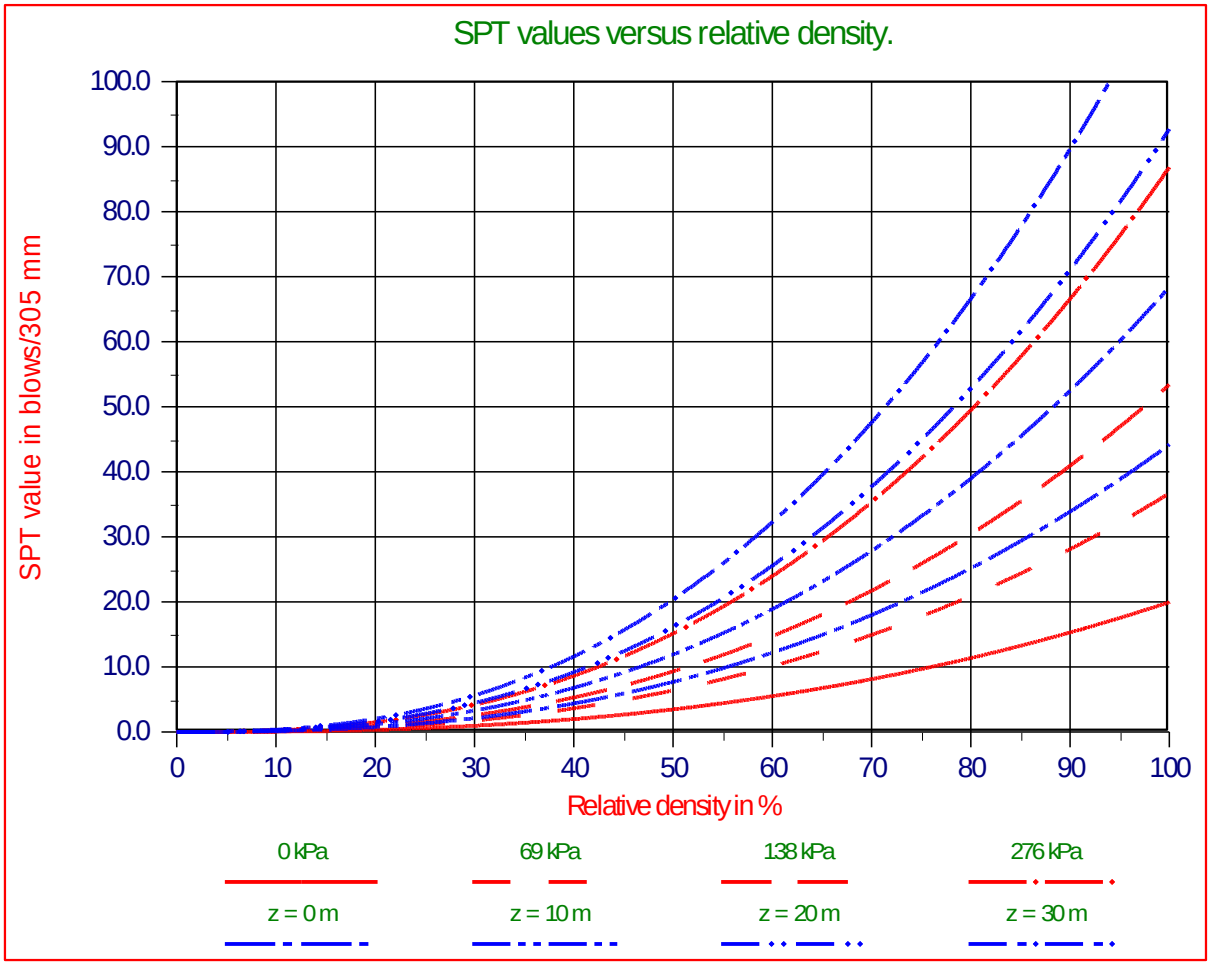

Figure 1-22: SPT values versus relative density (Miedema (1995).

Lambe & Whitman (1979), page 78 (Figure 1-22) give the relation between the SPT value, the relative density and the hydrostatic pressure in two graphs. With some curve-fitting these graphs can be summarized with the following equation (Miedema (1995)):

$$SPT = \left(1.82 + 0.221 \cdot \left(z + 10\right)\right) \cdot 10^{-4} \cdot RD^{2.52} \quad \textbf{(1-7)}$$

1.4.3.4. Porosity.

Porosity is the ratio of the volume of openings (voids) to the total volume of material. Porosity represents the storage capacity of the geologic material. The primary porosity of a sediment or rock consists of the spaces between the grains that make up that material. The more tightly packed the grains are, the lower the porosity. Using a box of marbles as an example, the internal dimensions of the box would represent the volume of the sample. The space surrounding each of the spherical marbles represents the void space. The porosity of the box of marbles would be determined by dividing the total void space by the total volume of the sample and expressed as a percentage.
The primary porosity of unconsolidated sediments is determined by the shape of the grains and the range of grain sizes present. In poorly sorted sediments, those with a larger range of grain sizes, the finer grains tend to fill the spaces between the larger grains, resulting in lower porosity. Primary porosity can range from less than one percent in crystalline rocks like granite to over 55% in some soils. The porosity of some rock is increased through fractures or solution of the material itself. This is known as secondary porosity.

$$n = \frac{V_v}{V_t} = \frac{V_v}{V_s + V_v} = \frac{e}{1 + e} \qquad \textbf{(1-8)}$$

1.4.3.5. Void ratio.

The ratio of the volume of void space to the volume of solid substance in any material consisting of void space and solid material, such as a soil sample, a sediment, or a powder.

$$e = \frac{V_v}{V_s} = \frac{V_v}{V_t - V_v} = \frac{n}{1 - n} \qquad \textbf{(1-9)}$$

The relations between void ratio **e** and porosity **n** are:

$$e = \frac{n}{1 - n} \quad \text{and} \quad n = \frac{e}{1 + e} \qquad \textbf{(1-10)}$$

1.4.3.6. Dilatation.

Dilation (or dilatation) refers to an enlargement or expansion in bulk or extent, the opposite of contraction. It derives from the Latin dilatare, "to spread wide". It is the increase in volume of a granular substance when its shape is changed, because of greater distance between its component particles. Suppose we have a volume **V** before the enlargement and a volume **V+dV** after the enlargement. Before the enlargement we name the porosity $\mathbf{n_i}$ (i from initial) and after the enlargement $\mathbf{n_{cv}}$ (the constant volume situation after large deformations). For the volume before the deformation we can write:

$$V = (1 - n_i) \cdot V + n_i \cdot V \qquad \textbf{(1-11)}$$

The first term on the right hand side is the sand volume, the second term the pore volume. After the enlargement we get:

$$V + dV = (1 - n_{cv}) \cdot (V + dV) + n_{cv} \cdot (V + dV) \qquad \textbf{(1-12)}$$

Again the first term on the right hand side is the sand volume. Since the sand volume did not change during the enlargement (we assume the quarts grains are incompressible), the volume of sand in both equations should be the same, thus:

$$(1 - n_i) \cdot V = (1 - n_{cv}) \cdot (V + dV) \qquad \textbf{(1-13)}$$

From this we can deduce that the dilatation **ε is:**

$$\varepsilon = \frac{dV}{V} = \frac{n_{cv} - n_i}{1 - n_{cv}} = \frac{dn}{1 - n_{cv}} \qquad \textbf{(1-14)}$$

1.4.4. Permeability.

Permeability is a measure of the ease with which fluids will flow though a porous rock, sediment, or soil. Just as with porosity, the packing, shape, and sorting of granular materials control their permeability. Although a rock may be highly porous, if the voids are not interconnected, then fluids within the closed, isolated pores cannot move. The degree to which pores within the material are interconnected is known as effective porosity. Rocks such as pumice and shale can have high porosity, yet can be nearly impermeable due to the poorly interconnected voids. In contrast, well-sorted sandstone closely replicates the example of a box of marbles cited above. The rounded sand grains provide ample, unrestricted void spaces that are free from smaller grains and are very well linked. Consequently, sandstones of this type have both high porosity and high permeability.
The range of values for permeability in geologic materials is extremely large. The most conductive materials have permeability values that are millions of times greater than the least permeable. Permeability is often directional in nature. The characteristics of the interstices of certain materials may cause the permeability to be significantly greater in one direction. Secondary porosity features, like fractures, frequently have significant impact on the permeability of the material. In addition to the characteristics of the host material, the viscosity and pressure of the fluid also affect the rate at which the fluid will flow.

Hydraulic conductivity or permeability **k** can be estimated by particle size analysis of the sediment of interest, using empirical equations relating either **k** to some size property of the sediment. Vukovic and Soro (1992) summarized several empirical methods from former studies and presented a general formula:

$$k = C \cdot \frac{g}{\nu_l} \cdot f(n) \cdot d_e^2 \qquad \textbf{(1-15)}$$

The kinematic viscosity ν_l is related to dynamic viscosity μ_l and the fluid (water) density ρ_l as follows:

$$\nu_l = \frac{\mu_l}{\rho_l} \qquad \textbf{(1-16)}$$

The values of **C**, **f(n)** and d_e are dependent on the different methods used in the grain-size analysis. According to Vukovic and Soro (1992), porosity **n** may be derived from the empirical relationship with the coefficient of grain uniformity **U** as follows:

$$n = 0.255 \cdot \left(1 + 0.83^{U}\right) \qquad \textbf{(1-17)}$$

Where **U** is the coefficient of grain uniformity and is given by:

$$U = \left(\frac{d_{60}}{d_{10}}\right) \qquad \textbf{(1-18)}$$

Here, d_{60} and d_{10} in the formula represent the grain diameter in (mm) for which, 60% and 10% of the sample respectively, are finer than. Former studies have presented the following formulae which take the general form presented in equation (1-15) above but with varying **C, f(n)** and d_e values and their domains of applicability.

Hazen's formula (1982) was originally developed for determination of hydraulic conductivity of uniformly graded sand but is also useful for fine sand to gravel range, provided the sediment has a uniformity coefficient less than 5 and effective grain size between 0.1 and 3mm.

$$k = 6 \cdot 10^{-4} \cdot \frac{g}{\nu_l} \cdot \left(1 + 10 \cdot (n - 0.26)\right) \cdot d_{10}^2 \qquad \textbf{(1-19)}$$

The Kozeny-Carman equation is one of the most widely accepted and used derivations of permeability as a function of the characteristics of the soil medium. The Kozeny-Carman equation (or Carman-Kozeny equation) is a relation used in the field of fluid dynamics to calculate the pressure drop of a fluid flowing through a packed bed of solids. It is named after Josef Kozeny and Philip C. Carman. This equation was originally proposed by Kozeny (1927) and was then modified by Carman (1937) and (1956) to become the Kozeny-Carman equation. It is not appropriate

for either soil with effective size above 3 mm or for clayey soils. The equation is only valid for laminar flow. The equation is given as:

$$k = d_e^2 \cdot \frac{\gamma_l}{\mu_l} \cdot \frac{e^3}{1+e} \cdot C \quad \text{or} \quad k = 8.3 \cdot 10^{-3} \cdot \frac{g}{\nu_l} \cdot \frac{n^3}{(1-n)^2} \cdot d_{10}^2 \qquad \textbf{(1-20)}$$

$$\text{With:} \quad \nu_l = \frac{\mu_l}{\rho_l} \text{ and } \gamma_l = \rho_l \cdot g$$

This equation holds for flow through packed beds with particle Reynolds numbers up to approximately 1.0, after which point frequent shifting of flow channels in the bed causes considerable kinetic energy losses. This equation can be expressed as "*flow is proportional to the pressure drop and inversely proportional to the fluid viscosity*", which is known as Darcy's law.

The Breyer method does not consider porosity and therefore, porosity function takes on value 1. Breyer formula is often considered most useful for materials with heterogeneous distributions and poorly sorted grains with uniformity coefficient between 1 and 20, and effective grain size between 0.06mm and 0.6mm.

$$k = 6 \cdot 10^{-4} \cdot \frac{g}{\nu_l} \cdot \log\left(\frac{500}{U}\right) \cdot d_{10}^2 \qquad \textbf{(1-21)}$$

The Slitcher formula is most applicable for grain-sizes between 0.01 mm and 5 mm.

$$k = 1 \cdot 10^{-2} \cdot \frac{g}{\nu_l} \cdot n^{3.287} \cdot d_{10}^2 \qquad \textbf{(1-22)}$$

The Terzaghi (1964) formula is most applicable for coarse sand. The Terzaghi equation:

$$k = C_t \cdot \frac{g}{\nu_l} \cdot \left(\frac{n-0.13}{\sqrt[3]{1-n}}\right)^2 \cdot d_{10}^2 \qquad \textbf{(1-23)}$$

Where the C_t = sorting coefficient and $6.1 \times 10^{-3} < C_t < 10.7 \times 10^{-3}$.

1.4.5. The Angle of Internal Friction.

Angle of internal friction for a given soil is the angle on the graph (Mohr's Circle) of the shear stress and normal effective stresses at which shear failure occurs. Angle of Internal Friction, **φ**, can be determined in the laboratory by the Direct Shear Test or the Triaxial Stress Test. Typical relationships for estimating the angle of internal friction, **φ**, are as follows:

Table 1-7: Empirical values for φ, of granular soils based on the standard penetration number, (From Bowels, *Foundation Analysis*).

SPT Penetration, N-Value (blows/ foot)	**φ** (degrees)
0	25 - 30
4	27 - 32
10	30 - 35
30	35 - 40
50	38 - 43

Table 1-8: Relationship between φ, and standard penetration number for sands, (From Peck 1974, *Foundation Engineering Handbook*).

SPT Penetration, N-Value (blows/ foot)	**Density of Sand**	**φ** (degrees)
<4	Very loose	<29
4 - 10	Loose	29 - 30
10 - 30	Medium	30 - 36
30 - 50	Dense	36 - 41
>50	Very dense	>41

Table 1-9: Relationship between φ, and standard penetration number for sands, (From Meyerhof 1956, *Foundation Engineering Handbook*).

SPT Penetration, N-Value (blows/ foot)	**Density of Sand**	**φ** (degrees)
<4	Very loose	<30
4 - 10	Loose	30 - 35
10 - 30	Medium	35 - 40
30 - 50	Dense	40 - 45
>50	Very dense	>45

Lambe & Whitman (1979), page 148 (Figure 1-23) give the relation between the SPT value and the angle of internal friction, also in a graph. This graph is valid up to 12 m in dry soil. With respect to the internal friction, the relation given in the graph has an accuracy of 3 degrees. A load of 12 m dry soil with a density of 1.67 ton/m^3 equals a hydrostatic pressure of 20 m.w.c. An absolute hydrostatic pressure of 20 m.w.c. equals 10 m of water depth if cavitation is considered. Measured SPT values at any depth will have to be reduced to the value that would occur at 10 m water depth. This can be accomplished with the following equation:

$$SPT_{10} = \frac{1}{(0.646 + 0.0354 \cdot z)} \cdot SPT_z \qquad \textbf{(1-24)}$$

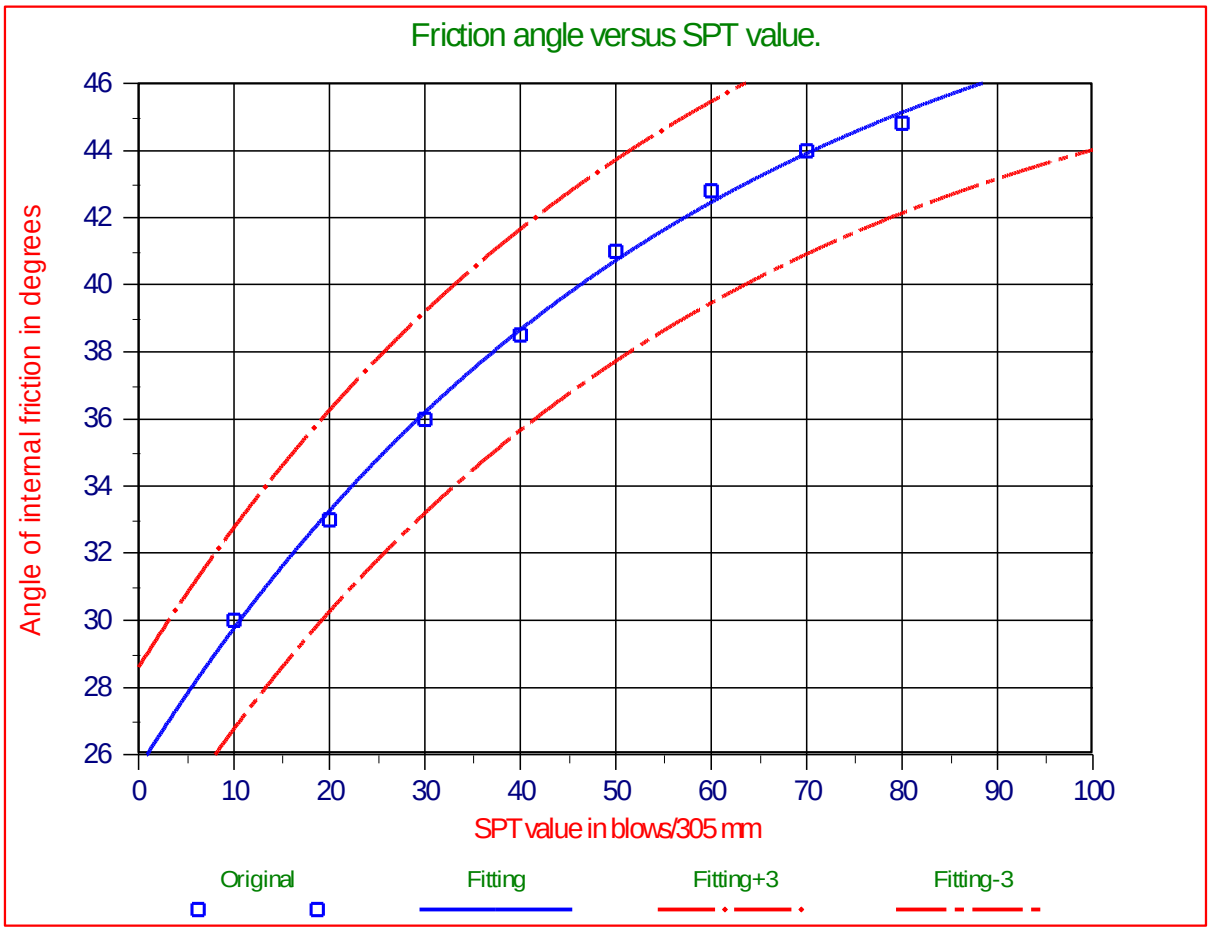

Figure 1-23: Friction angle versus SPT value (Miedema (1995).

With the aim of curve-fitting, the relation between the SPT value reduced to 10 m water depth and the angle of internal friction can be summarized to:

$$\varphi = 51.5 - 25.9 \cdot e^{-0.01753 \cdot SPT_{10}} \qquad \textbf{(1-25)}$$

1.4.6. The Angle of External Friction.

The external friction angle, δ, or friction between a soil medium and a material such as the composition from a retaining wall or pile may be expressed in degrees as the following:

Table 1-10: External friction angle φ values.

20º	steel piles (NAVFAC)
0.67·φ-0.83·φ	USACE
20º	steel (Broms)
3/4·φ	concrete (Broms)
2/3·φ	timber (Broms)
2/3·φ	Lindeburg
2/3·φ	for concrete walls (Coulomb)

The external friction angle can be estimated as **1/3·φ** for smooth retaining walls like sheet piles or concrete surfaces against timber formwork, or as **1/2·φ** to **2/3·φ** for rough surfaces. In the absence of detailed information the assumption of **2/3·φ** is commonly made.

1.4.7. Shear Strength.

1.4.7.1. Introduction.

Shear strength is a term used in soil mechanics to describe the magnitude of the shear stress that a soil can sustain. The shear resistance of soil is a result of friction and interlocking of particles, and possibly cementation or bonding at particle contacts. Due to interlocking, particulate material may expand or contract in volume as it is subject to shear strains. If soil expands its volume, the density of particles will decrease and the strength will decrease; in this case, the peak strength would be followed by a reduction of shear stress. The stress-strain relationship levels off when the material stops expanding or contracting, and when inter-particle bonds are broken. The theoretical state at which the shear stress and density remain constant while the shear strain increases may be called the critical state, steady state, or residual strength.
The volume change behavior and inter-particle friction depend on the density of the particles, the inter-granular contact forces, and to a somewhat lesser extent, other factors such as the rate of shearing and the direction of the shear stress. The average normal inter-granular contact force per unit area is called the effective stress.
If water is not allowed to flow in or out of the soil, the stress path is called an undrained stress path. During undrained shear, if the particles are surrounded by a nearly incompressible fluid such as water, then the density of the particles cannot change without drainage, but the water pressure and effective stress will change. On the other hand, if the fluids are allowed to freely drain out of the pores, then the pore pressures will remain constant and the test path is called a drained stress path. The soil is free to dilate or contract during shear if the soil is drained. In reality, soil is partially drained, somewhere between the perfectly undrained and drained idealized conditions. The shear strength of soil depends on the effective stress, the drainage conditions, the density of the particles, the rate of strain, and the direction of the strain.
For undrained, constant volume shearing, the Tresca theory may be used to predict the shear strength, but for drained conditions, the Mohr–Coulomb theory may be used.
Two important theories of soil shear are the critical state theory and the steady state theory. There are key differences between the steady state condition and the steady state condition and the resulting theory corresponding to each of these conditions.

1.4.7.2. Undrained Shear Strength.

This term describes a type of shear strength in soil mechanics as distinct from drained strength. Conceptually, there is no such thing as the undrained strength of a soil. It depends on a number of factors, the main ones being:

- Orientation of stresses
- Stress path
- Rate of shearing
- Volume of material (like for fissured clays or rock mass)

Undrained strength is typically defined by Tresca theory, based on Mohr's circle as:

$$\sigma_1 - \sigma_3 = 2 \cdot S_u = U.C.S. \qquad \textbf{(1-26)}$$

It is commonly adopted in limit equilibrium analyses where the rate of loading is very much greater than the rate at which pore water pressures that are generated due to the action of shearing the soil may dissipate. An example of this is rapid loading of sands during an earthquake, or the failure of a clay slope during heavy rain, and applies to most failures that occur during construction. As an implication of undrained condition, no elastic volumetric strains occur, and thus Poisson's ratio is assumed to remain 0.5 throughout shearing. The Tresca soil model also assumes no plastic volumetric strains occur. This is of significance in more advanced analyses such as in finite element analysis. In these advanced analysis methods, soil models other than Tresca may be used to model the undrained condition including Mohr-Coulomb and critical state soil models such as the modified Cam-clay model, provided Poisson's ratio is maintained at 0.5.

1.4.7.3. Drained Shear Strength.

The drained shear strength is the shear strength of the soil when pore fluid pressures, generated during the course of shearing the soil, are able to dissipate during shearing. It also applies where no pore water exists in the soil (the soil is dry) and hence pore fluid pressures are negligible. It is commonly approximated using the Mohr-Coulomb equation. (It was called "Coulomb's equation" by Karl von Terzaghi in 1942.) combined it with the principle of effective stress. In terms of effective stresses, the shear strength is often approximated by:

$$\tau = c + \sigma \cdot \tan(\varphi) \qquad \textbf{(1-27)}$$

The coefficient of friction μ is equal to tan(φ). Different values of friction angle can be defined, including the peak friction angle, φ'_p, the critical state friction angle, φ'_{cv}, or residual friction angle, φ'_r.
c' is called cohesion, however, it usually arises as a consequence of forcing a straight line to fit through measured values of (τ,σ')even though the data actually falls on a curve. The intercept of the straight line on the shear stress axis is called the cohesion. It is well known that the resulting intercept depends on the range of stresses considered: it is not a fundamental soil property. The curvature (nonlinearity) of the failure envelope occurs because the dilatancy of closely packed soil particles depends on confining pressure.

1.4.7.4. Cohesion (Internal Shear Strength).

Cohesion (in Latin cohaerere "stick or stay together") or **cohesive attraction** or **cohesive force** is the action or property of like molecules sticking together, being mutually attractive. This is an intrinsic property of a substance that is caused by the shape and structure of its molecules which makes the distribution of orbiting electrons irregular when molecules get close to one another, creating electrical attraction that can maintain a macroscopic structure such as a water drop. Cohesive soils are clay type soils. Cohesion is the force that holds together molecules or like particles within a soil. Cohesion, **c**, is usually determined in the laboratory from the Direct Shear Test. Unconfined Compressive Strength, UCS, can be determined in the laboratory using the Triaxial Test or the Unconfined Compressive Strength Test. There are also correlations for UCS with shear strength as estimated from the field using Vane Shear Tests. With a conversion of 1 kips/ft^2=47.88 kN/m^2.

$$c = \frac{U.C.S.}{2} \qquad \textbf{(1-28)}$$

Table 1-11: Guide for Consistency of Fine-Grained Soil, NAVFAC 7.02

SPT Penetration (blows/ foot)	**Estimated Consistency**	**UCS**(kPa)
<2	Very Soft	<24
2 - 4	Soft	24 - 48
4 - 8	Medium	48 - 96
8 - 15	Stiff	96 – 192
15 - 30	Very Stiff	192 – 388
>30	Hard	>388

Table 1-12: Empirical Values for Consistency of Cohesive Soil, (from Foundation Analysis, Bowels)

SPT Penetration (blows/ foot)	**Estimated Consistency**	**UCS** (kips/ft^2)
0 - 2	Very Soft	0 - 0.5
2 - 4	Soft	0.5 - 1.0
4 - 8	Medium	1.0 - 2.0
8 - 16	Stiff	2.0 - 4.0
16 - 32	Very Stiff	4.0 - 8.0
>32	Hard	>8

1.4.7.5. Adhesion (External Shear Strength).

Adhesion is any attraction process between dissimilar molecular species that can potentially bring them in close contact. By contrast, cohesion takes place between similar molecules.
Adhesion is the tendency of dissimilar particles and/or surfaces to cling to one another (cohesion refers to the tendency of similar or identical particles/surfaces to cling to one another). The forces that cause adhesion and cohesion can be divided into several types. The intermolecular forces responsible for the function of various kinds of stickers and sticky tape fall into the categories of chemical adhesion, dispersive adhesion, and diffusive adhesion.

1.4.8. UCS or Unconfined Compressive Strength.

UCS is one of the most basic parameters of rock strength, and the most common determination performed for bore ability predictions. It is measured in accordance with the procedures given in **ASTM D2938**, with the length to diameter ratio of 2 by using **NX**-size core samples. 3 to 5 **UCS** determinations are recommended to achieve statistical significance of the results. If the sample length to diameter ratio was greater or less than 2, ASTM recommends a correction factor that is applied to the **UCS** value determined from testing. **UCS** measurements are made using an electronic-servo controlled **MTS** stiff testing machine with a capacity of 220 kips. Loading data and other test parameters are recorded with a computer based data acquisition system, and the data is subsequently reduced and analyzed with a customized spreadsheet program.

The most important test for rock in the field of dredging is the uniaxial unconfined compressive strength (UCS). In the test a cylindrical rock sample is axial loaded till failure. Except the force needed, the deformation is measured too. So the complete stress-strain curve is measured from which the deformation modulus and the specific work of failure can be calculated. The unconfined compressive strength of the specimen is calculated by dividing the maximum load at failure by the sample cross-sectional area:

$$\sigma_c = \frac{F}{A} \qquad \textbf{(1-29)}$$

Figure 1-24: A UCS test facility (Timely Engineering Soil Tests, LLC).

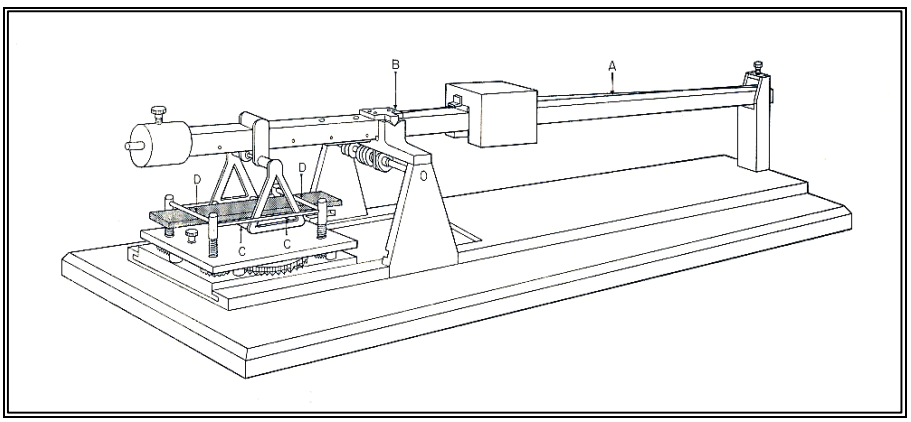

Figure 1-25: Bending (Vlasblom (2003-2007)).

1.4.9. Unconfined Tensile Strength.

The uniaxial unconfined tensile strength is defined in the same way as the compressive strength. Sample preparation and testing procedure require much effort and not commonly done. Another method to determine the tensile strength, also commonly not used, is by bending a sample.

1.4.10. BTS or Brazilian Tensile Strength.

Indirect, or **Brazilian**, tensile strength is measured using **NX**-size core samples cut to an approximate 0.5 length-to-diameter ratio, and following the procedures of **ASTM D3967**. **BTS** measurements are made using an electronic-servo controlled **MTS** stiff testing machine with a capacity of 220 kips. Loading data and other test parameters are recorded with a computer based data acquisition system, and the data is subsequently reduced and analyzed with a customized spreadsheet program. **BTS** provides a measure of rock toughness, as well as strength. The indirect tensile strength is calculated as follows (Fairhurst (1964)):

$$\sigma_T = \frac{2 \cdot F}{\pi \cdot L \cdot D} \qquad \textbf{(1-30)}$$

In bedded/foliated rocks, particular attention needs to be given to loading direction with respect to bedding/foliation. The rock should be loaded so that breakage occurs in approximately the same direction as fracture propagation between adjacent cuts on the tunnel face. This is very important assessment in mechanical excavation by tunnel boring machines. The most common used test to estimate, in an indirect way, the tensile strength is the Brazilian split test. Here the cylindrical sample is tested radial.

The validity of BTS to determine de UTS is discussed by many researchers. In general it can be stated that the BTS over estimates the UTS. According to Pells (1993) this discussion is in most applications in practice largely academic.

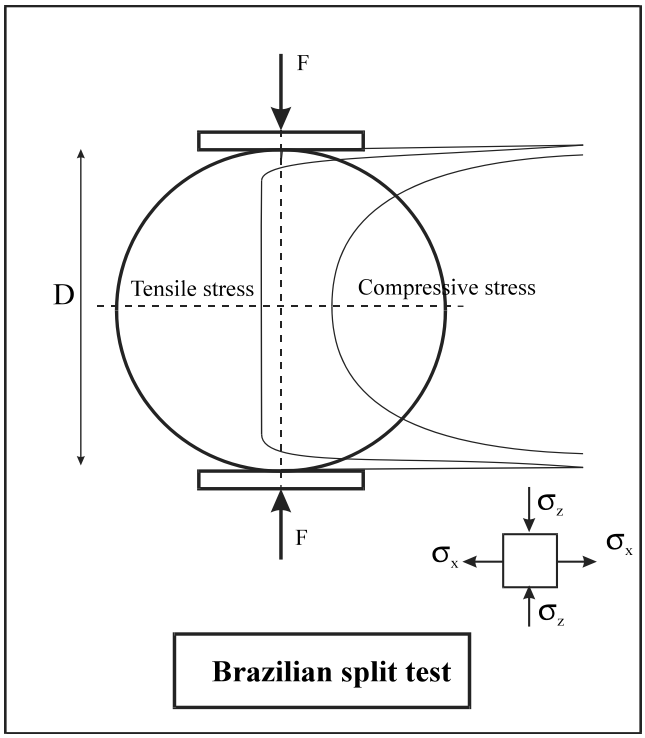

Figure 1-26: The Brazilian split test (Vlasblom (2003-2007)).

1.4.11. Hardness.

Hardness is a loosely defined term, referring the resistance to rock or minerals against an attacking tool. Hardness is determined using rebound tests (f.i. Schmidt hammer), indentation tests, (Brinell, Rockwell) or scratch tests (Mohs). The last test is based on the fact that a mineral higher in the scale can scratch a mineral lower in the scale.

Although this scale was established in the early of the 19th century it appeared that the increment of Mohs scale corresponded with a 60% increase in indentation hardness.

Table 1-13: The Mohs scale (source Wikipedia).

Mohs hardness	Mineral	Chemical formula	Absolute hardness.	Image
1	Talc	$Mg_3Si_4O_{10}(OH)_2$	1	
2	Gypsum	$CaSO_4 \cdot 2H_2O$	3	
3	Calcite	$CaCO_3$	9	
4	Fluorite	CaF_2	21	
5	Apatite	$Ca_5(PO_4)_3(OH^-,Cl^-,F^-)$	48	
6	Orthoclase	$KAlSi_3O_8$	72	
7	Quartz	SiO_2	100	
8	Topaz	$Al_2SiO_4(OH^-,F^-)_2$	200	
9	Corundum	Al_2O_3	400	
10	Diamond	C	1600	

1.5. Criteria & Concepts.

1.5.1. Failure Criteria.

After a soil reaches the critical state, it is no longer contracting or dilating and the shear stress on the failure plane τ_{crit} is determined by the effective normal stress on the failure plane σ_n' and critical state friction angle, φ_{cv}, :

$$\tau_{crit} = \sigma_n' \cdot \tan(\varphi_{cv}) \qquad \textbf{(1-31)}$$

The peak strength of the soil may be greater, however, due to the interlocking (dilatancy) contribution. This may be stated:

$$\tau_{peak} = \sigma_n' \cdot \tan(\varphi_{peak}) \qquad \textbf{(1-32)}$$

Where $\varphi_{peak} > \varphi_{cv}$. However, use of a friction angle greater than the critical state value for design requires care. The peak strength will not be mobilized everywhere at the same time in a practical problem such as a foundation, slope or retaining wall. The critical state friction angle is not nearly as variable as the peak friction angle and hence it can be relied upon with confidence. Not recognizing the significance of dilatancy, Coulomb proposed that the shear strength of soil may be expressed as a combination of adhesion and friction components:

$$\tau = \sigma' \cdot \tan(\varphi) + c' \qquad \textbf{(1-33)}$$

It is now known that the **c'** and **φ** parameters in the last equation are not fundamental soil properties. In particular, **c'** and **φ** are different depending on the magnitude of effective stress. According to Schofield (2006), the longstanding use of **c'** in practice has led many engineers to wrongly believe that **c'** is a fundamental parameter. This assumption that **c'** and **φ** are constant can lead to overestimation of peak strengths.

1.5.2. The Phi=0 Concept.

When a fast triaxial test is carried out, so an unconsolidated undrained test, it is very well possible that the pore pressures will be equal to the increase of the cell pressure. If a test at high cell pressure is carried out, the only difference with a test with a low cell pressure is the value of the pore pressures. The grain pressures will be almost equal in both cases and the result is, that we will find the same critical Mohr circle. So let's consider a series of unconsolidated undrained (UU) tests. Three specimens are selected and all are consolidated to 110 kPa. This brings the specimens to the end of step 1 in the UU test program. Now the confining pressures are changed to say 70, 140 and 700 kPa, without allowing further consolidation and the sheared undrained. The result, within experimental scatter, is that the shear stress or radius of the Mohr circle is about 35 kPa for each specimen.
So what happened?
When the confining pressure was changed, the pore pressure in the fully saturated specimens changed just as much as did the confining pressure, and the effective stress remained unchanged and equal in each specimen. Thus the effective stress remained 110 kPa and each specimen behaved during shear just as did the CU specimen. The shear stress and thus the radius of the Mohr circle did not increase and apparently the specimens did not encounter internal friction. This is called the phi=0 concept. In clays with a very low permeability and at a high deformation rate, like during the cutting of clay, the clay behaves like the internal friction angle is zero. So for cutting processes the phi=0 concept will be applied.

1.5.3. Factors Controlling Shear Strength of Soils.

The stress-strain relationship of soils, and therefore the shearing strength, is affected by:

1. Soil composition (basic soil material): mineralogy, grain size and grain size distribution, shape of particles, pore fluid type and content, ions on grain and in pore fluid.
2. State (initial): Defined by the initial void ratio, effective normal stress and shear stress (stress history). State can be described by terms such as: loose, dense, over consolidated, normally consolidated, stiff, soft, contractive, dilative, etc.
3. Structure: Refers to the arrangement of particles within the soil mass; the manner the particles are packed or distributed. Features such as layers, joints, fissures, slickensides, voids, pockets, cementation, etc., are part of the structure. Structure of soils is described by terms such as: undisturbed, disturbed, remolded,

compacted, cemented; flocculent, honey-combed, single-grained; flocculated, deflocculated; stratified, layered, laminated; isotropic and anisotropic.

4. Loading conditions: Effective stress path, i.e., drained, and undrained; and type of loading, i.e., magnitude, rate (static, dynamic), and time history (monotonic, cyclic).

The shear strength and stiffness of soil determines whether or not soil will be stable or how much it will deform. Knowledge of the strength is necessary to determine if a slope will be stable, if a building or bridge might settle too far into the ground, and the limiting pressures on a retaining wall. It is important to distinguish between failure of a soil element and the failure of a geotechnical structure (e.g., a building foundation, slope or retaining wall); some soil elements may reach their peak strength prior to failure of the structure. Different criteria can be used to define the "shear strength" and the "yield point" for a soil element from a stress-strain curve. One may define the peak shear strength as the peak of a stress strain curve, or the shear strength at critical state as the value after large strains when the shear resistance levels off. If the stress-strain curve does not stabilize before the end of shear strength test, the "strength" is sometimes considered to be the shear resistance at 15% to 20% strain. The shear strength of soil depends on many factors including the effective stress and the void ratio.
The shear stiffness is important, for example, for evaluation of the magnitude of deformations of foundations and slopes prior to failure and because it is related to the shear wave velocity. The slope of the initial, nearly linear, portion of a plot of shear stress as a function of shear strain is called the shear modulus

1.5.4. Friction, Interlocking & Dilation.

Soil is an assemblage of particles that have little to no cementation while rock (such as sandstone) may consist of an assembly of particles that are strongly cemented together by chemical bonds. The shear strength of soil is primarily due to inter-particle friction and therefore, the shear resistance on a plane is approximately proportional to the effective normal stress on that plane.[3] But soil also derives significant shear resistance from interlocking of grains. If the grains are densely packed, the grains tend to spread apart from each other as they are subject to shear strain. The expansion of the particle matrix due to shearing was called dilatancy by Osborne Reynolds. If one considers the energy required to shear an assembly of particles there is energy input by the shear force, T, moving a distance, x and there is also energy input by the normal force, N, as the sample expands a distance, y. Due to the extra energy required for the particles to dilate against the confining pressures, dilatant soils have greater peak strength than contractive soils. Furthermore, as dilative soil grains dilate, they become looser (their void ratio increases), and their rate of dilation decreases until they reach a critical void ratio. Contractive soils become denser as they shear, and their rate of contraction decreases until they reach a critical void ratio.
The tendency for a soil to dilate or contract depends primarily on the confining pressure and the void ratio of the soil. The rate of dilation is high if the confining pressure is small and the void ratio is small. The rate of contraction is high if the confining pressure is large and the void ratio is large. As a first approximation, the regions of contraction and dilation are separated by the critical state line.

1.5.5. Effective Stress.

Karl von Terzaghi (1964) first proposed the relationship for effective stress in 1936. For him, the term ‘effective’ meant the calculated stress that was effective in moving soil, or causing displacements. It represents the average stress carried by the soil skeleton. Effective stress (**σ'**) acting on a soil is calculated from two parameters, total stress (**σ**) and pore water pressure (**u**) according to:

$$\sigma' = \sigma - u \qquad \textbf{(1-34)}$$

Typically, for simple examples:

$$\sigma = \gamma_{soil} \cdot H_{soil} \text{ and } u = \gamma_w \cdot H_w \qquad \textbf{(1-35)}$$

Much like the concept of stress itself, the formula is a construct, for the easier visualization of forces acting on a soil mass, especially simple analysis models for slope stability, involving a slip plane. With these models, it is important to know the total weight of the soil above (including water), and the pore water pressure within the slip plane, assuming it is acting as a confined layer.
However, the formula becomes confusing when considering the true behavior of the soil particles under different measurable conditions, since none of the parameters are actually independent actors on the particles.

Consider a grouping of round quartz sand grains, piled loosely, in a classic ‘cannonball’ arrangement. As can be seen, there is a contact stress where the spheres actually touch. Pile on more spheres and the contact stresses

increase, to the point of causing frictional instability (dynamic friction), and perhaps failure. The independent parameter affecting the contacts (both normal and shear) is the force of the spheres above. This can be calculated by using the overall average density of the spheres and the height of spheres above.
If we then have these spheres in a beaker and add some water, they will begin to float a little depending on their density (buoyancy). With natural soil materials, the effect can be significant, as anyone who has lifted a large rock out of a lake can attest. The contact stress on the spheres decreases as the beaker is filled to the top of the spheres, but then nothing changes if more water is added. Although the water pressure between the spheres (pore water pressure) is increasing, the effective stress remains the same, because the concept of 'total stress' includes the weight of all the water above. This is where the equation can become confusing, and the effective stress can be calculated using the buoyant density of the spheres (soil), and the height of the soil above.

The concept of effective stress truly becomes interesting when dealing with non-hydrostatic pore water pressure. Under the conditions of a pore pressure gradient, the ground water flows, according to the permeability equation (Darcy's law). Using our spheres as a model, this is the same as injecting (or withdrawing) water between the spheres. If water is being injected, the seepage force acts to separate the spheres and reduces the effective stress. Thus, the soil mass becomes weaker. If water is being withdrawn, the spheres are forced together and the effective stress increases. Two extremes of this effect are quicksand, where the groundwater gradient and seepage force act against gravity; and the 'sandcastle effect', where the water drainage and capillary action act to strengthen the sand. As well, effective stress plays an important role in slope stability, and other geotechnical engineering and engineering geology problems, such as groundwater-related subsidence.

1.5.6. Pore Water Pressure: Hydrostatic Conditions.

If there is no pore water flow occurring in the soil, the pore water pressures will be hydrostatic. The water table is located at the depth where the water pressure is equal to the atmospheric pressure. For hydrostatic conditions, the water pressure increases linearly with depth below the water table:

$$u = \rho_w \cdot g \cdot z_w \qquad \textbf{(1-36)}$$

1.5.7. Pore Water Pressure: Capillary Action.

Due to surface tension water will rise up in a small capillary tube above a free surface of water. Likewise, water will rise up above the water table into the small pore spaces around the soil particles. In fact the soil may be completely saturated for some distance above the water table. Above the height of capillary saturation, the soil may be wet but the water content will decrease with elevation. If the water in the capillary zone is not moving, the water pressure obeys the equation of hydrostatic equilibrium, $\mathbf{u = \rho_w \cdot g \cdot z_w}$, but note that $\boldsymbol{z_w}$, is negative above the water table. Hence, hydrostatic water pressures are negative above the water table. The thickness of the zone of capillary saturation depends on the pore size, but typically, the heights vary between a centimeter or so for coarse sand to tens of meters for a silt or clay.
The surface tension of water explains why the water does not drain out of a wet sand castle or a moist ball of clay. Negative water pressures make the water stick to the particles and pull the particles to each other, friction at the particle contacts make a sand castle stable. But as soon as a wet sand castle is submerged below a free water surface, the negative pressures are lost and the castle collapses. Considering the effective stress equation, $\boldsymbol{\sigma' = \sigma - u_w}$, if the water pressure is negative, the effective stress may be positive, even on a free surface (a surface where the total normal stress is zero). The negative pore pressure pulls the particles together and causes compressive particle to particle contact forces.
Negative pore pressures in clayey soil can be much more powerful than those in sand. Negative pore pressures explain why clay soils shrink when they dry and swell as they are wetted. The swelling and shrinkage can cause major distress, especially to light structures and roads.

1.5.8. Darcy's Law.

Darcy's law states that the volume of flow of the pore fluid through a porous medium per unit time is proportional to the rate of change of excess fluid pressure with distance. The constant of proportionality includes the viscosity of the fluid and the intrinsic permeability of the soil.

$$Q = \frac{-K \cdot A}{\mu_l} \cdot \frac{(u_b - u_a)}{L} \qquad \textbf{(1-37)}$$

The negative sign is needed because fluids flow from high pressure to low pressure. So if the change in pressure is negative (in the *x*-direction) then the flow will be positive (in the *x*-direction). The above equation works well for a horizontal tube, but if the tube was inclined so that point b was a different elevation than point a, the equation would not work. The effect of elevation is accounted for by replacing the pore pressure by *excess pore pressure*, u_e defined as:

$$u_c = u - \rho_w \cdot g \cdot z \qquad \textbf{(1-38)}$$

Where *z* is the depth measured from an arbitrary elevation reference (datum). Replacing **u** by $\mathbf{u_e}$ we obtain a more general equation for flow:

$$Q = \frac{-K \cdot A}{\mu_l} \cdot \frac{\left(u_{c,b} - u_{c,a}\right)}{L} \qquad \textbf{(1-39)}$$

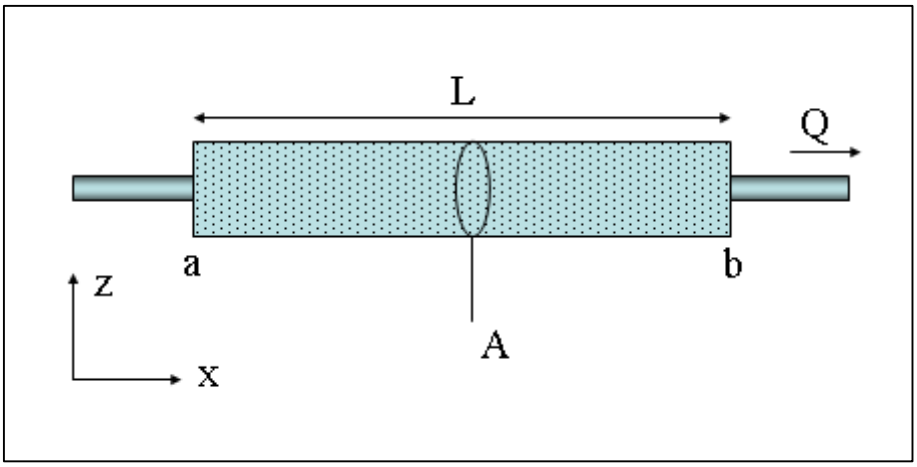

Figure 1-27: Diagram showing definitions and directions for Darcy's law.

Dividing both sides of the equation by A, and expressing the rate of change of excess pore pressure as a derivative, we obtain a more general equation for the apparent velocity in the x-direction:

$$q_x = \frac{-K}{\mu_l} \cdot \frac{du_c}{dx} \qquad \textbf{(1-40)}$$

Where q_x has units of velocity and is called the Darcy velocity, or discharge velocity. The seepage velocity (v_{sx} = average velocity of fluid molecules in the pores) is related to the Darcy velocity, and the porosity, n:

$$v_{s,x} = \frac{q_x}{n} \qquad \textbf{(1-41)}$$

Civil engineers predominantly work on problems that involve water and predominantly work on problems on earth (in earth's gravity). For this class of problems, civil engineers will often write Darcy's law in a much simpler form:

$$q_x = k \cdot i_x \qquad \textbf{(1-42)}$$

Where k is called permeability, and is defined as:

$$k = K \cdot \frac{\rho_l \cdot g}{\mu_l} \qquad \textbf{(1-43)}$$

And **i** is called the hydraulic gradient. The hydraulic gradient is the rate of change of total head with distance. Values are for typical fresh groundwater conditions, using standard values of viscosity and specific gravity for water at 20°C and 1 atm.

Table 1-14: Typical values of the permeability k.

Soil	Permeability (m/s)	Degree of permeability
Well sorted gravel	$10^{0}>k>10^{-2}$	Extremely high
Gravel	$10^{-2}>k>10^{-3}$	Very high
Sandy gravel, clean sand, fine sand	$10^{-3}>k>10^{-5}$	High to Medium
Sand, dirty sand, silty sand	$10^{-5}>k>10^{-7}$	Low
Silt, silty clay	$10^{-7}>k>10^{-9}$	Very low
Clay	$<10^{-9}$	Vitually impermeable
Highly fractured rocks	$10^{0}>k>10^{-3}$	Very high
Oil reservoir rocks	$10^{-4}>k>10^{-6}$	Medium to Low
Fresh sandstone	$10^{-7}>k>10^{-8}$	Very low
Fresh limestone, dolomite	$10^{-9}>k>10^{-10}$	Vitually impermeable
Fresh granite	$<10^{-11}$	Vitually impermeable

Table 1-15: Some permeabilities according to Hazen's equation.

Material	Permeability (m/s)	d_{10} (mm)
Uniform coarse sand	0.0036	0.6
Uniform medium sand	0.0009	0.3
Clean, well-graded sand	0.0001	0.1
Uniform fine sand	$36\cdot10^{-6}$	0.06
Well-graded fine sand	$4\cdot10^{-6}$	0.02
Silty sand	10^{-6}	0.01
Uniform silt	$36\cdot10^{-8}$	0.006
Sandy clay	$4\cdot10^{-8}$	0.002
Silty clay	10^{-8}	0.001
Clay	$64\cdot10^{-10}$	0.0008
Colloidal clay	$9\cdot10^{-11}$	0.00003

1.5.9. Brittle versus Ductile Failure.

The terms ductile failure and brittle failure are often used in literature for the failure of materials with shear strength and tensile strength.

"In materials science, ductility is a solid material's ability to deform under tensile stress; this is often characterized by the material's ability to be stretched into a wire. Malleability, a similar property, is a material's ability to deform under compressive stress; this is often characterized by the material's ability to form a thin sheet by hammering or rolling. Both of these mechanical properties are aspects of plasticity, the extent to which a solid material can be plastically deformed without fracture. Ductility and malleability are not always coextensive – for instance, while gold has high ductility and malleability, lead has low ductility but high malleability. The word ductility is sometimes used to embrace both types of plasticity.
A material is brittle if, when subjected to stress, it breaks without significant deformation (strain). Brittle materials absorb relatively little energy prior to fracture, even those of high strength. Breaking is often accompanied by a snapping sound. Brittle materials include most ceramics and glasses (which do not deform plastically) and some polymers, such as PMMA and polystyrene. Many steels become brittle at low temperatures (see ductile-brittle transition temperature), depending on their composition and processing. When used in materials science, it is generally applied to materials that fail when there is little or no evidence of plastic deformation before failure. One proof is to match the broken halves, which should fit exactly since no plastic deformation has occurred. Generally, the brittle strength of a material can be increased by pressure. This happens as an example in the brittle-ductile transition zone at an approximate depth of 10 kilometers in the Earth's crust, at which rock becomes less likely to fracture, and more likely to deform ductile." (Source Wikipedia).
In rock failure a distinction is made between brittle, brittle ductile and ductile failure. Factors determining those types of failure are the ductility number (ratio compressive strength over tensile strength), the confining pressure and the temperature. During dredging the temperature will have hardly any influence, however when drilling deep oil wells temperature will play an important role. The confining pressure, where the failure transit from brittle to ductile is called σ_{bp}.

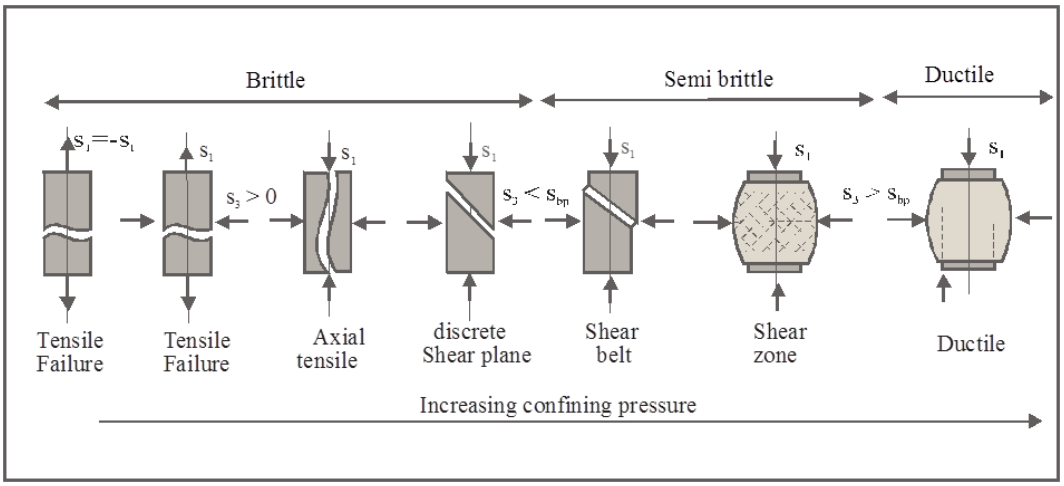

Figure 1-28: Brittle failure types (Vlasblom (2003-2007)).

Brittle failure occurs at relative low confining pressures $\sigma_3 < \sigma_{bp}$ en deviator stress $q=\sigma_1-\sigma_3 > \frac{1}{2}q_u$. The strength increases with the confining pressure, but decreases after the peak strength to a residual value. The presence of pore water can play an important role.
Brittle failure types are:

- Pure tensile failure with or without a small confining pressure.
- Axial tensile failure
- Shear plane failure

Brittle ductile failure is also called semi brittle. In the transition area where $\sigma_3 \approx \sigma_{bp}$, the deformations are not restricted to local shear planes or fractures but are divided over the whole area. The residual- strength is more or less equal to the peak strength.
Ductile failure. A rock fails ductile when $\sigma_3 >> q_u$ and $\sigma_3 > \sigma_{bp}$ while the force stays constant or increases some what with increasing deformation.

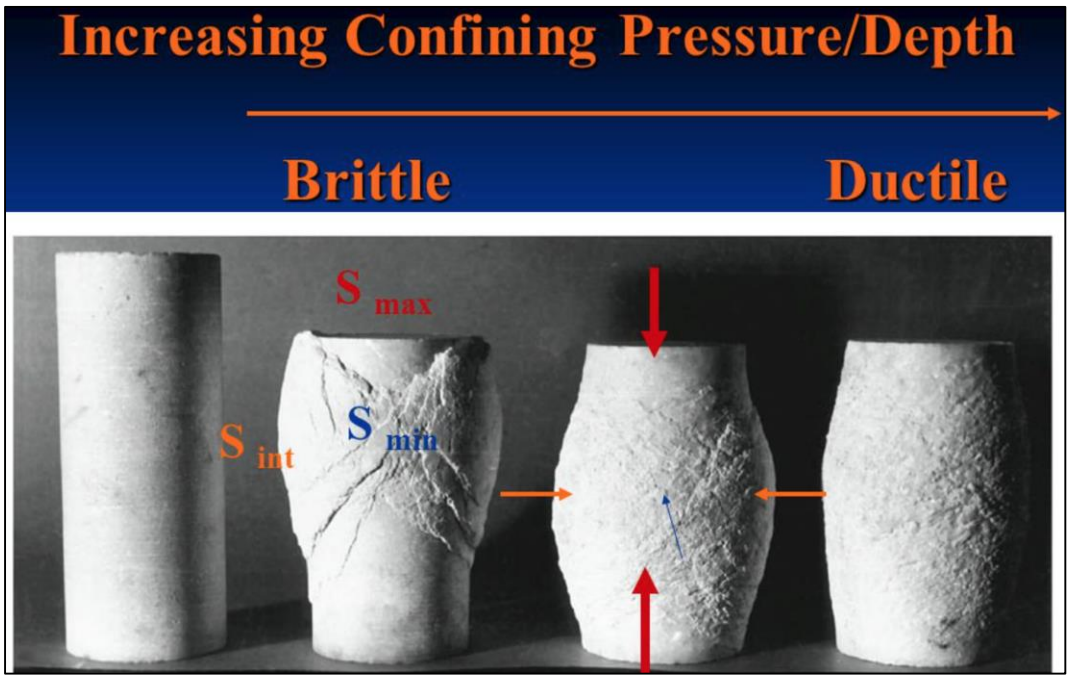

Figure 1-29: Brittle-ductile failure of marble (M.S. Patterson, Australian National University).

1.6. Soil Mechanical Tests.

1.6.1. Sieve Analysis.

The size distribution of gravel and sand particles are typically measured using sieve analysis. The formal procedure is described in ASTM D6913-04(2009). A stack of sieves with accurately dimensioned holes between a mesh of wires is used to separate the particles into size bins. A known volume of dried soil, with clods broken down to individual particles, is put into the top of a stack of sieves arranged from coarse to fine. The stack of sieves is shaken for a standard period of time so that the particles are sorted into size bins. This method works reasonably well for particles in the sand and gravel size range. Fine particles tend to stick to each other, and hence the sieving process is not an effective method. If there are a lot of fines (silt and clay) present in the soil it may be necessary to run water through the sieves to wash the coarse particles and clods through.
A variety of sieve sizes are available. The boundary between sand and silt is arbitrary. According to the Unified Soil Classification System, a #4 sieve (4 openings per inch) having 4.75mm opening size separates sand from gravel and a #200 sieve with an 0.075 mm opening separates sand from silt and clay. According to the British standard, 0.063 mm is the boundary between sand and silt, and 2 mm is the boundary between sand and gravel.

Figure 1-30: A set of sieves (Essa Australia from: www.directindustry.com).

1.6.2. Hydrometer Analysis.

The classification of fine-grained soils, i.e., soils that are finer than sand, is determined primarily by their Atterberg limits, not by their grain size. If it is important to determine the grain size distribution of fine-grained soils, the hydrometer test may be performed. In the hydrometer tests, the soil particles are mixed with water and shaken to produce a dilute suspension in a glass cylinder, and then the cylinder is left to sit. A hydrometer is used to measure the density of the suspension as a function of time. Clay particles may take several hours to settle past the depth of measurement of the hydrometer. Sand particles may take less than a second. Stoke's law provides the theoretical basis to calculate the relationship between sedimentation velocity and particle size. ASTM provides the detailed procedures for performing the Hydrometer test.
Clay particles can be sufficiently small that they never settle because they are kept in suspension by Brownian motion, in which case they may be classified as colloids.

1.6.3. Standard Penetration Test.

The standard penetration test (SPT) is an in-situ dynamic penetration test designed to provide information on the geotechnical engineering properties of soil. The test procedure is described in the British Standard BS EN ISO 22476-3, ASTM D1586 and Australian Standards AS 1289.6.3.1.

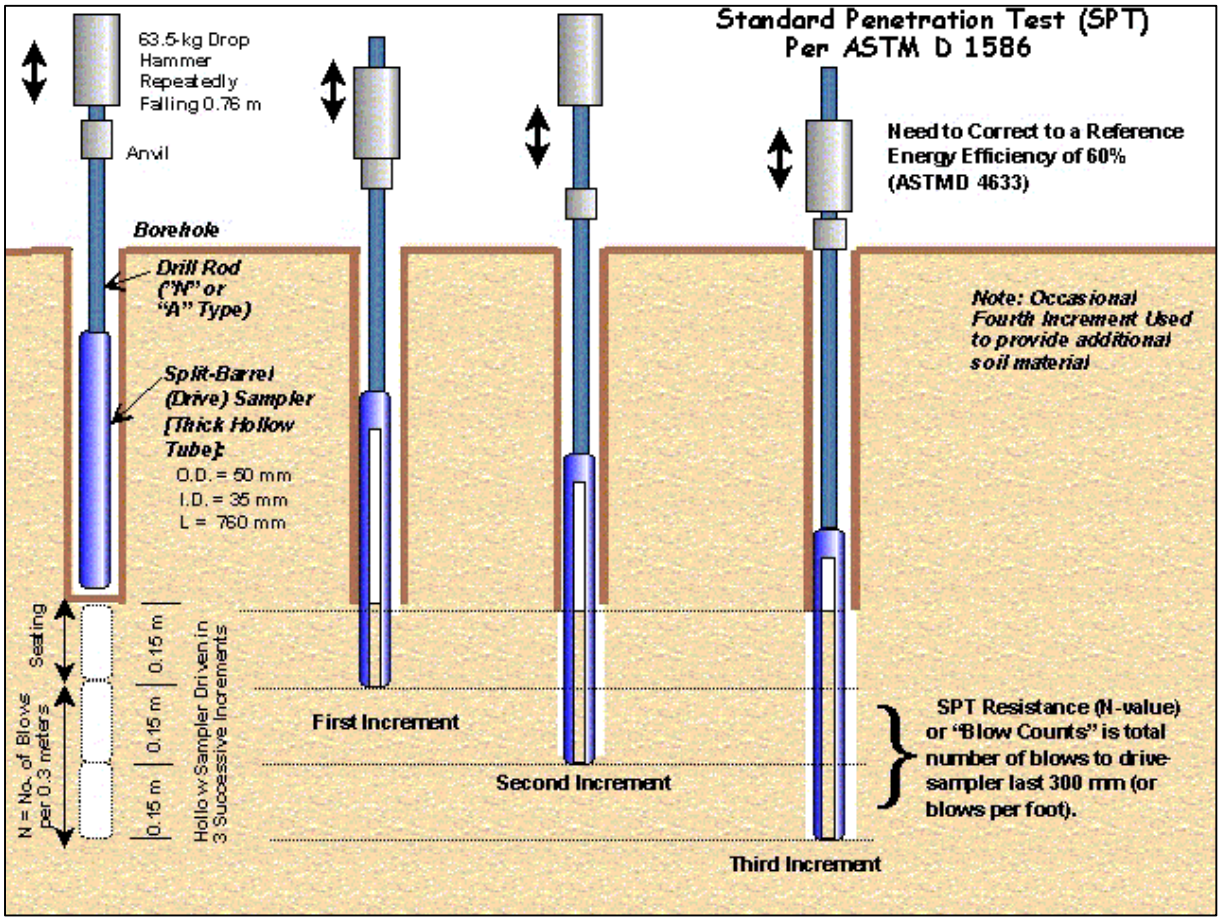

Figure 1-31: The Standard Penetration Test (www.shalviengineering.com).

The test uses a thick-walled sample tube, with an outside diameter of 50 mm and an inside diameter of 35 mm, and a length of around 650 mm. This is driven into the ground at the bottom of a borehole by blows from a slide hammer with a weight of 63.5 kg (140 lb) falling through a distance of 760 mm (30 in). The sample tube is driven 150 mm into the ground and then the number of blows needed for the tube to penetrate each 150 mm (6 in) up to a depth of 450 mm (18 in) is recorded. The sum of the number of blows required for the second and third 6 in. of penetration is termed the "standard penetration resistance" or the "N-value". In cases where 50 blows are insufficient to advance it through a 150 mm (6 in) interval the penetration after 50 blows is recorded. The blow count provides an indication of the density of the ground, and it is used in many empirical geotechnical engineering formulae.

The main purpose of the test is to provide an indication of the relative density of granular deposits, such as sands and gravels from which it is virtually impossible to obtain undisturbed samples. The great merit of the test, and the main reason for its widespread use is that it is simple and inexpensive. The soil strength parameters which can be inferred are approximate, but may give a useful guide in ground conditions where it may not be possible to obtain borehole samples of adequate quality like gravels, sands, silts, clay containing sand or gravel and weak rock. In conditions where the quality of the undisturbed sample is suspect, e.g. very silty or very sandy clays, or hard clays, it is often advantageous to alternate the sampling with standard penetration tests to check the strength. If the samples are found to be unacceptably disturbed, it may be necessary to use a different method for measuring strength like the plate test. When the test is carried out in granular soils below groundwater level, the soil may become loosened. In certain circumstances, it can be useful to continue driving the sampler beyond the distance specified, adding further drilling rods as necessary. Although this is not a standard penetration test, and should not

be regarded as such, it may at least give an indication as to whether the deposit is really as loose as the standard test may indicate.
The usefulness of SPT results depends on the soil type, with fine-grained sands giving the most useful results, with coarser sands and silty sands giving reasonably useful results, and clays and gravelly soils yielding results which may be very poorly representative of the true soil conditions. Soils in arid areas, such as the Western United States, may exhibit natural cementation. This condition will often increase the standard penetration value.
The SPT is used to provide results for empirical determination of a sand layer's susceptibility to earthquake liquefaction, based on research performed by Harry Seed, T. Leslie Youd, and others.
Despite its many flaws, it is usual practice to correlate SPT results with soil properties relevant for geotechnical engineering design. The reason being that SPT results are often the only test results available, therefore the use of direct correlations has become common practice in many countries.
Different correlations are proposed for granular and cohesive soils.

1.6.4. Cone Penetration Test.

The cone penetration test (CPT) is an in situ testing method used to determine the geotechnical engineering properties of soils and delineating soil stratigraphy. It was initially developed in the 1950s at the Dutch Laboratory for Soil Mechanics in Delft to investigate soft soils. Based on this history it has also been called the "Dutch cone test". Today, the CPT is one of the most used and accepted in situ test methods for soil investigation worldwide.
The test method consists of pushing an instrumented cone, with the tip facing down, into the ground at a controlled rate (usually 2 centimeters/second). The resolution of the CPT in delineating stratigraphic layers is related to the size of the cone tip, with typical cone tips having a cross-sectional area of either 10 or 15 cm^2, corresponding to diameters of 3.6 and 4.4 cm.
The early applications of CPT mainly determined the soil geotechnical property of bearing capacity. The original cone penetrometers involved simple mechanical measurements of the total penetration resistance to pushing a tool with a conical tip into the soil. Different methods were employed to separate the total measured resistance into components generated by the conical tip (the "tip friction") and friction generated by the rod string. A friction sleeve was added to quantify this component of the friction and aid in determining soil cohesive strength in the 1960s (Begemann, 1965). Electronic measurements began in 1948 and improved further in the early 1970s (de Reister, 1971). Most modern electronic CPT cones now also employ a pressure transducer with a filter to gather pore water pressure data. The filter is usually located either on the cone tip (the so-called U1 position), immediately behind the cone tip (the most common U2 position) or behind the friction sleeve (U3 position). Pore water pressure data aids determining stratigraphy and is primarily used to correct tip friction values for those effects. CPT testing which also gathers this piezometer data is called CPTU testing. CPT and CPTU testing equipment generally advances the cone using hydraulic rams mounted on either a heavily ballasted vehicle or using screwed-in anchors as a counter-force. One advantage of CPT over the Standard Penetration Test (SPT) is a more continuous profile of soil parameters, with CPTU data recorded typically at 2cm intervals.
In addition to the mechanical and electronic cones, a variety of other CPT-deployed tools have been developed over the years to provide additional subsurface information. One common tool advanced during CPT testing is a geophone set to gather seismic shear wave and compression wave velocities. This data helps determine the shear modulus and Poisson's ratio at intervals through the soil column for soil liquefaction analysis and low-strain soil strength analysis. Engineers use the shear wave velocity and shear modulus to determine the soil's behavior under low-strain and vibratory loads. Additional tools such as laser-induced fluorescence, X-ray fluorescence[1], soil conductivity/resistivity, membrane interface probe and cameras for capturing video imagery are also increasingly advanced in conjunction with the CPT probe. An additional CPT deployed tool used in Britain, Netherlands, Germany, Belgium and France is a piezocone combined with a tri-axial magnetometer. This is used to attempt to ensure that tests, boreholes, and piles, do not encounter unexploded ordnance (UXB) or duds. The magnetometer in the cone detects ferrous materials of 50 kg or larger within a radius of up to about 2 m distance from the probe depending on the material, orientation and soil conditions.
CPT for geotechnical applications was standardized in 1986 by ASTM Standard D 3441 (ASTM, 2004). ISSMGE provides international standards on CPT and CPTU. Later ASTM Standards have addressed the use of CPT for various environmental site characterization and groundwater monitoring activities. Particularly for geotechnical soil investigations, CPT is gaining popularity compared to standard penetration testing as a method of geotechnical soil investigation by its increased accuracy, speed of deployment, more continuous soil profile and reduced cost over other soil testing methods. The ability to advance additional in situ testing tools using the CPT direct push drilling rig, including the seismic tools described above, are accelerating this process.

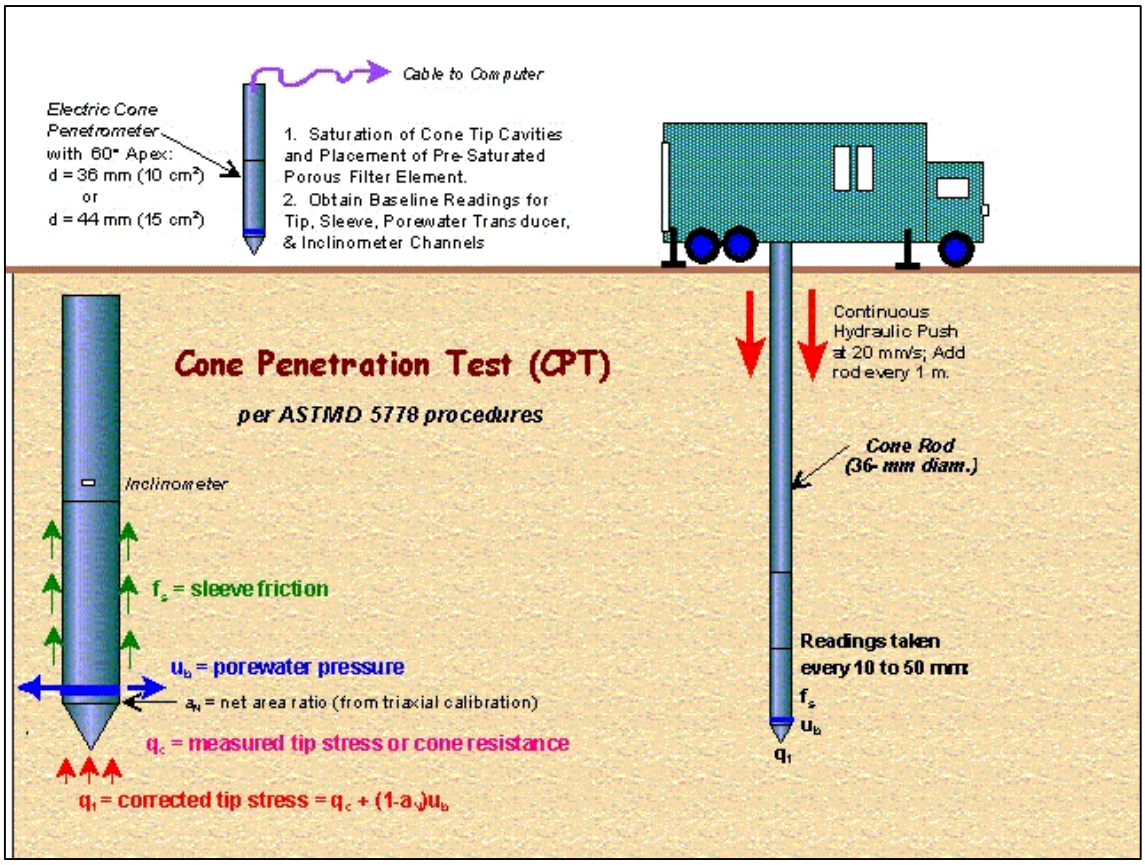

Figure 1-32: A typical CPT test setup (www.geotechdata.com).

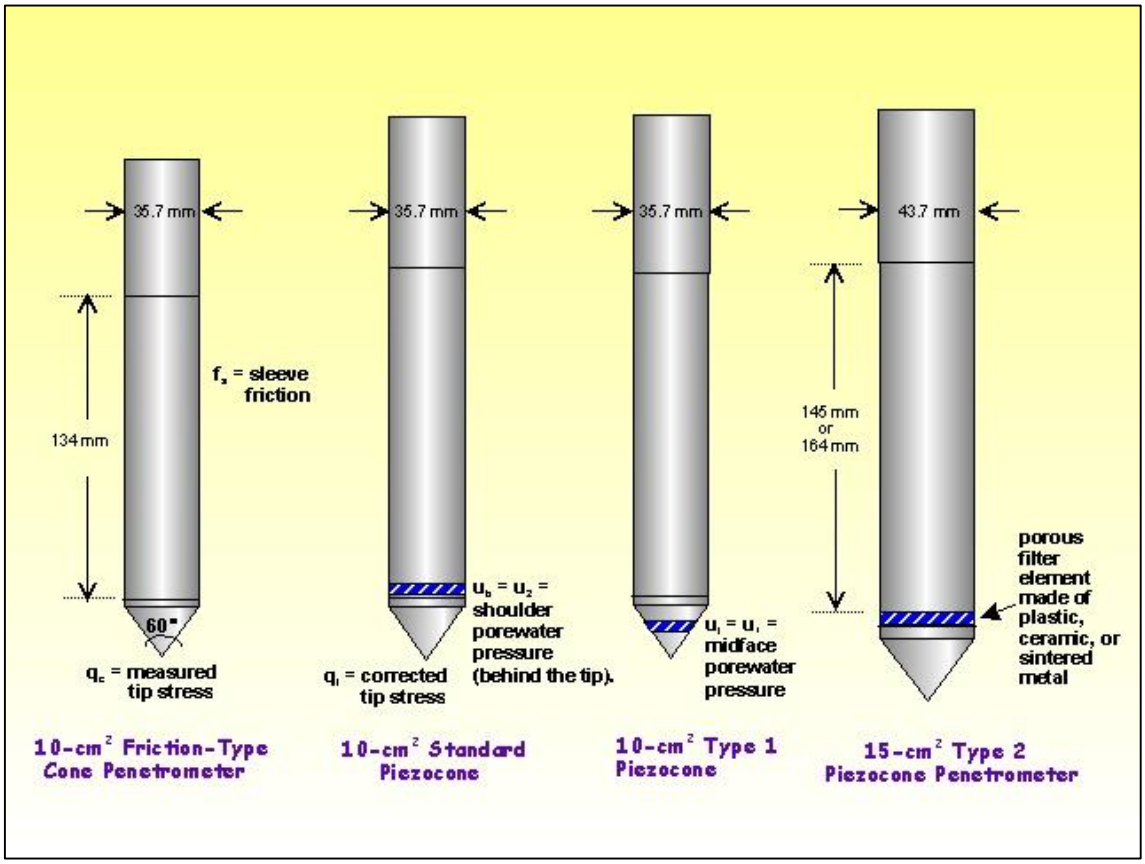

Figure 1-33: Several configurations of cones (www.geotechdata.info).

Figure 1-34: Several cone configurations.

1.6.5. Triaxial Test.

A triaxial shear test is a common method to measure the mechanical properties of many deformable solids, especially soil (e.g. sand, clay) and rock, and other granular materials or powders. There are several variations on the test. Although the name triaxial test suggests that the stresses would be different in three directions, this is not true in the test as is usually done. In this test with oil or water as confining medium, the confining pressures are equal in all directions (i.e. in terms of principal stresses: for a compression test: $\sigma_1 \neq \sigma_2 = \sigma_3$ and for tensile: $\sigma_1 = \sigma_2 \neq \sigma_3$). Only in a true triaxial test the stresses in all three directions can be different (i.e. $\sigma_1 \neq \sigma_2 \neq \sigma_3$). For loose granular materials like sand or gravel, the material is contained in a cylindrical latex sleeve with a flat, circular metal plate or platen closing off the top and bottom ends. This cylinder is placed into a bath of water (mostly water but may be any other fluid) to provide pressure along the sides of the cylinder. The top platen can then be mechanically driven up or down along the axis of the cylinder to squeeze the material. The distance that the upper platen travels is measured as a function of the force required to move it, as the pressure of the surrounding water is carefully controlled. The net change in volume of the material is also measured by how much water moves in or out of the surrounding bath. The test for cohesive (non-loose) materials (e.g. clay, rock) is similar to the test for loose granular materials. For rock testing the sleeve may be a thin metal sheeting rather than latex. Triaxial testing on rock is fairly seldom done because the high forces and pressures required to break a rock sample imply very costly and cumbersome testing equipment available at few laboratories in the world. During the test the pore pressures of fluids (e.g. water, oil) or gasses in the sample may be measured.

The principle behind a triaxial shear test is that the stress applied in the vertical direction (along the axis of the cylindrical sample) can be different from the stresses applied in the horizontal directions perpendicular to the sides of the cylinder, i.e. the confining pressure). In a homogeneous and isotropic material this produces a non-hydrostatic stress state, with shear stress that may lead to failure of the sample in shear. In non-homogeneous and anisotropic samples (e.g. bedded or jointed samples) failure may occur due to bending moments and, hence, failure may be tensile. Also combinations of bending and shear failure may happen in inhomogeneous and anisotropic material.
A solid is defined as a material that can support shear stress without moving. However, every solid has an upper limit to how much shear stress it can support. The triaxial test is designed to measure that limit. The stress on the platens is increased until the material in the cylinder fails and forms sliding regions within itself, known as shear bands. A motion where a material is deformed under shear stress is known as shearing. The geometry of the shearing in a triaxial test typically causes the sample to become shorter while bulging out along the sides. The

stress on the platen is then reduced and the water pressure pushes the sides back in, causing the sample to grow taller again. This cycle is usually repeated several times while collecting stress and strain data about the sample.
During the shearing, a granular material will typically have a net gain or loss of volume. If it had originally been in a dense state, then it typically gains volume, a characteristic known as Reynolds' dilatancy. If it had originally been in a very loose state, then contraction may occur before the shearing begins or in conjunction with the shearing.

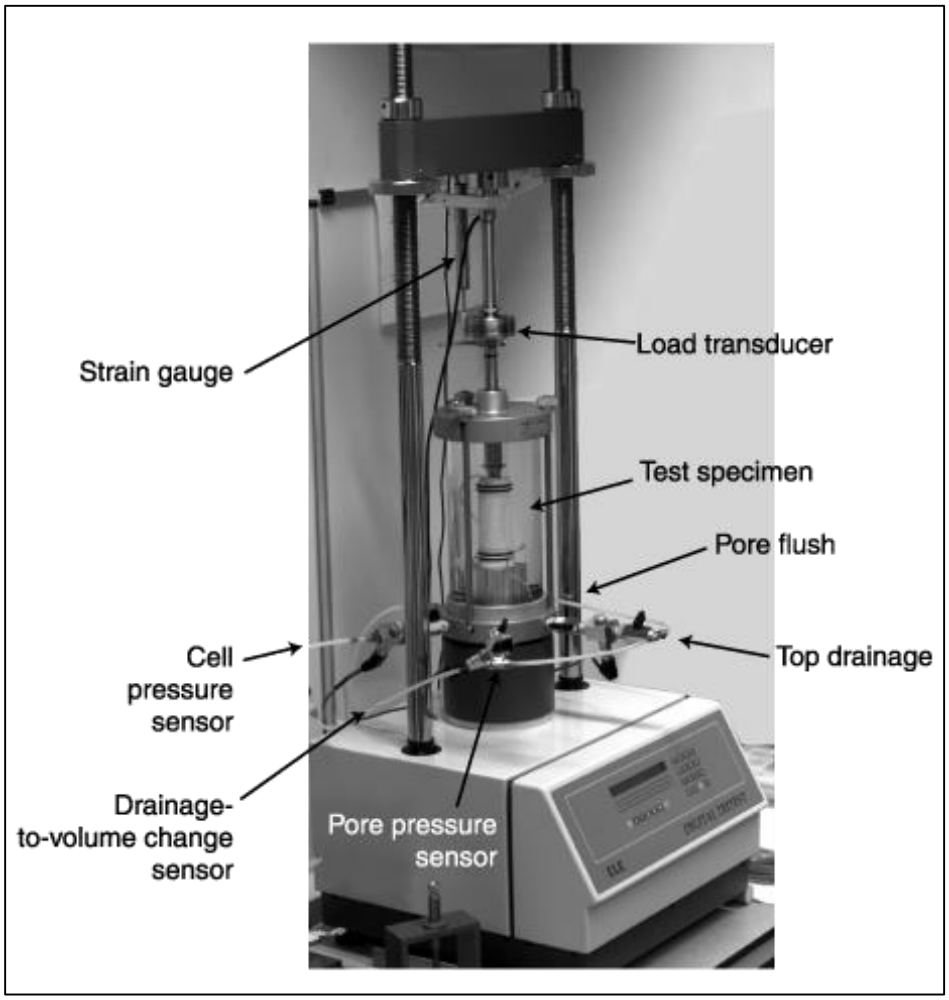

Figure 1-35: The Triaxial apparatus (www.geotechdata.info).

From the triaxial test data, it is possible to extract fundamental material parameters about the sample, including its angle of shearing resistance, apparent cohesion, and dilatancy angle. These parameters are then used in computer models to predict how the material will behave in a larger-scale engineering application. An example would be to predict the stability of the soil on a slope, whether the slope will collapse or whether the soil will support the shear stresses of the slope and remain in place. Triaxial tests are used along with other tests to make such engineering predictions.
The triaxial test can be used to determine the shear strength of a discontinuity. A homogeneous and isotropic sample (see above) fails due to shear stresses in the sample. If a sample with a discontinuity is orientated such that the discontinuity is about parallel to the plane in which maximum shear stress will be developed during the test, the sample will fail due to shear displacement along the discontinuity, and hence, the shear strength of a discontinuity can be calculated.

There are several variations of the triaxial test:

1.6.5.1. Consolidated Drained (CD).

In a consolidated drained test the sample is consolidated and sheared in compression with drainage. The rate of axial deformation is kept constant, i.e. is strain controlled. The idea is that the test allows the sample and the pore pressures to fully consolidate (i.e. adjust) to the surrounding stresses. The test may take a long time to allow the sample to adjust, in particular low permeability samples need a long time to drain and adjust stain to stress levels.

1.6.5.2. Consolidated Undrained (CU).

In a consolidated undrained test the sample is not allowed to drain. The shear characteristics are measured under undrained conditions and the sample is assumed to be fully consolidated under the stresses applied that should be similar to the field conditions. Test in particular used if a change in stress is to happen without time for further consolidation.

1.6.5.3. Unconsolidated Undrained (UU).

In an unconsolidated undrained test the sample is not allowed to drain. The sample is compressed at a constant rate (strain-controlled).

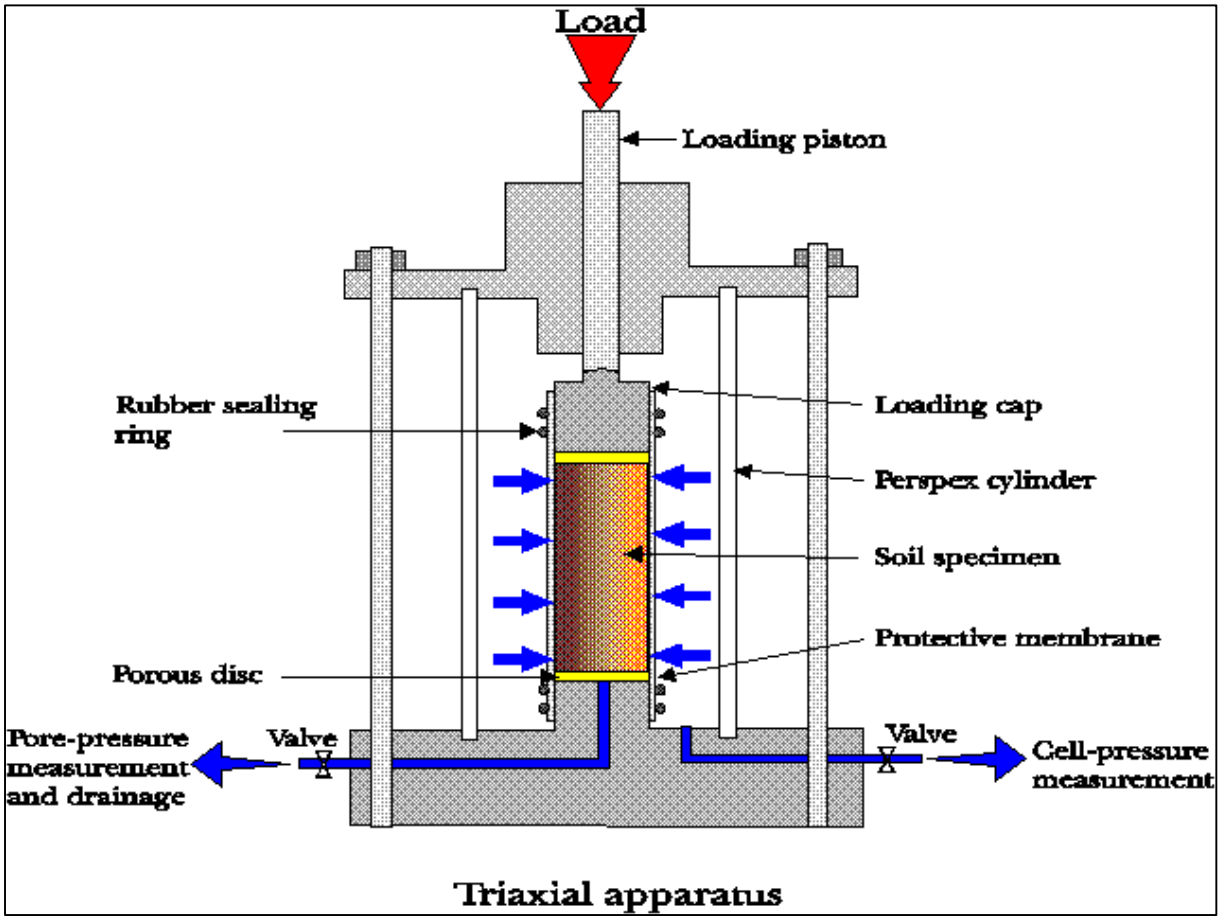

Figure 1-36: The Triaxial apparatus cross-section (civilblog.org).

1.6.6. Shear Test.

A direct shear test also known as shear box test is a laboratory or field test used by geotechnical engineers to measure the shear strength properties of soil or rock material, or of discontinuities in soil or rock masses. For soil the U.S. and U.K. standards defining how the test should be performed are ASTM D 3080 and BS 1377-7:1990 respectively to establish the shear strength properties of soil. It is also possible to estimate typical values of the shear strength parameters based on the type and classification of the soils. For rock the test is generally restricted to rock with (very) low (shear) strength. The test is, however, standard practice to establish the shear strength properties of discontinuities in rock.

The test is performed on three or four specimens from a relatively undisturbed soil sample. A specimen is placed in a shear box which has two stacked rings to hold the sample; the contact between the two rings is at approximately the mid-height of the sample. A confining stress is applied vertically to the specimen, and the upper ring is pulled laterally until the sample fails, or through a specified strain. The load applied and the strain induced is recorded at frequent intervals to determine a stress-strain curve for the confining stress.
Direct Shear tests can be performed under several conditions. The sample is normally saturated before the test is run, but can be run at the in-situ moisture content. The rate of strain can be varied to create a test of undrained or drained conditions, depending whether the strain is applied slowly enough for water in the sample to prevent pore-water pressure buildup.

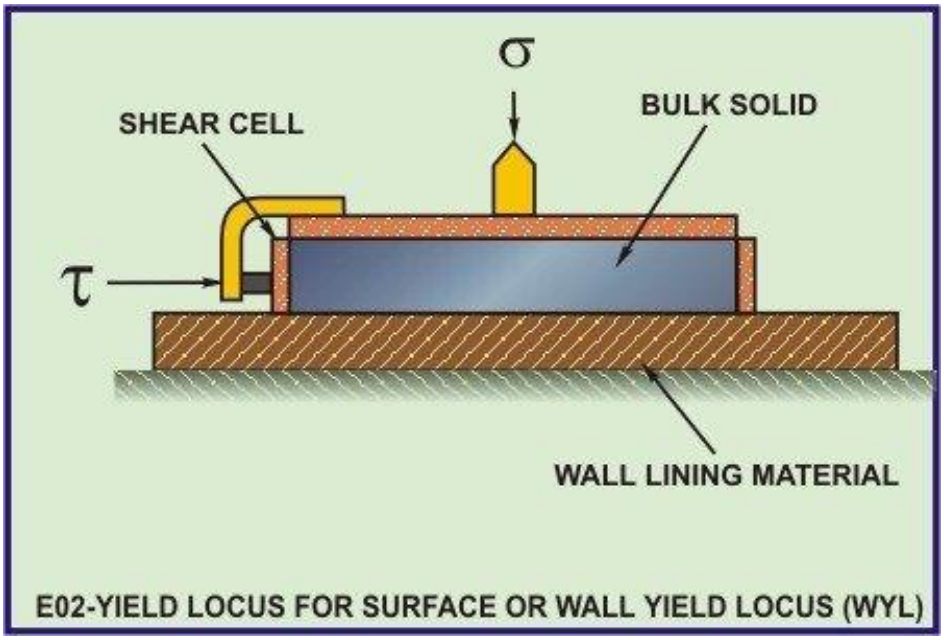

Figure 1-37: The direct shear test.

Several specimens are tested at varying confining stresses to determine the shear strength parameters, the soil cohesion (c) and the angle of internal friction (commonly friction angle) (φ). The results of the tests on each specimen are plotted on a graph with the peak (or residual) stress on the x-axis and the confining stress on the y-axis. The y-intercept of the curve which fits the test results is the cohesion, and the slope of the line or curve is the friction angle.

1.6.7. Point Load Test.

The Point Load Strength test is intended as an index test for the strength classification of rock materials. It may also be used to predict other strength parameters with which it is correlated, for example the unconfined compressive and the tensile strength. It is measured in accordance with the procedures recommended in **ASTM D5731**, usually with **NX**-size core samples. The testing machine consists of a loading frame, which measures the force required to break the sample, and a system for measuring the distance between the two platen contact points. Rock specimens in the form of either core, cut blocks, or irregular lumps are broken by application of concentrated load through a pair of spherically truncated, conical platens. The applied force at failure of the sample and distance between the platen tips are recorded in order to calculate the point load index as follows:

$$I_s = \frac{F}{D_e^2} \qquad (1\text{-}44)$$

Another test that is familiar with the Brazilian splitting test is the point load strength test. This test is executed either axial, diametrical or on irregular pieces. The point load test is frequently used to determine the strength when a large number of samples have to be tested. The tests give for brittle rocks, when tested under diametric loading, values reasonable close to the **BTS**. Also it is suggested that **PLS=0.8*BTS**, it is suggested to establish such a relation based on both tests.

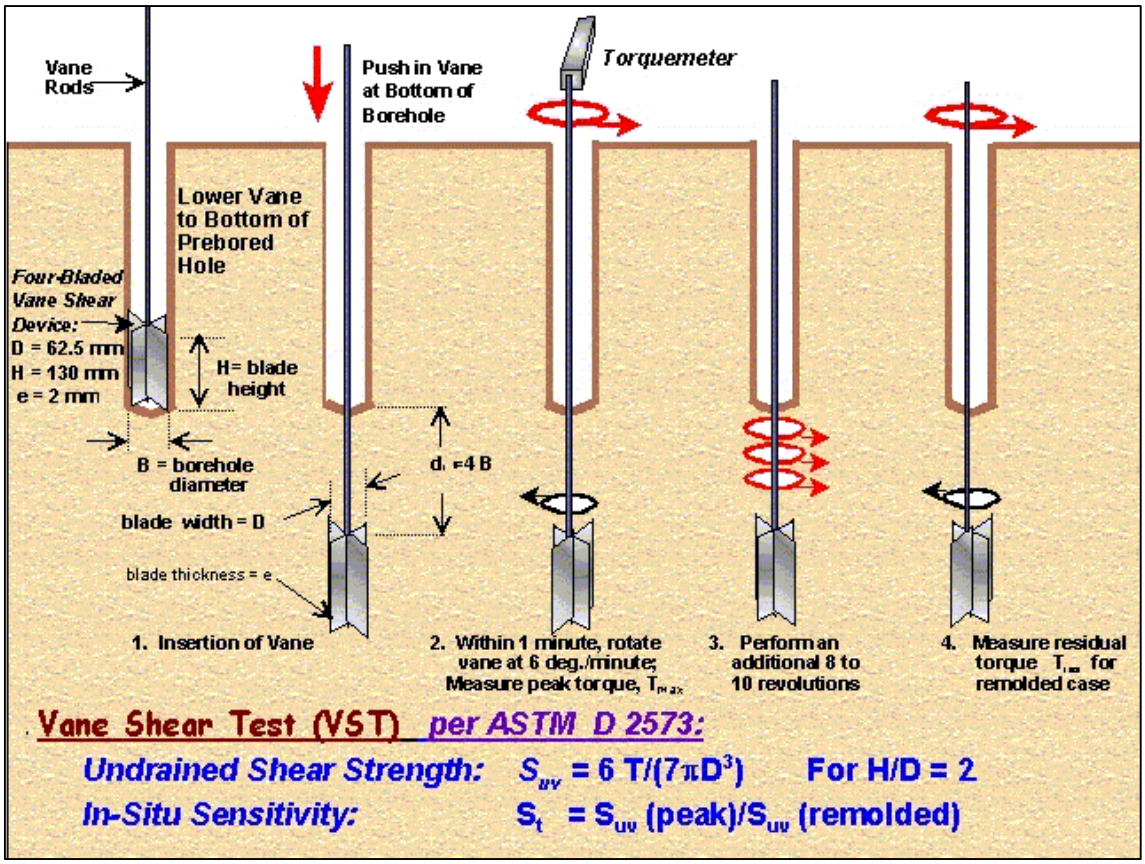

Figure 1-38: The vane shear test (English.geocpt.es).

Figure 1-39: Shear vane and Torvane for soil testing (www.humboldtmfg.com).

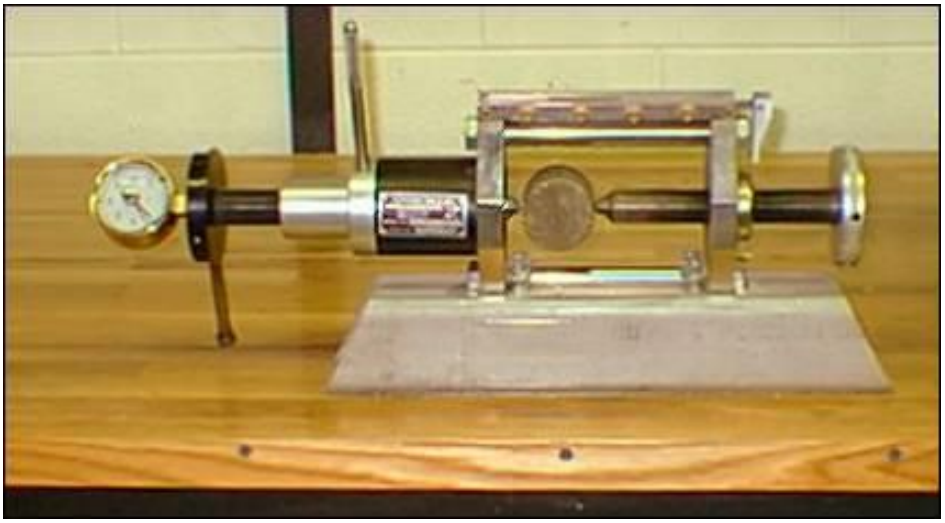

Figure 1-40: Point load test facility (inside.mines.edu).

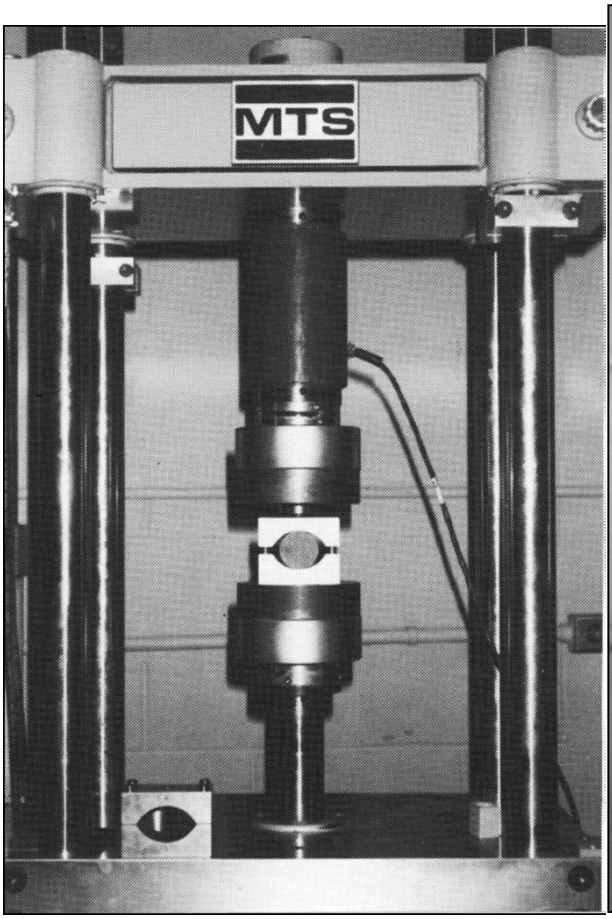

Figure 1-41: Brazilian splitting tension test.

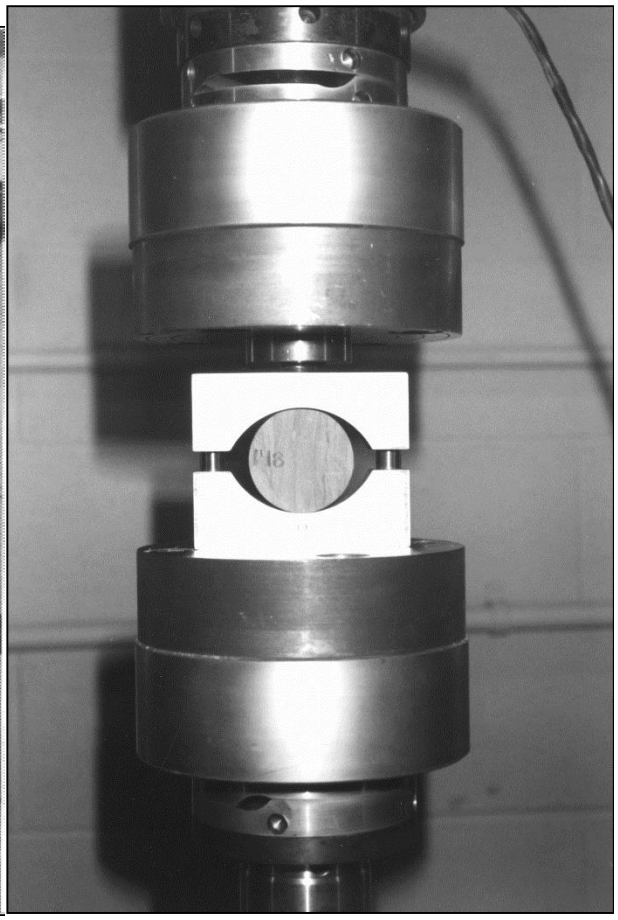

Figure 1-42: BTS zoomed.

Figure 1-43: A BTS test after failure.

1.7. Nomenclature.

G_s	Specific gravity	-
ρ_s	Density of the soil	kg/m^3
ρ_w	Density of water	kg/m^3
g	Gravitational constant (9.81 m/s^2)	m/s^2
M_t	Mass of the soil, total mass	kg
M_s	Mass of the solids	kg
M_w	Mass of the water	kg
M_a	Mass of the air	kg
V_t	Volume of the soil, total volume	m^3
V_s	Volume of the solids	m^3
V_w	Volume of the water	m^3
V_a	Volume of the air	m^3
ρ_t	Density of the soil	kg/m^3
γ_t	Unit weight of the soil	N/ m^3
g	Gravitational constant (9.81 m/s^2)	m/s^2
D_r	Relative density	-
e	Current void ratio of the soil in-situ	-
e_{max}	Void ratio of the soil at its loosest condition	-
e_{min}	Void ratio of the soil at its densest condition	-
n	Porosity of the soil in-situ	-
n_{max}	Porosity of the soil at its loosest condition	-
n_{min}	Porosity of the soil in its densest condition	-
V_v	Volume of the voids/pores	m^3
V_s	Volume of the solids/grains/particles	m^3
n	Porosity	-
e	Void ratio	-
C_t	Sorting coefficient	-
C	Sorting coefficient	-
K	Hydraulic conductivity	m^2

k	Permeability	**m/s**
f(n)	porosity function	**-**
C	sorting coefficient	
d_e	effective grain diameter	**mm**
d_{10}	Grain diameter where 10% is smaller	**mm**
d_{60}	Grain diameter where 60% is smaller	**mm**
U	Grain uniformity coefficient	**-**
ν	kinematic viscosity	
μ	Dynamic viscosity	**Pa.s**
ρ_w	Water density	**kg/m^3**
γ_w	Unit weight of water	**N/m^3**
Q	units of volume per time	**m^3/s**
K	intrinsic permeability	**m^2**
k	permeability	**m/s**
A	cross sectional area	**m^2**
L	Length	**m**
u_a	Start excess pore pressure	**Pa**
u_b	End excess pore pressure	**Pa**
μ	dynamic viscosity of the fluid	**Pa.s**
c	Cohesion	**kPa**
UCS	Unconfined Compressive Strength	**kPa**
V	The total volume of soil	**m^3**
n_i	Initial porosity	**-**
n_{cv}	Porosity at constant volume	**-**
ε	Dilatation	**-**
σ_c	Unconfined Compressive Strength	**kPa**
F	Maximum Failure Load	**kN**
A	Cross-sectional area of the core sample	**m^2**
E	Deformation modulus	**N/m^2**
W	Specific work of failure	**J/m^3**
σ_T	Brazilian Tensile Strength (BTS)	**kPa**
D	Diameter of the core sample	**m**
F	Maximum Failure Load	**kN**
L	Length of the core sample	**m**
I_S	Point load index	**kPa**
F	Failure load	**kN**
D_e	Distance between platen tips	**m**
D_e^2	= D^2 for diametrical test	**m^2**
D_e^2	= $4A/\pi$ = for axial, block and lump test	**m^2**
A	= W.D = minimum cross-sectional area of a plane through the platen contact points	**m^2**
ρ_w	Density of water	**kg/m^3**
z_w	Depth below the water table	**m**
u	Hydrostatic pressure	**kPa**
g	Gravitational constant	**m/s^2**
σ_1	the major principal stress	**kPa**
σ_3	the minor principal stress	**kPa**
τ	the shear strength $\tau = S_u$ (or sometimes c_u)	**kPa**
S_u	the undrained strength	**kPa**
σ'	$(\sigma - u)$ the effective stress	**kPa**
σ	Total stress applied normal to the shear plane	**kPa**
u	Pore water pressure acting on the same plane	**kPa**
φ	Effective stress friction angle or the angle of internal friction after Coulomb friction	**deg**
c'	Cohesion	**kPa**
τ	The shear strength $\tau = S_u$ (or sometimes c_u)	**kPa**

1.8. Notes.

Chapter 2: The Terminal Settling Velocity of Particles.

2.1. Introduction.

In many cases in hydraulic transport there will be equilibrium between erosion and deposition. In order to understand this, both deposition and erosion (initiation of motion) will be discussed. The settling velocity of grains depends on the grain size, shape and specific density. It also depends on the density and the viscosity of the carrier liquid the grains are settling in, it also depends upon whether the settling process is laminar or turbulent.
Most slurry transport models use the terminal settling velocity, the particle drag coefficient or the particle Froude number. So it is important to have a good unserstanding of these parameters.

2.2. The Equilibrium of Forces.

The settling velocity of grains depends on the grain size, shape and specific density. It also depends on the density and the viscosity of the liquid the grains are settling in, and it depends upon whether the settling process is laminar or turbulent. Discrete particles do not change their size, shape or weight during the settling process (and thus do not form aggregates). A discrete particle in a liquid will settle under the influence of gravity. The particle will accelerate until the frictional drag force of the liquid equals the value of the gravitational force, after which the vertical (settling) velocity of the particle will be constant (Figure 2-1), the so called terminal settling velocity.

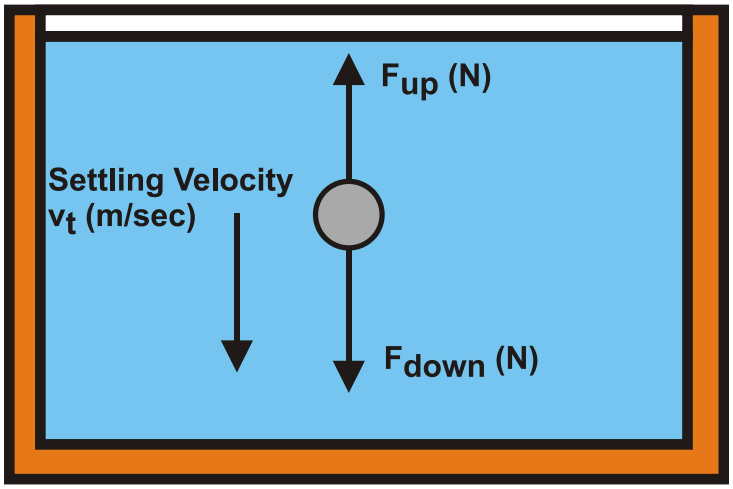

Figure 2-1: Forces on a settling particle.

The upward directed force on the particle, caused by the frictional drag of the liquid, can be calculated by:

$$F_{up} = C_D \cdot \frac{1}{2} \cdot \rho_l \cdot v_t^2 \cdot A \qquad (2\text{-}1)$$

The downward directed force, caused by the difference in density between the particle and the water can be calculated by:

$$F_{down} = (\rho_s - \rho_l) \cdot g \cdot V \cdot \psi \qquad (2\text{-}2)$$

In this equation a shape factor ψ is introduced to compensate for the shape of real sand grains. This shape factor is 1 for spheres and about 0.7 for real sand particles. The projected surface of the particle is:

$$A = \frac{\pi}{4} \cdot d^2 \qquad (2\text{-}3)$$

The volume of the particle is:

$$V = \frac{\pi}{6} \cdot d^3 \qquad \textbf{(2-4)}$$

In general, the terminal settling velocity v_t can be determined with the following equation:

$$v_t = \sqrt{\frac{4 \cdot g \cdot (\rho_s - \rho_l) \cdot d \cdot \psi}{3 \cdot \rho_l \cdot C_D}} \qquad \textbf{(2-5)}$$

The Reynolds number of the settling process determines whether the process is laminar or turbulent. The Reynolds number can be determined by:

$$Re_p = \frac{v_t \cdot d}{\nu_l} \qquad \textbf{(2-6)}$$

2.3. The Drag Coefficient.

In equation (2-5) all parameters are assumed to be known, except for the drag coefficient C_D.

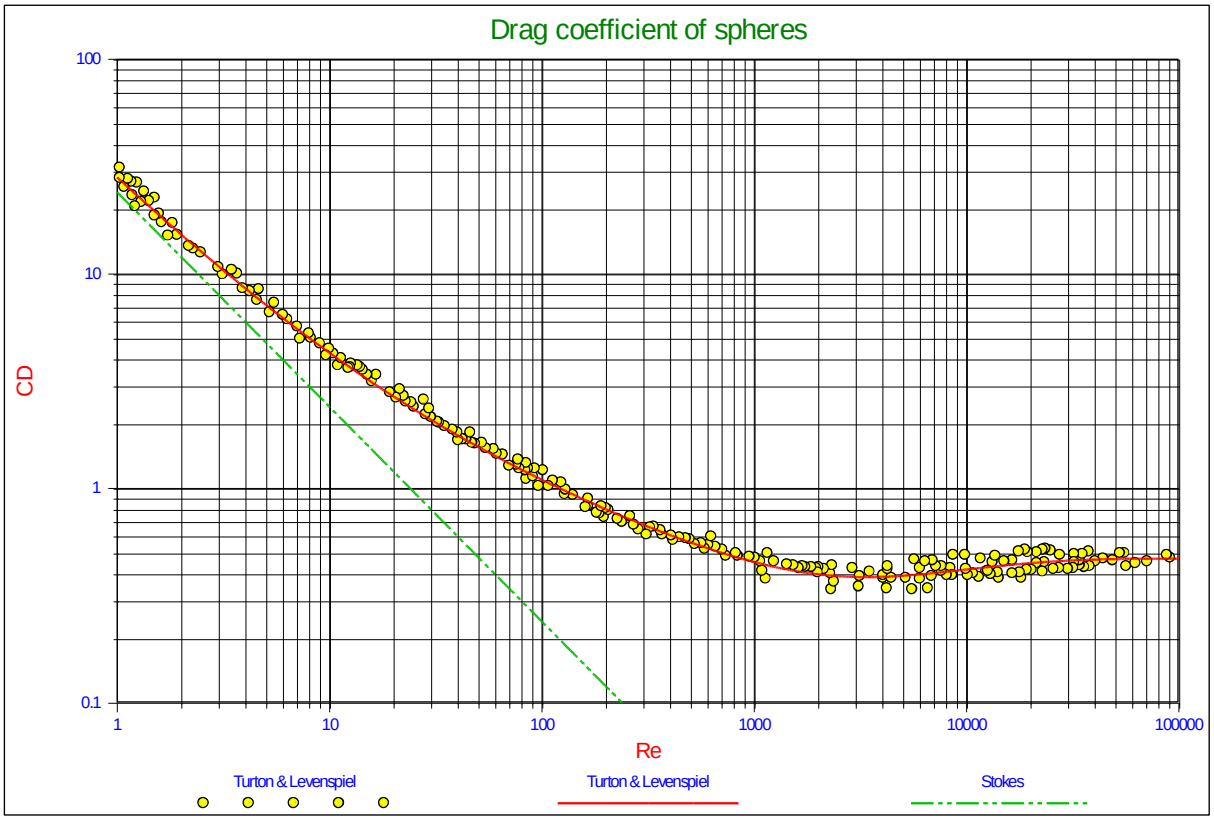

Figure 2-2: Experimental data for drag coefficients of spheres as a function of the Reynolds number (Turton & Levenspiel, 1986).

The drag coefficient C_D for spheres depends upon the Reynolds number according to:

The laminar region:

$$Re_p < 1 \qquad \Rightarrow \qquad C_D = \frac{24}{Re_p} \qquad \textbf{(2-7)}$$

The transitional region:

$$1 < Re_p < 2000 \quad \Rightarrow \quad C_D = \frac{24}{Re_p} + \frac{3}{\sqrt{Re_p}} + 0.34 \tag{2-8}$$

The turbulent region:

$$Re_p > 2000 \quad \Rightarrow \quad C_D = 0.445 \tag{2-9}$$

As can be seen from the above equations, the drag coefficient C_D is not continuous at the transition points of $Re_p=1$ and $Re_p=2000$. To get a smooth continuous curve the following equations can be applied:

The laminar region:

$$Re_p < 1 \quad \Rightarrow C_D = Re_p \cdot \left(\frac{24}{Re_p} + \frac{3}{\sqrt{Re_p}} + 0.34\right) + (1-Re_p) \cdot \frac{24}{Re_p} \tag{2-10}$$

The transitional region:

$$1 < Re_p < 2000 \quad \Rightarrow C_D = \frac{24}{Re_p} + \frac{3}{\sqrt{Re_p}} + 0.34 \tag{2-11}$$

The turbulent region:

$$Re_p > 10000 \quad \Rightarrow C_D = \frac{10000}{Re_p} \cdot \left(\frac{24}{Re_p} + \frac{3}{\sqrt{Re_p}} + 0.34\right) + \left(1 - \frac{10000}{Re_p}\right) \cdot 0.445 \tag{2-12}$$

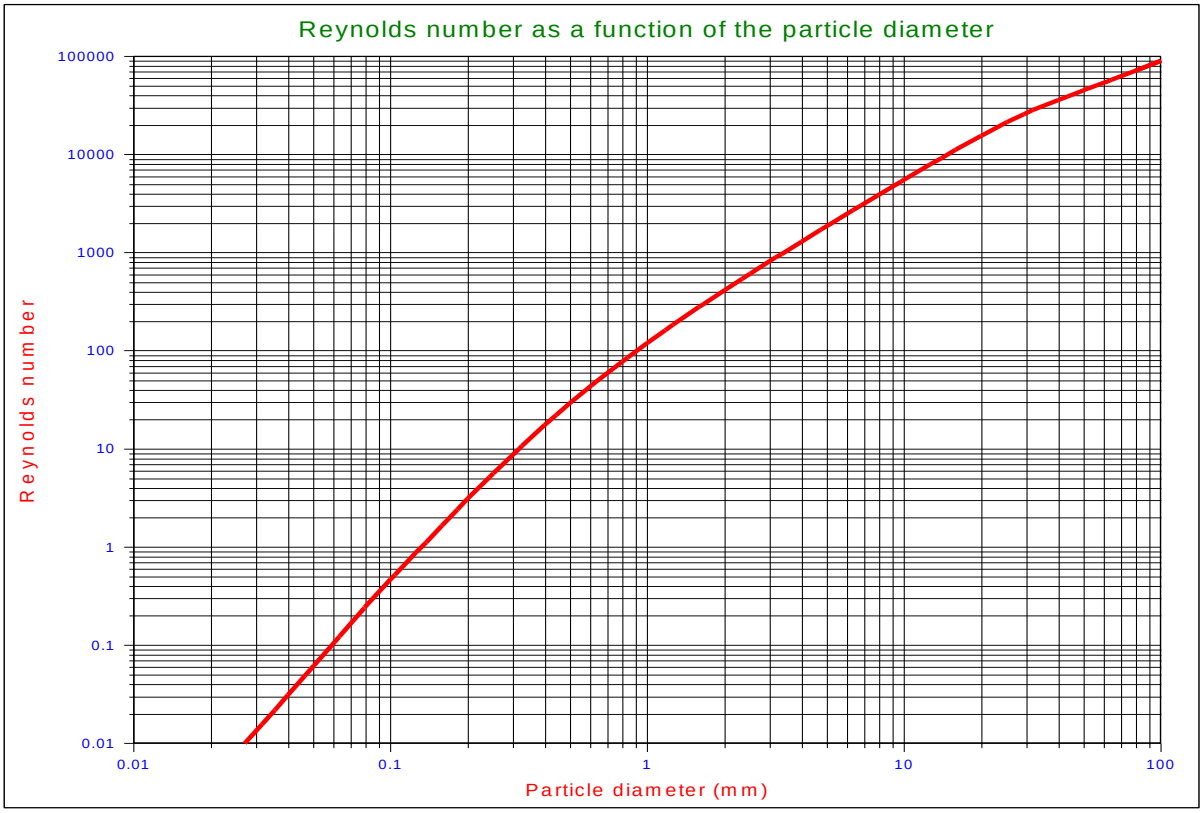

Figure 2-3: The particle Reynolds number as a function of the particle diameter.

Figure 2-3 shows the particle Reynolds number as a function of the particle diameter for sands and gravels, using the Ruby & Zanke (1977) equation.

Another equation for the transitional region has been derived by Turton & Levenspiel (1986):

$$C_D = \frac{24}{Re_p} \cdot (1 + 0.173 \cdot Re_p^{0.657}) + \frac{0.413}{1 + 16300 \cdot Re_p^{-1.09}} \qquad \textbf{(2-13)}$$

The models derived to describe the Shields curve use the drag coefficient of spheres and hardly any discussion about this has been found in literature, although it is known that for sands and gravels the drag coefficients, especially at large Reynolds numbers, are larger than the drag coefficient for spheres. Engelund & Hansen (1967) found the following equation based on measurements and found it best suited for natural sands and gravels (Julien, 1995):

$$C_D = \frac{24}{Re_p} + 1.5 \qquad \textbf{(2-14)}$$

It must be noted here that in general the drag coefficients are determined based on the terminal settling velocity of the particles. Wu & Wang (2006) recently gave an overview of drag coefficients and terminal settling velocities for different particle Corey shape factors. The result of their research is reflected in Figure 2-4. Figure 2-4 shows the drag coefficients as a function of the Reynolds number and as a function of the Corey shape factor. Figure 2-5 shows the drag coefficient for natural sands and gravels. The asymptotic value for large Reynolds numbers is about 1, while equation (2-14) shows an asymptotic value of 1.5.
For shells lying flat on the bed, the drag coefficient will be similar to the drag coefficient of a streamlined half body (0.09), which is much much smaller than the drag coefficient for settling (3). So there is a large asymmetry between the settling process and the erosion process of shells, while for more or less spherical sand particles the drag coefficient is considered to be the same in each direction.
Figure 2-6 shows the $\mathbf{C_D}$ coefficient as a function of the $\mathbf{Re_p}$ number. In the transition area the equations are implicit. Iteration 1 shows the resulting $\mathbf{C_D}$ values based on equations (2-7), (2-8) and (2-9), while iteration 2 shows the results based on equations (2-10), (2-11) and (2-12). It is clear from this figure that iteration 2 matches the observed data better than iteration 1, but equation (2-13) of Turton & Levenspiel (1986) matches the best. This is however for spheres and not for real sand and gravel particles.

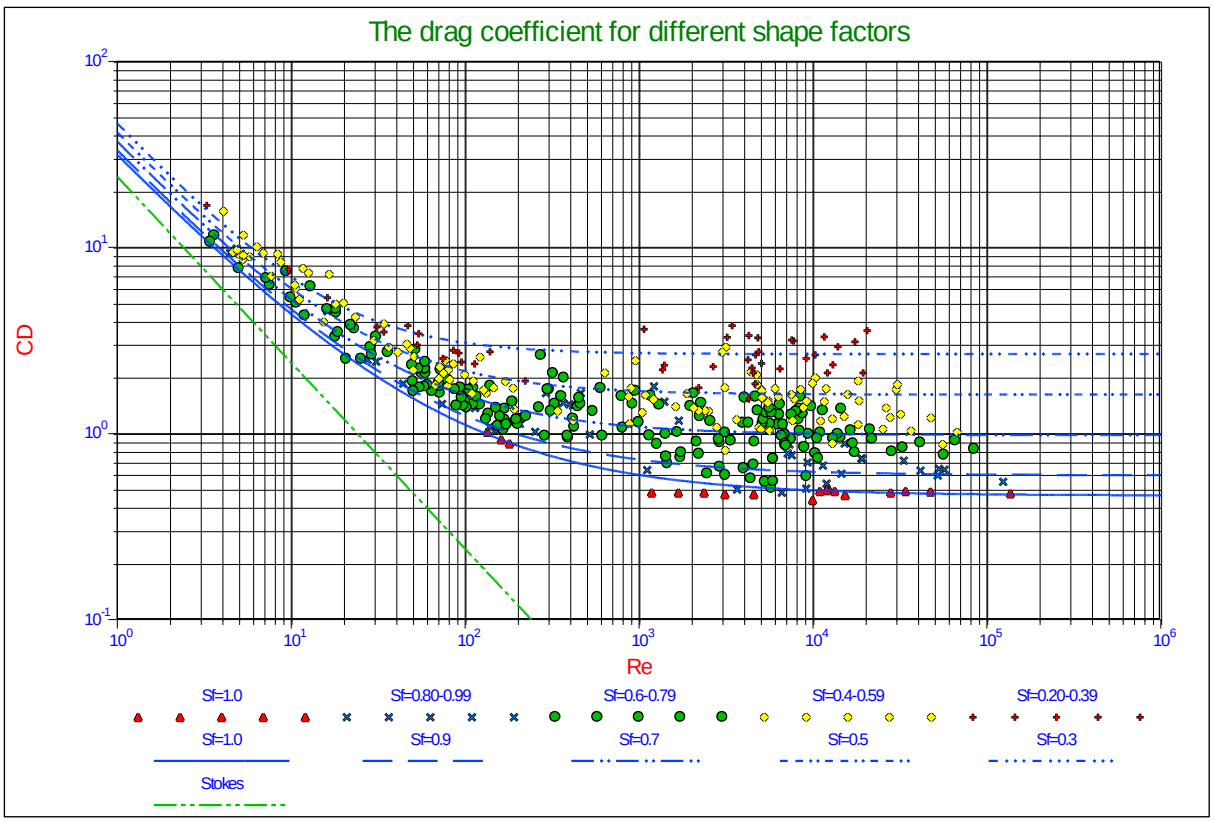

Figure 2-4: Drag coefficient as a function of the particle shape (Wu & Wang, 2006).

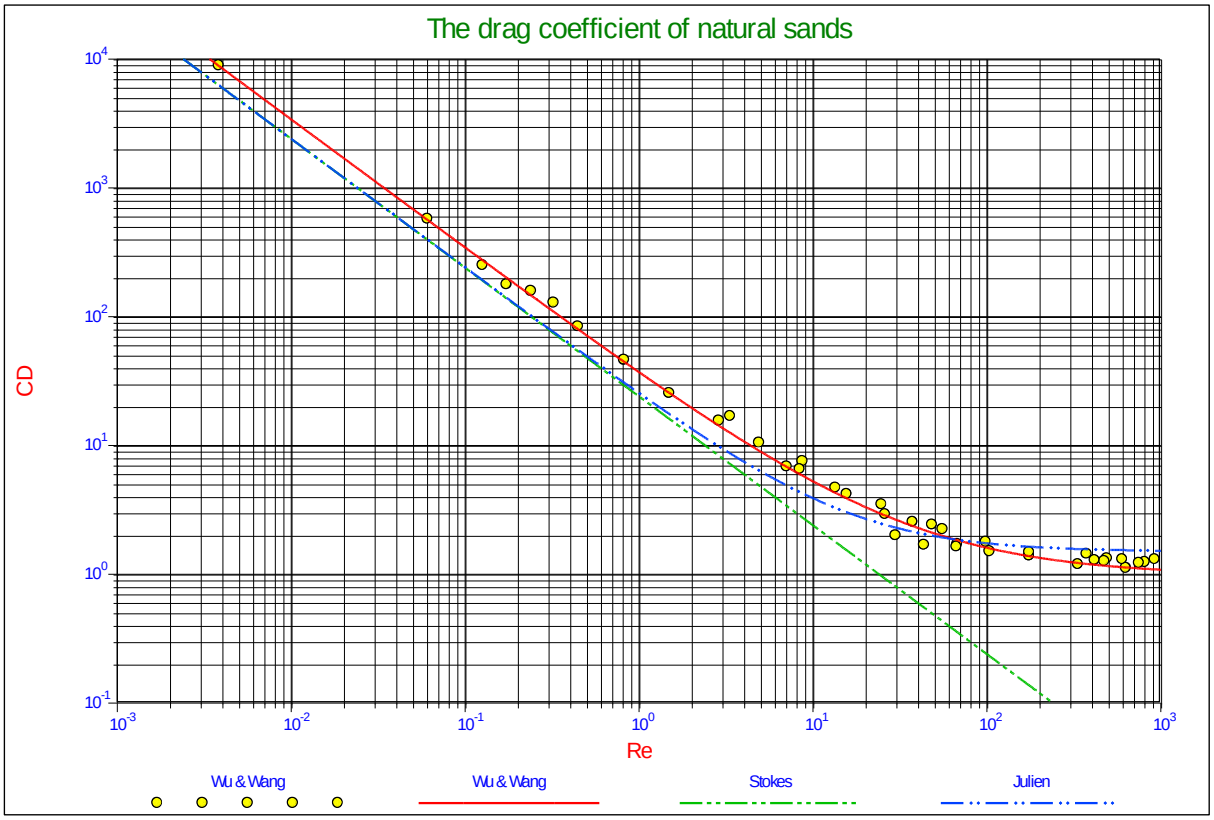

Figure 2-5: Drag coefficient for natural sediments (S_f=0.7) (Wu & Wang, 2006).

2.4. Terminal Settling Velocity Equations.

Stokes, Budryck and Rittinger used these drag coefficients to calculate settling velocities for laminar settling (Stokes), a transition zone (Budryck) and turbulent settling (Rittinger) of real sand grains. This gives the following equations for the settling velocity:

Laminar flow, **d<0.1 mm**, according to **Stokes**.

$$v_t = 424 \cdot R_{sd} \cdot d^2 \qquad \textbf{(2-15)}$$

Transition zone, **d>0.1 mm** and **d<1 mm**, according to **Budryck**.

$$v_t = 8.925 \cdot \frac{\left(\sqrt{(1 + 95 \cdot R_{sd} \cdot d^3)} - 1\right)}{d} \qquad \textbf{(2-16)}$$

Turbulent flow, **d>1 mm**, according to **Rittinger**.

$$v_t = 87 \cdot \sqrt{R_{sd} \cdot d} \qquad \textbf{(2-17)}$$

With the relative submerged density $\mathbf{R_{sd}}$ defined as:

$$R_{sd} = \frac{\rho_s - \rho_l}{\rho_l} \qquad \textbf{(2-18)}$$

In these equations the grain diameter is in mm and the settling velocity in mm/sec. Since the equations were derived for sand grains, the shape factor for sand grains is included for determining the constants in these equations.

Another equation for the transitional region (in m and m/sec) has been derived by Ruby & Zanke (1977):

$$v_t = \frac{10 \cdot \nu_l}{d} \cdot \left(\sqrt{1 + \frac{R_{sd} \cdot g \cdot d^3}{100 \cdot \nu_l^2}} - 1 \right) \qquad \textbf{(2-19)}$$

The effective drag coefficient can now be determined by:

$$C_D = \frac{4}{3} \cdot \frac{g \cdot R_{sd} \cdot d \cdot \psi}{v_t^2} \qquad \textbf{(2-20)}$$

Figure 2-7 shows the settling velocity as a function of the particle diameter for the Stokes, Budryck, Rittinger & Zanke equations.

In these equations the grain diameter is in mm and the settling velocity in mm/sec, except for the Zanke equation. Since the equations were derived for sand grains, the shape factor for sand grains is used for determining the constants in the equations. The shape factor can be introduced into the equations for the drag coefficient by dividing the drag coefficient by a shape factor ψ. For normal sands this shape factor has a value of 0.7. The viscosity of the water is temperature dependent. If a temperature of 10° is used as a reference, then the viscosity increases by 27% at 0° and it decreases by 30% at 20° centigrade. Since the viscosity influences the Reynolds number, the settling velocity for laminar settling is also influenced by the viscosity. For turbulent settling the drag coefficient does not depend on the Reynolds number, so this settling process is not influenced by the viscosity. Other researchers use slightly different constants in these equations but, these equations suffice to explain the basics of the Durand theory.

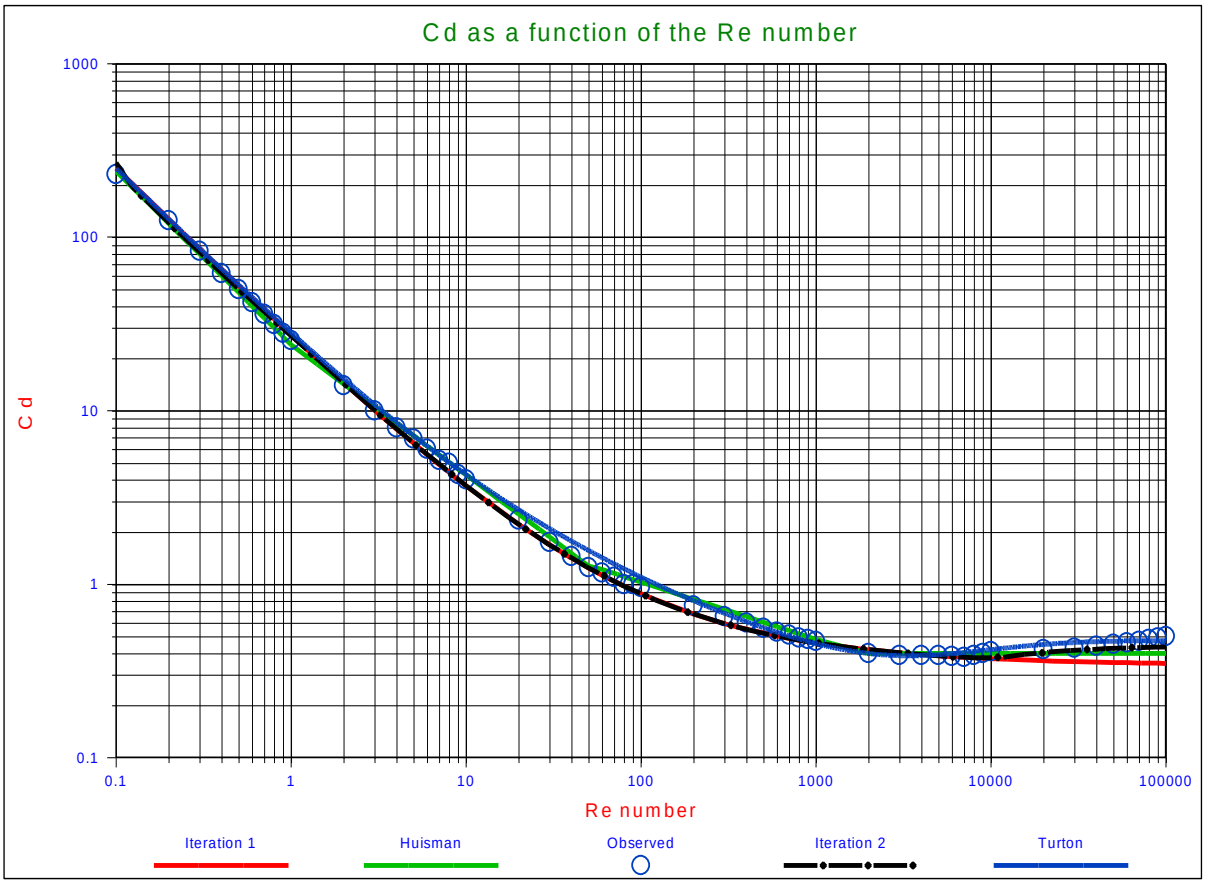

Figure 2-6: The drag coefficient as a function of the particle Reynolds number.

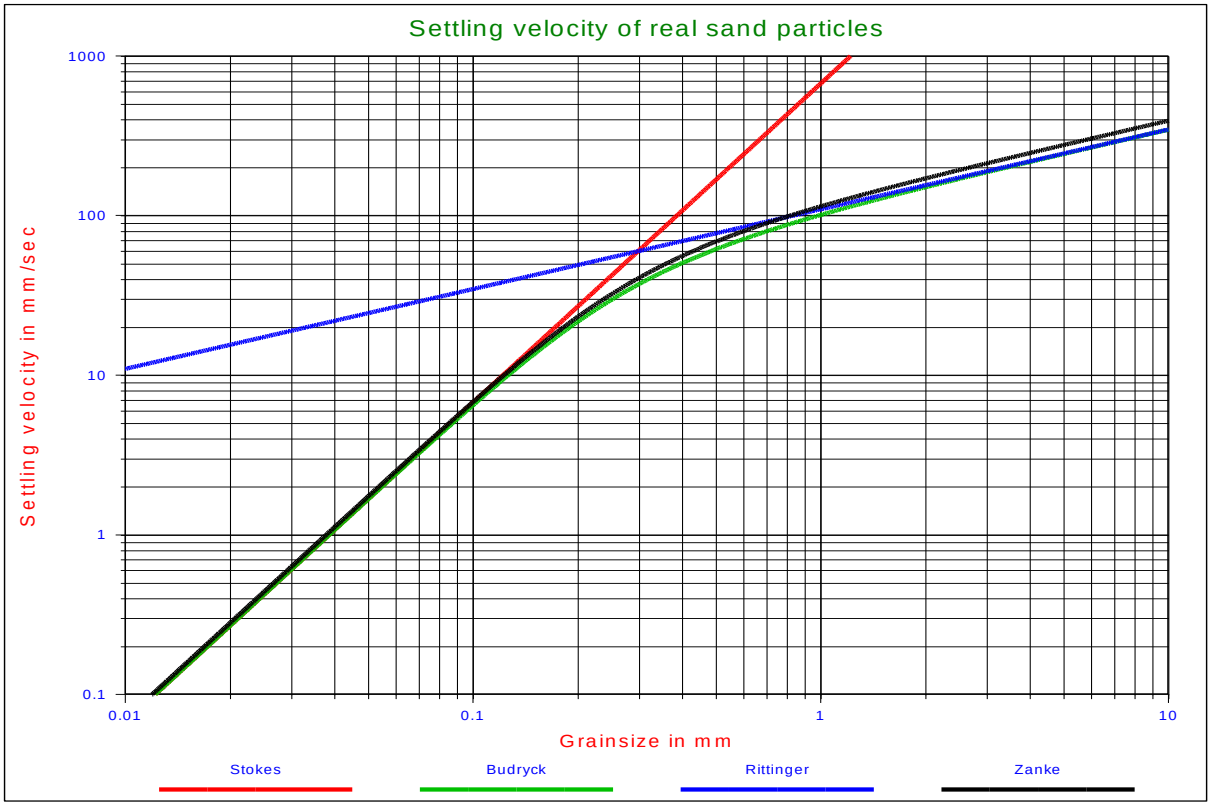

Figure 2-7: The settling velocity of individual particles.

The Huisman (1973-1995) Method.

A better approximation and more workable equations for the drag coefficient C_D may be obtained by subdividing the transition region, for instance:

$$Re_p < 1 \qquad C_D = \frac{24}{Re_p^1} \qquad \textbf{(2-21)}$$

$$1 < Re_p < 50 \qquad C_D = \frac{24}{Re_p^{3/4}} \qquad \textbf{(2-22)}$$

$$50 < Re_p < 1620 \qquad C_D = \frac{4.7}{Re_p^{1/3}} \qquad \textbf{(2-23)}$$

$$1620 < Re_p \qquad C_D = 0.4 \qquad \textbf{(2-24)}$$

This power approximation is also shown in Figure 2-6. Substitution of these equations in equation (2-19) gives:

$$Re_p < 1 \qquad v_t = \frac{1}{18} \cdot \frac{g^1}{\nu_l^1} \cdot R_{sd}^1 \cdot d^2 \qquad \textbf{(2-25)}$$

$$1 < Re_p < 50 \qquad v_t = \frac{1}{10} \cdot \frac{g^{0.8}}{\nu_l^{0.6}} \cdot R_{sd}^{0.8} \cdot d^{1.4} \qquad \textbf{(2-26)}$$

$$50 < Re_p < 1620 \qquad v_t = \frac{1}{2.13} \cdot \frac{g^{0.6}}{\nu_l^{0.2}} \cdot R_{sd}^{0.6} \cdot d^{0.8} \qquad \textbf{(2-27)}$$

$$1620 < Re_p \qquad v_t = 1.83 \cdot \frac{g^{0.5}}{\nu_l^{0}} \cdot R_{sd}^{0.5} \cdot d^{0.5} \qquad \textbf{(2-28)}$$

These equations are difficult to use in an actual case because the value of $\mathbf{Re_p}$ depends on the terminal settling velocity. The following method gives a more workable solution.

Equation (2-5) can be transformed into:

$$C_D \cdot Re_p^2 = \frac{4}{3} \cdot R_{sd} \cdot \frac{g}{\nu_l^2} \cdot d^3 \qquad \textbf{(2-29)}$$

This factor can be determined from the equations above:

$$Re_p < 1 \qquad C_D \cdot Re_p^2 = 24 \cdot Re_p \qquad \textbf{(2-30)}$$

$$1 < Re_p < 50 \qquad C_D \cdot Re_p^2 = 24 \cdot Re_p^{5/4} \qquad \textbf{(2-31)}$$

$$50 < Re_p < 1620 \qquad C_D \cdot Re_p^2 = 4.7 \cdot Re_p^{5/3} \qquad \textbf{(2-32)}$$

$$1620 < Re_p \qquad C_D \cdot Re_p^2 = 0.4 \cdot Re_p^2 \qquad \textbf{(2-33)}$$

From these equations the equation to be applied can be picked and the value of $\mathbf{Re_p}$ calculated. The settling velocity now follows from:

$$v_t = Re_p \cdot \frac{\nu_l}{d} \qquad \textbf{(2-34)}$$

The Grace Method (1986).

Following the suggestions of Grace (1986), it is found convenient to define a dimensionless particle diameter, which in fact is the Bonneville parameter (**d** in m and $\mathbf{v_t}$ in m/s):

$$D_* = d \cdot \left(\frac{R_{sd} \cdot g}{\nu_l^2} \right)^{1/3} \qquad \textbf{(2-35)}$$

And a dimensionless terminal settling velocity:

$$v_t^* = v_t \cdot \left(\frac{1}{\nu_l \cdot R_{sd} \cdot g} \right)^{1/3} \qquad \textbf{(2-36)}$$

Those are mutually related. Thus using the curve and rearranging gives directly the velocity $\mathbf{v_t}$ as a function of particle diameter **d**. No iteration is required. This described by analytic expressions appropriate for a computational determination of $\mathbf{v_s}$ according to Grace Method. Now $\mathbf{v_t}$ can be computed according to:

$$v_t = v_t^* \cdot \left(\frac{1}{\nu_l \cdot R_{sd} \cdot g} \right)^{-1/3} \qquad \textbf{(2-37)}$$

$$D^* < 3.8 \qquad v_t^* = \frac{\left(D^*\right)^2}{18} - 3.1234 \cdot 10^{-4} \cdot \left(D^*\right)^5 + 1.6415 \cdot 10^{-6} \cdot \left(D^*\right)^8 - 7.278 \cdot 10^{-10} \cdot \left(D^*\right)^{11} \qquad \textbf{(2-38)}$$

$$3.8 < D^* < 7.58 \qquad v_t^* = 10^{-1.5446 + 2.9162 \cdot \log(D^*) - 1.0432 \cdot \log(D^*)^2} \qquad \textbf{(2-39)}$$

$$7.58 < D^* < 227 \qquad v_t^* = 10^{-1.64758 + 2.94786 \cdot \log(D^*) - 1.09703 \cdot \log(D^*)^2 + 0.17129 \cdot \log(D^*)^3} \qquad \textbf{(2-40)}$$

$$227 < D^* < 3500 \qquad v_t^* = 10^{5.1837 - 4.51034 \cdot \log(D^*) + 1.687 \cdot \log(D^*)^2 - 0.189135 \cdot \log(D^*)^3} \qquad \textbf{(2-41)}$$

Figure 2-8 shows the terminal settling velocity for the iterative method according to equations (2-10), (2-11) and (2-12) and the methods of Huisman (1973-1995) and Grace (1986), using shape factors of 0.5 and 0.7. It can be seen that for small diameters these methods gives smaller velocities while for larger diameters larger velocities are predicted, compared with the other equations as shown in Figure 2-7. The iterative method gives larger velocities for the larger diameters, compared with the Huisman and Grace methods, but this is caused by the different way of implementing the shape factor. In the iterative method the shape factor is implemented according to equation 2, while with the Huisman and Grace methods the terminal settling velocity for spheres is multiplied by the shape factor according to equation (2-42). For the smaller grain diameters, smaller than 0.5 mm, which are of interest here, the 3 methods give the same results.

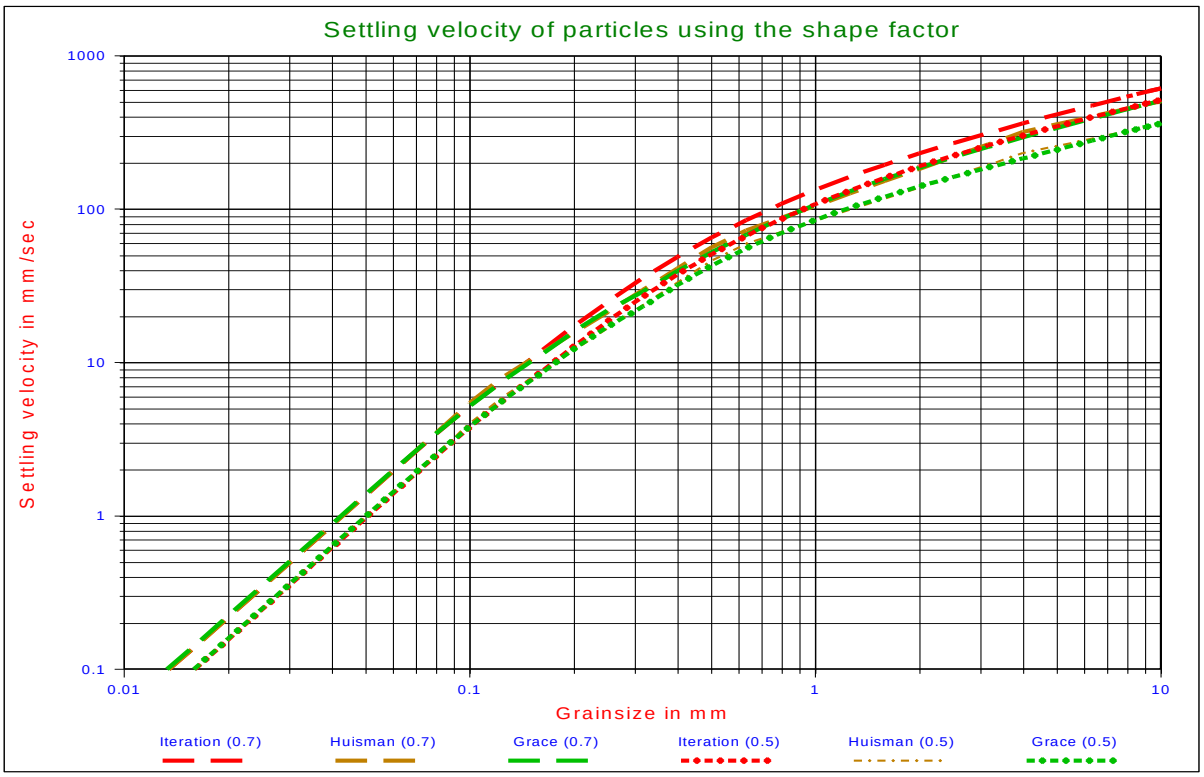

Figure 2-8: The settling velocity of individual particles using the shape factor.

2.5. The Shape Factor

In the range of particle Reynolds numbers from roughly unity to about 100, which is the range of interest here, a particle orients itself during settling so as to maximize drag. Generally this means that an oblate or lenticular particle, i.e. a shape with one dimension smaller than the other two, will settle with its maximum area horizontal. The drag of fluid on the particle then depends most critically on this area. This is also the area seen if the particle lies in a stable position on a flat surface. Therefore, for estimation of drag, the non-spherical particle is

characterized by the 'area equivalent diameter', i.e. the diameter of the sphere with the same projected area. For particles whose sizes are determined by sieving rather than microscopic analysis, the diameter is slightly smaller than the mesh size. However, unless the particles are needle shaped, the difference between the diameter and the screen opening is relatively small, generally less than 20%.

Although equation (2-5) contains a shape factor, basically all the equations in this chapter are derived for spheres. The shape factor ψ in equation (2-5) is one way of introducing the effect of the shape of particles on the terminal settling velocity. In fact equation (2-5) uses a shape factor based on the weight ratio between a real sand particle and a sphere with the same diameter. Another way is introducing a factor ξ according to:

$$\xi = \frac{v_t}{v_{ts}} \tag{2-42}$$

Where ξ equals the ratio of the terminal settling velocity of a non-spherical particle $\mathbf{v_t}$ and the terminal velocity $\mathbf{v_{ts}}$ of a spherical particle with the same diameter. The shape of the particle can be described by the volumetric shape factor **K** which is defined as the ratio of the volume of a particle and a cube with sides equal to the particle diameter so that **K=0.524** for a sphere:

$$K = \frac{volume\ of\ particle}{d^3} \tag{2-43}$$

The shape factor ξ is a function of the volumetric form factor **K** and the dimensionless particle diameter **D*** according to equation (2-35).

$$\log(\xi) = -0.55 + K - 0.0015 \cdot K + 0.03 \cdot 1000^{K-0.524} + \frac{-0.045 + 0.05 \cdot K^{-0.6} - 0.0287 \cdot 55000^{K-0.524}}{\cosh(2.55 \cdot (\log(D^*) - 1.114))} \tag{2-44}$$

This equation takes a simpler form for sand shaped particles with **K=0.26**:

$$\log(\xi) = -0.3073 + \frac{0.0656}{\cosh(2.55 \cdot (\log(D^*) - 1.114))} \tag{2-45}$$

A value of **K=0.26** for sand grains would give a volume ratio of 0.26/0.524=0.496 and thus a factor **ψ=0.496** in equation (2-5), while often a factor **ψ=0.7** is used.

Figure 2-9 shows the shape factor ξ as a function of the dimensionless particle diameter **d***, according to equation (2-44).

Figure 2-8 also shows the terminal settling velocity according to the methods of Huisman (1973-1995) and Grace (1986) using the shape factor according to equation (2-45). It can be seen clearly that both methods give the same results. One can see that the choice of the shape factor strongly determines the outcome of the terminal settling velocity.

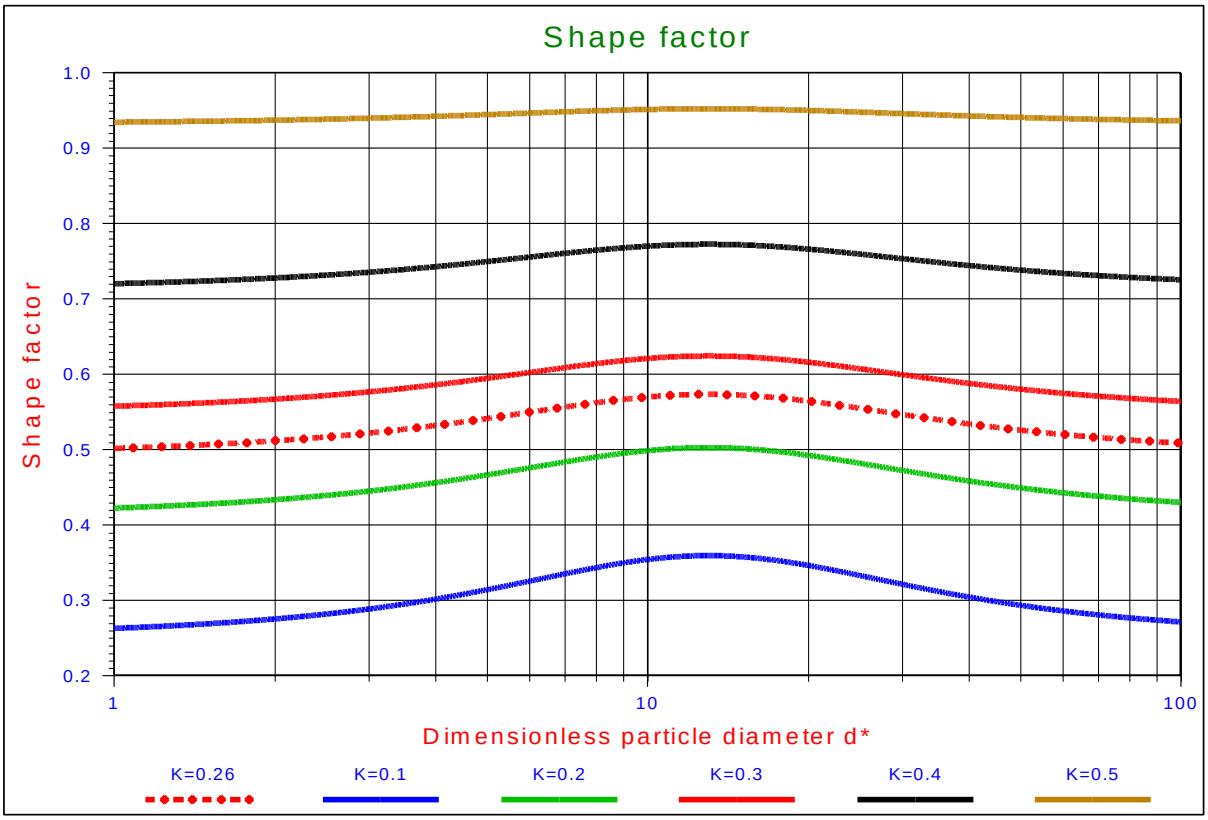

Figure 2-9: The shape factor ξ as a function of the dimensionless particle diameter D*.

2.6. Hindered Settling.

The above equations calculate the settling velocities for individual grains. The grain moves downwards and the same volume of water has to move upwards. In a mixture, this means that, when many grains are settling, an average upwards velocity of the water exists. This results in a decrease of the settling velocity, which is often referred to as hindered settling. However, at very low concentrations the settling velocity will increase because the grains settle in each other's shadow. Richardson and Zaki (1954) determined an equation to calculate the influence of hindered settling for volume concentrations C_{vs} between 0 and 0.3. The coefficient in this equation is dependent on the Reynolds number. The general equation yields:

$$\frac{v_{th}}{v_t} = (1 - C_{vs})^{\beta} \qquad \textbf{(2-46)}$$

The following values for β should be used according to Richardson and Zaki (1954):

$Re_p<0.2$	$\beta=4.65$	
$Re_p>0.2$ and $Re_p<1.0$	$\beta=4.35 \cdot Re_p^{-0.03}$	(2-47)
$Re_p>1.0$ and $Re_p<200$	$\beta=4.45 \cdot Re_p^{-0.1}$	
$Re_p>200$	$\beta=2.39$	

However this does not give a smooth continuous curve. Using the following definition does give a continuous curve:

$Re_p<0.1$	$\beta=4.65$	
$Re_p>0.1$ and $Re_p<1.0$	$\beta=4.35 \cdot Re_p^{-0.03}$	(2-48)
$Re_p>1.0$ and $Re_p<400$	$\beta=4.45 \cdot Re_p^{-0.1}$	
$Re_p>400$	$\beta=2.39$	

Other researchers found the same trend but sometimes somewhat different values for the power **β**. These equations are summarized below and shown in Figure 2-10.

According to Rowe (1987) this can be approximated by:

$$\beta = \frac{4.7 + 0.41 \cdot Re_p^{0.75}}{1 + 0.175 \cdot Re_p^{0.75}} \qquad \textbf{(2-49)}$$

Wallis (1969) found an equation which matches Rowe (1987) for small Reynolds numbers and Garside & Al-Dibouni (1977) for the large Reynolds numbers:

$$\beta = \frac{4.7 \cdot (1 + 0.15 \cdot Re_p^{0.687})}{1 + 0.253 \cdot Re_p^{0.687}} \qquad \textbf{(2-50)}$$

Garside & Al-Dibouni (1977) give the same trend but somewhat higher values for the exponent **β**.

$$\beta = \frac{5.1 + 0.27 \cdot Re_p^{0.9}}{1 + 0.1 \cdot Re_p^{0.9}} \qquad \textbf{(2-51)}$$

Di Felici (1999) finds very high values for **β** but this relation is only valid for dilute mixtures (very low concentration, less than 5%).

$$\beta = \frac{6.5 + 0.3 \cdot Re_p^{0.74}}{1 + 0.1 \cdot Re_p^{0.74}} \qquad \textbf{(2-52)}$$

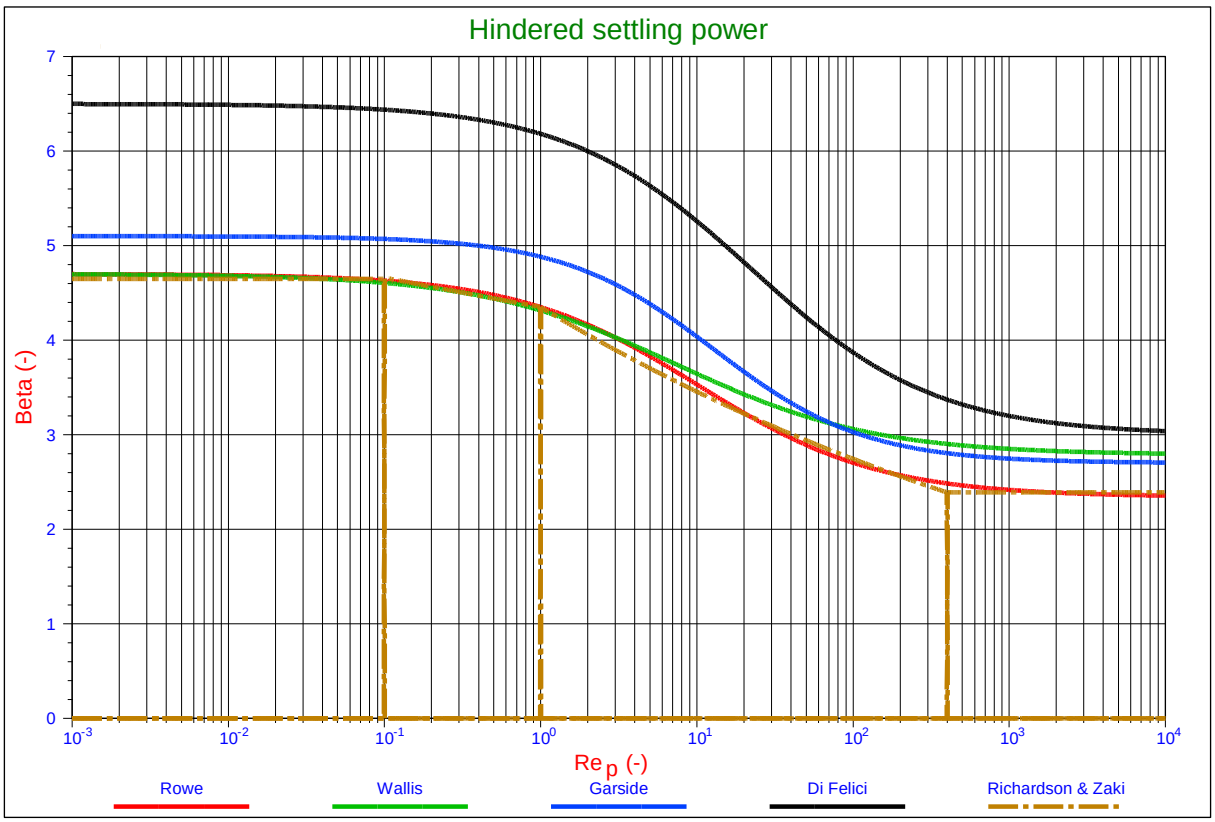

Figure 2-10: The hindered settling power according to several researchers.

2.7. Conclusions.

The equation of Ruby & Zanke (1977) will be used to determine the terminal settling velocity for sands and gravels. The equation of Richardson and Zaki (1954) will be used for hindered settling, with the equation of Rowe (1987) for the power **β** in the hindered settling equation. The DHLLDV framework is calibrated based on these equations.

Using different equations will result in slightly different hydraulic gradients and Limit Deposit Velocities, requiring the constants in the DHLLDV framework to be adjusted.

Particles with different shapes, like spheres or shells, and particles with different relative submerged densities may require different methods.

2.8. Nomenclature.

A	Cross section of particle	**m^2**
C_D	Drag coefficient	**-**
C_{vs}	Volumetric spatial concentration	**-**
d	Particle diameter	**m**
D_*	Bonneville parameter or dimensionless particle diameter	**-**
F_{down}	Downwards force on particle	**N**
F_{up}	Upwards force on particle	**N**
g	Gravitational constant 9.81 m/s^2	**m/s^2**
K	Volumetric form factor	**-**
Re_p	Particle Reynolds number	**-**
R_{sd}	Relative submerged density	**-**
v_t	Terminal settling velocity	**m/s**
v_t^*	Dimensionless terminal settling velocity	**-**
v_{th}	Hindered terminal settling velocity	**m/s**
v_{ts}	Terminal settling velocity sphere	**m/s**
V	Volume of particle	**m^3**
β	Hindered settling power	**-**
ρ_l	Density of carrier liquid	**ton/m^3**
ρ_s	Density of solid	**ton/m^3**
ψ	Shape factor	**-**
ξ	Shape factor	**-**
ν_l	Kinematic viscosity liquid	**m^2/s**

2.9. Notes.

Chapter 3: Pressure Losses with Homogeneous Liquid Flow.

3.1. Pipe Wall Shear Stress.

In general objects in a fluid flow experience a resistance proportional to the dynamic pressure of the fluid:

$$\frac{1}{2}\cdot\rho_l\cdot v_{ls}^2 \tag{3-1}$$

For an object in a fluid flow (like settling particles) the drag force on the object is the dynamic pressure times a characteristic cross section times a drag coefficient, giving:

$$F_{drag} = C_D\cdot\frac{1}{2}\cdot\rho_l\cdot v_{ls}^2\cdot A \tag{3-2}$$

The drag coefficient normally depends on the Reynolds number of the flow. Now with pipe flow, there is no flow around an object, but there is flow inside the pipe. The basic principles however remain the same, giving for the wall shear stress:

$$\tau_w = f\cdot\frac{1}{2}\cdot\rho_l\cdot v_{ls}^2 \tag{3-3}$$

The proportionality coefficient **f** is the so called Fanning friction factor, named after John Thomas Fanning (1837-1911). The friction force or drag force on a pipe with diameter $\mathbf{D_p}$ and length $\mathbf{\Delta L}$ is now:

$$F_{drag} = \tau_w\cdot A = f\cdot\frac{1}{2}\cdot\rho_l\cdot v_{ls}^2\cdot\pi\cdot D_p\cdot\Delta L \tag{3-4}$$

The pressure difference over the pipe with diameter $\mathbf{D_p}$ and length **L** is the drag force divided by the pipe cross section $\mathbf{A_p}$:

$$\Delta p = \frac{F_{drag}}{A_p} = \frac{f\cdot\frac{1}{2}\cdot\rho_l\cdot v_{ls}^2\cdot\pi\cdot D_p\cdot\Delta L}{\frac{\pi}{4}\cdot D_p^2} = 2\cdot f\cdot\frac{\Delta L}{D_p}\cdot\rho_l\cdot v_{ls}^2 \tag{3-5}$$

The notation using the Darcy friction factor also called the Darcy Weisbach friction factor or the Moody friction factor is more convenient here for using the dynamic pressure, giving:

$$\Delta p_l = \lambda_l\cdot\frac{\Delta L}{D_p}\cdot\frac{1}{2}\cdot\rho_l\cdot v_{ls}^2 \tag{3-6}$$

Note that the Darcy Weisbach friction factor is 4 times the Fanning friction factor. In terms of the shear stress this gives:

$$\tau_w = \frac{\lambda_l}{4}\cdot\frac{1}{2}\cdot\rho_l\cdot v_{ls}^2 = \frac{\lambda_l}{8}\cdot\rho_l\cdot v_{ls}^2 \tag{3-7}$$

The hydraulic gradient $\mathbf{i_w}$ (for water) or $\mathbf{i_l}$ (for a liquid in general) is:

$$i_l = i_w = \frac{\Delta p_l}{\rho_l\cdot g\cdot\Delta L} = \frac{\lambda_l\cdot v_{ls}^2}{2\cdot g\cdot D_p} \tag{3-8}$$

In this book the Darcy Weisbach friction factor is used.

3.2. The Darcy-Weisbach Friction Factor.

The value of the wall friction factor λ_l depends on the Reynolds number:

$$Re = \frac{v_{ls} \cdot D_p}{\nu_l} = \frac{\rho_l \cdot v_{ls} \cdot D_p}{\mu_l} \tag{3-9}$$

For laminar flow (Re<2320) the value of λ_l can be determined according to Poiseuille:

$$\lambda_l = \frac{64}{Re} \tag{3-10}$$

For turbulent flow (Re>2320) the value of λ_l depends not only on the Reynolds number but also on the relative roughness of the pipe ε/D_p. A general implicit equation for λ_l is the Colebrook-White (1937) equation:

$$\lambda_l = \frac{1}{\left(2 \cdot \log_{10}\left(\frac{2.51}{Re \cdot \sqrt{\lambda_l}} + \frac{0.27 \cdot \varepsilon}{D_p}\right)\right)^2} \tag{3-11}$$

For very smooth pipes the value of the relative roughness ε/D_p is almost zero, resulting in the Prandl & von Karman equation:

$$\lambda_l = \frac{1}{\left(2 \cdot \log_{10}\left(\frac{2.51}{Re \cdot \sqrt{\lambda_l}}\right)\right)^2} \tag{3-12}$$

At very high Reynolds numbers the value of $2.51/(Re \cdot \sqrt{\lambda_l})$ is almost zero, resulting in the Nikuradse (1933) equation:

$$\lambda_l = \frac{1}{\left(2 \cdot \log_{10}\left(\frac{0.27 \cdot \varepsilon}{D_p}\right)\right)^2} = \frac{5.3}{\left(2 \cdot \ln\left(\frac{0.27 \cdot \varepsilon}{D_p}\right)\right)^2} \tag{3-13}$$

Because equations (3-11) and (3-12) are implicit, for smooth pipes approximation equations can be used. For a Reynolds number between 2320 and 10^5 the Blasius equation gives a good approximation:

$$\lambda_l = 0.3164 \cdot \left(\frac{1}{Re}\right)^{0.25} \tag{3-14}$$

For a Reynolds number in the range of 10^5 to 10^8 the Nikuradse (1933) equation gives a good approximation:

$$\lambda_l = 0.0032 + \frac{0.221}{Re^{0.237}} \tag{3-15}$$

Figure 3-1 gives the so called Moody (1944) diagram, in this case based on the Swamee Jain (1976) equation.

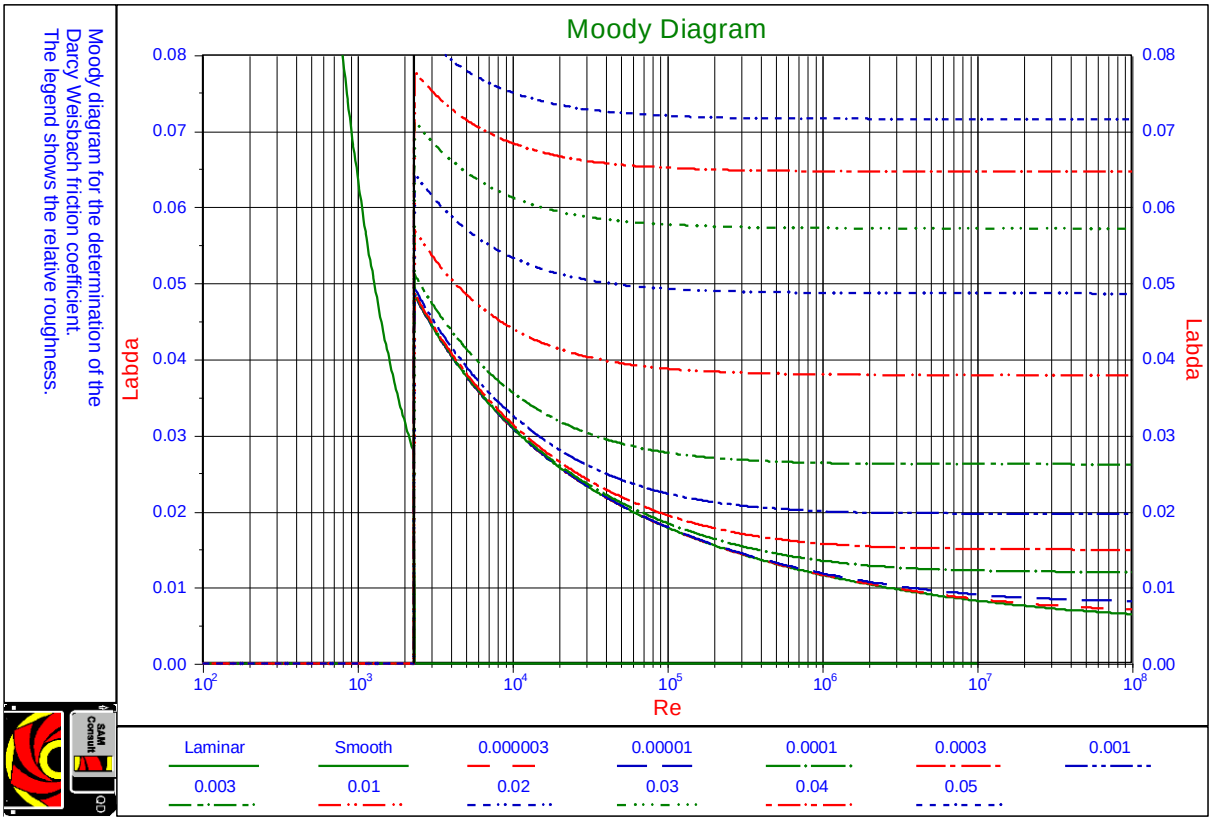

Figure 3-1: The Moody diagram determined with the Swamee Jain equation.

Over the whole range of Reynolds numbers above 2320 the Swamee Jain (1976) equation gives a good approximation:

$$\lambda_l = \frac{1.325}{\left(\ln\left(\frac{\varepsilon}{3.7 \cdot D_p} + \frac{5.75}{Re^{0.9}}\right)\right)^2} = \frac{0.25}{\left(\log_{10}\left(\frac{\varepsilon}{3.7 \cdot D_p} + \frac{5.75}{Re^{0.9}}\right)\right)^2} \qquad \textbf{(3-16)}$$

3.3. The Equivalent Liquid Model.

Assuming that the pressure losses in a pipe are proportional to the kinetic energy of the eddies and the kinetic energy of the eddies is proportional to the mixture density and the line speed and assuming that there are no losses due to sliding friction or collisions, the pressure losses can be determined by:

$$\Delta p_m = \lambda_l \cdot \frac{\Delta L}{D_p} \cdot \frac{1}{2} \cdot \rho_m \cdot v_{ls}^2 \qquad \textbf{(3-17)}$$

The hydraulic gradient $\mathbf{i_m}$ (for mixture) is now:

$$i_m = \frac{\Delta p_m}{\rho_l \cdot g \cdot \Delta L} = \frac{\rho_m}{\rho_l} \cdot \frac{\lambda_l \cdot v_{ls}^2}{2 \cdot g \cdot D_p} = \frac{\rho_m}{\rho_l} \cdot i_l \qquad \textbf{(3-18)}$$

The above assumptions are valid as long as the particles are small enough to be considered part of the eddies. So for larger particles this may not be true anymore.

3.4. Approximation of the Darcy-Weisbach Friction Factor.

It is obvious that the Darcy-Weisbach friction factor λ_l depends on the pipe diameter D_p and the line speed v_{ls}. This may be confused with a direct influence of the pipe diameter D_p and the line speed v_{ls}. So it is interesting to see how the Darcy-Weisbach friction factor λ_l depends on the pipe diameter D_p and the line speed v_{ls}. Figure 3-2 shows the Darcy-Weisbach friction factor for smooth pipes as a function of the line speed vls at a number of pipe diameters, while Figure 3-3 shows the Darcy-Weisbach friction factor as a function of the pipe diameter D_p at a number of line speeds. In both figures, the Darcy-Weisbach friction factor can be well approximated by a power function

$$\lambda_l = \alpha \cdot (v_{ls})^{\alpha_1} \cdot (D_p)^{\alpha_2} \qquad \textbf{(3-19)}$$

With:

$$\alpha = 0.01216 \quad \text{and} \quad \alpha_1 = -0.1537 \cdot (D_p)^{-0.089} \quad \text{and} \quad \alpha_2 = -0.2013 \cdot (v_{ls})^{-0.088} \qquad \textbf{(3-20)}$$

For laboratory conditions both powers are close to **-0.18**, while for real life conditions with higher line speeds and much larger pipe diameters this results in a power for the line speed of about α_1**=-0.155** and for the pipe diameter of about α_2**=-0.175**. This should be considered when analyzing the models for heterogeneous transport.

3.5. The Friction Velocity or Shear Velocity u_*.

The term ***friction velocity*** comes from the fact that $\sqrt{(\tau_w/\rho_l)}$ has the same unit as velocity and it has something to do with the wall friction force. The wall shear stress τ_w is often represented by friction velocity u_*, defined by:

$$u_* = \sqrt{\frac{\tau_w}{\rho_l}} = \sqrt{\frac{\lambda_l}{8}} \cdot v_{ls} \qquad \textbf{(3-21)}$$

3.6. The Thickness of the Viscous Sub Layer δ_v.

Very close to the pipe wall the flow is laminar in the so called viscous sub layer. The thickness of the viscous sub layer is defined as:

$$\delta_v = 11.6 \cdot \frac{\nu_l}{u_*} \qquad \textbf{(3-22)}$$

3.7. The Smallest Eddies.

The ratio between the largest eddies and the smallest eddies in turbulent pipe flow is of the magnitude of the Reynolds number to the power of ¾. Assuming that the largest eddies are of the magnitude of the pipe diameter, then this gives for the diameter of the smallest eddies:

$$d_e = \frac{D_p}{Re^{3/4}} = \frac{D_p^{1/4} \cdot \nu_l^{3/4}}{v_{ls}^{3/4}} \qquad \textbf{(3-23)}$$

Using the Blasius equation for the Darcy Weisbach friction factor, this gives for the ratio between the diameter of the smallest eddies to the thickness of the viscous sub layer:

$$\frac{d_e}{\delta_v} = 0.017 \cdot Re^{1/8} \qquad \textbf{(3-24)}$$

For Reynolds numbers ranging from 100,000 for small pipe diameters to 10,000,000 for large pipe diameters this gives a ratio of 0.072 to 0.127, so about 10%.

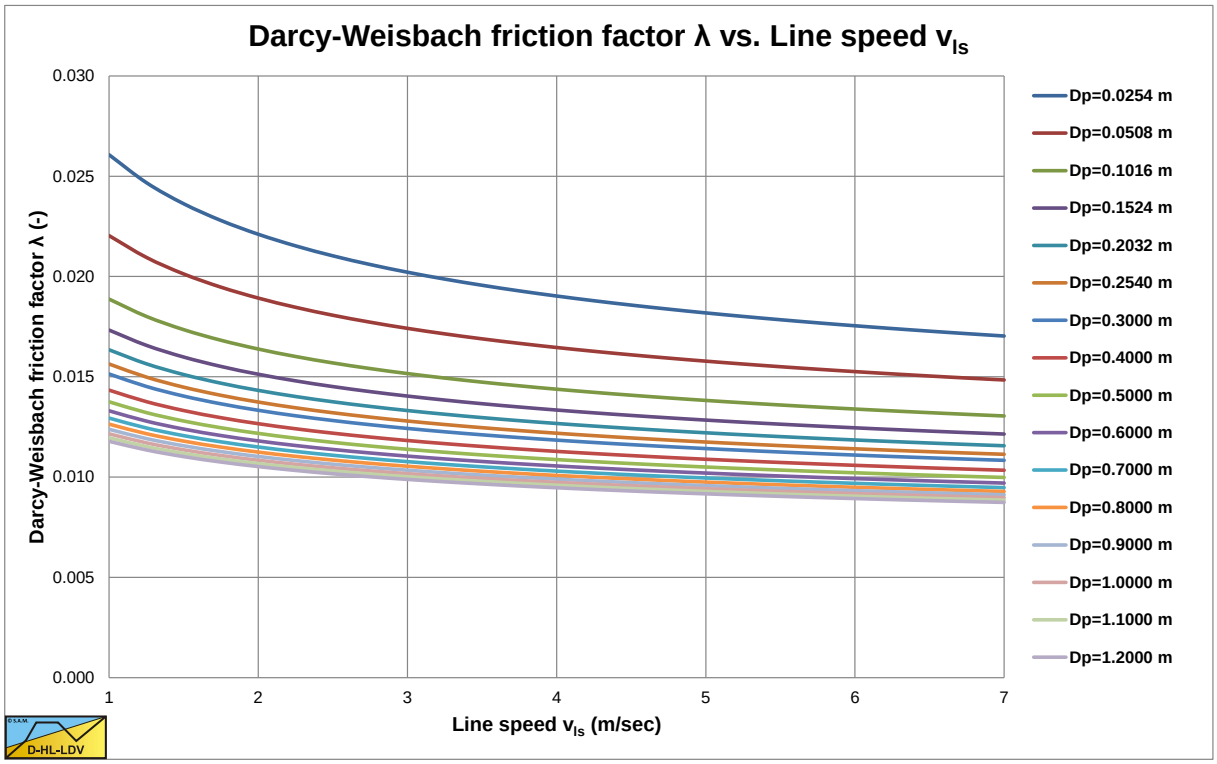

Figure 3-2: The Darcy-Weisbach friction factor λ_l for smooth pipes as a function of the line speed v_{ls}.

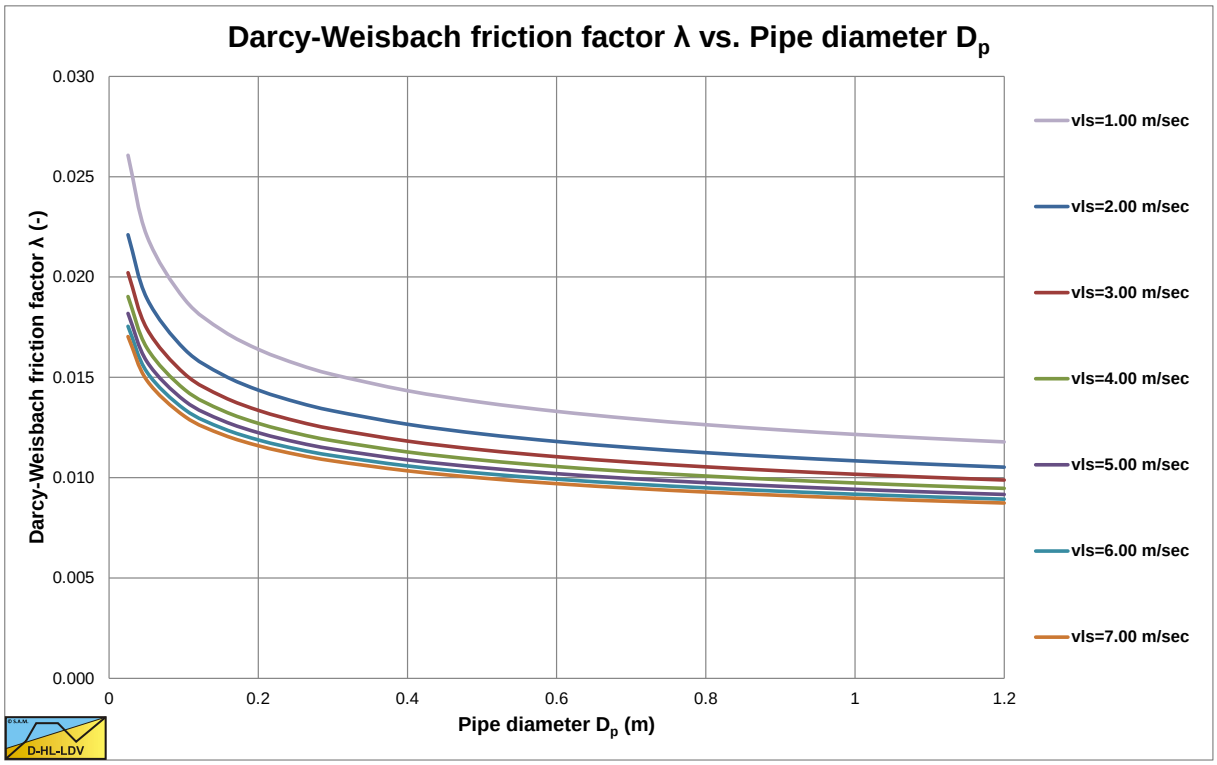

Figure 3-3: The Darcy-Weisbach friction factor λ_l for smooth pipes as a function of the pipe diameter D_p.

3.8. The Apparent Viscosity.

Einstein (1905) published an analysis for the viscosity of dilute suspensions. The result of this analysis is an equation giving the relation between the apparent dynamic viscosity and the volumetric concentration of the solids. The concentrations however are limited to low concentrations.

$$\mu_r = \frac{\mu_m}{\mu_l} = 1 + 2.5 \cdot C_{vs} \qquad \textbf{(3-25)}$$

Thomas (1965) collected data regarding the relative viscosity from 16 sources. The particle materials included polystyrene, rubber latex, glass and methyl methacrylate. The results are shown in Figure 3-4. In all studies, either the density of the suspending medium was adjusted or the viscosity of the suspending medium was sufficiently large that settling was unimportant. Examination of the experimental procedure used in these studies shows no basis for eliminating any of the data because of faulty technique; consequently, there must be at least one additional parameter that has not been accounted for. One parameter of importance is the absolute value of the particle diameter. For particles with diameters less than 1 to 10 microns, colloid-chemical forces become important causing non-Newtonian flow behavior. The result is a relative viscosity which increases as particle size is decreased, but which decreases to a limiting value as the shear rate is increased. For particles larger than 1 to 10 microns, the inertial effects due to the restoration of particle rotation after collision result in an additional energy dissipation and consequent increase in relative viscosity with increasing particle diameter.
In flow through capillary tubes, the increase in viscosity observed with large particle size suspensions is opposed by a decrease in viscosity caused by a tendency for particles to migrate toward the center of the tube as the particle diameter is increased. Examination of the data from which Figure 3-4 was prepared showed that in several cases the tests covered a sufficient range of shear rates or partied sizes that it was possible to extrapolate to conditions where particle size effects were negligible. For particles less than 1 micron diameter, the limiting value of the relative viscosity was obtained as the intercept of either a linear plot of **1/d** versus μ_m/μ_l or a linear plot of **1/(du/dr)** versus μ_m/μ_l. For particles larger than 1 to 10 microns, the limiting value of the relative viscosity was obtained as the intercept of a linear plot of **d** versus μ_m/μ_l. In the event that large particle size data were also available as a function of shear rate, the reduced particle size data were further corrected by plotting against **1/(du/ dr).** Treatment of the suitable data in this manner gave a unique curve for which the maximum deviation was reduced from three- to six fold over that shown in Figure 3-4, that is, to ± 7 % at C_{vs}**=0.2** and to ±13 % at C_{vs}**=0.5,** as is show in Figure 3-5.

Based on this Thomas (1965) derived an equation to determine the relative dynamic viscosity as a function of the concentration C_{vs} of the particles in the mixture.

$$\mu_r = \frac{\mu_m}{\mu_l} = 1 + 2.5 \cdot C_{vs} + 10.05 \cdot C_{vs}^2 + 0.00273 \cdot e^{16.6 \cdot C_{vs}} \qquad \textbf{(3-26)}$$

The Thomas (1965) equation can be used for pseudo homogeneous flow of small particles.

Figure 3-5 shows that the first two terms are valid to a volumetric concentration of about 6%. Adding the 3rd term extends the validity to a volumetric concentration of about 25%. Adding the 4th term extends the validity to a volumetric concentration of 60%, which covers the whole range of concentrations important in dredging applications.

Figure 3-6 shows experiments of Boothroyde et al. (1979) with Markham fines (light solids, high concentration) without using the Thomas (1965) viscosity. Figure 3-7 shows these experiments using the Thomas (1965) viscosity.

Figure 3-8 shows experiments of Thomas (1976) with iron ore (very heavy solids, medium concentration) without using the Thomas (1965) viscosity. Figure 3-9 shows these experiments using the Thomas (1965) viscosity.

In both cases the data points are above the ELM curves if the normal liquid viscosity is used. Using the Thomas (1965) viscosity correction places the data points very close to the ELM curves. Applying the Thomas (1965) viscosity gives a good result for the fines, as long as they behave like a Newtonian fluid.

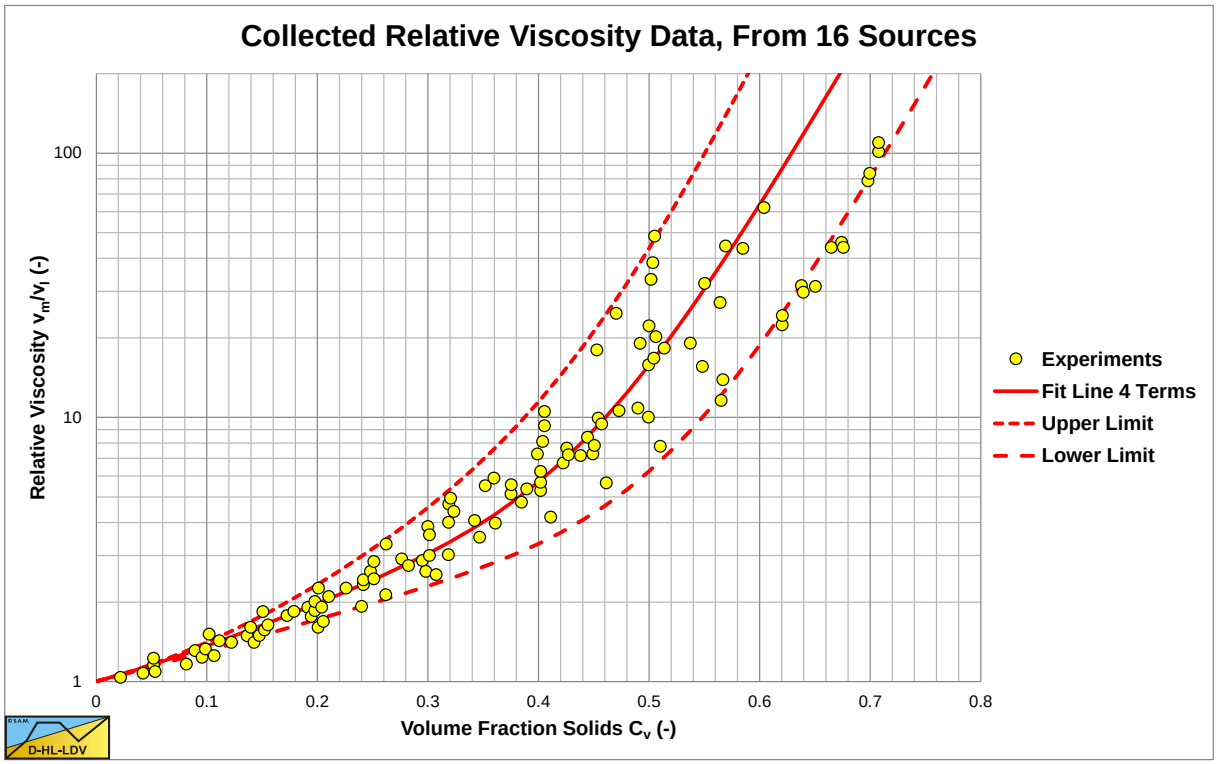

Figure 3-4: Collected relative viscosity data from 16 sources by Thomas (1965).

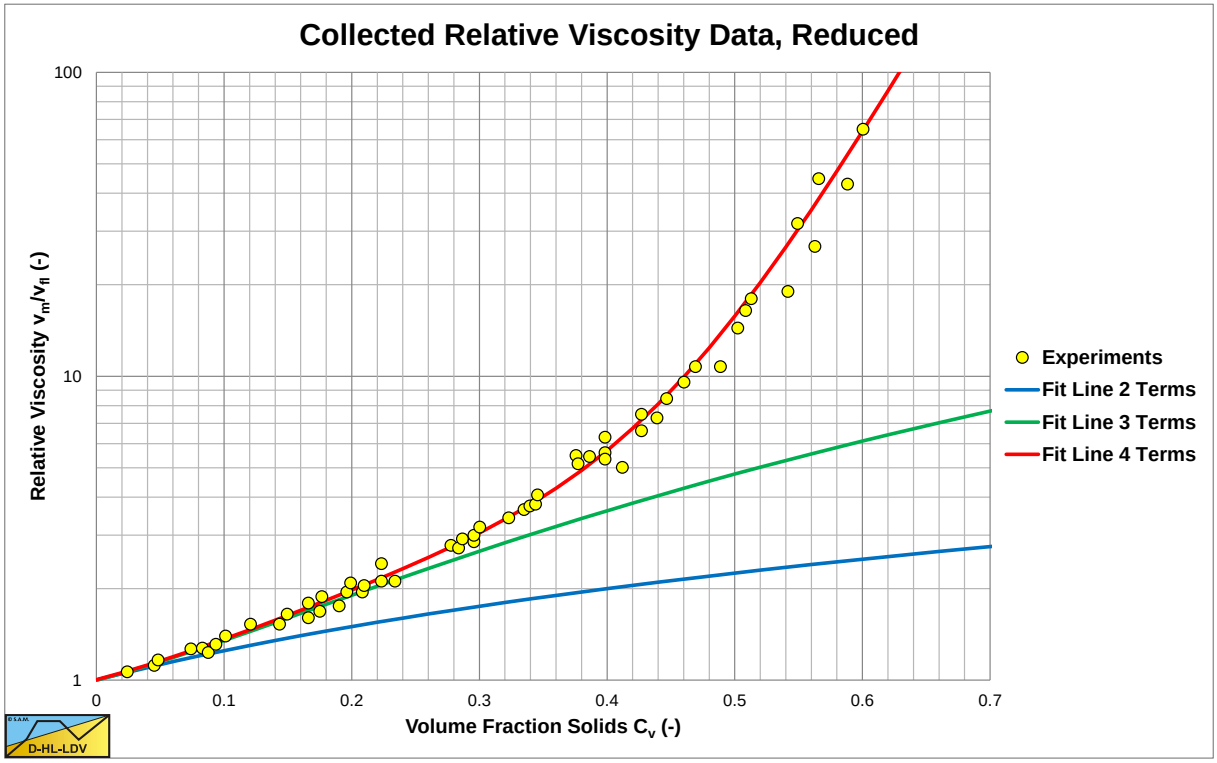

Figure 3-5: Collected relative viscosity data from 16 sources by Thomas (1965), reduced.

The limiting particle diameter for particles influencing the viscosity can be determined based on the Stokes number. A Stokes number of **Stk=0.1** gives a good first approximation. The velocity in the denominator is replaced by $\mathbf{6 \cdot D_p^{0.4}}$ as a first estimate of the LDV.

$$d = \sqrt{\frac{Stk \cdot 9 \cdot \rho_l \cdot \nu_l \cdot D_p}{\rho_s \cdot 6 \cdot D_p^{0.4}}} \qquad \textbf{(3-27)}$$

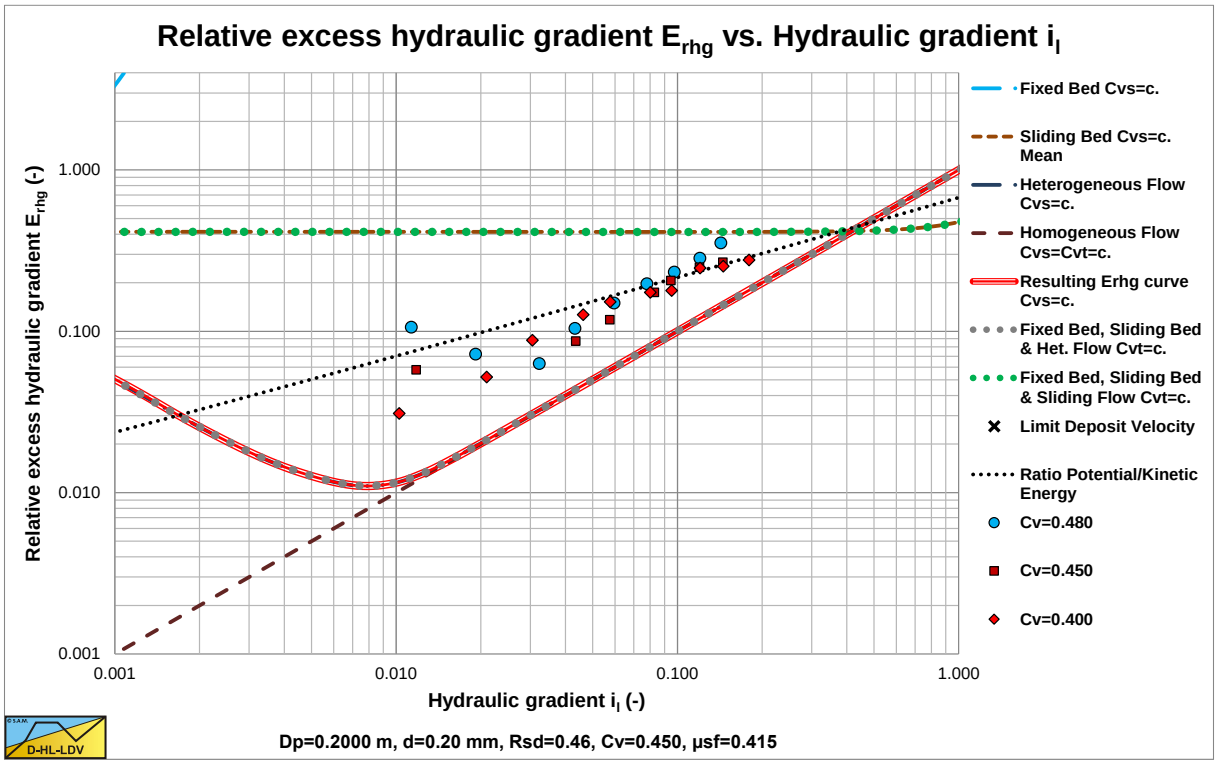

Figure 3-6: Markham fines Boothroyde et al. (1979), without Thomas (1965) viscosity.

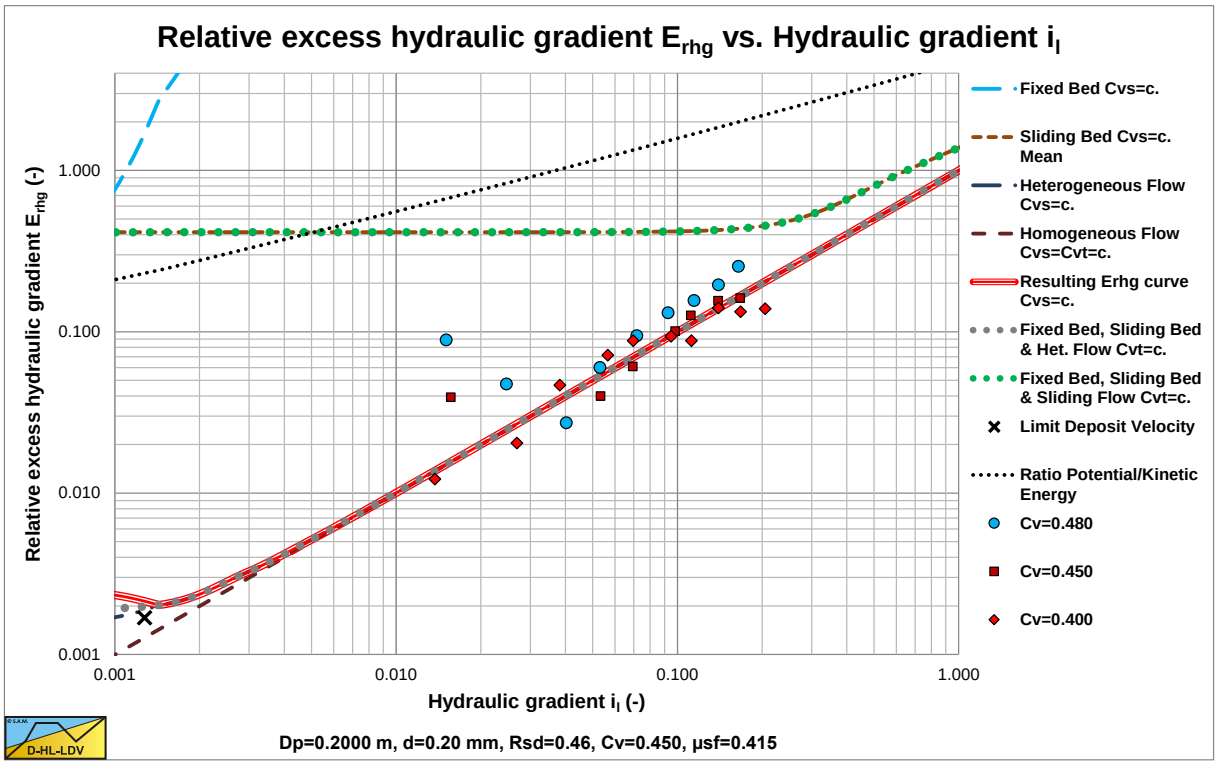

Figure 3-7: Markham fines Boothroyde et al. (1979), with Thomas (1965) viscosity.

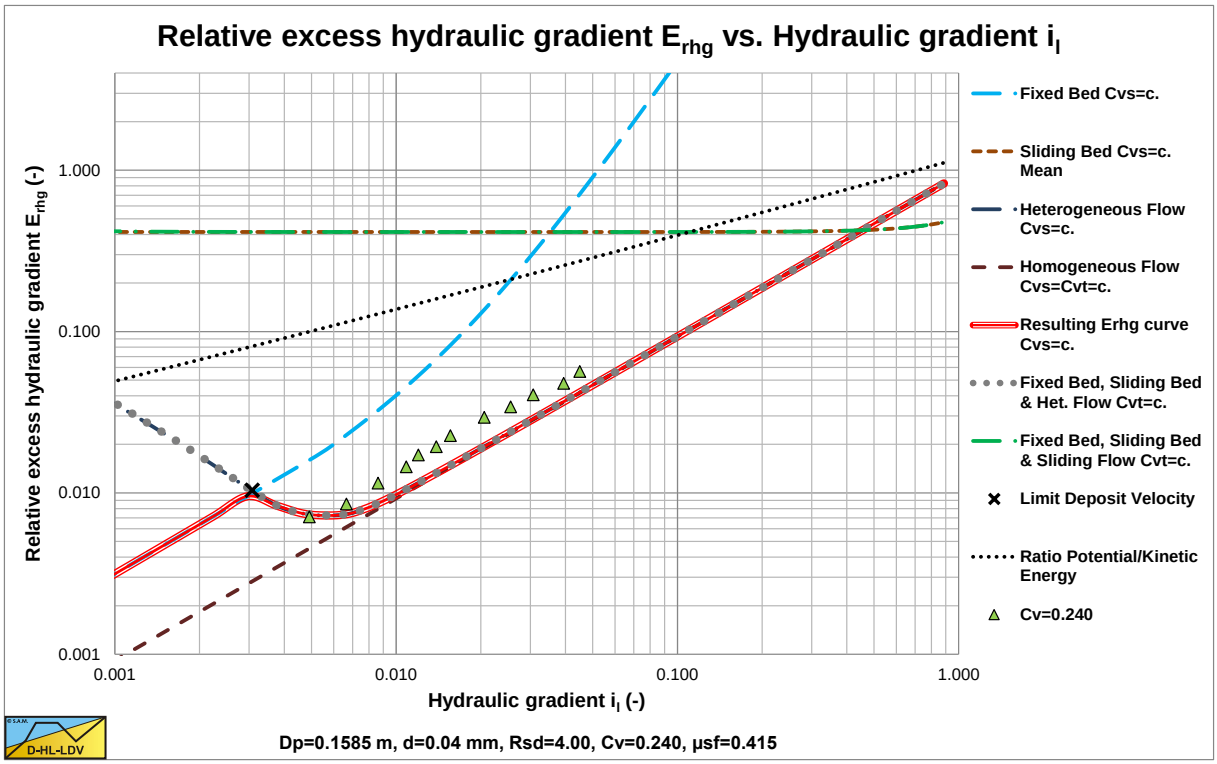

Figure 3-8: Iron ore Thomas (1976), without Thomas (1965) viscosity.

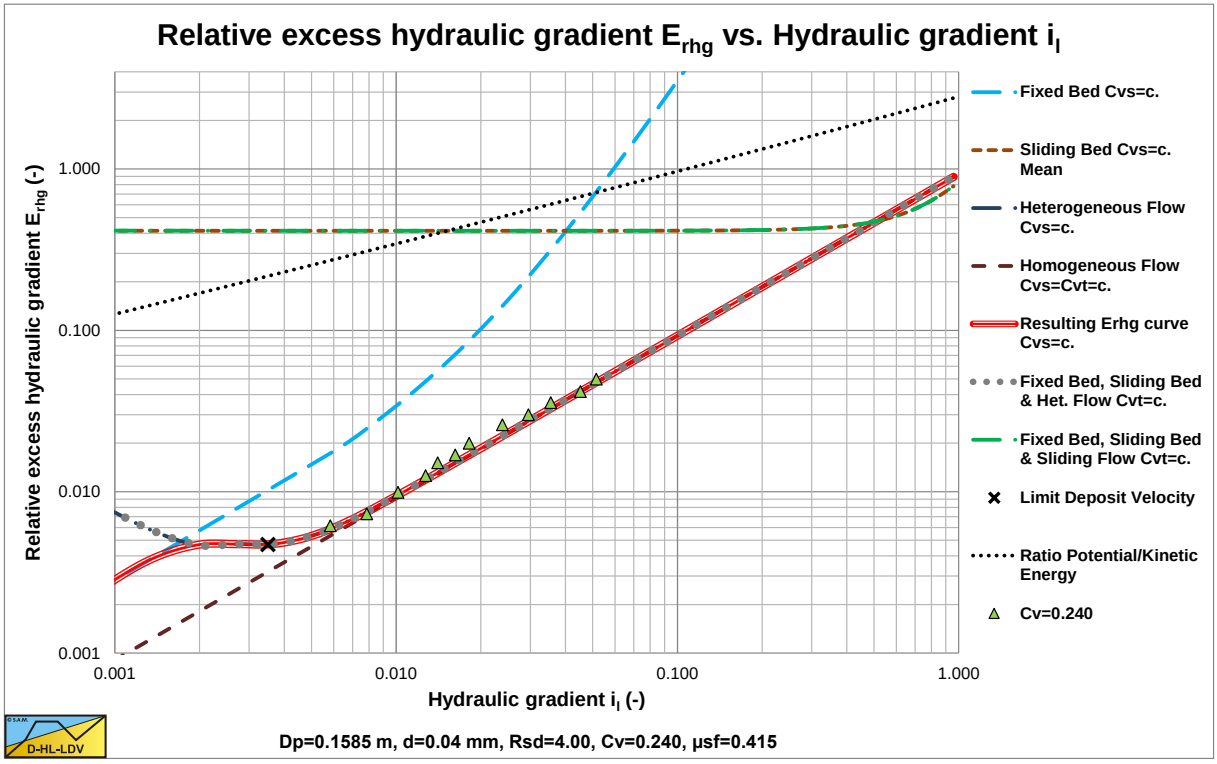

Figure 3-9: Iron ore Thomas (1976), with Thomas (1965) viscosity.

3.9. Nomenclature.

C_{vs}	Spatial volumetric concentration	**-**
D_p	Pipe diameter	**m**
g	Gravitational constant 9.81 m/sec^2	**m/s^2**
i, i_l, i_w	Hydraulic gradient	**m.w.c./m**
ΔL	Length of pipeline	**m**
Δp_l	Pressure difference over length ΔL	**kPa**
Re	Reynolds number of pipe flow	**-**
v_{ls}	Line speed	**m/s**
α	Proportionality constant	**-**
α_1	Power of line speed	**-**
α_2	Power of pipe diameter	**-**
ε	Roughness of pipe wall	**m**
λ_l	Darcy-Weisbach friction factor liquid to wall	**-**
ρ_l	Liquid density	**ton/m^3**
μ_l	Dynamic viscosity liquid	**Pa·s**
μ_m	Dynamic viscosity mixture	**Pa·s**
μ_r	Relative dynamic viscosity	**-**
ν_l	Kinematic viscosity liquid	**m^2/s**

3.10. Notes.

Chapter 4: The Delft Head Loss & Limit Deposit Velocity Framework.

4.1. Introduction.

4.1.1. Considerations.

In the last decades many head loss models for slurry transport have been developed. Not just for the dredging industry but also for coal and phosphate transport and in the chemical industries. Some models are based on the phenomena occurring combined with dimensionless parameters, resulting in semi-empirical equations (Durand, Condolios (1952), Gibert (1960), Worster & Denny (1955), Jufin Lopatin (1966),, Zandi & Govatos (1967), Fuhrboter (1961)), while others are based on physics with 2 and 3 layer models (Newitt et al. (1955), Doron & Barnea (1987), Wilson (1979), Matousek (2009)). The physical models are based on stationary transport in time and space, while the semi-empirical models may incorporate non-stationary or dynamical processes. An analysis of these models and of data collected from numerous publications for particles with densities ranging from 1.14 ton/m^3 to 3.65 ton/m^3, diameters ranging from 0.005 mm up to 45 mm, concentrations up to 45% and pipe diameters from 0.0254 m up to 0.9 m has led to an overall model of head losses in slurry transport, a sort of framework. The framework is based on 5 main flow regimes determining the source of energy losses. One can distinguish viscous friction losses, dry friction losses, potential energy losses, kinetic energy losses, Magnus lift work, turbulent lift work and turbulent eddy work. The losses do not have to occur at the same time. Usually one or two will be dominant depending on the flow regime.

Although sophisticated 2 and 3 layer models exist for slurry flow (here the flow of sand/gravel water mixtures), the main Dutch and Belgium dredging companies still use modified Durand & Condolios (1952) and Fuhrboter (1961) models, while the main dredging companies in the USA use a modified Wilson et al. (1992) model for heterogeneous transport. When asked why these companies don't use the more sophisticated models, they answer that they require models that match their inputs and they feel that the 2 and 3 layer models are still in an experimental phase, although these models give more insight in the physics. Usually the companies require a model based on the particle size distribution or $\mathbf{d_{50}}$, the pipe diameter $\mathbf{D_p}$, the line speed $\mathbf{v_{ls}}$, the relative submerged density $\mathbf{R_{sd}}$ and the temperature (the viscosity of the carrier liquid $\boldsymbol{\nu_l}$). Parameters like the bed associated hydraulic radius are not known in advance and thus not suitable. Usually the dredging companies operate at high line speeds above the limit deposit velocity (LDV) in the heterogeneous or homogeneous regime. This implies that the bed has dissolved and 2 and 3 layer models are not applicable anyway.

Still there is a need for improvement, since the existing models give reasonably good predictions for small diameter pipes, but not for large diameter pipes as used in dredging. Recent projects require line lengths up to 35 km with 5 to 6 booster pumps and large diameter pipes. Choosing the number of booster pumps and the location of the booster pumps depends on the head losses. However it should be considered that the slurry transport process is not stationary. Densities may vary from a water density of 1 ton/m^3 to densities of 1.6 ton/m^3 and particle size distributions will change over time. This results in a dynamic process where pumps, pump drives and slurry transport interact. The fundamental 2 and 3 layer models require a stationary approach, while the more empirical equations may take the dynamic effects as time and place averaged effects into account. The question is whether a semi empirical approach is possible, covering the whole range of pipe diameters and giving the empirical equations a more physical background, but still using the parameters available to the dredging industry.

Transporting sand with water through a pipeline, in general, results in an increase of the pressure required compared with pumping water or pure liquid. Since pressure times flow equals power and power times time equals energy, this can also be interpreted as an increase of the energy required to pump the solids. Energy or work also equals force times distance or stress times volume. The fact that more power is required to pump a solid liquid mixture compared with just pumping the liquid implies that there are additional energy losses and energy dissipation when pumping the solids. In order to go into detail to the model developed, first the different types of energy dissipation due to the solids effect are discussed.

Figure 4-1, **Figure 4-2**, **Figure 4-3** and **Figure 4-4** show the results of the energy approach for 8 sands ranging from **d=0.1 mm** up to **d=10 mm** in pipes with diameters of $\mathbf{D_p}$**=0.1524 m** and $\mathbf{D_p}$**=1 m**. For each pipe diameter the constant spatial volumetric concentration curves and the constant delivered volumetric concentration curves are shown.

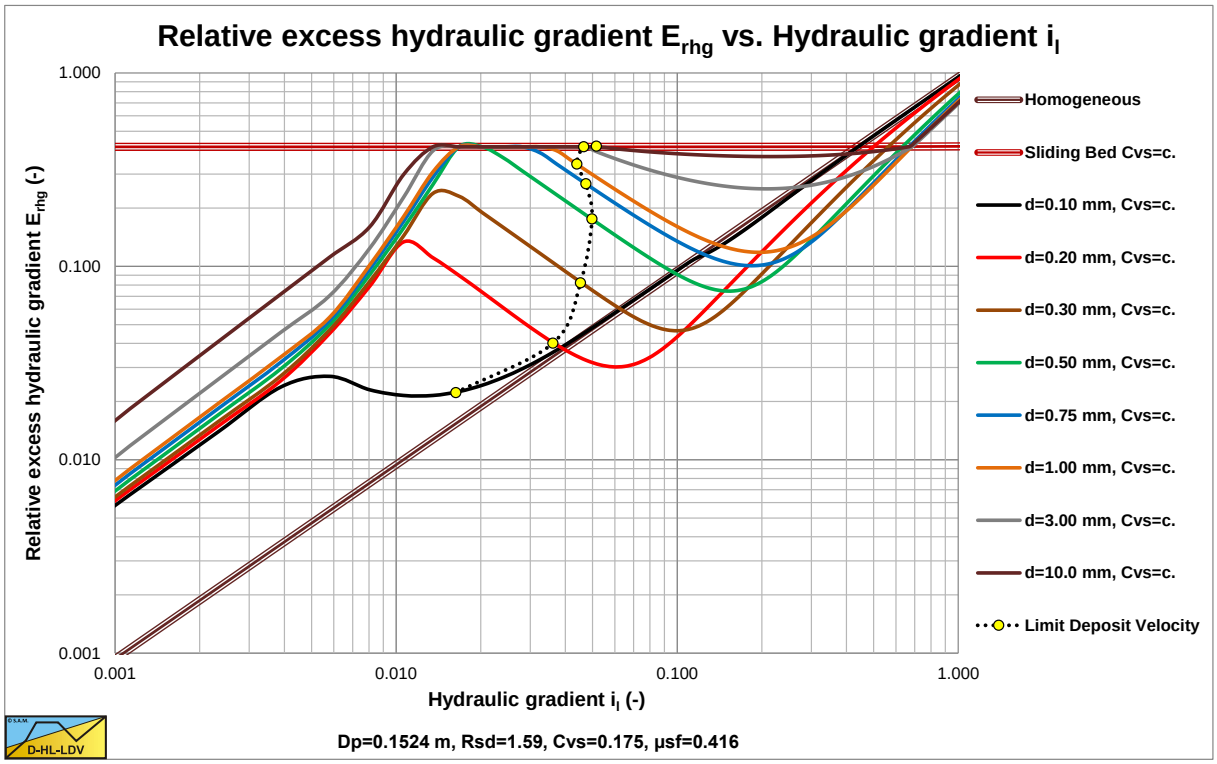

Figure 4-1: The relative excess hydraulic gradient as a function of the hydraulic gradient, constant C_{vs} and D_p=0.1524 m.

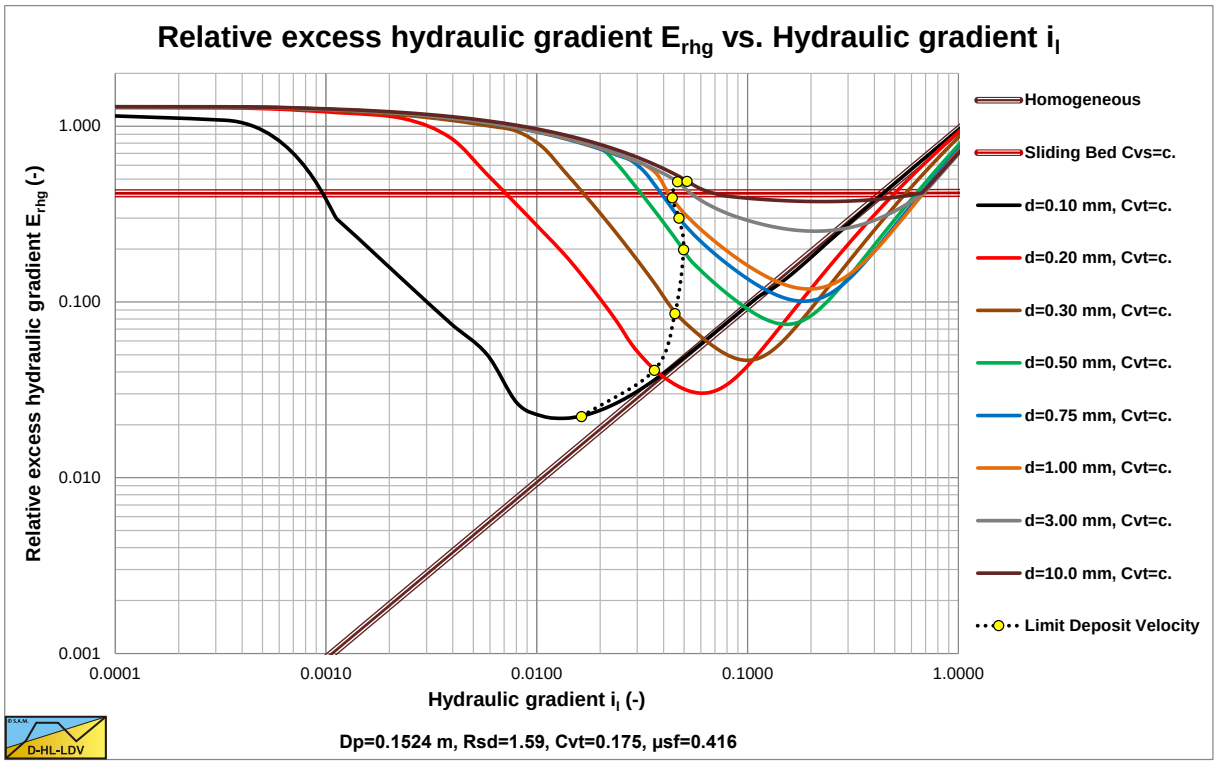

Figure 4-2: The relative excess hydraulic gradient as a function of the hydraulic gradient, constant C_{vt} and D_p=0.1524 m.

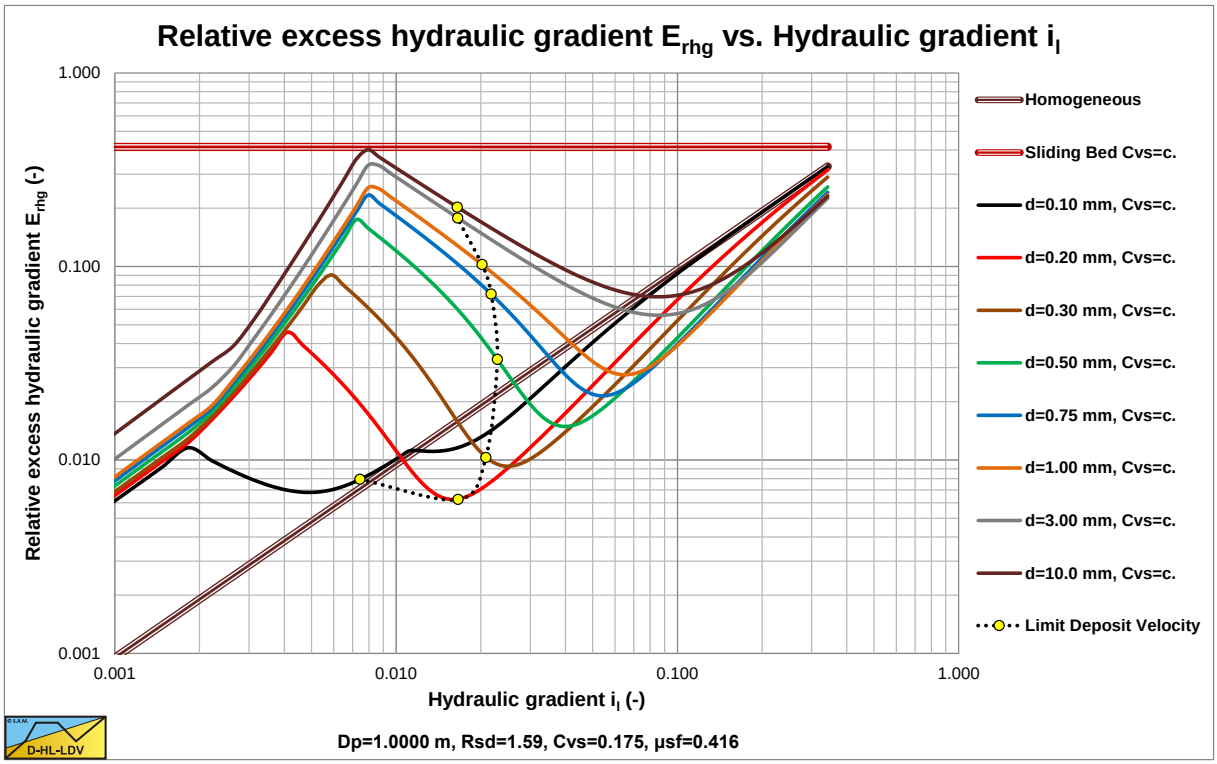

Figure 4-3: The relative excess hydraulic gradient as a function of the hydraulic gradient, constant C_{vs} and D_p=1 m.

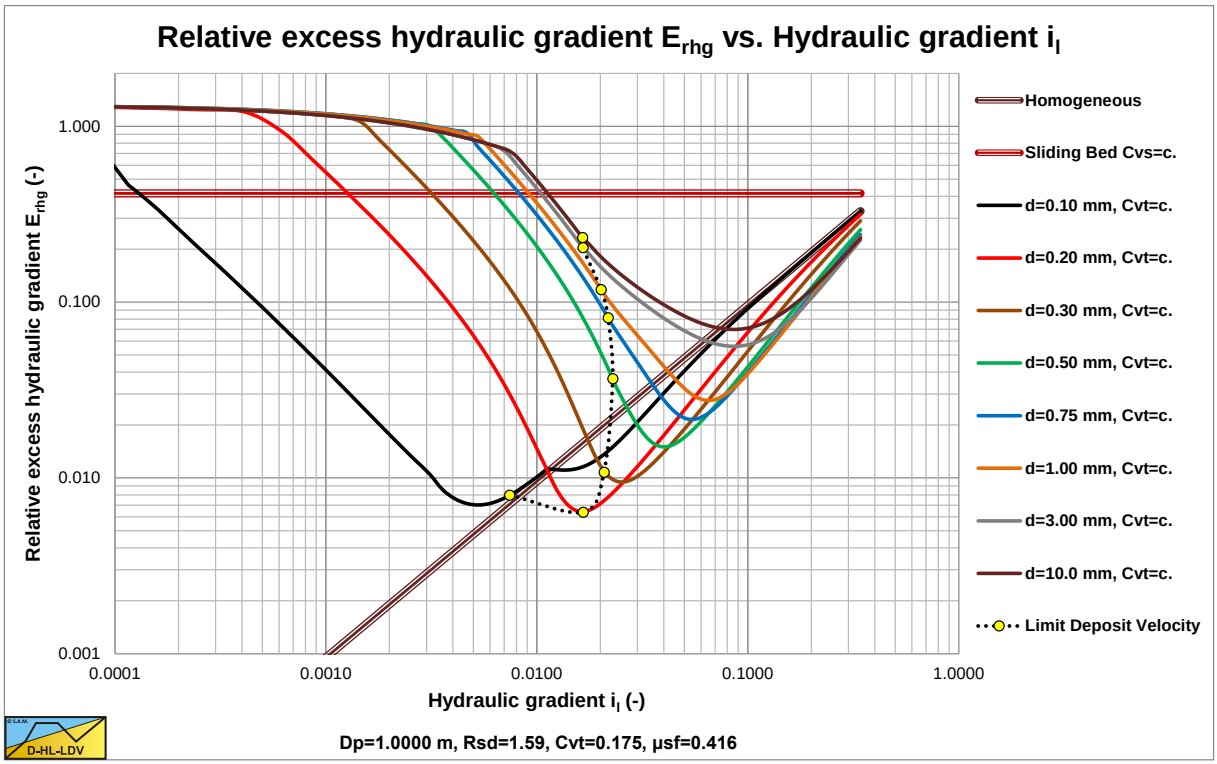

Figure 4-4: The relative excess hydraulic gradient as a function of the hydraulic gradient, constant C_{vt} and D_p=1 m.

It is clear that the flow regimes and the magnitude of the relative excess hydraulic gradient depends strongly on the pipe diameter and the particle diameter. In the large pipe a sliding bed will never occur in the constant spatial volumetric concentration case. In the small pipe however it will for particles larger than 0.5 mm. In the small pipe, the larger particles exceed the ratio $\mathbf{d/D_p>0.015}$ as set by Wilson et al. (1997), resulting in almost 100% stratified flow, here considered to be the sliding flow regime. In the large pipe this criterion is never met.

So head losses from experiments in pipes of 0.1524 m can hardly be translated into head losses for a pipe of 1 m as often used in dredging. The physical processes are different. Small pipe sliding bed versus large pipe no sliding bed and small pipe sliding flow versus large pipe no sliding flow. In fact the smaller the pipe diameter, the higher the probability of the occurrence of a sliding bed and sliding flow and the larger the pipe diameter, the lower the probability of the occurrence of a sliding bed and sliding flow. Only if the physical processes involved are similar, scaling is possible.

This explains why many equations and models from literature give good results for small pipe diameters, but deviate for large diameter pipes. The way energy is dissipated in small diameter pipes is often different from the way it is dissipated in large diameter pipes at operational line speeds. It also explains while a lot of research is focused on 2 and 3 layer transport with a sliding bed, which often occurs in small pipes, but much less in large pipes.

4.1.2. Energy Dissipation.

When a liquid is transported through a pipeline, energy is dissipated by viscous friction and by turbulence (assuming high Reynolds numbers). When solids are added, there will also be energy dissipation in the form of potential losses, kinetic losses and possibly friction losses and losses due to Magnus and turbulent lift work and turbulence in general.

- Potential energy losses. Because the solids are under the influence of gravity and the turbulence has to keep them floating. The potential energy losses will depend on the terminal settling velocity and be influenced by hindered settling. Since the settling process does not depend on the line speed, at a higher line speed the energy dissipation per unit of time will not change. This implies that the energy dissipation per unit of pipeline length is reversely proportional with the line speed. So at high line speeds the influence of the potential energy losses will diminish.
- Kinetic energy losses. Because the particles interact with the wall and with the turbulent eddies and in both cases they lose part of their kinetic energy. With the kinetic energy losses one may expect that the number of interactions is more or less constant in time, so at higher line speeds the number of interactions per unit of line length will decrease reversely proportional with the line speed, resulting in a decrease of the excess pressure due to the solids. At higher line speeds however the momentum of the particles also increases and it is more difficult to change the direction of the particles. This might decrease the number of interactions with the wall per unit of time. The total losses will be reversely proportional with the line speed to a power higher than 1, let's say a proportionality with a power between -1 and -2. The proportionality depends on the physical properties and the grading of the solids. Although near wall lift will exist at low line speeds, it is negligible until a certain line speed where the lift force is strong enough to keep the solids away from the wall. At this line speed there are no more interactions with the wall and the excess pressure collapses. At about the same line speed the lift forces start driving the solids to the center of the pipe resulting in a more homogeneous flow. The pure heterogeneous regime stops abrupt, because there are no more interactions with the wall, and the pseudo homogeneous regime starts, based on the work of lift forces and turbulence. The transition line speed depends on the particle and the pipe diameter. So the sudden regime change as described will only occur in uniform or very narrow graded sands.
- Sliding and rolling friction. Sliding and rolling friction occur if there is a sliding or moving bed or sheet flow. Forces are transmitted directly between particles and the internal and external friction coefficients determine the friction forces. These coefficients are dependent on the type of solids and the particle size distribution.
- Magnus lift work. When the thickness of the viscous sub-layer is bigger than the particle diameter, particles with rotation due to interactions with the wall will be subjected to Magnus lift forces. This will only occur for the combination of a low line speed and small particles. The Magnus lift forces will carry out work if they actually lift the particles, contributing to the energy losses. When the line speed increases, the thickness of the viscous sub-layer decreases and the particles do not fit in the viscous sub-layer anymore. The Magnus lift work will diminish when the size of the particles is bigger than the layer thickness. At a higher line speed, the turbulent lift and turbulent eddies will take over.
- Turbulent lift and eddy work. At high line speeds the turbulent lift and turbulent eddies becomes important. Since lift force times the distance over which it acts equals the work carried out, this will also result in energy losses. Since the lift force increases with the velocity gradient near the wall, the losses due to the lift force will increase with the line speed. At relatively low line speeds most solids will be transported in the bottom part of the pipeline, resulting in an asymmetrical concentration profile, matching heterogeneous flow. This results in an opposite asymmetrical velocity profile, with the highest flow at the top of the pipeline. Below a certain line speed the lift force on a particle is smaller than the weight of the particle and the lift force will not carry out any work. But above this transition velocity suddenly the particles will be lifted. The lift forces are dependent on the velocity gradient and thus will appear at the full circumference of the pipe, but they will first

start pushing the solids upwards from the bottom and thus start to create a more symmetrical concentration and velocity profile. With increasing line speed the concentration and velocity profile will get closer to the symmetrical profiles, matching pseudo homogeneous transport.

Resuming it can be stated that the potential and kinetic losses decrease with an increasing line speed with a power of the line speed between -1 and -2, while the losses due to near wall lift forces increase with an increasing line speed, until the pseudo homogeneous regime is reached. For each combination of particle and pipe diameter, there exists a transition line speed. Below this line speed kinetic losses dominate the excess pressure; above this line speed the work carried out by turbulent lift and eddy forces dominates the excess pressure. For uniform sand, kinetic losses and work carried out by lift forces will not occur at the same line speed. For graded sands a transition region, with respect to the line speed, will occur, the size of which depending on the grading. In the case where the particles are much smaller than the thickness of the viscous sub layer, theoretically there is Magnus lift if the particles are rotating. One may expect that the excess pressure due to the solids will continue decreasing with increasing line speed. In this case the excess pressure will reach zero asymptotically and there is no solids effect at very high line speeds. It is obvious that the collapse of the interactions with the wall, resulting in a collapse of the kinetic losses, due to the lift force, will happen at about the same line speed where the work of the lift forces starts increasing. This is the transition line speed between heterogeneous and pseudo homogeneous transport. It is not possible that the collapse of the kinetic losses appears at a line speed higher than the line speed where the work carried out by the lift forces starts, for uniform sands. It might be possible that this collapse appears at a slightly lower line speed, resulting in a collapse of the excess pressure, but at higher line speeds this will increase again because of the work of the lift forces.

Figure 4-5 shows a case where the transition velocity is the same for the collapse of the kinetic interactions and the start of the lift work. **Figure 4-6** shows a case where the transition velocity of the lift work is higher than the transition velocity for the collapse of the kinetic interactions. The latter results in a collapse of the relative excess hydraulic gradient. In both examples the same solids are used, but in the latter case the pipe diameter is bigger. Other experiments by Clift et al. (1982) with narrow graded 0.42 mm masonry sand, shows exactly the same phenomena.

Wilson et al. (1997) introduced the Stratification Ratio **R**, which in fact equals the relative excess hydraulic gradient. The higher the Stratification Ratio, the more asymmetrical the concentration and the velocity profile in the pipe. With increasing line speed, the Stratification Ratio decreases with power of 0.25-1.7, depending on the grading of the sand. However, once the transition line speed between heterogeneous and homogeneous transport is passed, the relative excess hydraulic gradient will increase again, while the stratification decreases. The term Stratification Ratio corresponds with the heterogeneous transport, with potential and kinetic losses, but not with the pseudo homogeneous transport with losses due to lift work. Therefore a new term is introduced, the **S**lip **R**elative **S**quared or $\mathbf{S_{rs}}$, which is the ratio between the slip velocity and the terminal settling velocity squared. Where the slip velocity is defined as; the contribution of the velocity difference between the line speed and the particle velocity to explain for the head losses. Mathematically the **S**tratification **R**atio **S**olids and the **S**lip **R**elative **S**quared are the same, but physically the **S**lip **R**elative **S**quared tells more about the physics of the heterogeneous hydraulic transport.

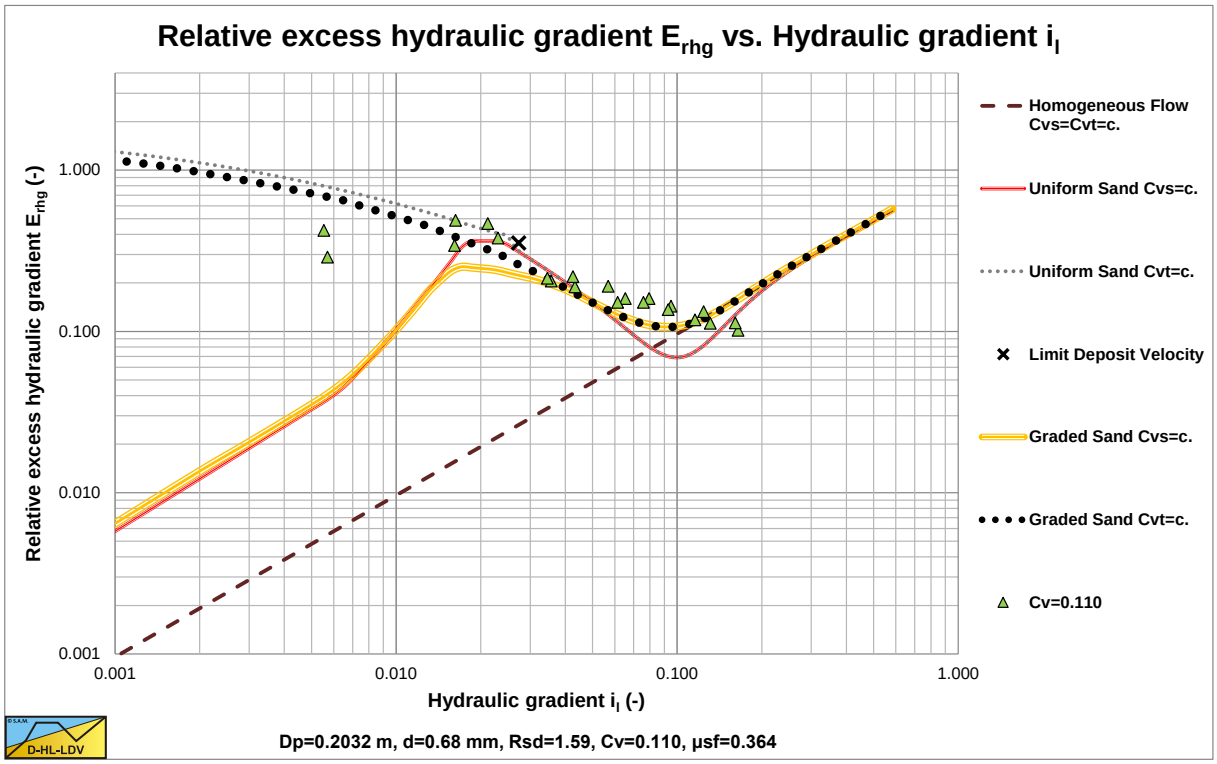

Figure 4-5: Behavior of narrow graded crushed granite slurry after Clift et al. (1982).

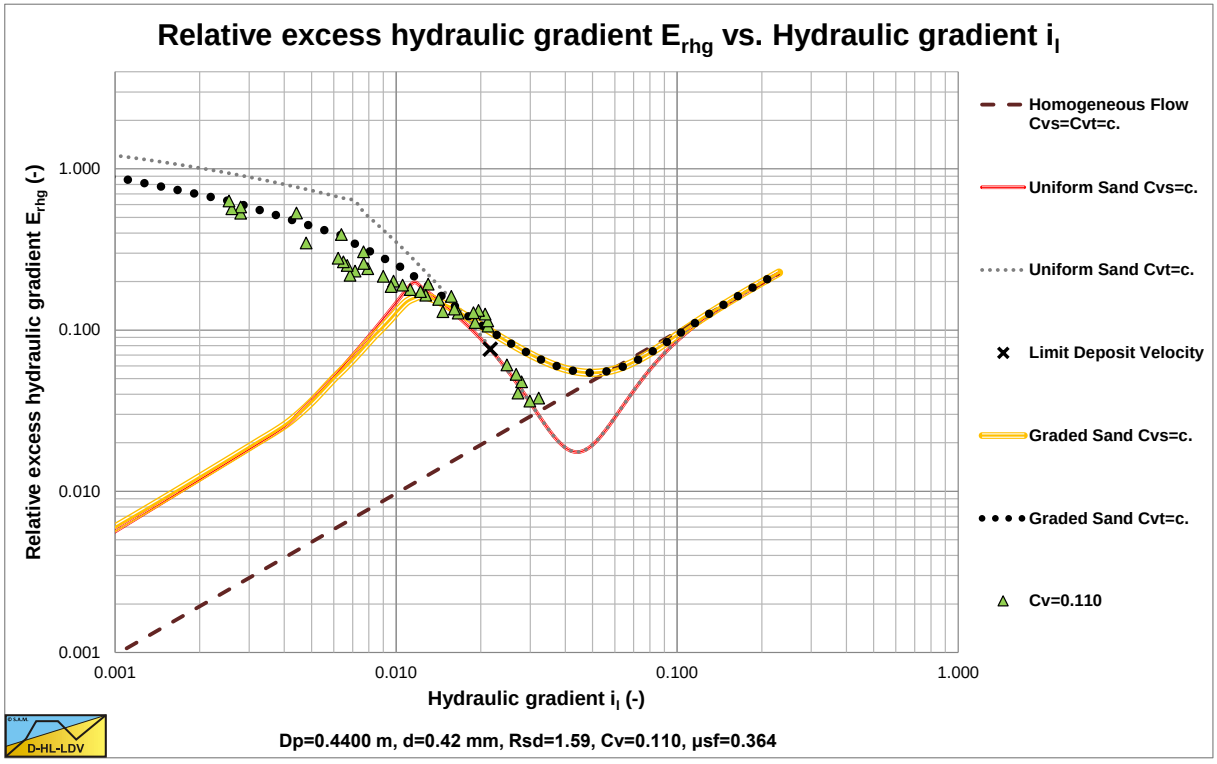

Figure 4-6: Behavior of narrow graded crushed granite slurry after Clift et al. (1982).

4.1.3. Starting Points.

Before discussing the Delft Head Loss & Limit Deposit Velocity (DHLLDV) model in detail, some starting points have to be pointed out. First of all, the model is based on a set of 4 sub-models for 4 main flow regimes. These sub-models are all based on a constant spatial volumetric concentration $\mathbf{C_{vs}}$. Curves for constant volumetric transport concentration $\mathbf{C_{vt}}$ are derived from the 4 sub-models based on the slip velocity $\mathbf{v_{sl}}$. The slip velocity $\mathbf{v_{sl}}$ is defined as the difference between the velocity of the mixture $\mathbf{v_{ls}}$ and the velocity of the solids $\mathbf{v_s}$:

$$v_{sl} = v_{ls} - v_s = v_{ls} \cdot \left(1 - \frac{v_s}{v_{ls}} \right) = v_{ls} \cdot \left(1 - \frac{C_{vt}}{C_{vs}} \right) \qquad \textbf{(4-1)}$$

For a certain control volume the volumetric transport concentration $\mathbf{C_{vt}}$ can be determined if the volumetric spatial concentration $\mathbf{C_{vs}}$ and the slip velocity $\mathbf{v_{sl}}$ are known, given a certain line speed $\mathbf{v_{ls}}$.

$$C_{vt} = \left(1 - \frac{v_{sl}}{v_{ls}} \right) \cdot C_{vs} \qquad \textbf{(4-2)}$$

Likewise, for a certain control volume, the volumetric spatial concentration $\mathbf{C_{vs}}$ can be determined if the volumetric transport concentration $\mathbf{C_{vt}}$ en the slip velocity $\mathbf{v_{sl}}$ are known, given a certain line speed $\mathbf{v_{ls}}$.

$$C_{vs} = \left(\frac{v_{ls}}{v_{ls} - v_{sl}} \right) \cdot C_{vt} \qquad \textbf{(4-3)}$$

These equations will be used a lot in the following derivations and are considered to be well known.

The 5 main flow regimes are:

1 A fixed bed regime or restricted pipe regime. The behavior of this main flow regime is, the solids form a bed at the bottom of the pipe. This bed is stationary (fixed), so the liquid has to flow through a restricted area above the bed, resulting in higher pressure losses. At higher line speeds it is probable that part of the solids start eroding and be transported heterogeneously above the bed. At the Limit Deposit Velocity, the bed has been eroded completely. As long as the pressure losses correspond with the behavior of flow through the restricted area above the bed, the flow regime is considered to be a fixed bed regime.

2 A sliding bed regime or sliding friction dominated regime. The behavior of this main flow regime is, the solids form a sliding bed at the bottom of the pipe. The pressure losses are the sum of the losses as a result of the sliding friction of the solids and the viscous friction of the liquid. At higher line speeds it is probable that part of the solids start eroding and be transported heterogeneously above the bed. At the Limit Deposit Velocity, the bed has been eroded completely. At higher concentration it is possible that sheet flow occurs and the sliding bed curve is followed right of the intersection with the heterogeneous transport curve. As long as the pressure losses correspond with the behavior of sliding friction, the pressure loss curves are parallel with the clean water resistance curve, the sliding bed regime is considered.

3 Heterogeneous transport or collision dominated regime. The behavior of this main flow regime is, the solids interact with the pipe wall through collisions. The solids are distributed non-uniformly over the cross section of the pipe with higher concentrations at the bottom of the pipe. This may be due to saltation or to Brownian motions of the particles in turbulent transport. For very small particles this may follow the fixed bed regime directly, for coarse particles this will follow the sliding bed regime.

4 Homogeneous transport. The behavior of this main flow regime is, the particles are uniformly distributed over the cross section of the pipe due to the mixing capability of the turbulent flow. The pressure losses behave according to Darcy Weisbach, but with the mixture density as the liquid density. For very fine particles the viscosity has to be adjusted by the apparent viscosity.

5 The sliding flow regime. If the ratio between the particle diameter and the pipe diameter is above a certain value and the spatial volumetric concentration is above about 5%, the turbulence is not capable of carrying the particles anymore. This will result in a high speed flow with the characteristics of sliding friction. So its named sliding flow.

Figure 4-8, **Figure 4-9** and **Figure 4-10** show the 4 main flow regimes for small, medium and large particles in an 0.1524 m (6 inch) pipeline. The abscissa, the horizontal axis, is the hydraulic gradient $\mathbf{i_l}$. The ordinate, the vertical axis, is the so called $\mathbf{E_{rhg}}$ value. The solid lines are the constant volumetric spatial concentration $\mathbf{C_{vs}}$ lines. The dashed lines the constant volumetric transport concentration $\mathbf{C_{vt}}$ lines.
The hydraulic gradient $\mathbf{i_w}$ (for water) or $\mathbf{i_l}$ (for a liquid in general) is:

$$i_l = i_w = \frac{\Delta p_l}{\rho_l \cdot g \cdot \Delta L} = \frac{\lambda_l \cdot v_{ls}^2}{2 \cdot g \cdot D_p} \qquad \textbf{(4-4)}$$

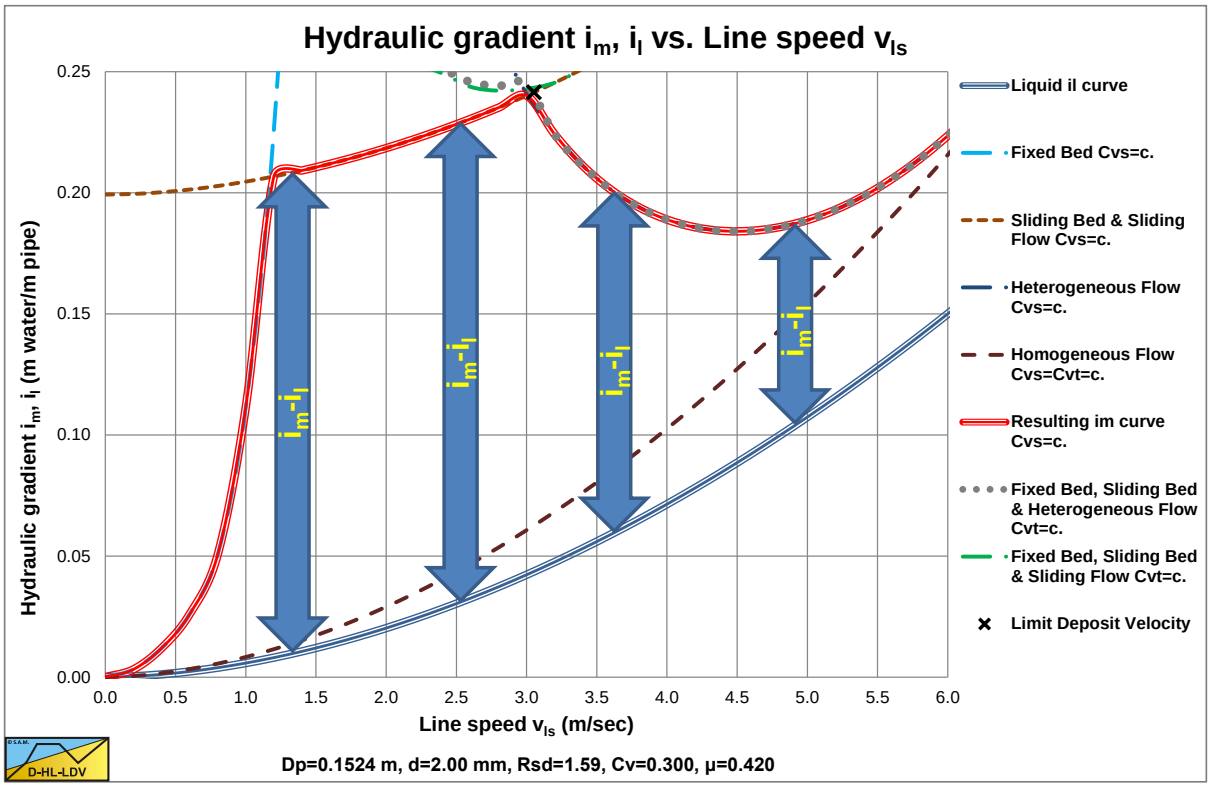

Figure 4-7: The hydraulic gradient i_m, i_l and excess hydraulic gradient i_m-i_l.

The **Relative Excess Hydraulic Gradient E_{rhg}** is the difference between the mixture gradient i_m and the hydraulic gradient i_l divided by the relative submerged density R_{sd} and the volumetric concentration C_{vs}. This E_{rhg} will also be referred to as the **solids effect**. The **Slip Relative Squared S_{rs}** is the **Slip Velocity** of a particle v_{sl} divided by the **Terminal Settling Velocity** of a particle v_t squared and this S_{rs} value is a good indication of the excess pressure losses due to the solids in the heterogeneous regime. The **Settling Velocity Hindered Relative S_{hr}** is the ratio between the hindered settling velocity $v_t \cdot (1-C_{vs}/\kappa c)^{\beta}$ and the line speed v_{ls}, divided by the relative submerged density R_{sd} and the volumetric concentration C_v. For all regimes the E_{rhg} value is:

$$E_{rhg} = \frac{i_m - i_l}{R_{sd} \cdot C_{vs}} \qquad \textbf{(4-5)}$$

In the heterogeneous regime the relation between these parameters is:

$$E_{rhg} = \frac{i_m - i_l}{R_{sd} \cdot C_{vs}} = S_{hr} + S_{rs} \qquad \textbf{(4-6)}$$

For very fine particles, the fixed bed regime transits directly to the heterogeneous regime, without the occurrence of the sliding bed regime. This can be seen in **Figure 4-8** because the intersection point is below the sliding bed curve. The Limit Deposit Velocity is at the transition between the heterogeneous regime and the homogeneous regime. Although there is some slip above the Limit Deposit Velocity, the slip and thus the difference between the constant volumetric spatial concentration C_{vs} lines and the constant volumetric transport concentration C_{vt} lines increases with a decreasing line speed at line speeds below the Limit Deposit Velocity.
For medium particles, **Figure 4-9**, the intersection point between the fixed bed regime and the heterogeneous regime lies above the sliding bed regime curve, meaning that the fixed bed regime is followed by the sliding bed regime, followed by the heterogeneous regime, with increasing line speed. The Limit Deposit Velocity is now somewhere between the intersection of the sliding bed regime with heterogeneous regime and the heterogeneous regime with the homogeneous regime. The larger the particle the closer is the Limit Deposit Velocity to the intersection of the sliding bed regime with heterogeneous regime.

For large particles, **Figure 4-10**, the behavior is similar to the medium particles, except for the fact that the Limit Deposit Velocity is at the intersection of the sliding bed regime with heterogeneous regime. The intersection point between the fixed bed regime and the heterogeneous regime will be at an increasing $\mathbf{E_{rhg}}$ value with an increasing particle diameter.

The examples given here are for an 0.1524 m pipe. For other pipe diameters, the sliding bed (constant sliding friction coefficient) and the homogeneous regime curves, will stay at the same position and do not depend on the pipe diameter. The fixed bed curve will move to the right with increasing pipe diameter, while the heterogeneous regime curve will move to the left with increasing pipe diameter. One could also say that both curves move downwards with an increasing pipe diameter.

The transitions between the main flow regimes are not instantaneously, but gradually. Special attention will be given to the transition between the heterogeneous regime and the homogeneous regime.

4.1.4. Approach.

The DHLLDV framework is based on uniform sands or gravels and constant spatial volumetric concentration.

1. An explanation of the framework of the Delft Head Loss & Limit Deposit Velocity model.
2. A detailed description of the 8 different flow regimes and 6 scenario's will be given.
3. The stationary bed regime without sheet flow and with sheet flow. The stationary bed without sheet flow is based on a 2 layer model for low line speeds and a 3 layer model for higher line speeds.
4. The sliding bed regime. The sliding bed is based on a 3 layer model showing an almost constant relative excess hydraulic gradient equal to the sliding friction coefficient.
5. The heterogeneous regime. The heterogeneous model is based on energy considerations, resulting in a two component model, potential energy losses and kinetic energy losses.
6. The homogeneous regime. The homogeneous model is based on the equivalent liquid model (ELM) with a correction based on a particle free viscous sub layer.
7. The sliding flow regime. The sliding flow model assumes a high speed flow with the macroscopic behavior of sliding friction.
8. A new model for the Limit Deposit Velocity is derived, consisting of 5 particle size regions and a lower limit. This model is based on the ratio of the potential energy of the particles to the energy in the liquid flow.
9. Based on the LDV a method is shown to construct slip velocity or slip ratio curves from zero line speed to the LDV. Based on the slip ratio, the constant delivered volumetric concentration curves can be constructed. The resulting model is compared with models from literature.
10. Knowing the slip ratio, the bed height for line speeds below the LDV can be determined. New equations are derived for this.
11. The transition from the heterogeneous regime to the homogeneous regime requires special attention. First of all, this transition line speed gives a good indication of the operational line speed and allows to compare the DHLLDV framework with many models from literature. Secondly the transition is not sharp, but depends on 3 velocities. The line speed where a particle still fits in the viscous sub layer, the transition line speed heterogeneous-homogeneous and the line speed where the lift force on a particle equals the submerged weight of the particle.
12. Finally the grading of the Particle Size Distribution (PSD) is discussed. A method is given to construct resulting head loss, slip velocity and bed height curves for graded sands and gravels.

The essential equations are given, with reference to the original equations. The purpose is to reproduce the DHLLDV framework, accompanied with flow charts.

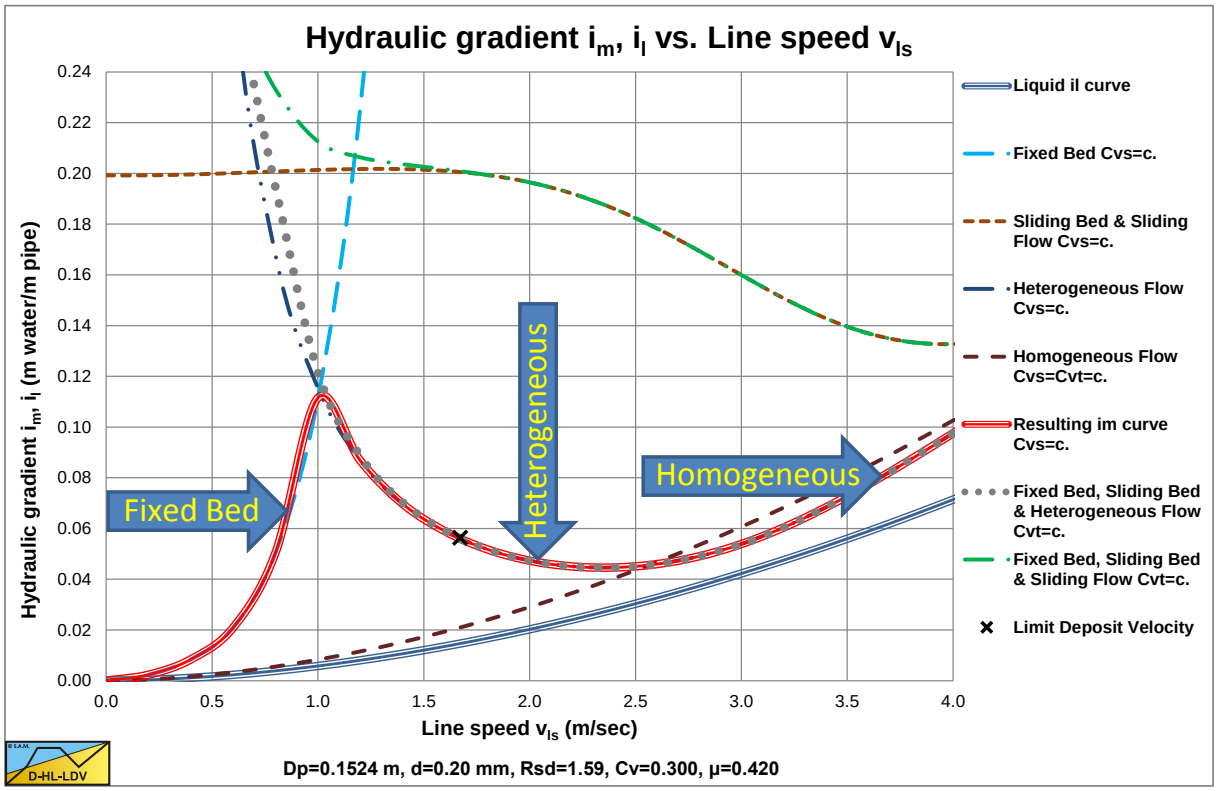

Figure 4-8: The 3 main flow regimes for fine particles.

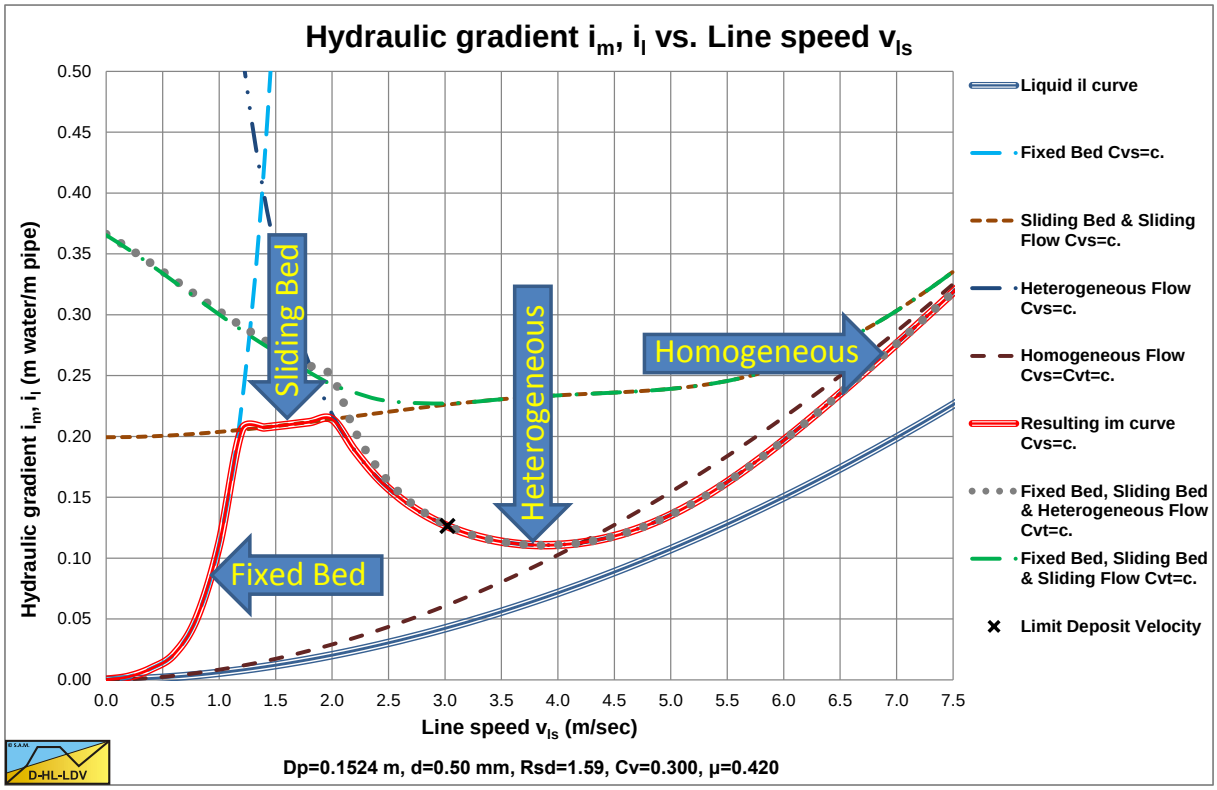

Figure 4-9: The 4 main flow regimes for medium particles.

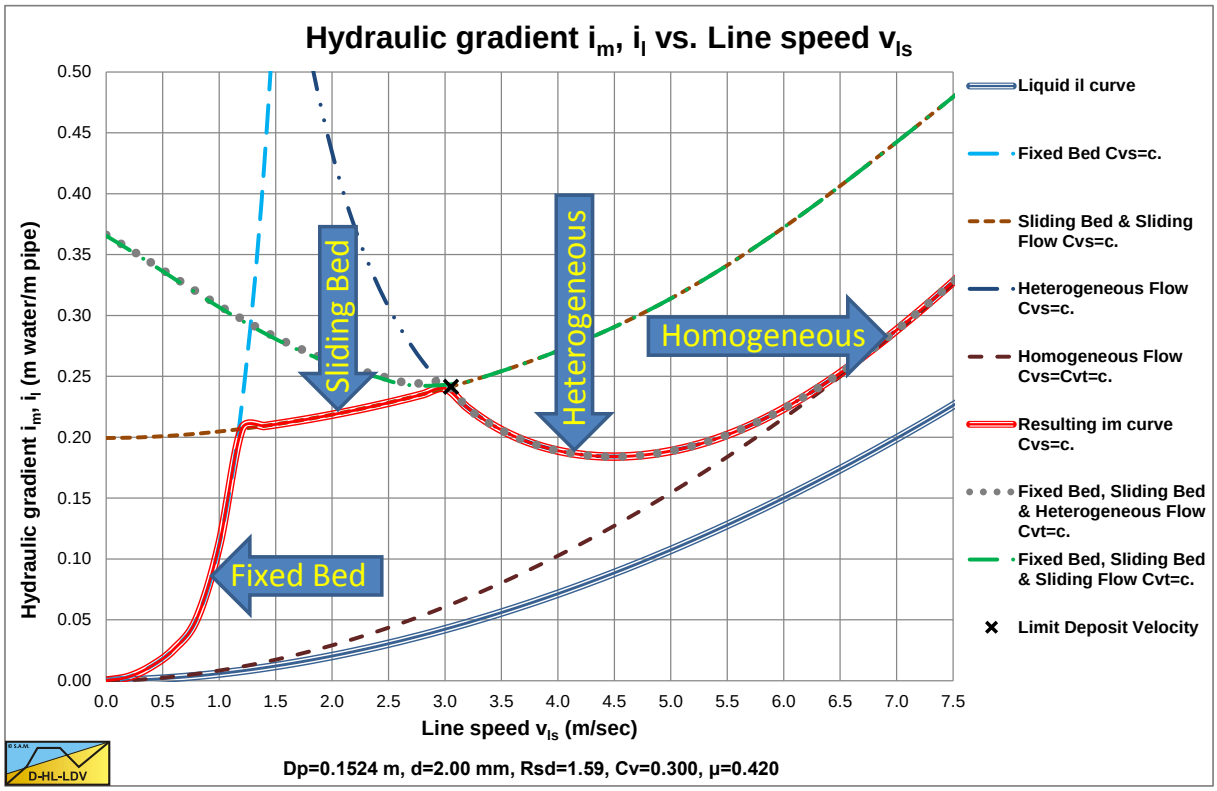

Figure 4-10: The 4 main flow regimes for coarse particles.

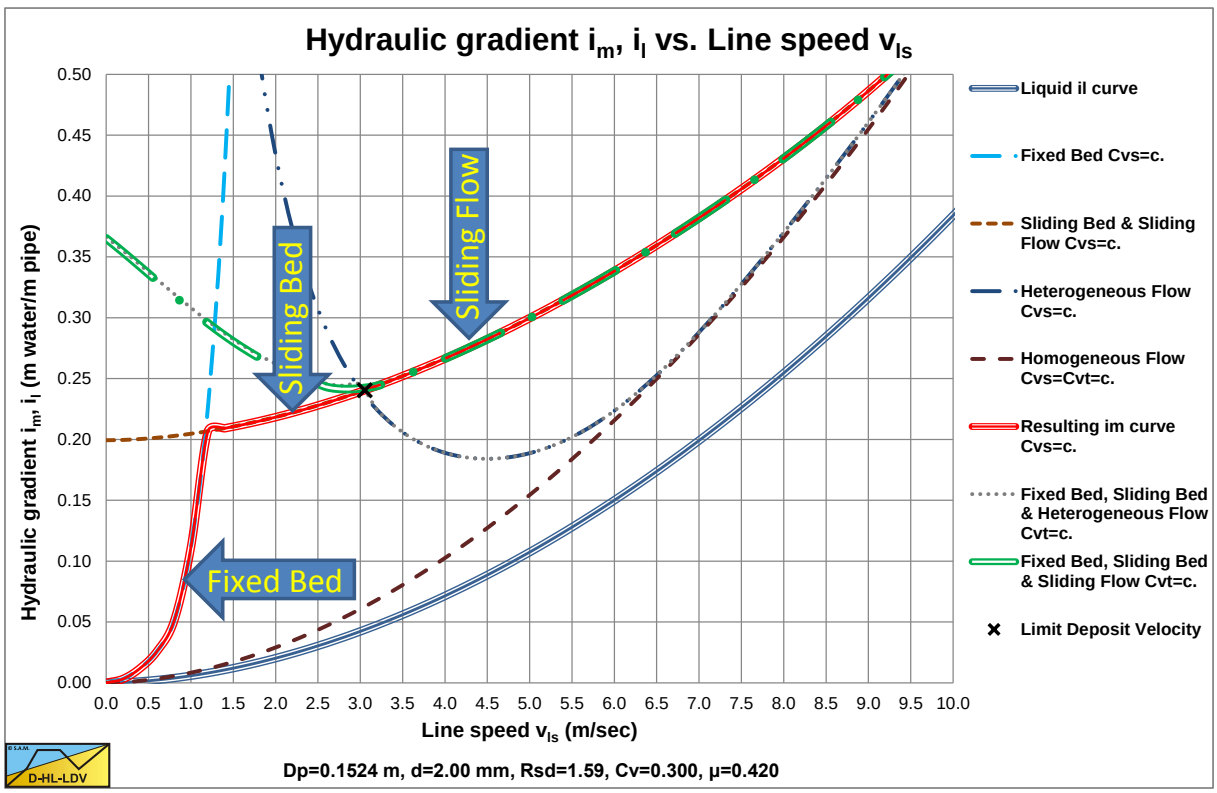

Figure 4-11: The 3 main flow regimes for coarse particles, including sliding flow.

4.1.5. Nomenclature Introduction.

C_{vs}	Spatial volumetric concentration	**-**
C_{vt}	Delivered (transport) volumetric concentration	**-**
d	Particle diameter	**m**
D_p	Pipe diameter	**m**
E_{rhg}	Relative excess hydraulic gradient	**-**
ELM	Equivalent Liquid Model	**-**
g	Gravitational constant 9.1 m/s^2	**m/s^2**
i_l	Liquid hydraulic gradient	**m/m**
i_w	Water hydraulic gradient	**m/m**
i_m	Mixture hydraulic gradient	**m/m**
ΔL	Length of pipe	**m**
LDV	Limit Deposit Velocity	**m/s**
Δp_l	Pressure difference	**kPa**
PSD	Particle Size Diagram	**-**
R_{sd}	Relative submerged density	**-**
S_{hr}	Settling velocity Hindered Relative	**-**
S_{rs}	Slip velocity Relative Squared	**-**
v_{ls}	Line speed	**m/s**
v_s	Velocity solids	**m/s**
v_{sl}	Slip velocity	**m/s**
v_t	Terminal settling velocity	**m/s**
ρ_l	Liquid density	**ton/m^3**
ρ_m	Mixture density	**ton/m^3**
κ_C	Concentration eccentricity hindered settling	**-**
λ_l	Darcy Weisbach friction factor	**-**
μ_{sf}	Sliding friction coefficient	**-**

4.2. Flow Regimes and Scenario's.

4.2.1. Introduction.

In dredging, the hydraulic transport of solids is one of the most important processes. Since the 50's many researchers have tried to create a physical mathematical model in order to predict the head losses in slurry transport. We can think of the models of Durand, Condolios, Gibert, Worster, Zandi & Govatos, Jufin Lopatin, Fuhrboter, Newitt, Doron, Wilson, Matousek and Turian & Yuan. Some models are based on phenomenological relations and thus result in semi empirical relations, others tried to create models based on physics, like the two and three layer models. It is however the question whether slurry transport can be modeled this way at all. Observations in our laboratory show a process which is often non-stationary with respect to time and space. Different physics occur depending on the line speed, particle diameter, concentration and pipe diameter. These physics are often named flow regimes; fixed bed, shearing bed, sliding bed, heterogeneous transport and (pseudo) homogeneous transport. It is also possible that more regimes occur at the same time, like, a fixed bed in the bottom layer with heterogeneous transport in the top layer.

It is the observation of the authors that researchers often focus on a detail and sub-optimize their model, which results in a model that can only be applied for the parameters used for their experiments. At high line speeds the volumetric spatial concentration (volume based) and the volumetric transport concentration (volume flux based) are almost equal, because all the particles are in suspension with a small slip related to the carrier liquid velocity. The difference of the head loss between the two concentrations will be within the margin of the scatter of the experiments. At low line speeds however, there may be a sliding or fixed bed, resulting in a big difference between the two concentrations and thus between laboratory and real life situations.

This chapter describes 8 flow regimes and 6 possible scenarios.

The flow regimes for constant spatial volumetric concentration $\mathbf{C_{vs}}$ are, from line speed zero with increasing line speed:
1: Fixed bed without suspension (fine particles) or sheet flow (coarse particles).
2: Fixed bed with suspension (fine particles) or sheet flow (coarse particles).
3: Fixed bed with suspension (fine particles) or sliding bed with sheet flow (coarse particles).
For fine to coarse particles $\mathbf{d/D_p<0.015}$:
5: Heterogeneous transport $\mathbf{C_{vs}\approx C_{vt}}$.
5/6: Pseudo homogeneous transport, $\mathbf{C_{vs}\approx C_{vt}}$.
6: Homogeneous transport, $\mathbf{C_{vs}\approx C_{vt}}$.
For very coarse particles $\mathbf{d/D_p>0.015}$:
7: Sliding flow.

The flow regimes for constant delivered volumetric concentration $\mathbf{C_{vt}}$ are, from line speed zero with increasing line speed:
8: Fixed bed with suspension (fine particles) or sheet flow (coarse particles).
4: Fixed bed with suspension (fine particles) or sliding bed with sheet flow (coarse particles).
For fine to coarse particles $\mathbf{d/D_p<0.015}$:
5: Heterogeneous transport $\mathbf{C_{vs}\approx C_{vt}}$.
5/6: Pseudo homogeneous transport, $\mathbf{C_{vs}\approx C_{vt}}$.
6: Homogeneous transport, $\mathbf{C_{vs}\approx C_{vt}}$.
For very coarse particles $\mathbf{d/D_p>0.015}$:
7: Sliding flow.

3 scenarios are based on a constant volumetric spatial concentration (usually in a laboratory) and 3 scenarios are based on a constant volumetric transport concentration (usually in real life). The flow regimes and scenarios are explained and examples of experiments are given. Based on the experimental evidence, one can conclude that the approach followed in this paper gives a good resemblance with the reality.

4.2.2. Concentration Considerations.

Based on an analysis of many experiments from literature, 8 flow regimes and 6 scenarios can be distinguished, which will be discussed in the next chapters. In order to understand these 8 flow regimes and 6 scenarios, the difference between the spatial volumetric concentration $\mathbf{C_{vs}}$ and the volumetric transport (delivered) concentration $\mathbf{C_{vt}}$ will first be discussed. In hydraulic transport, 2 definitions of the concentration are often used. Contractors are interested in the delivered volumetric concentration, also named the volumetric transport concentration $\mathbf{C_{vt}}$. $\mathbf{C_{vt}}$ is defined as the ratio between the volume flow of solids and the volume flow of the mixture. In general one can say that the average solids velocity will be smaller than the average mixture velocity. The difference is called the slip velocity. The spatial volumetric concentration $\mathbf{C_{vs}}$ is defined as the volume of solids divided by the volume of the mixture containing these solids. So the spatial volumetric concentration is based on a volume ratio, while the delivered volumetric concentration is based on a volume flux ratio. Concentration ($\mathbf{C_{vs}}$) is usually derived from density meter readings as:

$$C_{vs} = \frac{\rho_m - \rho_l}{\rho_s - \rho_l} \tag{4-7}$$

A radioactive density meter reads a density of the entire mass of slurry in the pipe, and thus is best suited to measuring $\mathbf{C_{vs}}$. In addition the placement of the meter in horizontal or vertical pipe, and the angle of the meter if in horizontal pipe, can affect the readings. A U-tube device reads the delivered density and is thus best suited to measuring $\mathbf{C_{vt}}$. In a closed loop system, we will know the volume of the closed loop and amount of material added, and thus can calculate $\mathbf{C_{vs}}$ directly, but not necessarily $\mathbf{C_{vt}}$. The volumetric delivered (transport) concentration is:

$$C_{vt} = \frac{\dot{V}_s}{\dot{V}_m} = \frac{Q_s}{Q_m} = \frac{v_s \cdot A_s}{v_m \cdot A_p} = \frac{v_s \cdot C_{vs} \cdot A_p}{v_m \cdot A_p} = C_{vs} \cdot \frac{v_s}{v_m} \tag{4-8}$$

The volumetric spatial concentration is based on the volume ratio solids/mixture according to:

$$C_{vs} = \frac{V_s}{V_m} \tag{4-9}$$

The slip velocity is defined as the difference between the velocity of the mixture and the velocity of the solids:

$$v_{sl} = v_m - v_s = v_m \cdot \left(1 - \frac{v_s}{v_m}\right) = v_m \cdot \left(1 - \frac{C_{vt}}{C_{vs}}\right) \tag{4-10}$$

Because of the fact that most experiments are carried out in a closed loop system, the concentration might be determined by the ratio of the volume of solids divided by the volume of the closed loop system.

$$C_{vs} = \frac{V_s}{V_{cl}} \tag{4-11}$$

This means that the concentration of solids in the liquid above the bed will be much smaller once a bed is formed. Now assume a bed with a porosity **n** of about 40% containing 50% of the solids, matching the $\mathbf{v_{50}}$ of Wilson (1997). This gives for the total bed volume in the closed loop system:

$$V_b = \frac{V_s}{2} \cdot \frac{1}{1-n} = \frac{C_{vs} \cdot V_{cl}}{2 \cdot (1-n)} \tag{4-12}$$

The volume of solids in suspension is the same, so the volume of the solids in the liquid is:

$$V_{s,s} = \frac{V_s}{2} \tag{4-13}$$

The volume of the mixture in suspension above the bed equals the closed loop volume minus the bed volume.

$$V_{m,s} = V_{cl} - V_b = V_{cl} - \frac{C_{vs} \cdot V_{cl}}{2 \cdot (1-n)} = V_{cl} \cdot \left(\frac{2 \cdot (1-n) - C_{vs}}{2 \cdot (1-n)} \right) \qquad \textbf{(4-14)}$$

The concentration of the solids in suspension is the volume of these solids, divided by the volume of the closed loop system minus the volume of the bed.

$$C_{vs,s} = \frac{V_s}{2 \cdot V_{m,s}} = \frac{C_{vs}}{2 \cdot \left(\frac{2 \cdot (1-n) - C_{vs}}{2 \cdot (1-n)} \right)} = \frac{(1-n) \cdot C_{vs}}{2 \cdot (1-n) - C_{vs}} \approx \frac{0.6 \cdot C_{vs}}{1.2 - C_{vs}} = \frac{C_{vs}}{2 - 1.66 \cdot C_{vs}} \qquad \textbf{(4-15)}$$

Of course the closed loop will not consist of just horizontal parts where a bed may occur, but the above example is just meant to give an indication.
This implies that at low volumetric concentrations $\mathbf{C_{vs}}$, the concentration in the suspension phase, the heterogeneous transport phase, is 50% of the total volumetric concentration. At a high concentration of $\mathbf{C_{vs}=0.3}$, the concentration of the heterogeneous phase is still reduced to 0.2. At a concentration of $\mathbf{C_{vs}=0.6}$, the above equation results in a concentration of 0.6, which makes sense, since this is solid sand and there is no suspension anymore. When experiments are carried out it should be clear which concentration is used. Is it the concentration based on the volume of the closed loop system, giving some constant volumetric spatial concentration? Is it the concentration based on radio active density meters in the pipe section where also the hydraulic gradient is measured, resulting in a spatial volumetric concentration? Or is the concentration measured with a U-tube resulting in a volumetric transport concentration. Now in a production situation there is not a closed loop system, but an open system. There is not a fixed amount of solids in the pipeline, which can be divided in a part in a bed and the rest in suspension. Instead, the supply at the suction mouth can vary from water to twice or more that the delivered concentration. In a stable situation, the production that enters the system is equal to the production that leaves the system. The concentration is determined at the suction mouth and although there may be a bed in part of the pipeline, this does not change the concentration, it just increases the line speed and concentration above the bed compared with a pipeline without a bed, due to the conservation of volume in the pipeline. The conclusion of the above considerations is that for a good interpretation of the results of experiments, the method of determining the concentration should be known. It is also important how the results are presented. Graf & Robinson (1970) for example, present their results based on a constant amount of solids in their closed loop system, while Doron & Barnea (1987) connect data points with constant volumetric transport concentration. The presentations of the results are different, while the physics are the same.

4.2.3. The 8 Flow Regimes Identified.

In literature different flow patterns or flow regimes are distinguished. Durand & Condolios (1952) distinguish 4 regimes, based on the particle size. Abulnaga (2002) also distinguished 4 regimes based on the actual flow of particles and their size. Matousek (2004) in his lecture notes distinguishes 6 flow regimes. Here we will consider 8 flow regimes and 6 scenarios for laboratory and real life conditions. These are:

Table 4-1: The 8 possible flow regimes.

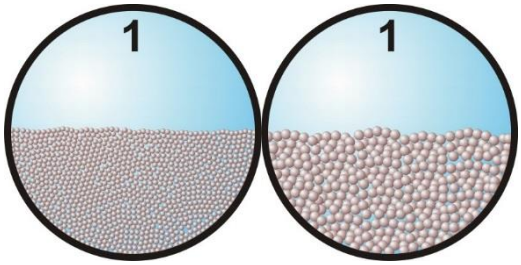

1: Fixed bed without suspension or sheet flow, constant C_{vs}.
Under laboratory circumstances with a constant spatial volumetric concentration $\mathbf{C_{vs}}$, at low line speeds all the particles are in a stationary (fixed) bed at the bottom of the pipe. Above the bed the liquid is flowing through a smaller cross-section $\mathbf{A_{flow}=A_{pipe}-A_{bed}}$. This gives a higher effective line speed $\mathbf{v_{ls,e}=v_{ls}\cdot A_{pipe}/A_{flow}}$. Since the bottom of this cross–section consists of particles, the Darcy-Weisbach friction factor λ has to be determined by taking a weighted average of the friction factor of the bed λ_b and the friction factor of the pipe wall λ_w. The method of Miedema & Matousek (2014) can be applied to determine the Darcy-Weisbach friction coefficient λ_b on the bed. This method does not distinguish between fine and coarse particles. The particle diameter is used for the roughness to determine the Darcy-Weisbach friction coefficient λ_b.
The Shields parameter is below a Shields value of about 1 so no sheet flow occurs.
The total pressure loss is thus determined by viscous friction on the bed and the pipe wall.

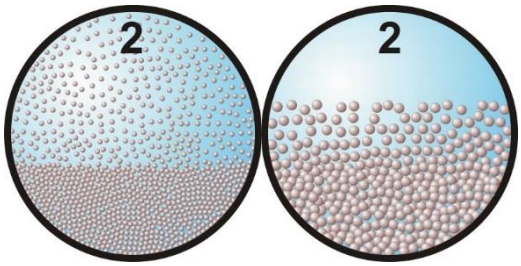

2: Fixed bed with suspension or sheet flow, constant C_{vs}.
Under laboratory circumstances with a constant spatial volumetric concentration $\mathbf{C_{vs}}$, at medium-low line speeds some of the particles are in a stationary (fixed) bed at the bottom of the pipe. Above the bed a suspension (fine particles) or a sheet flow (coarse particles) is flowing through a smaller cross-section $\mathbf{A_{flow}=A_{pipe}-A_{bed}}$. This gives a higher effective line speed $\mathbf{v_{ls,e}=v_{ls}\cdot A_{pipe}/A_{flow}}$. Since the bottom of this cross–section consists of particles, the Darcy-Weisbach friction factor λ has to be determined by taking a weighted average of the friction factor of the bed λ_b and the friction factor of the pipe wall λ_w. The method of Miedema & Matousek (2014) for sheet flow can be applied to determine the friction coefficient λ_b on the bed. This method does not distinguish between fine and coarse particles and gives an explicit relation for the Darcy-Weisbach friction factor.
The Shields parameter is above a critical Shields value, so sediment transport/erosion occurs.
The total pressure loss is thus determined by viscous friction and shear stresses in the sheet flow layer.

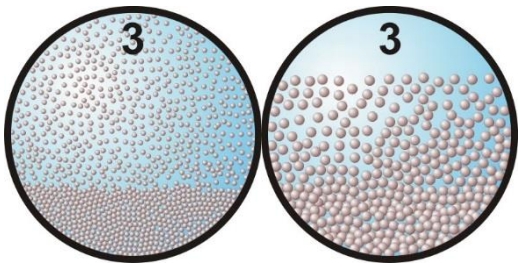

3: Fixed bed with suspension or sliding bed with sheet flow, constant C_{vs}.
Under laboratory circumstances with a constant spatial volumetric concentration $\mathbf{C_{vs}}$, for coarse particles the bed is sliding with sheet flow, where the thickness of the sheet flow layer increases with an increasing velocity difference between the flow above the bed and the bed, while for fine particles the shear stress on the bed is not high enough to make it start sliding, but more and more particles will be in suspension as the line speed increases. For fine particles the behavior starts following the heterogeneous behavior.
Since coarse particles in sheet flow require an upwards force at least equal to their submerged weight, which results from interparticle forces, an equal downwards force will act on the bed. The result is a total normal force between the bed and the pipe wall of about the submerged weight of the particles. From experiments it appears that this normal force is almost a constant, according to the Newitt et al. (1955) model. This vertical force times the friction coefficient μ_{sf} determines the sliding friction force. The friction coefficient μ_{sf} will have a value of about 0.415, but should preferably be determined by experiments, since it is a property of the particles.
The Shields parameter is above a critical Shields value, so sediment transport/erosion occurs.
The total pressure loss is thus determined by sliding friction between the bed and the pipe wall for coarse particles and by energy losses due to collisions for fine particles.

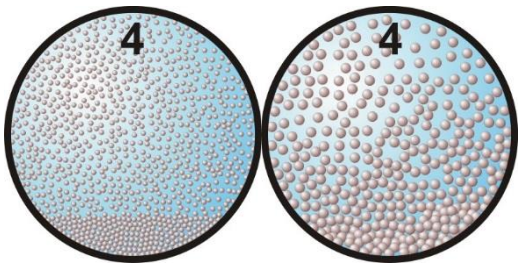

4: Fixed bed with suspension or sliding bed with sheet flow, constant C_{vt}.
Under laboratory circumstances with a constant spatial volumetric concentration $\mathbf{C_{vs}}$, for coarse particles the bed is sliding with sheet flow, where the thickness of the sheet flow layer increases further with an increasing velocity difference between the flow above the bed and the bed, while for fine particles the shear stress on the bed is not high enough to make it start sliding, but almost all particles will be in suspension as the line speed increases. For fine particles the behavior follows the heterogeneous behavior.
Since coarse particles in sheet flow require an upwards force at least equal to their submerged weight, which results from interparticle forces, an equal downwards force will act on the bed. The result is a total normal force between the bed and the pipe wall of about the submerged weight of the particles. From experiments it appears that this normal force is almost a constant, according to the Newitt et al. (1955) model. This vertical force times the friction coefficient μ_{sf} determines the sliding friction force. The friction coefficient μ_{sf} will have a value of about 0.415, but should preferably be determined by experiments, since it is a property of the particles.
The Shields parameter is above a critical Shields value, so sediment transport/erosion occurs.
The total pressure loss is thus determined by sliding friction between the bed and the pipe wall for coarse particles and by energy losses due to collisions for fine particles.

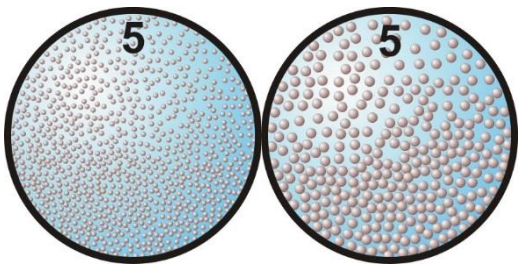

5: Heterogeneous transport, $C_{vt} \approx C_{vs}$.
The turbulent forces interacting with the particles are not strong enough to create a uniform composition throughout the cross-section of the pipe. A definite concentration gradient exists along the vertical profile of the pipe with the highest concentration at the bottom. There are no deposits and all the particles move in suspension or sheet flow. There is however an interaction between the particles and the bottom of the pipe. These interactions, collisions, cause the loss of kinetic energy of the particles and are the main cause of the pressure losses. Since the number of collisions per unit of time depends mainly on the terminal settling velocity of the particles, it will be almost constant, resulting in pressure losses that are reversely proportional with the line speed or the line speed to a higher power. The pressure losses can be determined according to Durand & Condolios (1952), Jufin & Lopatin (1966) or Miedema &Ramsdell (2013). The heterogeneous model is the same for fine and coarse particles.
The Shields parameter is very high above the Shields curve, resulting in suspension/saltation. The total pressure loss is determined by the collisions between the particles and the bottom of the pipe.

5/6: Pseudo homogeneous transport, $C_{vt} \approx C_{vs}$.
At the line speed where heterogeneous and homogeneous transport meet, there will be a transition between the two regimes. This transition depends on a number of velocities. If the thickness of the viscous sub-layer is bigger than the particle diameter, the particles will be subjected to Magnus lift. This Magnus lift will carry out work, resulting in higher pressure losses. If the velocity at which this occurs is near the transition velocity, this will play a role. If the turbulent lift force equals the submerged weight of the particle, this lift force will prevent the particles from hitting the bottom of the pipe, resulting in a sudden drop of the pressure losses. At slightly higher line speeds the lift force is strong enough to push the particles into the turbulent flow, where turbulent dispersion will take care of further mixing. In between there may be a gap resulting in almost no additional pressure losses. This occurs for particles with diameter from 0.1-0.5 mm with bigger pipe diameters. The pressure losses can be determined according to Miedema &Ramsdell (2013).
The Shields parameter is very high above the Shields curve, resulting in a suspension. The total pressure loss is determined by the collisions between the particles and the bottom of the pipe if they are present and by the work carried out by lift forces and turbulent dispersion.

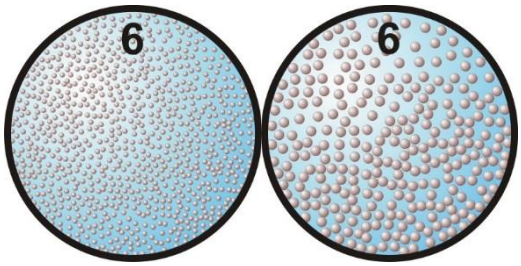

6: Homogeneous transport, $C_{vt} \approx C_{vs}$.
The turbulent forces interacting with the particles are so strong that the mixture has an almost uniform composition throughout the cross-section of the pipe. True homogeneous flows is not possible, since for the turbulent forces to overcome gravity, a concentration gradient has to exist. Pseudo homogeneous regimes usually occur with very fine particles or at very high line speeds. The pressure losses in this regime can be modeled using the adapted equivalent liquid model. It is assumed that the spatial volumetric concentration $\mathbf{C_{vs}}$ and the volumetric transport (delivered) concentration $\mathbf{C_{ts}}$ are almost equal.
The Shields parameter is very high above the Shields curve, resulting in a suspension. The total pressure loss is determined by the work carried out by lift forces and turbulent dispersion.

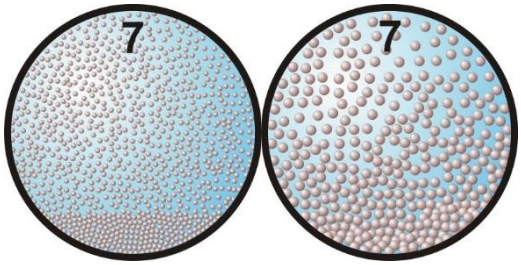

7: Sliding Flow.
At relatively low concentrations and relatively small particle diameters, the sliding bed regime will have a transition to the heterogeneous regime at the intersection of the two regimes. This is the result of lift forces strong enough to lift the particles and turbulent dispersion to mix them into a heterogeneous mixture. However when the weight of the bed is bigger than the total lift forces, this will not occur and the particles stay in the bed in a sort of sheet flow. A second reason may be that at high concentrations the space above the bed is not big enough to fully develop turbulence. When the line speed increases, the lift forces by turbulence will also increase and the sliding bed will finally vaporize into heterogeneous transport. The pressure losses in this regime are much higher than the pressure losses with heterogeneous transport at lower concentrations. The pressure losses can be determined according to Miedema &Ramsdell (2013). The term Sliding Flow is chosen, because there is flow but the flow resistance has the character of sliding friction.
The Shields parameter is far above the Shields curve, so sediment transport/erosion occurs.
The total pressure loss is thus determined by sliding friction between the bed and the pipe wall.

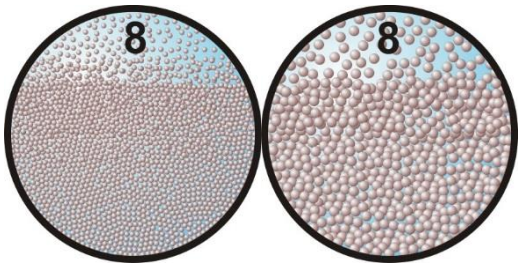

8: Fixed bed with suspension, constant C_{vt}.
Under real life conditions, there will be a "constant" volumetric transport concentration with decreasing line speed. There will be equilibrium between erosion and deposition, resulting in a certain bed height. Gibert (1960) has proposed that the Froude number will be equal to the Froude number at the Limit Deposit Velocity. In this case, the Limit Deposit Velocity is defined as the velocity where the sliding bed has vaporized due to erosion. With decreasing line speed, the bed height increases and so do the pressure losses. Once the bed height is known, the pressure losses can be determined according to the Newitt et al. (1955) model. This regime occurs if the relative excess hydraulic gradient is high enough to result in a sliding bed and so this will occur much more with small pipe diameters then with large pipe diameter.
The Shields parameter is above the Shields curve, so erosion occurs.
The total pressure loss is thus determined by sliding friction between the bed and the pipe wall.

4.2.4. The 6 Scenario's Identified.

In pipes with small diameters the hydraulic gradient will be relatively high, resulting in relatively high hydraulic gradients when transporting a mixture. This results in hydraulic gradients approaching the hydraulic gradient required to create a sliding bed. In pipes with large diameters the hydraulic gradient will be relatively small, also resulting in relatively small hydraulic gradients when transporting a mixture. This results in hydraulic gradients too small compared with the hydraulic gradient required to create a sliding bed.
The 9 regimes and 6 scenarios are shown in **Figure 4-12**, **Figure 4-13** and **Figure 4-14**. **Figure 4-12** shows the scenario **L1** for laboratory conditions and **R1** for real life conditions. **Figure 4-13** show the scenario's **L2** for laboratory conditions and **R2** for real life conditions. **Figure 4-14** show the scenario's **L3** for laboratory conditions and **R3** for real life conditions. The difference between laboratory conditions and real life conditions can be found at low line speeds where the volumetric spatial $\mathbf{C_{vs}}$ and transport $\mathbf{C_{vt}}$ concentrations differ substantially. At higher line speeds with heterogeneous and (pseudo) homogeneous transport it is assumed that the slip velocity $\mathbf{v_{sl}}$ is small compared with the line speed $\mathbf{v_{ls}}$.

4.2.5. Scenarios L1 & R1.

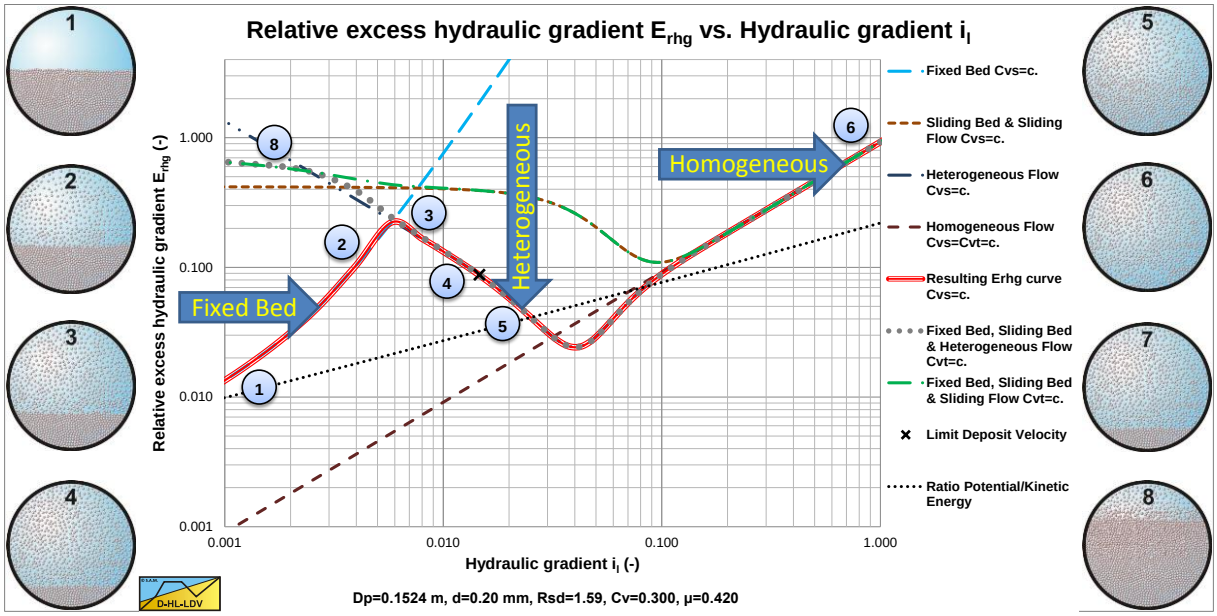

Figure 4-12: The definition of the pressure losses, scenario's L1 and R1, $E_{rhg}(i_l)$.

Table 4-2: Scenario's L1 and R1.

Scenario L1

Table 4-3: Indication of occurrence of L1.

D_p	d	C_v
<<	>>	>>
<	>	>
-	-	-
>	<	<
>>	<<	<<

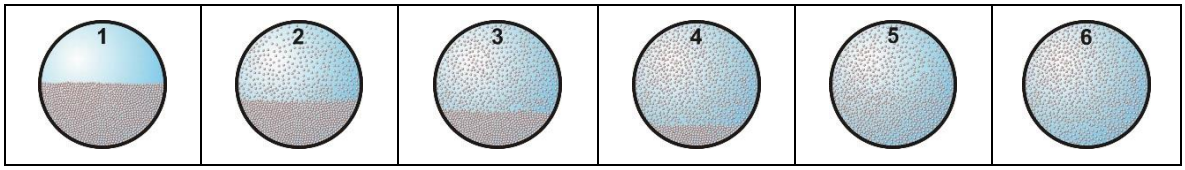

Starting at a line speed $\mathbf{v_{ls}=0}$, there will be a stationary (fixed) bed **(1)**. When the line speed is increased, there will not be erosion until the Shields parameter is high enough above the Shields curve. Increasing the line speed

further will result in erosion and suspension or saltation of the particles **(2)**. At the Limit Deposit Velocity, the bed is completely vaporized and the transport will have a transition from fixed bed to heterogeneous **(5)**. This also means that the excess pressure losses go from shear stress dominated to collision dominated. Increasing the line speed further, results in a transition region between heterogeneous transport and (pseudo) homogeneous transport **(6)**. At very high line speeds, the regime will be the homogeneous regime **(7)**. Whether this regime will be reached with practical line speeds depends completely on the combination of the parameters involved.

Scenario R1

Table 4-4: Indication of occurrence of R1.

D_p	d	C_v
<<	>>	>>
<	>	>
-	-	-
>	<	<
>>	<<	<<

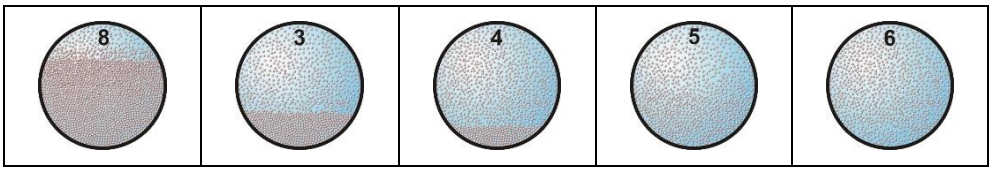

Starting at a line speed $\mathbf{v_{ls}=0}$, there will be equilibrium between erosion and deposition, resulting in a certain bed height. Above the bed there will be heterogeneous transport. At very low line speeds, the hydraulic gradient is so high that a sliding bed may occur. At higher line speeds, the hydraulic gradient drops, resulting in a stationary bed. With a stationary bed, the friction between the bed and the pipe wall is not fully mobilized. In fact the pressure losses depend on the heterogeneous behavior between the suspension and the bed **(9)**. At the Limit Deposit Velocity, the bed is completely vaporized and the transport will have a transition from fixed bed to heterogeneous transport **(5)**. This also means that the excess pressure losses go from shear stress dominated to collision dominated. Increasing the line speed further, results in a transition region between heterogeneous transport and (pseudo) homogeneous transport **(6)**. At very high line speeds, the regime will be the homogeneous regime **(7)**. Whether this regime will be reached with practical line speeds depends completely on the combination of the parameters involved.

4.2.6. Scenarios L2 & R2.

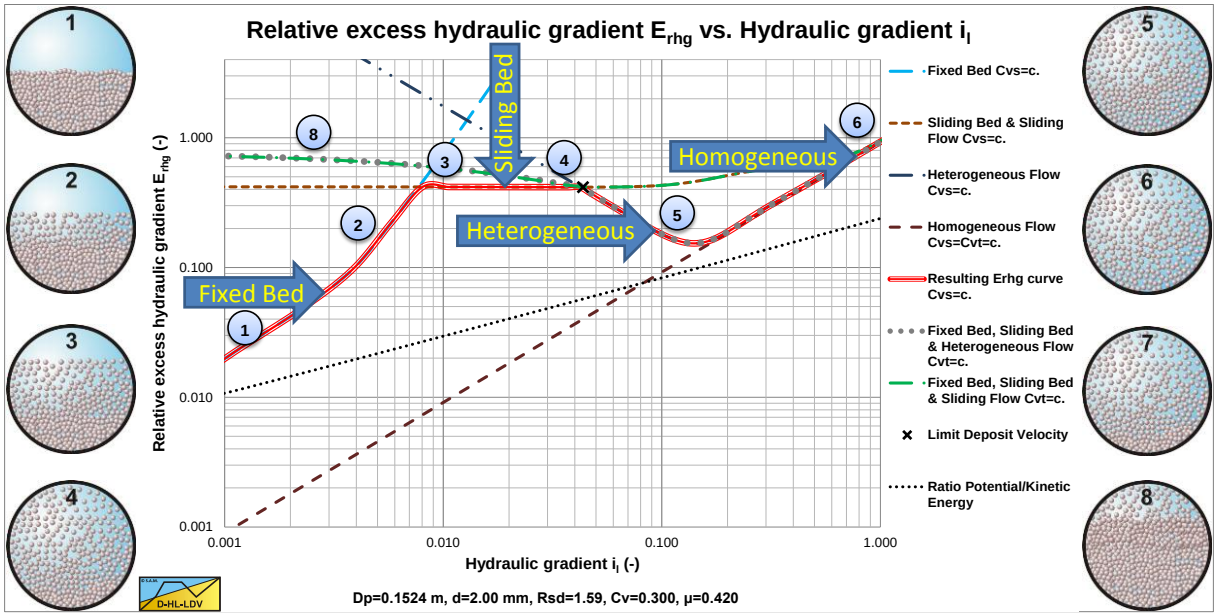

Figure 4-13: The definition of the pressure losses, scenario's L2 and R2, $E_{rhg}(i_l)$.

Table 4-5: Scenario's L2 and R2.

Scenario L2

Table 4-6: Indication of occurrence of L2.

D_p	d	C_v
<<	>>	>>
<	>	>
-	-	-
>	<	<
>>	<<	<<

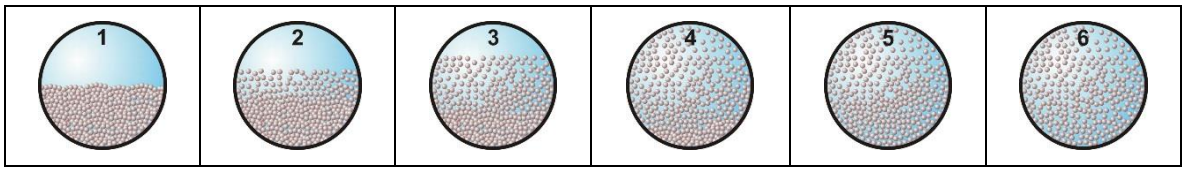

Starting at a line speed v_{ls}**=0**, there will be a stationary (fixed) bed **(1)**. When the line speed is increased, there will not be erosion until the Shields parameter is high enough above the Shields curve. Increasing the line speed further will result in erosion and suspension or saltation of the particles **(2)**. At a certain line speed, the hydraulic gradient is high enough to make the bed to start sliding **(3)**. Increasing the line speed further will result in an increase of the velocity of the bed and an increase of the erosion. The relative excess hydraulic gradient remains constant, because the weight of the suspension and the bed is a constant, resulting in an almost constant friction force. At the Limit Deposit Velocity, the bed is completely vaporized and the transport will have a transition from sliding bed to heterogeneous **(5)**. This also means that the excess pressure losses go from sliding friction dominated to collision dominated. Increasing the line speed further, results in a transition region between heterogeneous transport and (pseudo) homogeneous transport **(6)**. At very high line speeds, the regime will be the homogeneous regime **(7)**. Whether this regime will be reached with practical line speeds depends completely on the combination of the parameters involved.

Scenario R2

Table 4-7: Indication of occurrence of R2.

D_p	d	C_v
<<	>>	>>
<	>	>
-	-	-
>	<	<
>>	<<	<<

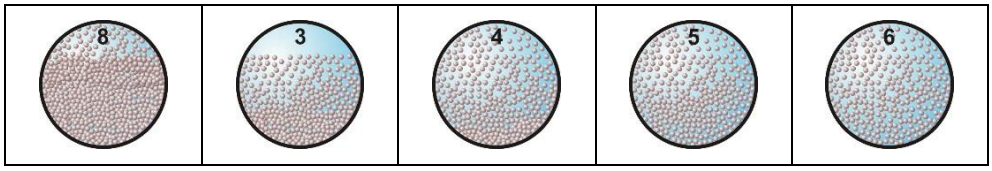

Starting at a line speed $\mathbf{v_{ls}=0}$, there will be equilibrium between erosion and deposition, resulting in a certain bed height. Gibert (1960) has proposed that the Froude number will be equal to the Froude number at the Limit Deposit Velocity. In this case the Limit Deposit Velocity is defined as the velocity where the sliding bed has vaporized due to erosion. With decreasing line speed, the bed height increases and so do the pressure losses **(4)**. At a certain line speed, the hydraulic gradient is high enough to make the bed to start sliding **(3)**. Increasing the line speed further will result in an increase of the velocity of the bed and an increase of the erosion. The relative excess hydraulic gradient remains constant, because the weight of the suspension and the bed is a constant, resulting in an almost constant friction force. At the Limit Deposit Velocity, the bed is completely vaporized and the transport will have a transition from sliding bed to heterogeneous **(5)**. This also means that the excess pressure losses go from sliding friction dominated to collision dominated. Increasing the line speed further, results in a transition region between heterogeneous transport and (pseudo) homogeneous transport **(6)**. At very high line speeds, the regime will be the homogeneous regime **(7)**. Whether this regime will be reached with practical line speeds depends completely on the combination of the parameters involved.

4.2.7. Scenarios L3 & R3.

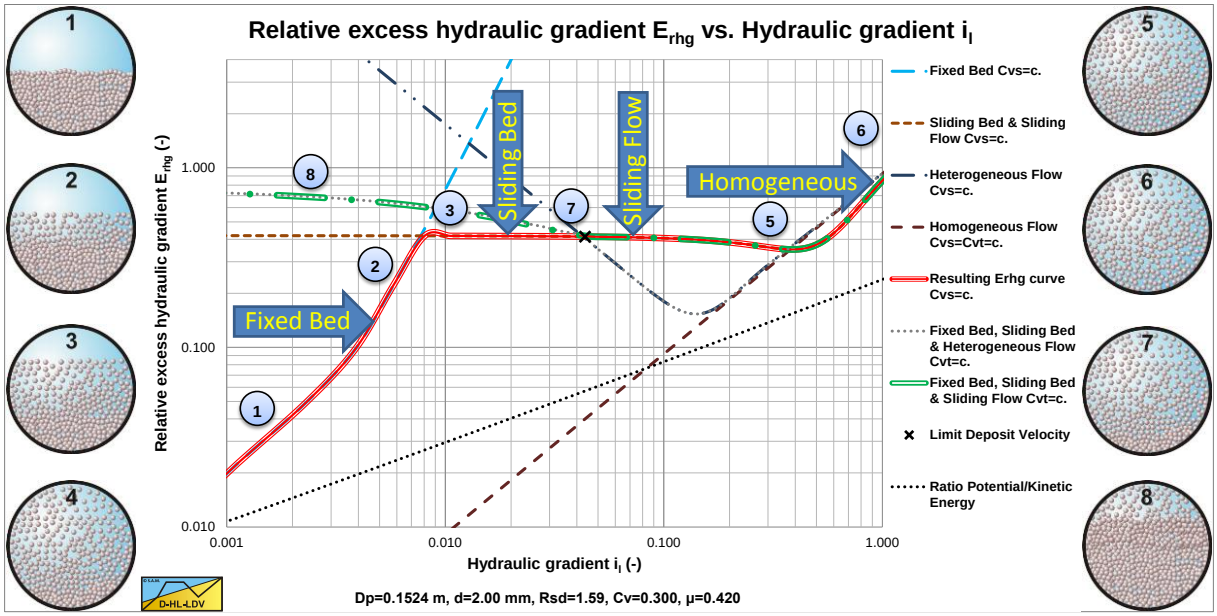

Figure 4-14: The definition of the pressure losses, scenario's L3 and R3, $E_{rhg}(i_l)$.

Table 4-8: Scenario's L3 and R3.

Scenario L3

Table 4-9: Indication of occurrence of L3.

D_p	d	C_v
<<	>>	>>
<	>	>
-	-	-
>	<	<
>>	<<	<<

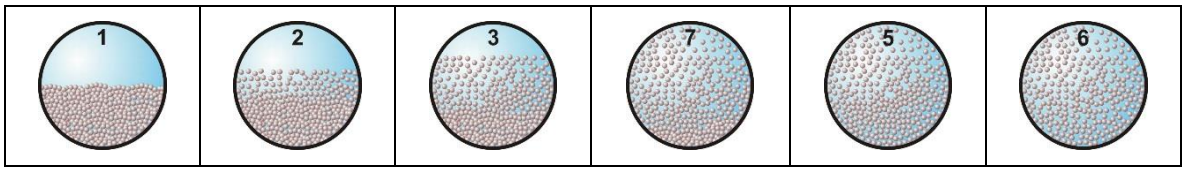

Starting at a line speed v_{ls}**=0**, there will be a stationary (fixed) bed **(1)**. When the line speed is increased, there will not be erosion until the Shields parameter is high enough above the Shields curve. Increasing the line speed further will result in erosion and suspension or saltation of the particles **(2)**. At a certain line speed, the hydraulic gradient is high enough to make the bed to start sliding **(3)**. Increasing the line speed further will result in an increase of the velocity of the bed and an increase of the erosion. The relative excess hydraulic gradient remains constant, because the weight of the suspension and the bed is a constant, resulting in an almost constant friction force. At the theoretical Limit Deposit Velocity, the shear stress on the bed and the resulting lift forces and turbulent dispersion are not strong enough to make the bed vaporize and create heterogeneous flow. The sheet flow occurs and there will be a sliding bed/sheet flow up to a higher line speed **(8)**. At a much higher line speed the sliding bed/sheet flow will erode and a pseudo homogeneous regime will occur **(6)**. At very high line speeds there will be a homogeneous regime **(7)**, but this will be at unreasonable high line speeds.

Scenario R3

Table 4-10: Indication of occurrence of R3.

D_p	d	C_v
<<	>>	>>
<	>	>
-	-	-
>	<	<
>>	<<	<<

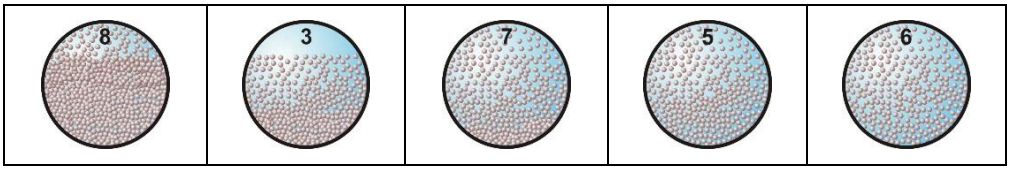

Starting at a line speed $\mathbf{v_{ls}=0}$, there will be equilibrium between erosion and deposition, resulting in a certain bed height. Gibert (1960) has proposed that the Froude number will be equal to the Froude number at the Limit Deposit Velocity. In this case the Limit Deposit Velocity is defined as the velocity where the sliding bed has vaporized due to erosion. With decreasing line speed, the bed height increases and so do the pressure losses **(4)**. At a certain line speed, the hydraulic gradient is high enough to make the bed to start sliding **(3)**. Increasing the line speed further will result in an increase of the velocity of the bed and an increase of the erosion. The relative excess hydraulic gradient remains constant, because the weight of the suspension and the bed is a constant, resulting in an almost constant friction force. At the theoretical Limit Deposit Velocity, the shear stress on the bed and the resulting lift forces and turbulent dispersion are not strong enough to make the bed vaporize and create heterogeneous flow. The sheet flow occurs and there will be a sliding bed/sheet flow up to a higher line speed **(8)**. At a much higher line speed the sliding bed/sheet flow will erode and a pseudo homogeneous regime will occur **(6)**. At very high line speeds there will be a homogeneous regime **(7)**, but this will be at unreasonable high line speeds.

4.2.8. Conclusions & Discussion.

From **Figure 4-12**, **Figure 4-13** and **Figure 4-14** it is clear that the characterization of flow regimes of Durand (1952), Abulnaga (2002) or Matousek (2004) is not adequate enough to identify all possible scenarios. Flow regime graphs like the ones published by Newitt (1955) or King (2002) (based on Turian & Yuan (1977)) already give a better understanding. These graphs however do not show the difference between laboratory and real life conditions and do not take the sheet flow effect into account, probably because the volumetric concentrations were not high enough.

4.3. Verification & Validation.

The **Relative Excess Hydraulic Gradient E_{rhg}** is the contribution of the solids to the relative hydraulic gradient. The word relative is used here because the hydraulic gradient is divided by the volumetric concentration C_v and the relative submerged density R_{sd} in order to determine the E_{rhg}. The E_{rhg} can be applied for all flow regimes. The relative submerged density R_{sd} is defined as:

$$R_{sd} = \frac{\rho_s - \rho_l}{\rho_l} \tag{4-16}$$

The **Slip Relative Squared S_{rs}** is the **Slip Velocity** of a particle v_{sl} divided by the **Terminal Settling Velocity** of a particle v_t squared and this S_{rs} value is a good indication of the excess pressure losses due to the kinetic energy losses of the solids. The **Settling Velocity Hindered Relative S_{hr}** is the ratio between the hindered settling velocity $v_t \cdot (1-C_v/\kappa)^{\beta}$ and the line speed v_{ls}, divided by the relative submerged density R_{sd} and the volumetric concentration C_v. The S_{hr} value gives a good approximation of the potential energy losses of the solids. The S_{hr} and S_{rs} are derived and can be applied for the heterogeneous regime.

$$E_{rhg} = \frac{i_m - i_l}{R_{sd} \cdot C_v} = R_{ss} = S_{hr} + S_{rs} = \left(\frac{v_t \cdot \left(1 - \frac{C_v}{\kappa_C}\right)^{\beta}}{v_{ls}} \right) + \left(\frac{v_{sl}}{v_t} \right)^2 \tag{4-17}$$

The **Stratification Ratio** of the **Solids R_{ss}** is a measure for the level of stratification of slurry as introduced by Wilson et al. (1997). A high stratification ratio means that the slurry is (almost) fully stratified; the liquid phase and the sediment (bed) phase are almost separated. Under laboratory conditions with constant volumetric spatial concentration C_{vs}, the S_{rs} is limited by the value of the friction coefficient μ, for a sliding bed with a high S_{rs} . The lower limit of the S_{rs} is when the heterogeneous regime transits to the (pseudo) homogeneous regime. Also here the S_{rs} is derived and can be applied for the heterogeneous regime only. Resuming, the E_{rhg} is valid for all flow regimes, the S_{rs} is valid for the heterogeneous regime and the friction factor μ is valid for the sliding bed regime. In the following examples the $E_{rhg}(i_l)$ graph will be used. The advantage of the $E_{rhg}(i_l)$ graph is that this type of graph is almost independent of the values of concentration C_v and relative submerged density R_{sd}, but also almost independent of the pipe wall roughness and the temperature (kinematic viscosity). A disadvantage may be that it will take more effort to transform this graph back to real life data. In these graphs always the lines for homogeneous (equivalent liquid) transport, heterogeneous transport, fixed bed (constant C_{vs}), sliding bed (both constant C_{vs} and constant C_{vt}) are drawn, in order to form a reference system.

4.3.1. L1: Fixed Bed & Heterogeneous, Constant C_{vs}.

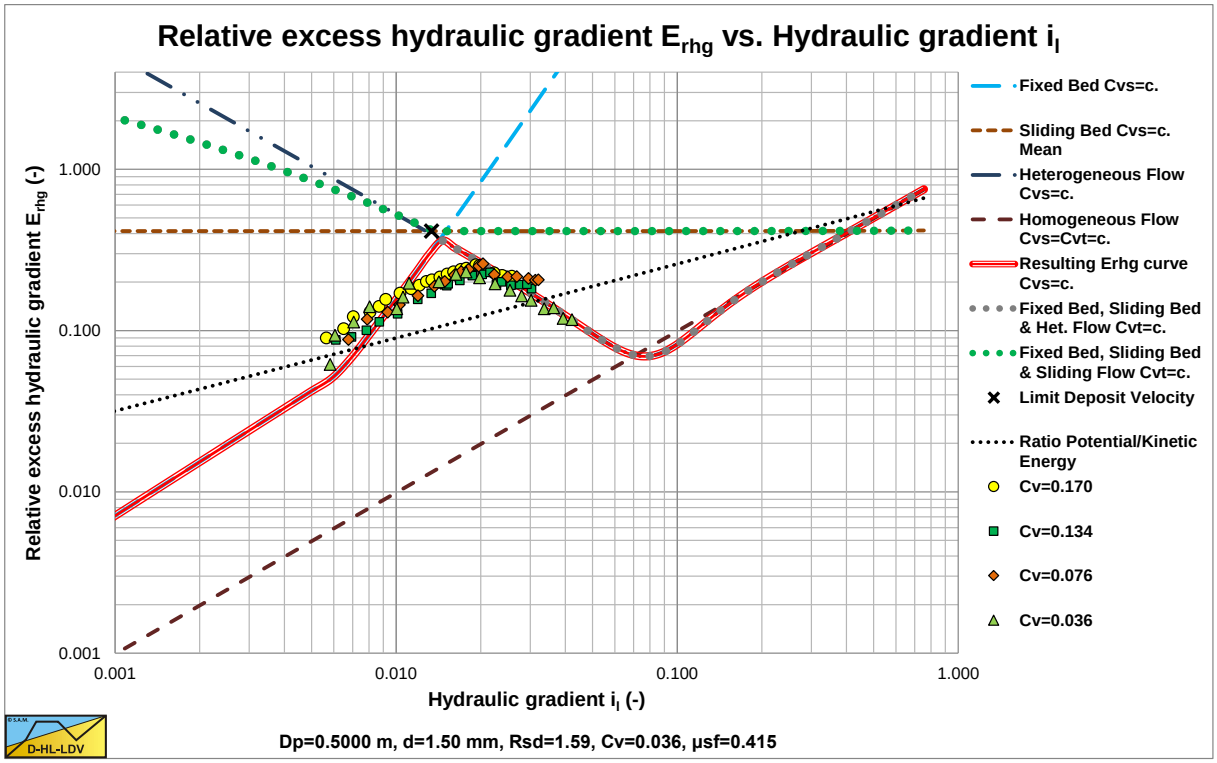

Figure 4-15: Kazanskij (1980), sand, low concentration

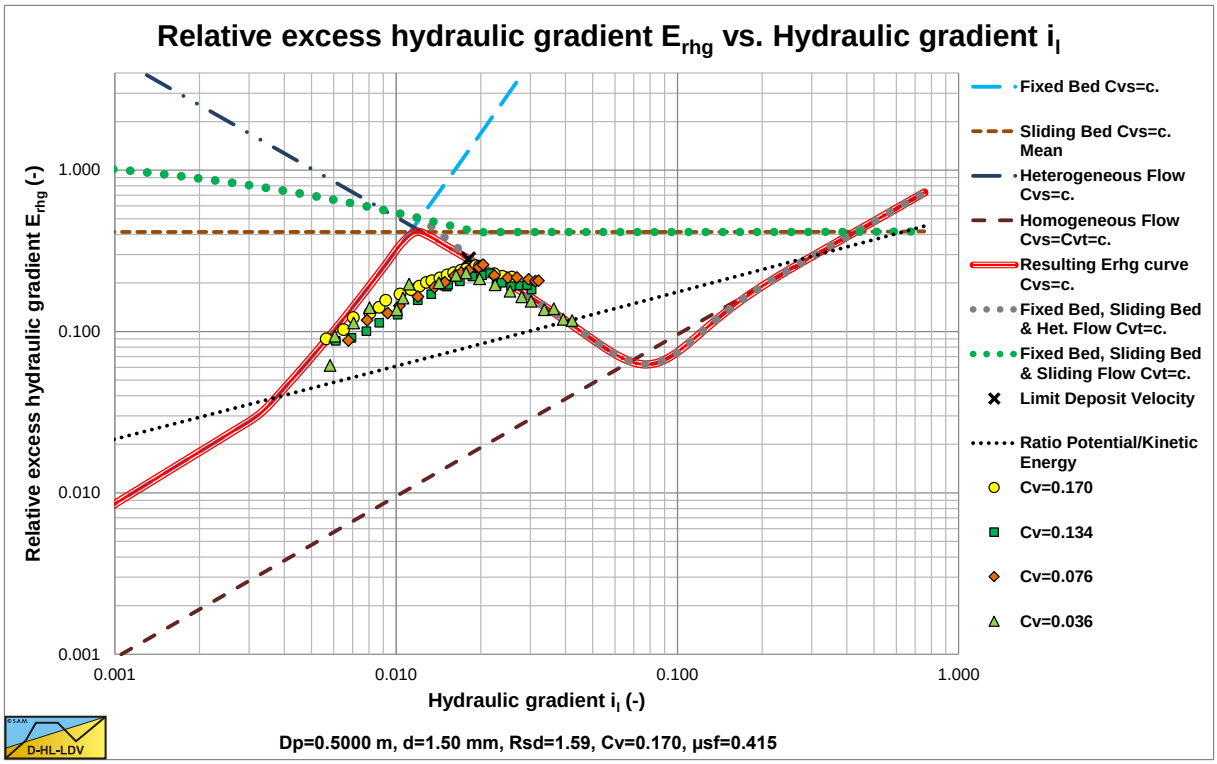

Figure 4-16: Kazanskij (1980), sand, high concentration

These experiments clearly show the transition of a fixed bed (flow regimes 1 and 2) to heterogeneous transport (flow regime 5) at a constant volumetric spatial concentration. The solid lines are drawn for a **C_{vs}=0.036 & 0.17** and may differ slightly for other concentrations. The transition is more smooth than the DHLLDV framework predicts.

4.3.2. R1: Heterogeneous, Constant C_{vt}.

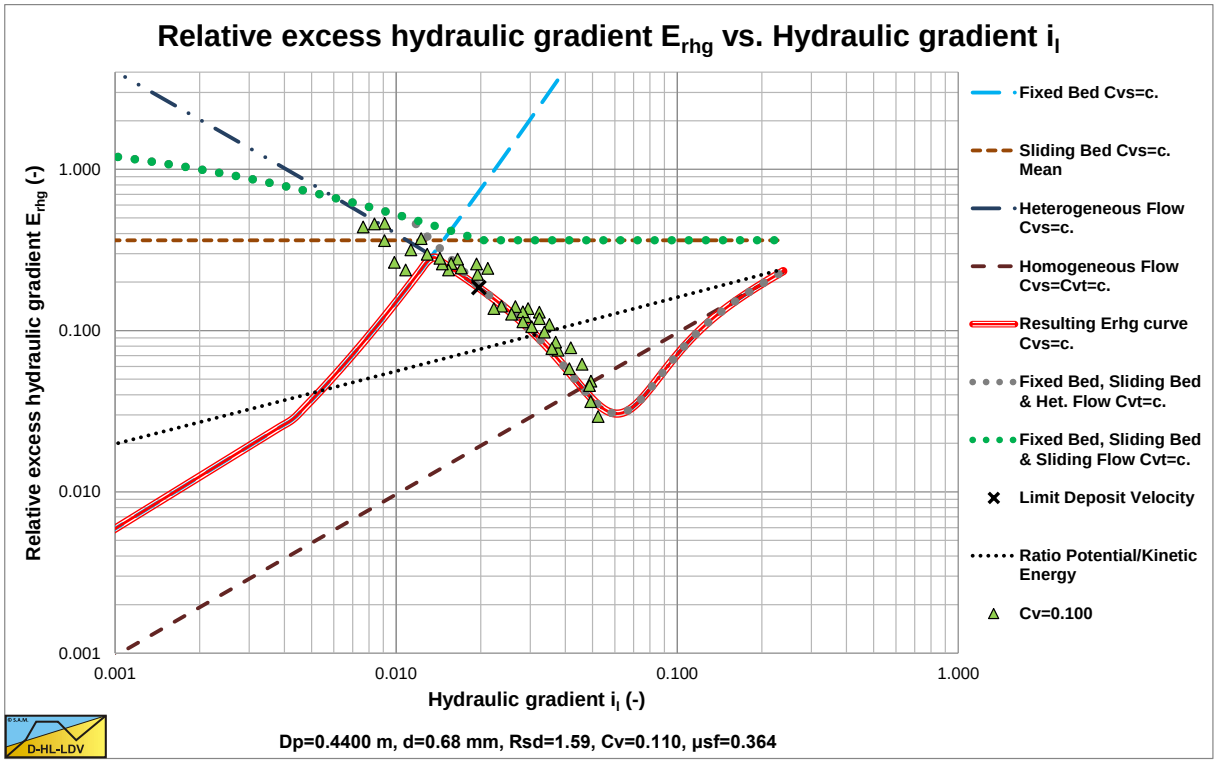

Figure 4-17: Clift et al. (1982), narrow graded crushed granite.

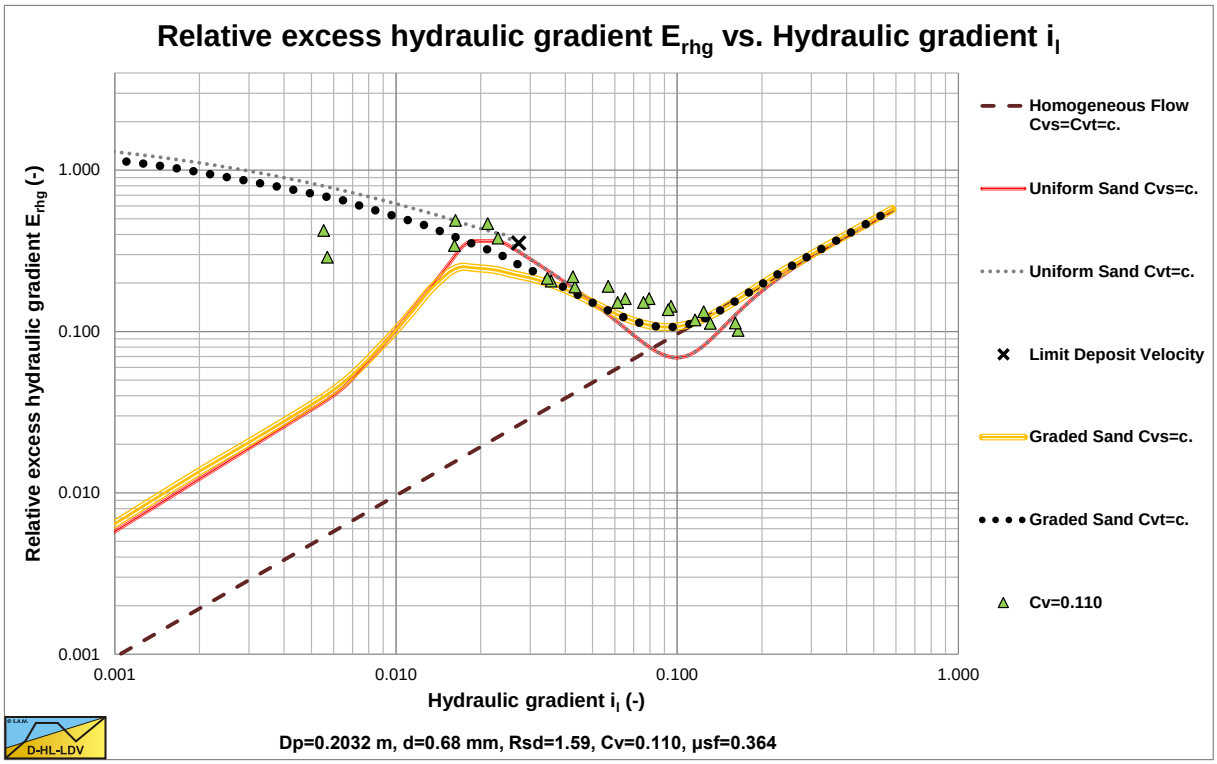

Figure 4-18: Clift et al. (1982), broad graded crushed granite.

These experiments show that at line speeds below the Limit Deposit Velocity and constant C_{vt}, the heterogeneous line is still followed. The grading of the sand makes the heterogeneous curve less steep, but this depends on the grading, the particle size and the pipe diameter.

4.3.3. L2: Fixed & Sliding Bed & Heterogeneous, Constant C_{vs}.

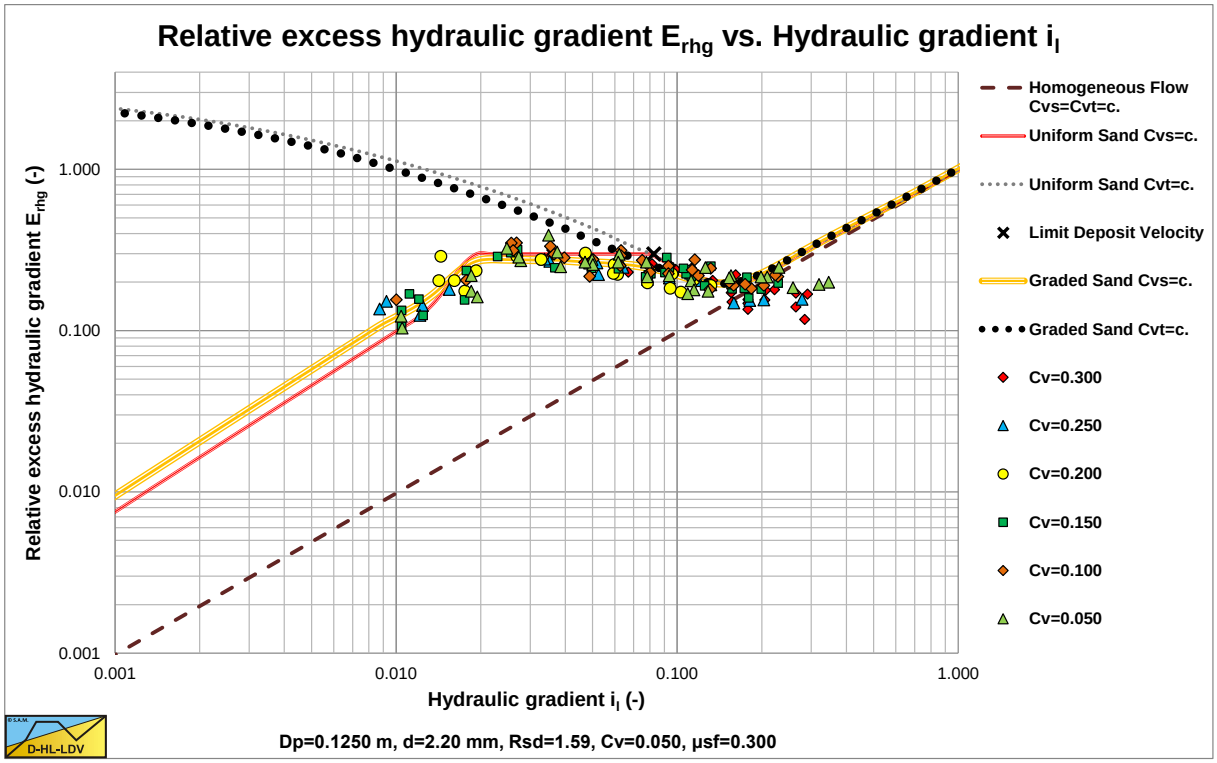

Figure 4-19: Wiedenroth (1967), coarse sand.

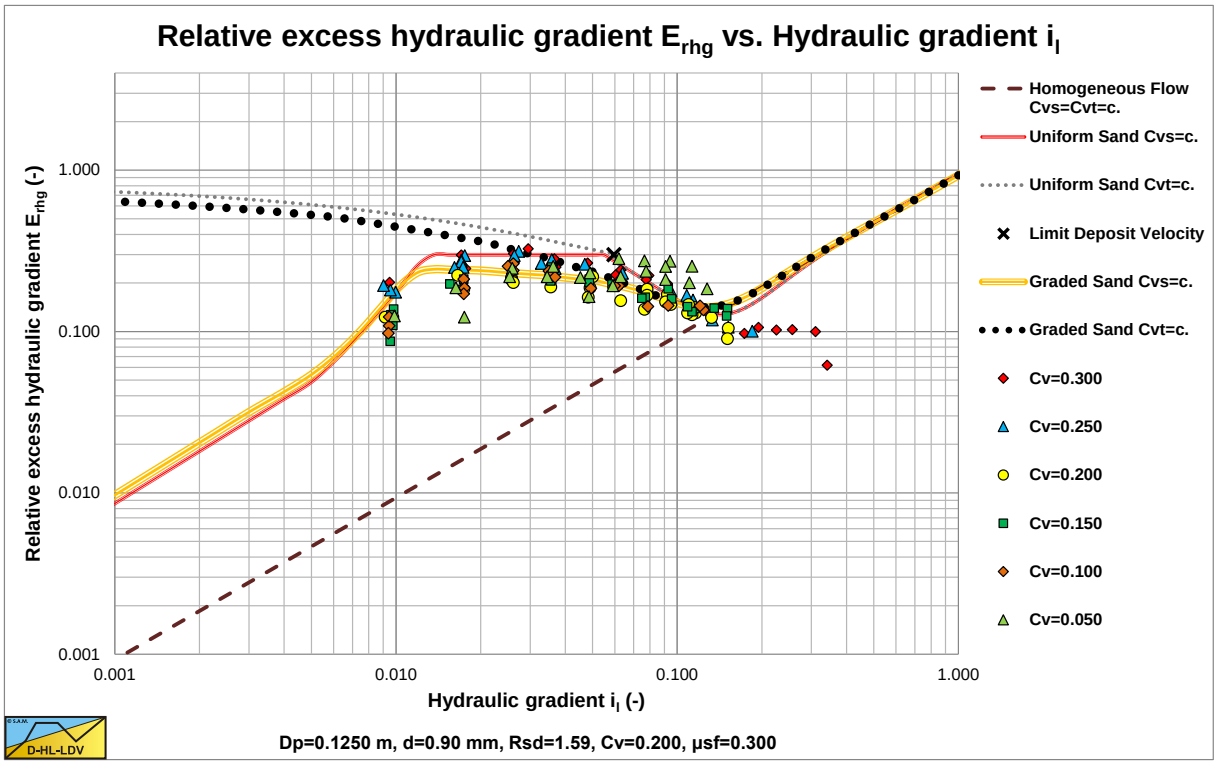

Figure 4-20: Wiedenroth (1967), medium sand.

These experiments at constant C_{vs}, show a fixed bed to sliding bed to heterogeneous behavior. In both figures it is clear that the curve for graded sands match the data points better. The effect of the grading is different for different particle sizes.

4.3.4. R2, R3: Sliding Bed & Sliding Flow, Constant C_{vt}.

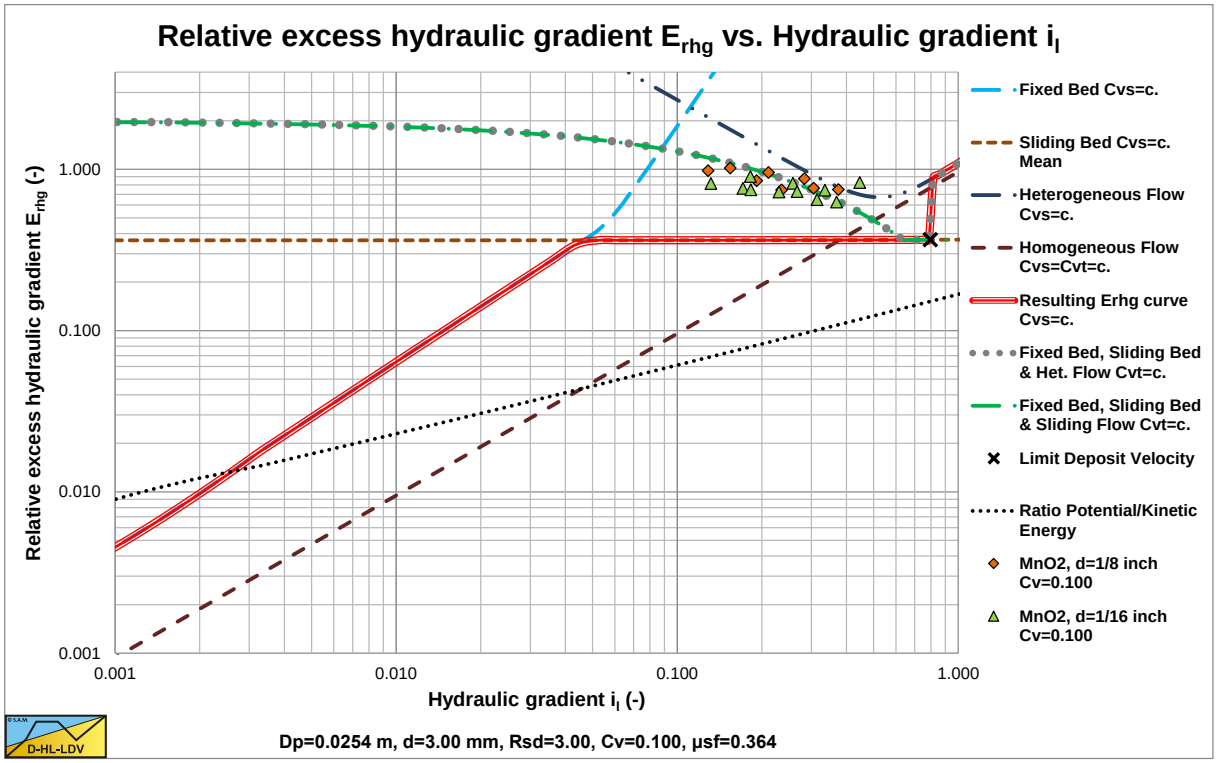

Figure 4-21: Newitt et al. (1955), MnO2.

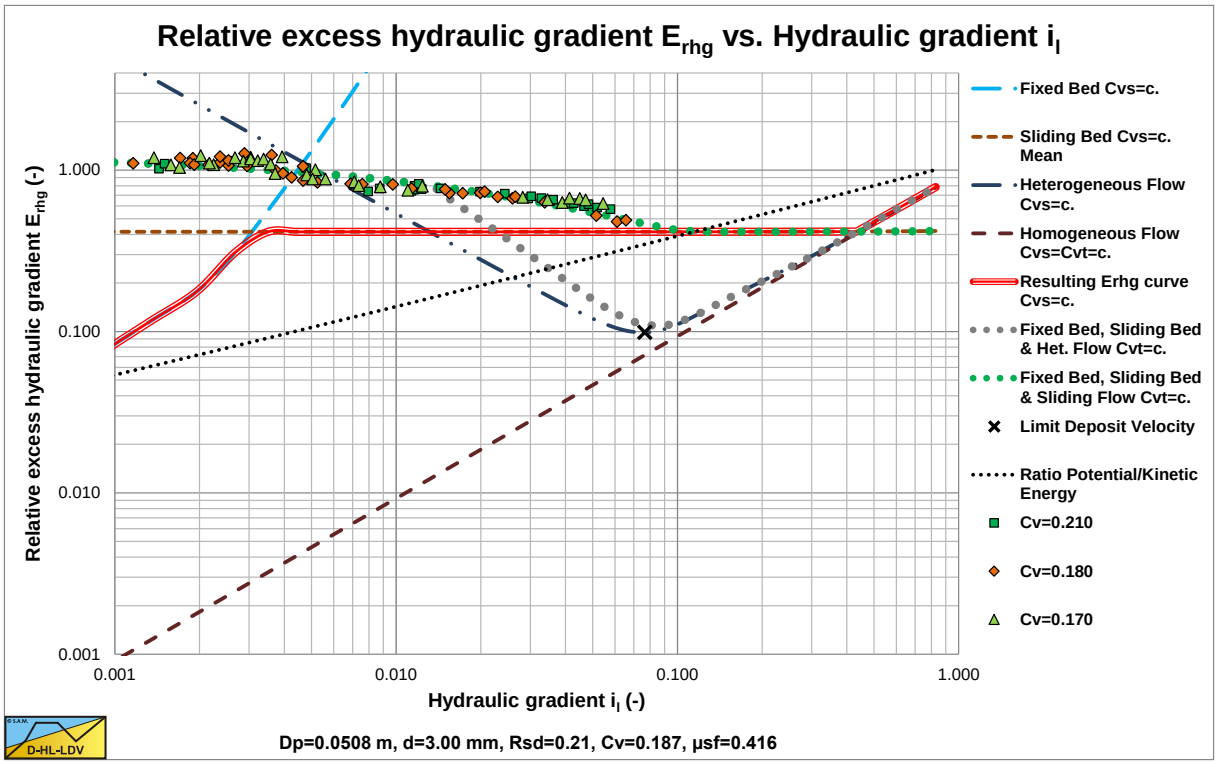

Figure 4-22: Doron & Barnea (1993), Acetal.

These experiments show the constant C_{vt} behavior at small line speeds, with a sliding/fixed bed and sliding flow behavior. The DHLLDV framework gives a good prediction for both heavy (MnO2) and light (Acetal) solids.

4.3.5. L1, R1, L2, R2:, Homogeneous.

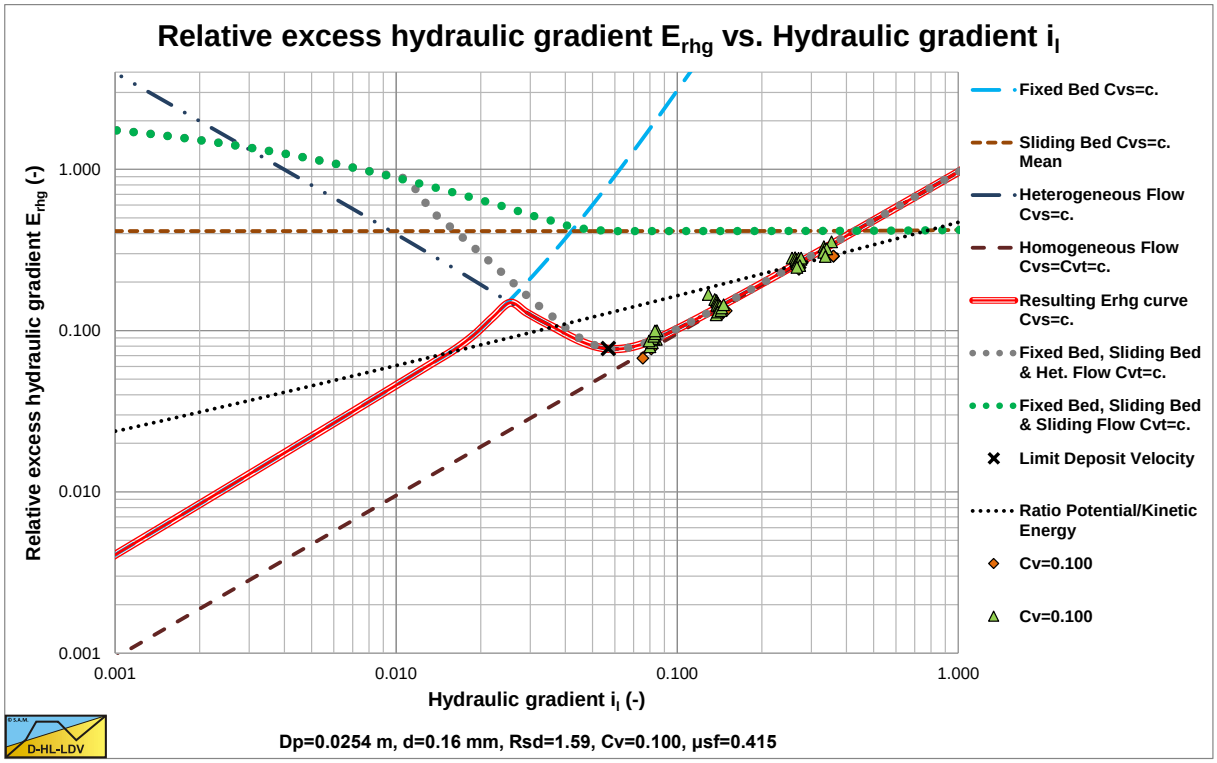

Figure 4-23: Babcock (1970), sand.

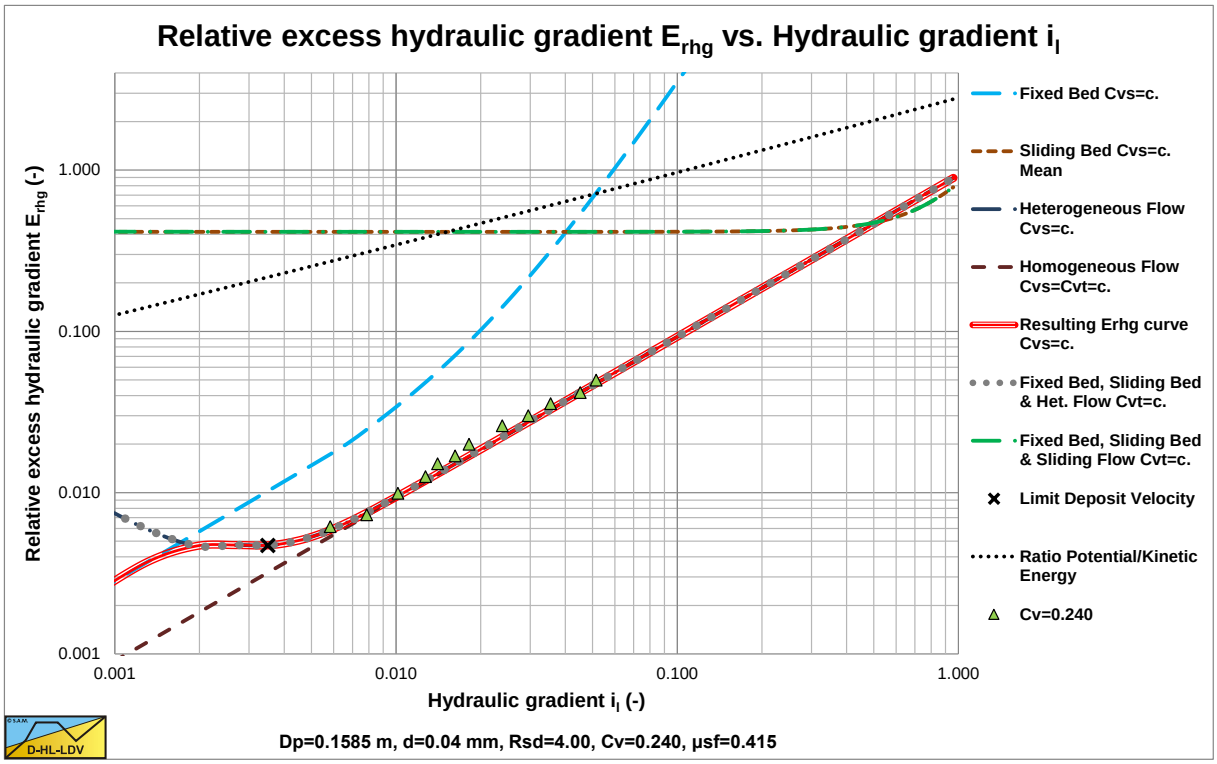

Figure 4-24: Thomas (1976), iron ore.

These experiments show homogeneous behavior, which occurs with small particles at relatively high line speeds. The Thomas (1976) graph also includes Thomas (1965) viscosity for very small particles.

4.3.6. L3, R3: Sliding Bed & Sliding Flow, Constant C_{vs}.

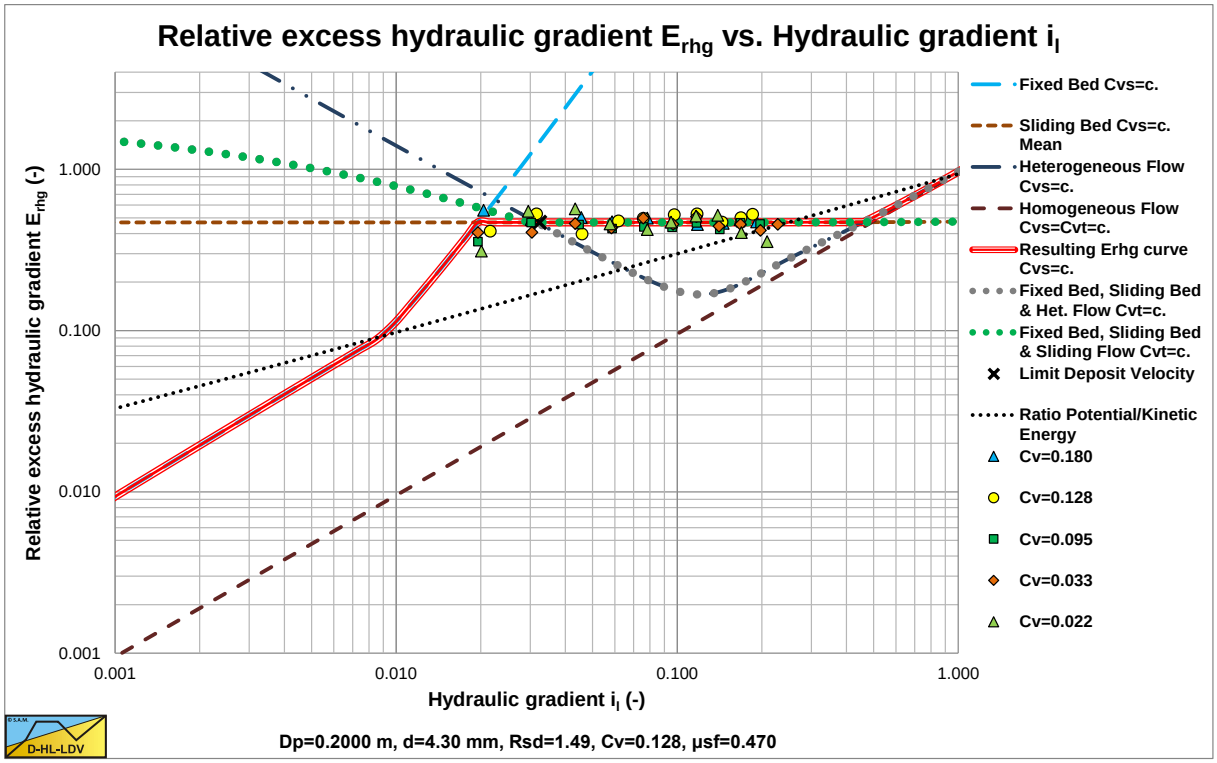

Figure 4-25: Boothroyde (1979), gravel.

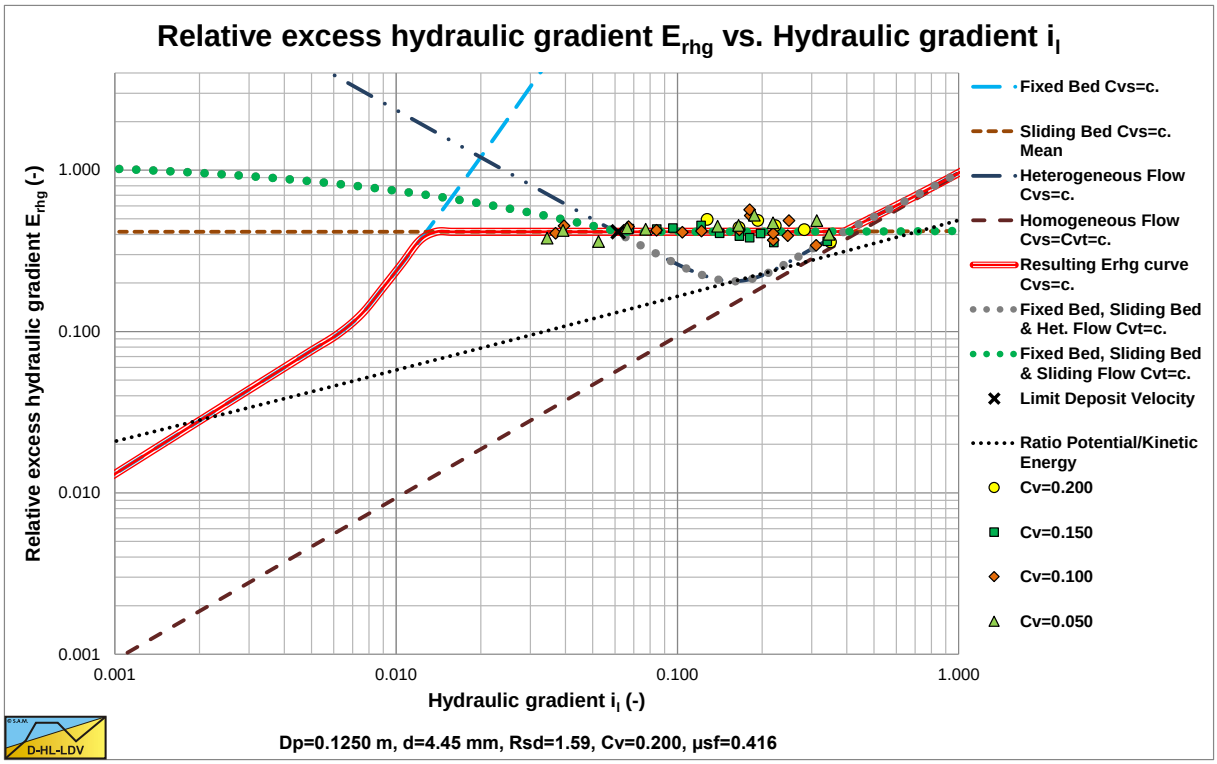

Figure 4-26: Wiedenroth (1967), gravel.

These experiments show the sliding bed and sliding flow regimes. Beyond the intersection point between a sliding bed and heterogeneous flow, the sliding flow curve is followed.

4.3.7. Discussion & Conclusions.

The experimental graphs are given without a lot of explanation, because they should talk for themselves. These graphs show the different flow regimes and sometimes more than one flow regime. In general there is a lot of scatter. This is caused in general by the way experiments were carried out and specifically the accuracy of the concentration measurements. Sometimes concentrations within a certain bandwidth (for example 10-15%) are given with an average mentioned on the graph (for example 12.5%). But in spite of the scatter, the graphs clearly show the different regimes.
From these graphs and the regime and scenario definitions, it should be clear that experiments carried out in very small pipelines, like 1 inch diameter pipelines, can never be compared with experiments in very large pipelines, like 1 m diameter pipelines. In a 1 m diameter pipeline it is difficult to get a sliding bed regime, while in a 1 inch diameter pipeline it is very difficult not to get a sliding bed regime, due to the high hydraulic gradients. It is like comparing laminar and turbulent flow.
Each regime has its own physical and mathematical model. The fixed bed regime can be modeled with flow through a restricted cross section using the Televantos (1979) method for determining the friction factor. The sliding bed regime and partly the sheet flow can be modeled using the Newitt et al. (1955) method, with the appropriate friction factor (0.35-0.7). The heterogeneous regime can be modeled with one of the existing equations or with the Miedema et al. (2013) model. The homogeneous regime can be modeled using the equivalent liquid model, using 100% of the solids or for example using 60% of the solids, like some authors do. For the fixed bed/sliding bed regimes below the Limit Deposit Velocity, a 2 layer or 3 layer model can be used, but the Durand & Condolios (1952) approach, considering a flow Froude number which is equal to the flow Froude number at the Limit Deposit Velocity, also gives good results.
Just carrying out some curve fits and drawing conclusions is very dangerous, because the experiments may cover 2 or more regimes. For example, if 50% of the experiments are in the heterogeneous regime and 50% of the experiments are in the homogeneous regime, a curve fit would give a horizontal line in the $\mathbf{E_{rhg}(i_l)}$ graph. If we look at experiments where 50% is in the fixed bed regime (constant $\mathbf{C_{vs}}$) and 50% is in the heterogeneous regime (for example **Figure 4-15** & **Figure 4-19**), the result of a curve fit is also a horizontal line. The cases however are completely different.
Recognizing the different regimes and especially the transitions between the different regimes is crucial in understanding what is physically happening.

4.4. Nomenclature Flow Regimes & Scenario's.

A_b	Cross section of the bed in the pipe	m^2
$A_{m,s}$	Cross section of the mixture in suspension above the bed	m^2
A_p	Cross section of the pipe	m^2
A_s	Cross section of the solids in the pipe	m^2
C_v	Volumetric concentration	-
C_{vs}	Volumetric spatial concentration	-
$C_{vs,s}$	Volumetric spatial concentration of the mixture in suspension above a fixed or sliding bed	-
C_{vt}	Volumetric transport (delivered) concentration	-
d	Particle diameter	mm
d_{50}	Median particle diameter - 50% by weight is smaller	mm
D_p	Pipe diameter	m
E_{rhg}	Relative Excess Hydraulic Gradient	-
i_m	Mixture head loss	m/m
i_l	LiquiDelft Head loss	m/m
i_w	Water head loss	m/m
n	Porosity	-
Q_m or $\dot{V}_m$	Flow rate of mixture	m^3/s
Q_s or $\dot{V}_s$	Flow rate of solids	m^3/s
R_{sd}	Relative submerged density	-
S_{rs}	Slip relative squared or Stratification ratio solids	-
v_{ls}	Velocity of the slurry, line speed	m/s
$v_{ls,e}$	Effective line speed. Line speed above the fixed or moving bed.	m/s
v_m	Velocity of the slurry, line speed (same as v_{ls})	m/s
v_s	Average velocity of the solids	m/s
v_{sl}	Slip velocity of the solids relative to the mixture	m/s
V_b	Volume of the bed	m^3
V_{cl}	Volume of the closed loop	m^3
V_m	Volume of the mixture in a pipe	m^3
$V_{m,s}$	Volume of the mixture in suspension above the bed	m^3
V_s	Volume of the solids in a pipe	m^3
$V_{s,s}$	Volume of the solids in suspension above the bed	m^3
v_t	Terminal settling velocity of the particles	m/s
λ	Darcy-Weisbach friction factor	-
κ_C	Concentration eccentricity factor.	-
μ_{sf}	Friction coefficient for a sliding bed	-
ρ_l, ρ_w	Density of the liquid	ton/ m^3
ρ_m	Density of the mixture	ton/ m^3
ρ_s	Density of the solids	ton/ m^3

4.5. Notes.

Chapter 5: Slurry Transport Models.

5.1. The DHLLDV Framework.

5.1.1. The Sliding Bed Regime.

For the sliding bed the same set of equations is used as for the stationary bed. The only difference is that for a stationary bed the bed velocity v_2 equals 0, while of course for a sliding bed the bed has a positive velocity v_2, smaller than v_1. A convenient parameter to show the results of the calculations is the **Relative Excess Hydraulic Gradient**. This parameter gives an almost dimensionless graph of the head losses.

$$E_{rhg} = \frac{i_m - i_l}{R_{sd} \cdot C_{vs}} \qquad (5\text{-}1)$$

Figure 5-1 shows the E_{rhg} parameter as a function of the relative volumetric concentration ($C_{vr}=C_{vs}/C_b$) and the relative line speed ($v_{ls}/v_{ls,ldv,max}$) for the weight approach sliding bed friction (Miedema & Ramsdell (2014)) and a sliding bed friction factor $\mu_{sf}=0.4$. The E_{rhg} parameter is very close to the sliding friction coefficient μ_{sf}, especially for relative line speeds up to 1.5, the region where most probably the sliding bed will occur.

So for the sliding bed regime the E_{rhg} parameter is defined to be equal to the sliding friction coefficient μ_{sf}.

$$E_{rhg} = \frac{i_m - i_l}{R_{sd} \cdot C_{vs}} = \mu_{sf} \qquad (5\text{-}2)$$

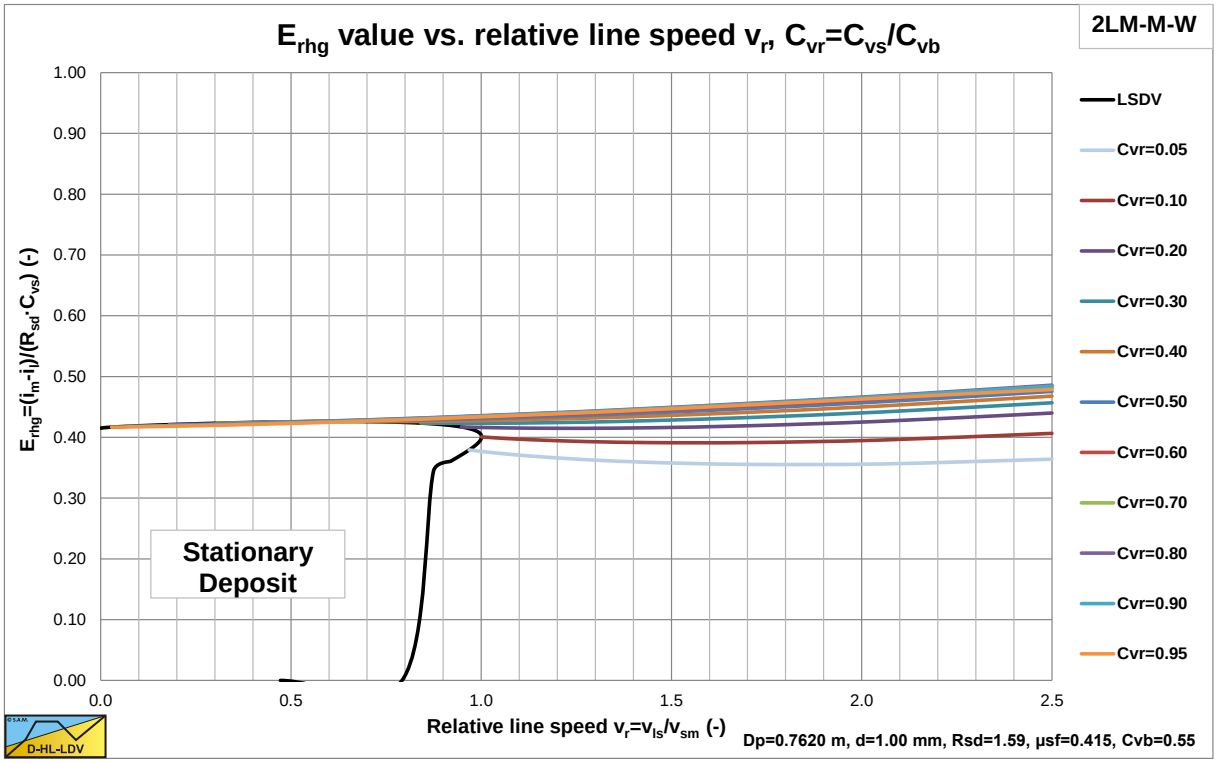

Figure 5-1: The E_{rhg} parameter versus the relative line speed.

The sliding friction coefficient μ_{sf} is the tangent of the external friction angle δ between the sand or gravel and the steel pipe wall. From soil mechanics it is known that the external friction angle δ is about 2/3 of the internal friction angle φ. This internal friction angle has a minimum of about 30° for loose packed sand, giving 20° for the external friction angle. The tangent of 20° is 0.364. Miedema & Ramsdell (2014) also analyzed the hydrostatic approach of Wilson et al. (1992) and the normal stress carrying the weight approach. These two approaches are similar up to a relative concentration of 0.5, giving an increase of the E_{rhg} parameter with a factor 1.3 compared to the weight approach as used here. In practice the relative concentration will be between 0 and 0.5 giving a multiplication

factor between 1 and 1.3 depending on the relative concentration. Taking an average gives a sliding friction factor of about 0.415. Resuming it can be stated that the E_{rhg} parameter should have a value of about 0.364 if the weight approach is applied, or a value of about 0.415 if the hydrostatic or normal stress carrying the weight approach are applied. In the current model a constant value of 0.415 is used to be on the safe side, resulting in hydraulic gradient curves parallel to the liquid curve as already observed by Newitt et al. (1955) and others.

5.1.2. The Heterogeneous Transport Regime.

Miedema & Ramsdell (2013) derived an equation for the **Relative Excess Hydraulic Gradient** for heterogeneous transport based on energy considerations. This equation consists of two parts. A first part for the contribution due to potential energy losses and a second part for the kinetic energy losses. The equation is based on uniform sands or gravels, but Miedema (2014) also derived a modified equation for graded sands and gravels. In its basic form the equation looks like:

$$E_{rhg} = \frac{i_m - i_l}{R_{sd} \cdot C_{vs}} = \frac{v_t \cdot \left(1 - \frac{C_{vs}}{\kappa_C}\right)^{\beta}}{v_{ls}} + \left(\frac{v_{sl}}{v_t}\right)^2 = S_{hr} + S_{rs} \qquad \textbf{(5-3)}$$

The **Settling** Velocity **Hindered Relative**, S_{hr}, is the **Hindered Settling Velocity** of a particle $v_t \cdot (1-C_{vs}/\kappa)^{\beta}$ divided by the line speed v_{ls}. The S_{hr} value gives the contribution of the potential energy losses to the **Relative Excess Hydraulic Gradient**. The S_{hr} is derived for and can be applied to the heterogeneous regime.
The **Slip Relative Squared** S_{rs} is the **Slip Velocity** of a particle v_{sl} divided by the **Terminal Settling Velocity** of a particle v_t squared and this S_{rs} value is a good indication of the **Relative Excess Hydraulic Gradient** due to the solids, since its contribution to the total is 90%-100%. The S_{rs} value gives the contribution of the kinetic energy losses to the **Relative Excess Hydraulic Gradient**. The S_{rs} is derived for and can be applied to the heterogeneous regime.

The potential energy term is explicit and all the variables involved are known, so this term can be solved. The kinetic energy term however contains the slip velocity, which is not known. The kinetic energy term has been derived by Miedema & Ramsdell (2013) based on kinetic energy losses due to collisions or interactions with the pipe wall or the viscous sub layer. This means that the slip velocity used in the above equation is not necessarily the average slip velocity, but it is the slip velocity necessary to explain the kinetic energy losses. The average slip velocity of the particles will probably be larger, but of the same magnitude. The derivation of the slip velocity equation for uniform sands or gravels will be subject of another paper, but the resulting equation for the E_{rhg} parameter is given here. Giving for the relative excess hydraulic gradient, the E_{rhg} parameter:

$$E_{rhg} = \frac{i_m - i_l}{R_{sd} \cdot C_{vs}} = S_{hr} + S_{rs} = \frac{v_t \cdot \left(1 - \frac{C_{vs}}{\kappa_C}\right)^{\beta}}{v_{ls}} + 7.5^2 \cdot \left(\frac{1}{\lambda_l}\right) \cdot \left(\frac{v_t}{\sqrt{g \cdot d}}\right)^{8/3} \cdot \left(\frac{(v_l \cdot g)^{1/3}}{v_{ls}}\right)^2 \qquad \textbf{(5-4)}$$

$$\kappa_C = 0.175 \cdot (1 + \beta)$$

The equation has been modified slightly since the original article of Miedema & Ramsdell (2013). The derivation is published in Miedema (2015).

5.1.3. The Homogeneous Transport Regime.

The basis of the homogeneous transport regime model is the equivalent liquid model (ELM). In terms of the relative excess hydraulic gradient, E_{rhg}, this can be written as:

$$E_{rhg} = \frac{i_m - i_l}{R_{sd} \cdot C_{vs}} = \frac{\lambda_l \cdot v_{ls}^2}{2 \cdot g \cdot D_p} = i_l \qquad \textbf{(5-5)}$$

Talmon (2013) derived an equation to correct the homogeneous equation (the ELM model) for the slurry density, based on the hypothesis that the viscous sub-layer hardly contains solids at very high line speeds in the

homogeneous regime. This theory results in a reduction of the resistance compared with the ELM, but the resistance is still higher than the resistance of clear water. Talmon (2013) used the Prandl approach for the mixing length, which is a 2D approach for open channel flow with a free surface. The Prandl approach was extended with damping near the wall to take into account the viscous effects near the wall, according to von Driest (Schlichting, 1968). Miedema (2015) extended the model with pipe flow and a concentration distribution, resulting in the following equations.

The value of the Darcy Weisbach wall friction factor λ_l depends on the Reynolds number:

$$Re = \frac{v_{ls} \cdot D_p}{\nu_l} \tag{5-6}$$

Over the whole range of Reynolds numbers above 2320 the Swamee Jain (1976) equation gives a good approximation:

$$\lambda_l = \frac{1.325}{\left(\ln\left(\frac{\varepsilon}{3.7 \cdot D_p} + \frac{5.75}{Re^{0.9}} \right) \right)^2} = \frac{0.25}{\left(\log_{10}\left(\frac{\varepsilon}{3.7 \cdot D_p} + \frac{5.75}{Re^{0.9}} \right) \right)^2} \tag{5-7}$$

For the resulting Darcy-Weisbach friction factor ratio this can be approximated by:

$$\frac{\lambda_m}{\lambda_l} = \frac{1}{\left(\frac{A_{C_v}}{\kappa} \cdot \ln\left(\frac{\rho_m}{\rho_l} \right) \cdot \sqrt{\frac{\lambda_l}{8}} + 1 \right)^2} \tag{5-8}$$

The hydraulic gradient i_l (for a liquid including the fine solids effect in general) is:

$$i_l = \frac{\Delta p_l}{\rho_l \cdot g \cdot \Delta L} = \frac{\lambda_l \cdot v_{ls}^2}{2 \cdot g \cdot D_p} \tag{5-9}$$

The relative excess hydraulic gradient E_{rhg} is now:

$$E_{rhg} = \frac{i_m - i_l}{R_{sd} \cdot C_{vs}} = i_l \cdot \frac{1 + R_{sd} \cdot C_v - \left(\frac{A_{C_v}}{\kappa} \cdot \ln\left(\frac{\rho_m}{\rho_l} \right) \cdot \sqrt{\frac{\lambda_l}{8}} + 1 \right)^2}{R_{sd} \cdot C_v \cdot \left(\frac{A_{C_v}}{\kappa} \cdot \ln\left(\frac{\rho_m}{\rho_l} \right) \cdot \sqrt{\frac{\lambda_l}{8}} + 1 \right)^2} = \alpha_E \cdot i_l \tag{5-10}$$

Table 5-1: Some A_ρ and A_{Cv} values.

	A_ρ	A_{Cv}
Law of the Wall	4.13	1.00
Nikuradse (no damping)	3.02	1.25
Prandtl (damping)	0.01	3.40
Average	1.05	2.20
Lower limit of data	5.43	0.80
Upper limit of data	1.67	1.80

A value of A_{Cv}**=1.3** is adviced.

5.1.4. The Resulting E_{rhg} Constant Spatial Volumetric Concentration Curve.

The hydraulic gradient for the mixture can be determined with:

$$i_m = i_l + E_{rhg} \cdot R_{sd} \cdot C_{vs} \quad \textbf{(5-11)}$$

and

$$p_m = i_l \cdot \rho_l \cdot g \cdot L + E_{rhg} \cdot R_{sd} \cdot C_{vs} \cdot \rho_l \cdot g \cdot L = p_l + p_s \quad \textbf{(5-12)}$$

5.1.5. Determining the Limit Deposit Velocity.

5.1.5.1. Introduction.

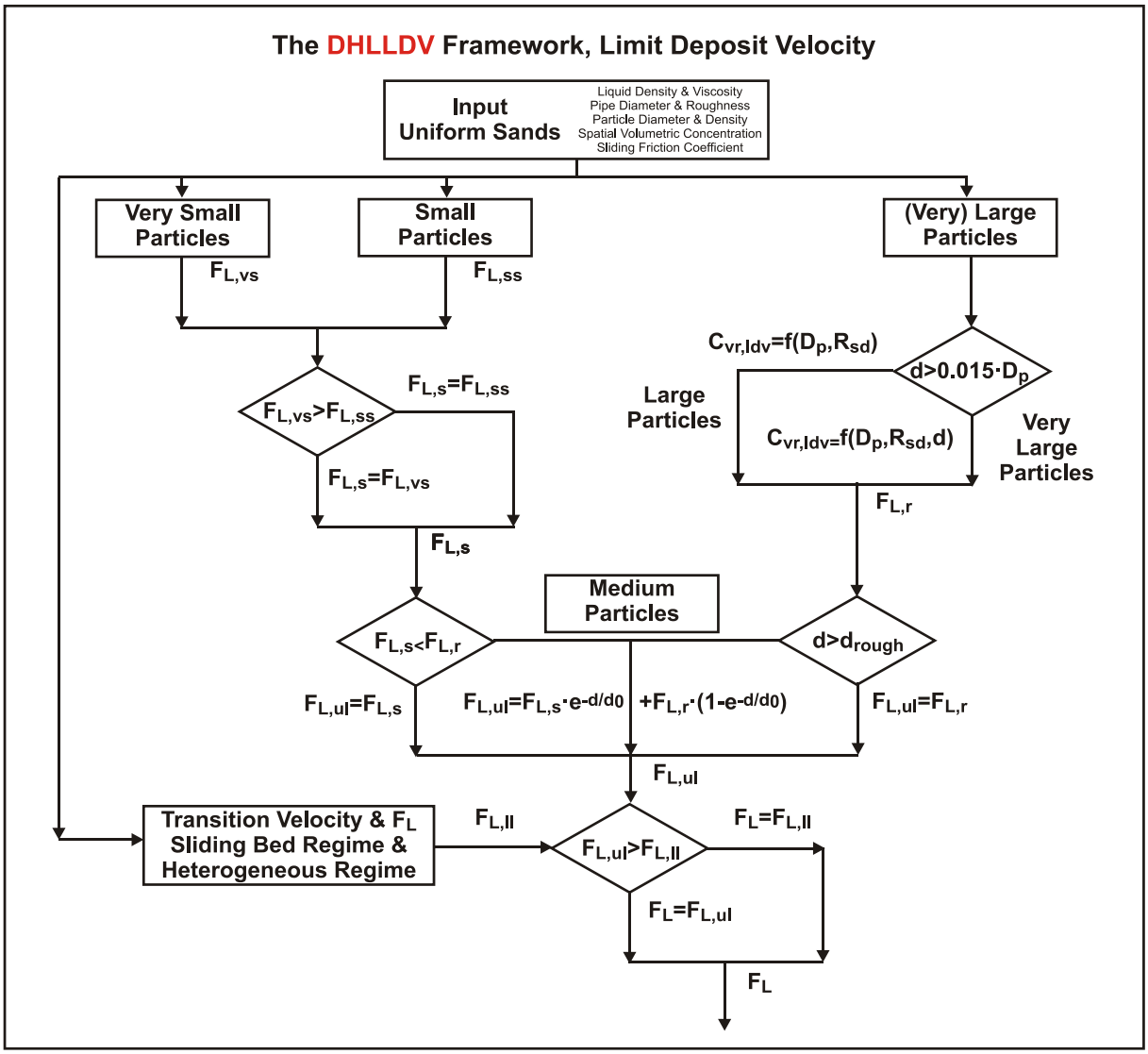

Figure 5-2: The algorithm to determine the Limit Deposit Velocity.

Figure 5-2 shows the algorithm to determine the Limit Deposit Velocity. The different steps are discussed in the next chapters.

5.1.5.2. Very Small & Small Particles.

For very small particles, smaller than about 50% of the thickness of the viscous sub layer, the LDV and the Froude number $\mathbf{F_L}$ are:

$$v_{ls,ldv} = 1.4 \cdot \left(\nu_l \cdot R_{sd} \cdot g\right)^{1/3} \cdot \sqrt{\frac{8}{\lambda_l}}$$

$$F_{L,vs} = \frac{v_{ls,ldv}}{\left(2 \cdot g \cdot R_{sd} \cdot D_p\right)^{1/2}} = \frac{1.4 \cdot \left(\nu_l \cdot R_{sd} \cdot g\right)^{1/3} \cdot \sqrt{\frac{8}{\lambda_l}}}{\left(2 \cdot g \cdot R_{sd} \cdot D_p\right)^{1/2}} \qquad \textbf{(5-13)}$$

For small particles and a smooth bed, in the case of sand particles smaller than about **d=0.15 mm**, this gives for the Limit Deposit Velocity:

$$v_{ls,ldv}^3 = \alpha_p^3 \cdot \frac{v_t \cdot \left(1 - \frac{C_{vs}}{\kappa_C}\right)^{\beta} \cdot C_{vs} \cdot \left(2 \cdot g \cdot R_{sd} \cdot D_p\right)}{\lambda_l} \qquad \textbf{(5-14)}$$

In terms of the Durand & Condolios LDV Froude number $\mathbf{F_L}$ factor this can be written as:

$$F_{L,ss} = \frac{v_{ls,ldv}}{\left(2 \cdot g \cdot R_{sd} \cdot D_p\right)^{1/2}} = \alpha_p \cdot \left(\frac{v_t \cdot \left(1 - \frac{C_{vs}}{\kappa_C}\right)^{\beta} \cdot C_{vs}}{\lambda_l \cdot \left(2 \cdot g \cdot R_{sd} \cdot D_p\right)^{1/2}} \right)^{1/3} \qquad \textbf{(5-15)}$$

$$\text{with:} \quad \alpha_p = 3.5 \cdot \left(\frac{1.65}{R_{sd}}\right)^{1/9}, \quad \kappa_C = 0.175 \cdot (1 + \beta)$$

The coefficient α_p**=3.5** is an upper limit. The minimum found is about 3.0, the average 3.25. To be on the safe side, the value of 3.5 should be used. To find the highest correlation with experimental data, the value of 3.25 should be used. With the following conditions the Froude number FL for very small and small particles can be determined:

$$\begin{aligned} &\text{If} \quad F_{L,vs} > F_{L,ss} \quad \Rightarrow \quad F_{L,s} = F_{L,vs} \\ &\text{If} \quad F_{L,vs} \le F_{L,ss} \quad \Rightarrow \quad F_{L,s} = F_{L,ss} \end{aligned} \qquad \textbf{(5-16)}$$

5.1.5.3. Large & Very Large Particles.

The Limit Deposit Velocity LDV is for medium and large particles and a rough bed:

$$v_{ls,ldv}^3 = \alpha_p^3 \cdot \frac{\left(1 - \frac{C_{vs}}{\kappa_C}\right)^{\beta} \cdot C_{vs} \cdot \left(\mu_{sf} \cdot C_{vb} \cdot \frac{\pi}{8}\right)^{1/2} \cdot C_{vr,ldv}^{1/2}}{\lambda_l} \cdot \left(2 \cdot g \cdot R_{sd} \cdot D_p\right)^{3/2} \qquad \textbf{(5-17)}$$

And the Durand & Condolios LDV Froude number:

$$F_{L,r} = \frac{v_{ls,ldv}}{\left(2 \cdot g \cdot R_{sd} \cdot D_p\right)^{1/2}} = \alpha_p \cdot \left(\frac{\left(1 - \frac{C_{vs}}{\kappa_C}\right)^{\beta} \cdot C_{vs} \cdot \left(\mu_{sf} \cdot C_{vb} \cdot \frac{\pi}{8}\right)^{1/2} \cdot C_{vr,ldv}^{1/2}}{\lambda_l} \right)^{1/3} \qquad \textbf{(5-18)}$$

The bed fraction at the Limit Deposit Velocity is, depending on the particle diameter to pipe diameter ratio:

$$d \le 0.015 \cdot D_p \qquad C_{vr,ldv} = 0.00012 \cdot D_p^{-1} \cdot \left(\frac{R_{sd}}{1.65}\right)^{-1} = \frac{0.0039}{2 \cdot g \cdot R_{sd} \cdot D_p}$$

$$d > 0.015 \cdot D_p \qquad C_{vr,ldv} = 0.00012 \cdot D_p^{-1} \cdot \left(\frac{R_{sd}}{1.65}\right)^{-1} \cdot \left(\frac{d}{0.015 \cdot D_p}\right)^{1/2} = \frac{0.0318}{2 \cdot g \cdot R_{sd} \cdot D_p} \cdot \left(\frac{d}{D_p}\right)^{1/2} \qquad \textbf{(5-19)}$$

5.1.5.4. The Resulting Upper Limit Froude Number.

The resulting upper limit of the Froude number $\mathbf{F_{L,ul}}$ value can now be determined according to (for sand):

$$F_{L,s} \le F_{L,r} \quad \Rightarrow \quad F_{L,ul} = F_{L,s}$$

$$F_{L,s} > F_{L,r} \quad \Rightarrow \quad F_{L,ul} = F_{L,s} \cdot e^{-d/d_0} + F_{L,r} \cdot \left(1 - e^{-d/d_0}\right)$$

$$d > d_{rough} \quad \Rightarrow \quad F_{L,ul} = F_{L,r} \qquad \textbf{(5-20)}$$

$$\text{with:} \quad d_0 = 0.00042 \cdot \left(\frac{1.65}{R_{sd}}\right)^{1/2} \quad \text{and} \quad d_{rough} = 2 \text{ mm for sand}$$

The value of 2 mm is valid for sand with $\mathbf{R_{sd} \approx 1.65}$, other materials will have a different value. This value will increase with decreasing solids density.

5.1.5.5. The Lower Limit.

The lower limit of the LDV is the transition velocity between the sliding bed regime and the heterogeneous regime, resulting in the transition velocity at:

$$v_{ls,ldv}^2 = \frac{v_t \cdot \left(1 - \frac{C_{vs}}{\kappa_C}\right)^{\beta} \cdot v_{ls,ldv} + \frac{7.5^2}{\lambda_l} \cdot \left(\frac{1}{\sqrt{C_x}}\right)^{8/3} \cdot \left(v_l \cdot g\right)^{2/3}}{\mu_{sf}} \qquad \textbf{(5-21)}$$

This equation shows that the transition between the sliding bed regime and the heterogeneous regime depends on the sliding friction coefficient. The equation derived is a second degree function and can be written as:

$$-v_{ls,ldv}^2 + \frac{v_t \cdot \left(1 - \frac{C_{vs}}{\kappa_C}\right)^{\beta}}{\mu_{sf}} \cdot v_{ls,ldv} + \frac{\frac{7.5^2}{\lambda_l} \cdot \left(\frac{1}{\sqrt{C_x}}\right)^{8/3} \cdot \left(v_l \cdot g\right)^{2/3}}{\mu_{sf}} = 0 \qquad \textbf{(5-22)}$$

With:

$$A = -1$$

$$B = \frac{v_t \cdot \left(1 - \frac{C_{vs}}{\kappa_C}\right)^{\beta}}{\mu_{sf}}$$

$$C = \frac{\frac{7.5^2}{\lambda_l} \cdot \left(\frac{1}{\sqrt{C_x}}\right)^{8/3} \cdot (v_l \cdot g)^{2/3}}{\mu_{sf}} \qquad \textbf{(5-23)}$$

$$v_{ls,ldv} = \frac{-B - \sqrt{B^2 - 4 \cdot A \cdot C}}{2 \cdot A}$$

In terms of the Durand & Condolios LDV Froude number $\mathbf{F_L}$ factor this can be written as:

$$F_{L,ll} = \frac{v_{ls,ldv}}{\left(2 \cdot g \cdot R_{sd} \cdot D_p\right)^{1/2}} \qquad \textbf{(5-24)}$$

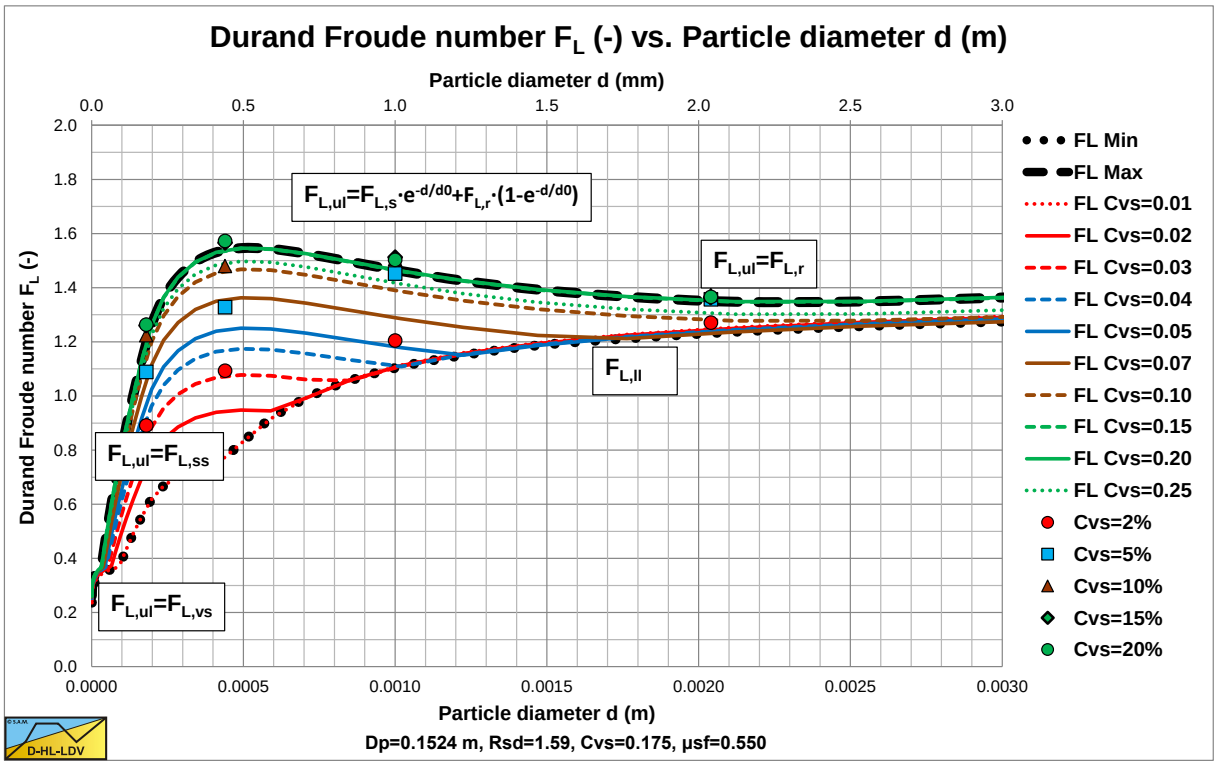

Figure 5-3: The resulting $F_L$curves.

5.1.5.6. The Resulting Froude Number.

The resulting Froude $\mathbf{F_L}$ value can now be determined according to:

$$F_{L,ul} \geq F_{L,ll} \quad \Rightarrow \quad F_L = F_{L,ul}$$

$$F_{L,ll} > F_{L,ul} \quad \Rightarrow \quad F_L = F_{L,ll} \qquad \textbf{(5-25)}$$

For small particles and/or concentrations near 20% and/or large pipe diameters, usually the upper limit Froude number will be valid. For large particles and/or low concentrations and/or very small to small pipe diameters, usually the lower limit Froude number will be valid.

Figure 5-3 shows the resulting LDV curves for a number of volumetric concentrations, including the Durand & Condolios (1952) data. The graph matches the graph as published by Durand (1953) very well. The use of the lower limit based on the transition sliding bed regime to heterogeneous regime is not exact, since this transition velocity will not be exact. It is possible that this lower limit should be set to 90% or 95% of this transition velocity. Here the theoretical transition velocity is used.

5.1.6. Nomenclature DHLLDV Framework.

A_{Cv}	Coefficient homogeneous regime (1.3 by default)	-
A_p	Cross section of the pipe	m^2
C_{vb}	Bed volumetric concentration	-
$C_{vb,max}$	Maximum bed volumetric concentration	-
C_{vB}	Concentration at the bottom of the pipe	-
C_D	Particle drag coefficient	-
C_{vs}	Spatial volumetric concentration	-
C_{vr}	Relative concentration C_{vs}/C_{vb}	-
$C_{vr,ldv}$	Relative concentration in bed at LDV	-
C_{vt}	Transport or delivered volumetric concentration	-
C_x	Durand & Condolios coefficient	-
d	Particle diameter	**m**
d_0	Particle diameter LDV transition region	**m**
D_H	Hydraulic diameter	**m**
D_p	Pipe diameter	**m**
E_{rhg}	Relative excess hydraulic gradient	-
$E_{rhg,SF}$	Relative excess hydraulic gradient in the sliding flow regime	-
$E_{rhg,HeHo}$	Relative excess hydraulic gradient in the heterogeneous/ homogeneous flow regimes	-
f	Fraction of fines	-
f	Factor determining sliding flow	-
F_L	Durand limit deposit velocity Froude number	-
$F_{L,s}$	Durand limit deposit velocity Froude number, smooth bed	-
$F_{L,ss}$	Durand limit deposit velocity Froude number, **s**mall particles **s**mooth bed	-
$F_{L,vs}$	Durand limit deposit velocity Froude number, smooth bed, **v**ery **s**mall particles	-
$F_{L,r}$	Durand limit deposit velocity Froude number, **r**ough bed, large particles	-
$F_{L,ul}$	Durand limit deposit velocity Froude number, **u**pper **l**imit	-
$F_{L,ll}$	Durand limit deposit velocity Froude number, **l**ower **l**imit	-
Fr_{DC}	Durand & Condolios Froude number	-
g	Gravitational constant (9.81)	m/s^2
h	Thickness of bed at LDV	**m**
i_l	Hydraulic gradient of liquid	-
i_m	Hydraulic gradient of mixture	-
$i_{m,i}$	Hydraulic gradient of i^{th} fraction of PSD	-
$i_{m,ldv}$	Hydraulic gradient mixture at LDV	-
K	Durand & Condolios constant (85)	-
m_p	Mass particle	**kg**
N	Zandi & Govatos deposit criterion	-
r	Position in pipe starting at the bottom	-
Re	Reynolds number based on velocity difference liquid flow - bed	-
R_{sd}	Relative submerged density	-
S_{hr}	**Settling** Velocity **Hindered Relative**	-
S_{rs}	**Slip** Velocity **Relative Squared**	-
u_*	Friction velocity	**m/s**
$u_{*,ldv}$	Friction velocity at the LDV	**m/s**
v_1	Average velocity above the bed	**m/s**
v_2	Velocity of the bed	**m/s**
v_{12}	Velocity difference bed interface (v_1-v_2)	**m/s**
v_{ls}	Cross-section averaged line speed	**m/s**
$v_{ls,ldv}$	Limit Deposit Velocity (LDV)	**m/s**
v_r	Relative line speed $v_{ls}/v_{ls,ldv,max}$ or v_{ls}/v_{sm}	**m/s**
v_{sl}	Slip velocity (velocity difference between particle and liquid)	**m/s**
v_{sm}	Maximum LSDV according to Wilson	**m/s**
v_t	Particle terminal settling velocity	**m/s**
v_{th}	Hindered settling velocity	**m/s**
v_{tv}	(Hindered) settling velocity in the vehicle (Wasp model)	**m/s**
$v_{tv,ldv}$	(Hindered) settling velocity in the vehicle (Wasp model) at LDV	**m/s**

α_h	Coefficient homogeneous equation	-
α_p	LDV factor	-
α_{sm}	Factor concentration distribution	-
β	Angle of bed with vertical	rad
β	Power of Richardson & Zaki hindered settling factor	-
β_{sm}	Relation sediment diffusivity eddy momentum diffusivity	-
φ	Internal friction angle	rad
δ	External friction angle	rad
λ_1, λ_l	Darcy Weisbach friction factor liquid to pipe wall	-
λ_{12}	Darcy Weisbach friction factor bed interface	-
κ	Von Karman constant (about 0.4)	-
κ_C	Concentration distribution constant	-
ρ_l	Density of liquid	ton/m^3
$\rho_{l,m}$	Density of liquid including fines	ton/m^3
ρ_m	Mixture density	ton/m^3
ρ_s	Density of solids	ton/m^3
ν_l	Kinematic viscosity liquid	m^2/s
μ_l	Dynamic viscosity liquid	Pa·s
$\mu_{l,m}$	Dynamic viscously liquid including fines	Pa·s
μ_{sf}	Sliding friction coefficient	-
$\tau_{2,sf}$	Shear stress bed – pipe wall due to sliding friction	kPa
τ_{12}	Bed shear stress	kPa
ξ	Slip ratio	-
ξ_0	Slip ratio asymptotically for line speed zero	-
ζ	Bed fraction	-

5.2. The Jufin & Lopatin (1966) Model.

5.2.1. Introduction.

The Jufin & Lopatin (1966) model was constructed as a proposal for the Soviet technical norm in 1966. The authors did not submit a new model but selected the best combination of correlations for the frictional head loss and the critical velocity from four models submitted by different Soviet research institutes. The four models submitted were tested by a large experimental database collected by a number of researchers. The database contained data from both laboratory and field measurements (including data from dredging installations). The data covered a wide range of pipeline sizes (24 – 900 mm) and particle sizes (sand and gravel, 0.25 - 11 mm). Some of the data on which the model is based can be found in the chapters about Silin, Kobernik & Asaulenko (1958), Kazanskij (1978) and on the website www.dhlldv.com.
Kazanskij (1972) gave a summary and sort of manual for the use of the Jufin-Lopatin model. First of all sands and gravels are divided into 4 groups, according to Table 5-2. The ψ^* parameter characterizes the particles and is comparable with the Durand & Condolios (1952) $\sqrt{C_x}$ parameter.

Table 5-2: Group classification of Jufin-Lopatin (1966), source Kazanskij (1972).

Group	Range	ψ^*
A	d<0.06 mm	-
B	d_{60}<10 mm d_{10}<10 mm<d_{60}	All ψ^*<=1.5, d_0<2.5 mm
C	d_{10}<10 mm<d_{60}	ψ^*>1.5, d_0>2.5 mm
D	d_{10}>10 mm	-

The particle diameter $\mathbf{d_0}$ is the average particle diameter, not a weighted particle diameter, and can be determined by:

$$d_0 = \frac{\sum_{i=1}^{100} d_i}{100} \quad \text{or} \quad d_0 = \frac{\sum_{i=10}^{90} d_i}{9} \tag{5-26}$$

So each fraction has the same weight in the determination of the $\mathbf{d_0}$ value. For uniform sands and gravels, the $\mathbf{d_0}$ is equal to the particle diameter.

5.2.2. Group A: Fines.

Group A covers the fines, silt. For silt Jufin & Lopatin (1966) use the ELM without the Thomas (1965) viscosity, so:

$$\Delta p_m = \lambda_l \cdot \frac{\Delta L}{D_p} \cdot \frac{1}{2} \cdot \rho_m \cdot v_{ls}^2 \tag{5-27}$$

The hydraulic gradient $\mathbf{i_m}$ (for mixture) is now:

$$i_m = \frac{\Delta p_m}{\rho_l \cdot g \cdot \Delta L} = \frac{\rho_m}{\rho_l} \cdot \frac{\lambda_l \cdot v_{ls}^2}{2 \cdot g \cdot D_p} \tag{5-28}$$

5.2.3. Group B: Sand.

Group B covers fine and medium sands, with possibly some fine gravel. The equation found by Jufin & Lopatin (1966) was based on the empirical experience, suggesting that the minimum hydraulic gradient at the velocity $\mathbf{v_{min}}$ was independent of the mixture flow properties and it was 3 times higher than the hydraulic gradient of water flow at the same velocity in a pipeline. This was also experienced in the American dredging industry (see Turner (1996)). Now most frictional head models follow the equation:

$$\Delta p_m = \Delta p_l \cdot \left(1 + 2 \cdot \Omega \cdot \left(\frac{1}{v_{ls}} \right)^3 \right) \qquad \text{with:} \quad v_{min} = \Omega^{1/3} \tag{5-29}$$

The minimum is found at the cube root of **Ω**, as is the case with the Durand/Condolios/Gibert, Newitt et al. and Fuhrboter models. The frictional-head-loss correlation by Jufin & Lopatin is:

$$\Delta p_m = \Delta p_l \cdot \left(1 + 2 \cdot \left(\frac{v_{min}}{v_{ls}} \right)^3 \right) \tag{5-30}$$

With, for quarts particles (sometimes a factor 5.3 is used instead of 5.5) :

$$v_{min} = 5.5 \cdot \left(C_{vt} \cdot \psi^* \cdot D_p \right)^{1/6} = 3.76 \cdot \left(C_{vt} \cdot \psi^* \cdot g \cdot D_p \right)^{1/6} = 3.46 \cdot \left(C_{vt} \cdot \psi^* \cdot g \cdot D_p \cdot R_{sd} \right)^{1/6} \tag{5-31}$$

And:

$$\psi^* = Fr_p^{3/2} = \left(\frac{v_t}{\sqrt{g \cdot d}} \right)^{3/2} \tag{5-32}$$

This can be written in a more general form for the hydraulic gradient according to:

$$i_m = i_l \cdot \left(1 + 2 \cdot 41.35 \cdot \left(C_{vt} \cdot \psi^* \cdot g \cdot D_p \cdot R_{sd} \right)^{1/2} \left(\frac{1}{v_{ls}} \right)^3 \right) \tag{5-33}$$

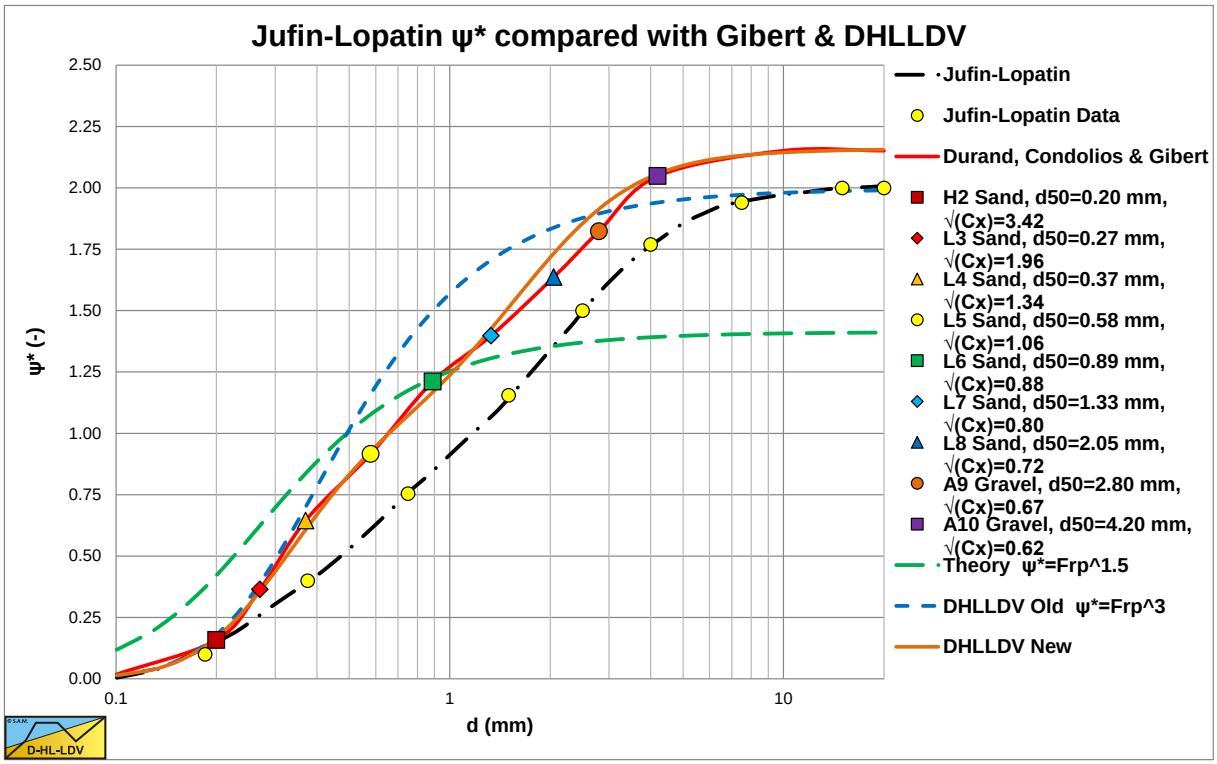

Figure 5-4: The Jufin-Lopatin ψ* compared to Gibert and DHLLDV.

Figure 5-4 shows the **ψ*** parameter of Jufin & Lopatin (1966) according to Kazanskij (1972). This parameter is compared with the equivalent parameters of Gibert (1960), Fuhrboter (1961) and the DHLLDV framework (Miedema S. A., 2014). The trends are similar, but especially for medium sands, the values differ.

Figure 5-5 shows a comparison in terms of the Gibert (1960) $\sqrt{C_x}$ value. Of course the trends are similar compared to Figure 5-4.

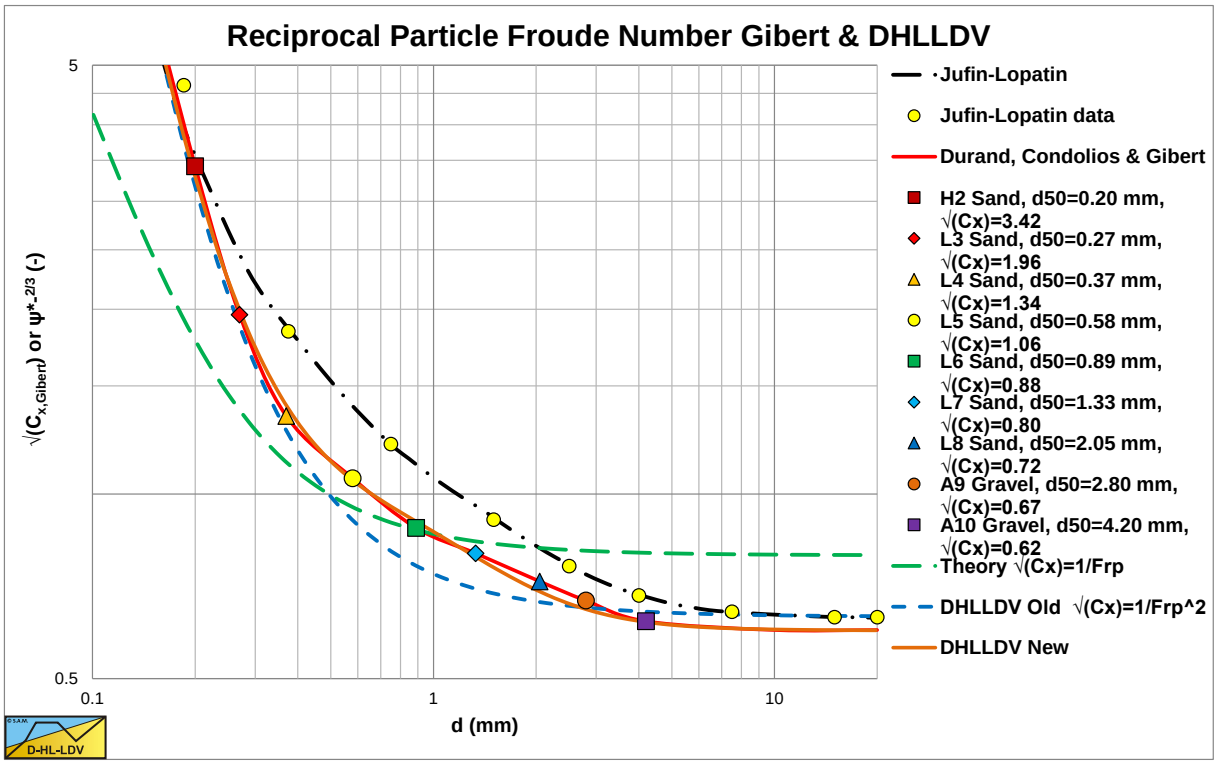

Figure 5-5: The reciprocal particle Froude number of Jufin-Lopatin, Gibert and DHLLDV.

Assuming the experiments are carried out with quarts this can be written as:

$$i_m = i_l \cdot \left(1 + 2 \cdot 41.35 \cdot \left(\frac{v_t}{\sqrt{g \cdot d}} \right)^{3/4} \cdot \left(g \cdot D_p \cdot R_{sd} \right)^{1/2} \cdot \left(C_{vt} \right)^{1/2} \left(\frac{1}{v_{ls}} \right)^3 \right) \qquad \textbf{(5-34)}$$

The term v_{min} should have the dimension of velocity, but in equation (5-31) it has the dimension of the cube root of velocity. This has to be compensated without violating the model of Jufin Lopatin. Now the product of kinematic viscosity ν and the gravitational constant g has the dimension of velocity to the 3rd power. It is not clear whether Jufin & Lopatin carried out experiments in liquids with different viscosities, but for dredging purposes it is neutral using this. This gives for v_{min}, using a kinematic viscosity of 10^{-6} m^2/sec and a gravitational constant of 9.81 m/sec^2:

$$v_{min} = 44.88 \cdot \left(C_{vt} \cdot \psi^* \cdot g \cdot D_p \cdot R_{sd} \right)^{1/6} \cdot \left(\nu_l \cdot g \right)^{2/9} \qquad \textbf{(5-35)}$$

Substituting this in equation (5-30) gives the equation for the hydraulic gradient.

$$i_m = i_l \cdot \left(1 + 2 \cdot 90389 \cdot \left(\frac{v_t}{\sqrt{g \cdot d}} \right)^{3/4} \cdot \left(g \cdot D_p \cdot R_{sd} \right)^{1/2} \cdot \left(\nu_l \cdot g \right)^{2/3} \cdot \left(C_{vt} \right)^{1/2} \left(\frac{1}{v_{ls}} \right)^3 \right) \qquad \textbf{(5-36)}$$

5.2.4. The Limit Deposit Velocity.

Jufin & Lopatin (1966) defined the Limit Deposit Velocity as (sometimes a value of 8 is used instead of 8.3):

$$v_{ls,\,ldv} = 8.3 \cdot \left(C_{vt} \cdot \psi^*\right)^{1/6} \cdot D_p^{1/3} \tag{5-37}$$

It is clear that this Limit Deposit Velocity also does not have the dimension of velocity, but the cube root of length. To give this Limit Deposit Velocity the dimension of velocity, the equation is modified to (for quarts and water):

$$v_{ls,\,ldv} = 9.23 \cdot \left(C_{vt} \cdot \psi^*\right)^{1/6} \cdot \left(2 \cdot g \cdot D_p \cdot R_{sd}\right)^{1/3} \cdot \left(\nu_l \cdot g\right)^{1/9} \tag{5-38}$$

Which can be written as:

$$v_{ls,\,ldv} = 9.23 \cdot \left(C_{vt}\right)^{1/6} \cdot \left(\frac{v_t}{\sqrt{g \cdot d}}\right)^{1/4} \cdot \left(2 \cdot g \cdot D_p \cdot R_{sd}\right)^{1/3} \cdot \left(\nu_l \cdot g\right)^{1/9} \tag{5-39}$$

Giving:

$$F_L = \frac{v_{ls,\,ldv}}{\left(2 \cdot g \cdot D_p \cdot R_{sd}\right)^{1/2}} = 9.23 \cdot \frac{\left(C_{vt}\right)^{1/6} \cdot \left(\frac{v_t}{\sqrt{g \cdot d}}\right)^{1/4} \cdot \left(\nu_l \cdot g\right)^{1/9}}{\left(2 \cdot g \cdot D_p \cdot R_{sd}\right)^{1/6}} \tag{5-40}$$

5.2.5. Broad Graded Sands or Gravels.

The effect of a broad particle size distribution is taken into account by determining an average value of the modified particle Froude number from values of the modified Froude number for soil fraction $\mathbf{p_i}$ of different size $\mathbf{d_i}$. The values for ψ* can also be taken from Table 5-2 or Figure 5-4.

$$\psi^* = Fr_{vt}^{1.5} = \sum_{i=1}^{n} Fr_{vt,i}^{1.5} \cdot p_i = \sum_{i=1}^{n} \psi^*(d_i) \cdot p_i \tag{5-41}$$

Table 5.1: Particle settling parameter for the Jufin-Lopatin (1966) model.

size fraction of solids, d [mm]	particle settling parameter, ψ* Jufin & Lopatin (1966)	particle settling parameter, ψ* Jufin (1971)
0.05 - 0.10	0.0204	0.02
0.10 - 0.25	0.0980	0.2
0.25 - 0.50	0.4040	0.4
0.50 - 1.00	0.7550	0.8
1.0 - 2.0	1.1550	1.2
2.0 - 3.0	1.5000	1.5
3.0 - 5.0	1.7700	1.8
5 - 10	1.9400	1.9
10 - 20	1.9700	2.0
>20	2.0000	2.0

5.2.6. Group C: Fine Gravel.

Group C is a transition between medium sized sand and coarse gravel. The equation for v_{min} has to be corrected according to:

$$v_{min} = 5.5 \cdot b \cdot \left(C_{vt} \cdot \psi^{*} \cdot D_p\right)^{1/6} = 3.76 \cdot b \cdot \left(C_{vt} \cdot \psi^{*} \cdot g \cdot D_p\right)^{1/6}$$

$$= 3.46 \cdot b \cdot \left(C_{vt} \cdot \psi^{*} \cdot g \cdot D_p \cdot R_{sd}\right)^{1/6} = 44.88 \cdot b \cdot \left(C_{vt} \cdot \psi^{*} \cdot g \cdot D_p \cdot R_{sd}\right)^{1/6} \cdot \left(\nu_l \cdot g\right)^{2/9} \quad \textbf{(5-42)}$$

Table 5-3: Correction factor a, source Kazanskij (1972) .

d_0	10 mm<d_0<20 mm				d_0>20 mm			
ρ_m (ton/m^3)	1.02	1.05	1.10	1.20	1.02	1.05	1.10	1.20
D_p<400 mm	1.01	1.18	1.34	1.48	1.11	1.30	1.48	1.68
400 mm<D_p<600 mm	1.14	1.31	1.47	1.64	1.27	1.46	1.62	1.81
600 mm<D_p	1.23	1.41	1.54	1.73	1.38	1.50	1.67	1.86

The correction factor **b** can be determined with:

$$b = 1 + \frac{(\psi - 1.5)}{(2.0 - 1.5)} \cdot (a - 1) \quad \textbf{(5-43)}$$

Where the factor **a** can be found in Table 5-3.

5.2.7. Group D: Coarse Gravel.

For Group D the correction factor is just **a**, according to Table 5-3.

$$v_{min} = 5.5 \cdot a \cdot \left(C_{vt} \cdot 2 \cdot D_p\right)^{1/6} = 3.76 \cdot a \cdot \left(C_{vt} \cdot 2 \cdot g \cdot D_p\right)^{1/6}$$

$$= 3.46 \cdot a \cdot \left(C_{vt} \cdot 2 \cdot g \cdot D_p \cdot R_{sd}\right)^{1/6} = 44.88 \cdot a \cdot \left(C_{vt} \cdot 2 \cdot g \cdot D_p \cdot R_{sd}\right)^{1/6} \cdot \left(\nu_l \cdot g\right)^{2/9} \quad \textbf{(5-44)}$$

5.2.8. Conclusions & Discussion.

The model of Jufin & Lopatin (1966) for Group A is the ELM model without a viscosity correction.
The models for Groups B, C and D are similar, but Groups C and D have a correction factor. In order to make the Jufin & Lopatin (1966) model comparable with other models, the basic equation is written in terms of the liquid hydraulic gradient plus the solids effect.

$$i_m = i_l + 2 \cdot 90389 \cdot \left(g \cdot D_p \cdot R_{sd} \cdot \psi^*\right)^{1/2} \cdot \left(v_l \cdot g\right)^{2/3} \cdot \left(C_{vt}\right)^{1/2} \left(\frac{1}{v_{ls}}\right)^3 \cdot \frac{\lambda_l \cdot v_{ls}^2}{2 \cdot g \cdot D_p}$$

$$= i_l + 90389 \cdot \frac{\lambda_l \cdot \left(\psi^* \cdot R_{sd}\right)^{1/2} \cdot \left(v_l \cdot g\right)^{2/3}}{\left(g \cdot D_p\right)^{1/2} \cdot \left(C_{vt}\right)^{1/2}} \cdot \frac{C_{vt}}{v_{ls}} \qquad \textbf{(5-45)}$$

The Darcy-Weisbach friction factor for a smooth pipe can be approached by:

$$\lambda_l = \alpha \cdot \left(v_{ls}\right)^{\alpha_1} \cdot \left(D_p\right)^{\alpha_2} \qquad \textbf{(5-46)}$$

With:

$$\alpha = 0.01216 \quad \text{and} \quad \alpha_1 = -0.1537 \cdot \left(D_p\right)^{-0.089} \quad \text{and} \quad \alpha_2 = -0.2013 \cdot \left(v_{ls}\right)^{-0.088} \qquad \textbf{(5-47)}$$

For laboratory conditions both powers are close to **-0.18**, while for real life conditions with higher line speeds and much larger pipe diameters this results in a power for the line speed of about α_1**=-0.155** and for the pipe diameter of about α_2**=-0.175**. This should be considered when analyzing the models for heterogeneous transport.

This gives for the Darcy-Weisbach friction factor in a dimensionless form:

$$\lambda_l = 0.01216 \cdot \left(v_{ls}\right)^{-0.155} \cdot \left(D_p\right)^{-0.175} \approx 0.1233 \cdot \left(v_{ls}\right)^{-0.155} \cdot \left(g \cdot D_p\right)^{-0.172} \cdot \left(v_l \cdot g\right)^{1/6} \qquad \textbf{(5-48)}$$

Substitution gives:

$$i_m = i_l + 11145 \cdot \frac{\left(\psi^* \cdot R_{sd}\right)^{1/2} \cdot \left(v_l \cdot g\right)^{5/6}}{\left(g \cdot D_p\right)^{0.672} \cdot \left(C_{vt}\right)^{1/2}} \cdot \frac{1}{v_{ls}^{0.155}} \cdot \frac{C_{vt}}{v_{ls}} \qquad \textbf{(5-49)}$$

With the solids effect factor S_k (to compare with Fuhrboter)defined as:

$$i_m = i_l + S_k \cdot \frac{C_{vt}}{v_{ls}} \qquad \textbf{(5-50)}$$

This gives for the solids effect factor S_k:

$$S_k = 11145 \cdot \frac{\left(\psi^* \cdot R_{sd}\right)^{1/2} \cdot \left(v_l \cdot g\right)^{5/6}}{\left(g \cdot D_p\right)^{0.672} \cdot \left(C_{vt}\right)^{1/2}} \cdot \frac{1}{v_{ls}^{0.155}} \qquad \textbf{(5-51)}$$

5.2.9. Nomenclature Early History & Empirical and Semi-Empirical Models.

a	Correction factor Jufin Lopatin	**-**
b	Correction factor Jufin Lopatin	**-**
C_D	Particle drag coefficient	**-**
C_{ms}	Spatial concentration by mass	**-**
C_v	Volumetric concentration	**-**
C_{vs}	Volumetric spatial concentration	**-**
C_{vt}	Volumetric transport/delivered concentration	**-**
C_x	Inverse particle Froude number squared according to Durand & Condolios **Fr_p^{-2}**	**-**
$C_{x,Gibert}$	Inverse particle Froude number squared according to Gibert	**-**
d	Particle diameter	**m**
d_0	Average particle diameter Jufin Lopatin	**m**
d_{10}	Particle diameter at which 10% by weight is smaller	**m**
d_{25}	Particle diameter at which 25% by weight is smaller	**m**
d_{50}	Particle diameter at which 50% by weight is smaller	**m**
d_{60}	Particle diameter at which 60% by weight is smaller	**m**
d_m	Mean particle diameter	**m**
D_p	Pipe diameter	**m**
$D_{p,H}$	Hydraulic diameter pipe cross section above bed	**m**
Du	Durand & Condolios constant (176-181) or (81-85)	**-**
E_{rhg}	Relative excess hydraulic gradient	**-**
f_l	Fanning friction factor liquid	**-**
f_m	Fanning friction factor mixture	
ELM	Equivalent Liquid Model	**-**
F_L, $F_{L,m}$	Durand & Condolios Limit Deposit Velocity coefficient	**-**
Fr_{ldv}	Flow Froude number at the Limit Deposit Velocity/critical velocity	**-**
Fr_{fl}	Flow Froude number	**-**
Fr_p	Particle Froude number **$1/\sqrt{C_x}$**	**-**
g	Gravitational constant	**$9.81 \cdot m/s^2$**
i	Hydraulic gradient	**m.w.c./m**
i_m	Hydraulic gradient mixture	**m.w.c./m**
i_w,i_l	Hydraulic gradient water/liquid	**-**
K	Durand & Condolios constant (176-181) or (81-85)	**-**
K	Constant others (Yagi, Babcock, etc.)	**-**
K	Wilson proportionality constant	**-**
K	Turian & Yuan constant	**-**
K_1	Newitt coefficient for heterogeneous transport (1100)	**-**
K_2	Newitt coefficient for sliding/moving bed (66)	**-**
L, ΔL	Length of the pipeline	**m**
LDV	Limit Deposit Velocity	**m/s**
LSDV	Limit of Stationary Deposit Velocity	**m/s**
MHGV	Minimum Hydraulic Gradient Velocity	**m/s**
N_{cr}	Zandi & Govatos parameter for Limit Deposit Velocity	**-**
p	Probability	**-**
p_{er}	Relative excess pressure	**-**
Δp	Head loss over a pipeline length **ΔL**	**kPa**
Δp_m	Head loss of mixture over a pipeline length **ΔL**	**kPa**
Δp_l, Δp_w	Head loss of liquid/water over a pipeline length **ΔL**	**kPa**
PSD	Particle Size Diagram/Distribution	**-**
R_{sd}	Relative submerged density	**-**
S_k	Solids effect factor Fuhrboter spatial concentration	**m/s**
S_{kt}	Solids effect factor Fuhrboter transport concentration	**m/s**
u_*	Friction velocity	**m/s**
v_{ls}	Line speed	**m/s**
$v_{ls,ldv}$	Limit Deposit Velocity (often called critical velocity)	**m/s**
$v_{ls,h-h}$	Transition velocity heterogeneous vs. homogeneous according to Newitt	**m/s**

$v_{ls,MHGV}$	Minimum Hydraulic Gradient Velocity	**m/s**
v_{min}	Minimum gradient velocity	**m/s**
v_t	Terminal settling velocity of particles	**m/s**
v_l	Average liquid velocity	**m/s**
v_p	Average velocity particle	**m/s**
v_s	Average velocity solids	**m/s**
x	Abscissa	**-**
y	Ordinate	**-**
α	Power in Yagi equation	**-**
α	Darcy Weisbach friction factor constant	**-**
α	Power of concentration in Turian & Yuan equation	**-**
α_1	Darcy Weisbach friction factor power	**-**
α_2	Darcy Weisbach friction factor power	**-**
β	Power of Richardson & Zaki equation	**-**
β	Power of Fanning friction factor liquid in Turian & Yuan equation	**-**
γ	Power of drag coefficient in Turian & Yuan equation	**-**
δ	Power of Froude number in Turian & Yuan equation	**-**
ρ_l	Liquid density	**ton/m^3**
ρ_w	Density of water	**ton/m^3**
ρ_m	Mixture density	**ton/m^3**
λ_l	Darcy-Weisbach friction factor liquid to wall	**-**
μ_{sf}	Friction coefficient for sliding bed (see also S_{rs})	**-**
Φ	Durand relative excess pressure as ordinate in different graphs	**-**
ψ	Durand abscissa, equations may differ due to historical development, later the relative submerged density has been added, sometimes the particle Froude number is omitted	**-**
ψ	Particle shape coefficient, usually near 0.7	**-**
ψ^*	Particle factor Jufin Lopatin	**-**
ν_w,ν_l	Kinematic viscosity of water/liquid	**m^2/s**
ν_m	Kinematic viscosity of mixture with Thomas equation	**m^2/s**
ν_r	Relative kinematic viscosity ν_m/ν_w	**-**
ξ	Particle shape factor	**-**
ξ	Slip ratio Yagi	**-**

5.3. The Wilson-GIW (1992) Model for Heterogeneous Transport.

5.3.1. The Full Model.

Assuming that 50% of the solids is moving in the bed by granular contact at a line speed of v_{50}, and assuming a friction coefficient μ_{sf} between the particles and the pipe wall, the friction force in a pipe with length ΔL is:

$$F_{sf} = \frac{\mu_{sf}}{2} \cdot A_p \cdot \Delta L \cdot C_v \cdot (\rho_s - \rho_l) \cdot g \qquad (5\text{-}52)$$

This gives an excess pressure due to the solids of:

$$\Delta p_m - \Delta p_l = \frac{F_{sf}}{A_p} = \frac{\mu_{sf}}{2} \cdot \Delta L \cdot C_v \cdot (\rho_s - \rho_l) \cdot g \qquad (5\text{-}53)$$

In terms of the hydraulic gradient this can be written as:

$$i_m - i_l = \frac{\Delta p_m - \Delta p_l}{\rho_l \cdot g \cdot \Delta L} = \frac{\mu_{sf}}{2} \cdot C_v \cdot \frac{(\rho_s - \rho_l)}{\rho_l} = \frac{\mu_{sf}}{2} \cdot C_v \cdot R_{sd} \qquad (5\text{-}54)$$

Wilson (1997) has defined a stratification ratio or relative solids effect, which tells which fraction of the particles, is in suspension and which part is in the fixed or moving bed, supported by granular contact. Wilson (1997) gives the following general equation for the head losses in hydraulic transport, where μ_{sf} equals the friction factor of a sliding bed, which he has determined to be μ_{sf}**=0.44**. For the 50% case this gives:

$$E_{rhg} = R = \frac{i_m - i_l}{R_{sd} \cdot C_v} = \frac{\Delta p_m - \Delta p_l}{\rho_l \cdot g \cdot \Delta L \cdot R_{sd} \cdot C_v} = \frac{\mu_{sf}}{2} \cdot \left(\frac{v_{50}}{v_{ls}} \right)^M \qquad (5\text{-}55)$$

When the line speed v_{ls} equals the v_{50}, the stratification ratio is 0.22 or half the friction coefficient μ_{sf}. This can be written in terms of pressures instead of hydraulic gradient as:

$$\Delta p_m = \Delta p_l + \frac{\mu_{sf}}{2} \cdot \rho_l \cdot g \cdot \Delta L \cdot \left(\frac{v_{50}}{v_{ls}} \right)^M \cdot R_{sd} \cdot C_v \qquad (5\text{-}56)$$

This equation can be written in the more generic form, matching the notations of the other theories:

$$\Delta p_m = \Delta p_l \cdot \left(1 + \frac{\mu_{sf} \cdot g \cdot R_{sd} \cdot D_p}{\lambda_l} \cdot (v_{50})^M \cdot \left(\frac{1}{v_{ls}} \right)^{2+M} \cdot C_v \right) \qquad (5\text{-}57)$$

For the line speed, where 50% of the particles is in granular contact, v_{50}, Wilson gives the following equation:

$$v_{50} = w_{50} \cdot \sqrt{\frac{8}{\lambda_l}} \cdot \cosh\left(\frac{60 \cdot d_{50}}{D_p} \right) \qquad (5\text{-}58)$$

When the power **M** equals 1, this equation has the same form as the equation of Durand & Condolios, Gibert, Fuhrboter, Jufin Lopatin and Newitt et al. The power **M** depends on the grading of the sand and can be determined by:

$$M = \left(0.25 + 13 \cdot \sigma^2 \right)^{-1/2} \qquad (5\text{-}59)$$

The variance **σ** of the PSD (Particle Size Distribution), can be determined by some ratio between the v_{50} and the v_{85}:

$$\sigma = \log\left(\frac{v_{85}}{v_{50}}\right) = \log\left(\frac{w_{85}\cdot\cosh\left(\frac{60\cdot d_{85}}{D_p}\right)}{w_{50}\cdot\cosh\left(\frac{60\cdot d_{50}}{D_p}\right)}\right) \qquad \textbf{(5-60)}$$

The terminal settling velocity related parameter **w**, the particle associated velocity, can be determined by:

$$w = 0.9\cdot v_t + 2.7\cdot\left(R_{sd}\cdot g\cdot\nu_l\right)^{1/3} \qquad \textbf{(5-61)}$$

It seems this equation mixes the homogeneous and heterogeneous regimes. For very small particles the second term gives a constant particle associated velocity, which matches homogeneous behavior at operational line speeds. Since the homogeneous behavior does not depend on the particle size, this gives a constant or asymptotic particle associated velocity.

5.3.2. The Simplified Wilson Model.

The model of Wilson can be simplified with some fit functions, according to:

$$v_{50} \approx 3.93\cdot\left(1000\cdot d_{50}\right)^{0.35}\cdot\left(\frac{R_{sd}}{1.65}\right)^{0.45}\cdot\left(\frac{\nu_{l,actual}}{\nu_{w,20}}\right)^{-0.25} \qquad \textbf{(5-62)}$$

In which the particle diameter d_{50} is in m and the resulting v_{50} in m/s. The third term on the right had side is the relative viscosity, the actual liquid viscosity divided by the viscosity of water at 20 degrees Centigrade. In normal dredging practice this term is about unity and can be neglected.

The exponent **M** is given by the approximation:

$$M \approx \left(\ln\left(\frac{d_{85}}{d_{50}}\right)\right)^{-1} \qquad \textbf{(5-63)}$$

Figure 5-6 shows the Wilson et al. (1992) model in $E_{rhg}(i_l)$ coordinates. The black dotted line is the $E_{rhg}=\mu_{sf}/2$ line. The yellow circle the point with $v_{ls}=v_{50}$. The heterogeneous Wilson lines have powers of **M=1.7, 1.0 & 0.25**. So heterogeneous lines always cross the yellow circle, the v_{50} point, and are rotated around this point depending on the power **M**. The higher the power **M**, the steeper the line in this graph.

5.3.3. Generic Equation.

Based on equation (5-57) and equation (5-62) and the assumption **M=1** for $d_{85}/d_{50}=2.72$ and assuming the liquid is water of 20 degrees Centigrade and the solids are sand (quarts), an equation is derived to compare Wilson with the other theories:

$$i_m = i_l\cdot\left(1+\frac{\mu_{sf}\cdot g\cdot R_{sd}\cdot D_p}{\lambda_l}\cdot\left(v_{50}\right)^M\cdot\left(\frac{1}{v_{ls}}\right)^{2+M}\cdot C_v\right) \qquad \textbf{(5-64)}$$

For the line speed v_{50}:

$$v_{50} \approx 3.93\cdot\left(1000\cdot d_{50}\right)^{0.35} = 44.1\cdot\left(d_{50}\right)^{0.35} \qquad \textbf{(5-65)}$$

This gives:

$$i_m = i_l \cdot \left(1 + \frac{\mu_{sf} \cdot g \cdot R_{sd} \cdot D_p}{\lambda_l} \cdot \left(44.1 \cdot \left(d_{50} \right)^{0.35} \right)^M \cdot \left(\frac{1}{v_{ls}} \right)^{2+M} \cdot C_v \right) \qquad \textbf{(5-66)}$$

Substituting equation (5-65) in equation (5-66) gives:

$$i_m = i_l \cdot \left(1 + 44.1^M \cdot \frac{\mu_{sf} \cdot g \cdot R_{sd} \cdot D_p}{\lambda_l} \cdot \left(d_{50} \right)^{0.35 \cdot M} \cdot \left(\frac{1}{v_{ls}} \right)^{2+M} \cdot C_v \right) \qquad \textbf{(5-67)}$$

With the friction coefficient of μ_{sf}**=0.44**, **M=1** and some simplifications, this gives:

$$i_m = i_l \cdot \left(1 + 19.4 \cdot \frac{g \cdot R_{sd} \cdot D_p}{\lambda_l} \cdot \left(d_{50} \right)^{0.35} \cdot \left(\frac{1}{v_{ls}} \right)^3 \cdot C_v \right) \qquad \textbf{(5-68)}$$

Giving each term the dimension of velocity gives:

$$i_m = i_l \cdot \left(1 + 27.64 \cdot \frac{g \cdot R_{sd} \cdot D_p}{\lambda_l} \cdot \left(g \cdot d_{50} \right)^{0.35} \cdot \left(\nu_l \cdot g \right)^{0.1} \cdot \left(\frac{1}{v_{ls}} \right)^3 \cdot C_v \right) \qquad \textbf{(5-69)}$$

Or:

$$i_m = i_l + 13.82 \cdot \left(g \cdot d_{50} \right)^{0.35} \cdot \left(\nu_l \cdot g \right)^{0.1} \cdot \frac{1}{v_{ls}} \cdot R_{sd} \cdot C_v \qquad \textbf{(5-70)}$$

The result is an equation where the excess pressure due to the solids is proportional to the pipe diameter $\mathbf{D_p}$ and almost proportional to the cube root of the $\mathbf{d_{50}}$ of the sand. There is no direct relation with the terminal settling velocity $\mathbf{v_t}$ or the particle drag coefficient $\mathbf{C_D}$.

5.3.4. Conclusions & Discussion.

The basic form of the equation for heterogeneous transport, equation (5-55), is of the type; hydraulic gradient mixture equals hydraulic gradient carrier liquid + solids effect. This implies that the hydraulic gradient of the carrier liquid and the solids effect are independent like in the Fuhrboter (1961) model. This in contrary with the Durand & Condolios (1952), Newitt et al. (1955) and the Jufin & Lopatin (1966) models. These are of the type; hydraulic gradient mixture equals hydraulic gradient carrier liquid times 1 + solids effect. Equations (5-69) and (5-70) show the Wilson equation for both types, with correct dimensions.
Basically the model shows straight lines in the $\mathbf{E_{rhg}(i_l)}$ graph with the $\mathbf{v_{50}}$**, 0.22** point as a pivot point. Depending on the value of the power **M**, the straight line pivots around this point. Figure 5-6 shows these straight line for powers of 0.25, 1.0 and 1.7. The power of 1.7 for uniform sands matches very well with the DHLLDV model for uniform sands.
The model gives good results if the physics on which it is based occur, medium sized particles.
For very fine particles in a large pipe there will never be a sliding bed. The stationary bed will vaporize (erode) with increasing line speed, probably without sheet flow, see Figure 5-7. The 50% stratification criterion is not valid here because the sliding friction is not 100% mobilized resulting in a much lower friction.
Very large particles will, almost always, be more than 50% stratified, resulting in a sliding bed or sliding flow, so the model is also invalid in this case, see Figure 5-8.

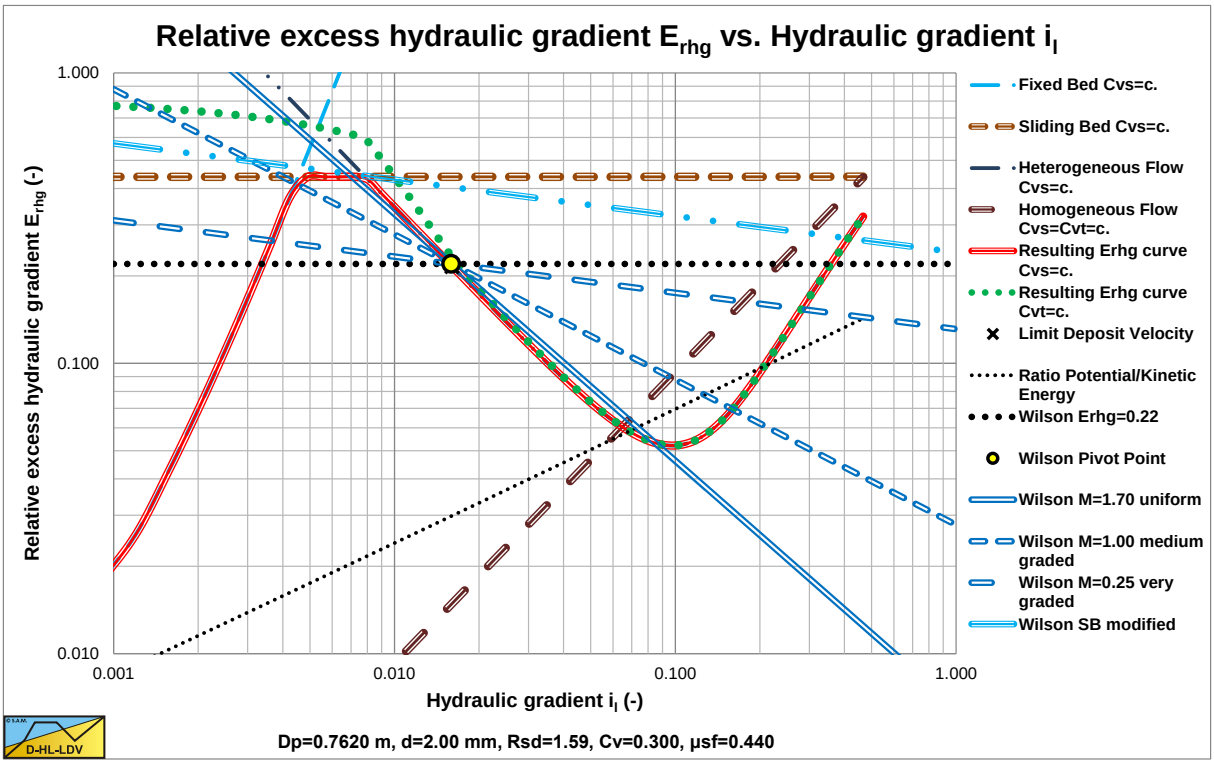

Figure 5-6: The power in the Wilson et al. (1992) model, d=2 mm.

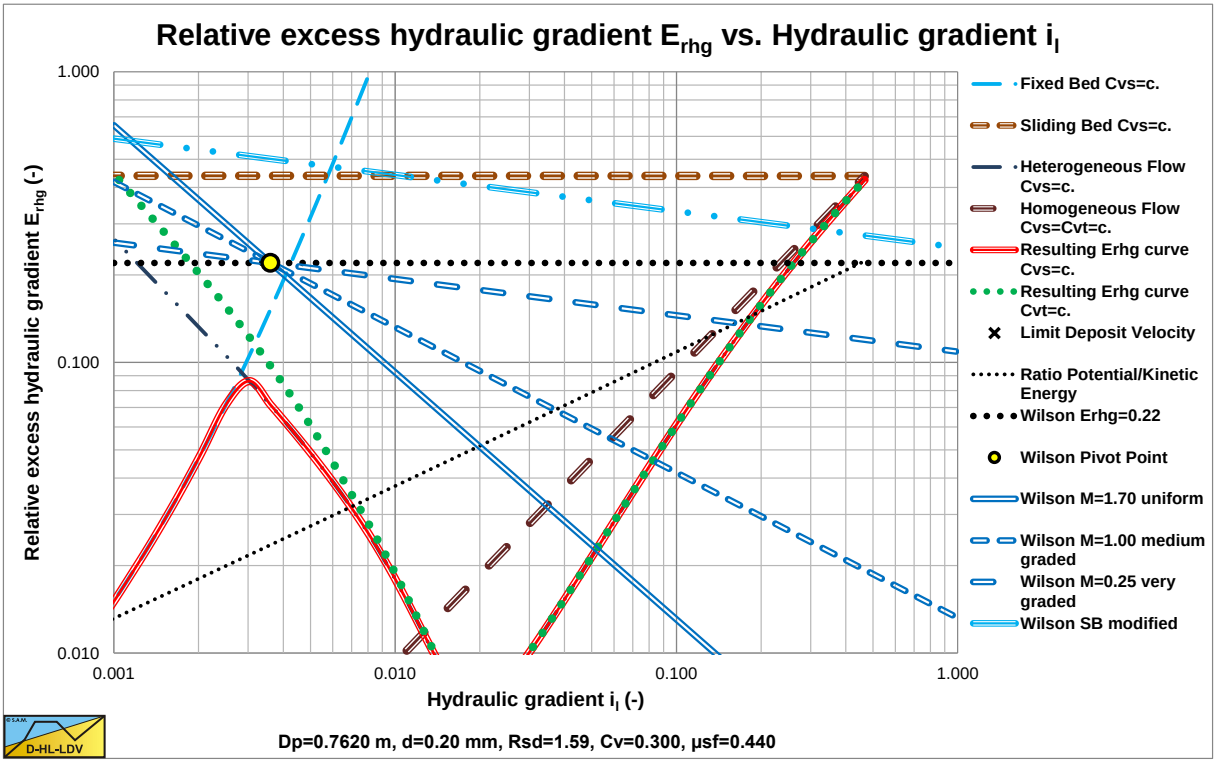

Figure 5-7: The power in the Wilson et al. (1992) model, d=0.2 mm.

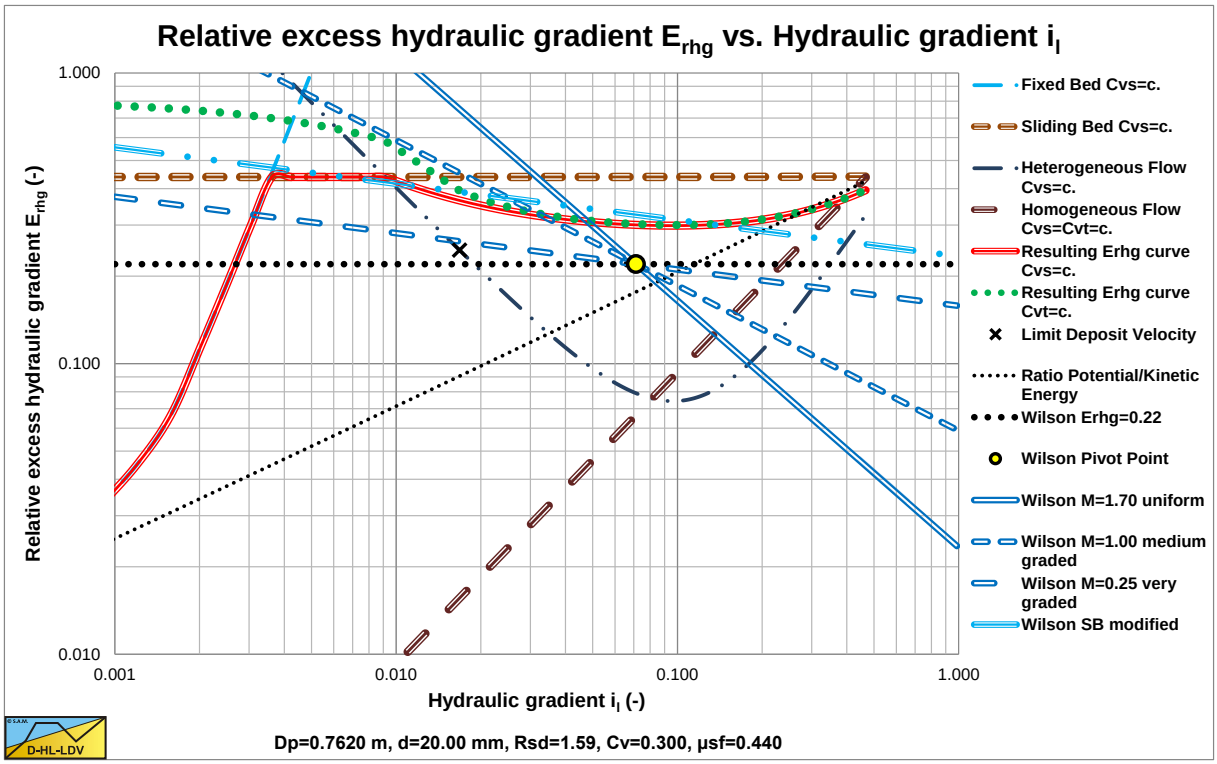

Figure 5-8: The power in the Wilson et al. (1992) model, d=20 mm.

In the 3 figures, the DHLLDV framework is used for comparison.

Wilson et al. (2006) suggests the following equation for full stratified flow, based on μ_{sf}=**0.4** (or **0.44**):

$$i_m = i_l + C_{vt} \cdot R_{sd} \cdot 2 \cdot \mu_{sf} \cdot \left(\frac{4 \cdot v_{sm}}{3 \cdot v_{ls}} \right)^{0.25} \quad \text{Based on } \mu_{sf} = 0.40 \qquad \text{or} \qquad i_m = i_l + C_{vt} \cdot R_{sd} \cdot 2 \cdot \mu_{sf} \cdot \left(\frac{v_{sm}}{v_{ls}} \right)^{0.25} \quad \text{Based on } \mu_{sf} = 0.44 \tag{5-71}$$

As is shown in Figure 5-8 there will be a discontinuity jumping from the heterogeneous model to the full stratified model, even if the same power of 0.25 is applied. In fact if more than 50% of the solids is stratified, the v_{50} point at E_{rhg}=**0.22** in the 3 graphs will never be reached.

5.3.5. Near Wall Lift.

Wilson et al. (2000) found that close to the bottom of the pipe the volumetric concentration is lower than just above the bottom of the pipe. They explain this phenomena as the effect of near wall turbulent lift. If there is a strong curvature of the velocity profile, which there is in turbulent flow close to the wall, particles in this flow will be subject to a lift force. This should not be mistaken with Magnus lift in a laminar flow (in the viscous sub-layer).

Wilson et al. (2010) introduced the lift force F_L on a particle as:

$$F_L = C_L \cdot \frac{1}{2} \cdot \rho_l \cdot u_*^2 \cdot \frac{\pi}{4} \cdot d^2 \tag{5-72}$$

And for the weight of the particle F_W:

$$F_W = (\rho_s - \rho_l) \cdot g \cdot \frac{\pi}{6} \cdot d^3 \tag{5-73}$$

Giving for the so called lift ratio L_R, the ratio of the lift force on a particle F_L to the weight of a particle F_W:

$$L_R = \frac{F_L}{F_W} = C_L \cdot \frac{3}{4} \cdot \frac{u_*^2}{R_{sd} \cdot g \cdot d} = \frac{3}{4} \cdot C_L \cdot \frac{\rho_l \cdot u_*^2}{\rho_l \cdot R_{sd} \cdot g \cdot d} = \frac{3}{4} \cdot C_L \cdot \theta = C_L \cdot \frac{3}{32} \cdot \frac{\lambda_l \cdot v_{ls}^2}{R_{sd} \cdot g \cdot d} \quad \textbf{(5-74)}$$

With: θ=Shields parameter.

This ratio will be referred to as the lift force to weight ratio or just the lift ratio. If this ratio is bigger than 1, particles will be lifted, otherwise gravity dominates. Now it is the question whether or not the lift force is completely correct, but it can be used as an indication. In Wilson et al. (2006) a lift coefficient C_L=**0.27** is mentioned.

The line speed where the lift ratio equals 1 can now be determined with:

$$v_{ls,L_R=1}^2 = \frac{32}{3} \cdot \frac{R_{sd} \cdot g \cdot d}{C_L \cdot \lambda_l} \quad \Rightarrow \quad v_{ls,L_R=1} = \left(\frac{32}{3} \cdot \frac{R_{sd} \cdot g \cdot d}{C_L \cdot \lambda_l} \right)^{0.5} \quad \textbf{(5-75)}$$

Now the idea is that in some circumstances particles will be lifted away from the bottom of the pipe, leaving a particle lean region near the wall, which is in agreement with the concentration profiles found. Medium sized particles show a hydraulic gradient below the ELM curve after passing this curve, see Figure 5-9. The asymptotic behavior for very high line speeds cannot be established from the data, since in general experiments are not carried out with very high line speeds, but at line speeds close to operational line speeds or lower. Figure 5-10 shows data from Blythe & Czarnotta (1995) also showing crossing the ELM. However these data points seem to return to the ELM at higher line speeds, or at least follow a parallel curve, not approaching the pure liquid behavior.

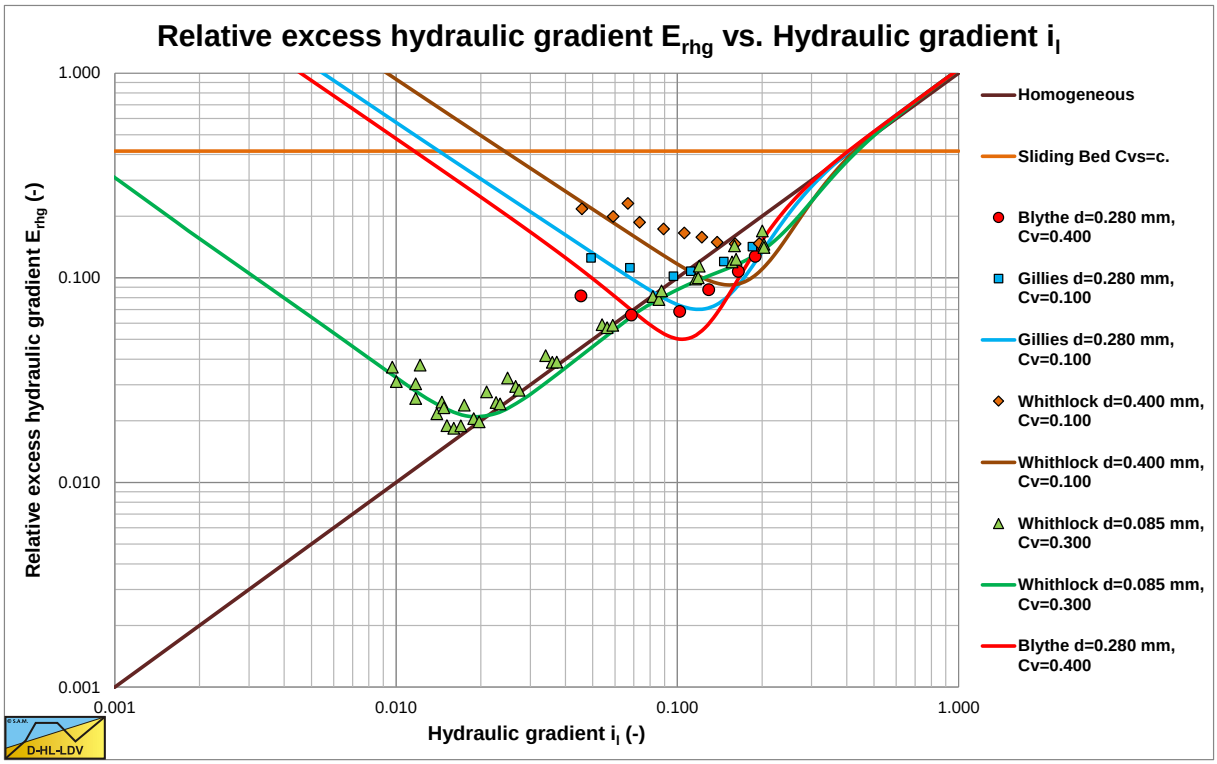

Figure 5-9: The data of Whithlock et al. (2004), Gillies (1993) and Blythe & Czarnotta (1995).

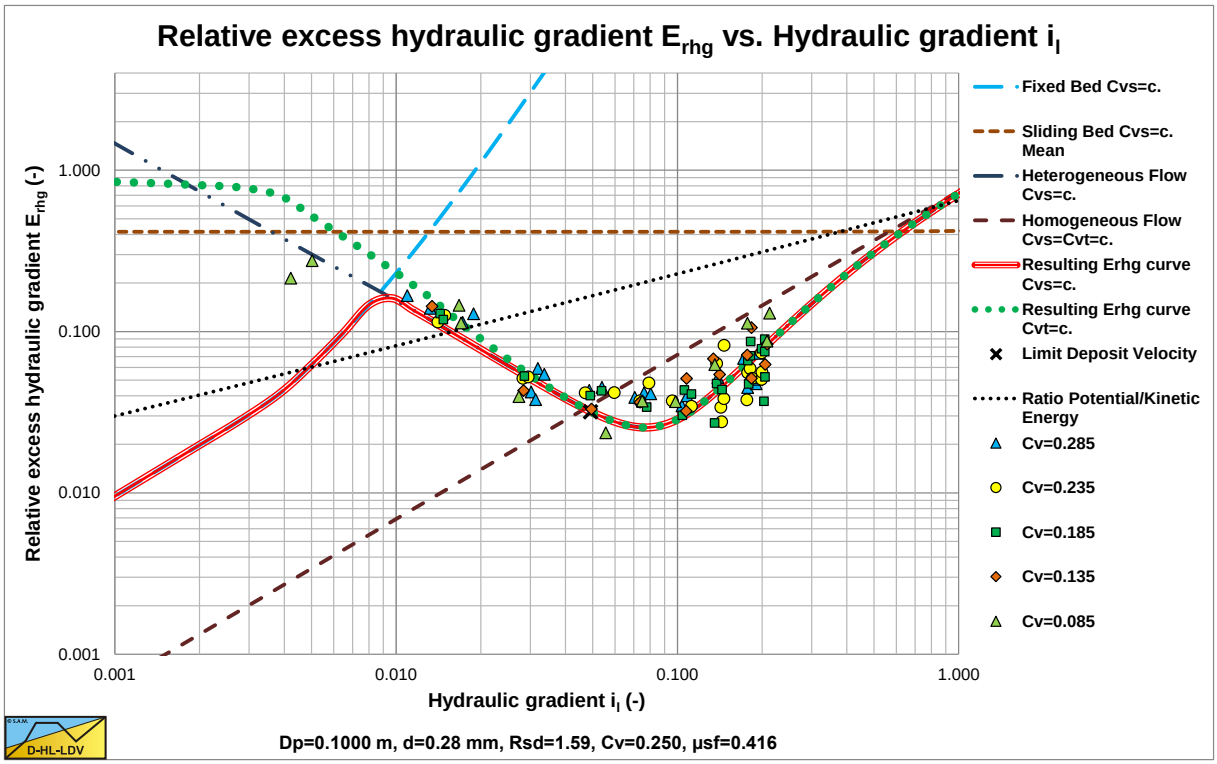

Figure 5-10: The data of Blythe & Czarnotta (1995).

Based on the so called shear Reynolds number:

$$Re_* = \frac{v_* \cdot d}{\nu_l} \tag{5-76}$$

A new expression has been derived for the stratification ratio **R**:

$$E_{rhg} = \frac{i_m - i_l}{R_{sd} \cdot C_{vt}} = R = \frac{0.93}{\theta \cdot (Re_*)^{1/3}} \tag{5-77}$$

The coefficient is slightly different from the original paper (0.93 instead of 0.7) because here the Shields parameter is applied. According to Wilson et al. (2010) the stratification ratio has an upper limit of 0.6. The shear velocity used in this Reynolds number is the shear velocity based on the terminal settling velocity of the particle. Now assuming a cylinder around the particle with diameter d and height d, the shear stress on the surface of this cylinder follows from the weight of the particle and the surface of this cylinder, so:

$$\tau_c \cdot \pi \cdot d^2 = (\rho_s - \rho_l) \cdot g \cdot \frac{\pi}{6} \cdot d^3$$

$$\tau_c = (\rho_s - \rho_l) \cdot g \cdot \frac{1}{6} \cdot d \tag{5-78}$$

Assuming a similar relation between the shear stress and the shear velocity gives:

$$\tau_c = \rho_l \cdot v_*^2 = (\rho_s - \rho_l) \cdot g \cdot \frac{1}{6} \cdot d$$

$$v_* = \left(\frac{(\rho_s - \rho_l)}{6 \cdot \rho_l} \cdot g \cdot d \right)^{1/2} = \left(\frac{R_{sd} \cdot g \cdot d}{6} \right)^{1/2} \qquad \textbf{(5-79)}$$

$$Re_* = \frac{v_* \cdot d}{\nu_l} = \frac{\left(\frac{R_{sd} \cdot g \cdot d}{6} \right)^{1/2} \cdot d}{\nu_l}$$

Now substituting both the Shields parameter and the shear Reynolds number in the stratification ratio equation gives:

$$E_{rhg} = \frac{i_m - i_l}{R_{sd} \cdot C_{vt}} = R = \frac{0.93}{\left(\frac{\lambda_l \cdot v_{ls}^2}{8 \cdot R_{sd} \cdot g \cdot d} \right) \cdot \left(\frac{\left(\frac{R_{sd} \cdot g \cdot d}{6} \right)^{1/2} \cdot d}{\nu_l} \right)^{1/3}} \qquad \textbf{(5-80)}$$

$$E_{rhg} = R = \frac{10 \cdot (R_{sd} \cdot g \cdot d)^{1/2} \cdot (R_{sd} \cdot g \cdot \nu_l)^{1/3}}{\lambda_l \cdot v_{ls}^2}$$

With this equation, the proportionality with the line speed is about -1.8. The Shields parameter has a proportionality of 2 because of the line speed squared and about -0.2 because of the Darcy Weisbach friction factor, resulting in a power of -1.8. The shear Reynolds number has a power of 0. So this totals to -1.8, which gives a slightly steeper decrease of the hydraulic gradient or stratification ratio of the original model having a power of -1.7 for uniform PSD's. The simplified heterogeneous model used:

$$E_{rhg} = R = \frac{i_m - i_l}{R_{sd} \cdot C_v} = \frac{\mu_{sf}}{2} \cdot \left(\frac{v_{50}}{v_{ls}} \right)^M \qquad \textbf{(5-81)}$$

With:

$$v_{50} \approx 3.93 \cdot (1000 \cdot d_{50})^{0.35} \cdot \left(\frac{R_{sd}}{1.65} \right)^{0.45} \cdot \left(\frac{v_{l,actual}}{v_{w,20}} \right)^{-0.25} \qquad \textbf{(5-82)}$$

$$v_{50} \approx 1.11 \cdot (d_{50})^{0.35} \cdot (R_{sd})^{0.45} \cdot (\nu_l)^{-0.25}$$

For sands and gravels this reduces to:

$$v_{50} \approx 44.1 \cdot (d_{50})^{0.35} \qquad \textbf{(5-83)}$$

Giving for the simplified equation (with μ_{sf}**=0.44** and **M=1.7**):

$$E_{rhg} = R = \frac{\mu_{sf}}{2} \cdot \left(\frac{44.1 \cdot (d_{50})^{0.35}}{v_{ls}} \right)^M = 137.4 \cdot \frac{d^{0.6}}{v_{ls}^{1.7}} \qquad \textbf{(5-84)}$$

The near wall lift based equation gives:

$$E_{rhg} = R = \frac{d^{1/2}}{\lambda_l \cdot v_{ls}^2} \qquad \textbf{(5-85)}$$

For medium sized sand particles in water and large pipe diameters (large flow Reynolds numbers), both equations are close. For example, a 1 mm particle gives a $\mathbf{v_{50}}$ of 3.93 m/s, resulting in **R=0.22** according to the simplified method. The near wall lift method results in **R=0.20**, assuming λ_l**=0.01** for large diameter pipes.
In both models the stratification ratio increases with increasing particle diameter and relative submerged density. However the relation of the viscosity is different. The simplified model shows a decreasing stratification ratio with increasing viscosity, while the near wal lift shows the opposite. For sands and gravels in water this will not have a significant influence, but for other solids and liquids it might. The appearance of the Darcy Weisbach friction factor in the denominator of the near wall lift equation results in some dependence of the pipe diameter. The dependence on the sliding friction coefficient is not present anymore in the near wall lift equation. Using the Shields parameter to explain for the stratification ratio seems interesting however.

5.3.6. The Demi-McDonald of Wilson (1979).

The LSDV of Wilson (1979) based on the 2 layer model was originally given as a nomographic chart, made with the help of Professor F.M. Woods. This nomographic chart is known as the demi-McDonald, because of the shape of the particle diameter curve. Figure 5-11 shows the demi-McDonald of Wilson (1979). The figure shows an example of the LSDV for a $\mathbf{D_p}$**=0.25 m** diameter pipe and a **d=1 mm** diameter particle. For solids with a density of $\boldsymbol{\rho_s}$**=2.65 ton/m^3** like sands and gravels, this gives an LSDV of about 3.1 m/s according to the left part of the nomogram. The right part shows that solids with a density of $\boldsymbol{\rho_s}$**=7.85 ton/m^3** like iron, give an LSDV of about 6.5 m/s.

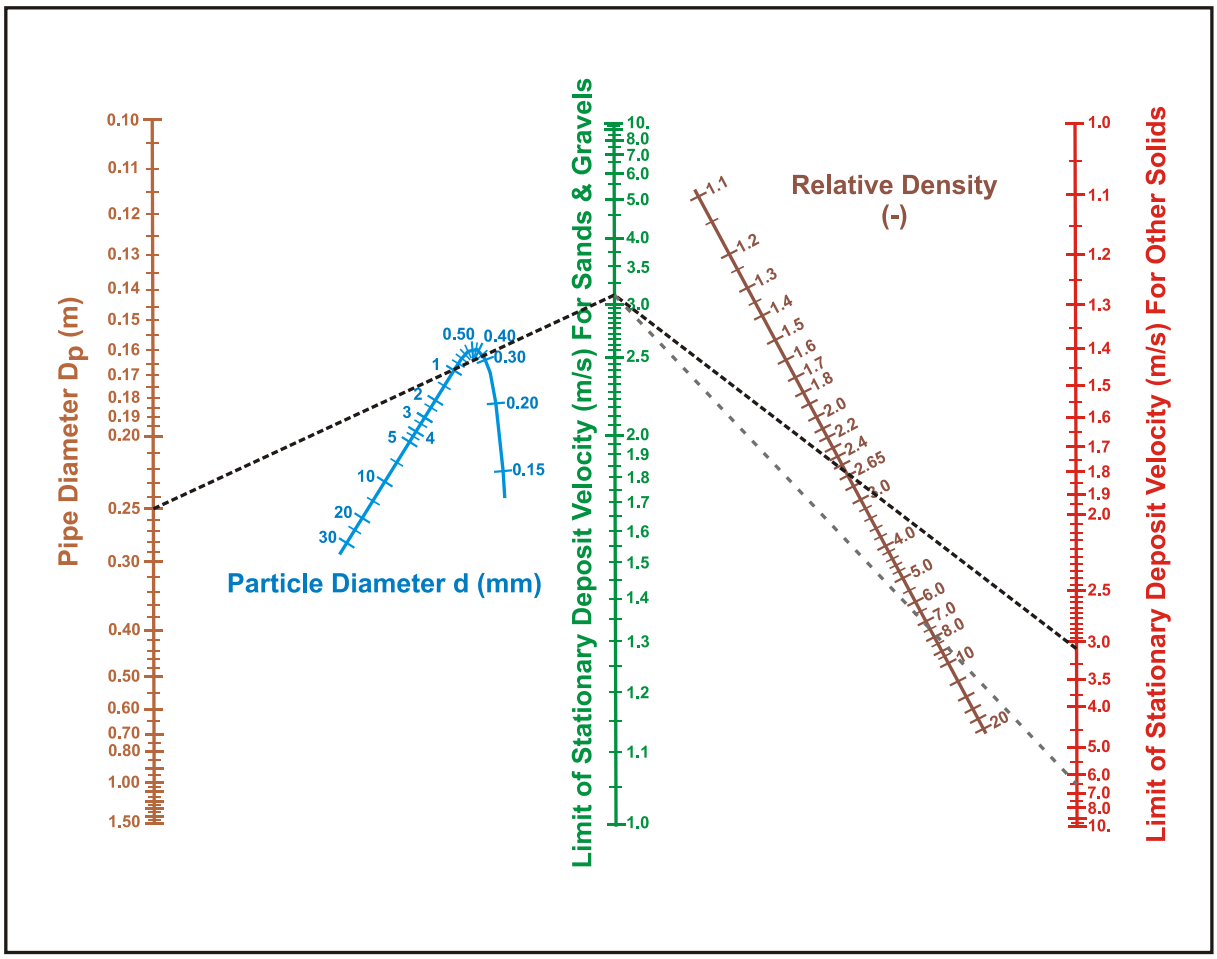

Figure 5-11: The demi-McDonald of Wilson (1979).

5.3.7. Nomenclature Wilson-GIW Models.

A_p	Cross section pipe	m^2
A_1	Cross section above bed	m^2
A_2	Cross section bed	m^2
C_{vb}	Volumetric spatial bed concentration	-
C_{vc}	Spatial volumetric concentration contact load	-
C_{vs}	Spatial volumetric concentration	-
$C_{vs,1}$	Spatial volumetric concentration in cross section 1	-
$C_{vs,2}$	Spatial volumetric concentration in cross section 2	-
$C_{vs,f}$	Spatial volumetric concentration homogeneous fraction	-
C_{vr}	Relative volumetric concentration $C_{vr}=C_{vs}/C_{vb}$	-
$C_{vr,max}$	Relative volumetric concentration at maximum LSDV	-
C_{vt}	Delivered (transport) volumetric concentration	-
$C_{vt,f}$	Delivered (transport) volumetric concentration homogeneous fraction	-
$C_{vt,ph}$	Delivered (transport) volumetric concentration pseudo homogeneous fraction	-
$C_{vt,h}$	Delivered (transport) volumetric concentration heterogeneous fraction	-
$C_{vt,s}$	Delivered (transport) volumetric concentration stratified fraction	-
d	Particle diameter	m
d_{50}	Particle diameter with 50% passing	m
D_H	Hydraulic diameter	m
D_p	Pipe diameter	m
E_{rhg}	Relative excess hydraulic gradient	-
F	Force	kN
$F_{1,l}$	Force between liquid and pipe wall	kN
$F_{12,l}$	Force between liquid and bed	kN
$F_{2,pr}$	Force on bed due to pressure	kN
$F_{2,sf}$	Force on bed due to friction	kN
$F_{2,l}$	Force on bed due to pore liquid	kN
F_n	Normal force	kN
F_w	Weight of bed	kN
F_{sf}	Friction force, sliding	kN
Fr	Froude number	-
g	Gravitational constant 9.81 m/s^2	m/s^2
i_{bed}	Hydraulic gradient sliding bed	m/m
i_{hom}	Hydraulic gradient homogeneous flow	m/m
i_l	Hydraulic gradient liquid	m/m
i_m	Hydraulic gradient mixture	m/m
i_{plug}	Hydraulic gradient plug flow	m/m
i_f	Hydraulic gradient homogeneous fraction	m/m
i_{ph}	Hydraulic gradient pseudo homogeneous fraction	m/m
i_h	Hydraulic gradient heterogeneous fraction	m/m
i_s	Hydraulic gradient stratified fraction	m/m
k_s	Bed roughness	m
ΔL	Length of pipe section	m
LDV	Limit Deposit Velocity	m/s
LSDV	Limit of Stationary Deposit Velocity	m/s
M	Power stratification ratio between 0.25 and 1.7	-
n	Porosity bed	-
O_p	Circumference pipe	m
O_1	Circumference pipe above bed	m
O_2	Circumference pipe in bed	m
O_{12}	Width of bed	m
Δp	Pressure difference	kPa
Δp_1	Pressure difference on cross section 1	kPa
Δp_2	Pressure difference on cross section 2	kPa
Δp_l	Pressure difference liquid	kPa
Δp_m	Pressure difference mixture	kPa

Δp_f	Pressure difference homogeneous fluid	**kPa**
q	Power to determine the normalised excess hydraulic gradient	**-**
Re	Reynolds number	**-**
R_{sd}	Relative submerged density	**-**
R	Stratification ratio	**-**
R_H	Hydraulic radius	**m**
S_f	Relative density homogeneous fraction + carrier liquid	**-**
S_{fp}	Relative density homogeneous & pseudo homogeneous fractions + carrier liquid	**-**
S_{fph}	Relative density homogeneous & pseudo homogeneous & heterogeneous fractions + carrier liquid	**-**
S_{fphs}	Relative density homogeneous & pseudo homogeneous & heterogeneous & stratified fractions + carrier liquid	**-**
S_m	Relative density mixture	**-**
S_s	Relative density solids	**-**
u_*	Friction velocity	**m/s**
v	Velocity	**m/s**
v_s	Limit of Stationary Deposit Velocity	**m/s**
v_t	Terminal settling velocity	**m/s**
v_{t*}	Dimensionless terminal settling velocity	**-**
v_u	Threshold velocity	**m/s**
v_{ls}	Line speed	**m/s**
v_1, $v_{1,m}$, v_r	Cross section averaged velocity above bed	**m/s**
v_2, $v_{2,m}$, v_b	Cross section averaged velocity bed	**m/s**
v_{sm}	Maximum Limit of Stationary Deposit Velocity (LSDV)	**m/s**
v_{50}	Line speed with 50% stratification	**m/s**
v_{85}	Line speed with 85% stratification	**m/s**
v_r	Relative line speed $v_r=v_{ls}/v_{sm}$	**-**
w_{50}	Particle associated velocity matching the d_{50}	**m/s**
w_{85}	Particle associated velocity matching the d_{85}	**m/s**
X	Fraction in general	**-**
X_f	Homogeneous fraction	**-**
X_{ph}	Pseudo homogeneous fraction	**-**
X_h	Heterogeneous fraction	**-**
X_s	Stratified fraction	**-**
y_b	Height of bed	**m**
α	Multiplication factor bed friction	**-**
α	Power to determine LSDV	**-**
β	Power to determine LSDV	**-**
β	Bed angle	**rad**
ε	Pipe wall roughness	**m**
ρ_l	Density carrier liquid	**ton/m^3**
ρ_s	Density solids	**ton/m^3**
ρ_m	Mixture density	**ton/m^3**
ρ_x	Density mixture with fraction X	**ton/m^3**
ρ_f	Density homogeneous fluid	**ton/m^3**
ρ_{fp}	Density homogeneous+pseudo homogeneous fluid	**ton/m^3**
ρ_{fph}	Density homogeneous+pseudo homogeneous+heterogeneous fluid	**ton/m^3**
ρ_{fphs}	Density homogeneous+pseudo homogeneous+heterogeneous+stratified fluid	**ton/m^3**
θ	Shields parameter	**-**
θ_c	Critical Shields parameter	**-**
λ	Darcy-Weisbach friction factor	**-**
λ_l	Darcy-Weisbach friction factor liquid-pipe wall	**-**
λ_1	Darcy-Weisbach friction factor with pipe wall	**-**
λ_2	Darcy-Weisbach friction factor with pipe wall, liquid in bed	**-**
λ_{12}	Darcy-Weisbach friction factor on the bed	**-**
λ_f	Darcy-Weisbach friction factor based on homogeneous fluid properties	**-**
ν_l	Kinematic viscosity	**m^2/s**
$\nu_{l,actual}$	Actual kinematic viscosity liquid	**m^2/s**

$\nu_{w,20}$	Kinematic viscosity of water at 20 degrees centigrade	**m^2/s**
ν_f	Kinematic viscosity homogeneous fluid	**m^2/s**
τ	Shear stress	**kPa**
τ_l	Shear stress liquid-pipe wall	**kPa**
$\tau_{1,l}$	Shear stress liquid-pipe wall above bed	**kPa**
$\tau_{12,l}$	Shear stress bed-liquid	**kPa**
$\tau_{2,l}$	Shear stress liquid-pipe in bed	**kPa**
$\tau_{2,sf}$	Shear stress from sliding friction	**kPa**
μ_{sf}	Sliding friction coefficient	**-**
μ_l	Dynamic viscosity liquid	**Pa·s**
μ_f	Dynamic viscosity homogeneous fluid	**Pa·s**
μ_r	Relative dynamic viscosity	**-**
σ_n	Normal stress	**kPa**
ζ	Normalised excess hydraulic gradient	**-**
ζ_∞	Normalised excess hydraulic gradient at infinite line speed	**-**

5.4. Notes.

Chapter 6: The Pump/Pipeline System.

6.1. Introduction.

A multi pump/pipeline system consists of components with different dynamic behaviour. To model such a system, one should start with simple mathematical descriptions of the sub-systems, to be able to determine the sensitivity of the behaviour of the system to changes in one of the sub-systems. The following sub-systems can be distinguished:
- The pump drive
- The centrifugal pump
- The sand/water slurry in the pipeline
- Flow control (if used)

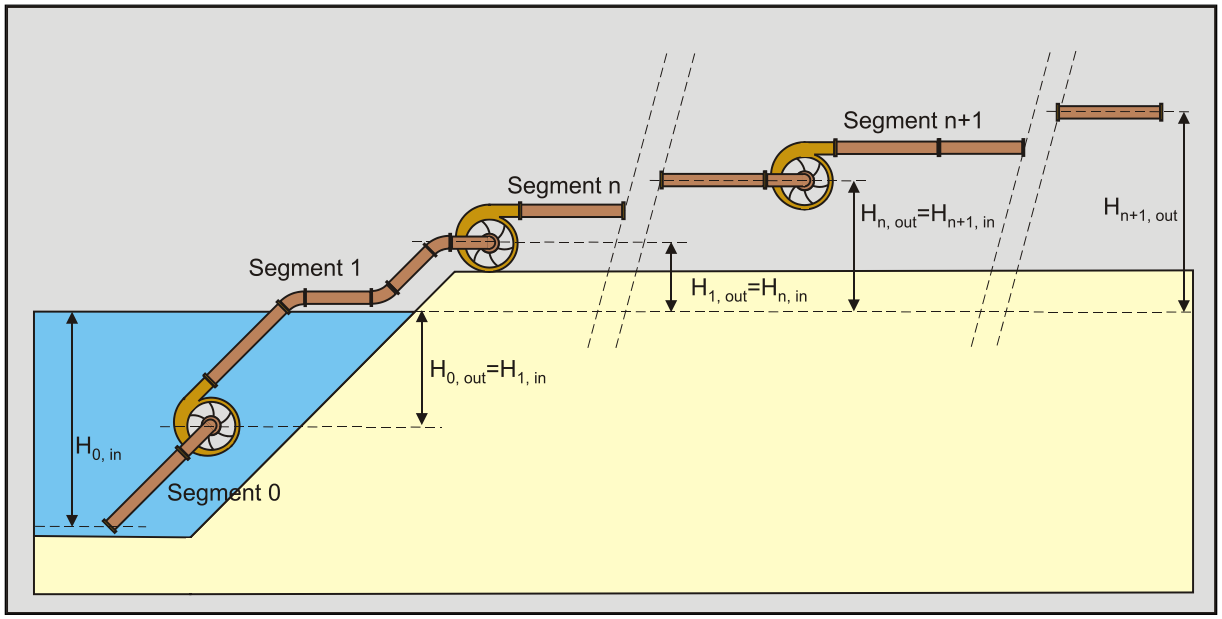

Figure 6-1: A pump –pipeline system.

The system is limited by cavitation at the entrance of each pump on one hand and by sedimentation of the solids resulting in plugging of the pipeline on the other hand. Cavitation will occur at high line velocities and/or at high solids concentrations in the suction pipe of the pump considered. Sedimentation will occur at line velocities below the so called critical velocity. The critical velocity depends on the grain distribution and on the solids concentration. In between these two limitations a stable transportation process is required. A steady state process is possible only if the solids properties and the solids concentration are constant in time. In practice however this will never be the case. Solids properties such as the grain size distribution will change as a function of time and place as will the solids concentration. The resistance of the slurry flow depends on the solids properties and concentration. If the total resistance of the slurry flow in a long pipeline is considered, changes of the solids properties and concentration at the suction mouth will result in slow changes of the total resistance, since only a small part of the pipeline is filled with the new slurry while most of the pipeline remains filled with the slurry that was already there, except from the slurry that has left the pipeline at the end. If the relatively short suction line is considered, this results in a much faster change of the vacuum at the inlet of the first pump.
The total head of a pump however, responds immediately to changes of the solids properties and concentration. If a sudden increase of the concentration is assumed, the total head of a pump will increase almost proportionally with the concentration. This will result in a higher flow velocity, but, because of the inertia of the slurry mass in the pipeline, the slurry mass will have to accelerate, so the flow velocity responds slowly on changes of the total head. The increase of the total head also causes an increase of the torque and power of the pump drive, resulting in a decrease of the pump drive revolutions and thus of the total head. Because of the inertia of pump and pump drive, there will not be an immediate response.
It is obvious that there is an interaction between all the different sub-systems. These interactions can be ranged from very slow to immediate. To be able to model the system, first the characteristic behaviour of the sub-systems should be known.

6.2. The Pump Drive.

Pump drives used in dredging are diesel direct drives, diesel/electric drives and diesel/hydraulic drives. In this paper the diesel direct drive, as the most common arrangement, is considered.
At nominal operating speed, the maximum load coincides with the nominal full torque point. If the torque is less then the nominal full torque, the engine speed usually rises slightly as the torque decreases. This is the result of the control of the speed by the governor. The extent of this depends upon the type of governor fitted.
If the engine load increases above the full torque point, the speed decreases and the engine operates in the full fuel range. With most diesel engines the torque will increase slightly as the speed decreases, because of a slightly increasing efficiency of the fuel pumps. When the load increases further, insufficient air is available to produce complete combustion and the engine stalls. The torque drops rapidly and heavily polluted gasses are emitted. The smoke limit has been reached. The speed range between the full torque point and the smoke limit is often referred to as the constant torque range.

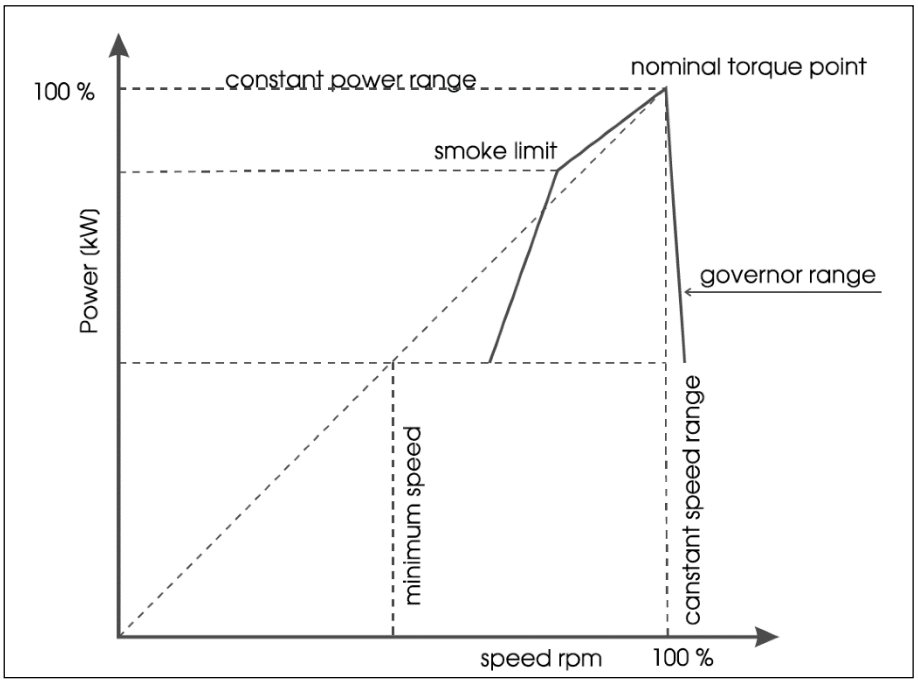

Figure 6-2: The speed-power curve of a diesel engine.

The torque/speed characteristic of the diesel engine can thus be approximated by a constant full torque upon the nominal operating speed, followed by a quick decrease of the torque in the governor range.
This characteristic however is valid for a steady state process of the diesel engine. When the speed of the diesel changes, the load will change, but also the inertia effects of the diesel have to be taken into account. The equation of motion of the diesel engine, gear box and centrifugal pump combination, reduced to the axis of the centrifugal pump, is:

$$\left(I_{d.e.} + I_{g.b.} + I_{c.p.}\right) \cdot \ddot{\varphi} = T_{d.e.} - T_{h.t.} \qquad \textbf{(6-1)}$$

In a steady state situation, the torque delivered by the diesel engine $\mathbf{T_{d.e.}}$ equals the torque required by the hydraulic transport $\mathbf{T_{h.t.}}$, so the angular acceleration of the diesel is zero. If $\mathbf{T_{d.e.}}$ is greater then $\mathbf{T_{h.t.}}$, the revolutions will increase, If $\mathbf{T_{d.e.}}$ is smaller then $\mathbf{T_{h.t.}}$, the revolutions will decrease. If the difference between these two torque's is approximated to be proportional with the difference between the actual angular velocity and the nominal operating angular velocity:

$$T_{d.e.} - T_{h.t.} = K_p \cdot \left(\dot{\varphi}_{s.p.} - \dot{\varphi}\right) \qquad \textbf{(6-2)}$$

The linear differential equation can be written as:

$$\left(I_{d.e.} + I_{g.b.} + I_{c.p.}\right) \cdot \ddot{\varphi} = K_p \cdot \left(\dot{\varphi}_{s.p.} - \dot{\varphi}\right) \quad \textbf{(6-3)}$$

With: $\left(I_{d.e.} + I_{g.b.} + I_{c.p.}\right) = I_t$ and $\tau_{d.e.} = \frac{K_p}{I_t}$ **(6-4)**

The solution of this first order system is:

$$\dot{\varphi} = \dot{\varphi}_0 + \left(\dot{\varphi}_{s.p.} - \dot{\varphi}_0\right) \cdot \left(1 - e^{-t/\tau_{d.e.}}\right) \quad \textbf{(6-5)}$$

In which $\dot{\varphi}_0$ is the angular velocity at an arbitrary time, defined as **t=0**. Using time domain calculations with a time step Δt, the angular velocity at time step **n** can now be written as a function of the angular velocity at time step **n-1** and the set point angular velocity $\dot{\varphi}_{s.p.}$ according to:

$$\dot{\varphi}_n = \dot{\varphi}_{n-1} + \left(\dot{\varphi}_{s.p.} - \dot{\varphi}_{n-1}\right) \cdot \left(1 - e^{-\Delta t/\tau_{d.e.}}\right) \quad \textbf{(6-6)}$$

6.3. The Centrifugal Pump.

Figure 6-3: Centrifugal pumps.

The behaviour of centrifugal pumps can be described with the Euler impulse moment equation:

$$\Delta p_E = \rho_f \cdot u_o \cdot \left(u_o - \frac{Q \cdot \cot(\beta_o)}{2 \cdot \pi \cdot r_o} \right) - \rho_f \cdot u_i \cdot \left(u_i - \frac{Q \cdot \cot(\beta_i)}{2 \cdot \pi \cdot r_i} \right) \quad \textbf{(6-7)}$$

For a known pump this can be simplified to:

$$\Delta p_E = \rho_f \cdot (C_1 - C_2 \cdot Q) \quad \textbf{(6-8)}$$

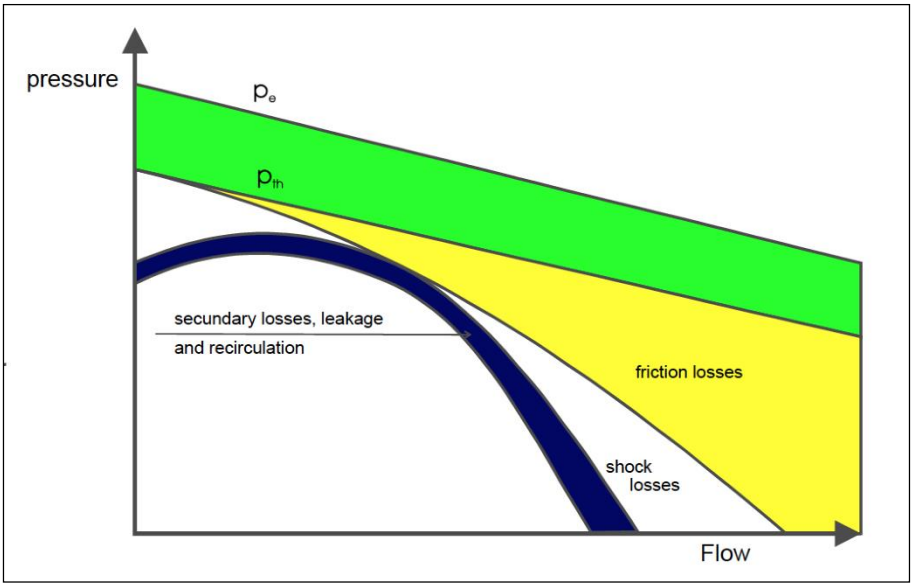

Figure 6-4: The pressure-flow curves.

Because of incongruity of impeller blades and flow, the finite number of blades, the blade thickness and the internal friction of the fluid, the Euler pressure Δp_E has to be corrected with a factor **k**, with a value of about 0.8. This factor however does not influence the efficiency. The resulting equation has to be corrected for losses from frictional contact with the walls and deflection and diversion in the pump and a correction for inlet and impact losses. The pressure reduction for the frictional losses is:

$$\Delta p_{h.f.} = C_3 \cdot \rho_f \cdot Q^2 \quad \textbf{(6-9)}$$

For a given design flow $\mathbf{Q_d}$ the impact losses can be described with:

$$\Delta p_{h.i.} = C_4 \cdot \rho_f \cdot (Q_d - Q)^2 \quad \textbf{(6-10)}$$

The total head of the pump as a function of the flow is now:

$$\Delta p_p = k \cdot \Delta p_E - \Delta p_{h.f.} - \Delta p_{h.i.} = \rho_f \cdot \left(k \cdot (C_1 - C_2 \cdot Q) - C_3 \cdot Q^2 - C_4 \cdot (Q_d - Q)^2 \right) \quad \textbf{(6-11)}$$

This is a second degree polynomial in **Q**. The fluid density ρ_f in the pump can be either the density of a homogeneous fluid (for water ρ_w) or the density of a mixture ρ_m passing the pump.
The total efficiency of the pump can be determined by dividing the power that is added to the flow $P_{fl} = \Delta p_p \cdot Q$ by the power that is output of the diesel engine $P_{d.e.} = k \cdot \Delta p_E \cdot Q + P_{d.f.}$ (in which $P_{d.f.}$ is the power required for the frictional losses in the gear box, the pump bearings, etc.), this gives:

$$\eta_p = \frac{(k \cdot \Delta p_E - \Delta p_{h.f.} - \Delta p_{h.i.}) \cdot Q}{k \cdot \Delta p_E \cdot Q + P_{d.f.}} \qquad \textbf{(6-12)}$$

For the efficiency curve a third degree polynomial approximation satisfies, while the power and torque curves approximate straight lines. The pump characteristics usually will be measured for a specific impeller diameter and number of revolutions.

6.4. Affinity Laws.

In a dynamic system however, the pump revolutions will change. This is on one hand the result of the torque/speed curve of the pump drive, on the other hand of manual or automatic flow control. This means that the pump characteristics should also be known at different pump speeds.
The so-called affinity laws describe the influence of a different impeller diameter or revolutions on the pump head, flow and efficiency:

$$\frac{p_1}{p_2} = \frac{n_1^2}{n_2^2} \cdot \frac{D_1^2}{D_2^2}, \quad \frac{Q_1}{Q_2} = \frac{n_1}{n_2} \cdot \frac{D_1^2}{D_2^2}, \quad \eta_1 = \eta_2 \qquad \textbf{(6-13)}$$

The efficiency does not change, but the value of the flow on the horizontal axis is shifted.
The affinity laws for the power and the torque can easily be derived from these equations.

$$\frac{P_1}{P_2} = \frac{p_1 \cdot Q_1 \cdot \eta_2}{p_2 \cdot Q_2 \cdot \eta_1} = \frac{n_1^3}{n_2^3} \cdot \frac{D_1^4}{D_2^4}, \quad \frac{T_1}{T_2} = \frac{P_1 \cdot n_2}{P_2 \cdot n_1} = \frac{p_1 \cdot Q_1 \cdot \eta_2 \cdot n_2}{p_2 \cdot Q_2 \cdot \eta_1 \cdot n_1} = \frac{n_1^2}{n_2^2} \cdot \frac{D_1^4}{D_2^4} \qquad \textbf{(6-14)}$$

If a ratio for the revolutions $\varepsilon_n = \frac{n}{n_m}$ and a ratio for the diameter $\varepsilon_D = \frac{D}{D_m}$ are given, the head and efficiency curves at a speed **n** and an impeller diameter **D** can be determined by:

$$Q = Q_m \cdot \varepsilon_n^1 \cdot \varepsilon_D^2 \qquad \textbf{(6-15)}$$

$$\Delta p_p = \alpha_0 \cdot Q^0 \cdot \varepsilon_n^2 \cdot \varepsilon_D^2 + \alpha_1 \cdot Q^1 \cdot \varepsilon_n^1 \cdot \varepsilon_D^0 + \alpha_2 \cdot Q^2 \cdot \varepsilon_n^0 \cdot \varepsilon_D^{-2} \qquad \textbf{(6-16)}$$

$$\eta_p = \beta_0 \cdot Q^0 \cdot \varepsilon_n^0 \cdot \varepsilon_D^0 + \beta_1 \cdot Q^1 \cdot \varepsilon_n^{-1} \cdot \varepsilon_D^{-2} + \beta_2 \cdot Q^2 \cdot \varepsilon_n^{-2} \cdot \varepsilon_D^{-4} + \beta_3 \cdot Q^3 \cdot \varepsilon_n^{-3} \cdot \varepsilon_D^{-6} \qquad \textbf{(6-17)}$$

In which $\mathbf{n_m}$, $\mathbf{D_m}$ and $\mathbf{Q_m}$ are the revolutions, impeller diameter and flow used in the measurements of the head and efficiency curves.
Based on this theory, the characteristics of two pumps used in the case study in this chapter, are given in Figure 6-5 and Figure 6-6. Both pumps are limited by the constant torque behaviour of the corresponding diesel engine in the full fuel range.

Figure 6-5 and Figure 6-6 give the pump characteristics for clear water. If a mixture is pumped however, the pump head increases because of the mixture density as has been pointed out when discussing equation (6-11) and the pump efficiency decreases because a heterogeneous mixture is flowing through the pump. The decrease of the efficiency depends upon the average grain diameter, the impeller diameter and the solids concentration and can be determined with (according to Stepanoff):

$$\eta_m = \left(1 - C_t \cdot \left(0.466 + 0.4 \cdot Log10\left(d_{50}\right)\right) / D\right) \qquad \textbf{(6-18)}$$

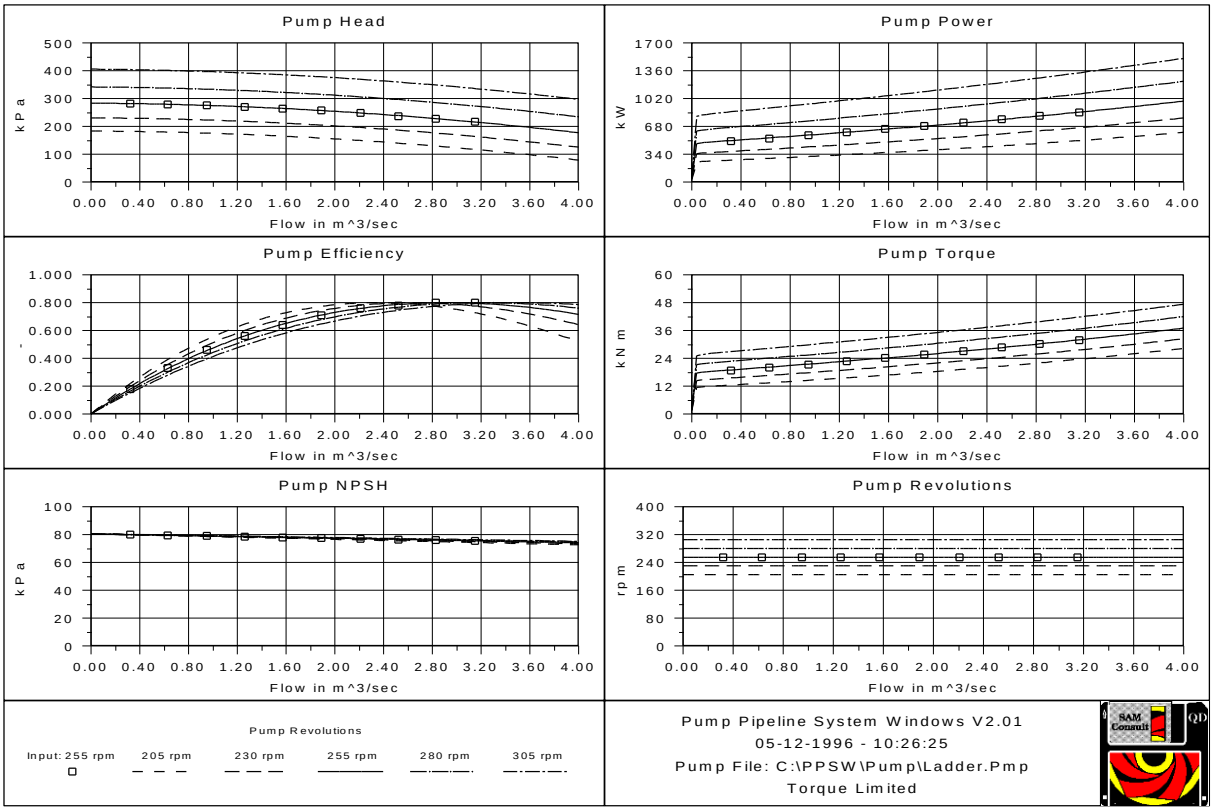

Figure 6-5: The characteristics of the ladder pump.

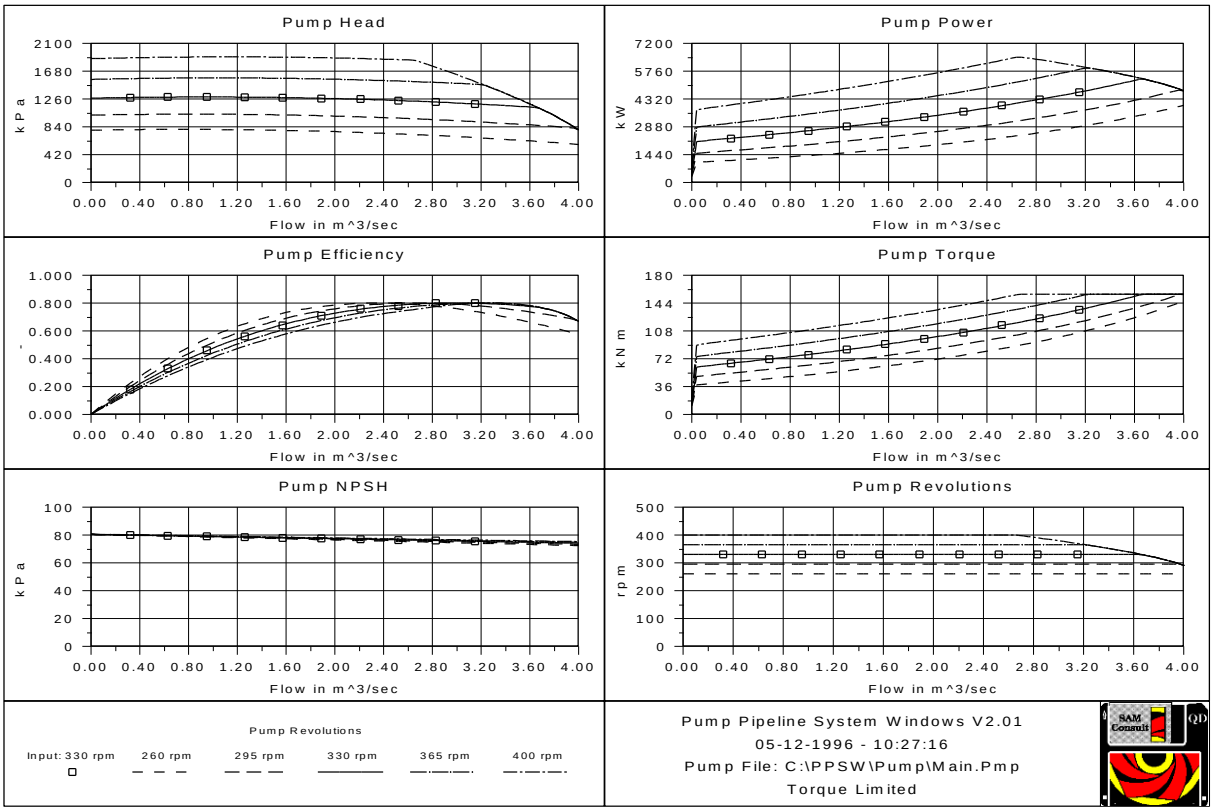

Figure 6-6: The characteristics of the main pump and the booster pump, torque limited.

6.5. Approximations.

The pump Q-H curve for water can be approximated by:

$$H = A + C \cdot Q^2 \qquad With: A = f \cdot H_D \qquad and \qquad C = \frac{(1-f) \cdot H_D}{Q_D^2} \tag{6-19}$$

The pump efficiency curve can be approximated by:

$$\eta_m = \eta_{max} \cdot \left(1 - \left(\frac{Q_D - Q}{Q_D} \right)^2 \right)^g \tag{6-20}$$

A factor **f** of about 1.25 and a power **g** of about 0.7 give good results. The design flow $\mathbf{Q_D}$ (m^3/s) and the design head $\mathbf{H_D}$ (kPa) follow from the requirements and can be used for one pump or for all pumps together.

6.6. The Total Head Losses.

The pressure at the inlet of the suction mouth of the cutter head or in the draghead is:

$$p_s = \rho_w \cdot g \cdot H_{sm} + 100 \tag{6-21}$$

The pressure losses from the suction mouth to the entrance of the first pump are:

$$p_{m,s} = \frac{1}{2} \cdot \rho_m \cdot v_{ls,s}^2 + \lambda_{w,s} \cdot \frac{L_s}{D_{p,s}} \cdot \frac{1}{2} \cdot \rho_w \cdot v_{ls,s}^2 + p_{s,s} + \sum_1^n \xi_{n,s} \cdot \frac{1}{2} \cdot \rho_m \cdot v_{ls,s}^2 + \rho_m \cdot g \cdot H_s + \rho_m \cdot L_s \cdot \dot{v}_{ls,s} \tag{6-22}$$

The pressure losses after the first pump (discharge losses) are:

$$p_{m,d} = \frac{1}{2} \cdot \rho_m \cdot \left(v_{ls,d}^2 - v_{ls,s}^2 \right) + \lambda_{w,d} \cdot \frac{L_d}{D_{p,d}} \cdot \frac{1}{2} \cdot \rho_w \cdot v_{ls,d}^2 + p_{s,d} + \sum_1^n \xi_{n,d} \cdot \frac{1}{2} \cdot \rho_m \cdot v_{ls,d}^2 + \rho_m \cdot g \cdot H_d + \rho_m \cdot L_d \cdot \dot{v}_{ls,d} \tag{6-23}$$

The absolute pressure at the inlet of the first pump is $\mathbf{p_s}$-$\mathbf{p_{m,s}}$ and should be above a certain minimum.

$$p_s - p_{m,s} > p_{lim} \tag{6-24}$$

The last term in equations (6-22) and (6-23) is the contribution of acceleration or deceleration of the mixture.

In a stationary situation, the mixture density has to be smaller than a certain limit to avoid cavitation in the first pump.

$$\rho_m < \frac{\rho_w \cdot g \cdot H_{sm} + 100 - p_{lim}}{\frac{1}{2} \cdot v_{ls,s}^2 + \lambda_{w,s} \cdot \frac{L_s}{D_{p,s}} \cdot \frac{1}{2} \cdot v_{ls,s}^2 + \sum_1^n \xi_{n,s} \cdot \frac{1}{2} \cdot v_{ls,s}^2 + g \cdot H_s} \tag{6-25}$$

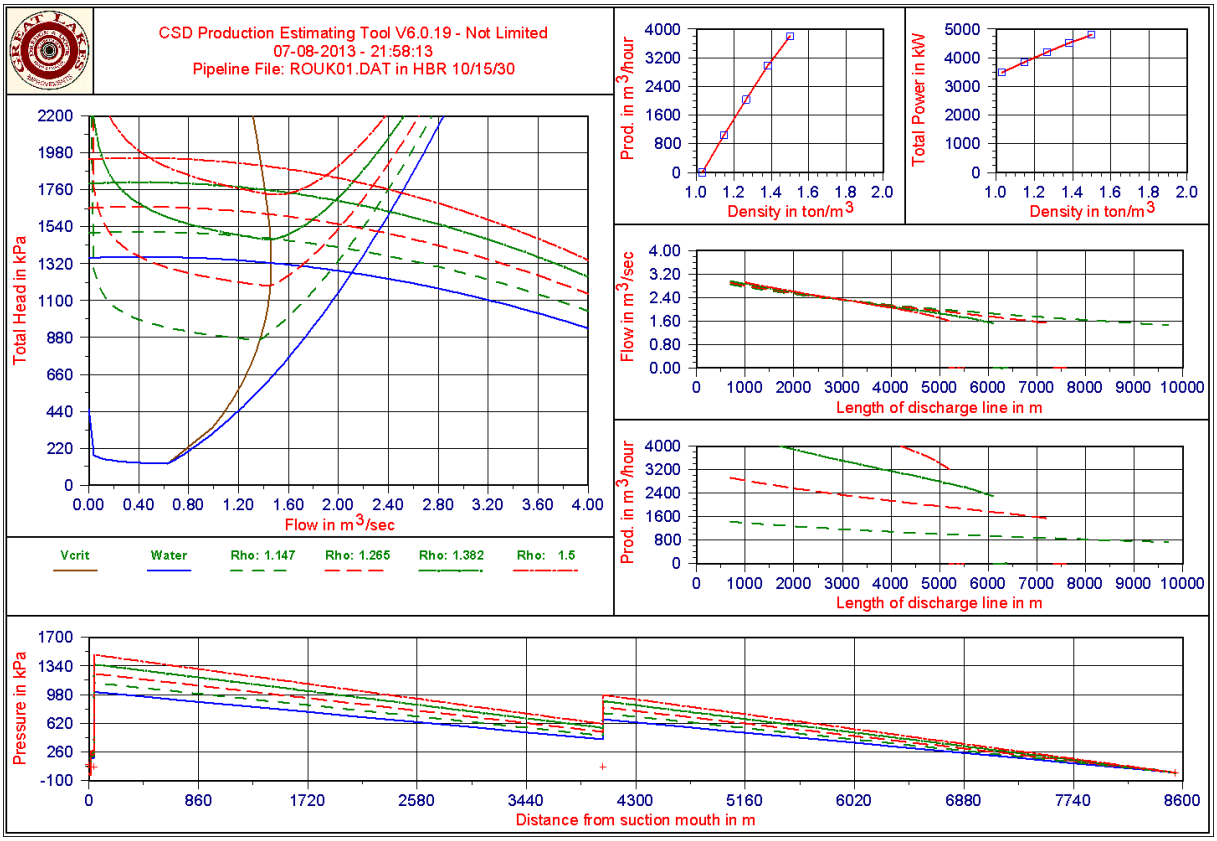

Figure 6-7: Characteristics of the pump/pipeline system, not limited.

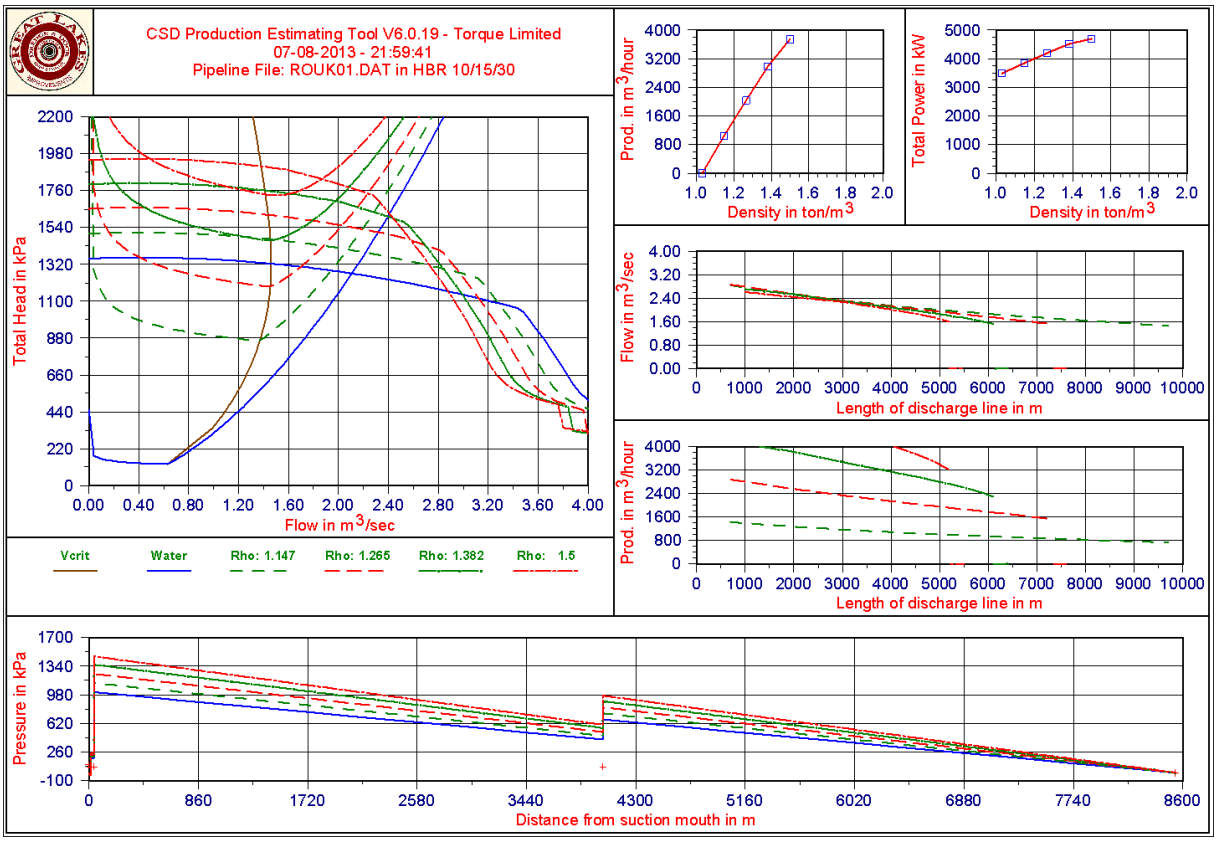

Figure 6-8: Characteristics of the pump/pipeline system, torque limited.

6.7. The Pump/Pipeline System Description.

In a steady state situation, the revolutions of the pumps are fixed, the line speed is constant and the solids properties and concentration are constant in the pipeline. The working point of the system is the intersection point of the pump head curve and the pipeline resistance curve. The pump curve is a summation of the head curves of each pump according to equation (6-16). The resistance curve is a summation of the resistances of the pipe segments and the geodetic head according to equations (6-22) and (6-23). Figure 6-7 and Figure 6-8 show this steady state situation for the system used in the case study at 6 densities ranging from clear water upto a density of 1.6 ton/m^3. In reality, the solids properties and concentration are not constant in time at the suction mouth. As a result of this, the solids properties and concentration are not constant as a function of the position in the pipeline. To be able to know these properties as a function of the position in the pipeline, the pipeline must be divided into small segments. These segments move through the pipeline with the line speed. Each time step a new segment is added at the suction mouth, while part of the last segment leaves the pipeline. Because the line speed is not constant, the length of the segment added is not constant, but equals the line speed times the time step. For each segment the resistance is determined, so the resistance as a function of the position in the pipeline is known. This way also the vacuum and the discharge pressure can be determined for each pump. If vacuum results in cavitation of one of the pumps, the pump head is decreased by decreasing the pump density, depending on the time the pump is cavitating. The dynamic calculations are carried out in the time domain, because most of the equations used are non-linear. The time step used is about 1 second, depending on the speed of the PC and the other tasks Windows has to carry out.

6.8. The Segmented Pipeline.

In reality, the solids properties and concentration are not constant in time at the suction mouth. As a result of this, the solids properties and concentration are not constant as a function of the position in the pipeline. To be able to know these properties as a function of the position in the pipeline, the pipeline must be divided into small segments. These segments move through the pipeline with the line speed. Each time step a new segment is added at the suction mouth, while part of the last segment leaves the pipeline. Because the line speed is not constant, the length of the segment added is not constant, but equals the line speed times the time step. For each segment the resistance is determined, so the resistance as a function of the position in the pipeline is known. This way also the vacuum and the discharge pressure can be determined for each pump. If vacuum results in cavitation of one of the pumps, the pump head is decreased by decreasing the pump density, depending on the time the pump is cavitating.

As mentioned before, each segment contains the mixture properties. The two most important properties are the mixture density and the grain size distribution. If a homogeneous transport model is considered, the grain distribution can be replaced by the characteristic factor depending on the grain size distribution. For a heterogeneous or two-phase transport model, the problem becomes much more complicated.

The segments move through the pipeline with the line speed, assuming that all of the contents of a segment move at the same speed. However if part of the mixture has settled at the bottom of the pipeline, this part will move with a much smaller velocity then the average velocity, while the mixture above the sediment will move with a velocity higher then the average. In a stationary situation this does not matter, as long as the transport model used takes this into account (the Durand model takes this into account), but in a non-stationary situation there may be temporary accumulation of solids. Also dunes may occur, moving through the pipeline. To implement these phenomena a longitudinal diffusion model has to be developed. The current administrative system in the simulation software is suitable for storing the information required to describe these phenomena. However the information stored has to be extended, since two-phase flow requires storage of two components, the bed load and the suspended material. With a time step in the simulation software of 0.1 to 0.2 seconds, the segment length varies (with a line speed of 5 m/s) from 0.5 to 1.0 m. The required length for a good description of dunes moving through the pipeline is unknown, but from experiments in our laboratory it seems a segment length of 0.5 m is still to high. An intuitive estimate of 0.1 to 0.2 m seems reasonable. The Durand model however has not been developed for a pipeline of only 0.1 m.

The mass conservation equation of a pipe segment can be described with equation (6-26). In this equation all terms give a mass flow. The sum of the mass flow of the suspended material and the bed load that enter a segment, should be equal to the sum of the suspended material and the bed load that leave the segment plus the material that settles in the segment. The last term on the right hand side is the settlement of suspended material into the bed. This term is positive when material settles (accumulates) in the segment.

$$Q_{in-s} + Q_{in-b} = Q_{out-s} + Q_{out-b} + Q_{s \rightarrow b} \qquad \textbf{(6-26)}$$

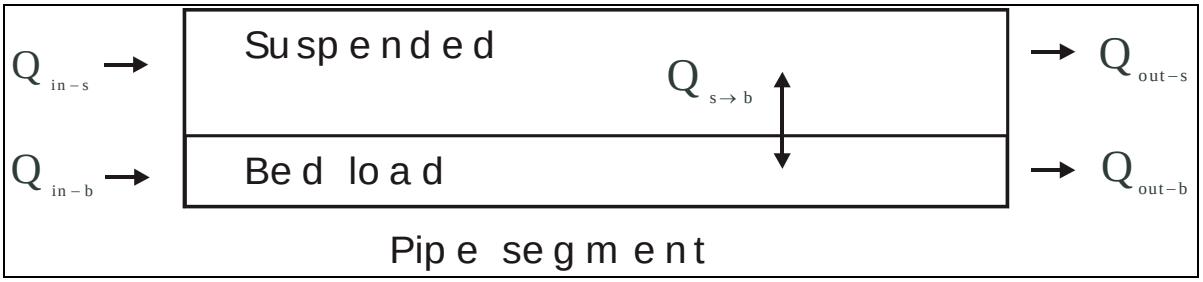

Figure 6-9: The mass equilibrium in a pipe segment.

The question is however; whether for a good description of the transport it suffices to administer the suspended load and the bed load in one segment moving through the pipeline. In fact the velocity of the suspended load will be higher then the average line speed and the velocity of the bed will be much smaller. The pipe segment should have to be split into two separate segments for the suspended load and for the bed load, moving at two different velocities through the system, in order to administer the two phase flow correctly. The current method of administering the contents of the segments is suitable for suspended load only at line speeds above the critical velocity.
A good description of the vertical diffusion between the suspended load and the bed load is not yet available and will be subject for further research. Erosion diffusion equations are used for hopper sedimentation as well, but these equation do not suffice Miedema and Vlasblom (1996).

6.9. The Inertial Effects in the Pipeline.

A steady state process requires a constant density and solids properties in the system and thus at the suction mouth. In practice it is known, that the solids properties and the density change with respect to time. As a result, the pump discharge pressure and vacuum will change with respect to time and the pipeline resistance will change with respect to time and place. A change of the discharge pressure will result in a change of the torque on the axis of the pump drive on one hand and in a change of the flow velocity on the other hand. The mixture in the pipeline has to accelerate or decelerate. Since centrifugal pumps respond to a change in density and solids properties at the moment the mixture passes the pump, while the pipeline resistance is determined by the contents of the pipeline as a whole, this forms a complex dynamic system.

The inertial pressure of the mixture has to be added to the resistance of the mixture. In fact, the inertial pressure is always equal to the difference between the total pressure generated by the pumps and the total resistance of the mixture in the pipeline system. If this difference is positive (the pump pressure has increased due to an increase of the mixture density), the mixture will accelerate. If negative, the mixture will decelerate.
As a result of the acceleration and deceleration, the mixture velocity (line velocity) will vary as a function of time. To realize a stable dredging process, it is required to have a line velocity that will not vary too much. The line velocity can be controlled by varying the revolutions of one of the dredge pumps, where the last pump is preferred. From the above one can distinguish the different effect by the time they require to change/occur:

1. Very fast (within a second), the change in discharge pressure of a centrifugal pump
2. Fast (seconds), the change in revolutions of the pump drive and the change in line speed (acceleration and deceleration)
3. Slow (minutes), filling up the pipeline with mixture or a change in mixture content

These effects can also be recognized in the equations describing the pump curve and the system curve. Equation (6-11) shows the effect of the fluid (mixture) density on the discharge pressure. Equation (6-6) shows the effect of a changing set point of the pump drive. Equations (6-22) and (6-23) contain the inertial effect in the most right term on the right hand side, while the effect of the changing mixture contents is described by the first term on the right hand side. Figure 6-7 and Figure 6-8 show the system curves and the pump curves for the system described in Figure 6-1, for 5 different densities, including clear water, for a stationary situation. The intersection points of each system and pump curve at one density are the working points for the system at that specific density.

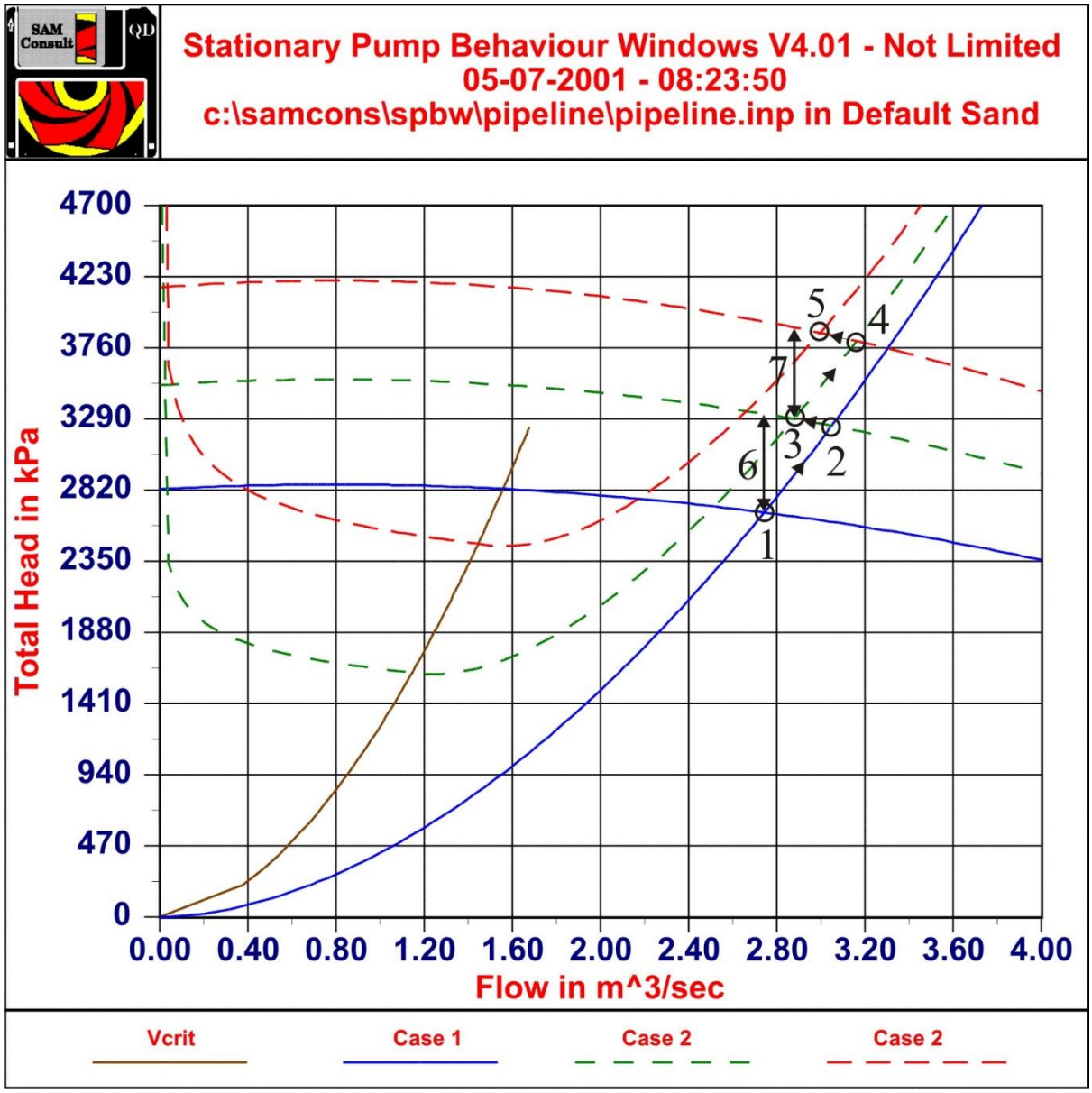

Figure 6-10: The system curves for 3 cases, accelerating.

Figure 6-10 is a representation of a number of phenomena that occur subsequently when the system (Figure 6-1) filled with water, is filled with mixture with a density of 1.6 ton/m^3. In this figure case 1 represents the system and the pump curve for the system filled with water. Case 2 represents the system with the pipeline filled with mixture up to a point just before the 3rd (booster) pump. Case 3 represents the system filled entirely with the mixture.

Now, what happens if a system filled with water is continuously filled with the mixture?

First the working point is point 1 in Figure 6-10. This is the intersection point of the pump and system curves for water. When mixture enters the system, within a few (about 8) seconds the mixture has reached the ladder and main pump, since the distance is only about 44 m and the line speed about 5 m/sec. At that moment, the discharge pressure of the ladder pump and main pump increase proportionally to the mixture density, resulting in a pump curve according to case 2 and a working point 2. The flow and thus the line speed will not change instantly because of the inertia of the fluid and solids mass in the pipeline. Number 6 shows the access pressure caused by the sudden increase of the discharge pressure. This access pressure has to take care of the acceleration of the pipeline contents. This acceleration will take in the order of 10-20 seconds.

The filling of the system continues and the resistance of the mixture slowly increases, so the working point moves from point 2 to point 3. With the line speed of 5 m/s, this will take about 400 seconds or almost 7 minutes. When the mixture reaches the booster pump, at once the discharge pressure increases, resulting in the pump curve

according to case 3, the top curve. The working point will move to point 4, while 7 represents the access pressure causing the acceleration of the pipeline contents. Moving from 3 to 4 will take 10-20 seconds. When the pipeline continues to be filled with mixture, the resistance increases, resulting in the working point moving from 4 to 5 in about 400 seconds.

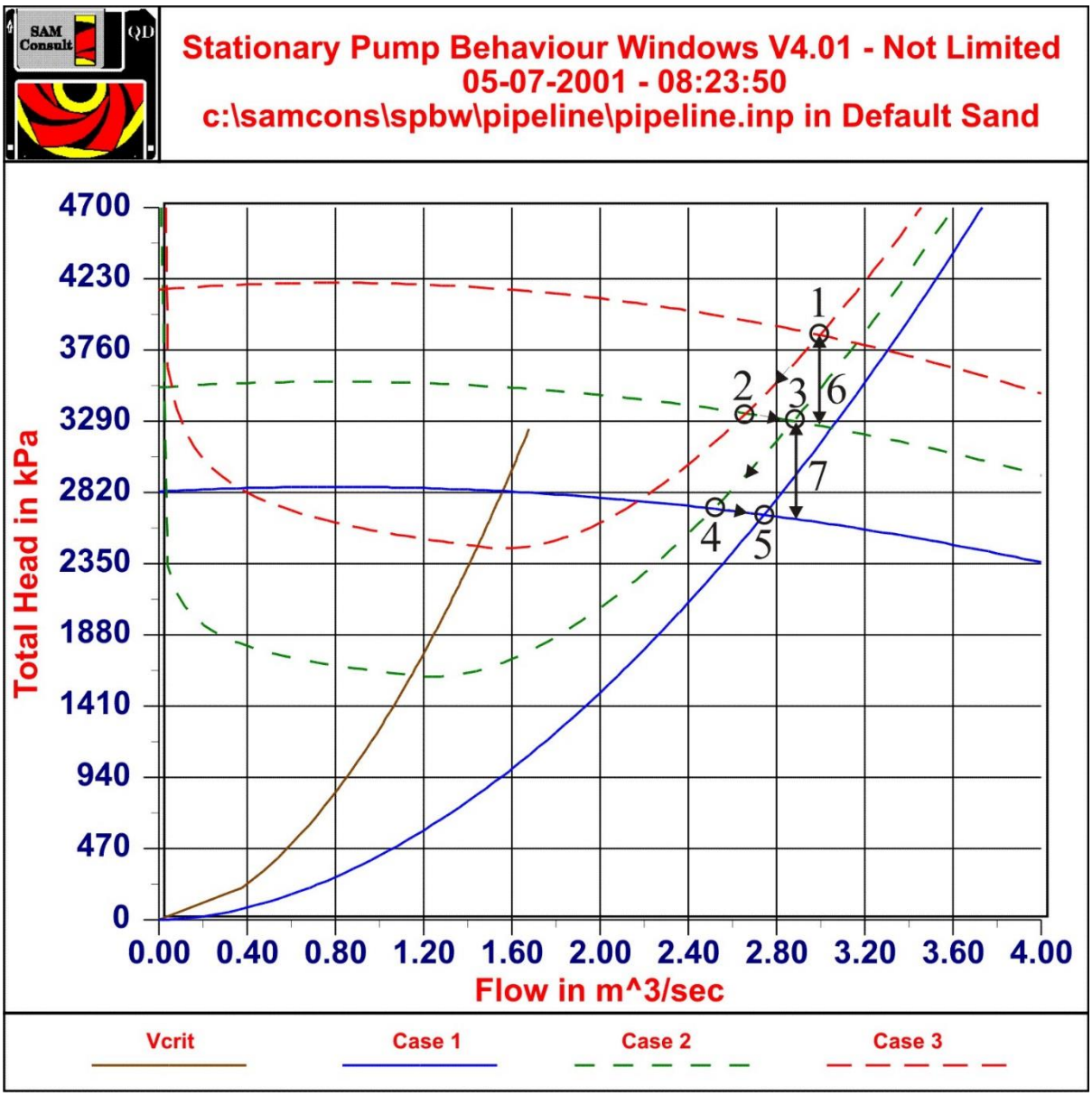

Figure 6-11: The system curves for 3 cases, decelerating.

Figure 6-11 shows the same procedure for a pipeline filled with a mixture of density 1.6 ton/m^3. In this case the pipeline, containing mixture of 1.6 ton/m^3, is filled with water, resulting in decreasing discharge pressures and pipeline resistance. The procedure is almost the inverse, but Figure 6-11 shows that the path followed is different. In working point 1, all the pumps and the pipeline are filled with the mixture. When the water reaches the ladder and main pump, the pump curve is decreased to case 2 and the new working point is point 2. 6 gives the deceleration pressure, so the contents of the pipeline will decelerate from 1 to 2 in about 10-20 seconds. From 2-3 the pipeline is filled with water up to the booster pump, resulting in a decrease of the resistance, taking about 400 seconds. When the water reaches the booster pump, the pump curve decreases again to case 1, resulting in working point 4. Again it takes 10-20 seconds to move from point 3 to point 4. At last the pipeline behind the booster pump is filled with water, resulting in a decrease of the resistance, taking about 400 seconds. The final working point is point 5. Both Figure 6-10 and Figure 6-11 give an example of the non-stationary effects in a multi-pump/pipeline system.

6.10. Case study.

The aim of this case study is twofold, first it shows events caused by the dynamic behaviour of the system that cannot be predicted by steady state calculations, second it shows the application of the above theory. A problem in defining a system and a scenario for the simulation is, that the system can consist of an infinite number of pump/pipeline combinations, while there also exists an infinite number of solids property/concentration distributions as a function of time. For this case study, a system is defined consisting of a suction line followed by three pump/pipeline units. The first pump is a ladder pump, with a speed of 200 rpm, an impeller diameter of 1.5 m and 1050 kW on the axis (see Figure 6-5). The second and the third pump run also at a speed of 200 rpm, have an impeller diameter of 2.4 m and 3250 kW on the axis (see Figure 6-6). The time constants of all three pumps are set to 4 seconds. The time constant of the density meter is set to 10 seconds. The suction line starts at 10 m below water level, has a length of 12 m and a diameter of 0.69 m. The ladder pump is placed 5 m below water level. The main pump and the booster pump are placed 10 m above water level. The pipeline length between ladder and main pump is 30 m, between main pump and booster pump 2000 m, as is the length of the discharge line. The pipe diameters after the ladder pump are 0.61 m. The total simulation lasts about 28 minutes and starts with the pipeline filled with water. After the pumps are activated, a mixture with a density of 1.6 ton/m^3 enters the suction mouth for a period of 2 minutes. A sand is used with a d_{15} of 0.25 mm, a d_{50} of 0.50 mm and a d_{85} of 0.75 mm. This density block wave moves through the system, subsequently passing the three pumps. For the simulation the following scenario is used:

00 minutes	start of simulation
01 minutes	start of ladder pump
04 minutes	start of main pump
07 minutes	start of booster pump
10 minutes	increase mixture density to about 1.6 ton/m^3
12 minutes	decrease mixture density to water density
12 minutes	take sample of density distribution in pipeline
17 minutes	take sample of density distribution in pipeline
22 minutes	take sample of density distribution in pipeline
28 minutes	stop simulation

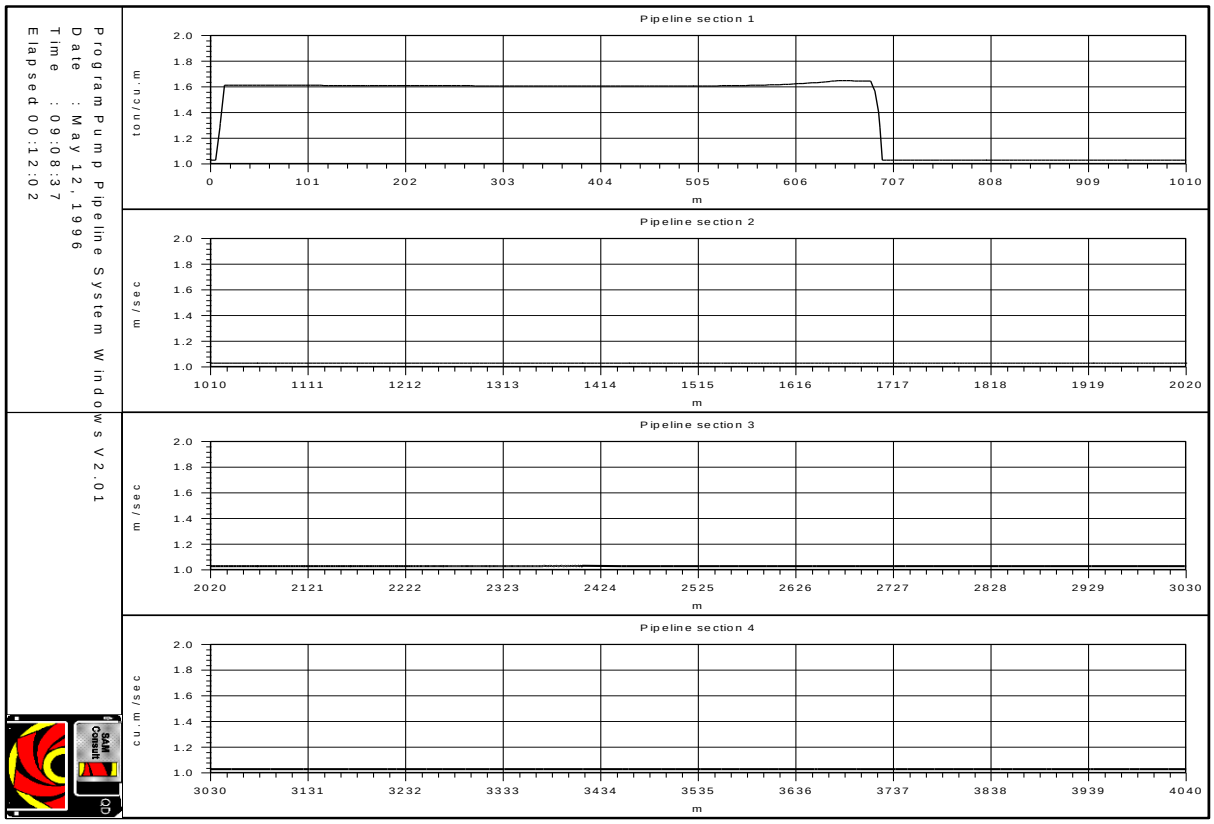

Figure 6-12: The density distribution in the pipeline after 12 minutes.

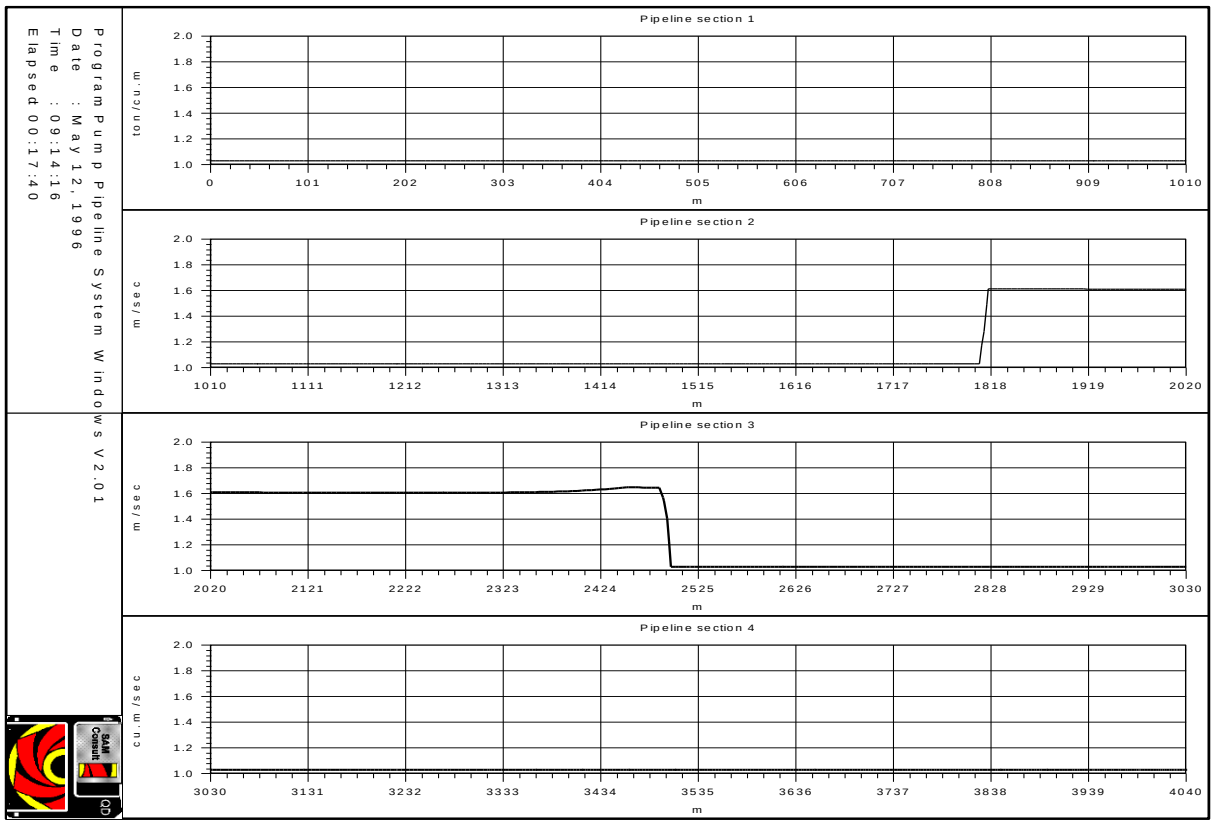

Figure 6-13: The density distribution in the pipeline after 17 minutes.

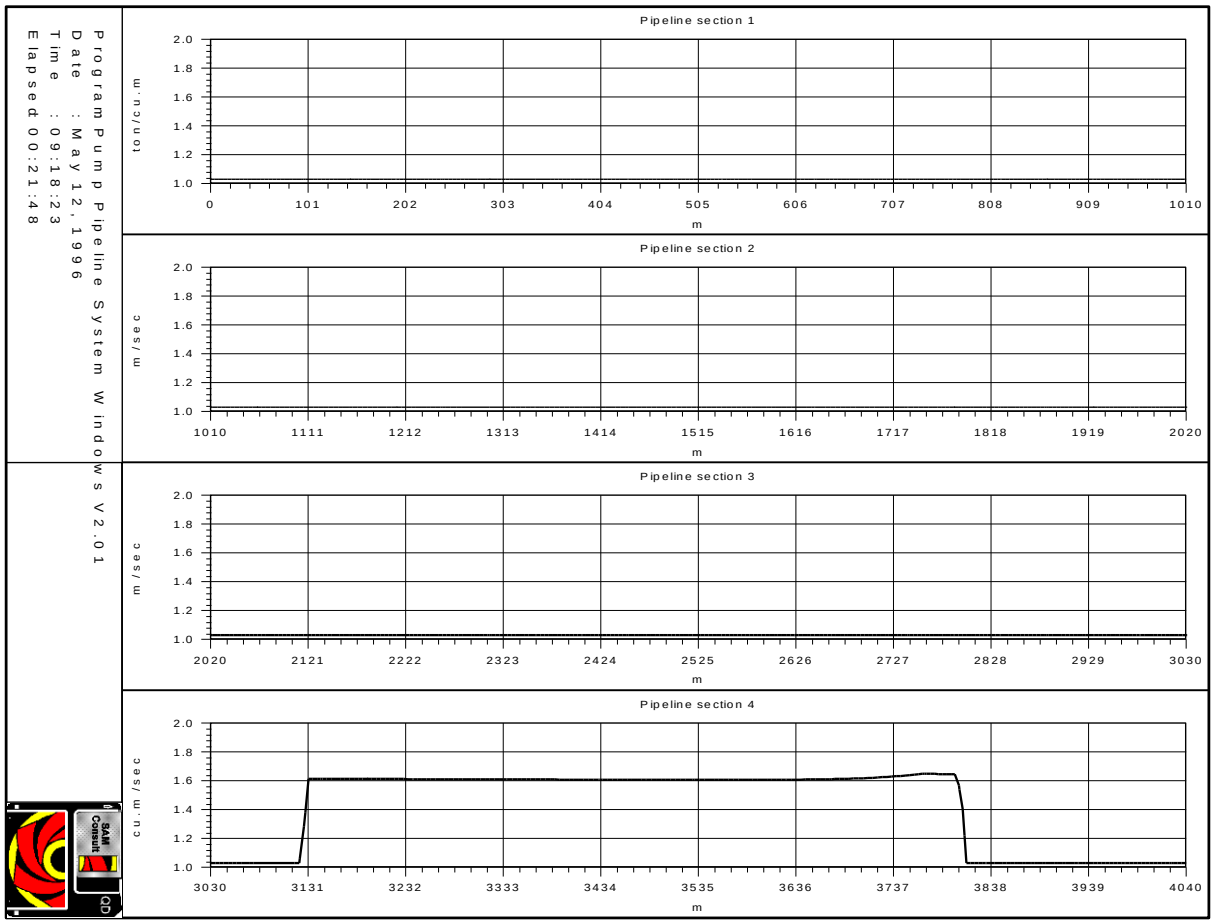

Figure 6-14: The density distribution in the pipeline after 22 minutes.

Figure 6-12, Figure 6-13 and Figure 6-14 show the density wave at 12, 17 and 22 minutes of simulation time. At 12 minutes the density wave occupies the suction line, the ladder pump and the main pump and part of the pipeline behind the main pump. At 17 minutes the density wave occupies the last part of the pipeline before the booster pump, the booster pump and the first part of the discharge line after the booster pump. At 22 minutes the density wave occupies the middle part of the discharge line. Figure 6-15 shows the line speed, the density, the total power consumed and the production as a function of time. The line speed, the density and the production are determined at the inlet of the ladder pump. The density is determined using the mathematical behaviour of a density transducer with a time constant of 10 seconds. Figure 6-16, Figure 6-17 and Figure 6-18 show the pump speed, power, vacuum and discharge pressure of the three pumps as a function of time.

As can be seen in Figure 6-15, the line speed increases slower then the pump speed, due to the inertial effect in the fourth term of equation (6-23). When the density wave passes the ladder and main pump (from 10 to 13 minutes), the discharge pressure of these pumps increases, resulting in a higher line speed. When the density wave passes the booster pump (from 16 to 19 minutes) the same occurs for the booster pump.
After about 10 minutes of simulation time, all three pumps are activated and a steady state situation occurs in the system. Then the mixture density at the suction mouth increases from water density to about 1.6 ton/m^3. First the resistance in the suction line increases, resulting in a sudden decrease of the ladder pump vacuum and discharge pressure. When the density wave reaches the ladder pump, the discharge pressure increases, due to the higher density. When after 2 minutes, the density decreases to the water density, first the resistance in the suction line decreases, resulting in an increase of the ladder pump vacuum and discharge pressure, followed by a decrease of the discharge pressure when the clear water reaches the ladder pump (see Figure 6-15). The distance between the ladder pump and the main pump is 30 m. With an average line speed of 5 m/s, the density wave passes the main pump 6 seconds after passing the ladder pump. The same phenomena as described for the ladder pump, occur 6 seconds later for the main pump (see Figure 6-17). Due to the increased discharge pressure of ladder and main pump during the density wave, the line speed will also increase (see Figure 6-15), but because of the inertial effects, this increase and 2 minutes later decrease is not as steep.

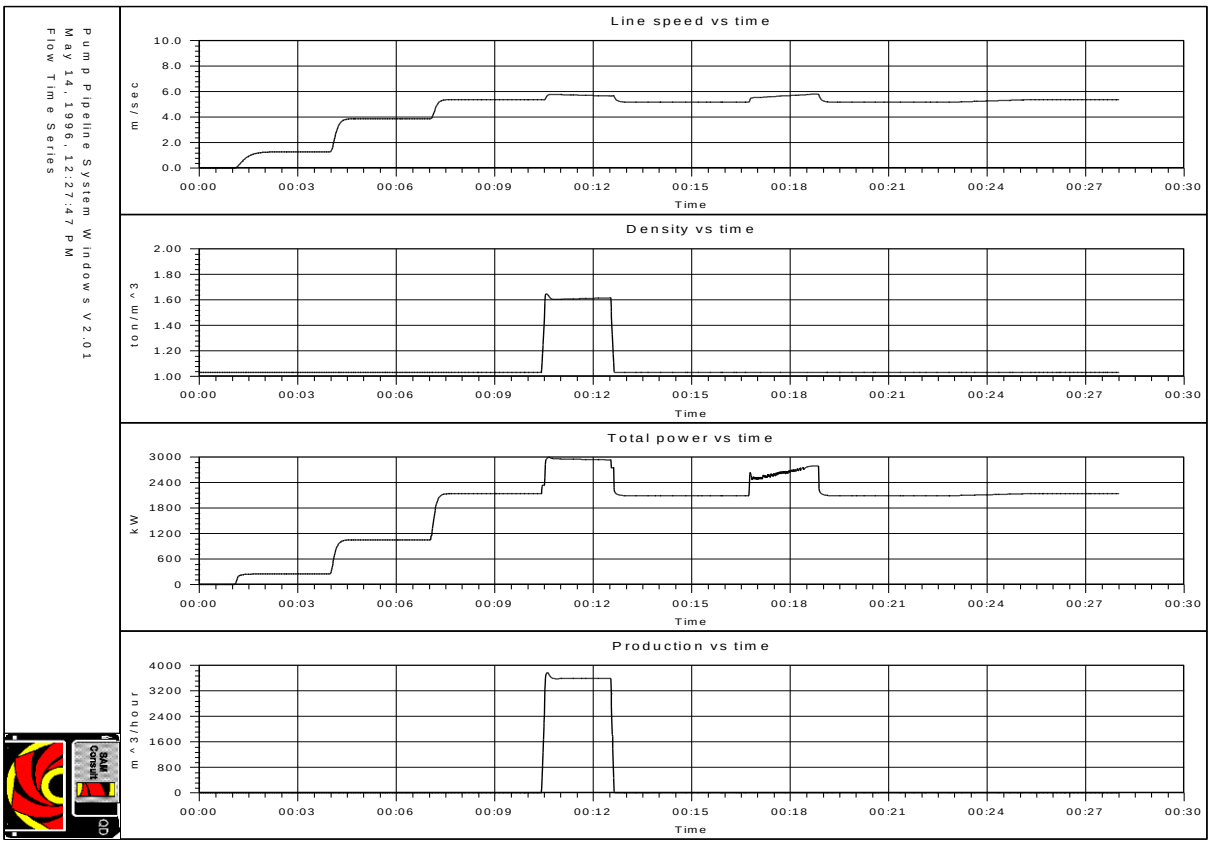

Figure 6-15: Line speed, density, total power and situ production as a function of time.

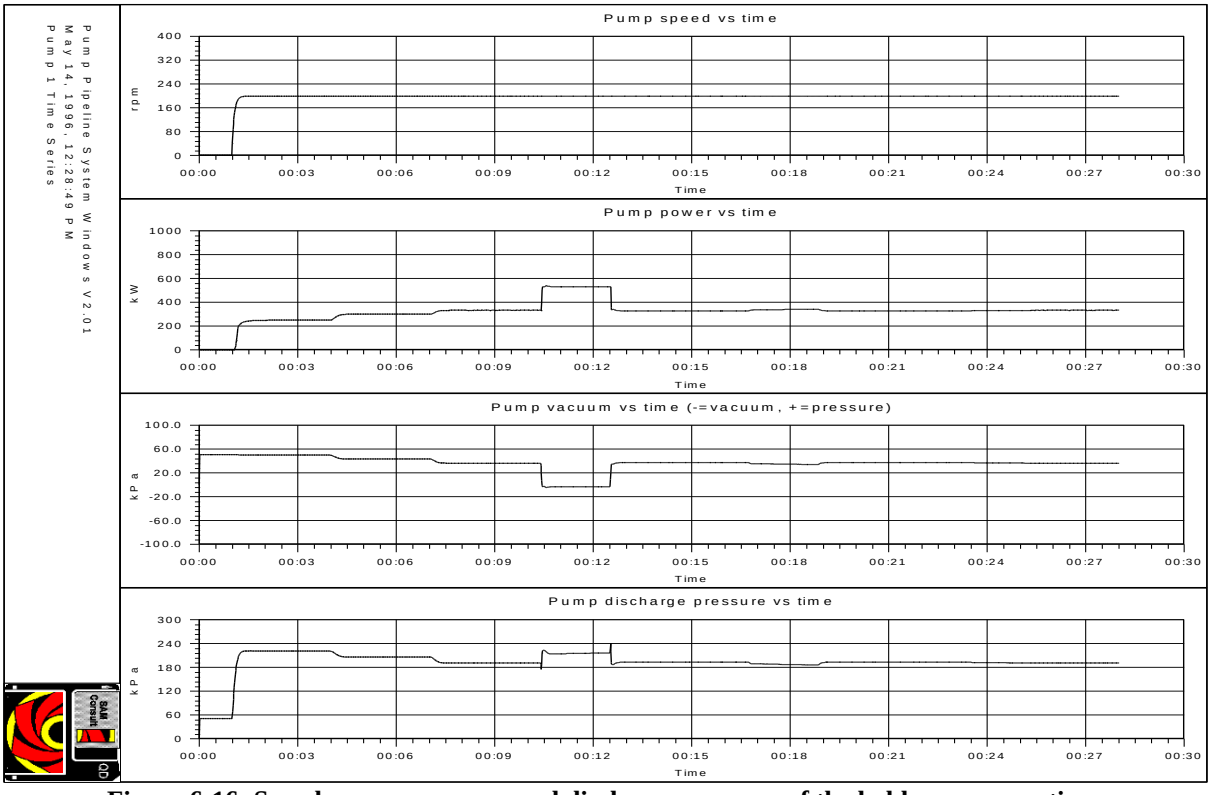

Figure 6-16: Speed, power, vacuum and discharge pressure of the ladder pump vs. time.

One could say that there is a time delay between the immidiate response of the discharge pressure of the pumps on changes in the density in the pumps and the response of the line speed on changes in the discharge pressure. At 12 minutes and about 15 seconds, the density wave has left the main pump, but has not yet reached the booster pump. The head of each pump is determined by the density of water, but the line speed is still determined by the

head resulting from the mixture and thus to high. The resistance in the pipe between main and booster pump is high because of the mixture, resulting in a decrease of the booster pump vacuum and discharge pressure. As the line speed decreases, the booster pump vacuum and discharge pressure will stay in a semi-steady state situation. When the density wave reaches the booster pump, the total head of the booster pump increases, resulting in an increase of the line speed. This occurs after about 16.5 minutes of simulation time. Since the total head of ladder and main pump does not change, the booster pump vacuum will have to decrease to pull harder on the mixture in the pipeline before the booster pump. This results in the occurence of cavitation of the booster pump, limiting the total head of the booster pump and thus the line speed. The cavitation causes a very instable behaviour of the booster pump as is shown in Figure 6-18. Since the density wave moves from the suction line to the discharge line, the booster pump vacuum and discharge pressure both increase when the density wave moves through the booster pump. After 18.5 minutes the density wave leaves the booster pump. The total head of the booster pump decreases sharply, while the line speed decreases slowly. The fluid in the pipeline before the booster pump pushes and the fluid after the booster pump pulls, resulting in a quick increase of the booster pump vacuum and a decrease in the booster pump discharge pressure. As the line speed decreases, the discharge pressure will increase again. After 23 minutes of simulation time, the density wave starts leaving the pipeline. 2 minutes later the density wave has complete left the system. Because of the decreasing resistance during this time-span, the line speed will increase slightly, resulting in a small decrease of the vacuum and discharge pressure of each pump, while the total head remains constant. The total power will also increase slightly because of this.
To stabilise the line speed to a specific value, flow control can be used. Flow control adjusts the speed of the last pump, in this case the booster pump. If the line speed is higher then a set point, the booster pump speed is decreased, if the line speed is lower, the booster pump speed is increased. To determine the correct booster pump speed, the total head is considered to be a summation of the heads of all of the pumps in the system. The head of the booster pump is considered to be proportional to the square of the booster pump speed and the total resistance is considered to be proportional to the square of the line speed, this gives:

$$\Delta p_{l.p.} + \Delta p_{m.p.} + \Delta p_{b.p.} = \Delta p_{l.p.} + \Delta p_{m.p.} + \alpha \cdot n^2 = \beta \cdot c^2 \qquad \textbf{(6-27)}$$

When the flow control is active, the heads of the ladder pump and the main pump do not change, so for the set point of the line speed:

$$\Delta p_{l.p.} + \Delta p_{m.p.} + \Delta p_{b.p.} = \Delta p_{l.p.} + \Delta p_{m.p.} + \alpha \cdot n_{f.c.}^2 = \beta \cdot c_{f.c.}^2 \qquad \textbf{(6-28)}$$

Assuming that the sum of the heads of ladder and main pump equals the head of the booster pump times a factor γ and dividing equation (6-28) by equation (6-27), the following can be derived:

$$n_{f.c.} = n \cdot \sqrt{(\gamma + 1) \cdot \left(\frac{c_{f.c.}}{c}\right)^2 - \gamma} \qquad \textbf{(6-29)}$$

By substituting: $\varepsilon = \left(\frac{c_{f.c.} - c}{c}\right)$ and using Taylor series approximation, this gives:

$$n_{f.c.} = n + n \cdot \tfrac{1}{2} \cdot (\gamma + 1) \cdot \varepsilon \cdot (\varepsilon + 2) \qquad \textbf{(6-30)}$$

Equation (6-30) is used to simulate flow control. The same scenario as above is used, except for the flow control that is activated after 8 minutes of simulation time. The set point for the line speed is set to 5 m/sec. Figure 6-19 and Figure 6-20 show the results of this simulation. As can be seen, the line speed changes rapidly when the density wave reaches or leaves one of the pumps. In about 15 seconds the flow control has adjusted the line speed to the set point. Figure 6-20 shows that the occurrence of cavitation is almost surpressed using the flow control. The booster pump speed tends to slightly oscillate. This is caused by applying several first order systems in series, resulting in a second or third order system. If the factor γ is choosen to high, the system is fast but tends to oscillate. If this factor is to small, the system responds very slow. In the simulation a value of 2 is used.

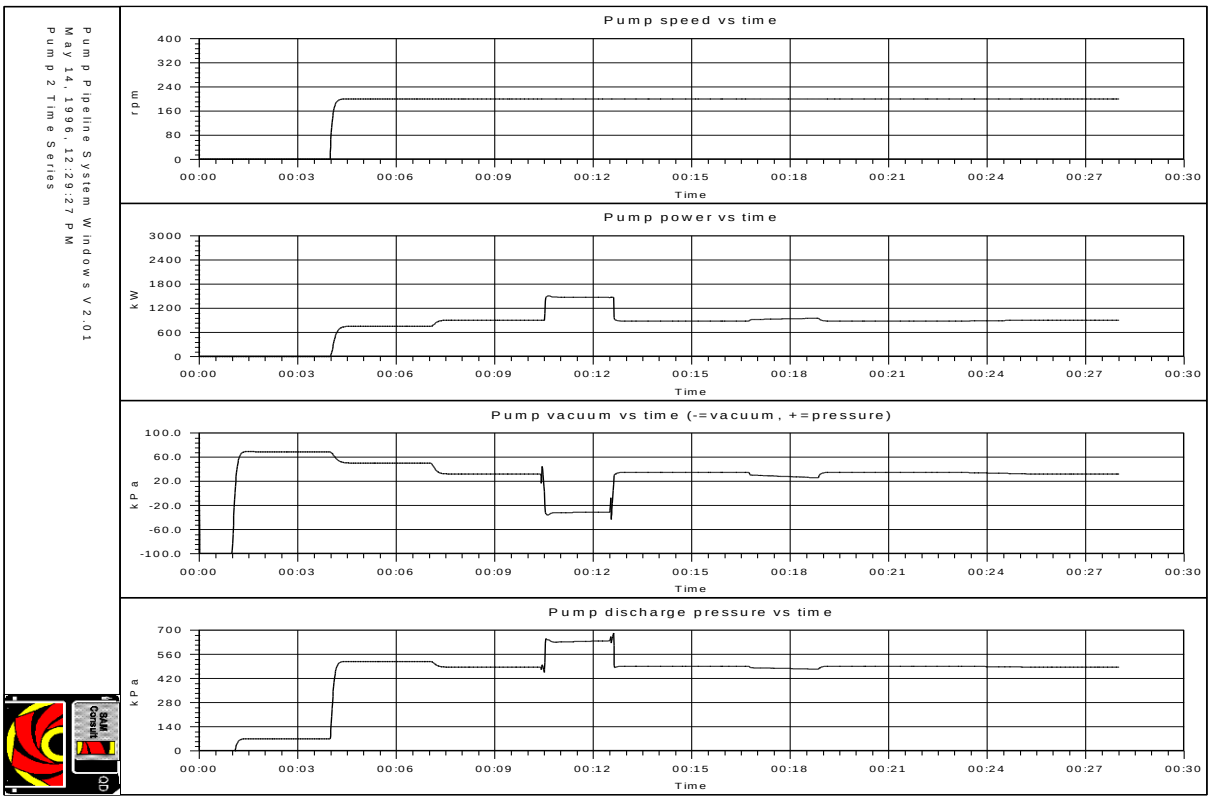

Figure 6-17: Speed, power, vacuum and discharge pressure of the main pump vs. time.

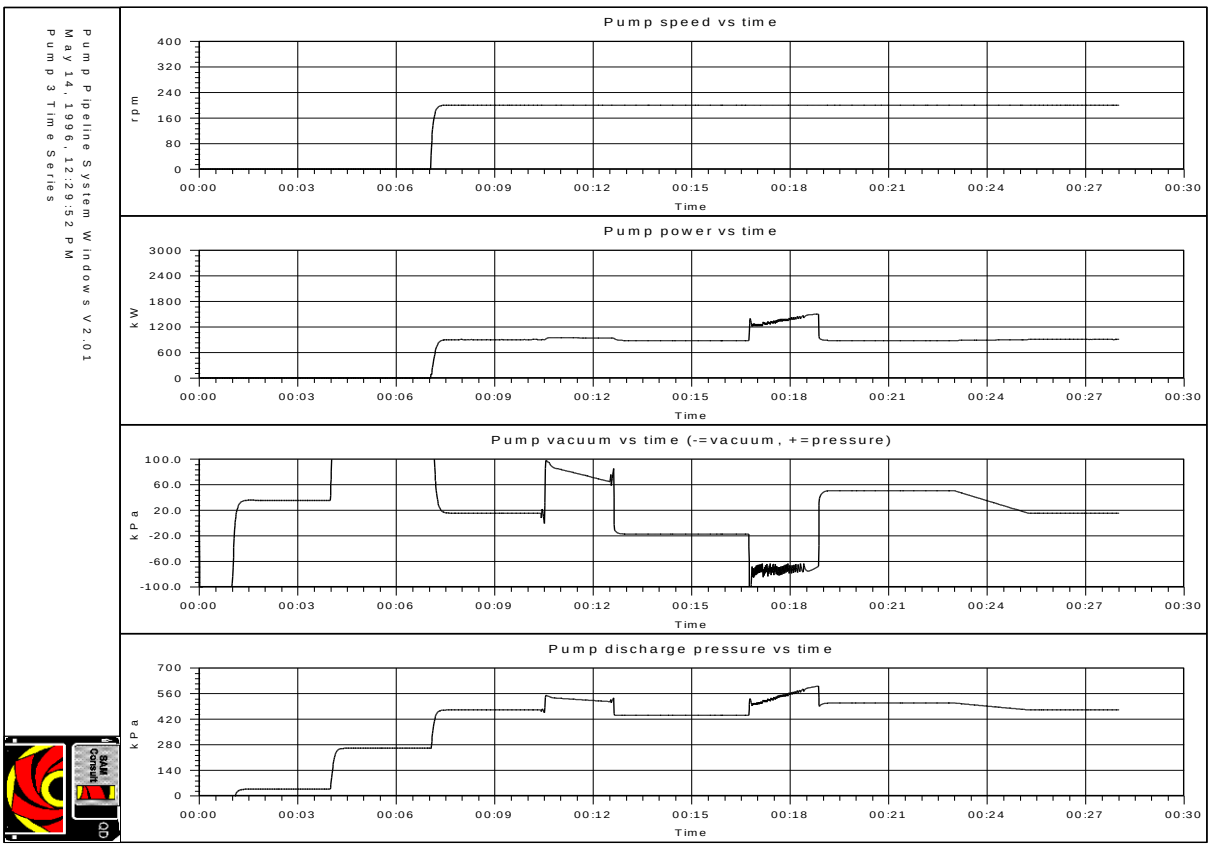

Figure 6-18: Speed, power, vacuum and discharge pressure of the booster pump vs. time.

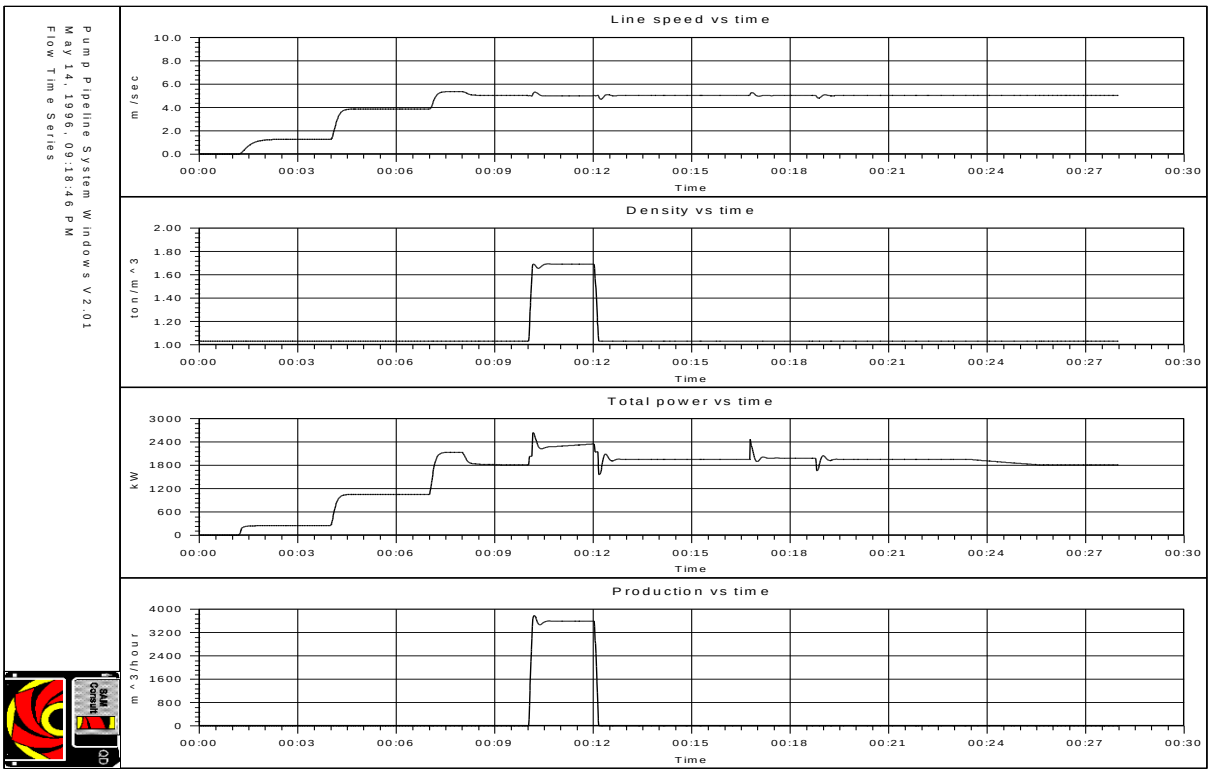

Figure 6-19: Line speed, density, total power and situ production as a function of time, with flow control.

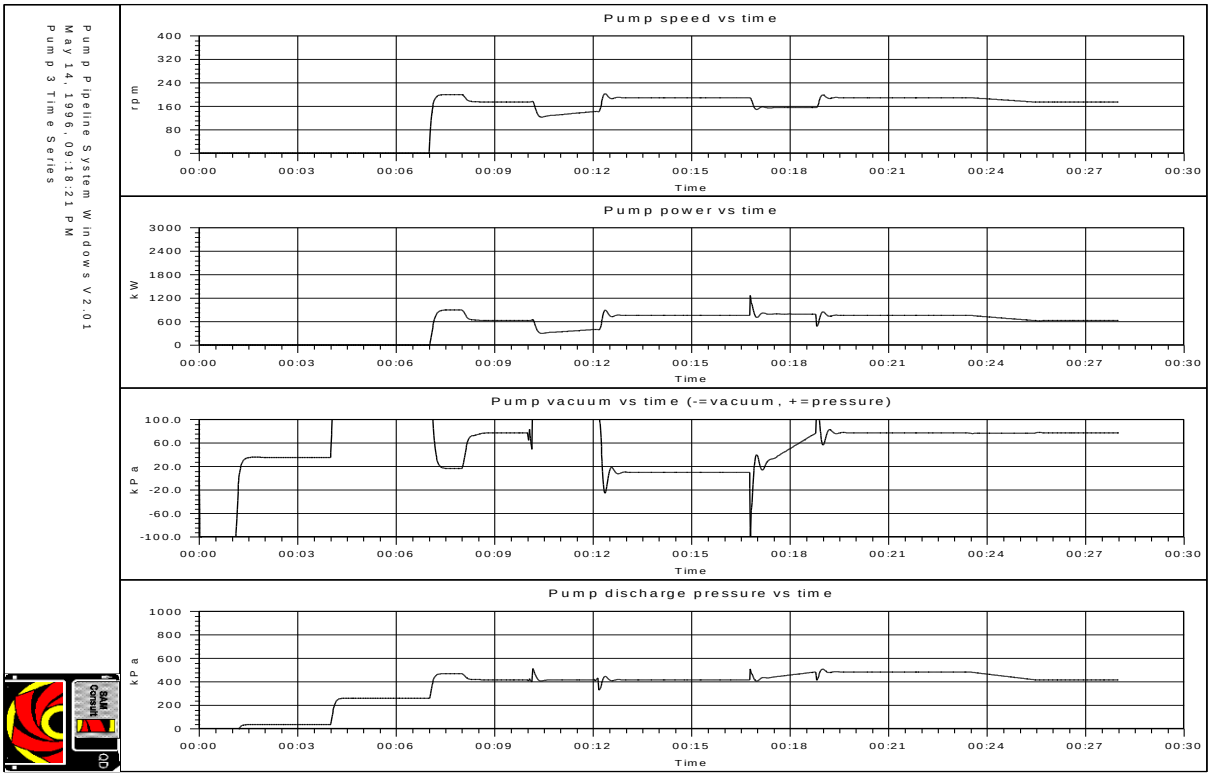

Figure 6-20: Speed, power, vacuum and discharge pressure of the booster pump vs. time, with flow control.

6.11. Conclusions and Discussion.

The behaviour of a multi pump/pipeline system is hard to understand. As mentioned before, an infinite number of system configurations and soil conditions exist. Systems are usually configured, based on steady state calculations, while the dynamic behaviour is ignored. Combining the steady state approach for pipeline resistance with the dynamic behaviour of pumps, pump drives and the second law of Newton, the dynamic behaviour can be simulated. However, a number of assumptions had to be made.

These assumptions are:

1. There is no longitudinal diffusion in the pipeline.
2. The pump drive behaves like a constant torque system.
3. The pipeline resistance is determined using the Durand theory.
4. The centrifugal pump obeys the affinity laws.

Whether these assumptions are valid will be subject of further research. The simulations however show the occurrence of phenomena that are known in practice.

Multi pump/pipeline systems can be configured in an infinite number of configurations. Phenomena that occur in one configuration do not have to occur in other configurations. So the configuration to carry out simulations to examine certain phenomena has to be chosen carefully. The configuration used in this paper is suitable for simulation of most phenomena. The examples show, that moving from one working point to the next working point, does not occur instantaneously, but with a time delay, where the time delay depends on the phenomena.

The simulation model used is very well suitable for fully suspended load, but has a deficiency for two phase flow. The main shortcoming is the fact that suspended load and bed load move through the system at two different velocities, not being equal to the average line speed.

A second shortcoming is the lack of availability of a good model for the vertical diffusion between the suspended load and the bed load. This will be subject for further research.

One should consider that mathematical modelling is an attempt to describe reality without having any presumption of being reality.

6.12. Nomenclature.

$C_{1,2,3,4}$	Coefficients	-
C_D	Drag coefficient	-
C_{vt}	Transport concentration	-
C_v	Volumetric concentration	-
C_{vs}	Spatial concentration	-
C_x	Drag coefficient	-
d	Grain/particle diameter	**m**
D	Impeller diameter	**m**
D_p	Pipe diameter	**m**
Fr	Froude number	-
g	Gravitational constant	**m/sec^2**
H	Height/elevation	**m**
I	Mass moment of inertia	**ton·m^3**
k	Constant	-
Kp	Proportionality constant	**kNms/rad**
L	Length of pipeline	**m**
n	Revolutions	**rpm**
p	Pressure	**kPa**
P	Power	**kW**
Q	Flow	**m^3/sec**
r	Radius	**m**
Re	Reynolds number	-
T	Torque	**kNm**
u	Tangetial velocity	**m/sec**
v_t	Settling velocity grains	**m/sec**
v_{ls}	Line speed	**m/sec**
α,β	Coefficients	-
β	Blade angle	**rad**
ε	Wall roughness	**m**
ε	Ratio	-
η	Efficiency	-
φ	Rotation angle of centrifugal pump	**rad**
$\dot{\varphi}$	Angular velocity of centrifugal pump	**rad/sec**
$\ddot{\varphi}$	Angular acceleration of centrifugal pump	**rad/sec^2**
λ	Darcy Weisbach friction coefficient	-
ν	Kinematic viscosity	**m^2/sec**
ρ	Density	**ton/m^3**
τ	Time constant	**sec**
ξ	Friction coefficient	-
ψ	Shape factor	-
	Indices	
c	Concentration	
cr	Critical	
c.p.	Centrifugal pump	

D	Design	
d	Discharge	
d.e.	Diesel engine	
d.f.	Dry friction	
f	Fluid	
g	Geodetic	
gr	Grain	
g.b.	Gear box	
h.f.	Hydraulic friction	
h.i.	Hydraulic impact	
h.p.	Hydraulic power	
h.t.	Hydraulic transport	
i	In	
m	Mixture	
m	Measured	
n	Revolutions	
o	Out	
p	Proportional	
p	Pump	
p	Pipe	
q	Quarts	
s.p.	Set point	
t.	Total	
w	Water	
0	Initial value (boundary condition)	
n	Number of time step	
E	Euler	
15	% passing	
50	% passing	
85	% passing	

6.13. Notes.

Chapter 7: Modeling of the Swing Winches of a Cutter Dredge.

7.1. Introduction.

The dredge motions consist of the six degrees of freedom of the pontoon complemented with the rotation of the ladder around the ladder bearings. This gives a total of 7 degrees of freedom (surge, sway, heave, roll, pitch, yaw and ladder rotation). For a dredge operating in still water, when wave forces are ignored, the motions in the horizontal plane are relevant (surge, sway and yaw) as well as the ladder rotation. The three pontoon motions can be reduced to the rotation around the spud if the spud is considered to be infinitely stiff. If the ladder rotation is considered not to be the result of a mass-spring system, but controlled by the ladder winch, only one equilibrium equation has to be solved, the rotation of the pontoon around the spud. The other 6 equilibrium equations are of interest when working offshore, when wave forces have to be taken into account, but using these equations increases the calculations to be carried out enormous.

7.2. The Motions of the Dredge.

The equilibrium equation of rotation around the spud is a second order non-linear differential equation, with the following external forces:

- The inertial forces of pontoon and ladder
- The water damping on pontoon and ladder
- The spring forces resulting from the swing wires
- The external forces resulting from the current
- The external forces resulting from the cutting process
- The external forces resulting from the swing winches
- The external forces resulting from the pipeline
- The reaction forces on the spud

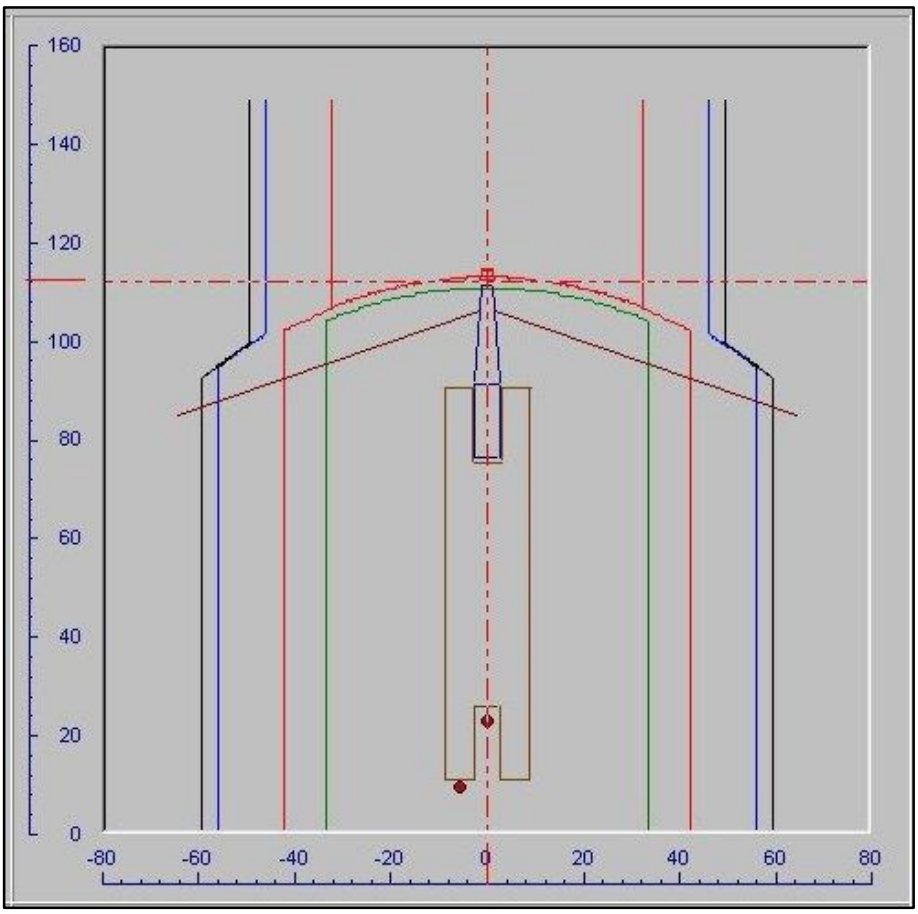

Figure 7-1: The display of the top view of the cutterdredge, also showing the channel.

1. The inertial forces (moments) determine whether there is an acceleration or deceleration of the rotation around the spud. These forces are the result of the equilibrium equation and thus of the external forces.
2. The water damping and the current forces depend on the value and the direction of the current and on the rotational speed of the pontoon around the spud.

3. The spring forces resulting from the swing wires and the forces resulting from the swing winches strongly depend on the characteristics of the winches and the wires and the winch control system. The position of the anchors in relation to the position of the spud and the position of the swing wire sheaves on the ladder determines the direction of the swing wire forces and thus of the resulting moments around the spud. Figure 4 shows the winch output of a research simulator.

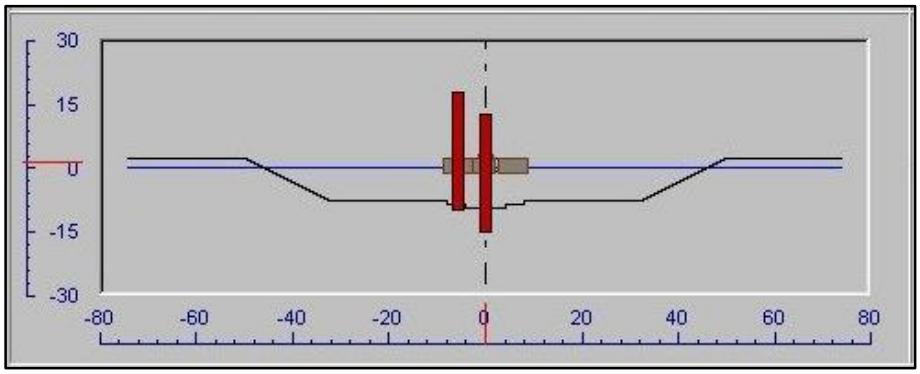

Figure 7-2: The display of the back view of the cutterdredge, also showing the cross-sectional channel profile.

4. The forces and moment excerted on the pontoon by the current influence the rotation around the spud depending on the current speed and the swing speed. For small values of the current speed this effect can however be neglected. For high values of the current speed the influence depends on the direction of the current and the swing angle. It may occur that the swing winches do not have enough power to pull back the pontoon out of a corner due to the angle of the swing wires and a high current speed.

5. The cutting forces and the cutting torque strongly influence the rotation around the spud, these will be discussed in the paragraph concerning the cutting forces.
6. The winch forces and the winch moment strongly influence the rotation around the spud, these will be discussed in the paragraph concerning the swing winch characteristics.

7. The forces resulting from the pipeline can be neglected if the position of the swivel elbow is close to the position of the work spud, because in this case this force hardly influences the rotation of the pontoon around the spud.

8. The reaction forces on the spud can be determined by the equilibrium equations of forces and complement this equilibrium. These forces however do not contribute to the moment around the spud.

The rotation of the pontoon around the spud is dominated by the cutting forces, the winch characteristics, the inertia of pontoon and ladder and placement of the anchors, while damping and current play a less important role. The equilibrium equation can be formulated as:

$$I_{yaw} \cdot \ddot{\varphi}_s + k_{yaw} \cdot \dot{\varphi}_s + c_{yaw} \cdot \varphi_s = M_{current} + M_{cutting} + M_{wires} + M_{pipe} + M_{spud} \qquad \textbf{(7-1)}$$

The water damping is combined with the current moment, the wire spring force, the pipeline moment and the spud moment are not taken into consideration. Equation 1 thus reduces to:

$$I_{yaw} \cdot \ddot{\varphi}_s = M_{current} + M_{cutting} + M_{wires} \qquad \textbf{(7-2)}$$

The equilibrium equation in question is non-linear, while some of the data is produced by interpolation from tables. This implies that the equation will have to be solved in the time domain, using a certain time step. This is also necessary because the simulation program has to interact with the console (the user input). To simulate the motions

of the dredge real time, a time step of at least two times per second is required. A time step of 5 to 10 times per second would be preferred.

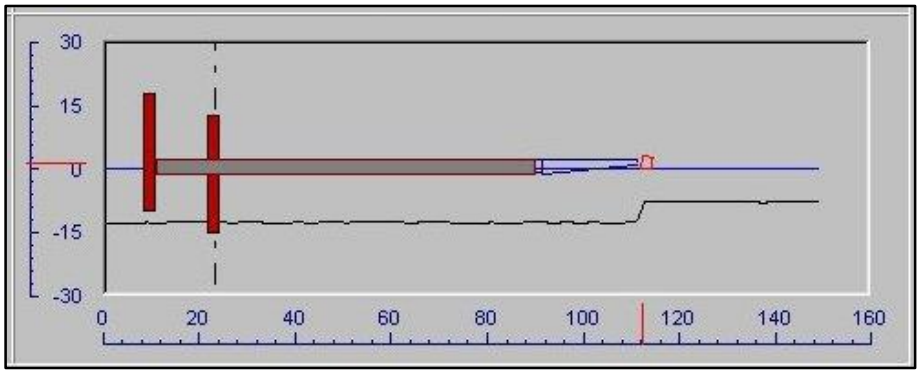

Figure 7-3: The display of the side view of the cutterdredge, also showing the longitudinal channel profile.

7.3. The Influence of the Swing Angle on the Wire Moment.

With fixed anchor positions, the angle of attack of the swing wires relative to the axis system of the pontoon, changes continuously with the value of the swing angle. With large swing angles this may result in a large decrease of the effective pulling or braking moment of the swing wires. This decrease of course depends on the anchor positions relative to the pontoon.

In this paper the following coordinate system definitions are applied:

1. The origin is placed in the centerline of the work spud.
2. The two wire sheaves are positioned on the centerline through the work spud and the cutterhead.
3. The positive swing direction is counter clock wise, with an angle of zero degrees when the centerline of the dredge matches the vertical axis (y-axis).
4. The distance from the center of the workspud to the center of the sheaves is L_{ss}.

With the coordinates if the swing sheaves on the ladder x_{ss} and y_{ss} according to:

$$x_{ss} = L_{ss} \cdot \sin(\varphi_s) \tag{7-3}$$

And

$$y_{ss} = L_{ss} \cdot \cos(\varphi_s) \tag{7-4}$$

The length of the port wire and the angle of the port wire with the centerline of the channel can be determined according to:

$$L_{pw} = \sqrt{(x_{ss} - x_{pw})^2 + (y_{ss} - y_{pw})^2} \tag{7-5}$$

and

$$\phi_{pw} = \arctan\left(\frac{x_{ss} - x_{pw}}{y_{ss} - y_{pw}}\right) \tag{7-6}$$

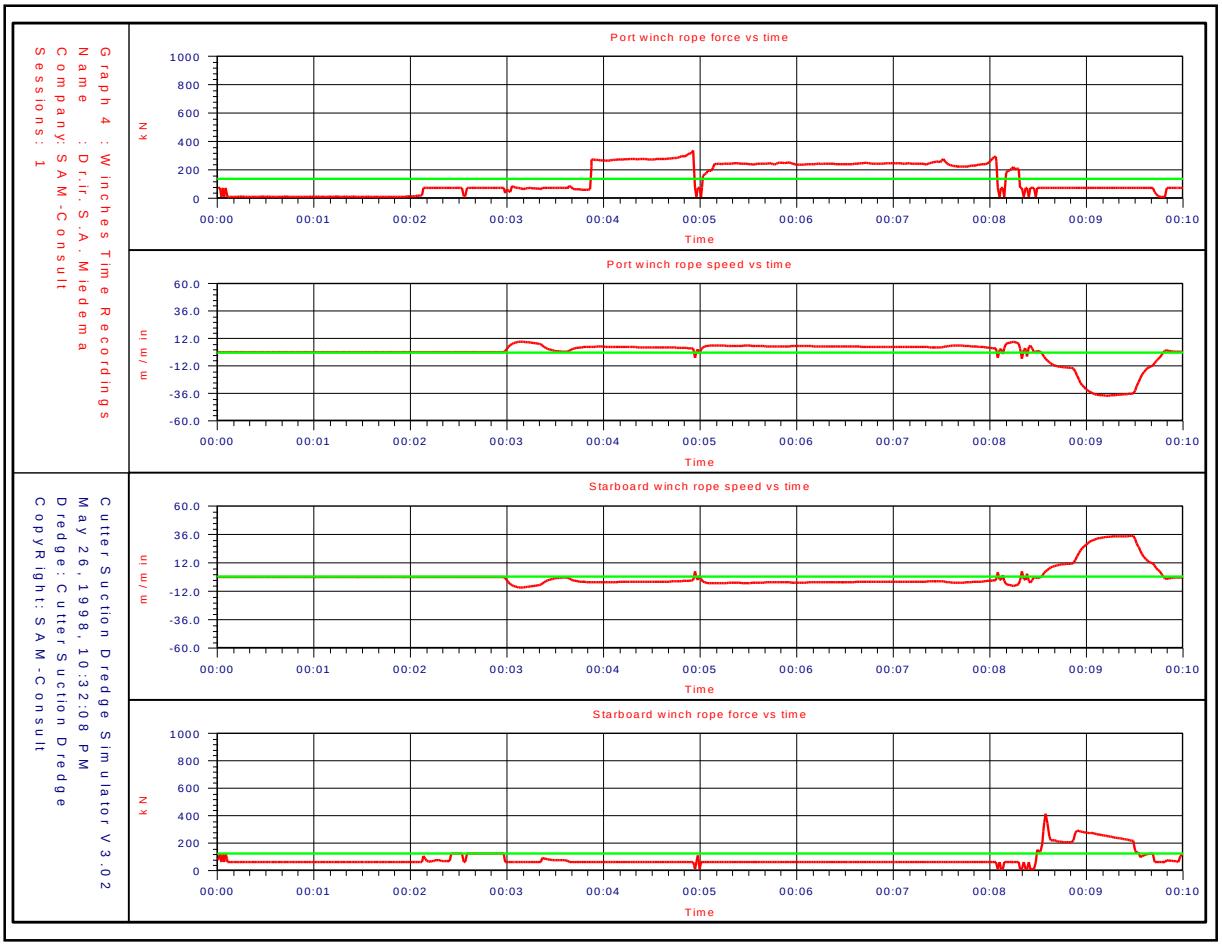

Figure 7-4: The output of the winch parameters.

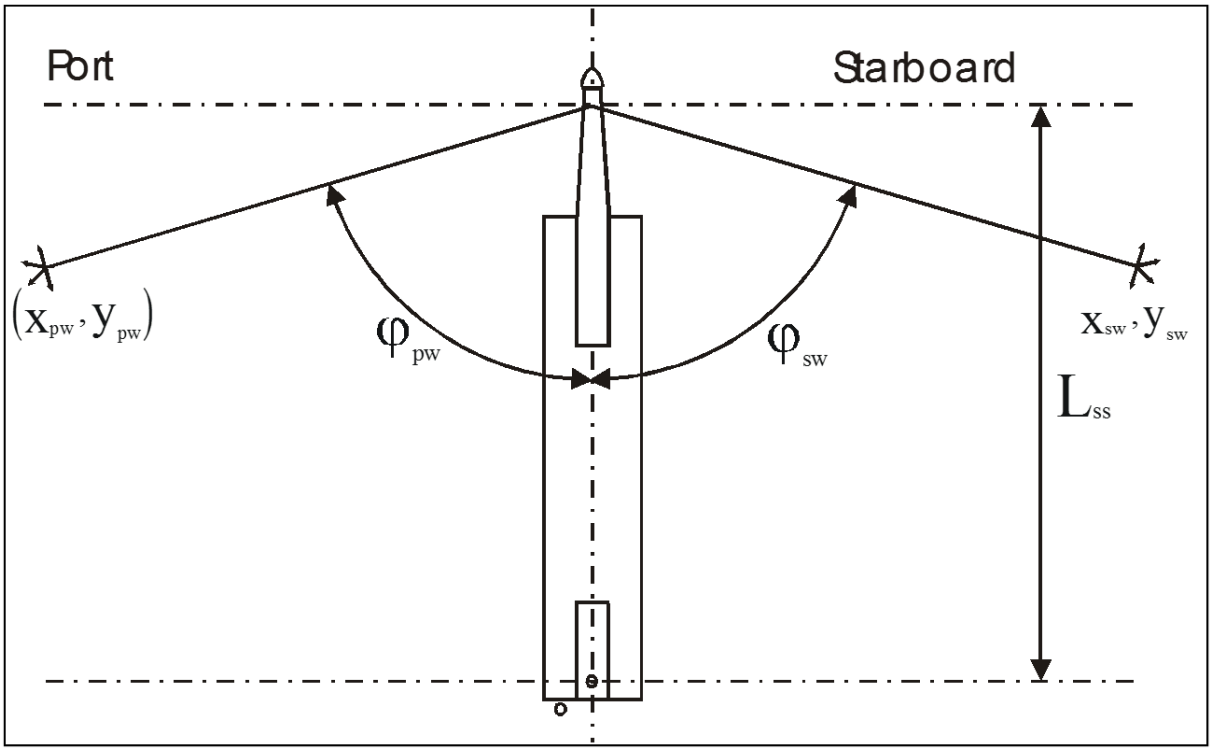

Figure 7-5: The coordinate system with the dredge in the neutral position.

The length of the starboard wire and the angle of the starboard wire with the centerline of the channel can be determined according to:

$$L_{sw} = \sqrt{(x_{ss} - x_{sw})^2 + (y_{ss} - y_{sw})^2} \tag{7-7}$$

and

$$\phi_{sw} = \arctan\left(\frac{x_{ss} - x_{sw}}{y_{ss} - y_{sw}}\right) \tag{7-8}$$

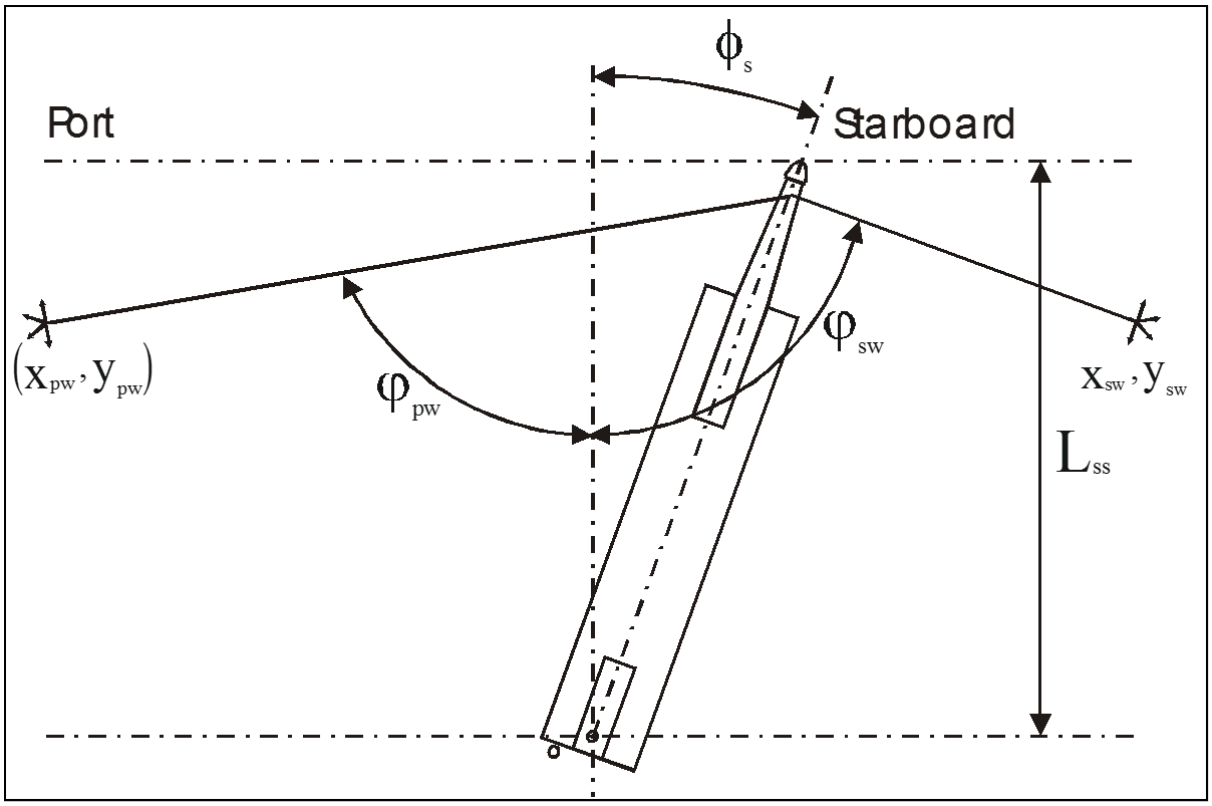

Figure 7-6: The coordinate system with the dredge at a swing angle ϕ_s.

The angle of the port wire with the centerline of the dredge is:

$$\phi_{pw} + \varphi_s \tag{7-9}$$

The angle of the starboard wire with the centerline of the dredge is:

$$\phi_{sw} - \varphi_s \tag{7-10}$$

The moment around the spud, resulting from the forces in the swing wires can now be determined by:

$$M_{wires} = F_{pw} \cdot L_{ss} \cdot \sin\left(\phi_{pw} + \varphi_s\right) - F_{sw} \cdot L_{ss} \cdot \sin\left(\phi_{sw} - \varphi_s\right) \tag{7-11}$$

The relation between the rope speed of the port wire and the angular speed of the dredge is now:

$$\dot{\varphi}_s \cdot L_{ss} = v_{pw} \cdot \sin\left(\phi_{pw} + \varphi_s\right) \tag{7-12}$$

The relation between the rope speed of the starboard wire and the angular speed of the dredge is now:

$$\dot{\varphi}_s \cdot L_{ss} = v_{sw} \cdot \sin\left(\phi_{sw} - \varphi_s\right) \tag{7-13}$$

This results in loss of effective power of both winches. The power mobilized by the winches to the angular speed of the dredge is:

$$P_{wm} = P_{pwm} - P_{swm} = F_{pw} \cdot v_{pw} \cdot \sin\left(\phi_{pw} + \varphi_s\right)^2 - F_{sw} \cdot v_{sw} \cdot \sin\left(\phi_{sw} - \varphi_s\right)^2 \tag{7-14}$$

The power consumed by the winches is:

$$P_w = P_{pw} + P_{sw} = F_{pw} \cdot v_{pw} + F_{sw} \cdot v_{sw} \tag{7-15}$$

7.4. The Winch Characteristics.

The torque speed characteristic of the winches consists of two parts if an electric drive is assumed. The first part runs from 0 revolution up to full revolutions and has a linear decrease of the torque, from a maximum at zero revolutions to the full torque at full revolutions. At this last point also the full power of the drive is reached. At higher revolutions the drive will use field weakening, while the power stays constant. In the simulator it is assumed that the characteristics for hauling and braking are equal. If one winch is in hauling mode, the other one will always be in braking mode.

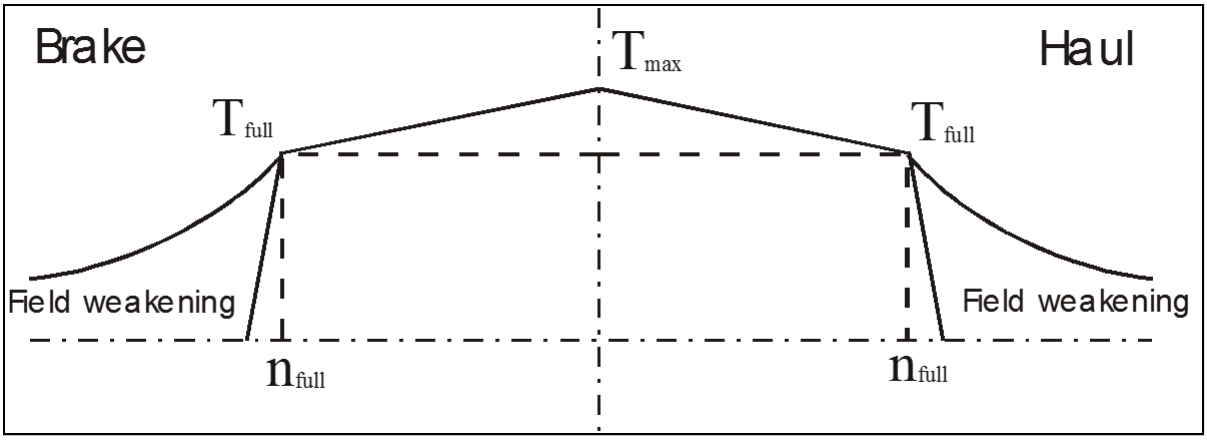

Figure 7-7: The torque-speed characteristic of the winches.

7.5. The Control System of the Winches.

The hauling winch is controlled by a setpoint for the winch revolutions. The braking winch is controlled by a setpoint for the braking torque. So for the hauling winch, the available torque results from the revolutions, while the pulling force also results from the drumdiameter and the number of layers on the drum. The mobilized torque also depends on the loads (cutter and current) and on the angular acceleration of the dredge around the spud pole.

Figure 7-8 shows the actual revolutions of the hauling winch, the setpoint of the hauling winch, the setpoint of the braking winch and the load curve for the hauling winch. The load curve includes the cutting process, the current and water damping and the braking winch. The difference between the available torque and the torque resulting for the loads is available for the acceleration of the pontoon. In the example given in Figure 7-8, it is assumed that the actual revolutions of the winch are smaller then the setpoint and that the available torque is larger then the required torque for compensating the loads.

The actual torque mobilized by the hauling winch, is always the resulting torque necessary to reach or stay on the setpoint. If in a certain situation, the torque available is less then the torque required, then the available maximum torque is assumed. In this case the working point is the intersection point of the load curve with the vertical dotted line through the setpoint of revolutions. The maximum available torque is not fully mobilized.

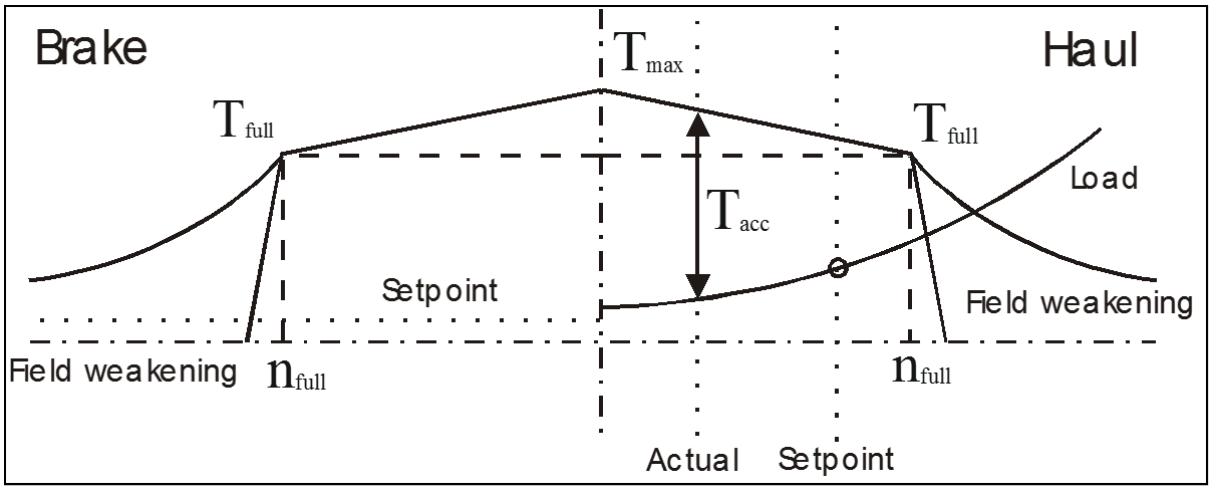

Figure 7-8: The torque-speed characteristic of the winches with the setpoints.
Case where the required torque is sufficient.

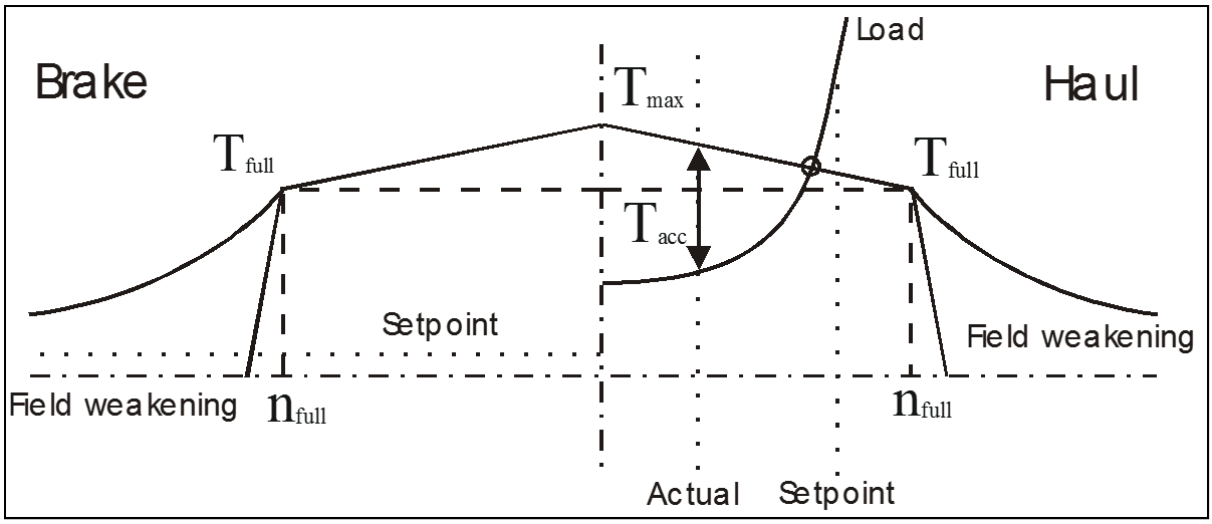

Figure 7-9: The torque-speed characteristic of the winches with the setpoints.
Case where the required torque in the setpoint is not sufficient.

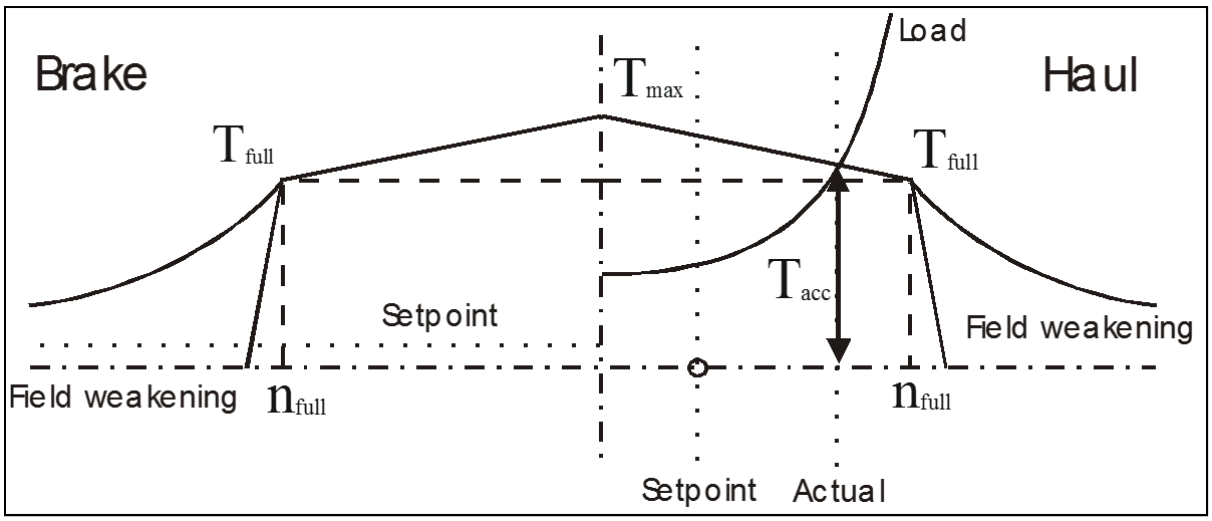

Figure 7-10: The torque-speed characteristic of the winches with the setpoints.
Case where the setpoint is smaller then the actual revolutions.

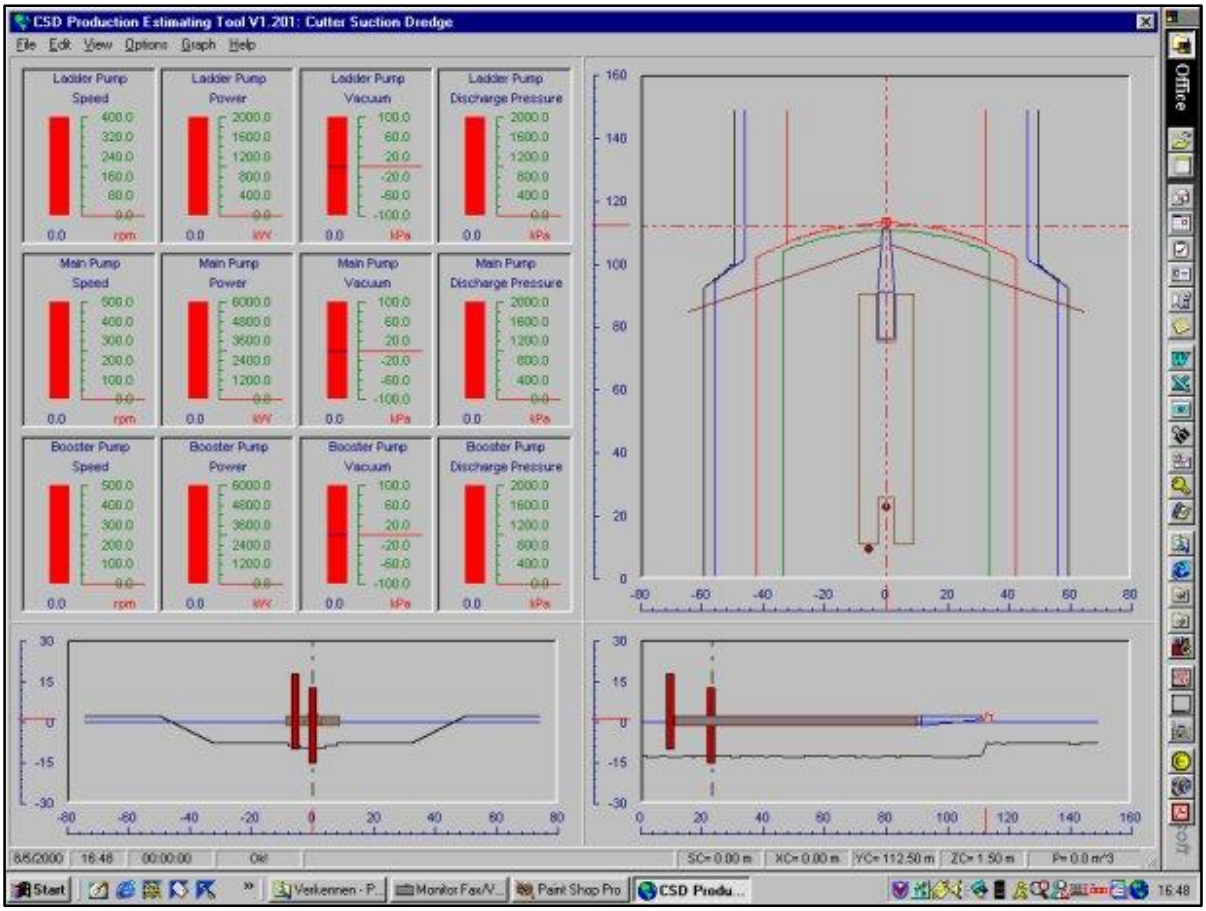

Figure 7-11: The dredge, winch and channel layout.

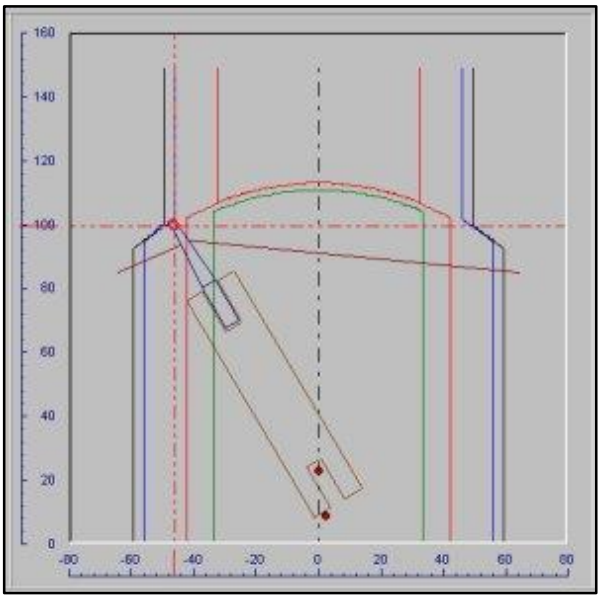

Figure 7-12: The dredge and anchor layout for case 1, port.

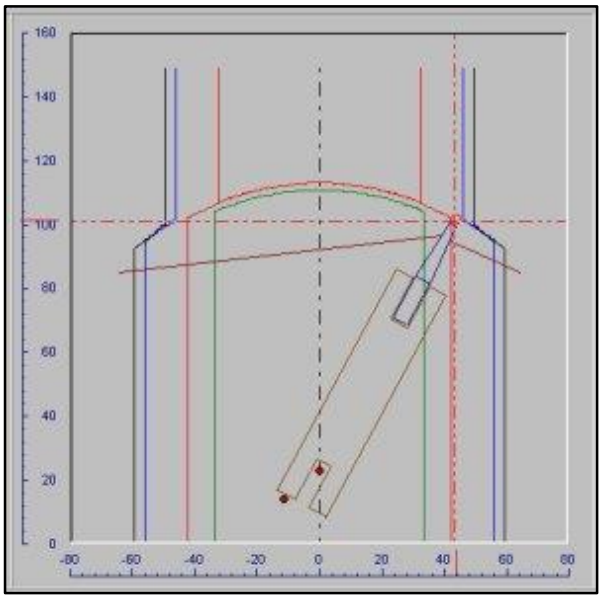

Figure 7-13: The dredge and anchor layout for case 1, starboard.

Figure 7-9 shows the case where the winch torque required in the setpoint is not sufficient. In this case, the working point is the intersection point of the load curve with the torque-speed curve. The maximum available torque is fully mobilized. The setpoint is not reached because there is not sufficient torque available.
Figure 7-10 shows the case where the setpoint is smaller then the actual revolutions. In this case, the pontoon will decelerate. The working point is the intersection point of the vertical through the setpoint and a minimum torque required keeping the wire from going slack.

7.6. Case Studies.

To show the behavior of the dredge-winch system two cases will be shown. In the first case the dredge starts on the centerline of the channel. The dredge and winch layouts are shown in Figure 7-11.

7.6.1. Case 1:

The winches have a drum diameter of 0.84 m, a full power of 158 kW at 8.87 rpm. The resulting full torque is 167 kNm. The anchor positions are symmetrical with respect to the centerline and are 65 m in horizontal direction and -21.5 m in vertical direction, away from the sheaves on the ladder. The ladder is not in contact with the bank and is moving free through the water. See Figure 7-12 and Figure 7-13.

The following actions are taken:

1. The setpoint for the swingspeed is set to 24 m/min to starboard.
2. The dredge swings from 0 to 30 degrees to starboard.
3. The setpoint for the swingspeed is set to 24 m/min to port.
4. The dredge swings from 30 degrees starboard to 30 degrees port.
5. The setpoint for the swingspeed is set to 24 m/min to starboard.
6. The dredge swings from 30 degrees port to the centerline.

Figure 7-14 shows the rope speeds and pulling forces for both the port and the starboard winch. It is clearly shown in the graphs in Figure 7-14 that, while the rope forces increase instantly, the rope speed increases or decreases according to a first or second order system. This is caused by the mass-spring-damper system according to equation 1, but also by the inertia of the winches themselves. In the simulator, the winches are modeled as a first order system. The winches and the dredge need some time to accelerate or decelerate.

The deceleration requires more time in case 1 then the acceleration, because the braking force is set to 30% of the maximum force, which is about 180 kN. The pulling force however, can be much higher, depending on the characteristic of the winches. Setting the braking force to a higher value, will increase the speed of the deceleration.

Typical for this case is, that the pulling wire is more and more perpendicular to the ladder when the swing angle approaches 30 degrees. This results in a decreasing pulling force, which can be seen in Figure 7-14. The braking force is set to a constant value and will only differ from this value if the braking force is larger then the torque-speed curve permits it to be. In that case the braking force will follow the torque speed curve.

7.6.2. Case 2:

The winches have a drum diameter of 0.84 m, a full power of 158 kW at 8.87 rpm. The resulting full torque is 167 kNm. The anchor positions are symmetrical with respect to the centerline and are 65 m in horizontal direction and +3.5 m in vertical direction, away from the sheaves on the ladder, as is shown in Figure 7-16 and Figure 7-17. The ladder is not in contact with the bank and is moving free through the water.

The following actions are taken:

1. The setpoint for the swingspeed is set to 24 m/min to starboard.
2. The dredge swings from 0 to 30 degrees to starboard.
3. The setpoint for the swingspeed is set to 24 m/min to port.
4. The dredge swings from 30 degrees starboard to 30 degrees port.
5. The setpoint for the swingspeed is set to 24 m/min to starboard.
6. The dredge swings from 30 degrees port to the centerline.

Figure 7-15 shows the rope speeds and pulling forces for both the port and the starboard winch. Because the anchors are moved 25 m forward in the channel, now the angle between the pulling wire and the ladder decreases when the dredge approaches the 30 degrees swing angle. This results in an increase of the pulling force as is visible in Figure 7-15. The start and stop behavior is almost equal to case 1.

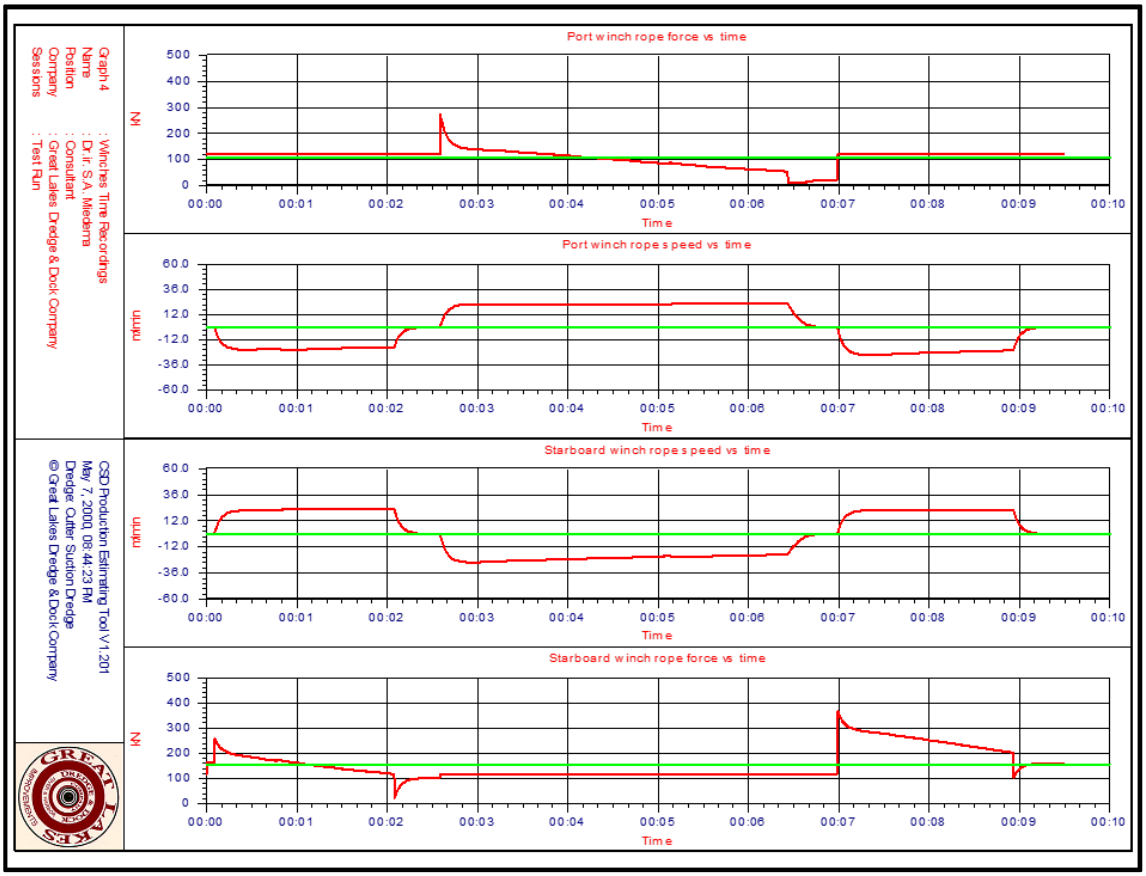

Figure 7-14: The rope speeds and forces for case 1.

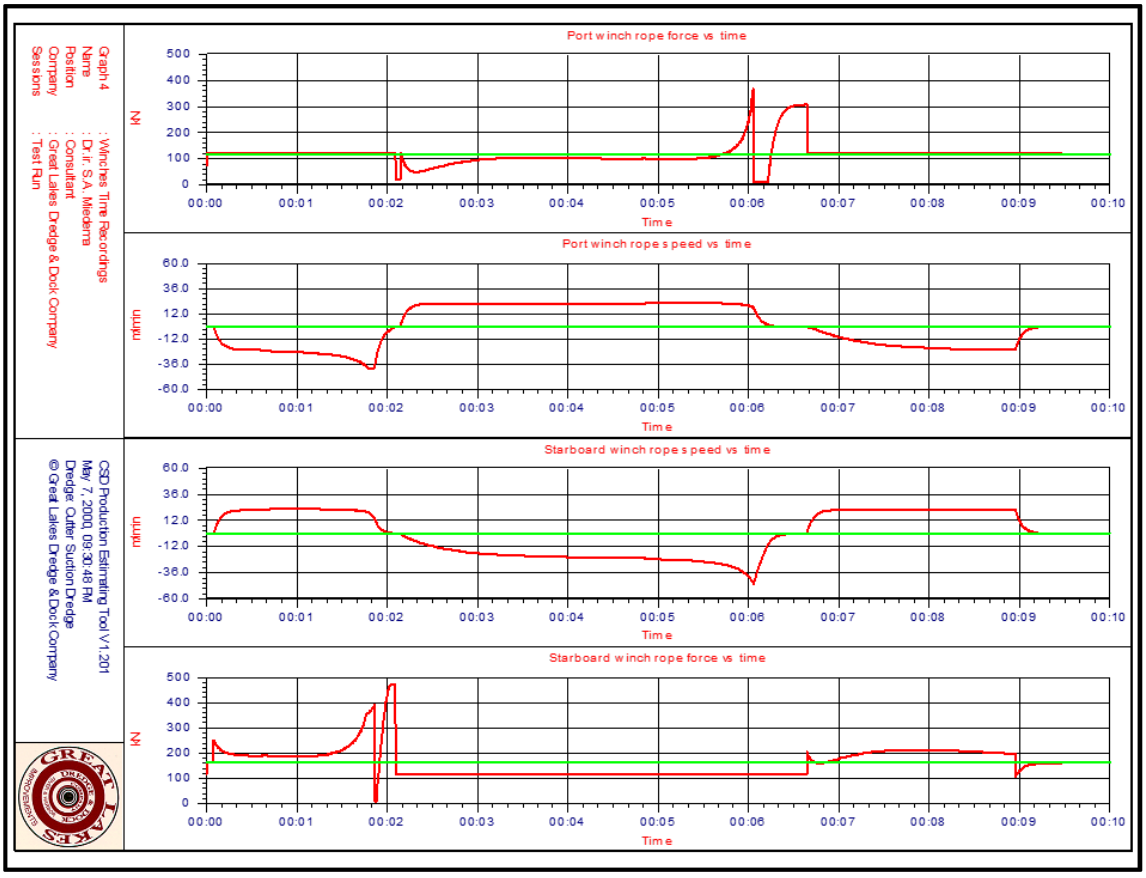

Figure 7-15: The rope speeds and forces for case 2.

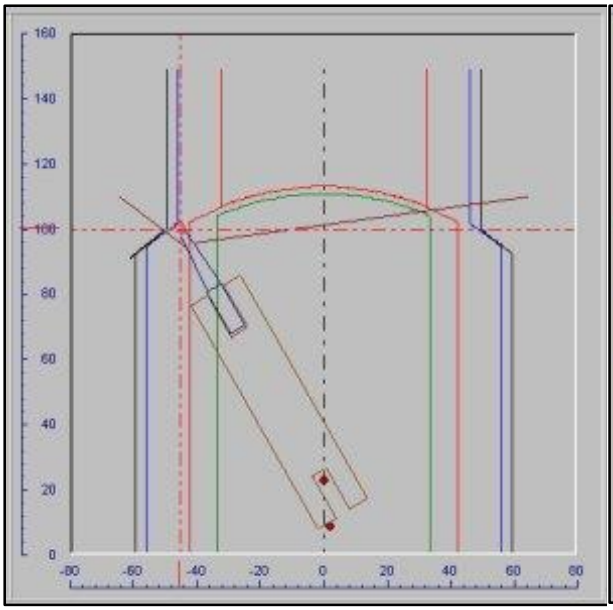

Figure 7-16: The dredge and anchor layout for case 2, port.

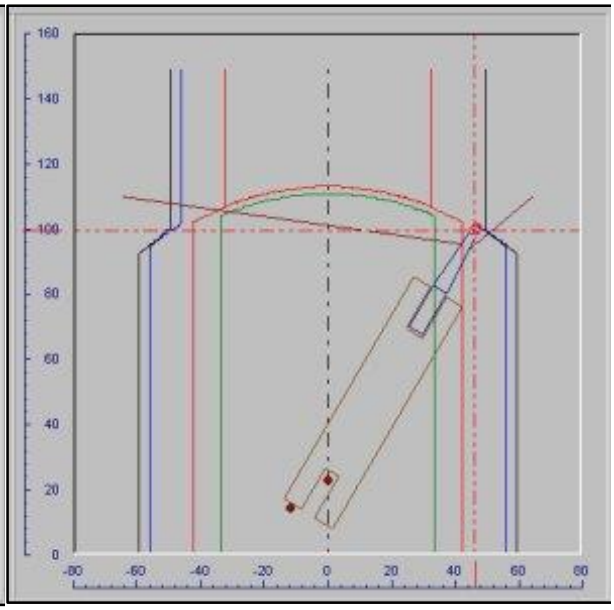

Figure 7-17: The dredge and anchor layout for case 2, starboard.

7.7. Conclusions.

The modeling of the winches and the wires consists of solving the equilibrium equation of motions of the dredge around the spudpole in combination with the characteristics of the winches. The two cases show that it takes about 10 seconds to accelerate to a swing speed of 24 m/min. The time required for the deceleration is of the same magnitude, but depends of course on the setpoint of the brake force.

The two cases also show, that the shape rope speed and force as a function of time, strongly depend on the position of the anchors relative to the sheave positions at the ladder. The two cases describe symmetrical configurations, which of course is not always the case. An infinite number of configurations can be chosen. Which configuration is the best depends on the work to be carried out and on the boundary conditions of the work to be carried out.

7.8. Nomenclature.

c_{yaw}	Spring constant of the yaw motion	**kNm/rad**
F_{pw}	Rope force of the port wire	**kN**
F_{sw}	Rope force of the starboard wire	**kN**
I_{yaw}	Mass moment of inertia of pontoon in yaw direction	**kNms^2/rad**
k_{yaw}	Damping coefficient of pontoon in yaw direction	**kNms/rad**
L_{pw}	Length of the port wire	**m**
L_{ss}	Distance from working spud to swing sheaves on ladder	**m**
L_{sw}	Length of starboard wire	**m**
$M_{current}$	Moment around the spud exerted by the current	**kNm**
$M_{cutting}$	Moment around the spud exerted by the cutting process	**kNm**
M_{pipe}	Moment around the spud exerted by the floating pipeline	**kNm**
M_{spud}	Moment around the spud exerted by the spud	**kNm**
M_{wires}	Moment around the spud exerted by the swing wires	**kNm**
n_{full}	Full revolutions of the swing winch	**rpm**
P_{pw}	Power of the port winch	**kW**
P_{pwm}	Power of the port winch mobilized on the dredge	**kW**
P_{sw}	Power of the starboard winch	**kW**
P_{swm}	Power of the starboard winch mobilized on the dredge	**kW**
P_{w}	Power of both winches	**kW**
P_{wm}	Power of both winches mobilized on the dredge	**kW**
T_{acc}	Winch torque available for acceleration or deceleration	**kNm**
T_{full}	Full torque of the winches	**kNm**
T_{max}	Maximum torque of the winches	**kNm**
v_{pw}	Rope speed of the port winch	**m/sec**
v_{sw}	Rope speed of the starboard winch	**m/sec**
x_{pw}	X coordinate of the port anchor	**m**
x_{ss}	X coordinate of the swing sheaves on the ladder	**m**
x_{sw}	X coordinate of the starboard anchor	**m**
y_{pw}	Y coordinate of the port anchor	**m**
y_{ss}	Y coordinate of the swing sheaves on the ladder	**m**
y_{sw}	Y coordinate of the starboard anchor	**m**
ϕ_s	Swing angle	**rad**
φ_{pw}	Port wire angle	**rad**
φ_{sw}	Starboard wire angle	rad

7.9. Notes.

Chapter 8: The Trailing Suction Hopper Dredge.

8.1. Introduction

In the last decennia there has been a strong development in the enlargement of TSHD's (Trailing Suction Hopper Dredges) from roughly 10.000 m^3 in the early 90's up to 50.000 m^3 expected loading capacity nowadays. Because of the economy of the loading process, but also environmental regulations, it is important to predict the overflow losses that are occurring.
For the estimation of the sedimentation process in TSHD's a number of models have been developed. The oldest model used is the Camp (1936), (1946) and (1953) model which was developed for sewage and water treatment tanks. Camp and Dobbins (1944) added the influence of turbulence based on the two-dimensional advection-diffusion equation, resulting in rather complicated equations. Miedema (1981) used the Camp model to develop an analytical model. Groot (1981) added the effects of hindered settling. Vlasblom & Miedema (1995) and Miedema & Vlasblom (1996) simplified the Camp equations by means of regression and included a rising sediment zone, as well as hindered settling and erosion and an adjustable overflow. Van Rhee (2002C) modified the implementation of erosion in the Camp model, but concluded that the influence is small due to the characteristics of the model. Ooijens (1999) added the time effect, since the previous models assume an instantaneous response of the settling efficiency on the inflow of mixture. Yagi (1970) developed a new model based on the concentration distribution in open channel flow.
The models mentioned above are all black box approaches assuming simplified velocity distributions and an ideal basin. Van Rhee (2002C) developed a more sophisticated model, the 2DV model. This model is based on the 2D (horizontal and vertical) Reynolds Averaged Navier Stokes equations with a k-ε turbulence model and includes suspended sediment transport for multiple fractions.

8.2. The Loading Cycle of a Hopper Dredge

The loading cycle of a TSHD is considered to start when the hopper is filled with soil and starts to sail to the dump area. This point in the loading cycle was chosen as the starting point in order to be able to show the optimal load in a graph. The loading cycle then consists of the following phases:

- Phase 1: The water above the overflow level flows away through the overflow. The overflow is lowered to the sediment level, so the water above the sediment can also flow away. In this way minimum draught is achieved. Sailing to the dump area is started.

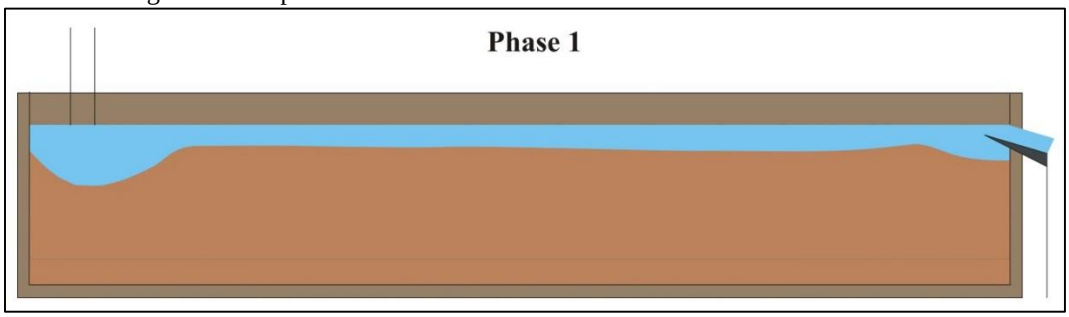

Figure 8-1: Phase 1 of the loading cycle.

- Phase 2: Continue sailing to the dump area.

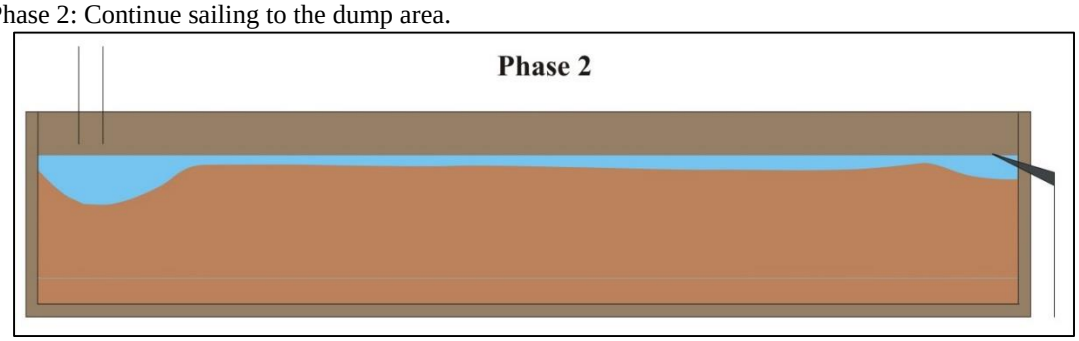

Figure 8-2: Phase 2 of the loading cycle.

- Phase 3: Dump the load in the dump area. Dumping can be carried out in 3 different ways, using the bottom dumping system, pumping ashore or rain bowing.

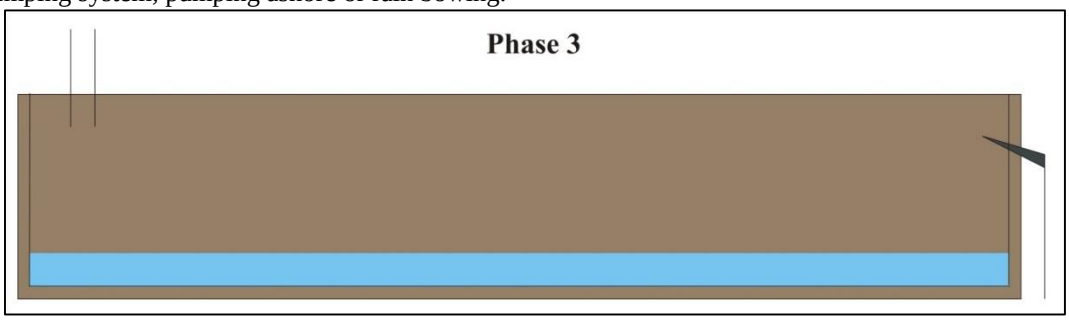

Figure 8-3: Phase 3 of the loading cycle.

- Phase 4: Pump the remaining water out of the hopper and sail to the dredging area. Often the water is not pumped out, but instead water is pumped in, to have the pumps as low as possible, in order to dredge a higher density, which should result in a shorter loading time.

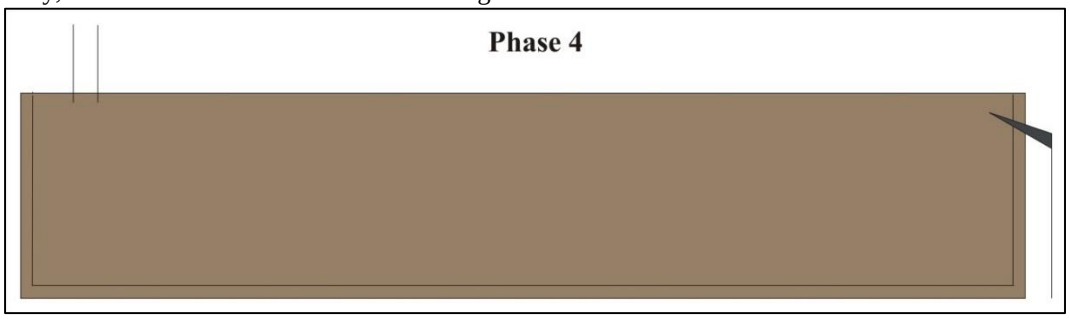

Figure 8-4: Phase 4 of the loading cycle.

- Phase 5: Start dredging and fill the hopper with mixture to the overflow level, during this phase 100% of the soil is assumed to settle in the hopper.

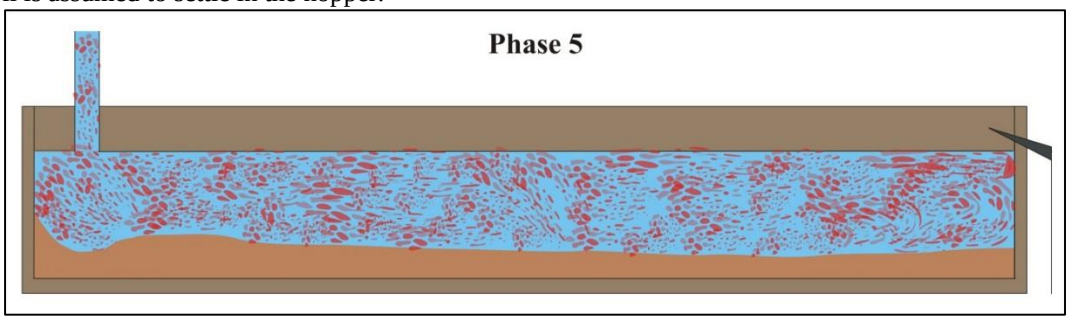

Figure 8-5: Phase 5 of the loading cycle.

- Phase 6: Continue loading with minimum overflow losses, during this phase a percentage of the grains will settle in the hopper. The percentage depends on the grain size distribution of the sand.

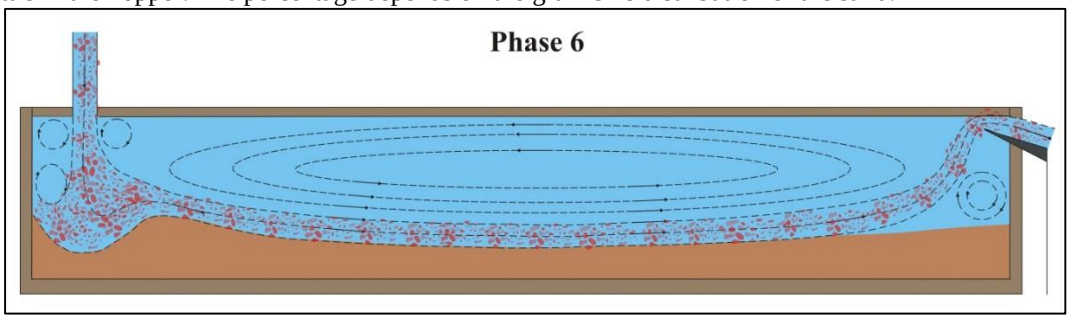

Figure 8-6: Phase 6 of the loading cycle.

- Phase 7: The maximum draught (CTS, Constant Tonnage System) is reached. From this point on the overflow is lowered.

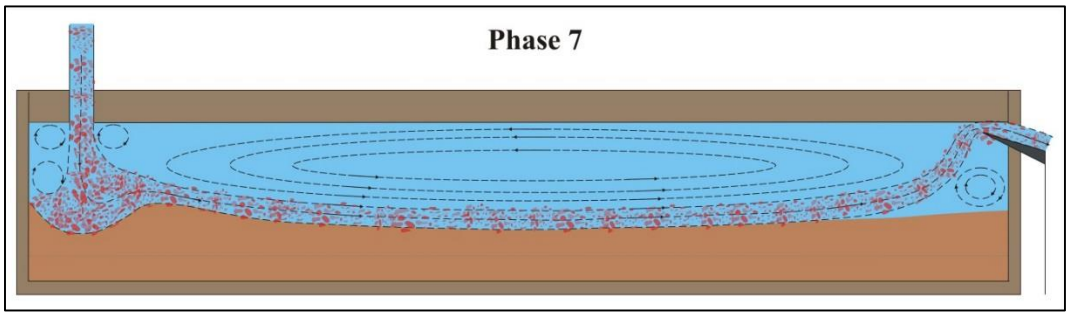

Figure 8-7: Phase 7 of the loading cycle.

- Phase 8: The sediment in the hopper is rising due to sedimentation, the flow velocity above the sediment increases, resulting in scour. This is the cause of rapidly increasing overflow losses.

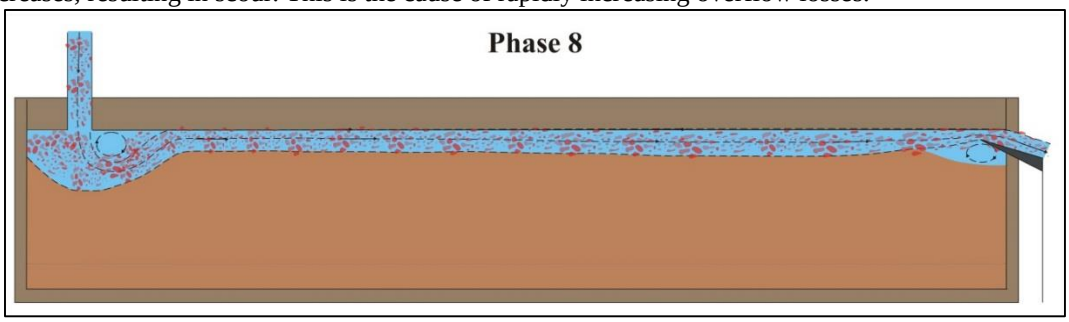

Figure 8-8: Phase 8 of the loading cycle.

Figure 8-9 and **Figure 8-10** show the total load, the effective load, the TDS and the overflow losses during these phases. The way each phase occurs in the cycle, depends on the type of hopper dredge, the working method and of course, the type of soil to be dredged.

Basically there are two main methods for loading the hopper. The 'Constant Volume System' (CVS). This system has a fixed overflow level so the effective volume of the hopper is constant. The TSHD is designed for filling the hopper with sediment with a density of 1.9-2.0 ton/m^3. The 'Constant Tonnage System' (CTS). The system has an adjustable overflow level. The hopper is designed for a density of 1.3-1.7 ton/m^3 in combination with a maximum tonnage. When the content of the hopper reaches the maximum tonnage, the overflow is lowered in order to keep the tonnage of the hopper content constant. This system has certain advantages, like reaching the maximum tonnage sooner than with CVS, resulting in the pumps to be as low as possible, giving a higher mixture density. De Koning (1977) has compared both systems.
The sedimentation in the hopper occurs during the phases 5, 6, 7 and 8. During phase 5 the hopper is filled with mixture until the overflow level is reached. During this phase 100% of the soil is assumed to stay in the hopper and settle. When the overflow level is reached, phase 6, depending on the grain distribution, a specified percentage of the soil will not settle and will leave the hopper via the overflow. During this phase scouring does not have much influence on the sedimentation process. When the maximum weight of the hopper contents is reached, the overflow will be lowered continuously in order to keep the weight of the hopper contents constant at its maximum (only CTS system). When the sediment level rises, phase 8, the flow velocity above the sediment increases and scouring will re suspend settled particles. The overflow losses increase with time. The transition between phase 5 and 6 is very sharp, as is the transition between the phases 6 and 7 for the graph of the total load, but this does not exist in the graph of the effective load (**Figure 8-10**). However, the transition between the phases 7 and 8 is not necessarily very sharp. When this transition occurs depends on the grain distribution of the soil dredged. With very fine sands this transition will be near the transition between phases 6 and 7, so phase 7 is very short or may not occur at all. With very coarse sands and gravel scouring is minimal, so phase 8 is hardly present. In this case the sediment level may be higher than the overflow level. With silt the phases 7 and 8 will not occur, since after reaching the overflow level the overflow losses will be 100%.

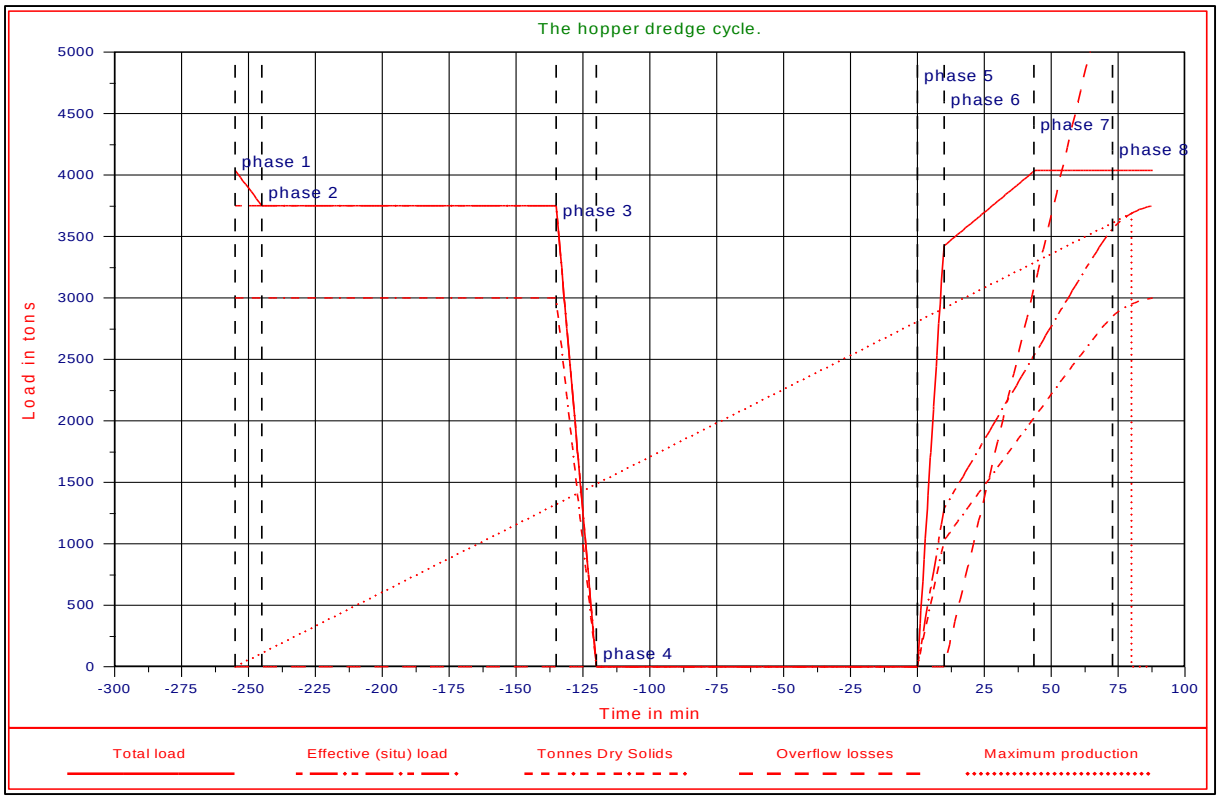

Figure 8-9: The loading cycle of a TSHD.

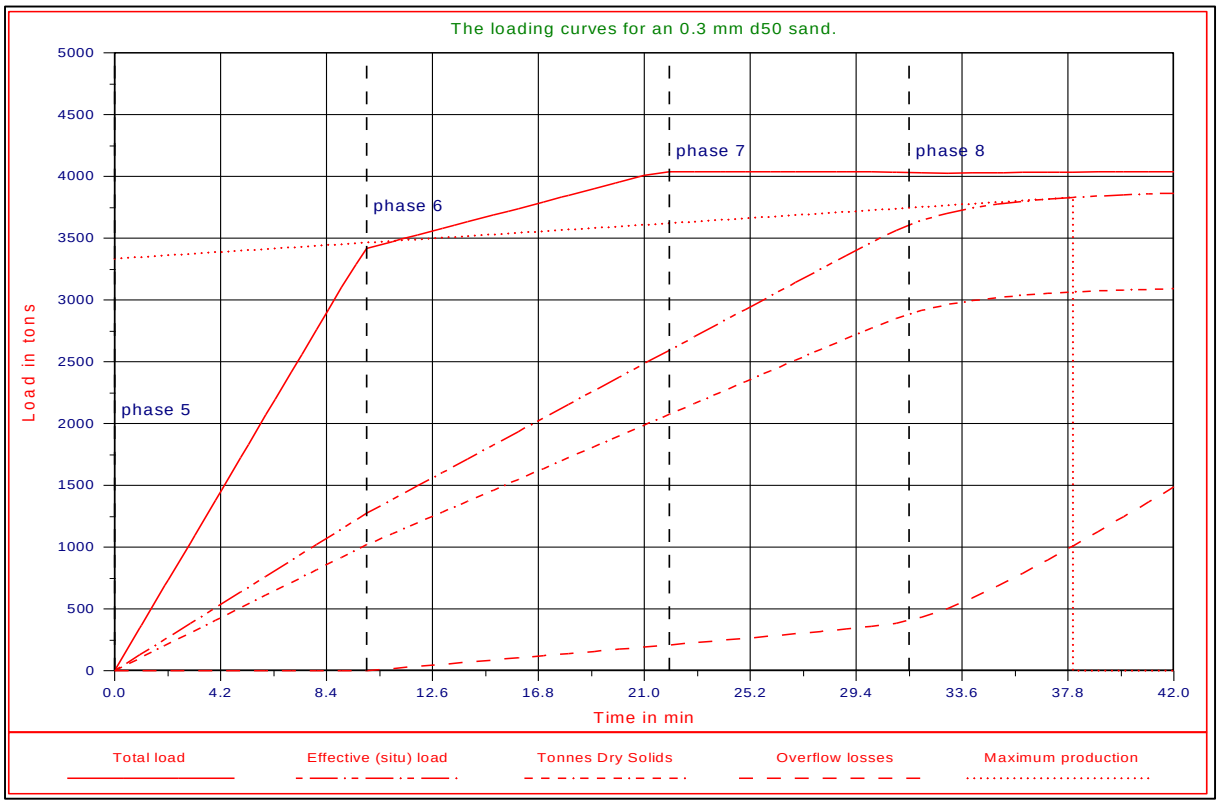

Figure 8-10: The loading part of the cycle of a TSHD.

So far the total load in the hopper has been described. A contractor is, of course, interested in the "Tonnes Dry Solids" (TDS) or situ cubic meters. The total load or gross load consists of the sediment with water in the pores and a layer of water or mixture above the sediment. The TDS consists of the weight of the soil grains only. The net weight in the hopper consists of the weight of the sediment, including the weight of the pore water. If the porosity of the sediment is considered to be equal to the in-situ porosity, then the volume of the sediment in the hopper equals the removed situ-volume. Although, in practice, there will be a difference between the in-situ porosity and the sediment porosity, here they will be considered equal. The net weight (weight of the sediment $\mathbf{W_s}$) is equal to the weight in the hopper $\mathbf{W_h}$ minus the weight of the water above the sediment $\mathbf{W_w}$:

$$W_s = W_h - W_w \tag{8-1}$$

The net volume (volume of the sediment $\mathbf{V_s}$) is equal to the volume of the hopper $\mathbf{V_h}$ minus the volume of the water above the sediment $\mathbf{V_w}$.

$$V_s = V_h - V_w \tag{8-2}$$

Multiplying the volumes with the densities gives:

$$V_s \cdot \rho_s = W_h - V_w \cdot \rho_w \quad \text{and} \quad V_w = V_h - V_s \tag{8-3}$$

$$V_s \cdot \rho_s = W_h - (V_h - V_s) \cdot \rho_w \tag{8-4}$$

$$V_s \cdot (\rho_s - \rho_w) = W_h - V_h \cdot \rho_w \tag{8-5}$$

Rearranging the terms of equation **(8-5)** gives an expression for the volume of situ cubic meters.

$$V_s = \frac{(W_h - V_h \cdot \rho_w)}{(\rho_s - \rho_w)} \tag{8-6}$$

Multiplying the situ volume $\mathbf{V_s}$ with the situ density $\boldsymbol{\rho_s}$ gives for the situ weight $\mathbf{W_s}$:

$$W_s = V_s \cdot \rho_s = \frac{(W_h - V_h \cdot \rho_w) \cdot \rho_s}{(\rho_s - \rho_w)} \tag{8-7}$$

To find the weight of the sand grains only (without the pore water), the situ density $\boldsymbol{\rho_s}$ has to be replaced by the quarts density (or particle density) $\boldsymbol{\rho_q}$:

$$TDS = W_s \cdot \frac{\rho_s - \rho_w}{\rho_q - \rho_w} \cdot \frac{\rho_q}{\rho_s} = \frac{(W_h - V_h \cdot \rho_w) \cdot \rho_q}{(\rho_q - \rho_w)} \tag{8-8}$$

The net weight (situ weight) according to equation **(8-7)** can be approximated by the total weight of the load in the hopper minus the weight of the same volume of water and the result multiplied by 2. For the TDS this factor is about 1.2, according to equation **(8-8)**. This is of course only valid for a specific density of the sediment of 2 tons per cubic meter.

With these equations the hopper cycle for the net weight and the TDS can be derived, this is shown in **Figure 8-9** and **Figure 8-10**. The hopper dredge is optimally loaded, when the effective load (weight) or the TDS divided by the total cycle time $\mathbf{dW_s/dt}$ reaches its maximum. This is shown in **Figure 8-9** and **Figure 8-10** and is the reason for the starting point of the loading cycle in Figure 8-9.

8.3. The Calculation Model.

Consider a rectangular hopper of width **W**, height **H** and length **L**. A mixture with a mixture density ρ_m and with a specified grain distribution is being dredged. Depending on the operational conditions such as dredging depth, the pump system installed, the grain distribution (PSD, Particle Size Distribution) and mixture density ρ_m, a mixture flow **Q** will enter the hopper. If the porosity **n** of the sediment is known, the flow of sediment can be determined according to:

The mass flow of the mixture into the hopper is:

$$Q_{in} \cdot \rho_m = Q_{in} \cdot (\rho_w \cdot (1-C_v) + \rho_q \cdot C_v) \quad \textbf{(8-9)}$$

The mass flow of the solids into the hopper is now:

$$\frac{dTDS}{dt} = Q_{in} \cdot \rho_q \cdot \frac{(\rho_m - \rho_w)}{(\rho_q - \rho_w)} = Q_{in} \cdot C_v \cdot \rho_q \quad \textbf{(8-10)}$$

From this, the mass flow of situ sediment into the hopper is:

$$\frac{dW_s}{dt} = Q_{in} \cdot C_v \cdot (\rho_q + e \cdot \rho_w) \quad \textbf{(8-11)}$$

With:

$$e = \frac{n}{(1-n)} \quad \textbf{(8-12)}$$

Part of this mass flow will settle in the hopper and another part will leave the hopper through the overflow. The ratio between these parts depends on the phase of the loading process. During phase 5 the hopper is loaded to the overflow level, so the mass flow into the hopper will stay in the hopper. This means that the total settling efficiency η_b during this phase equals 1. During phase 6 the loading continues until the maximum load in the hopper is reached (CTS). If scouring does not occur, the mass flow that will settle into the sediment can be calculated with equation (8-13) and (8-14), where the settling efficiency η_b should be determined with equation (8-56) and (8-57), 0.

The mass flow of the solids staying in the hopper is now:

$$\frac{dTDS}{dt} = Q_{in} \cdot C_v \cdot \rho_q \cdot \eta_b \quad \textbf{(8-13)}$$

From this, the mass flow of situ sediment into the hopper is:

$$\frac{dW_s}{dt} = Q_{in} \cdot C_v \cdot (\rho_q + e \cdot \rho_w) \cdot \eta_b \quad \textbf{(8-14)}$$

During phase 7 the loading continues, but with a CTS, the overflow is lowered to ensure that the total weight in the hopper remains constant. As scour does not yet occur, the above equation is still valid. During phase 8 scouring occurs. If scouring does occur, the mass flow that will settle into the sediment can also be calculated with equation (8-13) and (8-14), but the settling efficiency should be determined with equation (8-56) and (8-57) taking into account the effect of scouring. Scouring is the cause of increasing overflow losses. Scour depends upon the velocity of the flow above the sediment. Since in a hopper the sediment is not removed, the sediment level rises during the loading of the hopper. This means that the height of the mixture flow above the sediment decreases during the loading process, resulting in an increasing flow velocity. The scour velocity can now be determined by:

$$s_s = \frac{Q_{in}}{B \cdot H_w} \quad \textbf{(8-15)}$$

The height of the water/mixture layer $\mathbf{H_w}$ above the sediment, is equal to the overflow height **H** minus the sediment height $\mathbf{H_s}$:

$$H_w = H - H_s = H - \frac{W_s}{\rho_s \cdot W \cdot L} \tag{8-16}$$

The overflow height **H** is a constant for a Constant Volume System (CVS), but this height changes for a CTS, because the overflow is lowered from the moment, the maximum weight in the hopper is reached. If a maximum weight $\mathbf{W_m}$ is considered, the height of the layer of water above the sediment $\mathbf{H_w}$ for a CTS can be determined by:

$$H_w = \frac{W_m - \rho_S \cdot H_s \cdot B \cdot L}{\rho_W \cdot B \cdot L} \tag{8-17}$$

The hopper loading curve can now be determined by first calculating the time required to fill the hopper (phase 6), given a specified mixture flow $\mathbf{Q_{in}}$. From the mixture density $\boldsymbol{\rho_m}$ the mass and given a specified porosity, the volume of the sediment can be calculated. From this point the calculations are carried out in small time steps (phases 7 and 8). In one time step, first the height of the sediment and the height of the water layer above the sediment are determined. The height of the water layer can be determined with equation (8-16) for a CVS hopper and equation (8-17) for a CTS hopper. With equation (8-15) the scour velocity can now be determined. Using equations (8-55) the fraction of the grains that will be subject to scour can be determined. If this fraction $\mathbf{p_s}$ is zero equation (8-50) has to be used to determine the mass flow that will stay in the hopper. If this fraction is not equal to zero equation (8-56) has to be used. Equations (8-13) and (8-14) can now be used to determine the mass flow. This mass flow multiplied by the time step results in an increment of the sediment mass that is added to the already existing mass of the sediment. The total sediment mass is the starting point for the next time step. This is repeated until the overflow losses are 100%. When the entire loading curve is known, the optimum loading time can be determined. This is shown in **Figure 8-9**, where the dotted line just touches the loading curve of the effective (situ) load or the TDS. The point determined in this way gives the maximum ratio of effective load or TDS in the hopper and total cycle time. In chapter 2 and chapter 3 the determination of the settling efficiency $\boldsymbol{\eta_b}$ will be discussed in detail.

8.4. The Layer Thickness of the Layer of Water above Overflow Level

Where an obstacle is constructed on the bottom of an open channel, the water surface is raised and passes over it. Structures of this type are called weirs. Aside from special cases, flow over weirs may be regarded as steady, i.e. unchanging with respect to time, and suddenly varied, as in most hydraulic structures. The most important problem arising in connection with weirs is the relationship between the discharge over the weir and the characteristics of the weir. Many authors have suggested various relationships (e.g. Poleni, Weissbach, Boussinesq, Lauck, Pikalow) generally along the same theoretical lines and with similar results. So it seems satisfactory to introduce only the relationship of Weissbach.

$$Q_{out} = \frac{2}{3} \cdot C_e \cdot b \cdot \sqrt{2 \cdot g} \left(\left(h + \frac{v^2}{2 \cdot g} \right)^{3/2} - \left(\frac{v^2}{2 \cdot g} \right)^{3/2} \right) \tag{8-18}$$

If $\mathbf{h/(M+h)}$ tends towards zero (because **h** is small compared to **M**) then $\mathbf{v^2/2gh}$ also tends towards zero; so a simplified relationship can be reached as introduced first by Poleni about 250 years ago:

$$Q_{out} = \frac{2}{3} \cdot C_e \cdot b \cdot h \cdot \sqrt{2 \cdot g \cdot h} \tag{8-19}$$

The above equation (8-19) gives the relation between the layer thickness h and the flow $\mathbf{Q_{out}}$ for the stationary process. During the dredging process of a TSHD however, the process is not always stationary. At the start of the loading process when the overflow level is reached the layer of water will build up, while at the end when the pumps stop the layer thickness will decrease to zero. If the TSHD makes turns and the poor mixture is pumped overboard directly,

also the layer thickness will decrease and as soon as the mixture is pumped back in the hopper the layer will build up again.

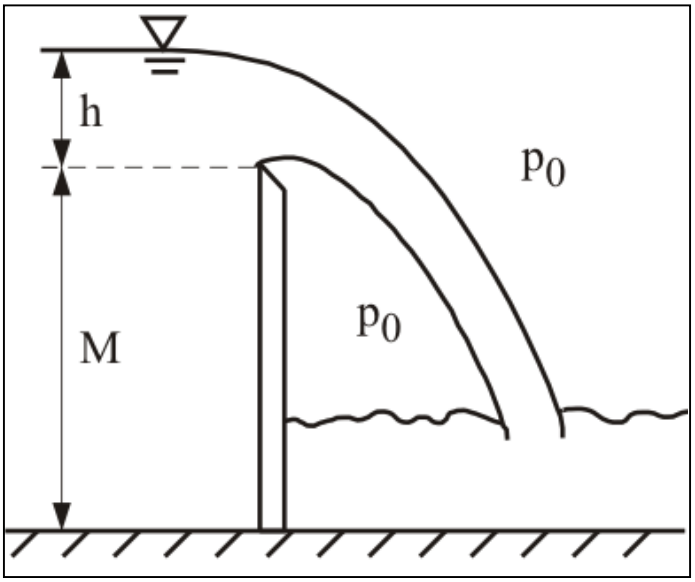

Figure 8-11: A sharp crested weir.

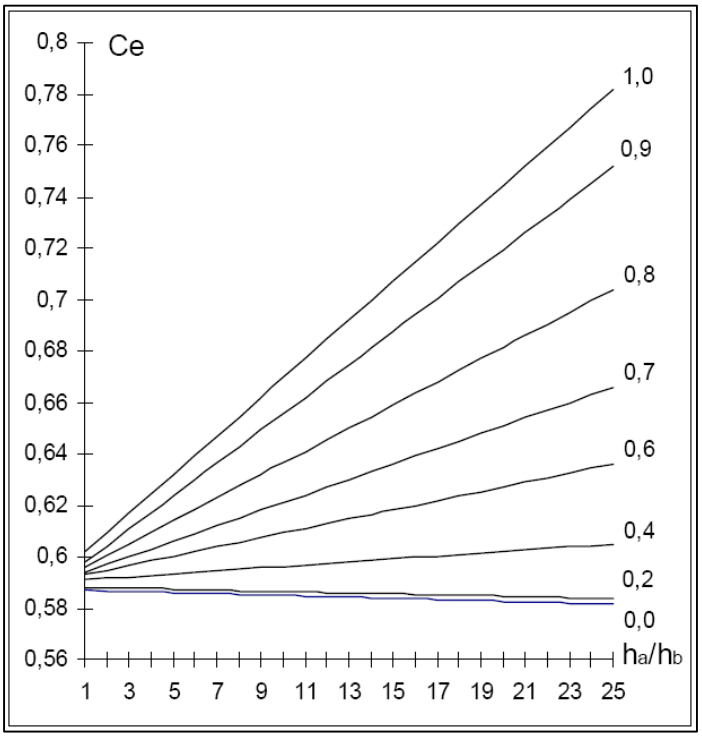

Figure 8-12: Values for the coefficient C_e as a function of $h_a/h_b=h/M$.

First the increase of the layer thickness will be considered. This increase per unit of time multiplied by the width and the length of the hopper equals the difference between the flow into the hopper and the flow leaving the hopper through the overflow according to:

$$b \cdot L \cdot \frac{dh}{dt} = Q_{in} - Q_{out} \qquad \textbf{(8-20)}$$

Substituting equation (8-19) in this equation gives a non-linear differential equation of the first order for the layer thickness **h**.

$$b \cdot L \cdot \frac{dh}{dt} = Q_{in} - C_e \cdot \frac{2}{3} \cdot \sqrt{2 \cdot g} \cdot b \cdot h^{3/2} \qquad \textbf{(8-21)}$$

This equation can be solved numerically, for example in Excel, using the starting condition **t=0**, **h=0** and the following two equations:

$$\Delta h = \frac{Q_{in} - C_e \cdot \frac{2}{3} \cdot \sqrt{2 \cdot g} \cdot b \cdot h^{3/2}}{b \cdot L} \cdot \Delta t \qquad \textbf{(8-22)}$$

$$h_{i+1} = h_i + \Delta h \qquad \textbf{(8-23)}$$

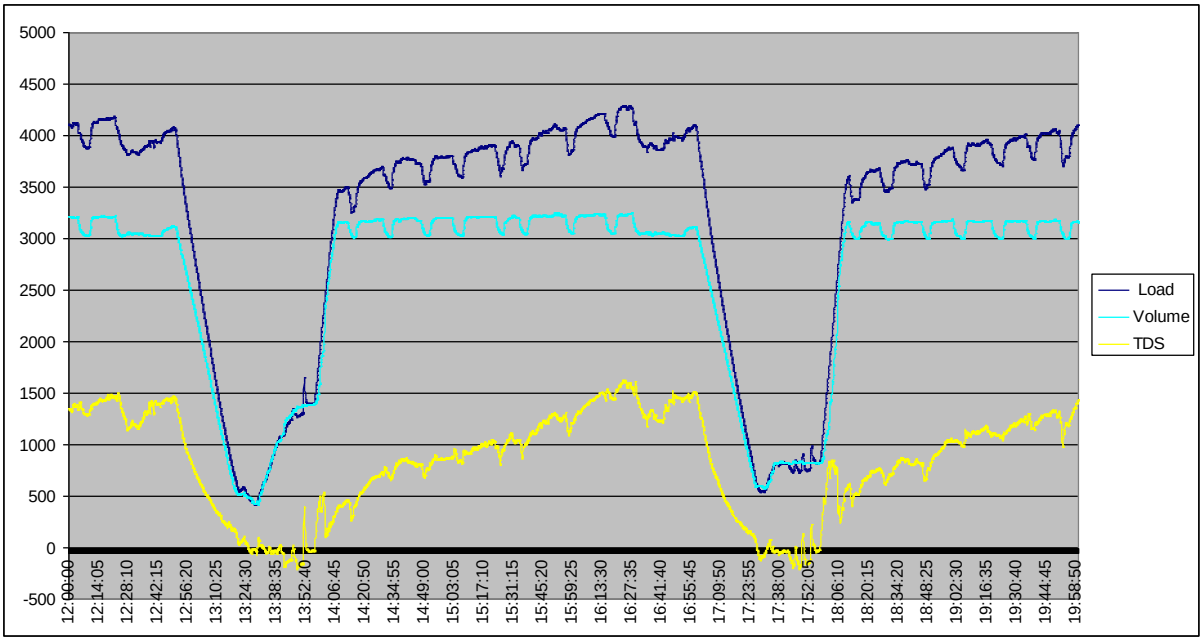

Figure 8-13: An example of a loading cycle of a TSHD with many turns.

In the equilibrium situation where $Q_{in}=Q_{out}$, the maximum layer thickness h_{max} is found according to:

$$h_{max} = \left(\frac{Q_{in}}{C_e \cdot \frac{2}{3} \sqrt{2 \cdot g} \cdot b} \right)^{2/3} = \left(\frac{Q_{in}}{2.95 \cdot C_e \cdot b} \right)^{2/3} \qquad \textbf{(8-24)}$$

From the start, **t=0**, until the maximum layer thickness is reached, h_{max}, the layer thickness **h** is a function of time that can be approximated according to:

$$h(t) = \left(\frac{Q_{in}}{2.95 \cdot C_e \cdot b} \right)^{2/3} \cdot \left\{ 1 - e^{\frac{-t}{0.452 \cdot L \cdot \left(\frac{2.95 \cdot C_e \cdot b}{Q_{in}} \right)^{1/3}}} \right\} = h_{max} \cdot \left\{ 1 - e^{-\frac{t}{\tau}} \right\} \qquad \textbf{(8-25)}$$

$$\tau = 0.452 \cdot L \cdot \left(\frac{2.95 \cdot C_e \cdot b}{Q_{in}} \right)^{1/3} = 0.452 \cdot L \cdot h_{max}^{-1/2} \qquad \textbf{(8-26)}$$

The decrease of the layer thickness h when the pumps are stopped or the poor mixture is pumped overboard follows from equation (8-20) when Q_{in} is set to zero, this can be approximated by:

$$\Delta h = \frac{-C_e \cdot \frac{2}{3} \cdot \sqrt{2 \cdot g} \cdot b \cdot h^{3/2}}{b \cdot L} \cdot \Delta t \qquad \textbf{(8-27)}$$

$$h_{i+1} = h_i + \Delta h \qquad \textbf{(8-28)}$$

Solving this gives:

$$h(t) = h_{max} - \frac{h_{max}}{\left(1 + C_d \cdot h_{max}^{2/3} \cdot t^{4/3}\right)} \quad \text{with:} \quad C_d = \frac{(3.27 + 0.0486 \cdot b)}{b^{0.22}} \cdot L^{-1.284} \qquad \textbf{(8-29)}$$

Figure 8-15 shows the discharge and the loading of the layer of water above the overflow level for a hopper with a length of 40 m, a width of 9 m and a height of 9 m and a flow of 5.8 m^3/sec. Both the exact solution and the approximation are shown versus an in situ measurement. The effective width of the overflow is assumed to be equal to the width of the hopper.

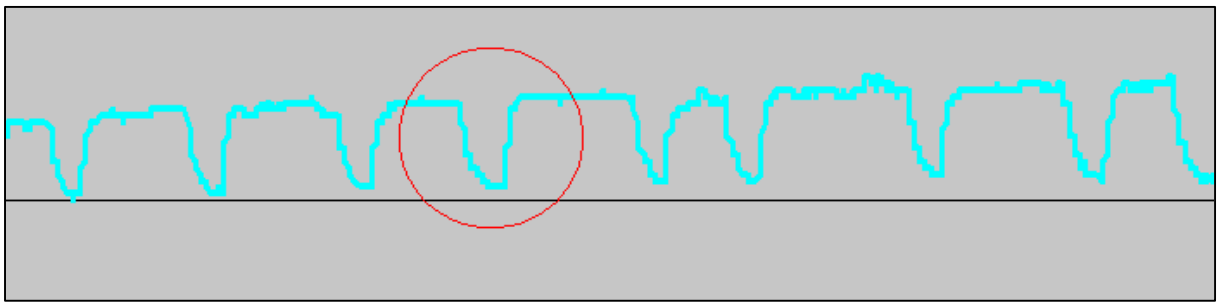

Figure 8-14: A close up of the hopper volume registration.

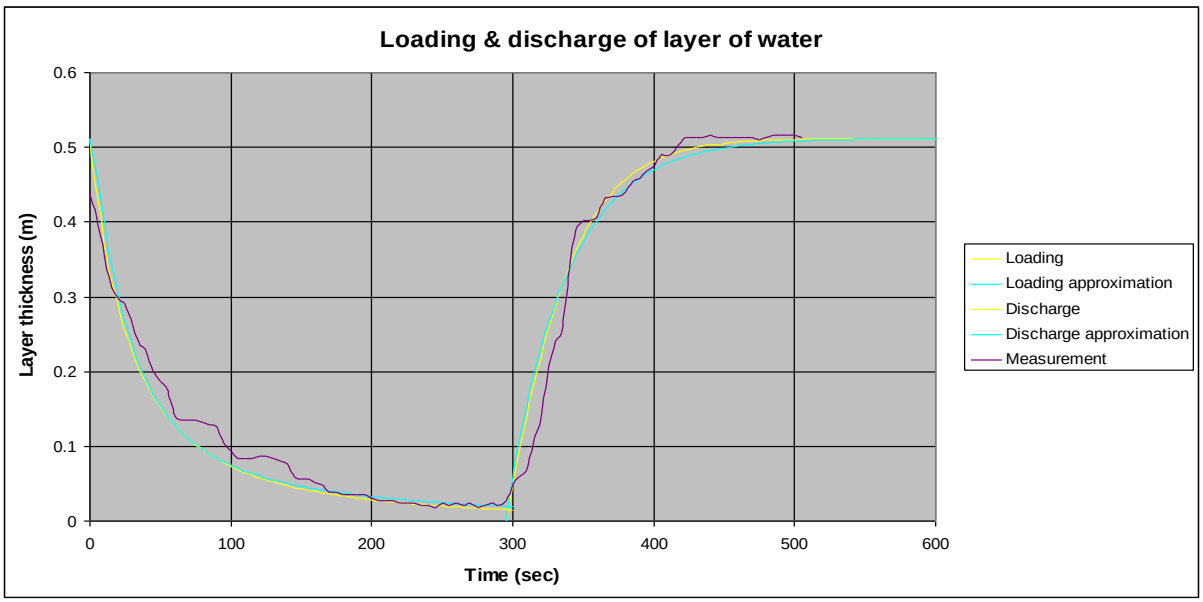

Figure 8-15: The layer thickness during a turn, registration and approximation.

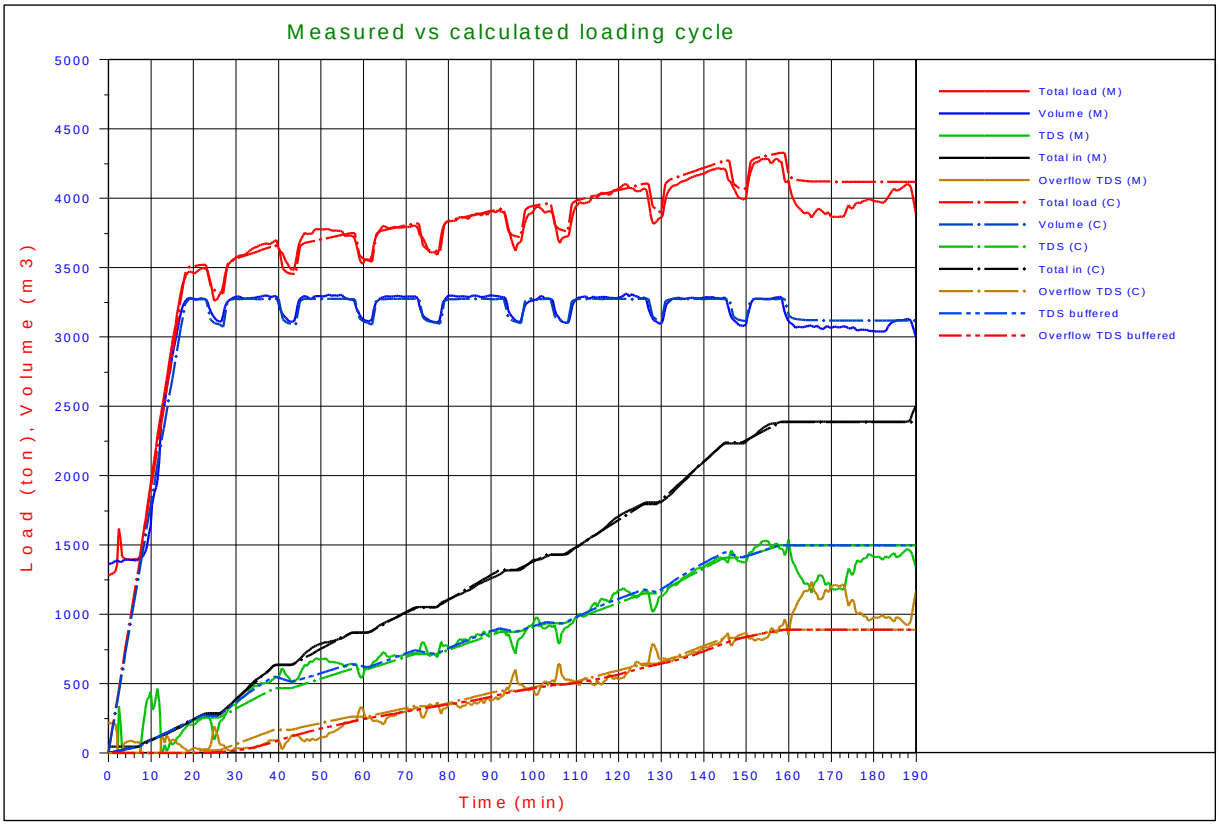

Figure 8-16: The cycle as registered is simulated with the theoretical model.

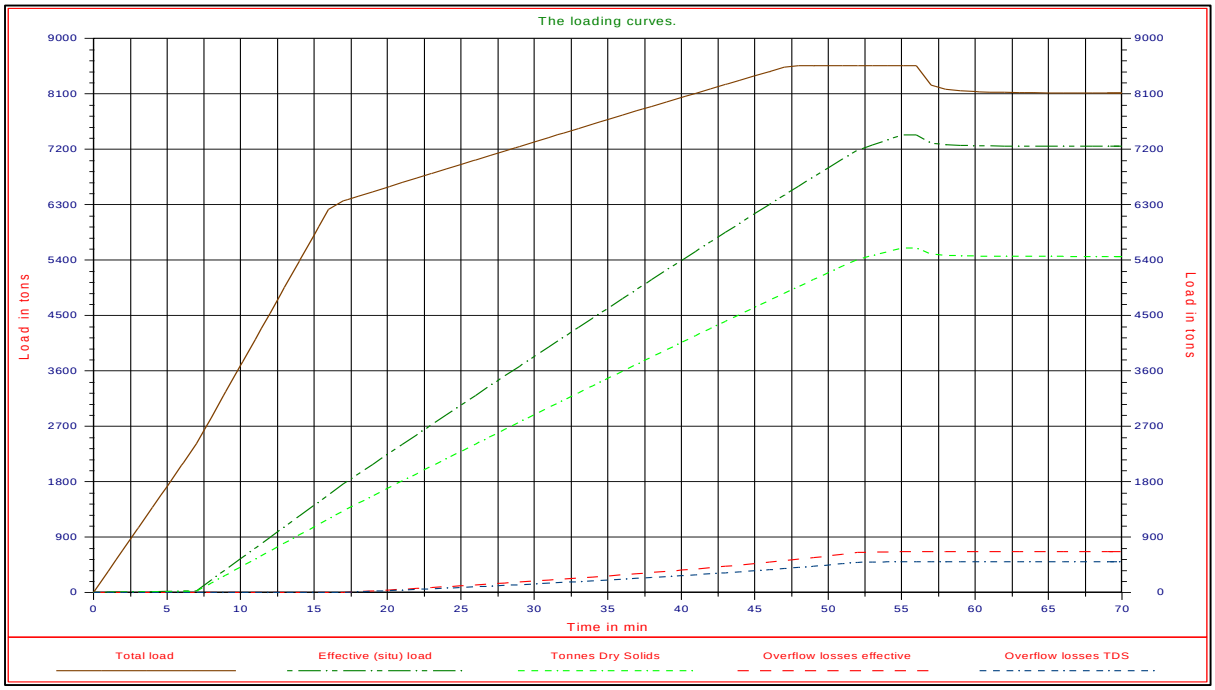

Figure 8-17: The decreasing of the height of the layer of water above the overflow at the end of the cycle.

8.5. The Storage Effect.

In the Miedema & Vlasblom model (1996) upon entrance of a particle in the hopper it is decided whether the particle will settle or not. In reality the particles that will not settle first have to move through the hopper before they reach the overflow. This means that these particles are part of the TDS in the hopper during the time they stay in the hopper. Ooijens (1999) discovered that using the time delay to determine the overflow losses improved the outcome of the Miedema & Vlasblom model (1996) considerably. Overflow losses with time delay can be derived from the overflow losses without a time delay according to the following equation:

$$ov_b(t) = \frac{1}{\tau} \cdot \int_{t-\tau}^{t} ov_c(t) \cdot dt + \frac{s}{\tau} \cdot \int_{0}^{t-\tau} (ov_c(t) - ov_b(t)) \cdot dt \qquad \textbf{(8-30)}$$

The first term in equation (8-30) gives the time delay for the situation with a constant bed height. Since the height of the bed increases during the loading process, the rising bed pushes part of the mixture out of the hopper. This is represented by the second term on the right hand.

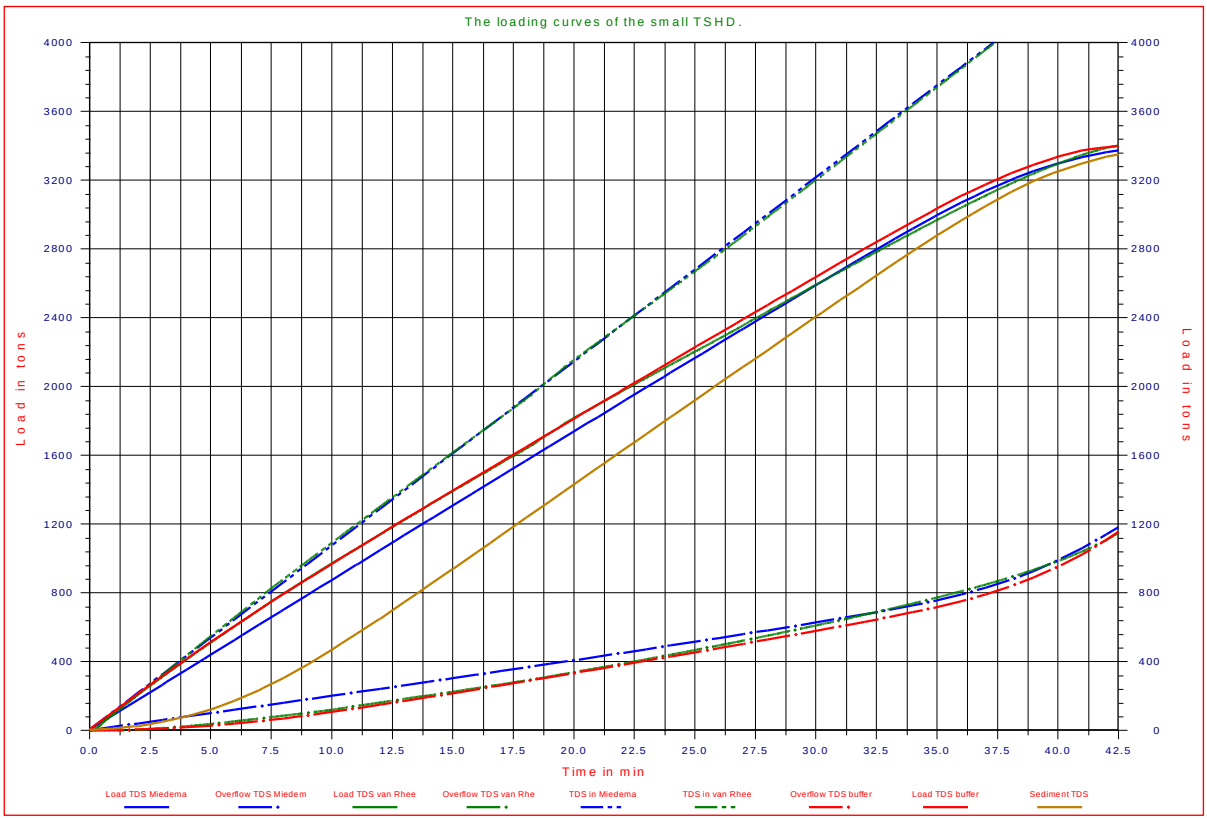

Figure 8-18: Loading curves according to Miedema & van Rhee (2007) with and without time delay.

Figure 8-18 shows the loading and overflow curves with and without the time delay or storage effect for a case considered by Miedema & van Rhee (2007). Table 8-1 gives the main data of the TSHD used in this case.

Table 8-1: The data of the TSHD used.

Hopper	Load	Volume	Length	Width	Empty height	Flow	Hopper load v_0	Mixture density
	ton	m^3	m	m	m	m^3/sec	m/sec	ton/m^3
Small	4400	2316	44.0	11.5	4.577	4	0.0079	1.3

From top to bottom Figure 8-18 contains 9 curves. The first two curves (blue and green) are almost identical and represent the TDS that enters the hopper. Since the flow and the density are constant, these curves are straight. The 3rd curve (red) represents the total TDS in the hopper according to the Miedema & Vlasblom (1996) model, so including the TDS that is still in suspension above the sediment of which part will leave the hopper through the overflow. The 4th curve (green) represents this according to van Miedema & van Rhee (2007). The 5th curve (blue)

represents the TDS that will stay in the hopper excluding the time delay effect, according to Miedema & Vlasblom (1996). The 6th (brown) curve represents the TDS in the sediment in the hopper. The 7th curve (blue) is the overflow losses according to Miedema & Vlasblom (1996), so excluding the time delay or buffering effect. The 8th curve (green) represents the overflow losses according to the 2DV model of van Rhee (2002C), which automatically includes the time delay effect. The 9th curve (red) represents the overflow losses according to the Miedema & Vlasblom (1996) model including the time delay effects according to equation (8-30).

8.6. The Hopper of a TSHD as an Ideal Settlement Basin.

As stated before, the ideal settlement basin is a rectangular basin with an entrance zone, a settlement and sedimentation zone and an overflow zone. The hopper geometry and configuration aboard of the TSHD can be quite different from the ideal situation, so a method to schematize the hopper dimensions is required.

1. The height **H** of the hopper can be defined best as the hopper volume divided by the hopper area **L·W**. This means that the base of the ideal hopper, related to the maximum overflow height is at a higher level than the ship's base. This assumption results in a good approximation at the final phases (7 and 8) of the loading process, while in phase 6 of the loading process the hopper is filled with mixture and so the material stays in the hopper anyway.

2. Near the loading chute of the hopper or in cases where a deep loading system is used, the turbulence of the flow results in a good and sufficient distribution of the concentration and particle size distribution over the cross-section of the hopper, so the entrance zone can be kept small. For example between the hopper bulkhead and the end of the loading chute.

3. In the ideal settlement basin there are no vertical flow velocities except those resulting from turbulence. However in reality vertical velocities do occur near the overflow, therefore it is assumed that the overflow zone starts where the vertical velocities exceed the horizontal velocities. An estimate of where this will occur can easily be made with a flow net.

4. Although the presence of beams and cylinder rods for the hopper doors does increase the turbulence, it is the author's opinion, that an additional allowance is not required, neither for the hopper load parameter, nor for the turbulence parameter.

5. As is shown in **Figure 8-6** and **Figure 8-7**, a density current may occur during the loading phases 6 and 7, resulting in a non-uniform velocity and density distribution. This does not affect the so called hopper load parameter as is proven in 0, so for the schematization of the hopper a uniform velocity and density distribution are assumed.

6. The validity of the schematizations and simplifications will be proven by some examples with model and prototype tests.

8.7. The Modified Camp Model.

Sedimentation is a treatment process where suspended particles, like sand and clay are re-moved from the water. Sedimentation can take place naturally in reservoirs or in compact settling installations. Sedimentation is applied in groundwater treatment installations for backwash water treatment and in TSHD's. In horizontal flow settling tanks water is uniformly distributed over the cross-sectional area of the tank in the inlet zone. A stable, non-turbulent, flow in the settling zone takes care for the settling of suspended matter in the settling zone. The sludge accumulates on the bottom, or is continuously removed. In the outlet zone the settled sludge must be prevented from being re-suspended and washed out with the effluent. Sedimentation occurs because of the difference in density between suspended particles and water. The following factors influence the sedimentation process: density and size of suspended particles, water temperature, turbulence, stability of flow, bottom scour and flocculation:

- Density, the higher the density of the particles, the faster the particles settle
- Size, the larger the particles are, the faster they settle
- Temperature, the lower the temperature of the water is, the higher the viscosity is, so the slower the particles settle
- Turbulence, the more turbulent the flow is, the slower the particles settle
- Stability, instability can result in short circuit flow, influencing the settling of particles
- Bottom scour, by bottom scour settled particles are re-suspended and washed out with the effluent

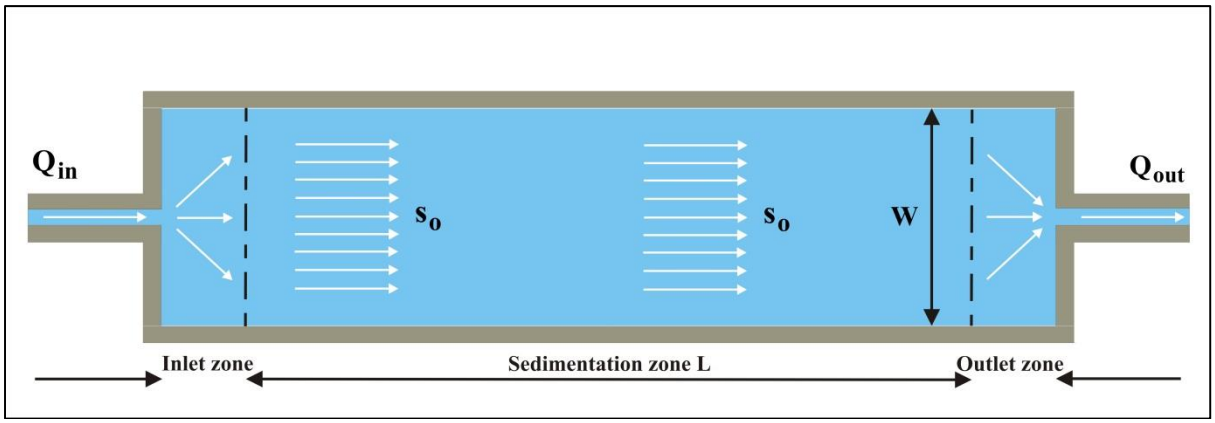

Figure 8-19: The top view of the ideal basin.

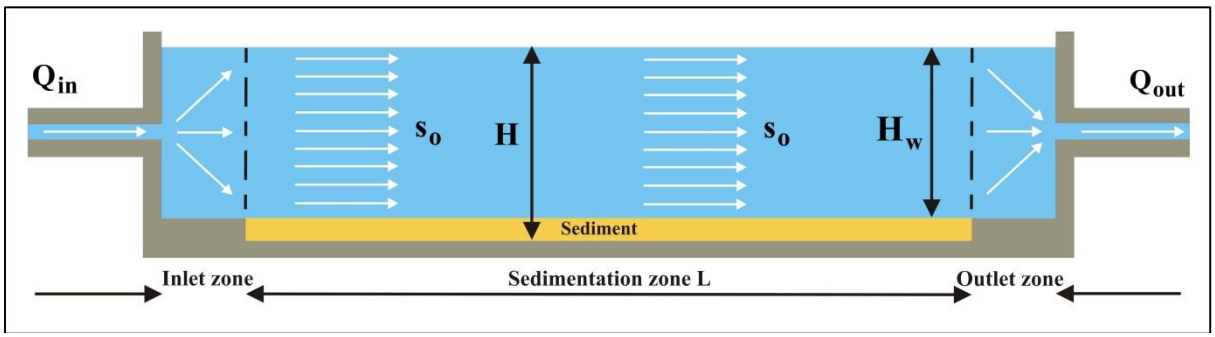

Figure 8-20: The side view of the ideal basin.

The ideal settlement basin consists of an entrance zone where the solid/fluid mixture enters the basin and where the grain distribution is uniform over the cross-section of the basin, a settlement zone where the grains settle into a sediment zone and a zone where the cleared water leaves the basin, the overflow zone. It is assumed that the grains are distributed uniformly and are extracted from the flow when the sediment zone is reached. Each particle stays in the basin for a fixed time and moves from the position at the entrance zone, where it enters the basin towards the sediment zone, following a straight line. The slope of this line depends on the settling velocity v and the flow velocity above the sediment s_o. Figure 8-19 shows a top view of the ideal settlement basin. Figure 8-20 shows the side view and Figure 8-21, Figure 8-22 and Figure 8-23 the path of individual grains. All particles with a diameter d_o and a settling velocity v_o will settle, a particle with this diameter, entering the basin at the top, reaches the end of the sediment zone. Particles with a larger diameter will all settle, particles with a smaller diameter will partially settle. Miedema & Vlasblom (1996) adapted the Camp model to be used for hopper sedimentation. The biggest difference between the original Camp (1936), (1946) and (1953) model and the Miedema & Vlasblom

model is the height H_w above the sediment zone. In the Camp model this is a fixed height, in the Miedema & Vlasblom model this height decreases during the loading process.

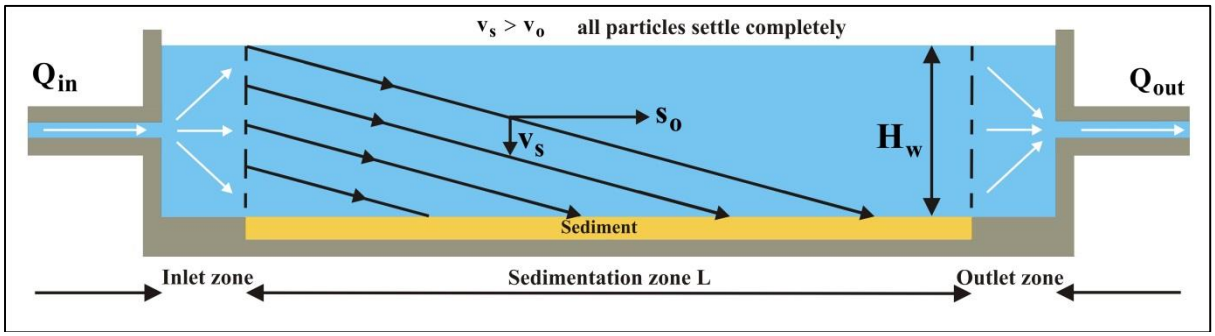

Figure 8-21: The path of a particle with a settling velocity greater than the hopper load parameter.

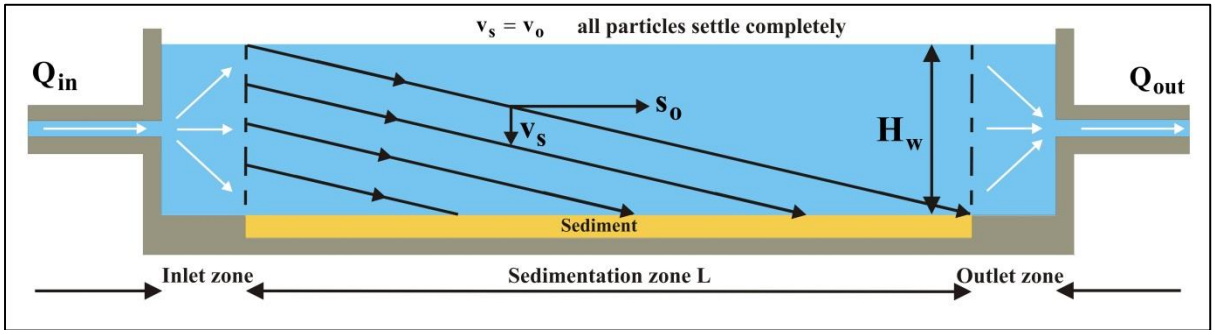

Figure 8-22: The path of a particle with a settling velocity equal to the hopper load parameter.

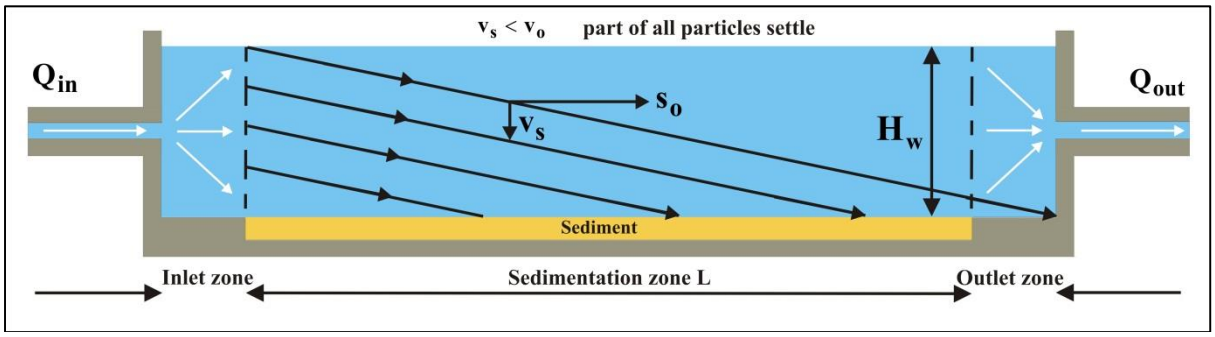

Figure 8-23: The path of a particle with a settling velocity smaller than the hopper load parameter.

The average horizontal velocity s_o in the basin, when the height H_w above the sediment is known (see equations (8-16) and (8-17)), equals to:

$$s_o = \frac{Q_{in}}{W \cdot H_w} \qquad \textbf{(8-31)}$$

The hopper load parameter v_o is defined as the settling velocity of a particle that enters the basin (hopper) at the top and reaches the sediment at the end of the basin, after traveling a distance **L,** see Figure 8-22. This can be determined according to (with a uniform velocity distribution):

$$\frac{v_o}{s_o} = \frac{H_w}{L} \quad \text{thus:} \quad v_o = s_o \cdot \frac{H_w}{L} = \frac{Q_{in}}{W \cdot L} \qquad \textbf{(8-32)}$$

If the velocity distribution is non-uniform, like in Figure 8-24, the hopper load parameter can be derived by integrating the horizontal velocity **s(z)** over the time the particle, entering at the top of the basin, needs to reach the sediment at the end, so traveling a horizontal distance **L**.

$$\int_0^T s(z)\cdot dt = L \qquad \textbf{(8-33)}$$

With:

$$T = \frac{H_w}{v'_o} \quad , \quad z = v'_o \cdot t \quad , \quad dz = v'_o \cdot dt \quad , \quad Q_{in} = W \cdot \int_0^{H_w} s(z)\cdot dz \qquad \textbf{(8-34)}$$

Equation (8-33) can be written as:

$$\frac{1}{v'_o}\cdot \int_0^{H_w} s(z)\cdot dz = \frac{1}{v'_o}\cdot \frac{Q_{in}}{W} = L \qquad \textbf{(8-35)}$$

Thus the hopper load parameter does not change because of a non-uniform velocity distribution.

$$v'_o = \frac{Q_{in}}{W \cdot L} = v_o \qquad \textbf{(8-36)}$$

During the transport of a particle from the top of the inlet to the overflow however, the sediment level rises by $\Delta H = v_{sed}\cdot\Delta t$, where Δt equals the traveling time of the particle and v_{sed} equals the sediment (bed) rise velocity. The thickness of the layer of fluid above the sediment thus decreases from H_w when the particle enters the hopper to $H_w - \Delta H$ when the particle reaches the sediment at the end of the hopper due to the settling velocity of the particle. The average thickness H_a of the layer of water above the sediment during the transport of the particle is now:

$$H_a = H_w - 0.5\cdot\Delta H \qquad \textbf{(8-37)}$$

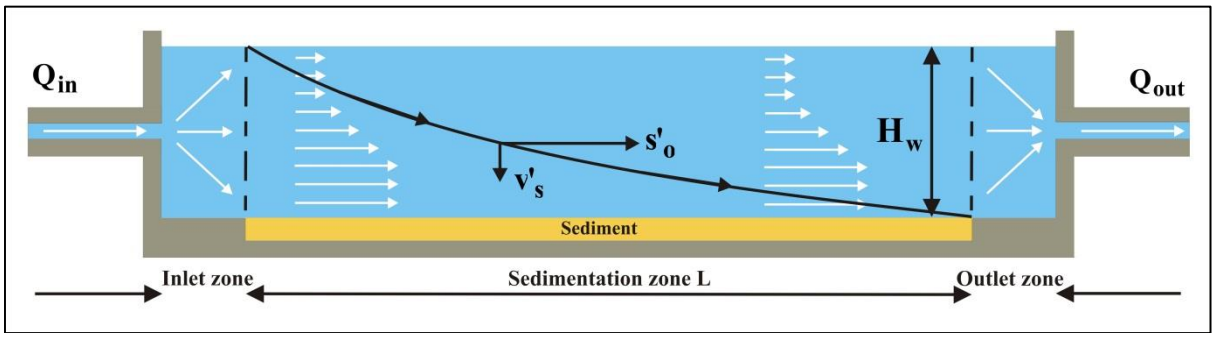

Figure 8-24: The path of a particle with a non-uniform velocity distribution.

The average horizontal velocity s_o in the hopper during the stay of the particle in the hopper is thus:

$$s_o = \frac{Q_{in}}{W\cdot(H_w - 0.5\cdot\Delta H)} = \frac{Q_{in}}{W\cdot H_a} \qquad \textbf{(8-38)}$$

The time it takes for the particle to be transported over the length of the hopper is thus:

$$\Delta t = \frac{L}{s_o} = \frac{W\cdot L\cdot H_a}{Q_{in}} \qquad \textbf{(8-39)}$$

The vertical distance traveled by a particle that enters the hopper at the top and just reaches the sediment at the end of the hopper is (see Figure 8-25):

$$v_{oo}\cdot\Delta t = v_{oo}\cdot\frac{W\cdot L\cdot H_a}{Q_{in}} = H_w - \Delta H = H_a - 0.5\cdot\Delta H \qquad \textbf{(8-40)}$$

This gives for the settling velocity of such a particle:

$$v_{oo} = \frac{Q_{in}}{W \cdot L \cdot H_a} \cdot (H_a - 0.5 \cdot \Delta H) = \frac{Q_{in}}{W \cdot L} \cdot \left(1 - \frac{0.5 \cdot \Delta H}{H_a}\right) \quad \textbf{(8-41)}$$

With:

$$\Delta H = v_{sed} \cdot \Delta t = v_{sed} \cdot \frac{W \cdot L \cdot H_a}{Q_{in}} \quad \textbf{(8-42)}$$

This gives for the modified hopper load parameter:

$$v_{oo} = \frac{Q_{in}}{W \cdot L} - \frac{v_{sed}}{2} \quad \textbf{(8-43)}$$

A smaller hopper load parameter means that smaller grains will settle easier. From Figure 8-21 the conclusion can be drawn that grains with a settling velocity greater than v_o will all reach the sediment layer and thus have a settling efficiency η_g of 1. Grains with a settling velocity smaller then v_o, Figure 8-23, will only settle in the sedimentation zone, if they enter the basin below a specified level. This gives for the modified settling efficiency of the individual grain:

$$\eta_{gg} = \left(\frac{v_s}{v_{oo}}\right) \quad \textbf{(8-44)}$$

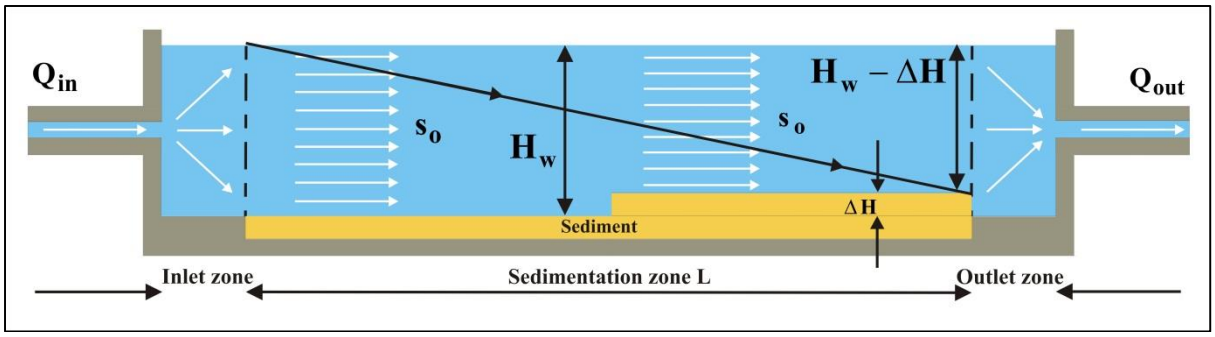

Figure 8-25: The effect of a rising sediment level.

In the case of a non-uniform velocity distribution, Figure 8-24, the settling efficiency can also be defined as the ratio of the horizontal distances traveled in the time a particle needs to reach the sediment, although this is not 100% true because the ratio of the vertical distance traveled gives the exact settling efficiency, it's a good approximation:

$$\eta_g = \left(\frac{L_{v_o}}{L_v}\right) \quad \textbf{(8-45)}$$

The horizontal distance traveled by a particle in the time to reach the sediment level is:

$$L_v = \int_0^T s(z) \cdot dt \quad \textbf{(8-46)}$$

With:

$$T = \frac{H_w}{v_s} \quad , \quad z = v_s \cdot t \quad , \quad dz = v_s \cdot dt \quad , \quad Q_{in} = W \cdot \int_0^{H_w} s(z) \cdot dz \qquad \textbf{(8-47)}$$

Equation (8-47) can be written as:

$$\frac{1}{v_s} \cdot \int_0^{H_w} s(z) \cdot dz = \frac{1}{v_s} \cdot \frac{Q_{in}}{W} = L_v \qquad \textbf{(8-48)}$$

This also gives a settling efficiency according to:

$$\eta_g = \left(\frac{v_s}{v_o} \right) \qquad \textbf{(8-49)}$$

The settling efficiency of a particle with a settling velocity smaller than the hopper load parameter $\mathbf{v_o}$, does not change due to a non-uniform velocity distribution. If the fraction of grains with a settling velocity greater than $\mathbf{v_o}$ equals $\mathbf{p_o}$, then the settling efficiency for a grain distribution $\boldsymbol{\eta_b}$ can be determined by integrating the grain settling efficiency for the whole grain distribution curve, according to Figure 8-26. The blue surface equals the basin settling efficiency according to equation (8-50).

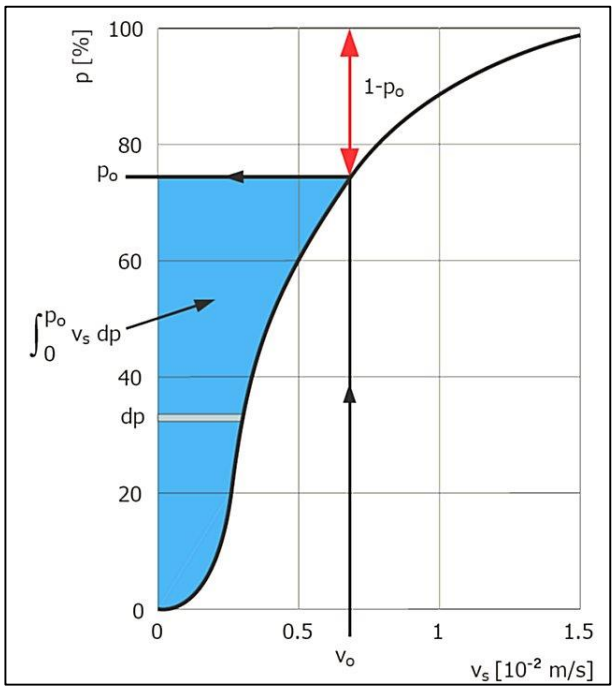

Figure 8-26: Determination of the basin settling efficiency.

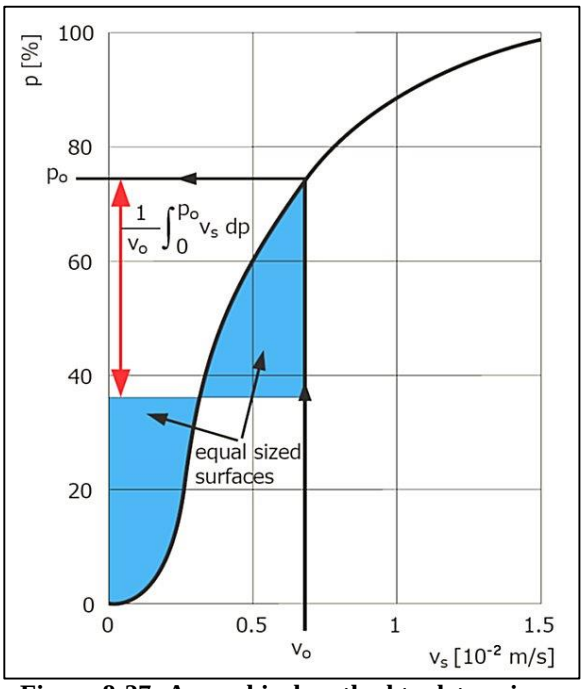

Figure 8-27: A graphical method to determine the settling efficiency.

$$\eta_b = (1 - p_o) + \int_0^{p_o} \eta_g \cdot dp \qquad \textbf{(8-50)}$$

In theory a particle is removed from the water when it reaches the bottom of the settling tank. In practice, however, it is possible that re-suspension of already settled particles occurs.
When the sediment level in the hopper is rising, the horizontal velocity increases and there will be a point where grains of a certain diameter will not settle anymore due to scour. First the small grains will not settle or erode and when the level increases more, also the bigger grains will stop settling, resulting in a smaller settling efficiency. The effect of scour is taken into account by integrating with the lower boundary $\mathbf{p_s}$. The fraction $\mathbf{p_s}$ is the fraction of the grains smaller then $\mathbf{d_s}$, matching a horizontal velocity in the hopper of $\mathbf{s_s}$.
The shear force of water on a spherical particle is:

$$\tau = \frac{1}{4} \cdot \lambda \cdot \frac{1}{2} \cdot \rho_w \cdot s_s^2 \qquad \textbf{(8-51)}$$

The shear force of particles at the bottom (mechanical friction) is proportional to the submerged weight of the sludge layer, per unit of bed surface (see Figure 8-28):

$$f = \mu \cdot N = \mu \cdot (1-n) \cdot (\rho_q - \rho_w) \cdot g \cdot d \qquad \textbf{(8-52)}$$

In equilibrium the hydraulic shear equals the mechanical shear and the critical scour velocity can be calculated. The scour velocity for a specific grain with diameter $\mathbf{d_s}$, according to Huisman (1973-1995) and (1980) is:

$$s_s = \sqrt{\frac{8 \cdot \mu \cdot (1-n) \cdot (\rho_q - \rho_w) \cdot g \cdot d_s}{\lambda \cdot \rho_w}} \qquad \textbf{(8-53)}$$

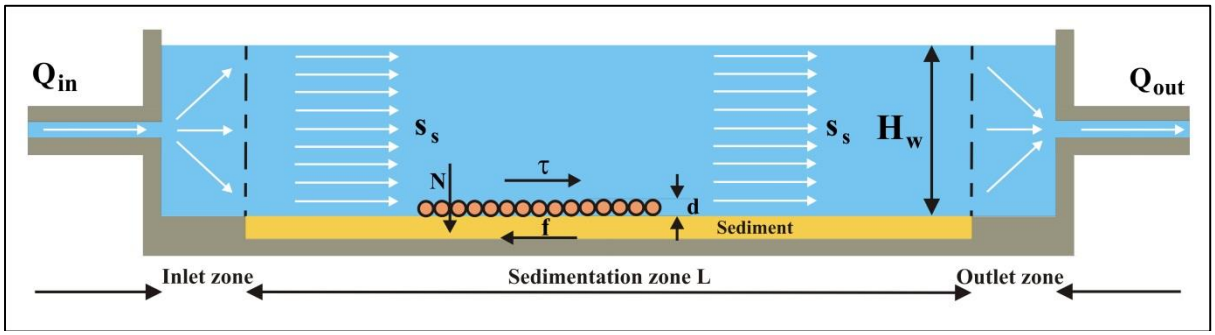

Figure 8-28: The equilibrium of forces on a particle.

With $\mu \cdot (1-n) = 0.05$ and $\lambda = 0.03$ this gives:

$$s_s = \sqrt{\frac{40 \cdot (\rho_q - \rho_w) \cdot g \cdot d_s}{3 \cdot \rho_w}} \qquad \textbf{(8-54)}$$

The particle diameter of particles that will not settle due to scour (and all particles with a smaller diameter) is:

$$d_s = \frac{3 \cdot \rho_w}{40 \cdot (\rho_q - \rho_w) \cdot g} \cdot s_s^2 \qquad \textbf{(8-55)}$$

Knowing the diameter $\mathbf{d_s}$, the fraction $\mathbf{p_s}$ that will not settle due to scour can be found if the PSD of the sand is known. Equation (8-54) is often used for designing settling basins for drinking water. In such basins scour should be avoided, resulting in an equation with a safety margin. For the prediction of the erosion during the final phase of the settling process in TSHD's a more accurate prediction of the scour velocity is required, which will be discussed in another chapter. The settling efficiency η_g, but this only occurs at the end of the loading cycle, can now be corrected for scour according to:

$$\eta_b = (1 - p_o) + \int_{p_s}^{p_o} \eta_g \cdot dp \qquad \textbf{(8-56)}$$

When $p_s > p_o$ this results in:

$$\eta_b = (1 - p_s) \qquad \textbf{(8-57)}$$

8.8. The Influence of Turbulence.

For the ideal settlement basin laminar flow is assumed. Turbulent flow will reduce the settling velocity of the grains and thus the total settling efficiency. Whether turbulent flow occurs, depends on the Reynolds number of the flow in the basin. Using the hydraulic radius concept this number is:

$$Re = \frac{Q_{in}}{\nu \cdot (W + 2 \cdot H_w)} \tag{8-58}$$

For a given flow Qi_n and viscosity ν the Reynolds number depends on the width **W** and the height H_w of the layer of fluid in the basin. A large width and height give a low Reynolds number. However this does not give an attractive shape for the basin from an economical point of view, which explains why the flow will be turbulent in existing basins.

Dobbins (1944) and Camp (1946) and (1953) use the two-dimensional turbulent diffusion equation to determine the resulting decrease of the settling efficiency.

$$s(z) \cdot \frac{\partial c}{\partial x} = \varepsilon_z \cdot \frac{\partial^2 c}{\partial z^2} + \left(v(c) + \frac{\partial \varepsilon_z}{\partial z} \right) \cdot \frac{\partial c}{\partial z} + \varepsilon_x \cdot \frac{\partial^2 c}{\partial x^2} \tag{8-59}$$

Assuming a parabolic velocity distribution instead of the logarithmic distribution, neglecting diffusion in the x-direction and considering the settling velocity independent of the concentration reduces the equation to:

$$\left(s_t - k \cdot (h - z)^2 \right) \cdot \frac{\partial c}{\partial x} = \varepsilon_z \cdot \frac{\partial^2 c}{\partial z^2} + v \cdot \frac{\partial c}{\partial z} \tag{8-60}$$

Because of the parabolic velocity distribution, the turbulent diffusion coefficient ε_z is a constant. A further simplification is obtained if the velocity **s** is assumed constant throughout the depth, meaning that the constant of the parabola **k** approaches zero. In this case the turbulent diffusion equation becomes:

$$\frac{\partial c}{\partial t} = s \cdot \frac{\partial c}{\partial x} = \varepsilon_z \cdot \frac{\partial^2 c}{\partial z^2} + v \cdot \frac{\partial c}{\partial z} \tag{8-61}$$

Huisman (1973-1995) in his lecture notes derives the diffusion-dispersion equation in a more general form, including longitudinal dispersion.

$$\frac{\partial c}{\partial t} + \frac{\partial (s \cdot c)}{\partial x} = \frac{\partial}{\partial x} \cdot \left(\varepsilon_x \cdot \frac{\partial c}{\partial x} \right) + \frac{\partial}{\partial z} \cdot \left(v \cdot c + \varepsilon_z \cdot \frac{\partial c}{\partial z} \right) \tag{8-62}$$

Assuming a steady and uniform flow, the longitudinal dispersion coefficient is independent of **x** and the settling velocity **v** independent of **z**. This reduces the equation 18 to:

$$s \cdot \frac{\partial c}{\partial x} = \varepsilon_z \cdot \frac{\partial^2 c}{\partial z^2} + v \cdot \frac{\partial c}{\partial z} + \varepsilon_x \cdot \frac{\partial^2 c}{\partial x^2} \tag{8-63}$$

By means of computations Huisman (1973-1995) shows that the retarding effect of dispersion may be ignored for the commonly applied width to depth ratio 3 to 5. This reduces equation (8-62) to equation (8-59) of Dobbins and Camp.

Groot (1981) investigated the influence of hindered settling and the influence of different velocity distributions using the following equation:

$$s \cdot \frac{\partial c}{\partial x} = v(c) \cdot \frac{\partial c}{\partial z} + c \cdot \frac{\partial v(c)}{\partial c} \cdot \frac{\partial c}{\partial z} + \frac{\partial}{\partial z} \cdot \left(\varepsilon(x,z) \cdot \frac{\partial c}{\partial z} \right) \tag{8-64}$$

The velocity distribution, the diffusion coefficient distribution and the distribution of the initial concentration did not have a significant influence on the computed results, but the results were very sensitive on the formulation of hindered settling. This formulation of course influences the settling velocity in general. Equation (8-63) can be solved analytically using separation of variables. The boundary conditions used by Camp and Dobbins describe the rate of vertical transport across the water surface and the sediment for **x=∞** and the concentration distribution at the inlet, these are:

$$\varepsilon \cdot \frac{\partial c}{\partial z} + v \cdot c = 0 \qquad \text{at the water surface} \qquad \textbf{(8-65)}$$

$$\varepsilon \cdot \frac{\partial c}{\partial z} + v \cdot c = 0 \qquad \text{at the sediment for } \mathbf{x=\infty}\text{, for the no-scour situation} \qquad \textbf{(8-66)}$$

$$c = f(z) \qquad \text{at the entrance for } \mathbf{x=0} \qquad \textbf{(8-67)}$$

This method, resulting in Figure 8-29, Figure 8-30 and Figure 8-31, gives the removal ration due to turbulence for a single grain. The removal ratio can be determined by summation of a series.
Solving equation (8-64) gives ($\mathbf{v \cdot H/2 \cdot \varepsilon_z}$) as the independent parameter on the horizontal axis and the removal ratio ($\mathbf{v/v_o}$=settling efficiency) on the vertical axis. Using a parabolic velocity distribution this can be substituted by:

$$\frac{v \cdot H}{2 \cdot \varepsilon_z} = \frac{v}{s_o} \cdot \frac{3}{\kappa} \cdot \sqrt{\frac{8}{\lambda}} = 122 \cdot \frac{v}{s_o} \qquad \text{with: } \kappa\mathbf{=0.4} \text{ and } \lambda\mathbf{=0.03} \qquad \textbf{(8-68)}$$

Figure 8-29, Figure 8-30 and Figure 8-31 give the removal ratio or settling efficiency for individual particles for values of **λ** of 0.01, 0.02 and 0.03.

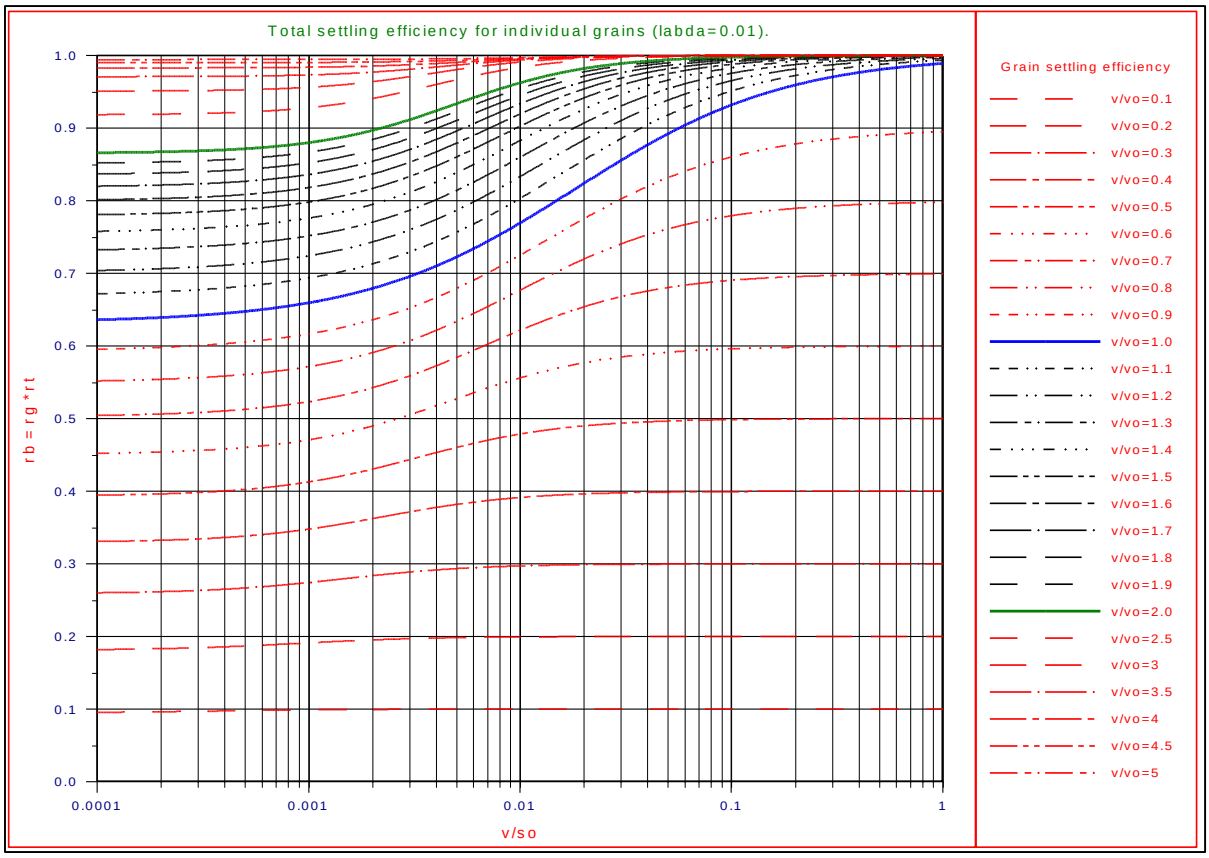

Figure 8-29: The total settling efficiency for λ=0.01.

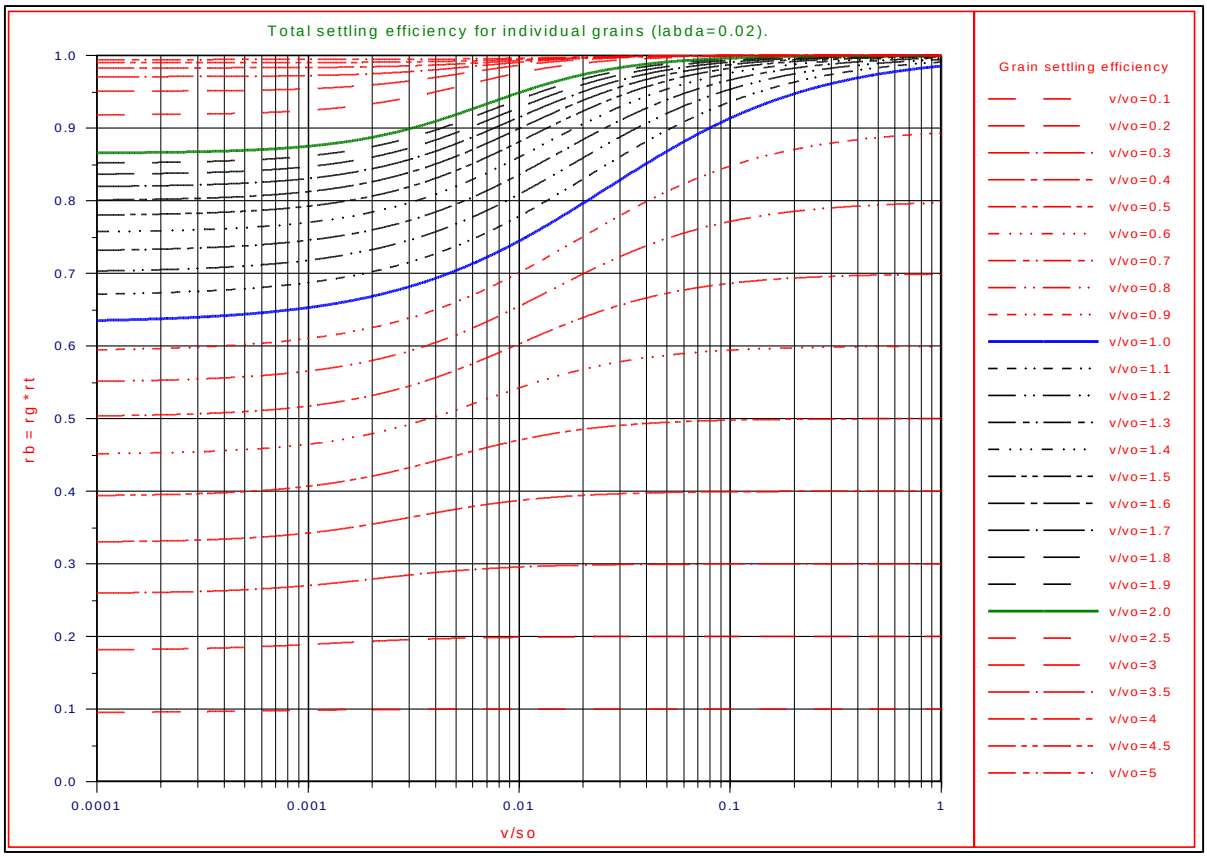

Figure 8-30: The total settling efficiency for λ=0.02.

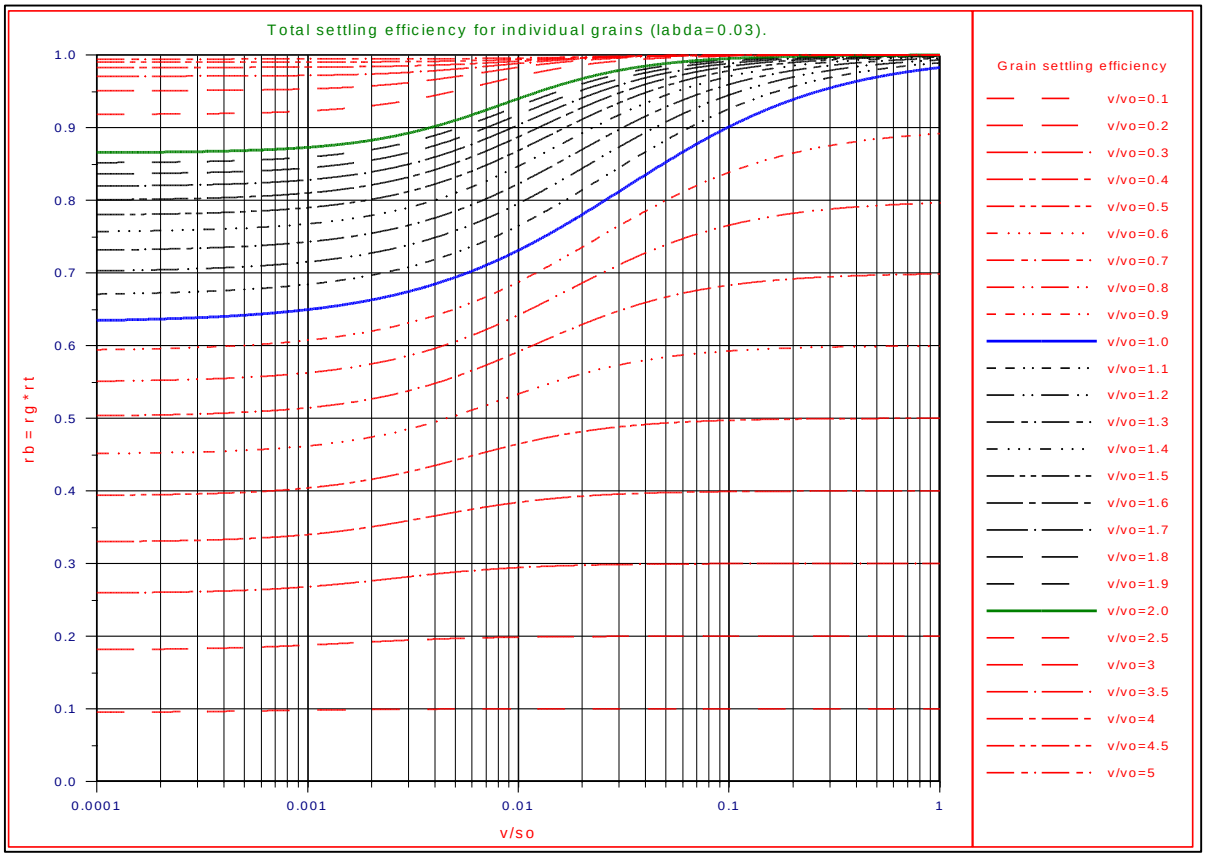

Figure 8-31: The total settling efficiency for λ=0.03.

The settling efficiency for $v/v_o<1$ can be approximated by equation (8-69), while equation (8-70) gives a good approximation for the case $v/v_o>1$:

$$\eta_t = \eta_g^{0} \cdot \left(1 - .184 \cdot \eta_g^{+.885-.20\cdot\eta_g} \cdot \left(1 - TanH\left(\eta_g^{-.13-.80\cdot\eta_g} \cdot \left(Log\left(\frac{v}{s_o}\right) - .2614 - .5 \cdot Log(\lambda) + \eta_g^{-.33-.94\cdot\eta_g}\right)\right)\right)\right) \quad \textbf{(8-69)}$$

$$\eta_t = \eta_g^{-1} \cdot \left(1 - .184 \cdot \eta_g^{-.69-.38\cdot\eta_g} \cdot \left(1 - TanH\left(\eta_g^{+.77-.08\cdot\eta_g} \cdot \left(Log\left(\frac{v}{s_o}\right) - .2614 - .5 \cdot Log(\lambda) + \eta_g^{+1.01-.18\cdot\eta_g}\right)\right)\right)\right) \quad \textbf{(8-70)}$$

The effect of turbulence is taken into account by multiplying the settling efficiency with the turbulence efficiency η_t according to Miedema & Vlasblom (1996). Since the turbulence efficiency is smaller than 1 for all grains according to the equations (8-69) and (8-70), the basin settling efficiency can be determined with equation (8-71), where p_s equals 0 as long as scour does not occur. So the total settling efficiency is now:

$$\eta_b = \int_{p_s}^{1} \eta_g \cdot \eta_t \cdot dp \quad \textbf{(8-71)}$$

8.9. Comparing the Miedema and the van Rhee Models.

8.9.1. Introduction.

This chapter is based on Miedema & van Rhee (2007).
In the past two decades the size of TSHD's has tripled and there are plans for TSHD's in the range of 50.000 m^3. When enlarging hoppers there are some limitations like the draught of the vessel and the line velocity in the suction lines. It's interesting to compare the influences of length, width, height ratio's, flow capacity and some other parameters on the production and the overflow losses of TSHD's. To do so, mathematical models have been developed to simulate the sedimentation process in the hopper. Two models will be used and compared, first the model of Vlasblom/Miedema (1995), Miedema/Vlasblom (1996) and Miedema (2008A) and second the more sophisticated 2DV model of van Rhee (2002C), which is verified and validated with model and prototype tests. Both models are explained briefly. With the two models 3 cases are analyzed, a 2316 m^3, a 21579 m^3 and a 36842 m^3 hopper. The results of the case studies give the following conclusions and recommendations:

- The two models give the same magnitude for the overflow losses, but the shape of the curves is different due to the differences in the physical modeling of the processes.
- Due to the lower losses the computed optimal loading time will be shorter for the Vlasblom /Miedema approach.
- The strong point of the van Rhee model is the accurate physical modeling, giving the possibility to model the geometry of the hopper in great detail, but also describing the physical processes in more detail.
- The van Rhee model is verified and validated with model and prototype tests and can be considered a reference model for other models.
- The strong point of the Miedema/Vlasblom model is the simplicity, giving a transparent model where result and cause are easily related.

From a scientific point of view it is interesting to compare the sophisticated van Rhee model with the simplified models and to do so, the van Rhee (2002C) model is compared with the Miedema (2008A) model. The comparison consists of a number of cases regarding real TSHD's. The following TSHD's will be compared:

Table 8-2: The data of the TSHD's used.

Hopper	Load	Volume	Length	Width	Empty height	Flow	Hopper load v_0	Mixture density
	ton	m^3	m	m	m	m^3/sec	m/sec	ton/m^3
Small	4400	2316	44.0	11.5	4.577	4	0.0079	1.3
Jumbo	41000	21579	79.2	22.4	12.163	14	0.0079	1.3
Mega	70000	36842	125.0	30.0	9.825	19	0.0051	1.3

Further it is assumed that all 3 TSHD's have a design density of 1.9 ton/m^3 and they operate according to the CVS system (no adjustable overflow). This gives a sand fraction of 0.54 and a porosity of 0.46. For the calculations a sand with a $\mathbf{d_{50}}$ of 0.4 mm is chosen, according to figure 1. The particle size distribution is chosen in such a way that there is a reasonable percentage of fines in order to have moderate overflow losses.

8.9.2. Case Studies with the Camp/Miedema Model.

The calculations according to the modified Camp/Miedema model as developed by Miedema (1981) and published by Vlasblom & Miedema (1995), Miedema & Vlasblom (1996) and Miedema (2008A) are carried out with the program TSHD (developed by Miedema). The effects of hindered settling, turbulence and scour and an adjustable overflow are implemented in this program as described previously.
The program assumes that first the hopper is filled with mixture up to the overflow level and all the grains entering the hopper during this phase will stay in the hopper, so the overflow losses are 0 during this phase. The table below shows the filling time, the total load and the TDS at the end of this phase.

Table 8-3: The hopper content after the filling phase.

Hopper	Load	Volume	Flow	Filling time	Total load	TDS	Overflow losses	Mixture density
	ton	m^3	m^3/sec	min	ton	ton	%	ton/m^3
Small	4400	2316	4	9.65	3011	1039	20.0	1.3
Jumbo	41000	21579	14	25.69	28053	9678	20.0	1.3
Mega	70000	36842	19	32.32	47895	16523	16.6	1.3

After this phase the program will determine the total settling efficiency and based on this the increase of the sediment and the overflow losses in time steps of 1 minute. Each time step the program checks whether or not scour occurs and if so which fraction of the PSD will not settle due to scour. Usually first there is a phase where scour does not occur. The overflow losses are determined by the settling efficiency according to the equations (8-69) and (8-70). If the hopper has a CTS system, each time the necessary overflow level is calculated and the overflow level is adjusted. In the cases considered a CVS system is assumed, so the overflow level is fixed. When the sediment level is so high that the velocity above the bed is very high, scour starts. This will happen at the end of the loading process. In the calculations the loading process is continued for a while, so the effect of scour is clearly visible. The results of the calculations are show in Figure 8-33, Figure 8-34 and Figure 8-35 for the Small, Jumbo and Mega hopper. The initial overflow losses of 20, 20 and 16.6% match the values of the hopper load parameter as mentioned in Table 8-2. The Mega hopper has a smaller hopper load parameter and thus also smaller initial overflow losses (without scour).

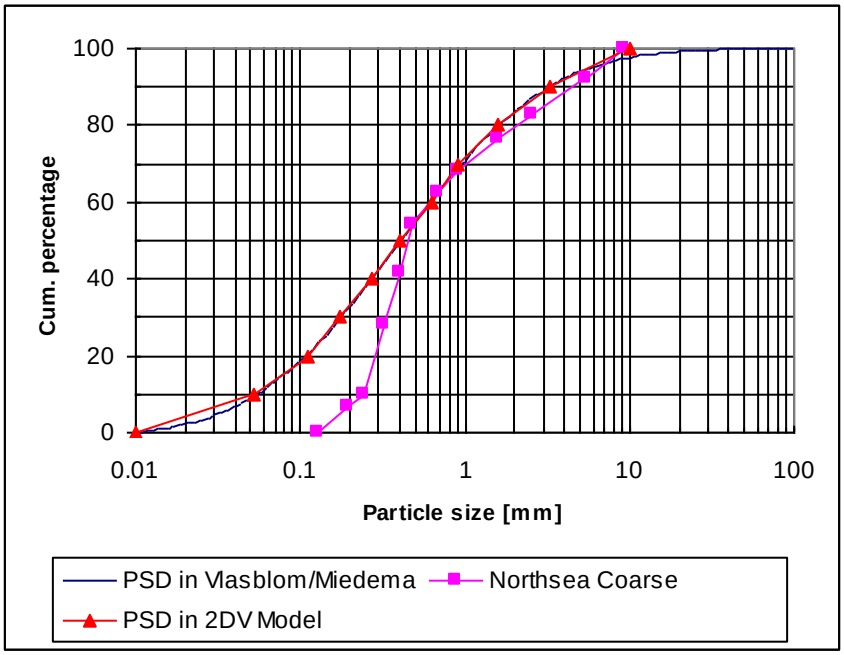

Figure 8-32: The 0.4 mm grain distribution.

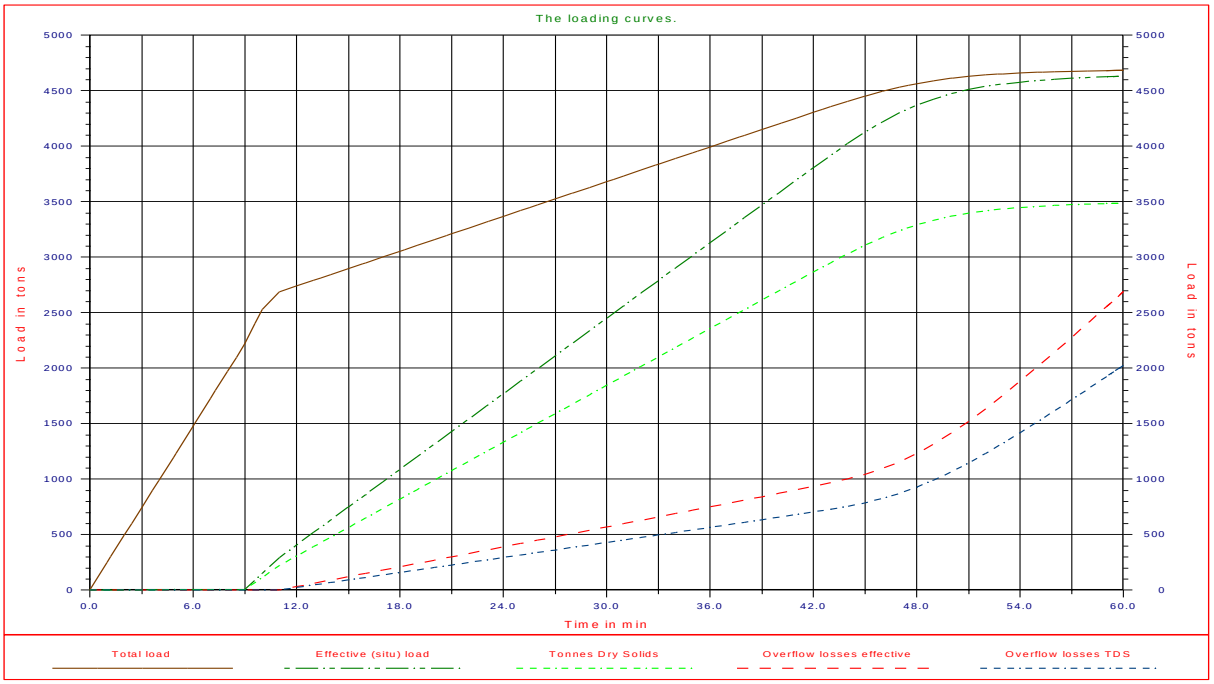

Figure 8-33: The loading curves of the Small TSHD.

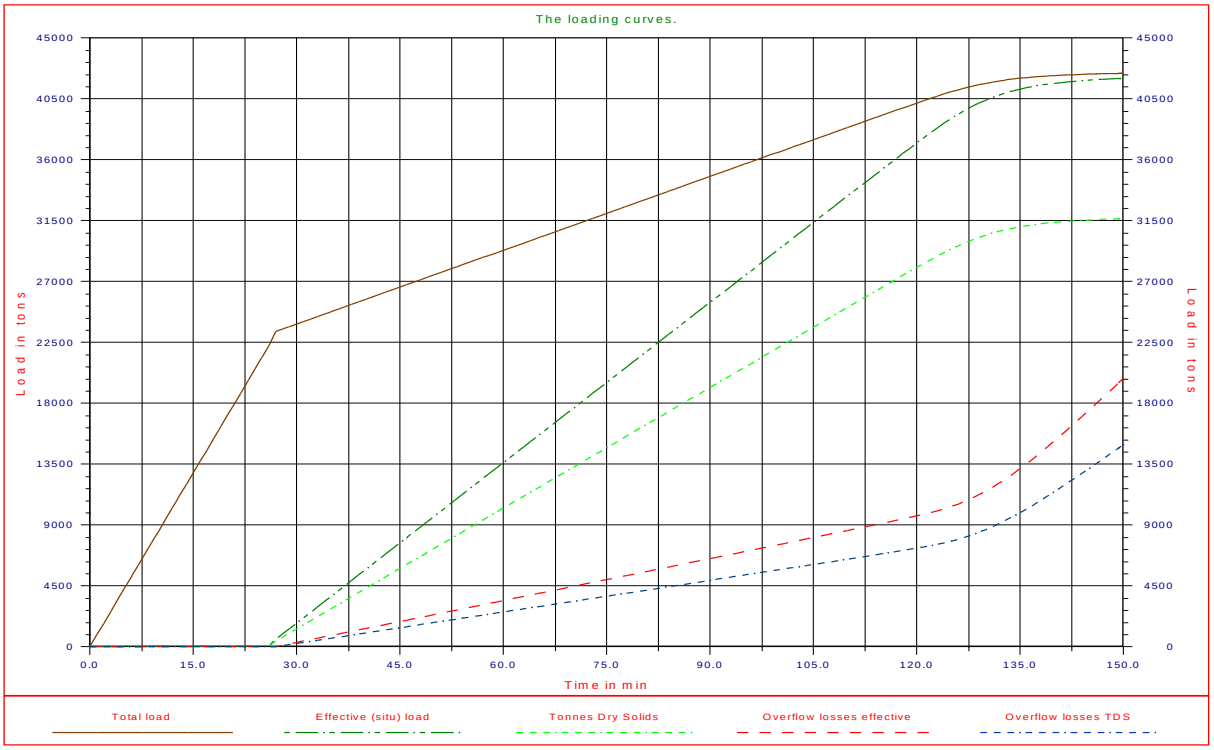

Figure 8-34: The loading curves of the Jumbo TSHD.

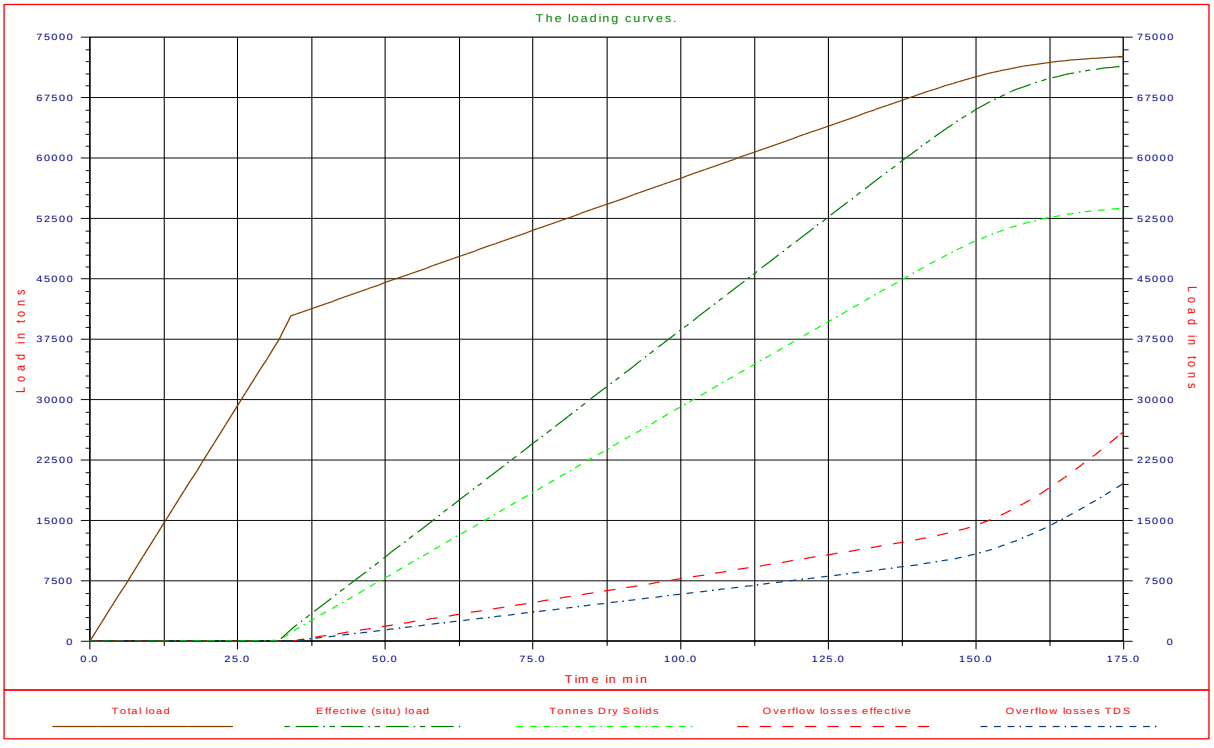

Figure 8-35: The loading curves of the Mega TSHD.

It should be noted that the optimum loading time, the loading time with the maximum production, depends on the total cycle, including sailing times, dumping time, etc. Since the calculations with the 2DV model start with a hopper full of water, also here first the hopper is filled with water, so the two models can be compared.

8.9.3. The 2DV Model

The settlement model described above provides a good approximation of the overflow losses. The influence of grain size, discharge, concentration and hopper geometry can be taken into account. Some influences however are not included in the model. For instance the influence of the inflow location, variation of water level at the start of dredging is not included. To overcome these limitations the 2DV hopper sedimentation model was developed (Van Rhee (2002A)). The model is based on the Reynolds Averaged Navier Stokes equations with a k-epsilon turbulence model. The model includes the influence of the overflow level of the hopper (moving water surface) and a moving sand bed due to the filling of the hopper. The influence of the particle size distribution (PSD) is included in the sediment transport equations. A summary of the model is described in Van Rhee (2002C). The total model is based on three modules (see Figure 8-36).

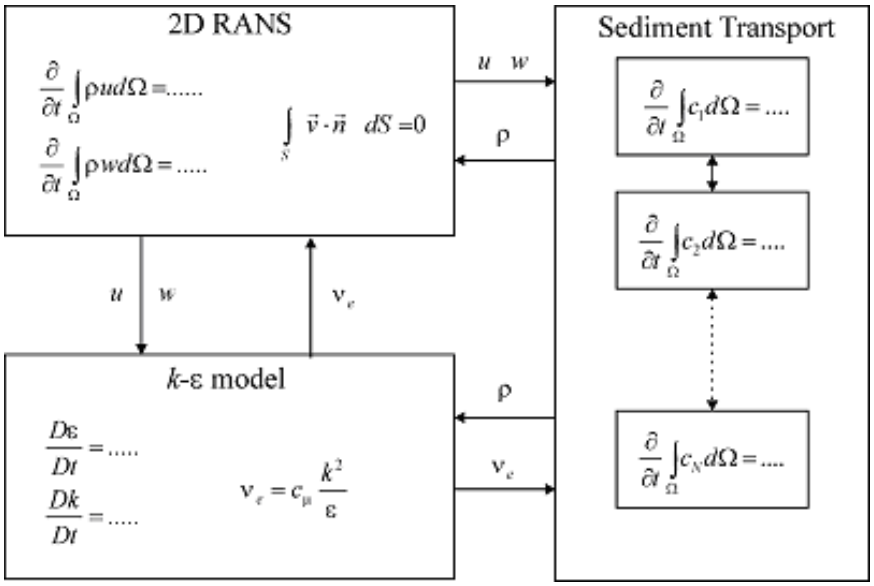

Figure 8-36: Overview of the 2DV model.

In the 2D RANS module the Reynolds Averaged Navier Stokes equations are solved (the momentum equations). The sediment transport module computes the distribution of suspended sediment in the hopper while the k-epsilon module is necessary for the turbulent closure. The modules have to be solved simultaneously because the equations are strongly coupled. In the momentum equations the density is present which follows from the sediment transport equations. The diffusive transport of sediment is governed by turbulence predicted by the k-epsilon model. The turbulence on the other hand is influenced by the density gradients computed in the sediment transport module.

Boundary conditions
The partial differential equations can be solved in case boundary conditions are prescribed. Different boundaries can be distinguished: Walls (sediment bed and side walls), water surface, inflow section and outflow section. At the walls the normal flow velocity is zero. The boundary condition for the flow velocity at the wall is computed using a so-called wall function (Rodi (1993), Stansby (1997)). The boundary conditions for the turbulent energy **k** en dissipation rate **ε** are consistent with this wall function approach. For the sediment transport equations the fluxes through vertical walls and water surface is equal to zero since no sediment enters or leaves the domain at these boundaries. At the sand bed for every fraction the sedimentation flux $\mathbf{S_i}$ is prescribed (the product of the near bed concentration and vertical particle velocity of a certain fraction). The influence of the bottom shear stress on the sedimentation is modeled using a reduction factor **R**.

$$S_i = R \cdot c_i \cdot w_{zj}$$

$$R = \begin{cases} 1 - \dfrac{\theta}{\theta_0} & \theta < \theta_0 \\ 0 & \theta \geq \theta_0 \end{cases} \qquad \textbf{(8-72)}$$

This simple relation between the reduction factor and Shields parameter **θ** is based on flume tests (Van Rhee (2002B)). The critical value for the Shields parameter proved to be independent of the grain size for the sands

tested (d50 < 300 μm). It will be clear that this approach can only be used when overall sedimentation (like in a hopper of a TSHD) will take place. When the Shields value exceeds the critical value no sedimentation will take place, but sediment already settled will not be picked up with this approach. Hence net erosion is not (yet) possible in the model.

At the inflow section the velocity and concentration is prescribed. The outflow boundary is only active when overflow is present, so when the mixture level in the hopper exceeds the overflow level. In that case the outflow velocity is prescribed, and follows simply from the ratio of the overflow discharge and the difference between the hopper and overflow level. For the other quantities the normal gradients are equal to zero (Neumann condition).
At the water surface a rigid-lid assumption is used since surface wave phenomena are not important for the subject situation. A rigid-lid can be regarded as a smooth horizontal plate covering the water surface in the hopper. Depending on the total volume balance inside the hopper this "plate" will be moved up and down.

Numerical approach
The momentum and sediment transport equations are solved using the Finite Volume Method to ensure conservation. The transport equations for the turbulent quantities k and are solved using the Finite Difference method. A Finite Difference Method is allays implemented on a rectangular (Cartesian) grid. Although a Finite Volume Method can be applied on any grid it is advantageous to use a Cartesian approach for this method as well especially when a staggered arrangement of variables is used. In general the flow domain is however not rectangular. The water surface can be considered horizontal on the length scale considered, but a sloping bottom will not coincide with the gridlines. Different approaches are possible. The first method is to use a Cartesian grid and to adjust the bottom cells (cut-cell method). Another method is to fit the grid at the bottom. In that case a boundary fitted non-orthogonal grid can be used. A third method is using grid transformation. By choosing an appropriate transformation the equations are solved on a Cartesian domain in transformed co-ordinates. Although this transformation allows for a good representation of a curved topography the method has the disadvantage that due to truncation errors in the horizontal momentum equation artificial flows will develop when a steep bottom encounters density gradients. These unrealistic flows can be partly suppressed when the diffusion terms are locally discretized in a Cartesian grid (Stelling (1994)). Since however in a hopper both large density gradients as steep bottom geometry can be present it was decided to develop the model in Cartesian co-ordinates with a cut-cell approach at the bed.
The computational procedure can only be outlined here very roughly. The flow is not stationary hence the system is evaluated in time. The following steps are repeated during time:

- Update the velocity field to time $\mathbf{t_{n+1}}$ by solving the NS-equations together with the continuity equation using a pressure correction method (SIMPLE-method (Patankar (1980)) using the density and eddy viscosity of the old time step $\mathbf{t_n}$.
- Update the turbulent quantities and to time $\mathbf{t_{n+1}}$ using the velocity field of $\mathbf{t_{n+1}}$. Compute the eddy-viscosity for the new time.
- Use the flow field of $\mathbf{t_{n+1}}$ to compute the grain velocities for the next time and update the concentrations for all fractions and hence the mixture density to time $\mathbf{t_{n+1}}$.
- Compute the new location for the bed level and mixture surface in the hopper

Results
The 2DV model is used to simulate the loading process for the three different cases. At the start of the simulation the hopper is filled with water. The results are shown in Figure 8-37, Figure 8-38 and Figure 8-39. In these figures the TDS in the hopper (settled in the bed and in suspension) and the cumulative overflow losses are plotted versus loading time.

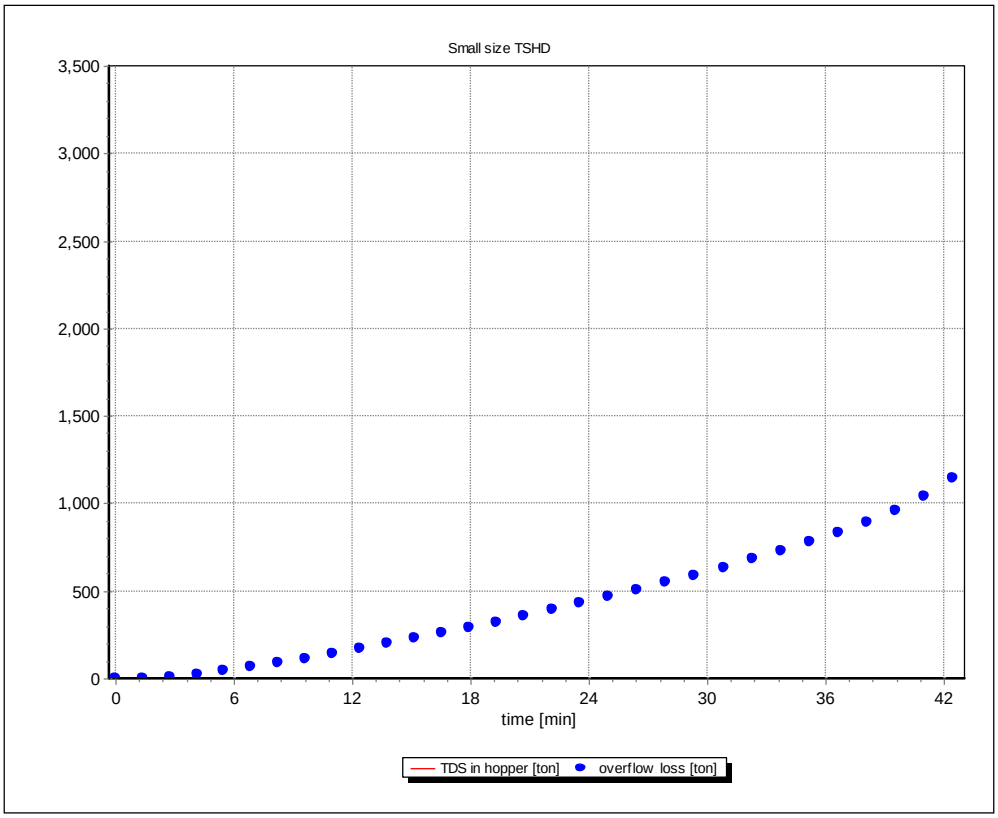

Figure 8-37: Loaded TDS and overflow losses as a function of time for a Small size TSHD.

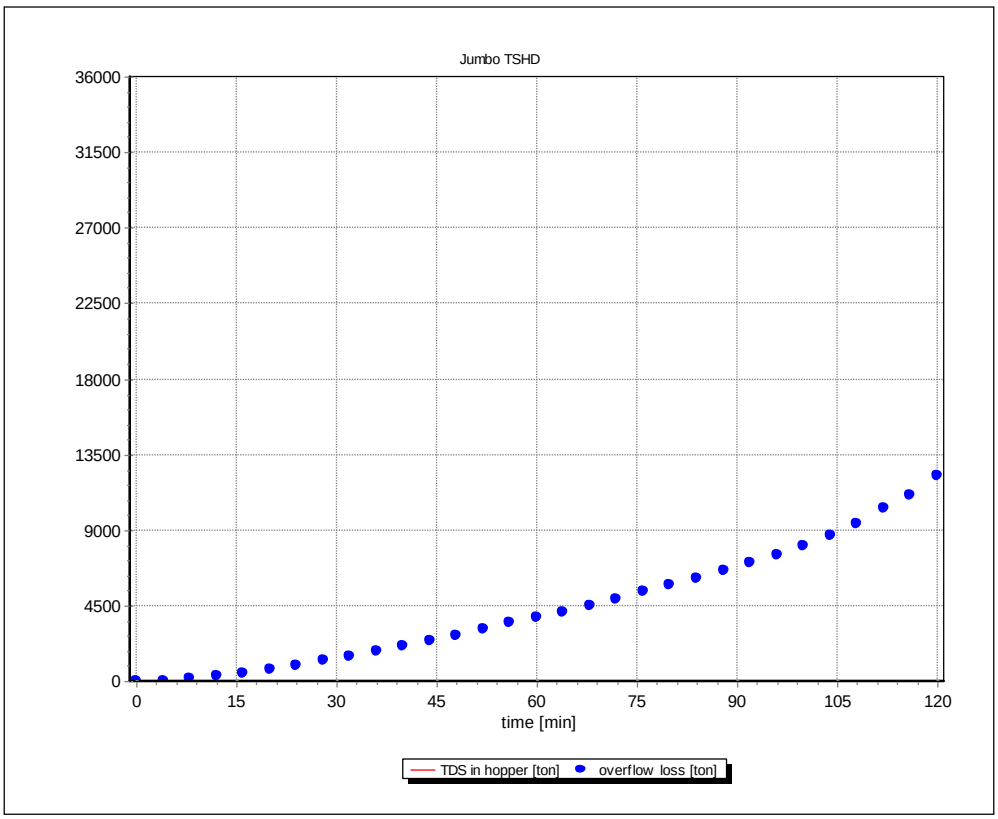

Figure 8-38: Loaded TDS and overflow losses as a function of time for Jumbo TSHD.

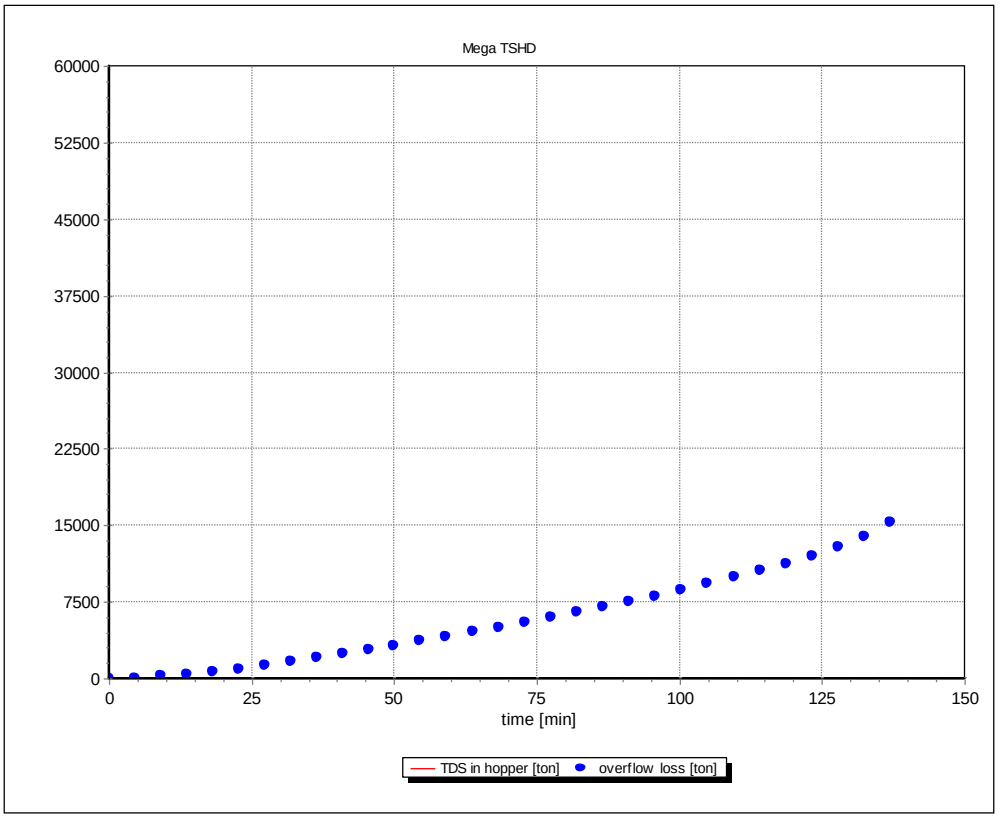

Figure 8-39: Loaded TDS and overflow losses as a function of time for a mega TSHD.

8.9.4. Comparison of the Two Models.

To compare the results of the two methods, first the differences in the models are summarized:

1. The physical modeling of the two methods is different; Miedema/Vlasblom/Camp is based on the Camp approach, while the 2DV model is based on the Reynolds Averaged Navier Stokes equations.
2. The van Rhee model starts with a hopper full of water, while the Miedema/Vlasblom/Camp model starts with an empty hopper.
3. The Miedema/Vlasblom/Camp model assumes 100% settling of the grains during the filling phase of the hopper.
4. The van Rhee model includes a layer of water above the overflow level, while the Miedema/Vlasblom/Camp model doesn't by default. But to compare the two models the height of the overflow level has been increased by the thickness of this layer of water and the results are shown in the Figure 8-40, Figure 8-41 and Figure 8-42. With the layer thickness according to: $H_l = \left(\frac{Q}{1.72 \cdot b} \right)^{2/3}$, where the constant 1.72 may vary. The width **W** is chosen for the width of the overflow **b** in the calculations. This gives a layer thickness of 34 cm for the small hopper and 51 cm for the Jumbo and the Mega hopper.

The results of the Small hopper and the Jumbo hopper are similar due to the same hopper load parameter of 0.0079 m/sec. The Mega hopper has a smaller hopper load parameter of 0.0051 m/sec, resulting in relatively smaller overflow losses. To compare the two models the graphs of the two models are combined and similarities and differences are discussed:

Similarities:

1. The overflow rate seems to be quite similar for all 3 hoppers, until the Miedema/Vlasblom/Camp approach reaches the scour phase. From this moment on the overflow rate increases rapidly.
2. It is obvious that at the end of the loading both models find the same amount of sand in all cases, since this matches the maximum loading capacity of the hopper in question. This observation explains the fact that the overflow losses of both models are almost the same at the time where the van Rhee simulation

stops (42 minutes for the Small hopper, 112 minutes for the Jumbo hopper and 137 minutes for the Mega hopper).

Differences:

1. The overflow losses in the van Rhee model are lower in the first phase, because in the Miedema/Vlasblom/Camp approach this occurs instantly, while the van Rhee approach considers the time the mixture needs to flow through the hopper and the effect of scour is very limited because a uniform flow velocity distribution over depth is assumed (leading to very low horizontal flow velocities) in this model. Only at the end of the loading stage the effect of the horizontal flow velocity on sedimentation becomes noticeable. For instance for the Small hopper the TDS loading curve is a straight line from the start of overflow up to 33 min after start dredging. After that time the loading rate decreases as a result of the increasing horizontal velocity. At t = 45 min the hopper is completely filled. Hence the influence of the velocity during the final loading stage is present for about 12 minutes.
2. In the 2DV model velocity distribution is not prescribed, but is determined by physics and depends on the inflow conditions. In general, due to the large density difference between the inflowing mixture and fluid already present in the hopper, density currents will develop. This will lead to a larger velocity close to the sand bed surface. Hence the effect of the flow velocity on sedimentation will be present from the start of dredging. This influence does not increase much during loading. The effect is more spread out over the loading cycle. The loading rate decreases gradually, but remains on a reasonable level unto the moment that the hopper is fully loaded. In the Miedema/Vlasblom/Camp loading rate reduces to zero at full load..
3. If optimum loading time is considered, the two models differ in that the van Rhee model gives 43, 112 and 137 minutes, while this will be around 38, 99 and 120 minutes in the Miedema/Vlasblom/Camp approach. Both models start with a hopper full of water, so this should be considered. The overflow losses in the final phase of the loading process are similar for both models.

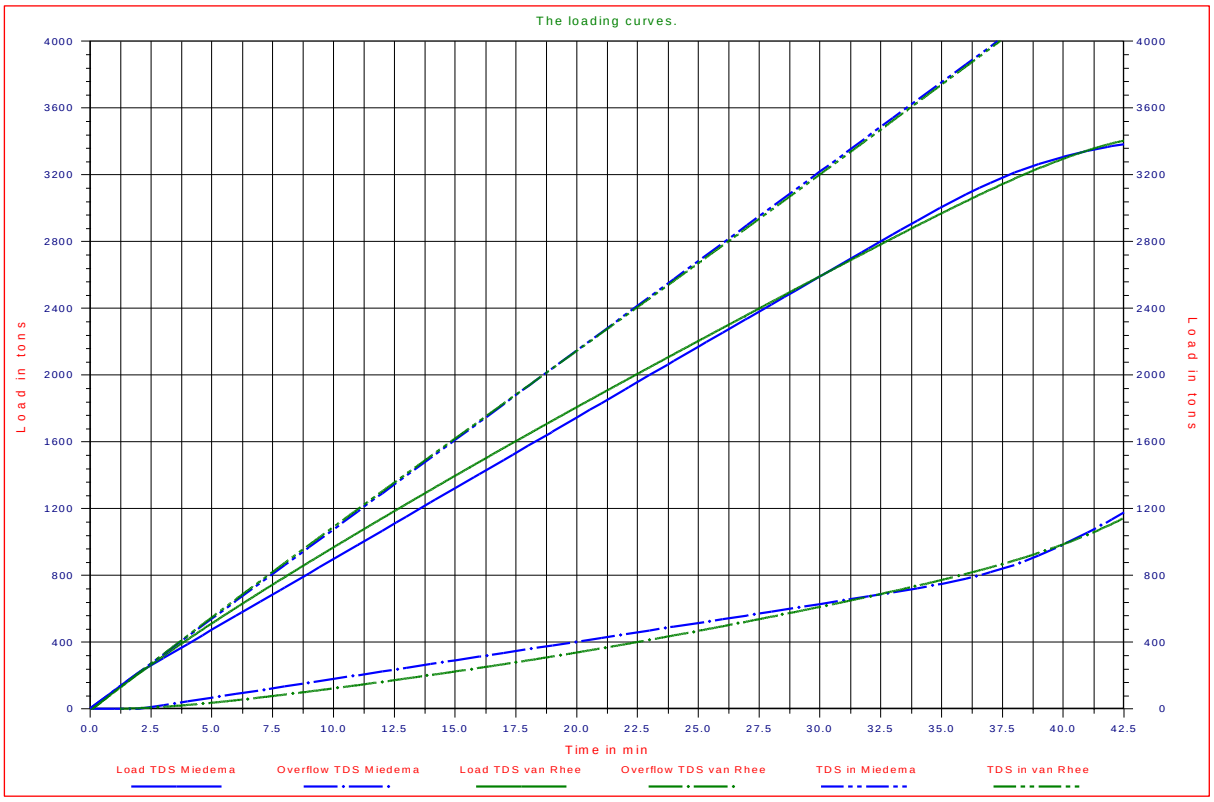

Figure 8-40: Comparison of the two models for the Small hopper.

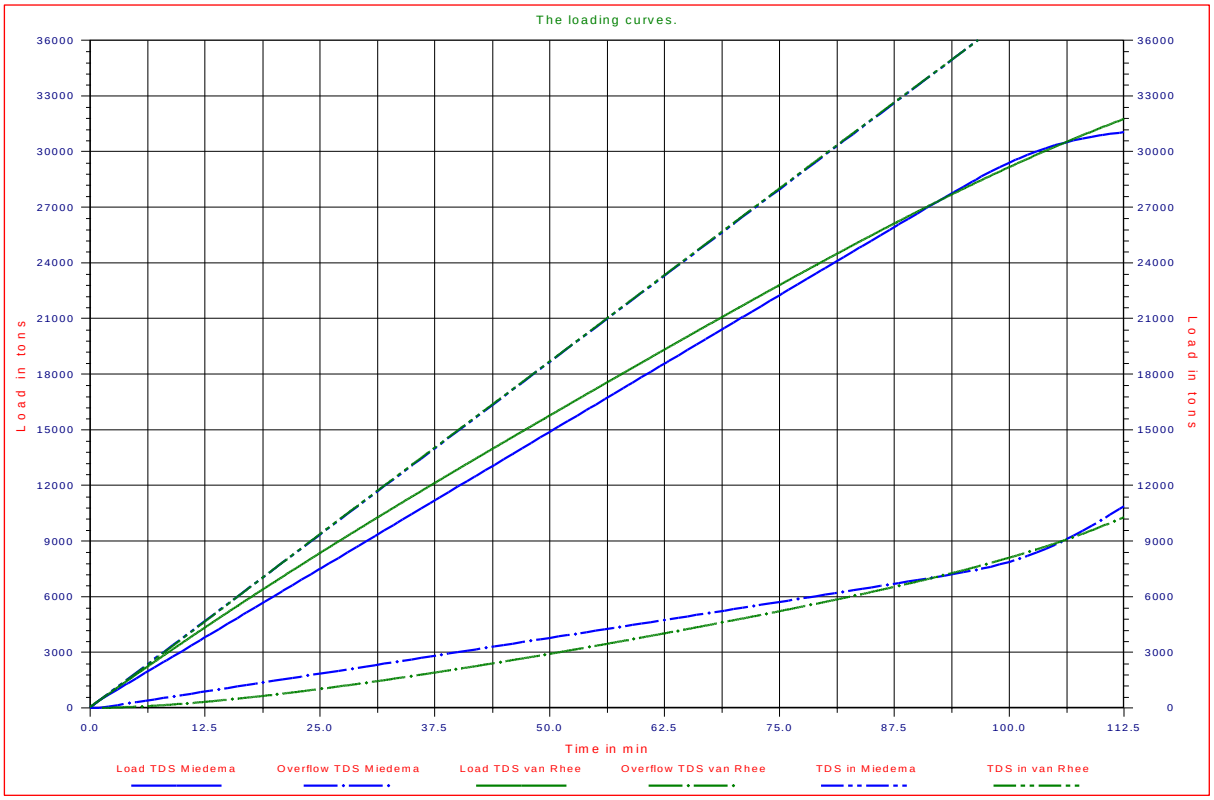

Figure 8-41: Comparison of the two models for the Jumbo hopper.

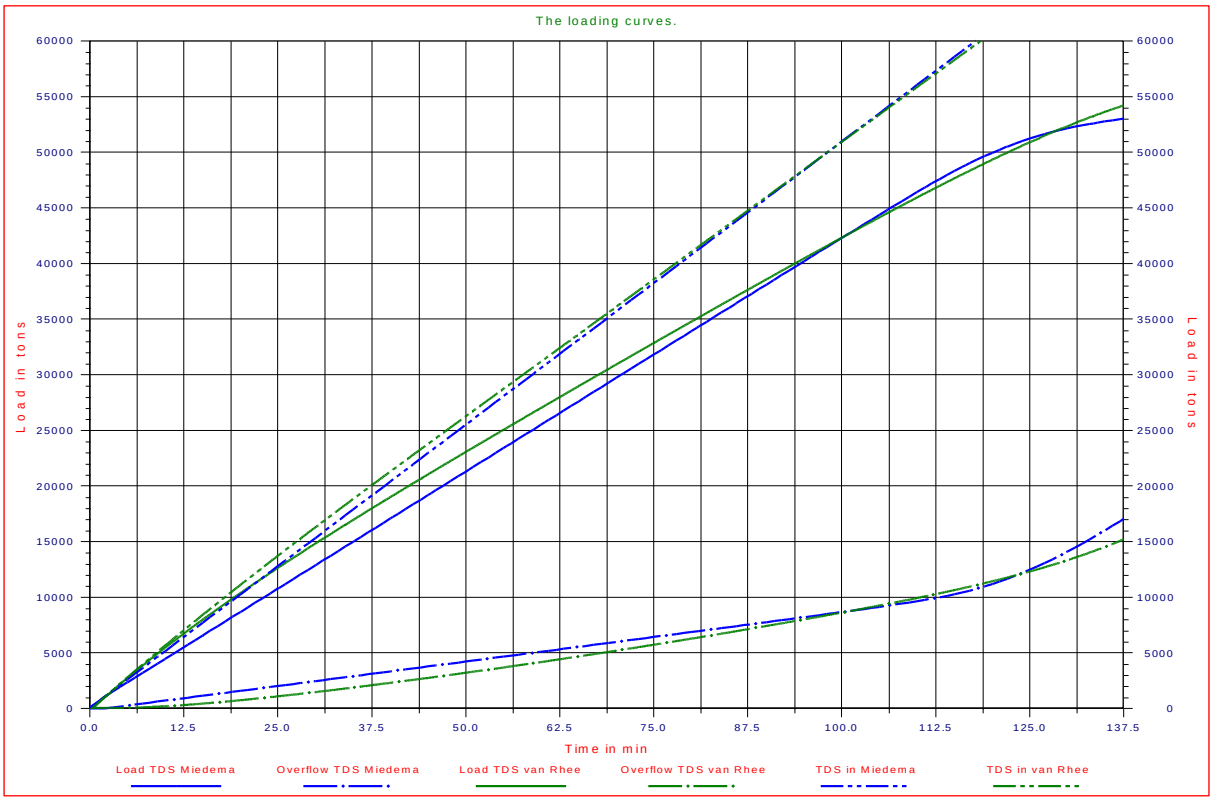

Figure 8-42: Comparison of the two models for the Mega hopper.

8.9.5. Conclusions

- The two models give the same magnitude for the overflow losses, but the shapes of the curves are different due to the differences in the physical modeling of the processes.
- Due to the lower losses the computed optimal loading time will be shorter for the Miedema/Vlasblom /Camp approach.
- The strong point of the van Rhee model is the accurate physical modeling, giving the possibility to model the geometry of the hopper in great detail, but also describing the physical processes in more detail.
- The van Rhee model is verified and validated with model and prototype tests and can be considered a reference model for other models.
- The strong point of the Miedema/Vlasblom/Camp model is the simplicity, giving a transparent model where result and cause are easily related.

8.10. A Sensitivity Analysis of the Scaling of TSHS's.

The loading process of TSHD's contains a number of non-linearity's:

1. The real hopper load parameter will vary during the loading process.
2. The turbulence settling efficiency.
3. The behavior of the layer of water above the overflow.
4. The behavior of hindered settling.
5. The effective concentration in the hopper.
6. The so called storage effect.

Based on all these non-linearity's it is not expected that TSHD's can be scaled easily, however the research in this paper shows that with the right choice of scale laws the TSHD's can be scaled rather well.
4 TSHD's are chosen, derived from Miedema & van Rhee (2007), but adapted to the scale laws. With each of these TSHD's simulations are carried out in 4 types of sand, 400 µm, 250 µm, 150 µm and 100 µm sand.

8.10.1. Scale Laws.

To compare TSHD's of different dimensions scale laws have to be applied in order to create identical loading processes. Scale laws should be based on the physical and the operational processes that occur. Further the shape of the hopper should be identical and the relation with the flow should match. It is however also important to decide which parameter or parameters to choose for the comparison of the TSHD's. When can the conclusion be drawn that two hoppers with different dimensions behave identical. The main parameter that is chosen for this comparison are the cumulative overflow losses. The cumulative overflow losses are the overflow losses expressed as TDS (Tonnes Dry Solids) divided by the total amount of TDS that has entered the hopper, from the start of the loading process until the moment of optimum loading.
The first important parameter to consider is the hopper load parameter (HLP) as described in equation (8-73). Here the hopper load parameter without the effect of the bed rise velocity is considered, because the bed rise velocity changes during the loading process and would result in changing scale laws. As stated before, the hopper load parameter is the settling velocity of a grain that will settle for 100%. Larger grains will also settle for 100%, but smaller grains will settle with a smaller percentage.

$$v_o = s_o \cdot \frac{H_w}{L} = \frac{Q_{in}}{W \cdot L} \qquad \textbf{(8-73)}$$

If two TSHD's with different dimensions have the same hopper load parameter, it can be expected that under similar conditions, the momentary overflow losses are equal and thus also the cumulative overflow losses. However the hopper load parameter does not take into consideration the effects of turbulence efficiency, hindered settling, and the storage effect and so on.

A second scale law could be that the ratios between Length, Width and Height are identical. If a length scale λ is considered this gives:

$$\lambda = \frac{L_1}{L_2} = \frac{W_1}{W_2} = \frac{H_1}{H_2} \quad \text{and} \quad \frac{HLP_1}{HLP_2} = 1 \quad \text{and} \quad \frac{Q_1}{Q_2} = \lambda^2 \quad \text{and} \quad \frac{T_{f1}}{T_{f2}} = \frac{V_1 / Q_1}{V_2 / Q_2} = \lambda \qquad \textbf{(8-74)}$$

Because the hopper load parameter is considered to be a constant, the flow **Q** will scale with the square of the length scale λ. The filling time $\mathbf{T_f}$, which is the time to fill the hopper up to the overflow level also scales with the length scale λ. To have similar processes for determining the optimum loading time, the travelling time, which is the sum of the sailing time to and from the dump area and the dumping time, should also be scaled with the length scale, assuming that the loading time is proportional to the filling time. Since the horizontal flow velocity in the hopper equals the flow **Q** divided by the width **W** and the height **H** of the hopper, the horizontal flow velocity is a constant and does not depend on the length scale. This also follows from the fact that the hopper load parameter is a constant. If it is assumed that the maximum line velocity in the suction pipes is a constant, for example 7 m/s and because the line velocity equals the flow velocity divided by 2 and divided by the cross section of one pipe, this implies that the pipe diameter should be proportional to the square root of the flow and thus be proportional to the length scale λ.
Because sand is difficult to scale and in reality the sand will be the same independent of the TSHD used, it is assumed that the sand is the same for all hopper sizes. This implies that the settling velocities are the same and looking at the equations (8-69) and (8-70) this means that the grain settling efficiency η_g does not depend on the

hopper size and the ratio v_s/s_o does not depend on the hopper size, since the horizontal flow velocity s_o does not depend on the hopper size. The resulting turbulence efficiency as calculated with equations (8-69) and (8-70) is thus not dependent on the hopper size, although it will change during the loading process.

8.10.2. The TSHD'S used.

Based on the scale laws and based on Miedema & van Rhee (2007), 4 TSHD's are chosen in a range from small to Mega. The main dimensions and additional parameters of these hoppers can be found in table 1 and 2.

Table 8-4: The main dimensions of the 4 TSHD's.

Hopper	Length (m)	Width (m)	Empty height (m)	Volume (m^3)	Design density (ton/m^3)	Maximum load (ton)	HLP (m/sec)
Small	40	10	5.0	2000	1.5	3000	0.008
Large	60	15	7.5	6750	1.5	10125	0.008
Jumbo	80	20	10.0	16000	1.5	24000	0.008
Mega	100	25	12.5	31250	1.5	46875	0.008

Table 8-5: Additional and derived quantities.

Hopper	Flow (m^3/sec)	Pipe diameter (m)	Filling time (min)	Sailing time (min)	Hydraulic diameter (m)	Reynolds number	Mixture density (ton/m^3)
Small	3.2	0.54	10.4	104	10	$0.64*10^6$	1.3
Large	7.2	0.81	15.6	156	15	$0.96*10^6$	1.3
Jumbo	12.8	1.08	20.8	208	20	$1.28*10^6$	1.3
Mega	20.0	1.35	26.0	260	25	$1.60*10^6$	1.3

Table 8-4 and Table 8-5 show a wide range of TSHD's from Small (2000 m^3) to Mega (31250 m^3) . As can be noted in the tables, the hopper load parameters are constant at 0.008 m/sec, which is the settling velocity of a grain a bit bigger than 100 µm. The design density of the TSHD's is chosen at 1.5 ton/m^3, which implies that the loading process will follow the Constant Tonnage Loading process. The total sailing and dumping time is chosen 10 times the filling time, which of course is arbitrary, but the resulting sailing times seem to be representative for the reality. The mixture density is chosen at 1.3 ton/m^3, which is high enough to take the influence of hindered settling into account. It should be noted that the Reynolds numbers of the horizontal flow in the hopper are not constant; the Reynolds numbers are proportional to the length scale λ. The question is whether or not this will influence the loading process. As stated before, it does not influence the turbulent settling efficiency, but it could influence the scour in the final phase of the loading process. Scour is influenced by the viscous friction of the fluid flowing over the bed. This friction depends on the relative roughness and the Reynolds number. The roughness of the sediment has the magnitude of the grain diameter which is in the range of 0.1-0.5 mm, while the hydraulic diameters of the 4 TSHD's are in the magnitude of 10-25 m. The largest relative roughness would occur for a 0.5 mm grain and a hydraulic diameter of 10 m, giving 0.0005/10=0.00005. The friction coefficient will be between 0.0175 and 0.0171, which hardly has an effect on the scour. Although there will always be some effect, it is not expected that this effect will have a big influence on the similarity of the loading processes of the 4 TSHD's. The sediment density is chosen at 1.9 ton/m^3, which means that the TDS is about 76% of the weight of the wet sediment.

For carrying out the simulations 4 grain distributions are chosen. All 4 grain distributions have a $\mathbf{d_{15}}$ for grains with a settling velocity smaller than the hopper load parameter in order to be sure there will be significant overflow losses. If grain distributions were chosen with almost 100% of the grains having a settling velocity above the hopper load parameter, this would result in very small cumulative overflow losses and a good comparison would be difficult. Table 8-6 gives the $\mathbf{d_{15}}$, $\mathbf{d_{50}}$ and $\mathbf{d_{85}}$ of the 4 grain distributions, while figure 12 shows the full PSD's.

Table 8-6: The characteristics of the 4 grain distributions.

	400 µm	250 µm	150 µm	100 µm
d_{15}	70 µm	80 µm	80 µm	50 µm
d_{50}	400 µm	250 µm	150 µm	100 µm
d_{85}	2000 µm	750 µm	300 µm	200 µm

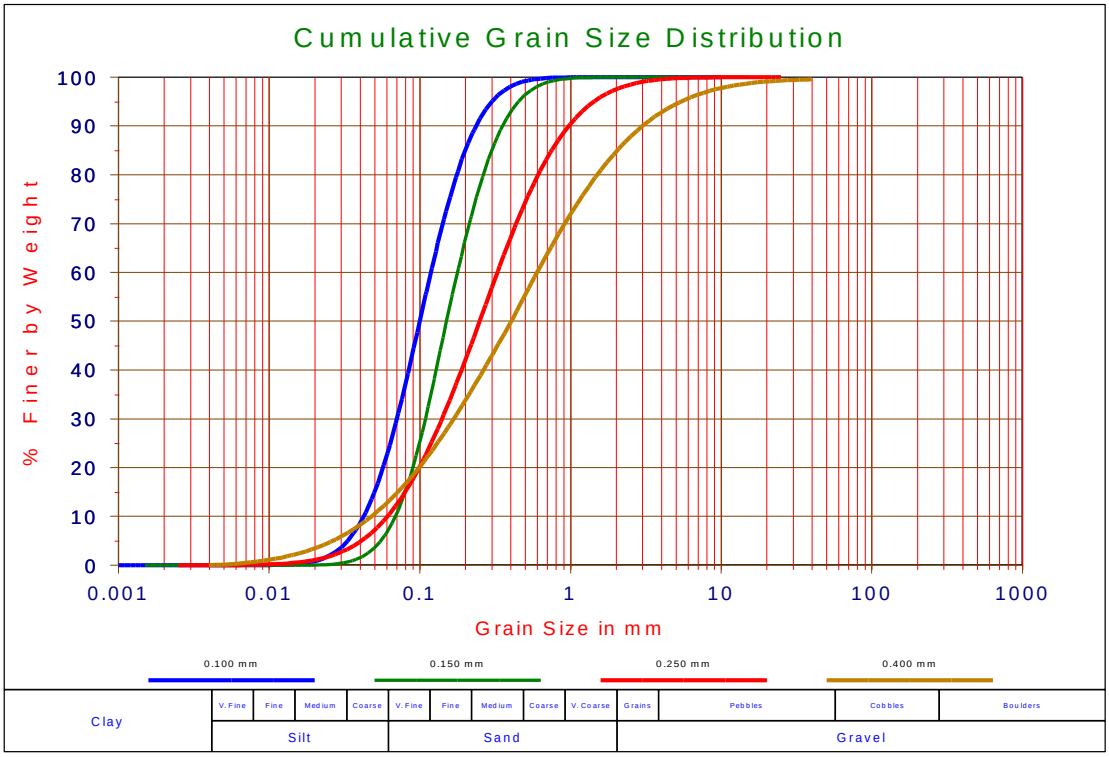

Figure 8-43: The 4 grain distributions.

8.10.3. Simulation Results.

The simulations of the loading process of the 4 TSHD's are carried out with software based on the model published by Miedema (2008A), including turbulence efficiency, hindered settling, the storage effect, the layer of water above the overflow and more. The results of these simulations are summarized in Table 8-7, Table 8-8, Table 8-9 and Table 8-10.

Table 8-7: The simulation results with the 0.400 mm sand.

400 µm sand	Loading time (min)	TDS (ton)	Overflow losses TDS (ton)	Cumulative overflow losses (%)	Production (ton/min)
Small	31.0	2174	476	18.0%	16.1
Large	46.5	7349	1594	17.8%	36.2
Jumbo	62.0	17440	3758	17.7%	64.5
Mega	77.5	34089	7313	17.7%	100.9

Table 8-8: The simulation results with the 0.250 mm sand.

250 µm sand	Loading time (min)	TDS (ton)	Overflow losses TDS (ton)	Cumulative overflow losses (%)	Production (ton/min)
Small	31.0	2146	503	19.0%	15.9
Large	46.5	7258	1685	18.8%	35.8
Jumbo	61.8	17218	3923	18.6%	63.7
Mega	77.3	33662	7651	18.5%	99.7

Table 8-9: The simulation results with the 0.150 mm sand.

150 µm sand	Loading time (min)	TDS (ton)	Overflow losses TDS (ton)	Cumulative overflow losses (%)	Production (ton/min)
Small	32.2	2104	645	23.5%	15.4
Large	48.2	7114	2149	23.2%	34.8
Jumbo	64.2	16887	3923	23.0%	62.0
Mega	80.3	33030	7651	23.0%	96.9

Table 8-10: The simulation results with the 0.100 mm sand.

100 µm sand	Loading time (min)	TDS (ton)	Overflow losses TDS (ton)	Cumulative overflow losses (%)	Production (ton/min)
Small	43.0	2111	1564	42.6%	14.3
Large	64.7	7145	5292	42.6%	32.3
Jumbo	86.0	16952	12452	42.3%	57.6
Mega	107.7	33149	24368	42.4%	90.1

To visualize the simulations, the graphs of the simulations of the Small TSHD and the Mega TSHD can be found in the Figure 8-44, Figure 8-45, Figure 8-46, Figure 8-47, Figure 8-48, Figure 8-49, Figure 8-50 and Figure 8-51. From these graphs and the above tables it will be clear that the cumulative overflow losses do not depend on the size of the TSHD in quantity and in shape op de loading and overflow curves. To understand the above tables and the following figures, they will be explained and discussed each.

Table 8-7, Table 8-8, Table 8-9 and Table 8-10 show the loading times in the second column, it is clear that the loading times are almost proportional to the length scale λ and they increase with increasing overflow losses. The finer the sand, the longer the loading time. The third column gives the TDS at the point of optimum loading. The TDS of a hopper filled with sediment is about 76% of the weight of the sediment, but since there is still some water on top of the sediment at the moment of optimum loading the TDS is a bit less. This means that the maximum TDS of the Small TSHD is 2280 tons, for the Large TSHD 7695 tons, for the Jumbo TSHD 18240 tons and for the Mega TSHD 35625 tons, so the assumption is correct. The TDS does not depend on the type of sand. The fourth column gives the overflow losses in tons TDS. Again TDS means, only the weight of the solids, excluding the pore water and the water on top of the sediment. The fifth column gives the cumulative overflow losses, which are almost constant for each type of sand. For the 400 µm sand about 17.8%, for the 250 µm about 18.7%, for the 150 µm sand about 23.2% and for the 100 µm sand about 42.4%. These cumulative overflow losses are the overflow losses in TDS, divided by the total amount of TDS that has entered the hopper. It is clear that the cumulative overflow losses do not seem to depend on the size of the TSHD, given the scale laws applied in the simulations. Apparently the scale laws applied are the correct scale laws for scaling TSHD's in order to get similar loading and sedimentation processes. It is interesting however to compare the cumulative overflow losses with the grain size distribution curves of the sands used. The hopper load parameter of 0.008 m/s matches a grain with a diameter of 0.112 mm. If the percentage of grains smaller than this diameter is considered and compared we the overflow losses, the following numbers are found. For the 400 µm sand, about 20% smaller than 0.112 mm and cumulative overflow losses of 17.8%, for the 250 µm sand, about 20% smaller than 0.112 mm and 18.7% cumulative overflow losses, for the 150 µm sand, about 26% smaller than 0.112 mm and 23.2% cumulative overflow losses and for the 100 µm sand, about 52% smaller than 0.112 mm and 42.4% cumulative overflow losses. Apparently, but not unexpected, the cumulative overflow losses have a strong relation with the percentage of the grains smaller than the grain diameter matching the hopper load parameter. There is however not a fixed relation, because the grains smaller than the diameter matching the hopper load parameter will still settle partially and this depends strongly on the steepness of the cumulative grain size distribution. In the examples given it is clear that the 400 µm sand and the 250 µm sand, both have about 20% smaller and both have a cumulative overflow loss of about 20%. The simulations however also take hindered settling, the effect of the concentration on the settling velocity, into account and in reality the TSHD might make turns, resulting in a more complicated loading process. The overflow losses will also depend on the concentration as will be discussed later. The last column shows the production and of course the production is decreasing if the cumulative overflow losses are increasing.

Figure 8-44 and Figure 8-45 give the loading curves of the Small and the Mega TSHD in order to see if not only the cumulative overflow losses are independent of the size of the TSHD, but also the shape of the loading curves. To understand these graphs the different curves are explained. The loading process starts with an empty hopper, so there is no water in the hopper. First for 10.4 minutes for the Small hopper and 26.0 minutes for the Mega hopper, the hopper is filled with mixture of 1.3 ton/m3. After that the loading continues until after about 22.4 minutes for the Small hopper and 57 minutes for the Mega hopper, the maximum load is reached as can be found in table 1, seventh column. After reaching the maximum load, the loading continues while the overflow is lowered in such a way that the total load in the hopper remains constant, replacing water above the sediment with sediment. After about 40 minutes for the Small hopper and about 100 minutes for the Mega hopper, the sediment level is so high and the layer of water above the sediment is so thin, that very high flow velocities occur above the sediment, preventing the grains the settle and resulting in scour. After a short while hardly any grains will settle and the optimum loading point is reached. Continuing after this point will result in a decrease of production and is thus useless.

The black solid line at the top is the total load in the hopper and it is obvious that this line stays at the maximum load once this is reached. The blue solid line is the total volume in the hopper, it can be seen that after reaching the maximum load, the total volume is decreasing because the overflow is lowered. The dashed red line shows the tangent method to determine the optimum loading point. The dashed brown line shows the weight of the sediment in the hopper, including the weight of the pore water. At the end of the loading this line is just below the maximum load line, because there is still a layer of water above the sediment, which does not count in the sediment weight. The black solid straight line gives the amount of TDS that enters the hopper, so the sum of sediment TDS and overflow TDS should be equal to this line. The highest solid brown line is the amount of TDS in the hopper, while the lowest solid brown line is the sediment volume. Finally the solid red line gives the overflow losses in TDS. It can be seen that until the mixture in the hopper reaches the overflow level, there are no overflow losses. After the hopper is filled the overflow losses follow an almost straight line, which curves to a steeper line when scour starts to occur.
Although the scales of Figure 8-44 and Figure 8-45 are different, it is clear that the different loading curves have similar shapes, so not only the cumulative overflow losses are independent of the size of the hopper, also the momentary overflow losses are.

Figure 8-46 and Figure 8-47 show the loading curves including the storage effect. So what exactly is this storage effect? When grains enter the hopper, it can already be calculated which fraction of the grains will settle and which fraction of the grains will leave the hopper through the overflow. Figure 8-44 and Figure 8-45 are based on such a calculation. Grains that will leave through the overflow however, first have to travel through the hopper before they actually leave the hopper through the overflow. One can say that these grains are temporary stored in the hopper, the so called storage effect. This means that if suddenly the loading process would stop before the optimum is reached, there are more grains and thus TDS in the hopper then would follow from the Figure 8-44 and Figure 8-45. It also means that the overflow losses at such a moment would be less. The amount of grains that will leave the hopper, but are still inside, depends on the time it takes for a particle to move from the entrance to the overflow and this depends on the flow velocity. The flow velocity will increase when the sediment level increases and at the end of the loading cycle this velocity is so high that the storage effect can be neglected. In the Figure 8-46 and Figure 8-47 the top thick solid black lines show the amount of TDS in the hopper (compare with Figure 8-44 and Figure 8-45, these contain the same lines but solid brown). Just above the thick solid black lines are the thin solid green lines. The difference between the thick solid black line and the thin solid green line is the amount of TDS that will leave through the overflow, but has not yet left. The thin solid brown line below the thick solid black line show how many grains have already settled, the difference between the two lines is the amount of grains that will settle, but has not yet settled. Finally the thick solid black line at the bottom gives the overflow losses as have already been shown in Figure 8-44 and Figure 8-45. The thin red line, below this line give the amount of TDS that have already left the hopper.

Figure 8-48 and Figure 8-49 show the grain distribution curves of the 100 µm for the Small and the Mega TSHD. The original distribution is the lines with the dots. Left from these are the red lines which give the distribution of the grains leaving the overflow, on average from the start of the loading until the optimum loading point. Right from the original distribution is the solid green line, showing the average distribution in the hopper. It can be concluded that the grain distributions are similar for the Small and the Mega TSHD.

Figure 8-50 and Figure 8-51 show the influence of the concentration and the amount of water in the hopper at the moment the loading starts, on the cumulative overflow losses and the cumulative efficiency. The dot in both graphs shows the result of the simulation carried out. It is obvious that Figure 8-50 and Figure 8-51 show similar graphs. The lines in the graphs are determined by an equation, derived as an attempt to predict the overflow losses with just one equation. The green solid line shows the cumulative overflow losses when the hopper is completely empty at the start of the loading process. The blue line when the hopper is filled with 50% water and the red line when its filled with 100% water. The graph shows the overflow losses as a function of the mixture concentration. These graphs are still experimental, but give good tendencies of the overflow losses.

8.10.4. Conclusions & Discussion.

The question before this research started, was how do the cumulative overflow losses behave when TSHD's are scaled from small to very big. The second question was, are that scale laws that should be applied when scaling TSHD's in order to create similar or maybe even identical processes.

First the answer on the second question, there are scale laws that should be applied and the main law is, to keep the hopper load parameter constant and from there derive the scale laws for the flow and other dimensions, but don't scale the sand.
If the scale laws are applied correctly, the simulations show that scaling the TSHD has hardly any influence on the cumulative overflow losses and the loading processes are similar.
The overflow losses however depend strongly on the position of the grain diameter match the hopper load parameter in the particle size distribution diagram. The fraction of the sand with diameters smaller than this diameter has a very strong relation with the cumulative overflow losses.

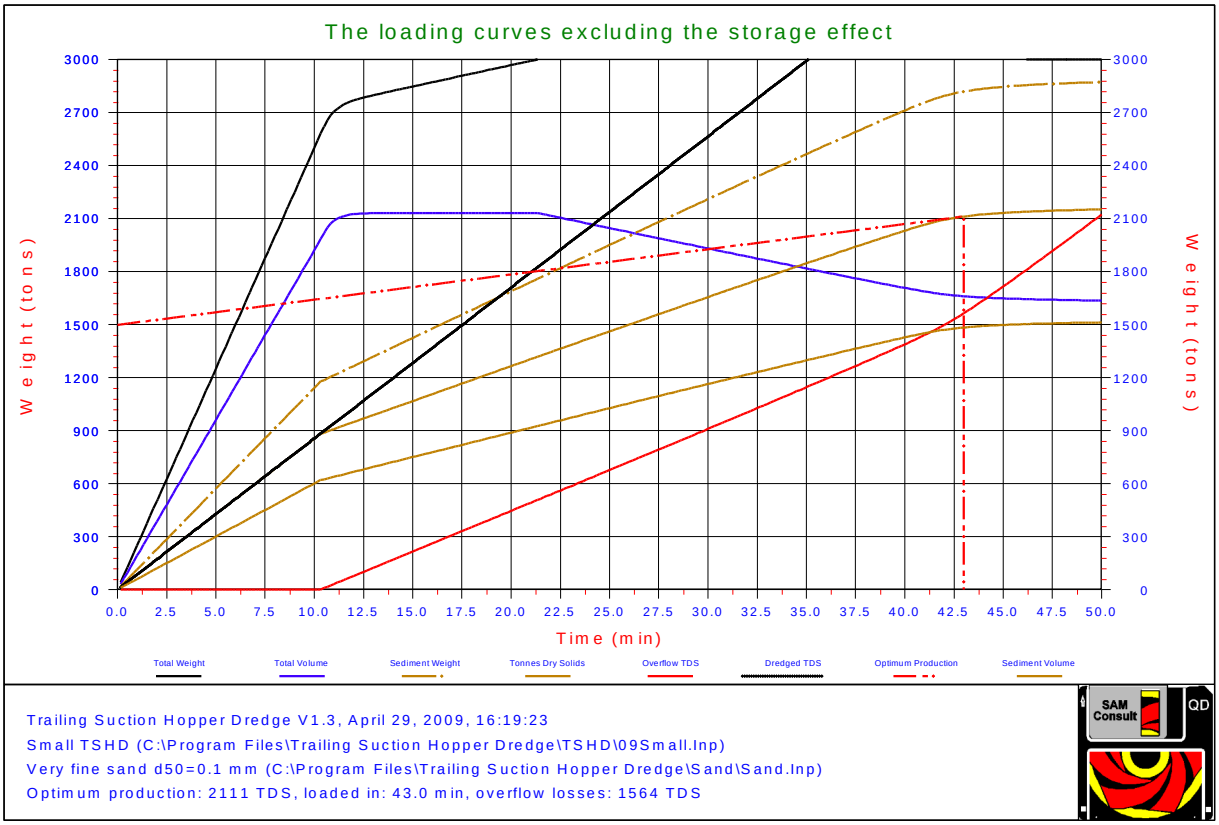

Figure 8-44: The loading curves for the Small TSHD.

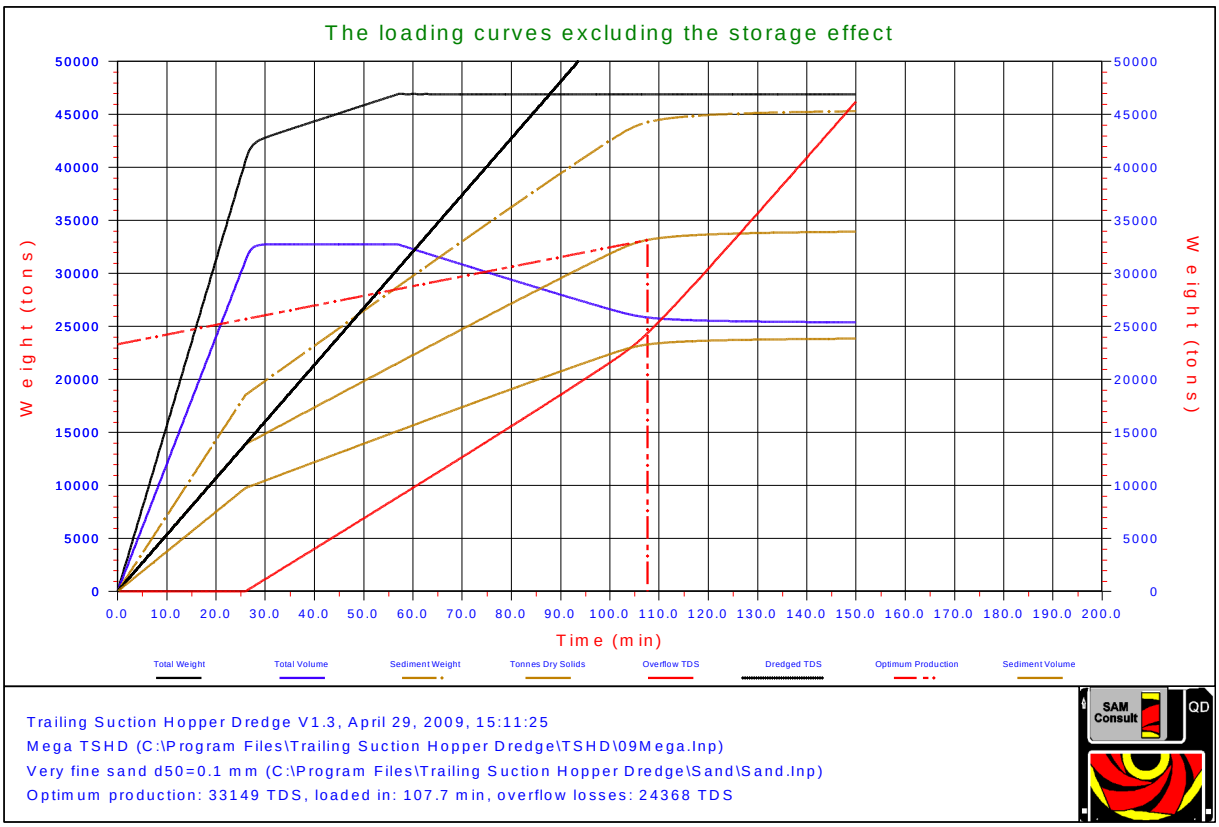

Figure 8-45: The loading curves for the Mega TSHD.

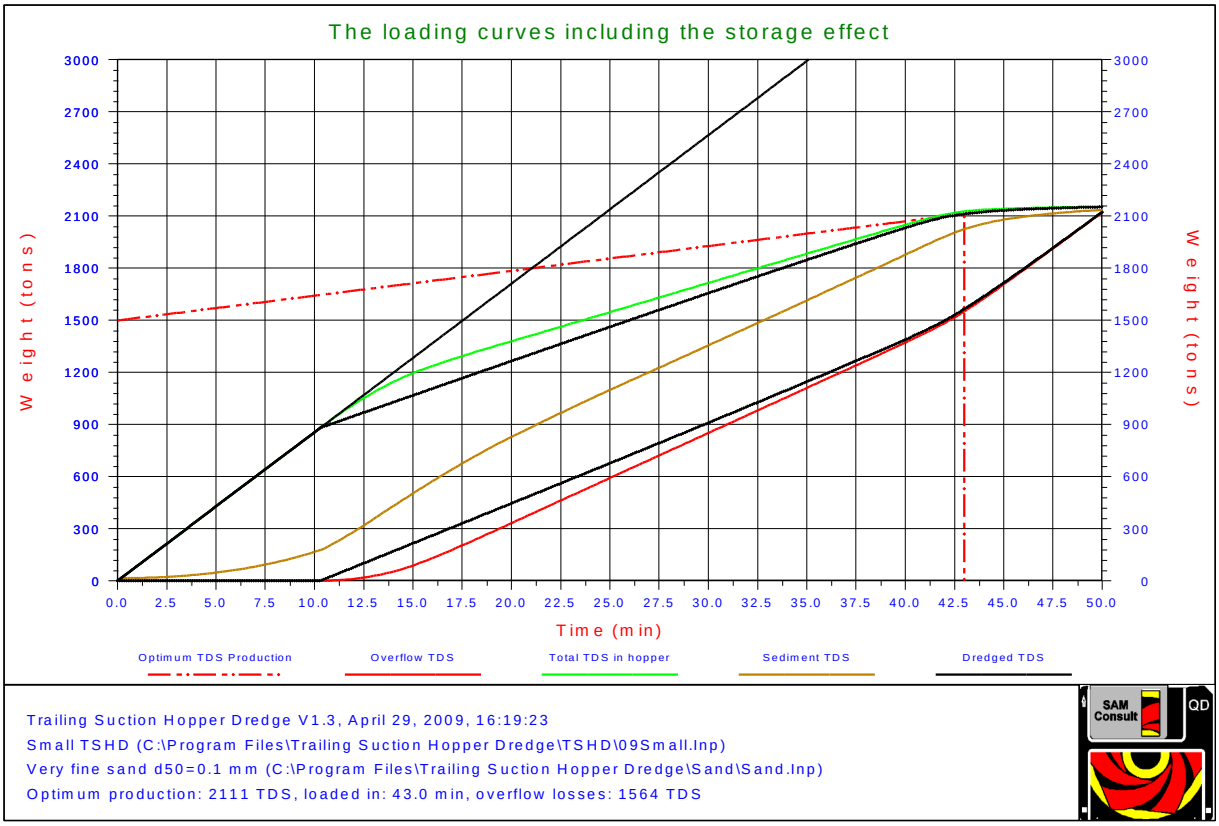

Figure 8-46: The loading curves including the storage effect for the Small TSHD.

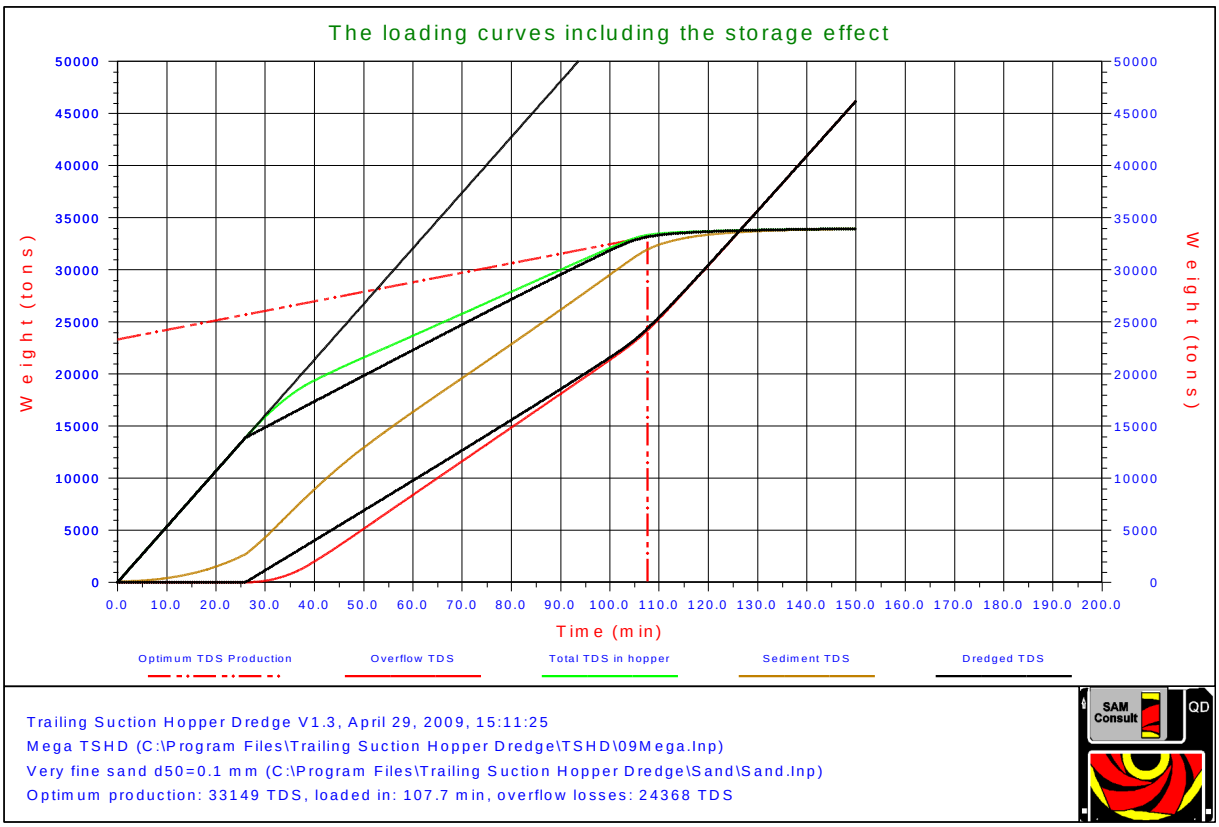

Figure 8-47: The loading curves including the storage effect for the Mega TSHD.

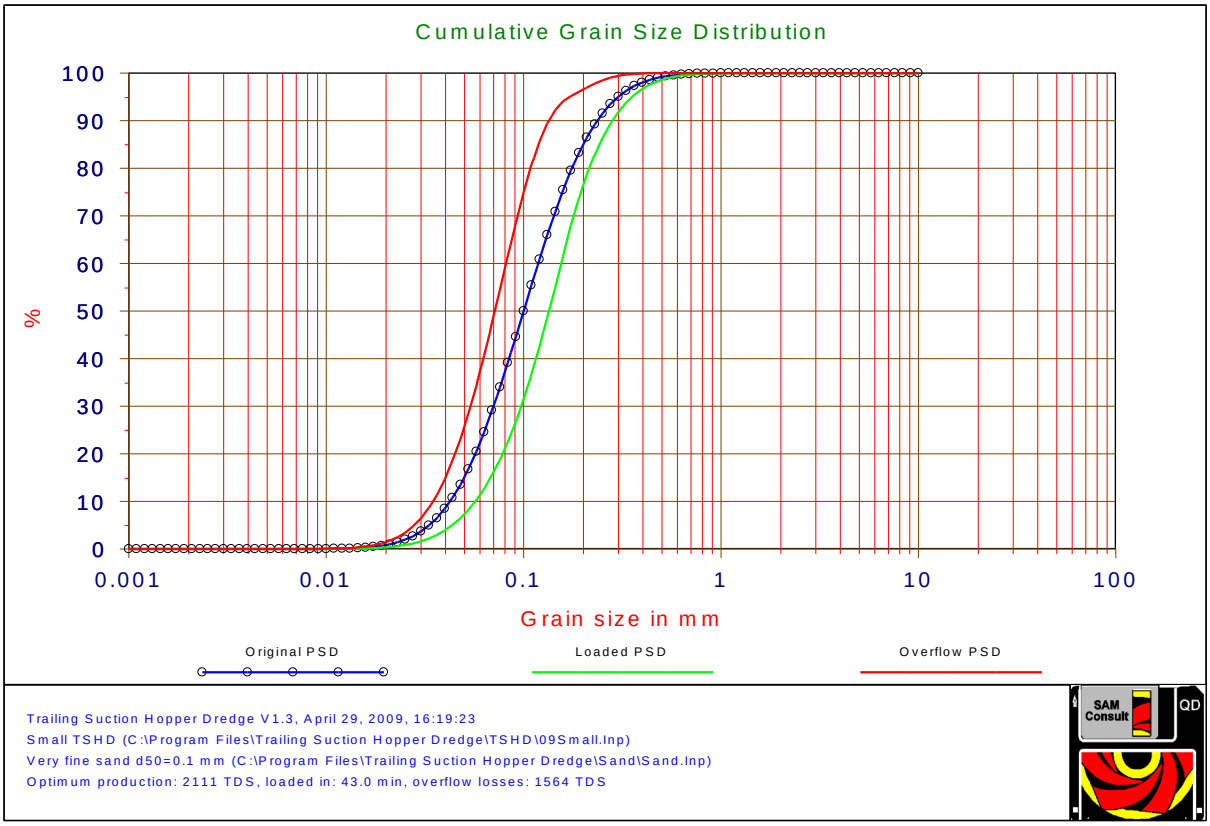

Figure 8-48: The grain distribution curves, original, overflow losses and sediment for the Small TSHD.

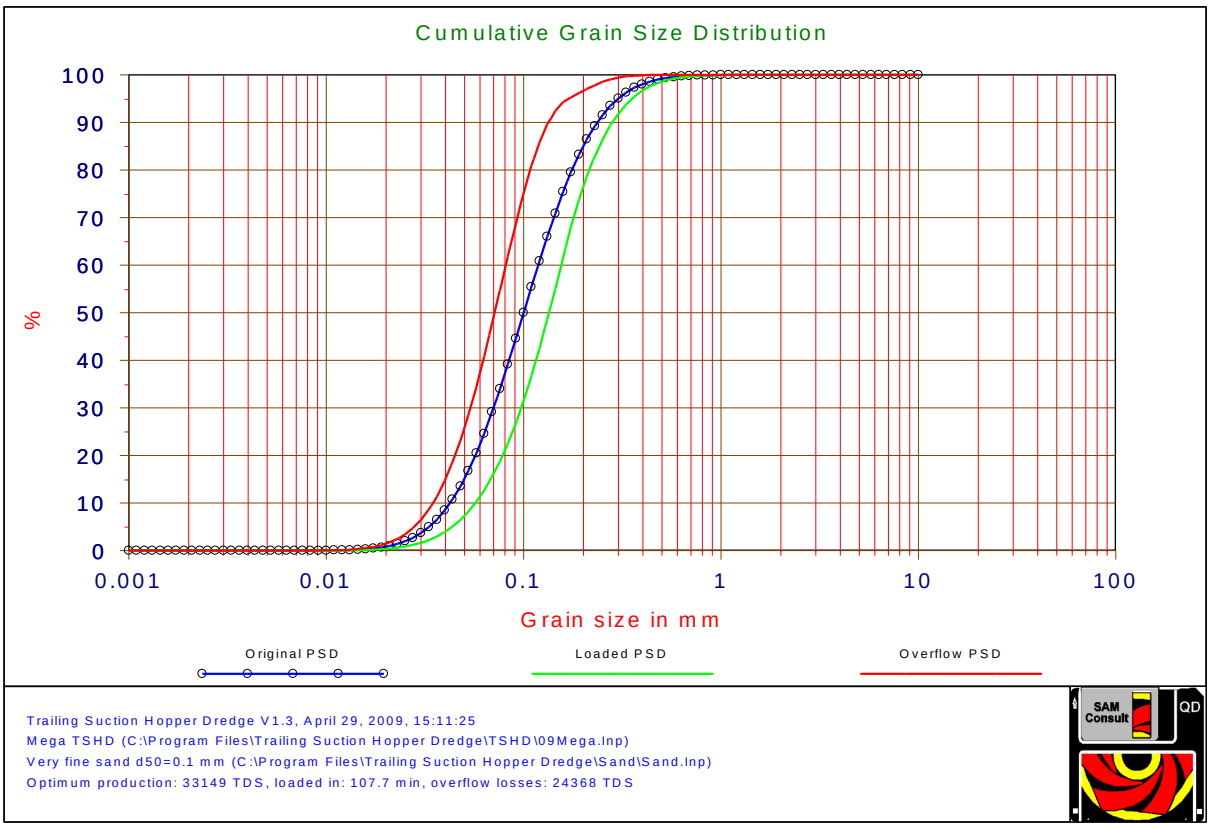

Figure 8-49: The grain distribution curves, original, overflow losses and sediment for the Mega TSHD.

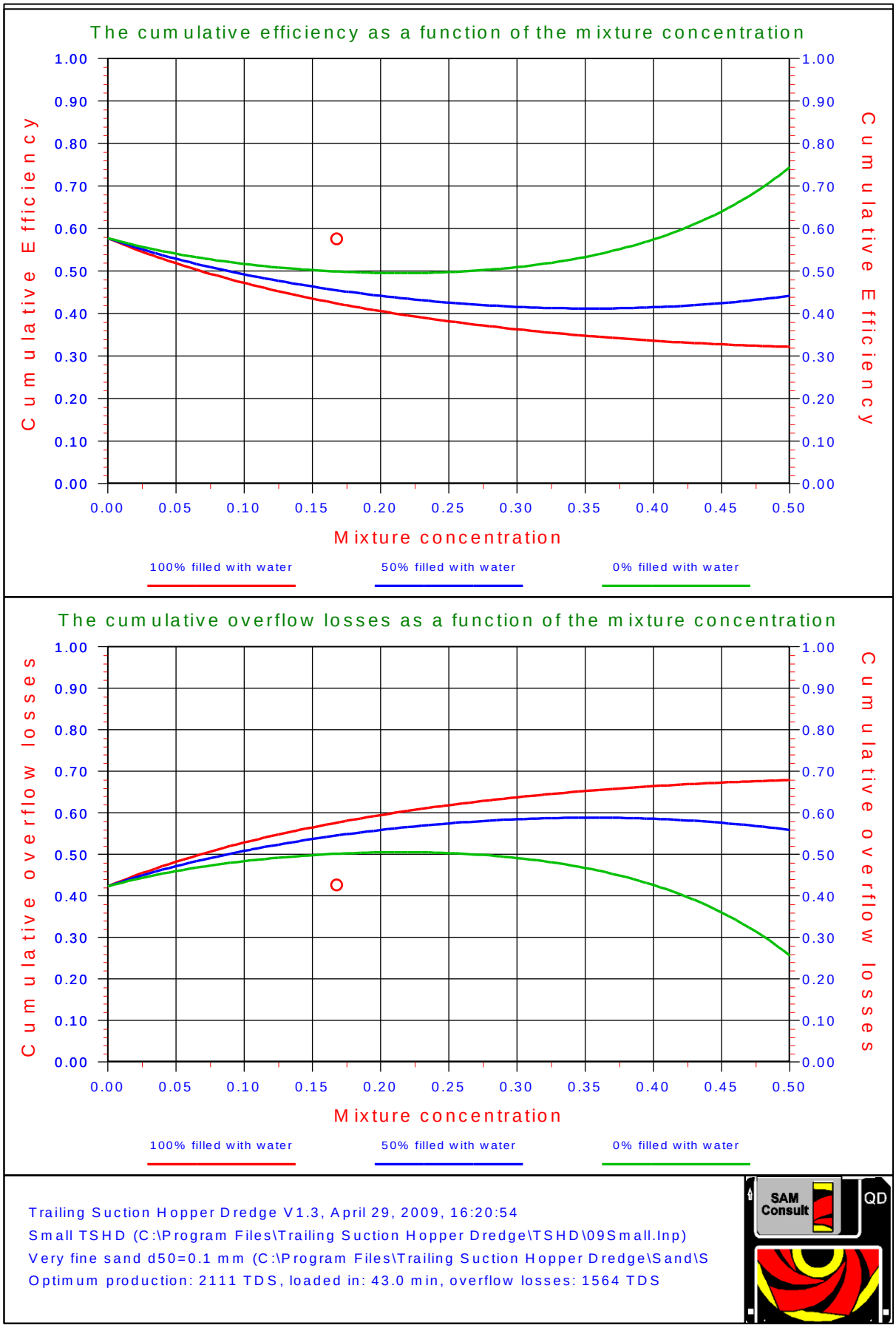

Figure 8-50: The overflow losses compared with an analytical model for the Small TSHD.

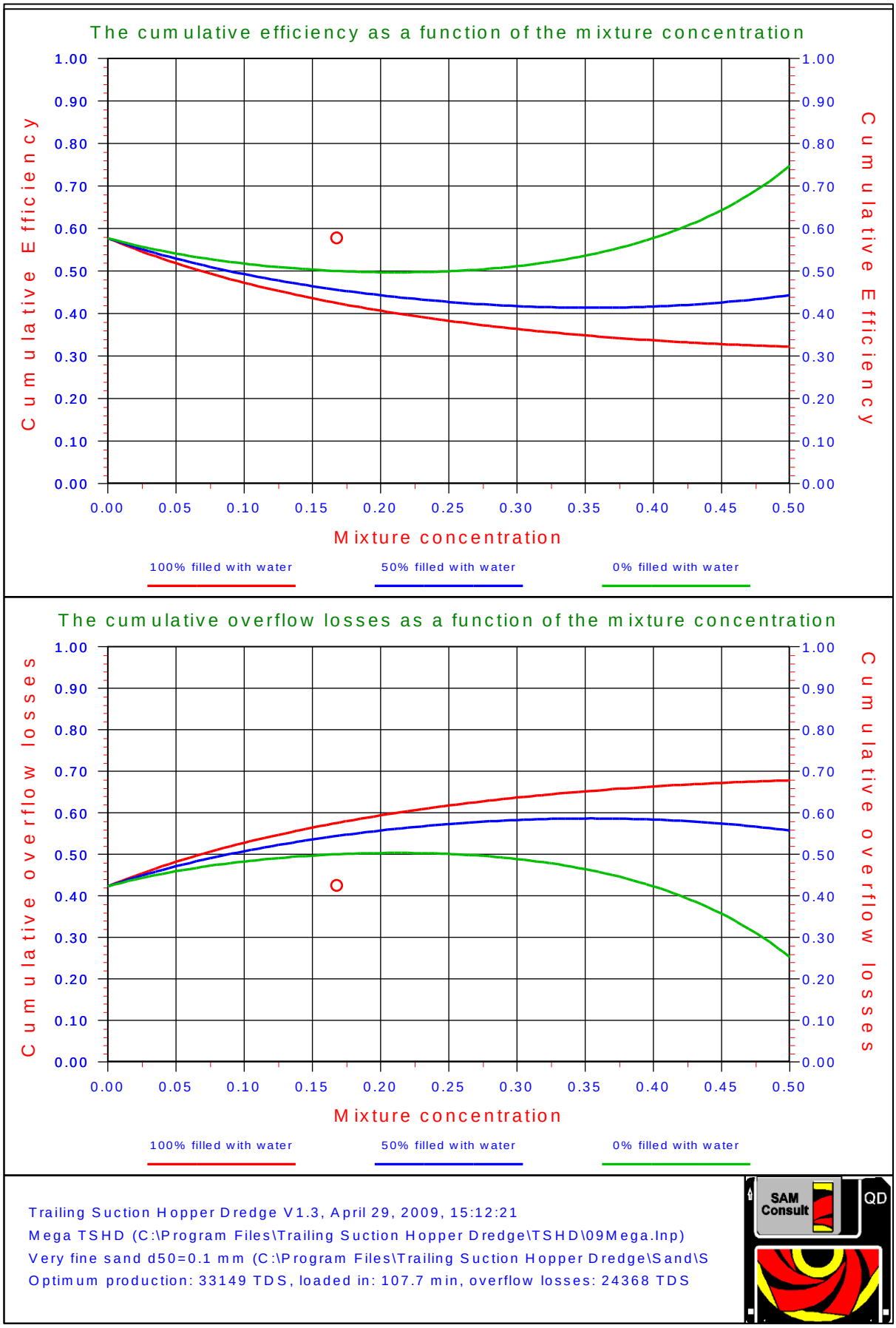

Figure 8-51: The overflow losses compared with an analytical model for the Mega TSHD.

8.11. Conclusions & Discussion.

The Camp and Dobbins model can be used to estimate loading time and overflow losses; however, the model should be tuned with measurements of the overflow rate in tons/sec as well as the particle size distribution in the overflow, as a function of time. The model can then also be used for the calculation of the decaying of the overflow plume in the dredging area.
If the model is used for the calculation of the production rate of the dredge a distinction has to be made whether the production is expressed in T.D.S./sec or in m^3/sec. In the first case the theory can be applied directly, while in the second case it has to be realized, that the overflow losses in T.D.S./sec do not always result in the same overflow loss in m^3/sec, since fine particles may situate in the voids of the bigger ones. The loss of fines does not reduce the total volume, but increases the void ratio. Although the fines leave the hopper in this case, they do not result in a reduction of the volume of the settled grains.
Those fractions which can be considered to apply to the overflow losses and those which do not, can be estimated from the difference between the real particle size distribution and the optimal particle size distribution, giving a maximum dry density, the so called Fuller distribution. If the gradient of the distribution curve for the fines is less steep then the corresponding gradient of the Fuller distribution, than that fraction of fines will not effectively contribute to the overflow losses if they are expressed in m^3/sec. In such a case, in-situ, the fines were situated in the voids of the courser grains. If the gradient is however steeper, the fines also form the grain matrix and the volume of settled grains will decrease if the fines leave the hopper through the overflow.
In the model a number of assumptions are made. Except from numerical values for the parameters involved, the Camp and Dobbins approach is used for the influence of turbulence, while separately the influence of scour is used instead of using it as a boundary condition.

The models of Miedema & Vlasblom (1996) and van Rhee (2002C) give the same magnitude for the overflow losses, but the shapes of the curves are different due to the differences in the physical modeling of the processes. Due to the lower losses the computed optimal loading time will be shorter for the Vlasblom /Miedema approach. The strong point of the van Rhee model is the accurate physical modeling, giving the possibility to model the geometry of the hopper in great detail, but also describing the physical processes in more detail. The van Rhee model is verified and validated with model and prototype tests and can be considered a reference model for other models. The strong point of the Miedema/Vlasblom model is the simplicity, giving a transparent model where result and cause are easily related.

One question before this research started, was how do the cumulative overflow losses behave when TSHD's are scaled from small to very big. The second question was, are that scale laws that should be applied when scaling TSHD's in order to create similar or maybe even identical processes.

First the answer on the second question, there are scale laws that should be applied and the main law is, to keep the hopper load parameter constant and from there derive the scale laws for the flow and other dimensions, but don't scale the sand. If the scale laws are applied correctly, the simulations show that scaling the TSHD has hardly any influence on the cumulative overflow losses and the loading processes are similar.
The overflow losses however depend strongly on the position of the grain diameter with respect to the hopper load parameter in the particle size distribution diagram. The fraction of the sand with diameters smaller than this diameter has a very strong relation with the cumulative overflow losses. A large silt fraction will increase these overflow losses.

Finally we have noted that the modified Hopper Load Parameter will reduce in magnitude compared with the unmodified Hopper Load Parameter. For particles with a settling efficiency greater than 1, this will not influence the settling efficiency, but for particles with a settling efficiency near 1 or smaller than 1, this may increase the settling efficiency slightly. So the sedimentation velocity in this respect has a positive effect on the cumulative settling efficiency. The current model seems to give rather accurate predictions. This conclusion is based on the comparison with the van Rhee model on one hand and the comparison with real data on the other hand.

Four effects are considered that were not part of the original Miedema & Vlasblom (1996) model, based on the Camp model. Those effects have been added later to the model by Miedema (2008A), (2008B), (2009A), (2009B), (2010) and Miedema & van Rhee (2007).

- Equations (8-25) and (8-29) give a good estimate of the thickness of the layer of water above the overflow level and Figure 8-15 proves that this estimate is accurate.
- The Shields approach is based on a fundamental force and moment equilibrium on grains and has been proven by many scientists in literature. Now the question is, which Shields curve to use. **Figure 8-52** shows 7 levels of erosion as defined by Delft Hydraulics (1972). To decide which of these 7 levels is appropriate for the

physics of the final stage of hopper loading, these physics should be examined. During this final stage, a high density mixture is flowing over the sediment. Part of the particles in this mixture flow will settle, part will not settle because the settling velocity is to low and part will not settle because of erosion and suspension. This process differs from the erosion process in the fact that there is not water flowing over the sediment, but a high density mixture. In fact the mixture is already saturated with particles and it is much more difficult for a particle to get eroded that in a clean water flow. One could call this hindered erosion. From the experience until now with the erosion model described (Miedema & van Rhee (2007)) and comparing it with other models, level 7 from Figure 8-52 should be chosen, this level is achieved by using **β=0.475**.

- The concentration of the mixture above the bed, often called the near bed concentration $\mathbf{c_b}$, can be estimated with equation **(8-75)**, and based on a black box approach. This concentration is used to determine the hindered settling effect on the settling velocity. Although equation **(8-75)** will not give the near bed concentration at a certain place at a certain time, it is derived for the entire hopper and loading cycle, it's a good estimate for determining the cumulative overflow losses.
- The storage, time delay or buffer effect can be implemented by using equation (8-30). Miedema & van Rhee (2007) compared both the Miedema & Vlasblom (1996) model, including the features as discussed here, and the sophisticated 2DV model, van Rhee (2002C). The result is shown in Figure 8-18. It is clear from this figure that there is a difference between the two methods if the storage effect is omitted in the Miedema & Vlasblom model, but including this storage effect gives almost the same results.
- It looks like the modified model gives results that match the van Rhee (2002C) model closely; of course the models are compared for just a few cases, specifically regarding the grain distributions used. This is remarkable because the physics of the two models are different. The van Rhee (2002C) model is based on the density flow as shown in Figure 8-6 and Figure 8-7, where there is an upward flow in the hopper. The modified model as presented here is based on the old Camp theory and assumes a uniform inflow of particles over the height of the hopper, as shown in Figure 8-20, a horizontal flow of the mixture and vertical downward transport of particles. So it seems that the dominating parameter in both models is the so called hopper load parameter, since this is the upward flow velocity in the van Rhee model and it is the settling velocity of a particle entering the hopper at the top and just reaching the sediment at the other end of the hopper in the Miedema & Vlasblom model.

Using the equations to determine the near bed concentration as derived here are based on known cumulative overflow losses and should thus not be used to predict overflow losses because that is a self-fulfilling prophecy. The modeling should be used to verify experiments where the near bed concentration is measured.
The use of the sedimentation or bed rise velocity to determine the sedimentation process when loading a TSHD with sand can only give good predictions if the correct near bed concentration is used and measured. Using the assumption that the near bed concentration equals the inflowing mixture concentration may lead to results that do not obey the conservation of mass principle.
Using the empirical equation (8-76) of van Rhee (2002C) to predict the overflow losses with the assumption that $\mathbf{c_b=c_{in}}$ is a good first approximation, but with some restrictions. It should be noted that van Rhee used the assumption of $\mathbf{c_b=c_{in}}$ to find this equation by curve fitting. The dimensionless overflow rate **S*** in this equation has to be considered to be the reciprocal of the settling efficiency, that is the correct physical meaning.
The analytical model derived in this paper matches this empirical equation, but has the advantage that sands with different grading can be taken into account.
The model derived for the sedimentation velocity, the near bed concentration and the overflow losses matches both the experiments as carried out by van Rhee (2002C) and Ooijens et al. (2001).
The model however is very sensitive for the values of the parameters **a** and **b** describing the PSD in equation (8-77), but with correct values, the model gives a very good prediction of the cumulative overflow losses.

$$\lambda = \frac{c_b}{c_{bed} \cdot \kappa} = \frac{c_b}{c_{in}} = \frac{\eta_{cum}}{\left(\eta_{cum} \cdot \kappa + \eta_p\right)} \qquad \textbf{(8-75)}$$

$$ov_{cum} = 0.39 \cdot (S'^{*} - 0.43) \qquad \textbf{(8-76)}$$

$$\log(d) = a \cdot p - b \qquad \textbf{(8-77)}$$

8.12. Nomenclature

a	Steepness of the PSD	**mm**
b	Offset of the PSD	**mm**
b	Width of the weir	**m**
c_b	Near bed concentration	**-**
c_{bed}	Bed/sediment concentration	**-**
c_{in}	Volume concentration	**-**
c_v , c_i	Volumetric concentration	**-**
C_e	Dimensionless discharge (contraction) coefficient with a value near 0.6.	**-**
C_d	Coefficient	**-**
C_D	Drag coefficient	**-**
C_L	Lift coefficient	**-**
d	Grain diameter	**mm**
d_o	Grain diameter matching the hopper load parameter	**mm**
d_{50}	Grain diameter at 50% of PSD	**mm**
d_s	Grain diameter (scour)	**m**
F_D	Drag force	**kN**
F_L	Lift force	**kN**
F_w	Submerged weight	**kN**
g	Gravitational constant (9.81)	**m/sec^2**
h	Height	**m**
h	is the overfall height (measured about a distance of 5·h upstream from the crest)	**m**
h_{max}	Maximum water layer thickness	**m**
H	Height of hopper	**m**
H_w	Height of the water above the sediment	**m**
H*	Dimensionless hopper load parameter	**-**
L	Length of basin	**m**
M	Height of the weir crest above the headwater bottom	**m**
n	Porosity	**-**
ov	Overflow losses	**-**
ov_{cum}	Cumulative overflow losses	**-**
p	Fraction of grains	**-**
p_o	Fraction of grains that settle partially (excluding turbulence)	**-**
p_{fs} , p_s	Fraction of grains that do no settle due to scour or fines	**-**
p_0	Atmospheric pressure	**kPa**
Q	Mixture flow	**m^3/sec**
$Q_{in,\ out}$	Mixture flow (in or out)	**m^3/sec**
Q_m	Mixture flow (mass)	**ton/sec**
R_d	Relative density	**-**
R	Reduction factor	**-**
s_o	Flow velocity in basin	**m/sec**
s_s	Scour velocity	**m/sec**
S*	Dimensionless overflow rate	**-**
S	Sedimentation flux	
t, T	Time	**sec**
TDS	Tonnes dry solid	**ton**
u_*	Shear velocity	**m/sec**
U_{cr}	Critical velocity above bed	**m/sec**
v	Mean velocity in the headwater this is equal to **Q/b (M + h)**	**m/sec**
v_c	Settling velocity including hindered settling	**m/sec**
v_o	Hopper load parameter	**m/sec**
v_s	Settling velocity of individual particle	**m/sec**
v_{sed}	Sedimentation/bed rise velocity	**m**
W	Width of basin	**m**
α	Fraction of hopper to be filled with mixture at start of loading process	**-**
α	Velocity factor	**-**
β	Power for hindered settling	**-**

β	Height factor	-
ε	Fraction of hopper filled with sediment when reaching the overflow	-
ρ_f	Density of fluid	ton/m^3
ρ_q	Density of particles (quarts=2.65)	ton/m^3
ρ_w	Density of water (1.025)	ton/m^3
ρ_m	Density of a sand/water mixture	ton/m^3
ρ_q	Density of quarts	ton/m^3
ρ_s	Density of sediment	ton/m^3
η	Settling efficiency	-
η_{cum}	Cumulative settling efficiency	-
η_g	Settling efficiency individual grain	-
η_b	Settling efficiency for basin	-
η_t	Turbulence settling efficiency for individual grain	-
η_p	Settling efficiency individual particle	-
λ	Concentration ratio c_b/c_{in}	-
λ	Viscous friction coefficient	-
κ	Concentration ratio c_{in}/c_{bed}	-
κ	Ratio mixture concentration versus bed concentration	-
μ	Settling velocity factor	-
μ	Friction coefficient	-
τ	Time constant	sec
ν	Kinematic viscosity	St
θ	Shields parameter	-

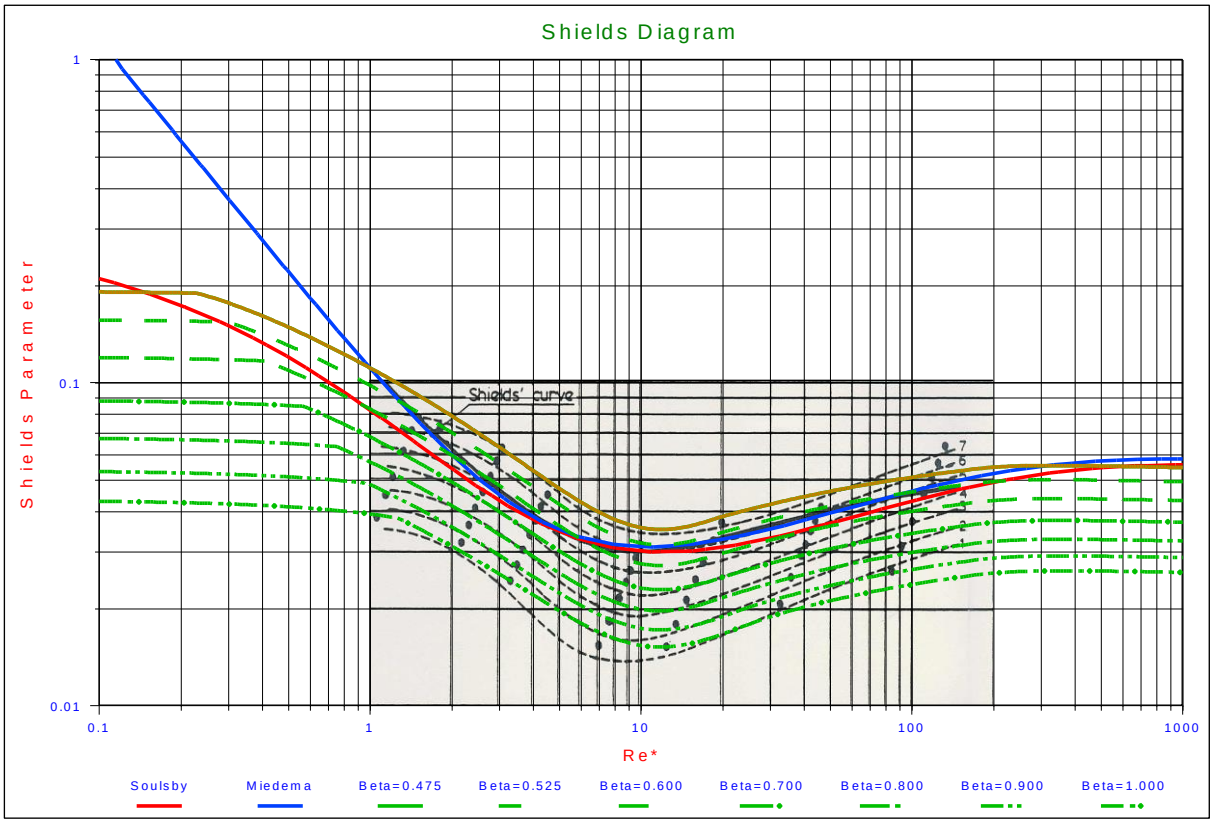

Figure 8-52: The 7 levels of erosion according to Delft Hydraulics (1972).

8.13. Notes.

Chapter 9: References.

Abelev, A., & Valent, P. (2010). *Strain rate dependency of strength of soft marine deposits of the Gulf of Mexico.* Stennis Space Center, MS 39529, USA.: Naval Research Laboratory.

Abulnaga, B. E. (2002). *Slurry Systems Handbook.* USA: McGraw Hill.

Azamathulla, H. M., & Ahmad, Z. (2013). Estimation of critical velocity for slurry transport through pipeline using adaptive neuro-fuzzy interference system and gene-expression programming. *Journal of Pipeline Systems Engineering and Practice.*, 131-137.

Babcock, H. A. (1970). The sliding bed flow regime. *Hydrotransport 1* (pp. H1-1 - H1-16). Bedford, England: BHRA.

Bagnold, R. A. (1954). Experiments on a gravity free dispersion of large solid spheres in a Newtonian fluid under shear. *Proceedings Royal Society, Vol. A225.*, 49-63.

Bagnold, R. A. (1957). The flow of cohesionless grains in fluids. *Phil. Trans. Royal Society, Vol. A249*, 235-297.

Bain, A. G., & Bonnington, S. T. (1970). *The hydraulic transport of solids by pipeline.* Pergamon Press.

Barker, A., Sayed, M., & Carrieres, M. (2004). Determination of iceberg draft, mass and cross sectional areas. *14th international offshore and polar engineering conference.* Toulon, France.

Barrette, P. (2011). Offshore pipeline protection against seabed scouring, an overview. *Cold Regions Science Technology, Vol. 69.*, 3-20.

Becker, S., Miedema, S., Jong, P., & Wittekoek, S. (1992). On the Closing Process of Clamshell Dredges in Water Saturated Sand. *WODCON XIII* (p. 22 pages). Bombay, India: WODA.

Becker, S., Miedema, S., Jong, P., & Wittekoek, S. (1992, September). The Closing Process of Clamshell Dredges in Water Saturated Sand. *Terra et Aqua, No. 49*, 22 pages.

Berg, C. H. (1998). *Pipelines as Transportation Systems.* Kinderdijk, the Netherlands: European Mining Course Proceedings, IHC-MTI.

Berg, C. v. (2013). *IHC Merwede Handbook for Centrifugal Pumps & Slurry Transportation.* Kinderdijk, Netherlands: IHC Merwede.

Berman, V. P. (1994). *Gidro i aerodinamiceskie osnovy rascota truboprovodnych sistem gidrokontejnernogo i vysokonapornogo pnevmaticeskogo transporta.* Lugansk: East Ukrainian State University.

Biot, M. (1941). General theory of three dimensional consolidation. *Journal of Applied Physics, vol. 12.*, 155-164.

Bishop, A. (1966). The strength of soils as engineering materials. *Geotechnique, vol. 16, no. 2.*, 91-128.

Bisschop, F., Miedema, S. A., Rhee, C. v., & Visser, P. J. (2014). Erosion experiments on sand at high velocities. *To be submitted to the Journal of Hydraulic Engineering*, 28.

Blasco, S. M., Shearer, J. M., & Myers, R. (1998). Seabed scouring by sea ice: scouring process and impact rates. *1st ice scour and arctic marine pipelines workshop, 13th international symposium on Okhotsk Sea and Sea Ice.*, (pp. 53-58). Mombetsu, Hokkaido, Japan.

Blatch, N. S. (1906). Discussion of Works for the purification of the water supply of Washington D.C. *Transactions ASCE 57.*, 400-409.

Blythe, C., & Czarnotta, Z. (1995). Determination of hydraulic gradient for sand slurries. *8th International Freight Pipeline Society Symposium*, (pp. 125-130). Pittsburg, USA.

Bonneville, R. (1963). *essais de synthese des lois debut d'entrainment des sediment sous l'action d'un courant en regime uniform.* Chatou: Bulletin Du CREC, No. 5.

Bonnington, S. T. (1961). *Estimation of Pipe Friction Involved in Pumping Solid Material.* BHRA, TN 708 (December 1961).

Boothroyde, J., Jacobs, B. E., & Jenkins, P. (1979). Coarse particle hydraulic transport. *Hydrotransport 6: 6th International Conference on the Hydraulic Transport of Solids in Pipes.* (p. Paper E1). BHRA.

Bourbonnair, J., & Lananyi, B. (1985). The mechanical behaviour of a frozen clay down to cryogenic temperatures. *4th symposium on ground freezing.*, (pp. 237-244). Sapporo, Japan.

Brakel, J. (1981). *Mathematisch model voor de krachten op een roterende snijkop van een in zeegang werkende snijkopzuiger.* Delft, Netherlands: Delft University of Technology - ScO/80/96.

Brauer, H. (1971). *Grundlagen der einphasen- und mehrphasenstromungen.* Verslag Sauerlander.

Bree, S. E. (1977). Centrifugal DredgePumps. *Ports & Dredging (10 issues, IHC Holland).*

Brooks, F. A., & Berggren, W. (1944). Remarks on turbulent transfer across planes of zero momentum exchange. *Transactions of the American Geophysics Union, Pt. VI.*, 889-896.

Brownlie, W. (1981). *Compilation of alluvial channel data: laboratory and field, Technical Report KH-R-43B.* Pasadena, California, USA: California Institute of Technology.

Buffington, J. M. (1999). The legend of A.F. Shields. *Journal of Hydraulic Engineering, 125*, 376–387.

Buffington, J. M., & Montgomery, D. R. (1997). A systematic analysis of eight decades of incipient motion studies, with special reference to gravel-bedded rivers. *Water Resources Research, 33*, 1993-2029.

Butterfield, R., & Andrawes, K. (1972). On the angles of friction between sand and plane surfaces. *Journal of Terramechanics, vol. 8, no. 4.*, 15-23.

Camenen, B., & Larson, M. (2013). Accuracy of Equivalent Roughness Height Formulas in Practical Applications. *Journal of Hydraulic Engineering.*, 331-335.
Camenen, B., Bayram, A. M., & Larson, M. (2006). Equivalent roughness height for plane bed under steady flow. *Journal of Hydraulic Engineering*, 1146-1158.
Camp, T. (1936). Study of rational design of settling tanks. *Sewage Works Journal 8-5.*, 742-758.
Camp, T. (1946). Sedimentation and the design of settling tanks. *ASCE Transactions*, 895-936.
Camp, T. (1953). Studies of sedimentation design. *Sewage & Industrial Wastes 25*, 1-14.
Carman, P. (1937). Fluid flow through granular beds. *Transactions Institute Chemical Engineering, 15, 150.*
Carman, P. (1956). *Flow of gases through porous media.* London: Butterworths Scientific Publications.
Charles, M. E. (1970). Transport of solids by pipeline. *Hydrotransport 1.* Cranfield: BHRA.
Chaskelberg, K., & Karlin. (1976). *Rascot gidrotransporta pesanych materialov.* Moskov: Gidromechanizacija.
Chen, X., & Miedema, S. A. (2014). NUMERICAL METHODS FOR MODELING THE ROCK CUTTING PROCESS IN DEEP SEA MINING. *OMAE 2014* (p. 10). San Francisco, USA: ASME.
Chin, C. O., & Chiew, Y. M. (1993). Effect of bed surface structure on spherical particle stability. *Journal of Waterway, Port, Coastal and Ocean Engineering, 119(3)*, 231–242.
Clift, R., Wilson, K. C., Addie, G. R., & Carstens, M. R. (1982). A mechanistically based method for scaling pipeline tests for settling slurries. *Hydrotransport 8* (pp. 91-101). Cranfield, UK.: BHRA Fluid Engineering.
Clift, R., Wilson, K., Addie, G., & Carstens, M. (1982). A mechanistically based method for scaling pipeline tests for settling slurries. *Hydrotransport 8* (pp. 91-101). Cranfield, UK.: BHRA.
Colebrook, C. F., & White, C. M. (1937). Experiments with Fluid Friction in Roughened Pipes. *Proceedings of the Royal Society of London. Series A, Mathematical and Physical Sciences 161 (906).* (pp. 367-381). London: Royal Society of London.
Coleman, N. L. (1967). A theoretical and experimental study of drag and lift forces acting on a sphere resting on a hypothetical stream bed. *International Association for Hydraulic Research,12th Congress, 3*, pp. 185-192.
Condolios, E., & Chapus, E. E. (1963A). Transporting Solid Materials in Pipelines, Part I. *Journal of Chemical Engineering, Vol. 70(13).*, 93-98.
Condolios, E., & Chapus, E. E. (1963B). Designing Solids Handling Pipelines Part II. *Journal of Chemical Engineering, Vol. 70(14).*, 131-138.
Condolios, E., & Chapus, E. E. (1963C). Operating solids pipelines, Part III. *Journal of Chemical Engineering, Vol. 70(15).*, 145-150.
Coulomb, C. (1776). Essai sur une application des regles des maximis et minimis a quelques problemes de statique relatifs a l'architecture. *Academie royale des sciences, Paris, Memoires de mathematique et de physique, vol. 7.*, 343-382.
Cox, C. M., Eygenraam, J. A., Granneman, C. C., & Njoo, M. (1995). A Training Si,ulator for Cutter Suction Dredgers: Bridging the Gap between Theory and Practice. *WODCON XIV* (p. 10). Amsterdam, The Netherlands.: WODA.
Crowe, C. T. (2006). *MultiPhase Flow Handbook.* Boca Raton, Florida, USA: Taylor & Francis Group.
Davies, J. T. (1987). Calculation of critical velocities to maintain solids in suspension in horizontal pipes. *Chemical Engineering Science, Vol. 42(7).*, 1667-1670.
Detournay, E., & Atkinson, C. (2000). Influence of pore pressure on the drilling response in low permeability shear dilatant rocks. *International Journal of Rock Mechanics & Mining Sciences, vol. 37.*, 1091-1101.
Dey, S. (1999). Sediment threshold. *Applied Mathematical Modelling*, 399-417.
Dey, S. (2003). Incipient motion of bivalve shells on sand beds under flowing water. *Journal of Hydraulic Engineering*, 232-240.
Dey, S. (2014). *Fluvial Hydrodynamics.* Kharagpur, India: Springer, GeoPlanet: Earth and Planetary Sciences.
DHL. (1972). *Systematic Investigation of Two Dimensional and Three Dimensional Scour, Report M648/M863.* Delft, Netherlands: Delft Hydraulics Laboratory.
Di Filice, R. (1999). The sedimentation velocity of dilute suspensions of nearly monosized spheres. *International Journal of Multiphase Flows 25*, 559-574.
Dobbins, W. (1944). Effect of Turbulence on Sedimentation. *ASCE Transactions Vol. 109, No. 2218*, 629-656.
Doron, P., & Barnea, D. (1993). A three layer model for solid liquid flow in horizontal pipes. *International Journal of Multiphase Flow, Vol. 19, No.6.*, 1029-1043.
Doron, P., & Barnea, D. (1995). Pressure drop and limit deposit velocity for solid liquid flow in pipes. *Chemical Engineering Science, Vol. 50, No. 10.*, 1595-1604.
Doron, P., & Barnea, D. (1996). Flow pattern maps for solid liquid flow in pipes. *International Journal of Multiphase Flow, Vol. 22, No. 2.*, 273-283.
Doron, P., Granica, D., & Barnea, D. (1987). Slurry flow in horizontal pipes, experimental and modeling. *International Journal of Multiphase Flow, Vol. 13, No. 4.*, 535-547.

References.

Doron, P., Simkhis, M., & Barnea, D. (1997). Flow of solid liquid mixtures in inclined pipes. *International Journal of Multiphase Flow, Vol. 23, No. 2.*, 313-323.

Duckworth, & Argyros. (1972). Influence of density ratio on the pressure gradient in pipes conveying suspensions of solids in liquids. *Hydrotransport 2.* Coventry: BHRA.

Durand, R. (1953). Basic Relationships of the Transportation of Solids in Pipes - Experimental Research. *Proceedings of the International Association of Hydraulic Research.* Minneapolis.

Durand, R., & Condolios, E. (1952). Etude experimentale du refoulement des materieaux en conduites en particulier des produits de dragage et des schlamms. *Deuxiemes Journees de l'Hydraulique.*, 27-55.

Durand, R., & Condolios, E. (1952). Etude experimentale du refoulement des materieaux en conduites en particulier des produits de dragage et des schlamms. (Experimental study of the discharge pipes materieaux especially products of dredging and slurries). *Deuxiemes Journees de l'Hydraulique.*, 27-55.

Durand, R., & Condolios, E. (1956). Donnees techniques sur le refoulement des mixture en conduites. *Revue de lÍndustriele Minerale, no. 22F*, 460-481.

Durand, R., & Condolios, E. (1956). *Technical data on hydraulic transport of solid materials in conduits.* Revue de L'Industrie Minerale, Numero Special 1F.

Durepaire, M. P. (1939). Contribution a létude du dragage et du refoulement des deblais a état de mixtures. *Annales des ponts et chaussees, Memoires I.*, 165-254.

Egiazarof, I. (1965). Calculation of non-uniform sediment concentrations. *Journal of the Hydraulic Division, ASCE, 91(HY4)*, 225-247.

Einstein, A. (1905). On the motion of small particles suspended in liquids at rest required by the molecular kinetic theory of heat. *Annalen der Physik Vol.17.*, 549-560.

Ellis, H. S., & Round, G. F. (1963). Laboratory studies on the flow of Nickel-Water suspensions. *Canadian Journal on Minerals & Mettalurgy, Bull. 56.*

Engelund, F., & Hansen, E. (1967). A monograph on sediment transport to alluvial streams. *Copenhagen: Technik Vorlag*.

Evans, I. (1962). A theory on basic mechanics of coal ploughing. *International symposium on mining research.*, (pp. 761-798).

Evans, I. (1964). The force required to cut coal with blunt wedges. *Mining Research Establishment Isleworth*.

Evans, I. (1965). The force required to cut coal with blunt wedges. *International journal of rock mechanics and mining science.*, 1-12.

Evans, I., & Pomeroy, C. (1966). *The strength, fracture and workability of coal.* Pergamon Press.

Fairhurst, C. (1964). On the validity of the Brazilian test for brittle materials. *International Journal of Rock Mechanics & Mining Sciences, vol. 1.*, 535-546.

Fenton, J. D., & Abbott, J. E. (1977). Initial movement of grains on a stream bed: The effect of relative protrusion. *Proceedings of Royal Society, 352(A)*, pp. 523–537. London.

Fowkes, R. S., & Wancheck, G. A. (1969). *Materials handling research: Hydraulic transportation of coarse solids.* U.S. Department of the interior, Bureau of Mines, Report 7283.

Franzi, G. (1941). *Sul moto dei liquidi con materie solide in suspensione.* Milano, Italy: Instituto di idraulica e costrusioni idrauliche dei politechnico di Milano, No. 47.

Fuhrboter, A. (1961). *Über die Förderung von Sand-Wasser-Gemischen in Rohrleitungen.* Mitteilungen des Franzius-Instituts, H. 19.

Fuhrboter, A. (1961). *Über die Förderung von Sand-Wasser-Gemischen in Rohrleitungen. (On the advances of sand -water mixtures in pipelines).* Mitteilungen des Franzius-Instituts, H. 19.

Gandhi, R. (2015, February). Personal communication.

Garcia, M. H. (2008). *Sedimentation Engineering* (Vol. 110). ASCE Manuals & Reports on Engineering Practise No. 110.

Garside, J., & Al-Dibouni, M. (1977). Velocity-Voidage Relationships for Fluidization and Sedimentation in Solid-Liquid Systems. *2nd Eng. Chem. Process Des. Dev., 16, 206*.

Gehking, K. (1987). *Rock Testing Procedures at VA's Geotechnical Laboratory in Zeltweg.* Zeltweg, Austria.: Voest Alphine, International Report TZU 48.

Gibert, R. (1960). Transport hydraulique et refoulement des mixtures en conduites. *Annales des Ponts et Chausees.*, 130(3), 307-74, 130(4), 437-94.

Gibert, R. (1960). Transport hydraulique et refoulement des mixtures en conduites. (Hydraulic transport and discharge pipes of mixtures). *Annales des Ponts et Chausees.*, 130(3), 307-74, 130(4), 437-94.

Gillies, D. P. (2013). *Particle contributions to kinematic friction in slurry pipeline flow, MSc Thesis.* University of Alberta, Department of Chemical Engineering.

Gillies, R. G. (1993). *Pipeline flow of coarse particles, PhD Thesis.* Saskatoon: University of Saskatchewan.

Gillies, R. G. (2015). Personal communication.

Gillies, R. G., & Shook, C. A. (2000A). Modeling high concentration settling slurry flows. *Canadian Journal of Chemical Engineering, Vol. 78.*, 709-716.

Gillies, R. G., Schaan, J., Sumner, R. J., McKibben, M. J., & Shook, C. A. (2000B). Deposition velocities for Newtonian slurries in turbulent flow. *Canadian Journal of Chemical Engineering, Vol. 78.*, 704-708.

Gillies, R. G., Shook, C. A., & Wilson, K. C. (1991). An improved two layer model for horizontal slurry pipeline flow. *Canadian Journal of Chemical Engineering, Vol. 69.*, 173-178.

Gillies, R. G., Shook, C. A., & Xu, J. (2004). Modelling heterogeneous slurry flows at high velocities. *The Canadian Journal of Chemical Engineering, Vol. 82.*, 1060-1065.

Glasstone, S., Laidler, K., & Eyring, H. (1941). *The theory of rate processes.* New York: McGraw Hill.

Gogus, M., & Kokpinar, M. A. (1993). Determination of critical flow velocity in slurry transporting pipeline systems. *Proceeding of the 12th International Conference on Slurry Handling and Pipeline Transport.* (pp. 743-757). Bedfordshire, UK.: British Hydraulic Research Group.

Govier, G. W., & Aziz, K. (1972). *The Flow of Complex Mixtures in Pipes.* New York: University of Calgary, Alberta, Canada.

Grace, J. (1986). Contacting modes and behaviour classification of gas-solid and other two-phase suspensions. *Canadian Journal of Chemical Engineering, vol. 64.*, 353-363.

Graf, W. H., & Pazis, G. C. (1977). Les phenomenes de deposition et d'erosion dans un canal alluvionnaire. *Journal of Hydraulic Research, 15*, 151-165.

Graf, W. H., Robinson, M. P., & Yucel, O. (1970). *Critical velocity for solid liquid mixtures.* Bethlehem, Pensylvania, USA.: Fritz Laboratory Reports, Paper 386. Lehigh University.

Graf, W. H., Robinson, M., & Yucel, O. (1970). The critical deposit velocity for solid-liquid mixtures. *Hydrotransport 1* (pp. H5-77-H5-88). Cranfield, UK: BHRA.

Grant, W. D., & Madsen, O. S. (1982). Movable bed roughness in unsteady oscillatory flow. *Journal Geophysics Resources*, 469-481.

Groot, J. (1981). *Rapport Beunbezinking (in Dutch).* Papendrecht: Royal Boskalis Westminster.

Grunsven, F. v. (2012). *Measuring the slip factor for various slurry flows using temperature calibrated Electrical Resistance Tomography.* Delft, The Netherlands.: Delft University of Technology.

Hansen, B. (1958). Line ruptures regarded as narrow rupture zones. *Earth Pressure Problems*, (pp. 39-48). Brussels.

Harada, E., Kuriyama, M., & Konno, H. (1989). Heat transfer with a solid liquid suspension flowing through a horizontal rectangular duct. *Heat Transfer Jap. Res. Vol. 18.*, 79-94.

Hatamura, Y., & Chijiiwa, K. (1975). Analyses of the mechanism of soil cutting, 1st report. *Bulletin of JSME, vol. 18, no. 120*, 619-626.

Hatamura, Y., & Chijiiwa, K. (1976A). Analyses of the mechanism of soil cutting, 2nd report. *Bulletin of the JSME, vol. 19, no. 131.*, 555-563.

Hatamura, Y., & Chijiiwa, K. (1976B). Analyses of the mechanism of soil cutting, 3rd report. *Bulletin of the JSME, vol. 19, no. 139.*, 1376-1384.

Hatamura, Y., & Chijiiwa, K. (1977A). Analyses of the mechanism of soil cutting, 4th report. *Bulletin of the JSME, vol. 20, no. 139.*, 130-137.

Hatamura, Y., & Chijiiwa, K. (1977B). Analyses of the mechanism of soil cutting, 5th report. *Bulletin of the JSME, vol. 20, no. 141.*, 388-395.

Hazen, A. (1982). Some physical properties of sands and gravels with special reference to their use in filtration. *24th Annual Report, Massachusetts State Board of Health, Pub. Doc. No. 34.*, 539-556.

He, J., & Vlasblom, W. (1998). Modelling of saturated sand cutting with large rake angles. *WODCON XV.* Las Vegas, USA: WODA.

He, J., Miedema, S., & Vlasblom, W. (2005). FEM Analyses Of Cutting Of Anisotropic Densely Compacted and Saturated Sand. *WEDAXXV/TAMU37.* New Orleans, Louisiana, USA: WEDA/TAMU.

Helmons, R. L., Miedema, S. A., & Rhee, C. v. (2014). A NEW APPROACH TO MODEL HYPERBARIC ROCK CUTTING PROCESSES. *OMAE 2014* (p. 9). San Francisco, USA: ASME.

Hepy, F. M., Ahmad, Z., & Kansal, M. L. (2008). Critical velocity for slurry transport through pipeline. *Dam Engineering, Vol. XIX(3).*, 169-184.

Hettiaratchi, D. (1967A). The mechanics of soil cultivation. *AES, no. 3/245/C/28.*

Hettiaratchi, D., & Reece, A. (1967B). Symmetrical three-dimensional soil failure. *Journal of Terramechanics 4 (3).*, 45-67.

Hettiaratchi, D., & Reece, A. (1974). The calculation of passive soil resistance. *Geotechnique 24, no. 3.*, 289-310.

Hettiaratchi, D., & Reece, A. (1975). Boundary wedges in two dimensional passive soil failure. *Geotechnique 25, no. 2.*, 197-220.

Hettiaratchi, D., Witney, B., & Reece, A. (1966). The calculation of passive pressure in two dimensional soil failure. *Journal of Agriculture Engineering Resources 11 (2)*, 89-107.

Hjulstrøm, F. (1935). Studies of the morphological activity of rivers as illustrated by the River Fyris. *Bulletin of the Geological Institute, 25*, 221–527. University of Uppsala.

References.

Hjulstrøm, F. (1939). Transportation of debris by moving water, in Trask, P.D., ed., Recent Marine Sediments. *A Symposium: Tulsa, Oklahoma, American Association of Petroleum Geologists*, (pp. 5-31). Tulsa, Oklahoma.

Hoek, E., & Brown, E. T. (1988). The Hoek-Brown Failure Criterion - a 1988 Update. *15th Canadian Rock Mechanics Symposium.*, (pp. 31-38).

Howard, G. W. (1938). Transportation of Sand and Gravel in a 4 Inch Pipe. *Transactions ASCE Vol. 104., No. 2039.*, 1334-1348.

Howard, G. W. (1939). Discussion on: Transportation of sand and gravel in a four inch pipe. *Transactions ASCE Vol. 104.*, 157, 316, 460, 1011.

Hsu. (1986). *Flow of non-colloidal slurries in pipeline.* PhD Thesis, University of Illinois.

Huisman, L. (1973-1995). *Sedimentation & Flotation 1973-1995.* Delft, Netherlands: Delft University of Technology.

Huisman, L. (1980). *Theory of settling tanks.* Delft, Netherlands: Delft University of Technology.

Hunt, J. N. (1954). The turbulent transport of suspended sediment in open channels. *Royal Society of London, Proc. Series A, Vol. 224(1158).*, 322-335.

Ikeda, S. (1982). Incipient motion of sand particles on side slopes. *Journal of the Hydraulic division, ASCE, 108*(No. HY1).

Ismail, H. M. (1952). Turbulent transfer mechanism and suspended sediment in closed channels. *Transactions of ASCE, Vol. 117.*, 409-446.

Iwagaki, Y. (1956). Fundamental study on critical tractive force. *Transactions of the Japanese Society of Civil Engineers, Vol. 41*, 1-21.

Joanknecht, L. (1973). *Mechanisch graaf onderzoek onder water.* Delft, Netherlands: Delft University of Technology.

Joanknecht, L. (1974). *Cutting forces in submerged soils.* Delft, Netherlands: Delft University of Technology.

Josselin de Jong, G. (1976). Rowe's stress dilatancy relation based on friction. *Geotechnique 26, no. 3*, 527-534.

Jufin, A. P. (1965). *Gidromechanizacija.* Moskau.

Jufin, A. P., & Lopatin, N. A. (1966). O projekte TUiN na gidrotransport zernistych materialov po stalnym truboprovodam. *Gidrotechniceskoe Strojitelstvo, 9.*, 49-52.

Jukes, P., Kenny, S., Panapitiya, U., Jafri, S., & Eltaher, A. (2011). Arctic and harsh environment pipeline trenching technologies and challenges. *OTC.* Houston: OTC.

Julien, P. (1995). Erosion and sedimentation. *Cambridge University Press*.

Kaitkay, P., & Lei, S. (2005). Experimental study of rock cutting under external hydrostatic pressure. *Journal of Materials Processing Technology, vol. 159.*, 206-213.

Karabelas, A. J. (1977). Vertical Distribution of Dilute Suspensins in Turbulent Pipe Flow. *AIChE Journal, Vol. 23(4).*, 426-434.

Karasik, U. A. (1973). Hydraulische Forderung von feinkorniqen Suspensionen (in russisch). *Gidromechanika, S.BO ff, Vol. 25. Kiew.*

Kaushal, D. R. (1995). *Prediction of particle distribution in the flow of multisized particulate slurries through closed ducts and open channels.* Delhi, India: I.I.T.. Department of Applied Mechanics, PhD Thesis.

Kaushal, D. R., & Tomita, Y. (2002B). Solids concentration profiles and pressure drop in pipeline flow of multisized particulate slurries. *International Journal of Multiphase Flow, Vol. 28.*, 1697-1717.

Kaushal, D. R., & Tomita, Y. (2002C). An improved method for predicting pressure drop along slurry pipeline. *Particulate Science and Technology: An International Journal, Vol. 20(4).*, 305-324.

Kaushal, D. R., & Tomita, Y. (2003B). Comparative study of pressure drop in multisized particulate slurry flow through pipe and rectangular duct. *International Journal of Multiphase Flow, Vol. 29.*, 1473-1487.

Kaushal, D. R., & Tomita, Y. (2013). Prediction of concentration distribution in pipeline flow of highly concentrated slurry. *Particulate Science and Technology: An International Journal, Vol. 31(1).*, 28-34.

Kaushal, D. R., Sato, K., Toyota, T., Funatsu, K., & Tomita, Y. (2005). Effect of particle size distribution on pressure drop and concentration profile in pipeline flow of highly concentrated slurry. *International Journal of Multiphase Flow, Vol. 31.*, 809-823.

Kaushal, D. R., Seshadri, V., & Singh, S. N. (2002D). Prediction of concentration and particle size distribution in the flow of multi-sized particulate slurry through rectangular duct. *Applied Mathematical Modelling, Vol. 26.*, 941-952.

Kaushal, D. R., Seshadri, V., & Singh, S. N. (2003A). Concentration and particle size distribution in the flow of multi-sized particulate slurry through rectangular duct. *Journal of Hydrology & Hydromechanics*, 114-121.

Kaushal, D. R., Tomita, Y., & Dighade, R. R. (2002A). Concentration at the pipe bottom at deposition velocity for transportation of commercial slurries through pipeline. *Powder Technology Vol. 125.*, 89-101.

Kazanskij, I. (1967). *Vyzkum proudeni hydrosmesi voda-pisek (untersuchung uber sans-wasser stromungen).* Mitteilungen des Franzius Instituts, Heft 33.

Kazanskij, I. (1972). *Berechnungsverfahren fur die Forderung von Sand-Wasser Gemischen in Rohrleitungen.* Hannover: Franzius Institut, Heft 33.

Kazanskij, I. (1978). Scale-up effects in hydraulic transport theory and practice. *Hydrotransport 5* (pp. B3: 47-74). Cranfield, UK: BHRA Fluid Engineering.

Kazanskij, I. (1980). Vergleich verschiedener Rohrmaterialen in Bezug auf Verschleiss und Energieverbrauch beim Hydrotransport in Rohrleitungen. *VDI Berichte Nr. 371*, pp. 51-58.

Kelessidis, V., & Maglione, R. (2008). Yield stress of water bentonite dispersions. *Colloids and Surfaces A: Physicochemical Engineering Aspects 318.*, 217-226.

Kelessidis, V., Tsamantaki, C., & Dalamarinis, P. (2007). Effect of pH and electrolyte on the rheology of aqueous Wyoming bentonite dispersions. *Applied Clay Science 38.*, 86-96.

Kesteren, W. G. (1995). Numerical simulations of crack bifurcation in the chip forming cutting process in rock. In G. B. Karihaloo (Ed.), *Fracture of brittle disordered materials: concrete, rock and ceramics.* (pp. 505-524). London, UK.: E&FN Spon.

King, R. P. (2002). *Introduction to Practical Fluid Flow.* University of Utah.: Butterworth Heineman.

Kokpinar, M. A., & Gogus, M. (2001). Critical velocity in slurry transport in horizontal pipelines. *Journal of Hydraulic Engineering, Vol. 127(9).*, 763-771.

Koning, J. d. (1977). Constant Tonnage Loading System of Trailing Suction Hopper Dredges. *International Course on Modern Dredging* (p. D6). The Hague, The Netherlands: Delft University of Technology & KIVI.

Koning, J. d., Miedema, S., & Zwartbol, A. (1983). Soil/Cutterhead Interaction under Wave Conditions. *WODCON X.* Singapore: WODA.

Korzajev, M. (1964). Metod rascota parametrov gidrotransporta gruntov. *Gidromechanizacija, Moskau*.

Kozeny, J. (1927). *Uber kapillare leitung des wassers in boden.* Wien: Sitzungsber. Akad. Wiss. Wien, Math. Naturwiss. Kl. Abt. 2a, 136, 271-306.

Kril, S. I. (1990). *Nopernye vzvesenesuscie potoki (pressurised slurry flows).* Kiev: Naukova Dumka.

Krivenko. (1970). Energieverlust in zwei phasen stromungen in hochkonzentrierten grobdispersionen. *Gidromechanica, Kiev.*

Kumar, U., Mishra, R., Singh, S. N., & Seshadri, V. (2003). Effect of particle gradation on flow characteristics of ash disposal pipelines. *Powder Technology Vol. 132.*, 39-51.

Kumar, U., Singh, S. N., & Seshadri, V. (2008). Prediction of flow characteristics of bimodal slurry in horizontal pipe flow. *Particulate Science and Technology, Vol. 26.*, 361-379.

Kurihara, M. (1948). On the critical tractive force. *Research Institute for Hydraulic Engineering*, Report No. 3, Vol. 4.

Lahiri, S. K. (2009). *Study on slurry flow modelling in pipeline.* Durgapur, India: National Institute of Technology, Durgapur, India.

Lambe, T., & Whitman, R. (1979). *Soil mechanics, SI version.* New York: John Wiley & Sons.

Lane, E. W., & Kalinske, A. A. (1941). Engineering calculations of suspended sediment. *Trans. Am. Geophysics Union, Vol. 20(3).*, 603-607.

Leussen, W. v., & Os, A. v. (1987 December). Basic research on cutting forces in saturated sand. *Journal of Geotechnical Engineering, vol. 113, no. 12.*, 1501-1516.

Leussen, W., & Nieuwenhuis, J. (1984). Soil mechanics aspects of dredging. *Geotechnique 34, no. 3.*, 359-381.

Liefferink, D. M., Alvarez Grima, M., Miedema, S. A., Plat, R., & Rhee, C. v. (2014). Failure mechanism of cutting submerged frozen clay in an arctic trenching process. *OTC 2014.* Houston, Texas, USA.: OTC.

Lobanov, V., & Joanknecht, L. (1980). The cutting of soil under hydrostatic pressure. *WODCON IX.* Vancouver, Canada: WODA.

Longwell, P. A. (1977). *Mechanics of Fluid Flow.* New York: McGraw Hill.

Luckner, T. (2002). Zum Bewegungsbeginn von Sedimenten. *Dissertation.* Darmstadt, Germany: Technische Universitat Darmstadt.

Ma, Y. (2001). *Mathematical model analysis for the saturated sand cutting with large cutting angles in the non-vavitation situation.* Delft, Netherlands: Delft University of Technology, Report: 2001.BT.5581.

Ma, Y., Ni, F., & Miedema, S. (2006A). Calculation of the Blade Cutting Force for small Cutting Angles based on MATLAB. *The 2nd China Dredging Association International Conference & Exhibition, themed Dredging and Sustainable Development.* Guangzhou, China: CHIDA.

Ma, Y., Ni, F., & Miedema, S. (2006B). Mechanical Model of Water Saturated Sand Cutting at Blade Large Cutting Angles. *Journal of Hohai University, ISSN 1009-1130, CN 32-1591*.

Madsen, O. S., Wright, L. D., Boon, J. D., & Chrisholm, T. A. (1993). *Wind stress, bed roughness and sediment suspension on the inner shelf during an extreme storm event.* Continental Shelf Research 13, 1303-1324.

Mantz, P. A. (1977). Incipient transport of fine grains and flakes by fluids—Extended Shields diagram. *Journal of Hydraulic Division, ASCE, 103(6)*, 601-615.

Matousek, V. (1996). Solids Transportation in a Long Pipeline Connected with a Dredge. *Terra et Aqua 62.*, 3-11.

References.

Matousek, V. (1997). *Flow Mechanism of Sand/Water Mixtures in Pipelines, PhD Thesis.* Delft, Netherlands: Delft University of Technology.

Matousek, V. (2004). *Dredge Pumps & Slurry Transport, Lecture Notes.* Delft: Delft University of Technology.

Matousek, V. (2007). Interaction of slurry pipe flow with a stationary bed. *Journal of the South African Institute of Mining and Metallurgy, 107(6).*, 367-374.

Matousek, V. (2009). Predictive model for frictional pressure drop in settling-slurry pipe with stationar deposit. *Powder Technology*, 367-374.

Matousek, V. (2011). Solids Transport Formula in Predictive Model for Pipe Flow of Slurry above Deposit. *Particulate Science and Technology, Vol. 29(1).*, 89-106.

Matousek, V., & Krupicka, J. (2009). On equivalent roughness of mobile bed at high shear stress. *Journal of Hydrology & Hydromechanics, Vol. 57-3.*, 191-199.

Matousek, V., & Krupicka, J. (2010). Modeling of settling slurry flow around deposition limit velocity. *Hydrotransport 18* (p. 12). Rio de Janeiro, Brazil: BHR Group.

Matousek, V., & Krupicka, J. (2010). Semi empirical formulae for upper plane bed friction. *Hydrotransport 18* (pp. 95-103). BHRA.

Matousek, V., & Krupicka, J. (2011). Unified model for coarse slurry flow with stationary and sliding bed. *15th International Conference on Transport & Sedimentation of Solid Particles.*, (p. 8). Wroclaw, Poland.

Matousek, V., & Krupicka, J. (2011). Unified model for coarse slurry flow with stationary and sliding bed. *Transport and Sedimentation of Solid Particles, 15th*, (p. 9). Wroclav, Poland.

Matousek, V., Krupicka, J., & Picek, T. (2013). Validation of transport and friction formulae for upper plane bed by experiments in rectangular pipe. *Journal of Hydrology and Hydromechanics.*, 120-125.

Meijer, K. (1981). *Berekening van spanningen en deformaties in verzadigde grond.* Delft, Netherlands: Delft Hydraulics Laboratory, Report R914 part 1.

Meijer, K. (1985). *Computation of stresses and strains in saturated soil, PhD Thesis.* Delft, Netherlands: Delft University of Technology.

Meijer, K., & Os, A. (1976). Pore pressures near a moving under water slope. *Geotechnical Engineering Division ASCE 102, no. GT4.*, 361-372.

Merchant, M. (1944). Basic mechanics of the metal cutting process. *Journal of Applied Mechanics, vol. 11A.*, 168-175.

Merchant, M. (1945A). Mechanics of metal cutting process, orthogonal cutting and a type 2 chip. *Journal of Applied Physics, vol. 16, no. 5.*, 267-275.

Merchant, M. (1945B). Mechanics of metal cutting, plasticity conditions in orthogonal cutting. *Journal of Applied Physics, vol. 16, no. 6.*, 318-324.

Meyer-Peter, E., & Muller, R. (1948). Formulas for bed load transport. *2nd Meeting of the International Association for Hydraulic Structures Research.*, (pp. 39-64).

Miedema, S. (1981). *The flow of dredged slurry in and out hoppers and the settlement process in hoppers.* Delft, The Netherlands: Delft University of Technology, ScO/81/105, 147 pages.

Miedema, S. (1995). Production Estimation Based on Cutting Theories for Cutting Water Saturated Sand. *WODCON IV* (p. 30 pages). Amsterdam, The Netherlands: WODA.

Miedema, S. (2008A). An Analytical Approach to the Sedimentation Process in Trailing Suction Hopper Dredges. *Terra et Aqua 112*, 15-25.

Miedema, S. (2008B). An analytical method to determine scour. *WEDA XXVIII & Texas A&M 39.* St. Louis, USA: Western Dredging Association (WEDA).

Miedema, S. (2009A). The effect of the bed rise velocity on the sedimentation process in hopper dredges. *Journal of Dredging Engineering, Vol. 10, No. 1*, 10-31.

Miedema, S. (2009B). A sensitivity analysis of the scaling of TSHD's. *WEDA 29 & TAMU 40 Conference.* Phoenix, Arizona, USA: WEDA.

Miedema, S. (2010). Constructing the Shields curve, a new theoretical approach and its applications. *WODCON XIX* (p. 22 pages). Beijing, September 2010: WODA.

Miedema, S. A. (1981). *The soil reaction forces on a crown cutterhead on a swell compensated ladder.* Delft, The Netherlands: Delft University of Technology.

Miedema, S. A. (1982). The Interaction between Cutterhead and Soil at Sea. *Dredging Day November 19th* (p. 25 pages in Dutch). Delft, The Netherlands: Delft University of Technology.

Miedema, S. A. (1982). *The mathematical modeling of the soil reaction forces on a cutterhead and the development of the computer program DREDMO.* Delft, The Netherlands: Delft University of Technology.

Miedema, S. A. (1984A). *Mathematical Modeling of a Seagoing Cutter Suction Dredge.* Delft, The Netherlands: Delft University of Technology/KIVI.

Miedema, S. A. (1984B, October). The Cutting of Densely Compacted Sand under Water. *Terra et Aqua, No. 28*, 4-10.

Miedema, S. A. (1985A, September). Derivation of the Differential Equation for Sand Pore Pressures. *Dredging and Port Construction*, 35.
Miedema, S. A. (1985B, July). Mathematical Modeling of the Cutting of Densely Compacted Sand Under Water. *Dredging and Port Construction*, 22-26.
Miedema, S. A. (1986A). The Application of a Cutting Theory on a Dredging Wheel. *WODCON XI* (p. 14 pages). Brighton, UK: WODA.
Miedema, S. A. (1986B, June). Underwater Soil Cutting: a Study in Continuity. *Dredging and Port Construction*, 47-53.
Miedema, S. A. (1987 September). *The Calculation of the Cutting Forces when Cutting Water Saturated Sand, PhD Thesis.* Delft: Delft University of Technology.
Miedema, S. A. (1989). On the Cutting Forces in Saturated Sand of a Seagoing Cutter Suction Dredge. *WODCON XII* (p. 27 pages). Orlando, Florida, USA: WODA.
Miedema, S. A. (1989, December). On the Cutting Forces in Saturated Sand of a Seagoing Cutter Suction Dredge. *Terra et Aqua, No. 41*, 27 pages.
Miedema, S. A. (1992). New developments of cutting theories with respect to dredging, the cutting of clay. *WODCON XIII.* Bombay, India: World Dredging Association (WODA).
Miedema, S. A. (1994). On the Snow-Plough Effect when Cutting Water Saturated Sand with Inclined Straight Blades. *ASCE Dredging 94* (p. 24 pages). Orlando, Florida, USA: ASCE.
Miedema, S. A. (1995). Dynamic Pump/Pipeline Behavior Windows. *Software*. Delft, The Netherlands: SAM-Consult.
Miedema, S. A. (1995). Production Estimation Based on Cutting Theories for Cutting Water Saturated Sand. *WODCON IV* (p. 30 pages). Amsterdam, The Netherlands: WODA.
Miedema, S. A. (1996). Modeling and Simulation of the Dynamic Behavior of a Pump/Pipeline System. *17th Annual Meeting & Technical Conference of WEDA.* (p. 10). New Orleans, USA.: WEDA.
Miedema, S. A. (1999). Considerations in Building and using Dredge Simulators. *WEDA XIX & TAMU 31* (p. 10). Louisville, Kentucky, USA: WEDA.
Miedema, S. A. (1999). Considerations on limits of dredging processes. *19th Annual Meeting & Technical Conference of the Western Dredging Association.* Louisville, Kentucky, USA: WEDA/TAMU.
Miedema, S. A. (2000). The modelling of the swing winches of a cutter dredge in relation with simulators. *Texas A/M 32nd Annual Dredging Seminar.* Warwick, Rhode Island, USA: WEDA/TAMU.
Miedema, S. A. (2003). The Existence of Kinematic Wedges at Large Cutting Angles. *CHIDA Dredging Days.* Shanghai, China: CHIDA.
Miedema, S. A. (2004). The Cutting Mechanisms of Water Saturated Sand at Small and Large Cutting Angles. *International Conference on Coastal Infrastructure Development - Challenges in the 21st Century.* Hongkong: ICCD.
Miedema, S. A. (2005). The Cutting of Water Saturated Sand, the FINAL Solution. *WEDAXXV/TAMU37.* New Orleans, Louisiana, USA: WEDA/TAMU.
Miedema, S. A. (2006A). The Cutting of Water Saturated Sand, the Solution. *CEDA African Section: Dredging Days.* Tangiers, Morocco: CEDA.
Miedema, S. A. (2006B). The Cutting of Water Saturated Sand, the Solution. *The 2nd China Dredging Association International Conference & Exhibition, themed Dredging and Sustainable Development.* Guangzhou, China: CHIDA.
Miedema, S. A. (2009). New Developments Of Cutting Theories With Respect To Dredging, The Cutting Of Clay And Rock. *WEDA XXIX/Texas A/M 40.* Phoenix, Arizona, USA: WEDA/TAMU.
Miedema, S. A. (2010). New Developments of Cutting Theories with respect to Offshore Applications. *ISOPE* (p. 8). Beijing, China.: ISOPE.
Miedema, S. A. (2012A). Constructing the Shields Curve: Part A Fundamentals of the Sliding, Rolling and Lifting Mechanisms for the Entrainment of Particles. *Journal of Dredging Engineering, Vol. 12.*, 1-49.
Miedema, S. A. (2012B). Constructing the Shields Curve: Part B Sensitivity Analysis, Exposure & Protrusion Levels, Settling Velocity, Shear Stress & Friction Velocity, Erosion Flux and Laminar Main Flow. *Journal of Dredging Engineering, Vol. 12.*, 50-92.
Miedema, S. A. (2013). An overview of theories describing head losses in slurry transport. A tribute to some of the early researchers. *OMAE 2013, 32nd International Conference on Ocean, Offshore and Arctic Engineering.* (p. 18). Nantes, France: ASME.
Miedema, S. A. (2013). Constructing the Shields Curve: Part C Cohesion by Silt, Hjulstrom, Sundborg. *OMAE* (p. 22). Nantes: ASME.
Miedema, S. A. (2013S). *Software MS Excel 2LM & 3LM.* Retrieved from The Delft Head Loss & Limit Deposit Velocity Model: www.dhlldv.com
Miedema, S. A. (2014). An analytical approach to explain the Fuhrboter equation. *Maritime Engineering, Vol. 167, Issue 2.*, 68-81.

References.

Miedema, S. A. (2014). *Dredging Processes Hydraulic Transport.* Delft, Netherlands: Delft University of Technology.

Miedema, S. A. (2014). *The Delft Sand, Clay & Rock Cutting Model.* (1st ed.). Delft: IOS Press, Delft University Press. doi:10.3233/978-1-61499-454-1-i

Miedema, S. A. (2014B). An analysis of slurry transport at low line speeds. *ASME 2014 33rd International Conference on Ocean, Offshore and Arctic Engineering, OMAE.* (p. 11). San Francisco, USA.: ASME.

Miedema, S. A. (2014C). An analytical approach to explain the Fuhrboter equation. *Maritime Engineering, Vol. 167(2).*, 1-14.

Miedema, S. A. (2014W). *DHLLDV/Experiments*. Retrieved from The Delft Head Loss & Limit Deposit Velocity Model.: www.dhlldv.com

Miedema, S. A. (2015). A head loss model for homogeneous slurry transport. *Journal of Hydrology & Hydrodynamics, Vol. 63(1).*, 1-12.

Miedema, S. A. (2015). Head Loss Model for Slurry Transport in the Heterogeneous Regime. *Submitted to the Journal of Ocean Engineering.*

Miedema, S. A. (2015A). A head loss model for homogeneous slurry transport. *Journal of Hydrology & Hydrodynamics, Vol. 1.*, 14 pages.

Miedema, S. A. (2015B). Head Loss Model for Slurry Transport in the Heterogeneous Regime. *Journal of Ocean Engineering. Accepted.*

Miedema, S. A. (2015B). THE SLIP RATIO OR HOLDUP FUNCTION IN SLURRY TRANSPORT. *Dredging Summit and Expo 2015.* (p. 12). Houston, Texas, USA.: WEDA.

Miedema, S. A. (2015C). Head Loss Model for Slurry Transport in the Heterogeneous Regime. *Journal of Ocean Engineering.*

Miedema, S. A., & Becker, S. (1993). The Use of Modeling and Simulation in the Dredging Industry, in Particular the Closing Process of Clamshell Dredges. *CEDA Dredging Days* (p. 26 pages). Amsterdam, The Netherlands: CEDA.

Miedema, S. A., & Frijters, D. (2003). The Mechanism of Kinematic Wedges at Large Cutting Angles - Velocity and Friction Measurements. *23rd WEDA Technical Conference/35th TAMU Dredging Seminar* (p. 14 pages). Chicago, Illinois, USA: WEDA/TAMU.

Miedema, S. A., & Frijters, D. (2004). The wedge mechanism for cutting of water saturated sand at large cutting angles. *WODCON XVII.* Hamburg, Germany: WODA.

Miedema, S. A., & He, J. (2002B). The Existance of Kinematic Wedges at Large Cutting Angles. *WEDA XXII Technical Conference/34th Texas A/M Dredging Seminar* (p. 20 pages). Denver, Colorado, USA: WEDA/TAMU.

Miedema, S. A., & Ma, Y. (2002A). The Cutting of Water Saturated Sand at Large Cutting Angles. *ASCE Dredging 02* (p. 16 pages). Orlando, Florida, USA: ASCE.

Miedema, S. A., & Matousek, V. (2014). An explicit formulation of bed friction factor for sheet flow. *International Freight Pipeline Society Symposium, 15th.* (p. 17 pages). Prague, Czech Republic: IFPS.

Miedema, S. A., & Ramsdell, R. C. (2011). Hydraulic transport of sand/shell mixtures in relation with the critical velocity. *Terra et Aqua, Vol. 122.*

Miedema, S. A., & Ramsdell, R. C. (2013). A head loss model for slurry transport based on energy considerations. *World Dredging Conference XX* (p. 14). Brussels, Belgium: WODA.

Miedema, S. A., & Ramsdell, R. C. (2014). An Analysis of the Hydrostatic Approach of Wilson for the Friction of a Sliding Bed. *WEDA/TAMU* (p. 21). Toronto, Canada: WEDA.

Miedema, S. A., & Ramsdell, R. C. (2014A). The Delft Head Loss & Limit Deposit Velocity Model. *Hydrotransport* (p. 15). Denver, USA.: BHR Group.

Miedema, S. A., & Ramsdell, R. C. (2014B). An Analysis of the Hydrostatic Approach of Wilson for the Friction of a Sliding Bed. *WEDA/TAMU* (p. 21). Toronto, Canada: WEDA.

Miedema, S. A., & Ramsdell, R. C. (2015). The Limit Deposit Velocity Model, a New Approach. *Journal of Hydrology & Hydromechanics, submitted.*, 15.

Miedema, S. A., & Vlasblom, W. J. (1996). Theory for Hopper Sedimentation. *29th Annual Texas A&M Dredging Seminar & WEDA Conference.* (p. 10). New Orleans, USA.: WEDA.

Miedema, S. A., & Yi, Z. (2001). An Analytical Method of Pore Pressure Calculations when Cutting Water Saturated Sand. *Texas A/M 33nd Annual Dredging Seminar* (p. 18 pages). Houston, USA: WEDA/TAMU.

Miedema, S. A., & Zijsling, D. (2012). Hyperbaric rock cutting. *OMAE International Conference on Ocean, Offshore and Arctic Engineering* (p. 14). Rio de Janeiro, Brazil: ASME.

Miedema, S. A., Riet, E. J., & Matousek, V. (2002). Theoretical Description And Numerical Sensitivity Analysis On Wilson Model For Hydraulic Transport Of Solids In Pipelines. *WEDA Journal of Dredging Engineering.*

Miedema, S., & Rhee, C. v. (2007). A sensitivity analysis on the effects of dimensions and geometry of Trailing Suction Hopper Dredges. *WODCON*. Orlando, Florida, USA: WODA.

Miedema, S., & Vlasblom, W. (1996). Theory of Hopper Sedimentation. *29th Annual Texas A&M Dredging Seminar*. New Orleans: WEDA/TAMU.

Miller, D., & Bruggers, D. (1980). Soil and permafrost conditions in the Alaskan Beaufort Sea. *OTC 1980*. Houston, Texas, USA.: OTC.

Ming, G., Ruixiang, L., Ni, F., & Liqun, X. (2007). Hydraulic transport of coarse gravel. *WODCON XVIII*. Orlando, Florida, USA: WODA.

Mitchell, J. (1976). *Fundamentals of soil behavior*. John Wiley & Sons, Inc.

Mitchell, J., Campanella, R., & Singh, A. (1968). Soil creep as a rate process. *Journal SMFD, vol. 94, no. 1, ASCE*.

Mogi, K. (1966). Pressure dependence of rock strength and transition from brittle fracture to ductile flow. *Bulletin Earthquake Res. Inst. Japan, Vol. 44.*, 215-232.

Moody, L. F. (1944). Friction Factors for Pipe Flow. *Transactions of the ASME 66 (8).*, 671-684.

Morsi, S., & Alexander, A. (1972). An investigation of particle trajectories in two-phase flow systems. *Journal of Fluid Mechanics, Vol. 55*, 193-208.

Mukhtar, A. (1991). *Investigations of the flow of multisized heterogeneous slurries in straight pipe and pipe bends.* Delhi, India: PhD Thesis, IIT.

Newitt, D. M., Richardson, M. C., Abbott, M., & Turtle, R. B. (1955). Hydraulic conveying of solids in horizontal pipes. *Transactions of the Institution of Chemical Engineers Vo.l 33.*, 93-110.

Nezu, I., & Nakagawa, H. (1993). *Turbulence in Open Channel Flows.* A. A. Balkema.

Ni, F., Zhao, L., Matousek, V., Vlasblom, W. J., & Zwartbol, A. (2004). Two phase flow of highly concentrated slurry in a pipeline. *Journal of Hydrodynamics, Series B, Vol. 16, No. 3.*, 325-331.

Ni, F., Zhao, L., Xu, L., & Vlasblom, W. J. (2008). A model calculation for flow resistance in the hydraulic transport of sand. *WODCON 18* (pp. 1377-1384). Orlando, Florida, USA: WODA.

Nielsen, P. (1981). Dynamics and geometry of wave generated ripples. *Journal of Geophysics Research, Vol. 86.*, 6467-6472.

Nikuradse, J. (1933, July/August). Stromungsgesetze in rauen Rohren. *VDI Forschungsheft 361, Beilage zo "Forschung auf dem Gebiete des Ingenieurwesens", Ausgabe B, Band 4.*

Nishimatsu, Y. (1972). The mechanics of rock cutting. *International Journal of Rock Mechanics & Mining Science, vol. 9.*, 261-270.

Nnadi, F. N., & Wilson, K. C. (1992). Motion of contact load particles at high shear stress. *Journal of Hydraulic Engineering, Vol. 118.*, 1670-1684.

Nnadi, F. N., & Wilson, K. C. (1995). Bed Load Motion at High Shear Stress: Dune Washout and Plane Bed Flow. *Journal of Hydraulic Engineering, Vol. 121.*, 267-273.

O'Brien, M. P. (1933). Review of the theory of turbulent flow and its relations to sediment transportation. *Transactions of the American Geophysics Union, Vol. 14.*, 487-491.

O'Brien, M. P., & Folsom, R. G. (1939). The transportation of sand in pipelines. *Vol. 3,No. 7 of University of California publications in engineering.*

Ooijens, S. (1999). Adding Dynamics to the Camp Model for the Calculation of Overflow Losses. *Terra et Aqua 76*, 12-21.

Ooijens, S., Gruijter, A. d., Nieuwenhuizen, A., & Vandycke, S. (2001). Research on Hopper Settlement Using Large Scale Modeling. *CEDA Dredging Days 2001* (pp. 1-11). Rotterdam: CEDA.

Oroskar, A. R., & Turian, R. M. (1980). The hold up in pipeline flow of slurries. *AIChE, Vol. 26.*, 550-558.

Os, A. G. (1976). Snelle deformatie van korrelvormig materiaal onder water. *PT-P31, no. 12*, 735-741.

Os, A. G. (1977A). Behavior of soil when excavated under water. In *International course on modern dredging.* The Hague, Netherlands.

Os, A. G. (1977B). Snelle deformatie van korrelvormig materiaal onder water. *PT-B32, no. 8.*, 461-467.

Osman, M. (1964). The mechanics of soil cutting blades. *J.A.E.R. 9 (4)*, 313-328.

Osterkamp, T. (2001). *Sub-Sea Permafrost, Encyclopaedia of Ocean Sciences (2902-2912).*

Palmer, A. (1999). Speed effects in cutting and ploughing. *Geotechnique 49, no. 3.*, 285-294.

Paphitis, D. (2001). Sediment movement under unidirectional flows: an assesment of empirical threshold curves. *Coastal Engineering*, 227-245.

Parzonka, W., Kenchington, J. M., & Charles, M. E. (1981). Hydrotransport of solids in horizontal pipes: Effects of solids concentration and particle size on the deposit velocity. *Canadian Journal of Chemical Engineering, Vol. 59.*, 291-296.

Patankar, S. (1980). *Numerical heat transfer and fluid flow.* New York, USA: McGraw-Hill.

Peker, S. M., & Helvaci, S. S. (2008). *Solid-Liquid Two Phase Flow.* Amsterdam, The Netherlands: Elsevier.

Poloski, A. P., Etchells, A. W., Chun, J., Adkins, H. E., Casella, A. M., Minette, M. J., & Yokuda, S. (2010). A pipeline transport correlation for slurries with small but dense particles. *Canadian Journal of Chemical Engineering, Vol. 88.*, 182-189.

References.

Postma, H. (1967). Sediment transport and sedimentation in the estuarine environment. *Estuaries, AAAS, Washington D.C. Publ. 83.*, 158-179.

Prandl, L. (1925). Z. angew. *Math. Mech. 5 (1)*, 136-139.

Pugh, F. J., & Wilson, K. C. (1999). Role of the interface in stratified slurry flow. *Powder Technology, Vol. 104.*, 221-226.

Pugh, F. J., & Wilson, K. C. (1999). Velocity and concentration distribution in sheet flow above plane beds. *Journal of Hydraulic Engineering*, 117-125.

Raalte, G., & Zwartbol, A. (1986). Disc bottom cutterhead, a report on laboratory and field tests. *WODCON XI.* Brighton, UK: WODA.

Rafatian, N., Miska, S., Ledgerwood III, L., Hughes, B., Ahmed, R., Yu, M., & Takach, N. (2009). Experimental study of MSE of a single PDC cutter under simulated pressurized conditions. *SPE/IADC 119302 Drilling Conference & Exhibition.* Amsterdam, Netherlands: SPE International.

Ramsdell, R. C., & Miedema, S. A. (2010). Hydraulic transport of sand/shell mixtures. *WODCON XIX*. Beijing, China.: WODA.

Ramsdell, R. C., & Miedema, S. A. (2013). An overview of flow regimes describing slurry transport. *WODCON XX* (p. 15). Brussels, Belgium.: WODA.

Ramsdell, R. C., Miedema, S. A., & Talmon, A. (2011). Hydraulic transport of sand/shell mixtures. *OMAE 2011*. Rotterdam, Netherlands.: ASME.

Randal, R. E., Jong, P. S., & Miedema, S. A. (2000). Experiences with Cutter Suction Dredge Simulator Training. *WEDA/TAMU* (p. 10). Rhode Island, USA: WEDA.

Raudviki, A. J. (1990). *Loose Boundary Hydraulics.* University of Auckland: Pergamon Press.

Ravelet, F., Bakir, F., Khelladi, S., & Rey, R. (2012). Experimental study of hydraulic transport of large particles in horizontal pipes. *Experimental Thermal and Fluid Science*, 13.

Reece, A. (1965). The fundamental equation of earth moving machinery. *Symposium Earth Moving Machinery.* London: Institute of Mechanical Engineering.

Reichardt, H. (1951). Vollstandige Darstellung der Turbulenten Geswindigkeitsverteilung in Glatten Leitungen. *Zum Angew. Math. Mech., 3(7)*, 208-219.

Rhee, C. v. (2002A). The influence of the bottom shear stress on the sedimentation of sand. *11th International Symposium on Transport and Sedimentation of Solid Particles.* Ghent, Belgium.

Rhee, C. v. (2002B). Numerical modeling of the flow and settling in a Trailing Suction Hopper Dredge. *15th International Conference on Hydrotransport.* Banff, Canada.

Rhee, C. v. (2002C). *On the sedimentation process in a Trailing Suction Hopper Dredger.* Delft, Netherlands: Delft University of Technology, PhD Thesis.

Rhee, C., & Steeghs, H. (1991 June). Multi blade ploughs in saturated sand, model cutting tests. *Dredging & Port Construction*.

Richardson, J. F., & Zaki, W. N. (1954). Sedimentation & Fluidization: Part I. *Transactions of the Institution of Chemical Engineering 32*, 35-53.

Riet, E. J., Matousek, V., & Miedema, S. A. (1995). A Reconstruction of and Sensitivity Analysis on the Wilson Model for Hydraulic Particle Transport. *Proc. 8th Int. Conf. on Transport and Sedimentation of Solid Particles.* Prague, Czech Republic.

Riet, E. J., Matousek, V., & Miedema, S. A. (1996). A Theoretical Description and Numerical Sensitivity Analysis on Wilson's Model for Hydraulic Transport in Pipelines. *Journal of Hydrology & Hydromechanics*.

Rijn, L. v. (1984). Sediment transport: Part I: Bed load transport. *Journal of Hydraulic Engineering, Vol. 110(10)*, 1431-1456.

Rijn, L. v. (1993). *Principles of Sediment Transport, Part 1.* . Blokzijl: Aqua Publications.

Roberts, J., Jepsen, R., Gotthard, D., & Lick, W. (1998). Effects of particle size and bulk density on erosion of quartz particles. *Journal of Hydraulic Engineering*, 1261-1267.

Robinson, M. P. (1971). *Critical deposit velocities for low concentration solid-liquid mixtures. MSc Thesis.* Lehigh University, Fritz Laboratory.

Robinson, M. P., & Graf, W. H. (1972). *Critical deposit velocities for low concentration sand water mixtures. ASCE National Water Resources EnVg Meeting Preprint 1637, January 1972. Paper 1982.* Atlanta, Georgia, USA.: Lehigh University, Fritz Laboratory.

Rodi, W. (1993). *Turbulence models and their application in hydraulics, a state of the art review.* IAHR, Third Edition.

Rouse, H. (1937). Modern conceptions of the mechanics of fluid turbulence. *Transactions of the American Society of Cicil Engineers, Vol. 102*, 463-505, Discussion 506-543.

Rowe, P. (1962). The stress dilatancy relation for static equilibrium of an assembly of particles in contact. *Proceedings Royal Society A269.* (pp. 500-527). Royal Society.

Rowe, P. (1987). A convinient empirical equation for estimation of the Richardson-Zaki exponent. *Chemical Engineering Science Vol. 42, no. 11*, 2795-2796.

Rowe, P. N. (1987). A convinient empirical equation for estimation of the Richardson-Zaki exponent. *Chemical Engineering Science Vol. 42, no. 11*, 2795-2796.

Roxborough, F. (1987). The role of some basic rock properties in assessing cuttability. *Seminar on Tunnels - Wholly Engineered Structures* (pp. 1-21). Canberra, Australia: AFCC.

Saffman, P. G. (1965). The lift on small sphere in a slow shear low. *Journal of Fluid Mechanics, 22*, 385-400.

Sanders, R. S., Sun, R., Gillies, R. G., McKibben, M., Litzenberger, C., & Shook, C. A. (2004). Deposition Velocities for Particles of Intermediate Size in Turbulent Flows. *Hydrotransport 16* (pp. 429-442). Santiago, Chile.: BHR Group.

Schaan, J., & Shook, C. A. (2000). Anomalous friction in slurry flows. *Canadian Journal of Chemical Engineering, Vol. 78.*, 726-730.

Scheurel, H. G. (1985). *Rohrverschleiss beim hydraulischen feststoffentransport.* Karlsruhe: Universitat Karlsruhe.

Schiller, R. E., & Herbich, J. B. (1991). *Sediment transport in pipes. Handbook of dredging.* New York: McGraw-Hill.

Schlichting, H. (1968). *Boundary layer theory.* 6th ed. New York: McGraw-Hill.

Schrieck, G. (1996). *Introduction to Dredging Engineering.* Delft, the Netherlands: Delft University of Technology.

Segal, G. (2001). *Sepra analysis programmers guide, standard problems and users manual.* Leidschendam, Netherlands: Ingenieursbureau Sepra.

Sellgren, A., & Wilson, K. (2007). Validation of a four-component pipeline friction-loss model. *Hydrotransport 17* (pp. 193-204). BHR Group.

Seshadri, V., Singh, S. N., & Kaushal, D. R. (2006). A model for the prediction of concentration and particle size distribution for the flow of multisized particulate suspensions through closed ducts and open channels. *Particulate Science and Technology: An International Journal.*, 239-258.

Shields, A. (1936). Anwendung der Aehnlichkeitsmechanik und der Turbulenzforschung auf die Geschiebebewegung. *Mitteilung der Preussischen Versuchsanstalt fur Wasserbau und Schiffbau, Heft 26, Berlin.* Belin.

Shook, C. A., Geller, L., Gillies, R. G., Husband, W. H., & Small, M. (1986). Experiments with coarse particles in a 250 mm pipeline. *10th International Conference on the Hydraulic Transport of Solids in Pipelines (Hydrotransport 10).* (pp. 219-227). Cranfield, UK.: BHRA Fluid Eng.

Shook, C. A., Gillies, R. G., & Sanders, R. S. (2002). *Pipeline Hydrotransport with Application in the Oil Sand Industry.* Saskatoon, Canada: Saskatchewan Research Council, SRC Publication 11508-1E02.

Shook, C., & Roco, M. (1991). *Slurry Flow, Principles & Practice.* Boston: Butterworth Heineman.

Silin, M. O., Kobernik, S. G., & Asaulenko, I. A. (1958). *Druckhohenverluste von Wasser und Wasser-Boden-Gemischen in Rohrleitungen grossen Durchmessers.* Ukrain: Dopovidi Akad. Nauk. Ukrain RSR.

Silin, N. A., & Kobernik, S. G. (1962). Rezimy raboty zemlijesosnych snarjadov, Kijev.

Simons, D. (1957). *Theory and design of stable channels in alluvial material.* PhD thesis: Colorado State University.

Sinclair, C. G. (1962). The limit deposit velocity of heterogeneous suspensions. *Proceedings Symposium on the Interaction Btween Fluids and Particles.* Institute of Chemical Engineers.

Smoldyrev. (1970). *Truboprowodnyi transport(rohrleitungstransport).* Moskau.

Sobota, J., & Kril, S. I. (1992). Liquid and solid velocity during mixture flow. *Proceedings 10th International Colloquium Massenguttransport durch Rohrleitungen.*, (p. K). Meschede, Germany.

Sohne, W. (1956). Some basic considerations of soil mechanics as applied to agricultural engineering. *Grundlagen der landtechnik (7).*, 11-27.

Soleil, G., & Ballade, P. (1952). Le transport hydraulique des materiaux dans les travaux publics, observations des resultats d'essais en grandeur nature. *Deuxiemes Journees de l'Hydraulique*, 9-26.

Soulsby, R., & Whitehouse, R. (1997). Threshold of sediment motion in coastal environment. *Proceedings Pacific Coasts and Ports.* (pp. 149-154). Christchurch, New Zealand: University of Canterbury.

Souza Pinto, T. C., Moraes Junior, D., Slatter, P. T., & Leal Filho, L. S. (2014). Modelling the critical velocity for heterogeneous flow of mineral slurries. *International Journal of Multiphase Flow, 65.*, 31-37.

Soydemir, C. (1977). Potential models for shear strength generation in soft marine clays. *International Symposium on Soft Clay.* Bangkok, Thailand.

Spelay, R., Hashemi, S. A., Gillies, R. G., Hegde, R., Sanders, R. S., & Gillies, D. G. (2013). Governing friction loss mechanisms and the importance of offline characterization tests in the pipeline transport of dense coarse particle slurries. *Proceedings of the ASME 2013 Fluids Engineering Division Summer Meeting.* (pp. 1-7). Incline Village, Nevada, USA.: FEDSM2013.

Stam, P. (1983). *Analyse ten behoeve van het ontwerp van een klei snijdende sleepkop, CO/82/129.* Delft, Netherlands: Delft University of Technology.

Stansby, P. (1997). Semi-implicit finite shallow-water flow and solute transport solver with k-epsilon turbulence model. *International Journal for Numerical Methods in Fluids, vol. 25.*, 285-313.

References.

Steeghs, H. (1985A). Snijden van zand onder water, part I. *Ports & Dredging no. 121*.

Steeghs, H. (1985B). Snijden van zand onder water, part II. *Ports & Dredging no. 123.*

Stelling, G., & Kester, J. (1994). On the approximation of horizontal gradients in sigma coordinates for bathymetry with steep bottom slopes. *International Journal for Numerical Methods in Fluids, vol. 18*, 915-935.

Stevenson, P., Cabrejos, F. J., & Thorpe, R. B. (2002). Incipient motion of particles on a bed of like particles in hydraulic and pneumatic conveying. *Fourth World Congress of Particle Technology, Sydney, 21st–25th July (paper 400).* Sydney.

Stevenson, P., Thorpe, R. B., & Davidson, J. F. (2002). Incipient motion of a small particle in the viscous boundary-layer at a pipe wall. *Chemical Engineering Science, 57*, 4505–4520.

Sundborg, A. (1956). The River Klarålven: Chapter 2. The morphological activity of flowing water erosion of the stream bed. *Geografiska Annaler, 38*, 165-221.

Swamee, P. K. (1993). Critical depth equations for irrigation canals. *Journal of Irrigation and Drainage Engineering, ASCE.*, 400-409.

Swamee, S. E., & Jain, K. A. (1976). Explicit equations for pipe-flow problems. *Journal of the Hydraulics Division (ASCE) 102 (5).*, 657-664.

Talmon, A. (2013). Analytical model for pipe wall friction of pseudo homogeneous sand slurries. *Particulate Science & technology: An International Journal*, 264-270.

Talmon, A. M. (2011). Hydraulic Resistance of Sand-Water Mixture Flow in Vertical Pipes. *T&S, Transport and Sedimentation of Solid Particles* (pp. 137-147). Wroclaw, Poland: T&S.

Talmon, A. M. (2013). Analytical model for pipe wall friction of pseudo homogeneous sand slurries. *Particulate Science & technology: An International Journal*, 264-270.

Televantos, Y., Shook, C. A., Carleton, A., & Street, M. (1979). Flow of slurries of coarse particles at high solids concentrations. *Canadian Journal of Chemical Engineering, Vol. 57.*, 255-262.

Terzaghi, K., & Peck, R. (1964). *Soil mechanics in engineering practise.* New York: John Wiley & Sons.

Thomas, A. (1976). SCALE-UP METHODS FOR PIPELINE TRANSPORT OF SLURRIES. *International Journal of Mineral Processing, Vol. 3.*, 51-69.

Thomas, A. D. (1979). Predicting the deposit velocity for horizontal turbulent pipe flow of slurries. *International Journal of Multiphase Flow, Vol. 5.*, 113-129.

Thomas, A. D. (2014). Slurries of most interest to the mining industry flow homogeneously and the deposit velocity is the key parameter. *HydroTransport 19.* (pp. 239-252). Denver, Colorado, USA.: BHR Group.

Thomas, D. G. (1962). Transport Characteristics of Suspensions: Part VI. Minimum velocity for large particle size suspensions in round horizontal pipes. *A.I.Ch.E. Journal, Vol.8(3).*, 373-378.

Thomas, D. G. (1965). Transport characteristics of suspensions: VIII. A note on the viscosity of Newtonian suspensions of uniform spherical particles. *Journal Of Colloidal Sciences, Vol. 20.*, 267-277.

Turian, R. M., & Yuan, T. F. (1977). Flow of slurries in pipelines. *AIChE Journal, Vol. 23.*, 232-243.

Turian, R. M., Hsu, F. L., & Ma, T. W. (1987). Estimation of the critical velocity in pipeline flow of slurries. *Powder Technology, Vol. 51.*, 35-47.

Turnage, G., & Freitag, D. (1970). Effects of cone velocity and size on soil penetration resistance. *ASEA 69-670.*

Turner, T. (1996). *Fundamentals of Hydraulic Dredging.* New York: ASCE.

Turton, R., & Levenspiel, O. (1986). A short note on the drag correlation for spheres. *Powder technology Vol. 47*, 83-85.

Vanoni, V. A. (1975). *Sedimentation Engineering: American Society of Civil Engineers, Manuals and Reports on Engineering Practice. No. 54. P.745.*

Verhoef, P. (1997). *Wear of rock cutting tools: Implications for site investigation of rock dredging projects.* Delft, Netherlands: Balkema Rotterdam.

Verruijt, A. (1983). *Soil Mechanics.* Delft: DUM, Netherlands.

Vlasak, P. (2008). *Laminar, transitional and turbulent flow of fine grained slurries in pipelines.* Prague.: Czech Technical University in Prague, Fakulty of Civil Engineering.

Vlasak, P., Kysela, B., & Chara, Z. (2012). FLOW STRUCTURE OF COARSE-GRAINED SLURRY IN A HORIZONTAL PIPE. *Journal of Hydrology & Hydromechanics, Vol. 60.*, 115-124.

Vlasblom, W. (2003-2007). *Rock Cutting, Lecture Notes.* Delft, Netherlands: Delft University of Technology.

Vlasblom, W., & Miedema, S. (1995). A Theory for Determining Sedimentation and Overflow Losses in Hoppers. *WODCON IV.* Amsterdam, Netherlands: WODA.

Vocadlo, J. J. (1972). Prediction of pressure gradient for the horizontal turbulent flow of slurries. *Hydrotransport 2.* Coventry: BHRA.

Vocadlo, J. J., & E., C. M. (1972). Prediction of pressure gradient for the horizontal turbulent flow of slurries. *Conference on the Hydraulic Transport of Solids in Pipes.* Warwick, England: British Hydromechanics Research Association.

Vukovic, M., & Soro, A. (1992). Determination of hydraulic conductivity of porous media from grain size composition. *Water Resources Publications, Littleton, Colorado.*

Wallis, G. (1969). *One Dimensional Two Phase Flow.* McGraw Hill.
Wasp, E. J. (1963). Cross country coal pipeline hydraulics. *Pipeline News.*, 20-28.
Wasp, E. J., & Slatter, P. T. (2004). Deposition velocities for small particles in large pipes. *12th International Conference on Transport & Sedimentation of Solid Particles*, (pp. 20-24). Prague, Czech Republic.
Wasp, E. J., Kenny, J. P., & Gandhi, R. L. (1977). Solid liquid flow slurry pipeline transportation. *Transactions Technical Publications*.
Wasp, E. J., Kenny, J. P., Aude, T. C., Seiter, R. H., & Jacques, R. B. (1970). Deposition velocities transition velocities and spatial distribution of solids in slurry pipelines. *Hydro Transport 1, paper H42.* (pp. 53-76). Coventry: BHRA Fluid Engineering.
Weibull, W. (1939). A statistical theory of the strength of materials. *Royal Swedish Institute of Engineers, 151:1.*
Weijermars, R. (1997-2011). *Principles of rock mechanics.* Delft, Netherlands: Alboran Science Publishing.
Welte, A. (1971). Grundlagen der Berechnung der Rohrleitungsdruckverluste. *Konstruction 23, Heft 5 & 6.*
Westendorp, J. H. (1948). *Verslag literatuurstudie over persen van zand M.276.* Delft, Netherlands: Delft Hydraulics Laboratory.
White, C. M. (1940). The equilibrium of grains on the bed of a stream. *Proceedings Royal Society of London, A174*, pp. 322-338.
Whitlock, L., Wilson, K. C., & Sellgren, A. (2004). Effect of near-wall lift on frictional characteristics of sand slurries. *Hydrotransport 16* (pp. 443-454). Cranfield, UK.: BHR Group.
Wiberg, P. L., & Smith, J. D. (1987A). Calculations of the critical shear stress for motion of uniform and heterogeneous sediments. *Water Resources Research, 23*(8), 1471–1480.
Wiberg, P., & Smith, J. (1987B). Initial motion of coarse sediment in streams of high gradient. *Proceedings of the Corvallis Symposium.* IAHS Publication No. 165.
Wiedenroth, W. (1967). *Untersuchungen uber die forderung von sand wasser gemischen durch rohrleitungen und kreiselpumpen.* Hannover: PhD Thesis, Technische Hochschule Hannover.
Wikramanayake, P. N., & Madsen, O. S. (1991). *Calculation of movable bed friction factors.* Vicksburg, Mississippi.: Tech. Rep. DACW-39-88-K-0047, 105 pp., Coastal Eng. Res. Cent.,.
Wilson, K. C. (1965). *Application of the minimum entropy production principle to problems in two-phase flow, PhD Thesis.* Kingston, Ontario, Canada.: Queens University.
Wilson, K. C. (1966). Bed Load Transport at High Shear Stress. *Journal of the Hydraulics Division*, 49-59.
Wilson, K. C. (1970). Slip point of beds in solid liquid pipeline flow. *Journal of Hydraulic Division, Vol 96(HY1)*, 1-12.
Wilson, K. C. (1970). Slip point of beds in solid-liquid pipeline flow. *Proceedings American Society of Civil Engineers, Vol. 96, HY1*.
Wilson, K. C. (1972). A Formula for the Velocity Required to Initiate Particle Suspension in Pipeline Flow. *Hydrotransport 2* (pp. E2 23-36). Warwick, UK.: BHRA Fluid Engineering.
Wilson, K. C. (1974). Coordinates for the Limit of Deposition in Pipeline Flow. *Hydrotransport 3* (pp. E1 1-13). Colorado School of Mines, Colorado, USA.: BHRA Fluid Engineering.
Wilson, K. C. (1975). Stationary Deposits and Sliding Beds in Pipes Transporting Solids. *Dredging Technology* (pp. C3 29-40). College Station, Texas, USA.: BHRA Fluid Engineering.
Wilson, K. C. (1976). A Unified Physically based Analysis of Solid-Liquid Pipeline Flow. *Hydrotransport 4* (pp. A1 1-16). Banff, Alberta, Canada: BHRA Fluid Engineering.
Wilson, K. C. (1979). Deposition limit nomograms for particles of various densities in pipeline flow. *Hydrotransport 6* (p. 12). Canterbury, UK: BHRA Fluid Engineering.
Wilson, K. C. (1980). Analysis of Slurry Flows with a Free Surface. *Hydrotransport 7* (pp. 123-132). Sendai, Japan: BHRA Fluid Engineering.
Wilson, K. C. (1984). Analysis of Contact Load Distribution and Application to Deposition Limit in Horizontal Pipes. *Journal of Pipelines, Vol. 4.*, 171-176.
Wilson, K. C. (1986). Effect of Solids Concentration on Deposit Velocity. *Journal of Pipelines, Vol. 5.*, 251-257.
Wilson, K. C. (1987). Analysis of Bed Load Motion at High Shear Stress. *Journal of Hydraulic Engineering, Vol. 113.*, 97-103.
Wilson, K. C. (1988). Evaluation of interfacial friction for pipeline transport models. *Hydrotransport 11* (p. B4). BHRA Fluid Engineering.
Wilson, K. C. (1989). Mobile Bed Friction at High Shear Stress. *Journal of Hydraulic Engineering, Vol. 115.*, 825-830.
Wilson, K. C., & Addie, G. R. (1997). Coarse particle pipeline transport: effect of particle degradation on friction. *Powder Technology, Vol. 94.*, 235-238.
Wilson, K. C., & Brown, N. P. (1982). Analysis of Fluid Friction in dense Phase Pipeline Flow. *The Canadian Journal of Chemical Engineering, Vol. 60.*, 83-86.

References.

Wilson, K. C., & Judge, D. G. (1976). New Techniques for the Scale-Up of Pilot Plant Results to Coal Slurry Pipelines. *Proceedings International Symposium on Freight Pipelines.* (pp. 1-29). Washington DC, USA: University of Pensylvania.

Wilson, K. C., & Judge, D. G. (1977). Application of Analytical Model to Stationary Deposit Limit in Sand Water Slurries. *Dredging Technology* (pp. J1 1-12). College Station, Texas, USA.: BHRA Fluid Engineering.

Wilson, K. C., & Judge, D. G. (1978). Analytically based Nomographic Charts for Sand-Water Flow. *Hydrotransport 5* (pp. A1 1-12). Hannover, Germany: BHRA Fluid Engineering.

Wilson, K. C., & Judge, D. G. (1980). New Techniques for the Scale-up of Pilot Plant Results to Coal Slurry Pipelines. *Journal of Powder & Bulk Solids Technology.*, 15-22.

Wilson, K. C., & Nnadi, F. N. (1990). Behavior of Mobile Beds at High Shear Stress. *Proceedings Coastal Engineering 22.*, (pp. 2536-2541). Delft.

Wilson, K. C., & Pugh, F. J. (1988). Dispersive Force Basis for Concentration Profiles. *Journal of Hydraulic Engineering, Vol. 114, No. 7.*, 806-810.

Wilson, K. C., & Pugh, F. J. (1988). Dispersive Force Modelling of Turbulent Suspension in Heterogeneous Slurry Flow. *The Canadian Journal of Chemical Engineering, Vol. 66.*, 721-727.

Wilson, K. C., & Sellgren, A. (2001). *Hydraulic transport of solids, Pump Handbook, pp. 9.321-9.349.* McGraw-Hill.

Wilson, K. C., & Sellgren, A. (2003). Interaction of Particles and Near-Wall Lift in Slurry Pipelines. *Journal of Hydraulic Engineering, Vol. 129.*, 73-76.

Wilson, K. C., & Sellgren, A. (2010). Behavior of intermediate particle slurries in pipelines. *Hydrotransport 18* (pp. 117-128). Rio de Janeiro: BHR Group.

Wilson, K. C., & Sellgren, A. (2012). Revised Method for Calculating Stratification Ratios for Heterogeneous Flows. *14th International Conference on Transport & Sedimentation of Solid Particles.*, (pp. 334-340).

Wilson, K. C., & Watt, W. E. (1974). Influence of Particle Diameter on the Turbulent Support of Solids in Pipeline Flow. *Hydrotransport 3* (pp. D1 1-9). Colorado School of Mines, Colorado, USA.: BHRA Fluid Engineering.

Wilson, K. C., Addie, G. R., & Clift, R. (1992). *Slurry Transport using Centrifugal Pumps.* New York: Elsevier Applied Sciences.

Wilson, K. C., Addie, G. R., Clift, R., & Sellgren, A. (1997). *Slurry Transport using Centrifugal Pumps.* Glasgow, UK.: Chapman & Hall, Blackie Academic & Professional.

Wilson, K. C., Addie, G. R., Sellgren, A., & Clift, R. (2006). *Slurry transport using centrifugal pumps.* New York: Springer Science+Business Media Inc.

Wilson, K. C., Clift, R., & Sellgren, A. (2002). Operating points for pipelines carrying concentrated heterogeneous slurries. *Powder Technology, Vol. 123.*, 19-24.

Wilson, K. C., Clift, R., Addie, G. R., & Maffet, J. (1990). Effect of Broad Particle Grading on Slurry Stratification Ratio and Scale-up. *Powder Technology, 61.*, 165 - 172.

Wilson, K. C., Sanders, R. S., Gillies, R. G., & Shook, C. A. (2010). Verification of the near wall model for slurry flow. *Powder Technology, Vol. 197.*, 247-253.

Wilson, K. C., Sellgren, A., & Addie, G. R. (2000). Near-wall fluid lift of particles in slurry pipelines. *10th Conference on Transport and Sedimentation of Solid Particles.* Wroclav, Poland: T&S10.

Wilson, K. C., Streat, M., & Bantin, R. A. (1972). Slip model correlation of dense two phase flow. *Hydrotransport 2* (pp. B1 1-10). Warwick, UK: BHRA Fluid Engineering.

Wilson, W. E. (1942). Mechanics of flow with non colloidal inert solids. *Transactions ASCE Vol. 107.*, 1576-1594.

Wismer, R., & Luth, H. (1972A). Performance of Plane Soil Cutting Blades. *Transactions of ASEA.*

Wismer, R., & Luth, H. (1972B). Rate effects in soil cutting. *Journal of Terramechanics, vol. 8, no. 3.*, 11-21.

Wood, D. J. (1966). An explicit friction factor relationship. *Civil Engineering, Vol. 36, ASCE.*, 60-61.

Worster, R. C., & Denny, D. F. (1955). Hydraulic transport of solid materials in pipelines. *Institution of Mechanical Engineers (London)*, 563-586.

Wu, W., & Wang, S. (2006). Formulas for sediment porosity and settling velocity. *Journal of Hydraulic Engineering, 132(8)*, 858-862.

Yagi, T. (1970). Sedimentation effects of soil in hopper. *WODCON III* (pp. 1-22). Singapore: WODA.

Yagi, T., Okude, T., Miyazaki, S., & Koreishi, A. (1972). *An Analysis of the Hydraulic Transport of Solids in Horizontal Pipes.* Nagase, Yokosuka, Japan.: Report of the Port & Harbour Research Institute, Vol. 11, No. 3.

Yalin, M. S., & Karahan, E. (1979). Inception of sediment transport. *ASCE Journal of the Hydraulic Division, 105*, 1433–1443.

Yi, Z. (2000). *The FEM calculation of pore water pressure in sand cutting process by SEPRAN.* Delft, Netherlands: Delft University of Technology, Report: 2001.BT.5455.

Yi, Z., & Miedema, S. (2001). Finite Element Calculations To Determine The Pore Pressures When Cutting Water Saturated Sand At Large Cutting Angles. *CEDA Dredging Days* (p. 20 pages). Amsterdam, The Netherlands: CEDA.

Yi, Z., & Miedema, S. (2002). Finite Element Calculations To Determine The Pore Pressures When Cutting Water Saturated Sand At Large Cutting Angles. *CEDA Dredging Days* (p. 20 pages). Amsterdam, The Netherlands: CEDA.

Zandi, I. (1971). Hydraulic transport of bulky materials. In I. Zandi, *Advances in Solid–Liquid Flow in Pipes and its Applications.* (pp. 1-38). Oxford: Pergamon Pres.

Zandi, I., & Govatos, G. (1967). Heterogeneous flow of solids in pipelines. *Proc. ACSE, J. Hydraul. Div.,, 93(HY3).*, 145-159.

Zanke, U. C. (1977). *Berechnung der Sinkgeschwindigkeiten von Sedimenten.* Hannover, Germany: Mitteilungen Des Francius Instituts for Wasserbau, Heft 46, seite 243, Technical University Hannover.

Zanke, U. C. (2001). *Zum Einfluss der Turbulenz auf den Beginn der Sedimentbewegung.* Darmstadt, Germany: Mitteilungen des Instituts fur Wasserbau und Wasserwirtschaft der TU Darmstadt, Heft 120.

Zanke, U. C. (2003). On the influence of turbulence on the initiation of sediment motion. *International Journal of Sediment Research, 18*(1), 17–31.

Zeng, D., & Yao, Y. (1988). Investigation on the relationship between soil metal friction and sliding speed. *2nd Asian Pacific Conference of ISTVS.* Bangkok, Thailand.

Zeng, D., & Yao, Y. (1991). Investigation on the relationship between soil shear strength and shear rate. *Journal of Terramechanics, 28 (1).*

Zijsling, D. (1987). Single cutter testing - a key for PDC bit development (SPE 16529). *Offshore Europe 87.* Aberdeen, Scotland.

Chapter 10: List of Figures.

List of Figures.

Chapter 11: List of Tables.

OE4607 Introduction Dredging Engineering.
MSc Offshore & Dredging Engineering
Delft University of Technology

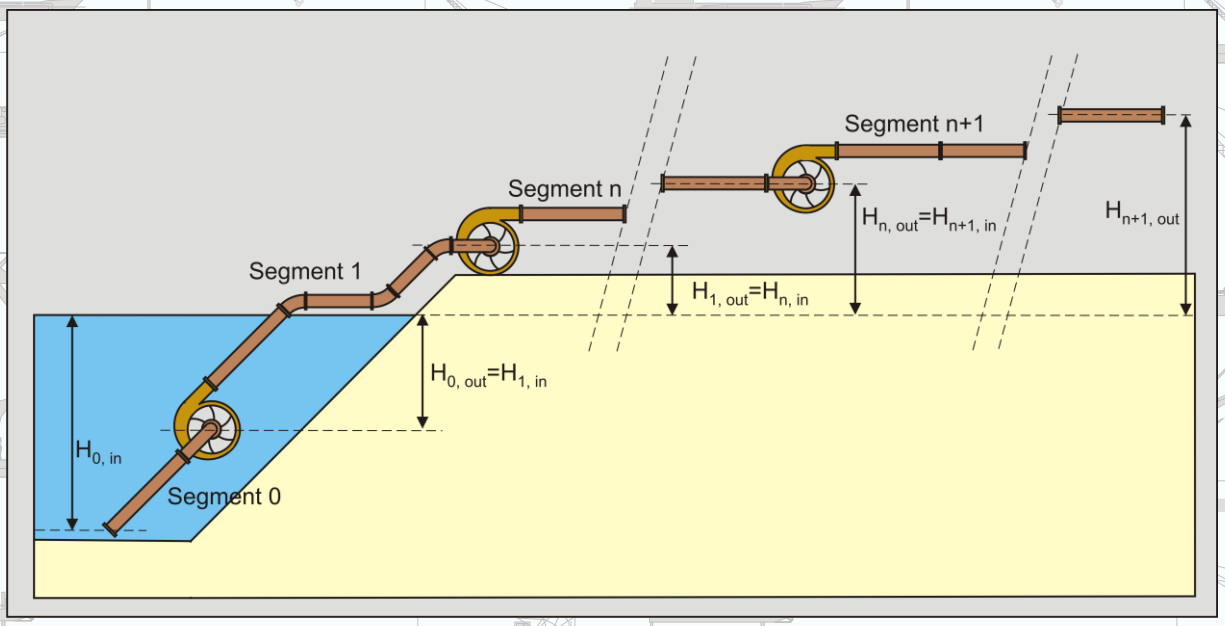

by

Dr.ir. Sape A. Miedema